UNIVERSITY OF FORT HARE

Faculty of Science & Agriculture

Chemistry Department

Preparation and Evaluation of Lignocellulose-Montmorillonite Nanocomposites for the Adsorption of some Heavy Metals and Organic Dyes from Aqueous Solution

By

Tavengwa Bunhu
(Student Number: 200804148)

SUBMITTED TO THE UNIVERSITY OF FORT HARE IN FULFILLMENT OF THE REQUIREMENTS FOR THE DEGREE OF DOCTOR OF PHILOSOPHY IN CHEMISTRY

OCTOBER 2011

Preface

This thesis presents work performed by the author in the Department of Chemistry, University of Fort Hare, King Williams Town Rd, Alice, 5700, from March 2008 to June 2011 under the supervision of Dr L. Tichagwa.

This work is the original work of the author and has not been submitted in part, or in whole, to any other university. Where use has been made of the work of others, it has been duly acknowledged in the text.

Dedications

This work is dedicated to my wife Caroline, my son Tawananyasha Blessed and my daughter Makanakaishe Rejoice.

Acknowledgements

God Almighty sustained and carried me through my studies and I am so grateful.

I would like to thank my supervisor, Dr L. Tichagwa for her invaluable guidance and support throughout my PhD research. My achievements during my PhD research would not have been possible without her excellent guidance and support.

I extend my gratitude to my colleagues for their assistance in various ways: Mr P. Nyamukamba, Mr H. Mungondori, Dr R. Butcher and all departmental staff who were genuinely interested in my work and supportive. The project would not have been successful if it was not for the technical assistance provided by Mr N. C. Manene and Mr M. Nwamadi with the AAS, UV-Vis, FTIR and TGA operation.

I would like to thank my family for their encouragement and support. I owe special thanks to Thandisile Mcako, Pumeza Fata, Anita Mgweje and Ayanda Matu for their assistance.

Abstract

The need to reduce the cost of adsorption technology has led scientists to explore the use of many low cost adsorbents especially those from renewable resources. Lignocellulose and montmorillonite clay have been identified as potentially low cost and efficient adsorbent materials for the removal of toxic heavy metals and organic substances from contaminated water. Montmorillonite clay has good adsorption properties and the potential for ion exchange. Lignocellulose possesses many hydroxyl, carbonyl and phenyl groups and therefore, both montmorillonite and lignocellulose are good candidates for the development of effective and low cost adsorbents in water treatment and purification.

The aim of this study was to prepare composite materials based on lignocellulose and montmorillonite clay and subsequently evaluate their efficacy as adsorbents for heavy metal species and organic pollutants in aqueous solution. It was also important to assess the adsorption properties of the modified individual (uncombined) lignocellulose and montmorillonite.

Lignocellulose and sodium-exchanged montmorillonite (NaMMT) clay were each separately modified with methyl methacrylate (MMA), methacrylic acid (MAA) and methacryloxypropyl trimethoxysilane (MPS) and used as adsorbents for the removal of heavy metals and dyes from aqueous solution. The lignocellulose and NaMMT were modified with MMA, MAA and MPS through free radical graft polymerisation and/or condensation reactions. NaMMT was also modified through Al-pillaring to give AlpMMT. The materials were characterised by fourier transform infrared spectroscopy (FTIR), thermogravimetric analysis (TGA), scanning electron microscopy (SEM) and small angle X-ray scattering (SAXS) and characterisation results showed that the modification of the montmorillonite with MAA, MMA and MPS was successful.

The modified lignocellulose and montmorillonite materials were evaluated for the adsorption of heavy metal ions (Cd^{2+} and Pb^{2+}) from aqueous solution by the batch method. The adsorption isotherms and kinetics of both Cd^{2+} and Pb^{2+} onto the NaMMT clay, AlpMMT and lignocellulose materials are presented. The Langmuir isotherm was found to be the best fit for the adsorption of both heavy metals onto all the adsorbents. AlpMMT showed very poor uptake for heavy metals (both Cd^{2+} and Pb^{2+}). PMMAgMMT, PMAAgMMT, PMAAgLig and PMPSgLig showed improved adsorption for both heavy metals. The mechanism of heavy metal adsorption onto the adsorbents was best represented by the pseudo second-order kinetic model. PMPSgLig, NaMMT and AlpMMT showed relatively high adsorption capacities for methyl orange, while the adsorption of neutral red was comparable for almost all the adsorbents. Neither the Langmuir model nor the Freundlich model was found to

adequately describe the adsorption process of dyes onto all the adsorbents. The pseudo second-order model was found to be the best fit to describe the adsorption mechanism of both dyes onto all the adsorbents. The modification of lignocellulose and montmorillonite with suitable organic groups can potentially produce highly effective and efficient adsorbents for the removal of both heavy metals and dyes from contaminated water.

Novel adsorbent composite materials based on lignocellulose and montmorillonite clay (NaMMT) were also prepared and evaluated for the removal of pollutants (dyes and heavy metals) from aqueous solution. The lignocellulose-montmorillonite composites were prepared by in situ intercalative polymerisation, using methyl methacrylate, methacrylic acid and methacryloxypropyl trimethoxysilane (MPS) as coupling agents. The composite materials were characterised by FTIR, TGA, TEM and SAXS. SAXS diffractograms showed intercalated nanocomposites of PMMAgLig-NaMMT and PMAAgLig-NaMMT, whereas PMPSgLig-NaMMT showed a phase-separated composite and the same results were confirmed by TEM.

The lignocellulose-montmorillonite composites were assessed for their adsorption properties for heavy metal ions (Cd^{2+} and Pb^{2+}) and dyes (methyl orange and neutral red) from aqueous solution. Among these composite materials, only PMAAgLig-NaMMT showed a marked increase in the uptake of both Cd^{2+} and Pb^{2+} relative to lignocellulose and montmorillonite when used independently. The adsorption data were fitted to the Langmuir and Freundlich isotherms, as well as to the pseudo first-order and pseudo second-order kinetic models. The data were best described by the Langmuir isotherm and the pseudo second-order kinetic model.

On the adsorption of dyes, only PMPSgLig-NaMMT showed enhanced adsorption of methyl orange (MetO) compared with lignocellulose and montmorillonite separately. The enhanced adsorption was attributed to the synergistic adsorption due to the presence of MPS, lignocellulose and NaMMT. Competitive adsorption studies were carried out from binary mixtures of MetO and Cd^{2+} or Pb^{2+} in aqueous solution. The adsorption process of MetO onto the composite material was found to follow the Freundlich adsorption model, while the mechanism of adsorption followed both the pseudo first-order and pseudo second-order models. This particular composite can be used for the simultaneous adsorption of both heavy metals and organic dyes from contaminated water. The adsorption of neutral red to the composite materials was comparable and the pseudo second-order kinetic model best described the adsorption mechanism.

List of Abbreviations

NaMMT: Sodium-exchanged montmorillonite

Lig: Lignocellulose

MMA: Methyl methacrylate

MAA: Methacrylic acid

MPS: Methacryloxypropyl trimethoxysilane

DBTDL: Dibutyltin dilaurate

PMMA: Poly (methyl methacrylate)

PMAA: Poly (methacrylic acid)

PMPS: Poly (methacryloxypropyl trimethoxysilane)

PMMAgMMT: Poly (methyl methacrylate) grafted montomorillonite

PMMAgLig: Poly (methyl methacrylate) grafted lignocellulose

PMAAgMMT: Poly (methacrylic acid) grafted montmorillonite

PMAAgLig: Poly (methacrylic acid) grafted lignocellulose

PMPSgMMT: Methacryloxypropyl trimethoxysilane grafted montmorillonite

PMPSgLig: Methacryloxypropyl trimethoxysilane grafted lignocellulose

PMAAgLig-NaMMT: Poly (methacrylic acid) modified lignocellulose-montmorillonite nanocomposite

PMMAgLig-NaMMT: Poly (methyl methacrylate) modified lignocellulose-montmorillonite nanocomposite

PMPSgLig-NaMMT: Methacryloxypropyl trimethoxysilane modified lignocellulose-montmorillonite nanocomposite

Lig-NaMMT: Lignocellulose-montmorillonite nanocomposite without polymer

MetO: Methyl orange

NeuR: Neutral red

FTIR: Fourier-transform infrared spectroscopy

TGA: Thermogravimetric analysis

XRD: X-ray diffraction

TEM: Transmission electron microscopy

SEM: Scanning electron microscopy

UV-Vis: Ultraviolet visible spectroscopy

AAS: Atomic absorption spectroscopy

Table of Contents

Chapter 1

Introduction

1.0 Introduction

Water supports all forms of life on earth. The availability of clean water to the human population is of paramount importance. The United Nations reports that though access to improved drinking water has expanded, nearly one billion people do not have safe drinking water (United Nations MDGs, 2008).

As the world population increases, water consumption also increases. Some observers have estimated that by 2025, more than half of the world population will be facing water-based vulnerability or a water crisis (Kulshreshtha, S. N., 1998; Rijsberman, F. R., 2006). There are several manifestations of the water crisis and these include: ground water overdrafting leading to diminished agricultural returns, regional conflicts over scarce water resources, reduced access to safe drinking water due to pollution of water resources. The shortage of fresh water also impacts negatively on biodiversity including aquatic life.

Water pollution is a major problem in the global context and has even been suggested to be the leading cause of death and disease worldwide (UN-Water, 2010). There are now regulations governing the disposal of industrial waste water in terms of toxic chemicals content. People around the globe are also being urged to use water responsibly for present and future generations, and there is a lot of technological advancement dealing with the recycling of industrial water and/or its treatment before it is discharged into the environment.

1.1 Water pollution

Water pollution has in some cases, been defined as any human-caused contamination of water that reduces its usefulness to humans and other organisms in nature (United States Environmental Protection Agency EPA-905-F-97-011, 1997). Most of the pollution of water supplies comes from anthropogenic sources which include contaminants such as herbicides, pesticides, fertilizers, hazardous industrial chemicals, detergents, pathogens, heavy metals, organic solvents and textile dyes that find their way into water supplies.

The recent oil spills in the Gulf of Mexico (USA) and Yellow River (China) and the 'toxic red sludge flood' in Hungary serve as examples of human-caused water pollution (Tran, M., 2010; Watts, J., 2010; Bryant, B., 2011). Apart from such disasters, industrial waterborne waste presents a major potential hazard to natural water systems. Industrial waste water can contain either organic or inorganic toxic matter, which is released into natural waterways, and consequently find its way into water supplies. Organic matter may cause deoxygenation by promoting microbial growth and inorganic waste may cause eutrophication of water bodies or be directly toxic to the various forms of life in rivers and other aquatic systems.

1.2 Health risks of heavy metals and organic pollutants

Heavy metals such as cadmium (Cd^{2+}) and lead (Pb^{2+}) are some of the most toxic inorganic contaminants found in the environment (Chowdhury, B. A. et al, 1987; Jin, T. et al, 2004). The two heavy metals are released into the aquatic systems from a number of industries such as metal plating, smelting, mining, cadmium-nickel and lead batteries, phosphate fertilizers, paint industries, leather tanning, pigments, textiles and alloy industries as well as from sewage (Kadirvelu, K. et al, 2003; Kobya, M. et al, 2005; Halttunen, T., 2007). Food is the most important source of cadmium among the non-smoking population (Nawrot, T. S. et al, 2010).

Exposure to Cd^{2+} has been associated with renal damage (Järup, L. et al, 2000) and osteoporosis (Kazantzis, G., 2004). Cadmium exposure has also been linked to prostate and renal cancer (Kazantzis, G., 2004; Nawrot, T. et al, 2010). Both Cd^{2+} and Pb^{2+} have been associated with adverse renal and negative bone effects (Alfvén, T. et al, 2002). The permissible limit of Cd^{2+} in drinking water set by the World Health Organisation 2010 guidelines is 3 µg/L.

Lead (Pb^{2+}) accumulation in the body has been reported to disturb processes such as haemoglobin synthesis, renal function and is reported to cause neurological and behavioural disturbances in children (Halttunen, T. 2007). It was reported that even low blood Pb^{2+} concentrations have been associated with cognitive impairment in children as measured by intelligence quotient (IQ) tests (Committee on Environmental Health: Paediatrics, 2005). Increased bone Pb^{2+} concentrations are associated with attentional dysfunction, aggression and delinquency. Children followed from infancy with blood lead (Pb^{2+}) measurements up to adolescence showed that the effects of Pb^{2+} exposure are long lasting if not permanent (Committee on Environmental Health: Paediatrics, 2005). Pb^{2+} is often found in drinking water at concentrations over guidelines set by the World Health Organisation (WHO), 2010 of 10 µg/L. Lead contamination of drinking water often results from the corrosion of

lead-containing plumbing pipes. Cadmium and lead are both found in considerable concentrations as a result of point contamination, e.g. from industry.

Among the organic contaminants, chlorinated organic solvents have been used in industries such as in metal cleaning and degreasing, dry-cleaning, leather tanning, pharmaceuticals, dyes and paints, adhesives, aerosols, lubricants, heat-transfer fluids, plasticizers, cleaning solvents and the manufacture of various chemicals. (Yanga, H. C. et al, 2007). Some chlorinated organic compounds also form during chlorination. Contaminants such as chlorinated organic solvents are known human carcinogens, with a potential for wide reaching impact on public health.

Other pollutants such as organic dyes are also quite common in industry especially the textiles sector (Zhang, G. et al, 2011). Apart from the textiles sector, industries such as food, plastic, rubber, paper, cosmetics, etc. use significant amounts of dyes in their products (Attia, A. A. et al, 2008). Industrial waste water contaminated with dyes is often discharged into natural water ways. Most dyes are claimed to be inert and non-toxic at the concentration of discharge into the environment (Annadurai, G. et al, 2002). However, some food dyes like tartrazine were found to have an adverse effect on the behaviour of young mice (Tanaka, T. et al, 2008), and also inflamed the stomach lining of rats when tartrazine was given in the diet for a prolonged period of time. Mehedi, N. et al, 2009 studied the reproductive behaviour of mice fed on tartrazine diet. The investigators concluded that excessive tartrazine consumption can result in adverse effects on the male reproductive system (Tanaka, T. et al, 2008).

Methyl orange is an azo-dye commonly used in the textile, food, leather, pulp and paper industries. However, it is reported to show some toxicity to plants (Parshetti, G. K. et al, 2010). Therefore, concerns exist regarding the ecological impact of the release of azo-dyes like methyl orange into the environment (Sabnis, R. W. et al, 2010). Neutral red was reported to bind to DNA (Wang, Y. T. et al, 1999; Ni, Y. N. et al, 2007) and such interaction may result in mutations in DNA during replication (Huang, C. Z. et al, 2001; Heli, H. et al, 2004). Dyes also impart colour to water making it aesthetically less pleasant. The presence of dyes in surface water also blocks solar radiation from reaching aquatic organisms, thus negatively affecting the balance of aquatic ecosystems. In addition, the release of dyes into water streams may result in the formation of toxic carcinogenic degradation products (Namasivayam, C. et al, 2006). The removal of organic contaminants, especially dyes from industrial effluent is therefore important.

1.3 Removal of heavy metals from water

A number of techniques are available for the removal of inorganic pollutants (heavy metals) from industrial waste water. The removal of heavy metals from (drinking) water can be achieved through precipitation, flocculation, solvent extraction, ion exchange, reverse osmosis, etc. (Arief, V. C. et al, 2008).

Reverse osmosis, although very effective, is a cost-prohibitive process as the membranes get easily spoiled requiring frequent replacement (Flemming, H. C., 1997). Chemical precipitation methods are not very suitable when pollutants are present in trace amounts and also a large amount of sludge is produced. Ion exchange is expensive. Solvent extraction or electrolytic processes are also used at times but are considered to be cost-effective only for concentrated solutions (Nomanbhay, S. M. et al, 2005).

The process of adsorption has now become one of the preferred methods for the removal of toxic contaminants from water as it has been found to be effective, economical, versatile and relatively simple (Garg, V. K. et al, 2004). Adsorption has the additional advantages of applicability at very low concentrations, suitability for using batch and continuous processes, ease of operation, little sludge generation, possibility of regeneration and reuse of adsorbents and low capital cost (Garg, V. K. et al, 2004). The adsorption process has acquired global importance for reducing the problem of contamination of water and air. The process has become a significant addition to Green Chemistry endeavours.

Activated carbon (granular or powdered) is the traditionally used adsorbent, and has been applied with good success for the removal of both heavy metals and organic pollutants from contaminated water. It has attractive properties such as large surface area, microporosity, and high adsorption capacity (Gürses, A. et al, 2004). However, its use is limited due to high cost in terms of both capital and regeneration. The regeneration of activated carbon for reuse (though highly desirable) is said to result in rapid loss of its adsorption capacity (Garg, V. K. et al, 2004). These and other factors have lent impetus to the continuing search for better, low cost adsorbing materials with the potential for easy regeneration.

1.4 Removal of organic contaminants from water

The problems highlighted above indeed call for appropriate measures to be taken in order to reduce or eliminate the occurrence or presence of biological, organic and inorganic pollutants from existing

water supplies. A number of strategies are in place to remove these biological and toxic chemical pollutants from both industrial waste water and drinking water. The strategy employed depends on the type of contaminant present, whether biological, organic or inorganic.

For some organic solvents, technologies such as solvent-vapour extraction, air sparging, steam flooding, cosolvent/alcohol flooding, surfactant-addition, in situ oxidation, electrical heating, electrokinetics, in-well stripping, etc., can be employed for zone remediation (Keane, M. A., 2003). Incineration is quite widely used for treating or destroying hazardous waste. Novel technologies include organics destruction via advanced oxidation processes (Lampron, K. J. et al, 2001; Yanga, H. C. et al, 2007), biological processes, membrane technology, novel adsorbents and chemical oxidation (Keane, M. A. et al, 2003). Biological oxidation is applicable to biodegradable organics but conversion is very slow in case of chlorinated organics (Lampron, K. J. et al, 2001; Hoong, L. J., 2005). Catalytic treatment under non-oxidising conditions is a promising process whereby hazardous chlorinated organics are converted to reusable products with minimal toxic emissions (Schreier, C. G. et al, 1995; Keane, M. A., 2003). Other options applicable include reverse osmosis, ion exchange, co-precipitation and adsorption on activated carbon (Gopal, K. et al, 2004). Reverse osmosis is able to remove most of the organic pollutants but not in sufficient quantities. Modern dyes are highly stable, thus making conventional physicochemical and biological treatment methods ineffective for their removal. Conventional methods for the removal of dyes from water include coagulation and flocculation, electro-floatation, precipitation, ion exchange, membrane filtration, electrochemical destruction, irradiation, biological (Khehra, M. S. et al, 2005) and ozonation (Garg, V. K. et al, 2004).

Nonetheless, poor performance and/or excessive costs have made these approaches less than satisfactory for the remediation of some of the organic contaminants at many contaminated sites. Chlorinated organics are inherently difficult to combust and the release of toxic chlorinated gases is highly undesirable. Biological processes (though potentially effective) require well controlled growth conditions for the microorganisms and may not always be practical (Schreier, C. G. et al, 1995).

The removal of dissolved contaminants by adsorption onto solid adsorbents is reported to be a more promising technique over others for wastewater treatment on considering initial cost, process design, operation, sludge generation, recyclability of process, etc., (Keane, M. A., 2003; Garg, V. K. et al, 2004).

1.5 Nanotechnology in water treatment

Nanotechnology has found widespread use in areas such as drug research, material chemistry and the environment, information and communication, heavy industry, consumer goods (textiles and cosmetics) and energy. Nanotechnology-based methods for water treatment and purification are an area that is now being widely explored.

Nanotechnology in water treatment includes such techniques as the use of carbon nanotubes as nanofilter membranes (only water molecules can pass along their interior while viruses, bacteria, toxic metal ions and other organic molecules are excluded) (Srivastava, A. et al, 2004; Raval, H. D. et al, 2009). Cyclodextrin nanoporous polymer is reported to be effective in the removal of a range of organic contaminants (Crini, G., 2005; Salipira, K. L. et al, 2007). Nanocatalyst-based technologies such as nanoscale zero-valent iron (Zhang, H, 2006; Tanboonchuy, V. et al, 2010), nanoscale titanium dioxide photocatalyst (Fujishima, A. et al, 2006; Ahn, W. H. et al, 2007), titanium dioxide nanoparticle adsorbent (Baumgardner, A. C., 2005), nanostructured iron oxide adsorbent (Hristovski, K. et al, 2008), as well as magnetic nanoparticles such as magnetoferritin (Dickson, D. P. E. et al, 1997) are also being developed for use in water purification. Most of these techniques are still being developed and for them to be viable in the developing world, they have to be relatively simple and inexpensive to install, operate, and maintain.

Zeolites are used as ion exchange media or adsorbents in cartridges or columns for the removal of metal contaminants including arsenic, lead, copper, zinc, cadmium, nickel and silver. Ceramic filters, though not nanofilters are widely used for water purification throughout the world. The filters are made of clays mixed with sawdust or wheat flour to increase porosity, and have micro-scale pores effective for removing bacteria from water (Clasen, T. F. et al, 2004). Such ceramic filters can be viewed as composites based on clay and lignocellulose. Nanocomposites are being widely investigated in many industries because of their enhanced properties relative to the properties of their constituents when evaluated independently.

1.5.1 Nanocomposites

Nanocomposites are a class of composites that are particle-filled polymers for which at least one dimension of the dispersed particles is in the nanometer scale. Some of these are materials created by introducing nanoparticles into a macroscopic material. Nanoparticles have the advantage of an increased surface area to volume ratio. When brought into a bulky material, nanoparticles can strongly influence the thermal and mechanical properties of the material. Nanocomposites based on nanoclay (montmorillonite) and synthetic polymers have been widely investigated and are reported in the

literature, especially for the development of structural materials where tremendous property improvements have been achieved (Kord, B. et al, 2010). Such properties include mechanical strength, resistance to chemical attack, as well as resistance to thermal degradation (Zhao, Y. et al, 2006).

In water treatment, polymer-clay nanocomposites have been used in the preparation of nanofiltration membranes (Jeong, B. H. et al, 2007) and for adsorption (Khaydarov, R. A. et al, 2010). Nanocomposites based on cyclodextrines and carbon nanotubes have been prepared and assessed in the adsorption of chlorinated organics from water (Salipira, K. L. et al, 2007). They were found to perform better than the conventional material, activated carbon. Poly (pyrrole)-carbon nanotube nanocomposite was assessed for its adsorption properties in the removal of negatively charged anions, like perchlorate from water (Lin, Y. et al, 2006). Montarges, E. et al, 1995 also reported synthesizing a nanocomposite of poly (ethylene oxide)-poly (propylene oxide)-Al_{13}-pillared montmorillonite for possible application in the removal of chlorinated organics from water by adsorption.

The use of synthetic polymers and carbon nanotubes in the preparation of nanocomposites promises to yield highly effective materials for water treatment and purification. However, the high cost involved especially in the synthesis of carbon nanotubes and also the production of petroleum monomers makes it less viable. In addition, the petroleum monomers are not easily biodegradable and therefore will present another environmental challenge. In view of this, it is desirable to explore the use of locally available, renewable and biodegradable materials in the development of nanocomposites for water treatment and purification. This research project seeks to use such materials as lignocellulose from wood and montmorillonite clay for the preparation of low cost nanocomposite adsorbents.

Biomass (lignocellulose) and clays (montmorillonite) are now receiving much attention in the search for low cost, efficient and effective water treatment and purification materials since they are readily and widely available. Lignocellulose as a biopolymer possesses many functional groups which can serve as adsorption sites for the removal of both heavy metals and organic pollutants from water. Clays, especially smectites have been widely investigated as adsorbents for inorganic and organic pollutants from aqueous solution. Of the smectite family of clays, montmorillonite has received much attention owing to its high surface area, high cation exchange capacity, swelling properties in water and its potential for ion-exchange (Ahmaruzzaman, M., 2008). Simple modification of both lignocellulose (Ngah, W. S. W. et al, 2008) and montmorillonite (Bhattacharyya, K. G. et al, 2007) can yield materials with enhanced adsorption properties. Nevertheless, one drawback with the use of montmorillonite directly is the challenge of handling powders of such a small particle size (nano-scale).

Though nanocomposites based on lignocellulose and montmorillonite have been reported before (Zhao, Y. et al, 2006), there is no report in the literature on their use as adsorbents in water purification. Previous works have shown the presence of a synergistic effect in composite materials. An investigation by Ake, C. L. et al, 2001, where a composite material of activated carbon and montmorillonite was assessed for its uptake of Pb^{2+} from aqueous solution, showed enhanced adsorption of Pb^{2+} by the composite compared with the two individual materials. In another study, it was shown that modification of montmorillonite clay with a surfactant followed by aluminium-pillaring gave a material that could adsorb both organic and inorganic contaminants from an aqueous mixture of the two (Jiang, J. Q. et al, 2003). Normally, a combination of two or more of the above highlighted techniques is used to completely remove organic and inorganic pollutants from contaminated water. Therefore, a method or technique where both organic and inorganic pollutants are removed simultaneously would be highly desirable.

1.6 Problem statement

In this study, nanocomposites based on lignocellulose and montmorillonite clay (which are relatively cheap materials) are prepared with the hope of achieving materials with enhanced adsorption properties (through some synergistic adsorbent properties of the individual materials) for use in the simultaneous removal of both organic dyes and heavy metals from aqueous solution. Such nanocomposites can also help circumvent problems associated with the handling of nano-scale montmorillonite clay particles through immobilization on the micron-sized lignocellulose.

1.7 Aims and objectives

The overall aim of this study was to prepare modified lignocellulose, modified montmorillonite and lignocellulose/montmorillonite nanocomposite materials, perform material characterisation and evaluate their efficacy as adsorbents for the removal of heavy metals (Cd^{2+} and Pb^{2+}) and organic pollutants (methyl orange and neutral red) from aqueous solution.

In meeting the above goal, the following specific objectives are to be realised:
- To investigate the modification of both lignocellulose and montmorillonite clay through grafting with polymers (poly (methacrylic acid), poly (methyl methacrylate) and poly (methacryloxypropyl trimethoxysilane)).

- To increase the surface area of montmorillonite through aluminium-pillaring, and hopefully improve the adsorption capacity of the clay.

- To couple the aluminium-pillared montmorillonite with lignocellulose using each of the three polymers highlighted above to form lignocellulose-montmorillonite nanocomposites.

- To evaluate the adsorption properties of the montmorillonite and lignocellulose separately (before/after modification and as nanocomposites) by carrying out batch adsorption experiments using heavy metals (Cd^{2+} and Pb^{2+}) and dyes (methyl orange and neutral red) as model pollutants.

- To determine the adsorption capacity of each adsorbent material by applying some commonly used adsorption isotherms and kinetic models.

- To carry out of competitive adsorption studies of heavy metals mixed together with methyl orange or neutral red on selected adsorbents.

- To assess the recyclability of selected adsorbents by carrying out adsorption-desorption experiments.

1.8 Delineation and delimitations of the study

According to Sun, Y. et al, 2002, the purpose of lignocellulose pre-treatment is to remove lignin and hemicellulose, reduce cellulose crystallinity and increase the porosity of materials. The investigators observed that the removal of lignin and hemicellulose is necessary for ethanol production from lignocellulosic material. The removal of lignin and hemicellulose might reduce the number of adsorption sites, and consequently reduce the adsorption capacity of the resultant material. Therefore, in this study, lignocellulose refers to plane tree leaf biomass that has been ground, soxhlet extracted using an ethanol:water solvent mixture and dried appropriately to a free flowing powder of particle size of ≤300 μm. The soxhlet extraction with an ethanol:water solvent mixture was viewed as a gentle pre-treatment method that would remove water soluble organic compounds, increase the porosity of lignocellulose but leave the lignin, hemicellulose and cellulose undisturbed.

Aluminium-pillaring of sodium-exchanged montmorillonite (NaMMT) clay was carried out in order to increase the surface area of the clay, and hopefully the adsorption capacity (Manohar, D. M. et al, 2006). The aluminium-pillared montmorillonite (AlpMMT) clay was intended for use in the preparation of lignocellulose-montmorillonite nanocomposites. However, due to the poor uptake of heavy metals onto the AlpMMT, the nanocomposites were prepared using NaMMT instead.

1.9 Outline of thesis

This thesis has three main sections and consists of a total of eight chapters. The first section is made up of Chapters 1 and 2 which deal with the introduction and literature review. Chapter 1 contains a general introduction to the thesis. The aims and objectives of this study are also presented including the outline of the thesis. Chapter 2 is the literature review on the chemistry of lignocellulose and montmorillonite clay, previous work on their use as adsorbents and the different modifications carried out on the two materials. The nanocomposites of the two materials and their preparation are also presented.

The second section consists of Chapters 3, 4 and 5 which present the experimental work carried out to achieve the objectives of this thesis. This section focuses on the preparation of the adsorbent materials. Chapter 3 presents the details of the chemical reagents used in this study as well as the pre-treatment of lignocellulose and montmorillonite clay. A general description of the syntheses and characterisation techniques are also presented. The characterisation techniques are presented at the end of the Chapter 3. The detailed procedure followed in the aluminium-pillaring of the montmorillonite clay is presented in Chapter 4 including the variation of different parameters during the pillaring process. The second part of the chapter presents the results from the characterisation of the different aluminium-pillared montmorillonite clay samples prepared. Chapter 5 covers the procedures used for the grafting of the three different organic polymers onto lignocellulose and onto montmorillonite clay. The grafting of the separate materials (lignocellulose and montmorillonite) was followed by the preparation of lignocellulose-montmorillonite nanocomposites. The grafted materials and the nanocomposites were characterised using different techniques. Also included are the results obtained from the characterisation of the polymer-grafted materials and the nanocomposites.

The third section of the thesis consists of Chapters 6 and 7 which cover the evaluation of the prepared adsorbents for their adsorption of heavy metals and dyes from aqueous solution. The procedures for the adsorption of heavy metals are reported in Chapter 6 while data (isotherms and kinetics) from the adsorption experiments and the discussion are presented at the end of the chapter. Chapter 7 presents the adsorption of methyl orange and neutral red onto the different adsorbent materials. This also includes the results and discussion of the adsorption isotherms and kinetics. The adsorption results are discussed in relation to the modification performed on each material.

Chapter 8 gives a general conclusion of the research and recommendations for future work.

1.10 References

1. Ahmaruzzaman, M. Adsorption of phenolic compounds on low-cost adsorbents: A review. *Advances in Colloid and Interface Science*, **2008**, *143*, 48–67.

2. Ahn, W. Y.; Sheeley, S. A.; Rajh, T.; Cropek, D. M. Photocatalytic reduction of 4-nitrophenol with arginine-modified titanium dioxide nanoparticles. *Applied Catalysis B: Environmental*, **2007**, *74*, 103–110.

3. Ake, C. L.; Mayura, K.; Huebner, H. J.; Bratton, G. R.; Phillips, T. D. Development of clay-based composites for the sorption of lead from water. *Journal of Toxicology and Environmental Health Part A*, **2001**, *63*, 459–475.

4. Alfvén, T.; Järup, L.; Elinder, C. G. Cadmium and lead in blood in relation to low bone mineral density and tubular proteinuria. *Environmental Health Perspectives*, **2002**, *110* (7), 699-702.

5. Annadurai, G.; Juang, R. S.; Lee, D. J. Use of cellulose-based wastes for adsorption of dyes from aqueous solutions. *Journal of Hazardous Materials*, **2002**, *B92*, 263–274.

6. Arief, V. O.; Trilestari, K.; Sunarso, J.; Indraswati, N.; Ismadji, S. Recent progress on biosorption of heavy metals from liquids using low cost biosorbents: Characterization, biosorption parameters and mechanism studies. *Clean*, **2008**, *36* (12), 937 – 962.

7. Attia, A. A.; Girgis, B. S.; Fathy, N. A. Removal of methylene blue by carbons derived from peach stones by H_3PO_4 activation: Batch and column studies. *Dyes and Pigments*, **2008**, *76*, 282-289.

8. Baumgardner, A. C. Arsenic removal using titanium dioxide agglomerated nanoparticle adsorbents. *M.Sc. Dissertation, Arizona State University*, **2005**.

9. Bhattacharyya, K. G.; Gupta, S. S. Influence of acid activation of kaolinite and montmorillonite on adsorptive removal of Cd(II) from water. *Industrial & Engineering Chemistry Research*, **2007**, *46,* 3734-3742.

10. Bryant, B. Deepwater Horizon and the Gulf oil spill - the key questions answered. http://www.guardian.co.uk/environment/2011/apr/20/deepwater-horizon-key-questions-answered (Accessed - 12/09/2011).

11. Chowdhury, B. A.; Chandra, R. K. Biological and health implications of toxic heavy metals. *Progress in Food & Nutritional Science*, **1987**, *11* (1), 55-113.

12. Clasen, T. F.; Brown, J.; Collin, S.; Suntura, O.; Cairncross, S. Reducing diarrhea through the use of household-based ceramic water filters: a randomized, controlled trial in rural Bolivia. *American Journal of Tropical Medicine and Hygiene*, **2004**, *70* (6), 651–657.

13. Committee on Environmental Health. Lead exposure in children: prevention, detection, and management. *Paediatrics*, **2005**, *116*, 1036-1046.

14. Crini, G. Recent developments in polysaccharide-based materials used as adsorbents in wastewater treatment. *Progress in Polymer Science*, **2005**, *30*, 38–70.

15. Dickson, D. P. E.; Walton, S. A. Properties of magnetoferritin: a novel biomagnetic nanoparticle. *NanoStructured Materials*, **1997**, *9*, 595-598.

16. Flemming, H. C. Reverse osmosis membrane biofouling. *Experimental Thermal and Fluid Science*, **1997**; *14*, 382-391

17. Fujishima, A.; Rao, T. N.; Tryk, D. A. Titanium dioxide photocatalysis. *Journal of Photochemistry and Photobiology C: Photochemistry Reviews*, **2000**, *1*, 1–21.

18. Garg, V. K.; Kumar, R.; Gupta, R. Removal of malachite green dye from aqueous solution by adsorption using agro-industry waste: a case study of *Prosopis cineraria*. *Dyes and Pigments*, **2004**, *62*, 1–10.

19. Gopal, K.; Srivastava, S. B.; Shukla, S.; Bersillon, J. L. Contaminants in drinking water and its mitigation using suitable adsorbents: an overview. *Journal of Environmental Biology*, **2004**, *25*, 469–475.

20. Gürses, A.; Karaca, S.; Dŏgar Ç.; R. Bayrak; M. Açıkyıldız; M. Yalçın. Determination of adsorptive properties of clay/water system: methylene blue sorption. *Journal of Colloid and Interface Science*, **2004**, *269*, 310–314.

21. Halttunen, T. Removal of cadmium, lead and arsenic from water by lactic acid bacteria. *Functional Foods Forum, Department of Biochemistry and Food Chemistry, University of Turku*. **2007**.

22. Heli, H.; Bathaie, S. Z.; Mousavi, M. F. Electrochemical investigation of neutral red binding to DNA at the surface. *Electrochemistry Communications*, **2004**, *6*, 1114–1118.

23. Hoong, L. J. Degradation of 2-chlorophenol in water using advanced oxidation processes. *M. Sc. Dissertation, University Putra Malaysia*, **2005**.

24. Hristovski, K.; Westerhoff, P.; Möller, T.; Sylvester, P.; Condit, W.; Mash, H. Simultaneous removal of perchlorate and arsenate by ion-exchange media modified with nanostructured iron hydroxide. *Journal of Hazardous Materials*, **2008**, *152* (1), 397-406.

25. Huang, C. Z.; Li, Y. F.; Feng, P. A spectrophotometric study on the interaction of neutral red with double-stranded DNA in large excess. *Talanta*, **2001**, *55*, 321–328.

26. Järup, L.; Hellström, L.; Alfvén, T.; Carlsson, M. D.; Grubb, A.; Persson, B.; Pettersson, C.; Spång, G.; Schütz, A.; Elinder, C. G. Low level exposure to cadmium and early kidney damage: the OSCAR study. *Occupational & Environmental Medicine*, 2000, *57*, 668-672.

27. Jeong, B. H.; Hoek, E. M. V.; Yan, Y.; Subramani, A.; Huang, X.; Hurwitz, G.; Ghosh, A. K.; Jawor, J. Interfacial polymerization of thin film nanocomposites: A new concept for reverse osmosis membranes. *Journal of Membrane Science*, **2007**, *294*, 1–7.

28. Jiang, J. Q.; Zeng, Z. Comparison of modified montmorillonite adsorbents Part II: The effects of the type of raw clays and modification conditions on the adsorption performance. *Chemosphere*, **2003**, *53*, 53–62.

29. Jin, T.; Nordberg, G.; Ye, T.; Bo, M.; Wang, H.; Zhu, G.; Kong, Q.; Bernard, A. Osteoporosis and renal dysfunction in a general population exposed to cadmium in China. *Environmental Research*, **2004**, *96*, 353–359.

30. Kadirvelu, K.; Namasivayam, C. Activated carbon from coconut coirpith as metal adsorbent: adsorption of Cd (II) from aqueous solution. *Advances in Environmental Research*, **2003**, *7*, 471–478.

31. Kazantzis, G. Cadmium, osteoporosis and calcium metabolism. *Biometals*, **2004**, *17*, 493–498.

32. Keane, M. A. Advances in greener separation processes – case study: recovery of chlorinated aromatic compounds. *Green Chemistry*, **2003**, *5*, 309–317.

33. Khaydarov, R. A.; Khaydarov, R. R.; Gapurova, O. Water purification from metal ions using carbon nanoparticle-conjugated polymer nanocomposites. *Water Research*, **2010**, *44*, 1927 – 1933.

34. Khehra, M. S.; Saini, H. S.; Sharma, D. K.; Chadhaa, B. S.; Chimni, S. S. Decolorization of various azo dyes by bacterial consortium. *Dyes and Pigments*, **2005**, *67*, 55-61.

35. Kobya, M.; Demirbas, E.; Senturk, E.; Ince, M. Adsorption of heavy metal ions from aqueous solutions by activated carbon prepared from apricot stone. *Bioresource Technology*, **2005**, *96*, 1518–1521.

36. Kord, В.; Hemmasi, A. H.; Ghasemi, I. Properties of PP/wood flour/organomodified montmorillonite nanocomposites. *Wood Science Technology,* DOI 10.1007/s00226-010-0309-7.

37. Kulshreshtha, S. N. "A Global Outlook for Water Resources to the Year 2025". *Water Resources Management*, **1998**, *12* (3), 167–184. (doi:10.1023/A:1007957229865).

38. Lampron, K. J.; Chiu, P. C.; Cha, D. K. Reductive dehalogenation of chlorinated ethenes with elemental iron: the role of microorganisms. *Water Research*, **2001**, *35* (13), 3077–3084.

39. Lin, Y.; Cui, X.; Bontha, J. Electrically controlled anion exchange based on polypyrrole and carbon nanotubes nanocomposite for perchlorate removal. *Environmental Science Technology*, **2006**, *40* (12), 4004-4009.

40. Manohar, D. M.; Noeline, B. F.; Anirudhan, T. S. Adsorption performance of Al-pillared bentonite clay for the removal of cobalt(II) from aqueous phase. *Applied Clay Science*, **2006**, *31*, 194-206.

41. Mehedi, N.; Ainad-Tabet, S.; Mokrane, N.; Addou, S.; Zaoui, C.; Kheroua, O.; Saidi, D. Reproductive toxicology of tartrazine (FD and C Yellow No. 5) in Swiss albino mice. *American Journal of Pharmacology and Toxicology*, **2009**, *4* (4), 130-135.

42. Montarges, E.; Michot, L. J.; Lhote, F.; Fabien, T.; Villieras, F. Intercalation of A1$_{13}$-polyethyleneoxide complexes into montmorillonite clay. *Clays and Clay Minerals,* **1995**, *43* (4), 417-426.

43. Namasivayam, C.; Sangeetha, D. Recycling of agricultural solid waste, coir pith: Removal of anions, heavy metals, organics and dyes from water by adsorption onto ZnCl2 activated coir pith carbon. *Journal of Hazardous Materials*, **2006**, *B135*, 449–452.

44. Nawrot; T. S.; Staessen, J. A.; Roels, H. A.; Munters, E.; Cuypers, A.; Richart, T.; Ruttens, A.; Smeets, K.; Clijsters, H.; Vangronsveld, J. Cadmium exposure in the population: from health risks to strategies of prevention. *Biometals*, **2010**, *23*, 769–782.

45. Ngah, W. S. W.; Hanafiah, M. A. K. M. Removal of heavy metal ions from wastewater by chemically modified plant wastes as adsorbents: A review. *Bioresource Technology;* **2008**; *99*; 3935–3948.

46. Ni, Y. N.; Zhong, X. Z. Investigation of the interaction of DNA and neutral red by fluorescence spectroscopic analysis. *Chinese Chemical Letters*, **2007**, *18* (5), 569-572.

47. Nomanbhay, S. M.; Palanisamy, K. Removal of heavy metal from industrial wastewater using chitosan coated oil palm shell charcoal. *Electronic Journal of Biotechnology*, **2005**, *8* (1), 43-53.

48. Parshetti, G. K.; Telke, A. A.; Kalyani, D. C.; Govindwar, S. P. Decolorization and detoxification of sulfonated azo dye methyl orange by *Kocuria rosea* MTCC 1532. *Journal of Hazardous Materials*, **2010**, *176*, 503–509.

49. Raval, H. D.; Gohil J. M. Carbon nanotube membrane for water desalination. : *International Journal of Nuclear Desalination*, **2009**, *3* (4), 360 - 368.

50. Rijsberman, F. R. Water scarcity: Fact or fiction? Agricultural Water Management, **2006**, *80*, 5–22.

51. Sabnis, R. W. Handbook of Biological Dyes and Stains: Synthesis and Industrial Applications. John Wiley and Sons, **2010**, 116-117.

52. Salipira, K. L.; Mamba, B. B.; Krause. R. W.; Malefetse, T. J.; Durbach, S. H. Carbon nanotubes and cyclodextrin polymers for removing organic pollutants from water. *Environmental Chemistry Letters*, **2007**, *5*, 13–17.

53. Schreier, C. G.; Reinard, M. Catalytic hydrodehalogenation of chlorinated ethylenes using palladium and hydrogen for the treatment of contaminated water. *Chemosphere*, **1995**, *35*, 3475-3487.

54. Srivastava, A.; Srivastava, O. N.; Talapatra, S.; Vajtai, R.; Ajayan, P. M. Carbon nanotube filters. *Nature Materials*, **2004**, *3*, 610 – 614.

55. Sun, Y.; Cheng, J. Hydrolysis of lignocellulosic materials for ethanol production: a review. *Bioresource Technology*, **2002**, *83*, 1-11.

56. Tanaka, T.; Takahashi, O.; Oishi, S, Akio Ogata. Effects of tartrazine on exploratory behavior in a three-generation toxicity study in mice. *Reproductive Toxicology*, **2008**, *26*, 156–163.

57. Tanboonchuy, V.; Hsu, J. C.; Grisdanurak, N.; Liao, C. H. Arsenate removal by nano zero-valent iron in the gas bubbling system. *World Academy of Science, Engineering and Technology*, **2010**, *65*, 263-265.

58. The Millennium Development Goals Report **2008**, United Nations, *http://www.un.org/millenniumgoals/pdf/The%20Millennium%20Development%20Goals%20 Report%202008.pdf* (Accessed – 10/10/2009).

59. Tran, M. Hungary toxic sludge heading towards the Danube. http://www.guardian.co.uk/world/2010/oct/06/toxic-sludge-hungary-danube? INTCMP=ILCNETTXT3487, **2010** (Accessed - 12/09/2011).

60. United States Environmental Protection Agency EPA-905-F-97-011, August 1997

61. UN-Water. UN-Water statement on water quality. *www.unwater.org*, **2010**, (Accessed - 06/10/2011).

62. Wang, Y. T.; Zhao, F. L.; Li, K. A.; Tong, S. T. Molecular spectroscopic study of DNA binding with neutral red and application to assay of nucleic acids. *Analytica Chimica Acta*, **1999**, *396*, 75–81.

63. Watts, J. Chinese environment officials fail to stop oil slick from polluting Yellow river. http://www.guardian.co.uk/environment/2010/jan/04/oil-spill-china-yellow-river (Accessed - 12-09-2011).

64. WHO Guidelines, Cadmium in drinking-water. WHO/SDE/WSH/03.04/80/Rev/1, 2010, http://www.who.int/water_sanitation_health/dwq/chemicals/cadmium.pdf (Accessed - 13/09/2011).

65. WHO Guidelines, Lead in drinking-water. WHO/SDE/WSH/03.04/09/Rev/1, 2010, http://www.who.int/water_sanitation_health/dwq/chemicals/lead.pdf (Accessed - 13/09/2011).

66. Yanga,H. C.; Choa, Y. J.; Eunb, H. C.; Kima, E. H. Destruction of chlorinated organic solvents in a two-stage molten salt oxidation reactor system. *Chemical Engineering Science*, **2007**, *62*, 5137 – 5143.

67. Zhang, G.; Li, X.; Li, Y.; Wu, T.; Sun, D.; Lu, F. Removal of anionic dyes from aqueous solution by leaching solutions of white mud. *Desalination*, **2011**, *274* (1-3), 255–261.

68. Zhang, H.; Jin, Z.; Han L.; Qin, C. Synthesis of nanoscale zero-valent iron supported on exfoliated graphite for removal of nitrate. *Transactions of Nonferrous Metals Society of China*, **2006**, *16*, 345-349.

69. Zhao, Y.; Wang, K.; Zhu, F.; Xue, P.; Jia, M. Properties of poly(vinyl chloride)/wood flour/montmorillonite composites: Effects of coupling agents and layered silicate. *Polymer Degradation and Stability*, **2006**, *91*, 2874-2883.

Chapter 2

Literature Review

2.0 Introduction

The supply of clean water to the human population is of high importance. Many water treatment methods are currently available for the removal of biological (pathogens), organic and inorganic pollutants. Waste water is normally treated by: chemical precipitation (USEPA, 2000), evaporation, reverse osmosis, electrodialysis, phytoextraction and ultrafiltration (Li, Y. H. et al, 2003; Sprynskyy, M. et al, 2006; Mobasherpour, I. et al, 2011). These technologies are generally practical and applicable only to concentrated wastewaters but are ineffective when applied to lowly concentrated wastewaters such as those with heavy metal ion concentrations less than 100 ppm (Muhammad, N. et al, 1998; Pavasant, P. et al, 2006).

Waste waters contaminated with organic pollutants like chlorophenols and dyes can be treated through advanced oxidation technology, electrochemical methods, microbiological decomposition, ozonation, coagulation and membrane filtration (Lata, H. et al, 2008; Lin, J. X. et al, 2008; Zhang, G. et al, 2011). Removal of pollutants by adsorbents is a method which has been reported to be simple (in terms of operation), cost-effective and efficient for the removal of both organic and inorganic pollutants from contaminated waters (Nigam, P. et al, 1996; Robinson, T. et al, 2001; Annadurai, G. et al, 2002).

2.1 Adsorption technology in water treatment

Adsorption has gained importance in water purification. Amongst all the water treatment methods proposed, using adsorbents is one of the most popular. With a proper design of the adsorption process, high-quality treated effluents can be produced (Crini, G., 2005). It is recognized as an effective, efficient and economic method for water decontamination applications and for separation.

Adsorption is an equilibrium separation process which is an established technology in waste water treatment. Adsorption is defined as the transfer or preferential accumulation of certain components (solute) of a fluid phase to the surface of a solid adsorbent. Figure 2.1 shows the accumulation of a solute onto the surface of a solid adsorbent during the process of adsorption.
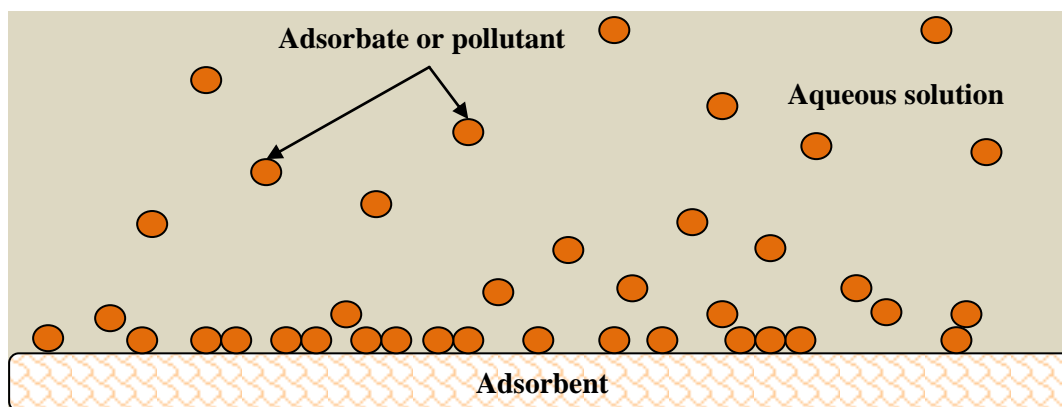
Figure 2.1: Schematic showing the process of adsorption of solute onto a solid adsorbent.

The accumulation of the adsorbate on the solid surface is due to a number of interactions with the chemical groups on the surface of the adsorbent. Such interactions vary from one adsorbent to another and will also depend on the pH of the medium, the salt concentration and the presence of ligands in the medium. Some of the reported interactions include: ion-exchange, complexation, coordination/chelation, electrostatic interactions, acid-base interactions, hydrogen bonding, hydrophobic interactions, physical adsorption and precipitation (Crini, G., 2005). The decontamination of polluted waters through adsorption can be achieved through one or a combination of two or more of these interactions.

The biggest barrier to the application of this process by industry is the high cost of adsorbent materials currently available for commercial use. The cost of adsorption technology can be reduced if the adsorbent is available at a low cost. As a result, numerous low-cost alternative adsorbents have been proposed and these include agricultural lignocellulosic waste, zeolites, flyash and clay minerals.

2.2 Types of adsorbents used in water treatment

There are generally three broad classes of adsorbents and these include organic, biological and mineral adsorbents. Organic adsorbents include polymeric materials such as polysaccharides. Of great interest in this category are the cyclodextrin polymers, chitosan and starch. Cyclodextrins possess a nanoporous structure. The mineral adsorbents are those adsorbents derived from mineral deposits like activated carbon (from coal), zeolites and clay. Crini, G., 2005 listed some of the types of adsorbents used in water treatment and these included: activated carbon, zeolites, polymeric materials, clays and lignocellulosic adsorbents. Dabrowski, A., 2001 classified activated carbon (together with molecular carbon sieves, mesocarbon microbeads, fullerenes, carbonaceous nanomaterials, etc.) under carbon adsorbents. There are also other types such as polymer-nanoclay nanocomposite (Montarges, E. et al, 1998), carbon nanotubes (Li, Y. H. et al, 2003), poly (pyrrole)-carbon nanotube nanocomposite (Lin,

18

Y. et al, 2006), cyclodextrin-carbon and nanotube nanocomposite (Salipira, K. L. et al, 2007) adsorbents.

The following section describes the use of biological materials as adsorbents for both organic and inorganic pollutants from aqueous solution.

2.3 Biological adsorbents in water treatment

Biological adsorbent materials include bacterial or fungi biomass, agricultural waste biomass and wood biomass. There are many reports in the literature on the use of bacteria and fungi biomass for the removal of a wide range of pollutants from contaminated water. Such studies include the work by Yu, J. et al, 2007 in which they assessed the adsorption of Pb^{2+} and Cd^{2+} onto cystine-modified yeast biomass. They reported adsorption capacities of 192 and 65 mg/g for Pb^{2+} and Cd^{2+}, respectively. Denizli, A. et al, 2005 studied the adsorption of chlorophenols onto dead and dried fungus (*Pleurotus sajor caju*) biomass. The investigators reported adsorption capacities of 89.40 (phenol), 159.5 (*o*-chlorophenol), 189.0 (*p*-chlorophenol) and 373.2 mg/g (2,4,6-trichlorophenol). Bell, J. P. et al, 1987 reported the adsorption of pesticides (lindane, diazinon, malathion, 2-chlorobiphenyl and pentachlorophenol) onto *Rhizopus arrhizas* (fungi) biomass. Antizar-Ladislao, B. et al, 2004 used bacteria biomass for the biosorption of chlorophenols from aqueous solution. Halttunen, T. et al, 2007 used lactic acid bacteria biomass for the adsorption of Pb^{2+} from aqueous solution and reported an adsorption capacity of 176 mg/g. There are many other studies performed using microbial biomass for the removal of both organic and inorganic pollutants from water through adsorption (Tobin, J. M. et al, 1984; Li, Z. et al, 2006; Tong, M. et al, 2007; Yu, J. et al, 2007). Wilke, A. et al, 2006 reported the adsorption of heavy metals (Zn, Pb, Ni and Cd) onto thirty strains of algae.

The use of bacteria and fungi biomass for adsorption purposes is attractive and very promising judging from the relatively high adsorption capacities reported. However, the need for special media and attention in the culturing of these microbes adds to the total cost of the biosorbent, and it means that the adsorbent may not be readily available. Agricultural waste, wood and tree leaves biomass (also referred to as lignocellulose) have attracted greater attention because of their wide availability, low cost and the fact that there is no need for special growth media as with bacteria and fungi. Lignocellulosic biomass can also be easily harvested and used for adsorption purposes with simple modification. Section 2.4 below looks at the chemistry of lignocellulosic material as well as its application as an adsorbent for the removal of diverse pollutants from aqueous solution.

2.4 Lignocellulose

Lignocellulose is one of the most abundant materials in the world. As mentioned in Section 2.3, its source ranges from trees to agricultural residues. It has been traditionally used as firewood, building material and animal food. Presently, the exploitation of lignocellulose has increased especially in the pulp and paper industry, chemical industry, as well as the thermal power industry (biofuel). The following section deals with the chemical composition of lignocellulose in more detail.

2.4.1 Chemical composition of lignocellulose

Lignocellulosic material refers to plant biomass that is chemically composed of cellulose, hemicellulose and lignin (Howard, R. L. et al, 2003). Displayed in Figure 2.2 is the general structure of lignocellulose. Lignocellulose has many hydroxyl and carbonyl groups which are expected to interact with polyphenols, dyes or heavy metal ions by hydrogen bonding, hydrophobic interaction or complexation (FitzPatrick, M. et al, 2010).

Cellulose polymer chains are arranged into highly ordered and tightly packed cellulose fibrils by hydrogen bonds between adjacent cellulose chains. The fibrils are linked together by hemicellulose (amorphous polymers of different sugars) as well as other polymers like pectin (Taherzadeh, M. J. et al, 2008). The fibrils are covered by lignin which acts as the adhesive or glue keeping the cellulose fibrils together. The fibrils associate into a cellulose bundle or macrofibril (Figure 2.2).
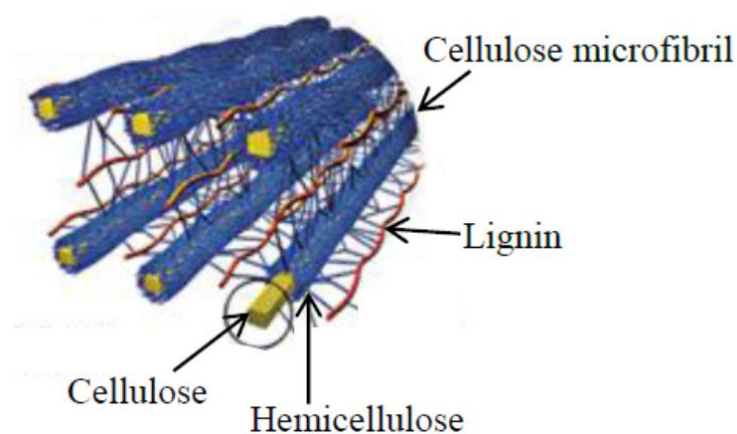
Figure 2.2: Structure of lignocellulose (Ritter, S. K., 2008).

The chemical components of lignocellulose can be classified into four major categories. These are cellulose, hemicelluloses, lignin and extractives. Cellulose, lignin and hemicelluloses comprise the largest percentage by mass while extractives account for just a small percentage. Lignocellulosic

material can be used as an adsorbent with minimal treatment or can be modified accordingly for the removal of different pollutants. Such pollutants can be organic, inorganic and microbial contaminants. The following section looks at the chemical structure of lignin in more detail.

2.4.1.1 Lignin

Lignin is a random copolymer of phenyl-propane units which serves as the matrix or glue of cellulose and hemicellulose (Howard, R. L. et al, 2003). Figure 2.3 displays the chemical structure of lignin. It can be seen from the structure that lignin possesses many functional groups which can serve as adsorption sites for the uptake of both organic and inorganic contaminants from water. Such groups include phenyl, carbonyl and hydroxyl groups.
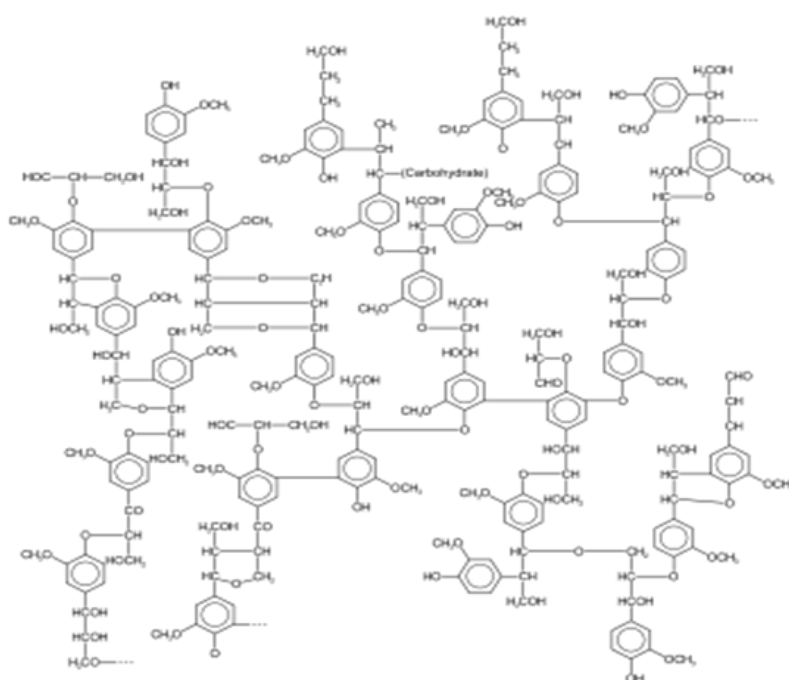
Figure 2.3: Structure of lignin (Kirk, T. K. et al, 1987).

The exposed oxygen centres are expected to interact with heavy metals, while the phenolic groups can interact with benzenes, chlorophenol and azo dyes. These functional groups make lignin an attractive adsorbent for water treatment. Lignin constitutes about 20 - 30% of the total plant weight. The following section discusses the structure of cellulose.

2.4.1.2 Cellulose

Cellulose is a linear polymer of glucose linked via α-1,4-glycosidic linkages and is usually arranged in microcrystalline structures and is very difficult to dissolve or hydrolyse under ordinary conditions. Figure 2.4 shows the chemical structure of cellulose. The cellulose content in wood varies between 40 – 50% depending on the species.

21
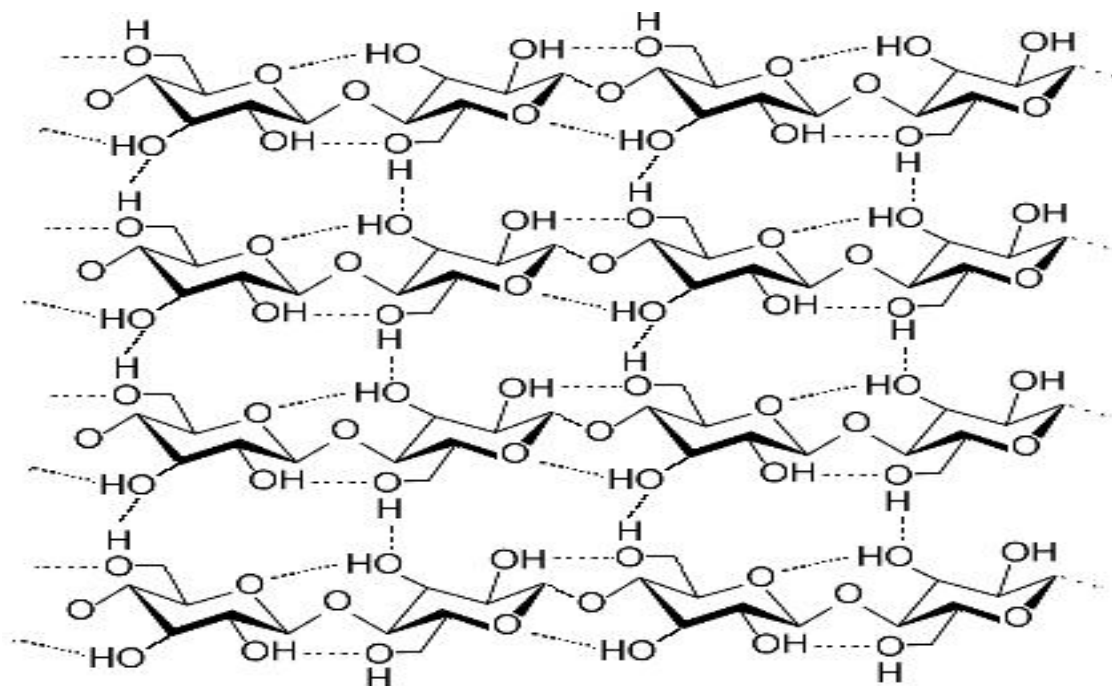
Figure 2.4: Chemical structure of cellulose (http://www.doitpoms.ac.uk/tlplib/wood/structure).

The OH groups in a cellulose chain can form intramolecular and intermolecular hydrogen bonding within the chain and between adjacent chains, respectively. The chains are arranged in a parallel fashion into bundles, which form microfibrils and these are oriented in the cell wall structure (Taherzadeh, M. J. et al, 2008). Again, the presence of the oxygen atoms in the cellulose structure provides adsorption sites for heavy metals, while the alkyl groups are expected to act as adsorption sites for organic pollutants. The last major component of lignocellulose is hemicellulose and this is described in the next section.

2.4.1.3 Hemicellulose

Hemicellulose is a branched copolymer of C5 sugars (xylose, arabinose) and C6 sugars (mannose, galactose, glucuronic acid). Polymer chains of hemicellulose are short and amorphous, making them partially soluble or swellable in water. Hemicellulose has similar chemical or functional groups as cellulose. Figure 2.5 displays some of the chemical structures of the monomer units found in hemicellulose.
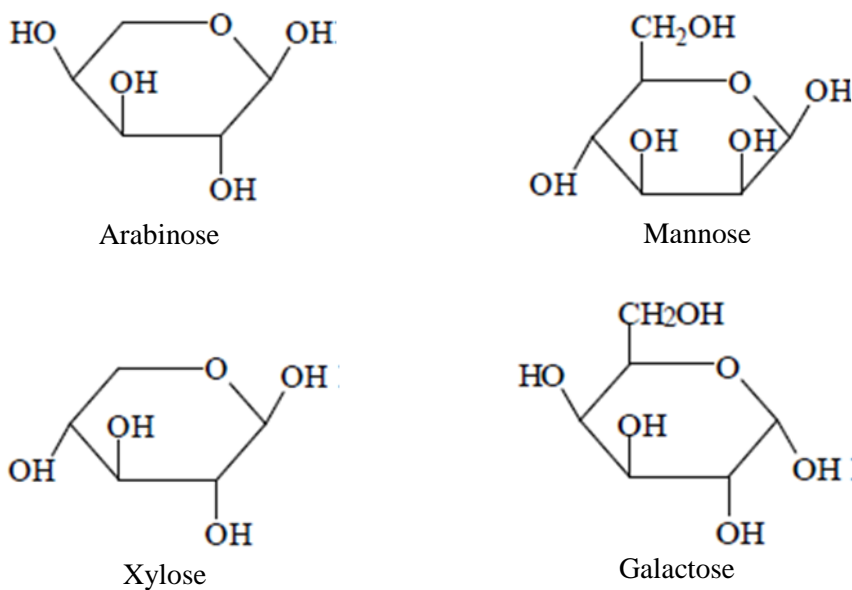
Figure 2.5: Chemical structures of some of the monomer units of hemicellulose (Laine, C., 2005).

2.4.2 Application of lignocellulosic materials as adsorbents

Lignocellulosic materials have been widely applied as adsorbents for both organic and inorganic contaminants (Jiang, J. Q. et al, 2003; Izadyar, S. et al, 2007). This is due to their potentially high adsorption capacities, as well as low cost. Plant waste is inexpensive as it has little or no economic value.

Arief, V. O. et al, 2008 reviewed the characterization of biosorbents, the biosorption parameters, as well as the studies on the adsorption mechanism. The review was more focused on the adsorption of heavy metals onto different biomass-based adsorbents. The authors highlighted that the most important groups involved in heavy metal adsorption in *Mangrove* leaves include -OH, NH_2, C=C, C=O, NO_2 and C-O, as determined by FTIR. For other types of biomass like *Arundo donax* and *Prosopis ruscofilia* wood sawdust, the main functional groups were C-OH, C-C, - OH and C-O. It can be said that the types of functional groups may vary depending on the type of biomass. Analysis of the heavy metal loaded biosorbent showed shifts in the absorption bands of the functional groups.

Most of the adsorption studies have focused on untreated plant waste as reviewed by Ngah, W. S. W. et al, 2008. A comparison of adsorption efficiencies between chemically modified and unmodified adsorbents was also reported. In this study, the use of adsorbents obtained from plant waste and their methods of modification were investigated.

Section 2.4.2.1 below reviews the work carried out on the application of lignocellulosic material for the adsorption of organic pollutants from aqueous solution.

2.4.2.1 Adsorption of heavy metals

This section reviews the published works on the adsorption of heavy metals onto lignocellulosic material. As mentioned in Section 2.4.1, the many functional groups present in the lignocellulose make it a potentially good adsorbent material for heavy metals from aqueous solution. Bhatnagar, A. et al, 2010 reviewed the potential use of several agricultural wastes as adsorbents for the removal of heavy metals from water. A wide range of agricultural waste is being developed for possible use for the removal of a diversity of pollutants from water.

Krishnani, K. K. et al, 2009 used sugarcane bagasse for the adsorption of metal ions (Cd^{2+}, Pb^{2+}, Cu^{2+}, Ni^{2+}, Co^{2+} and Mn^{2+}) from aqueous solution. The sugarcane bagasse was first treated with steam by immersing in water in an autoclave. Adsorption capacities of 9.33 mg/g (Pb^{2+}) and 1.82 mg/g (Cd^{2+}) were obtained. These values were higher than the capacities obtained for the untreated bagasse. Neem tree leaves were evaluated for their heavy metal ions adsorption properties from aqueous solution (Oboh, I. et al, 2009). The leaves were just washed with distilled water, dried, ground to powder and then used for adsorption experiments. A removal efficiency of about 41.45% was recorded for Pb^{2+}. King, P. et al, 2007 reported the use of *Syzygium cumini* L leaf biomass for the adsorption of Pb^{2+}. The leaf biomass was cleaned by washing with deionized water several times, followed by drying and grinding the leaves to powder. The powdered leaf biomass was then used for adsorption studies.

Shin, E. W. et al, 2005 used *Juniperous monosperma* biomass modified by sulfonation for the adsorption of Cd^{2+} from aqueous solution. Sulfonation was found to double the uptake of Cd^{2+} from aqueous solution compared with the unmodified biomass. An adsorption capacity of about 17 mg/g was obtained, an improvement of about five times that of the untreated biomass. Nameni, M. et al, 2008 investigated the adsorption of Cr (IV) from aqueous solution by wheat bran.

As a lignocellulosic material, sawdust exhibits affinity for different xenobiotics. Sawdust has been used for the removal of Cu (II) from aqueous solutions (Bajpai, S. K. et al, 2007). The sawdust was grafted with acrylamide and sodium acrylate to produce a cation exchange material. Potassium persulfate was used as the initiator for the grafting reaction. The cation exchange material had an adsorption capacity of 20.0 mg/g for Cu (II). Meena, A. K. et al, 2008 investigated the adsorption of heavy metals (Cr IV, Pb^{2+}, Hg^{2+} and Cu^{2+}) by treated *Acacia Arabica* sawdust. The sawdust was treated with NaOH followed by treatment with H_2SO_4. The authors reported an adsorption capacity of 52.38 mg/g for Pb^{2+}.

Baral, S. S. et al, 2006 used chemically treated sawdust for the adsorption of Cr (VI) from aqueous solution. The treatment of the sawdust was the same as that reported by Vazquez, G. et al above. The

authors found that the adsorption of Cr (VI) decreased with increase in adsorbent dose and increased with increase in initial adsorbate concentration. They reported an adsorption capacity of 9.55 mg/g for Cr (VI). Ahmad, A. et al, 2009 investigated the adsorption of Pb (II) and Cu (II) onto Meranti wood. The Meranti sawdust was washed with distilled water followed by the immobilization of pigments and water-soluble substances by treating with formaldehyde solution in a 1:4 ratio (sawdust: formaldehyde, w/v). The sawdust was observed to poorly adsorb both Cu (II) and Pb (II) according to the Freundlich model (which was the best fit for the adsorption data).

Wheat bran has been investigated for the adsorption of Cr (VI). The powder was used for adsorption experiments without washing or any physical or chemical treatment. The adsorption capacity was found to be very low, 0.942 mg/g. Coconut coir pith was assessed for its adsorption properties towards Cr (IV) after modifying with hexadecyltrimethylammonium bromide (Namasivayam, C. et al, 2008). The authors reported an adsorption capacity of 76.3 mg Cr (IV) per gram of adsorbent.

Han, R. et al, 2005 assessed the biosportion of Pb^{2+} onto cereal chaff. The cereal chaff was not subjected to any pre-treatment save for drying and then screening with sieves. An adsorption capacity of 12.5 mg/g was obtained for Pb^{2+} adsorption from aqueous solution.

Orange peels have been investigated as potential adsorbents for the removal of heavy metals from aqueous solution (Xuan, Z. et al, 2006). The authors treated the orange peels with 0.1 M NaOH at room temperature, followed by treatment with increasing concentrations of citric acid. They reported an increase in the adsorption capacity after this treatment with adsorption capacities of up to 252 mg of Pb^{2+} per gram of biomass being achieved. Baig, T. H. et al, 1999 reported the removal of heavy metals (Pb^{2+}, Cd^{2+}, Cu^{2+}, etc.) by *Solanum Elaeagfolium* biomass treated with a solution of NaOH. The treatment of the biomass with NaOH is reported to have enhanced the uptake of heavy metals. The authors reported adsorption capacities of 20.6 mg/g (Pb^{2+}) and 18.9 mg/g (Cd^{2+}).

Kumar, U. et al, 2006 investigated the adsorption of Cd (II) from aqueous solution onto pretreated rice husks. The rice husk was pretreated separately with NaOH, HCl, Na_2CO_3, and epichlorohydrin for four hours to give different types of adsorbents. The adsorbed amount of Cd (II) was found to decrease after treatment of the rice husk with HCl. Wong, K. K. et al, 2003 investigated the adsorption of Pb (II) and Cu (II) onto rice husk modified with tartaric acid. They recorded an adsorption capacity of 108 and 29 mg/g for the adsorption of Pb (II) and Cu (II), respectively.

Bello, O. S. et al, 2010 assessed the adsorption of Pb^{2+} ions onto activated carbon produced from palm oil fruit fibre. It was reported that the adsorption capacity of the activated carbon for Pb^{2+} was higher compared with the raw biomass. According to a review by Arief, V. O. et al, 2008, soxhlet extraction

of *Sargassum* biomass followed by soaking in hydrochloric acid solution was found to result in the loss of active sites for the adsorption of metal ions. Thus, low heavy metal adsorption capacities were recorded on the resultant materials. The pre-treatment of lignocellulose with acids may not help improve the uptake of heavy metal ions from solution.

A lot of adsorption studies have also been conducted using microbial biomass. Many researchers are currently involved in the investigation of the application of algal and yeast biomass to accumulate and remove toxic and valuable heavy metals from waste water. The work by Duncan, J. R. et al (WRC Report No. 616/1/03) details the use of yeast (*S. cerevisiae*) and algae (*Spirulina*) for the biosorption of heavy metals from contaminated industrial waste water. The yeast is a by-product of alcohol fermentation industries. The authors realized a complete removal of Cu^{2+}, Cr^{2+} and Ni^{2+} from electroplating waste water, whilst on average, 82% (Zn^{2+}) and 83% (Cd^{2+}) was removed from the waste water when they used chemically modified yeast biomass.

Halttunen, J. et al, 2007 investigated the adsorption of Pb^{2+} and Cd^{2+} onto specific lactic acid bacteria. Significant removal of heavy metals was achieved and the removal efficiency was observed to be metal and bacterial strain specific. Relatively high metal ion removal capacities of 54.7 and 175.7 mg/g dry mass for Cd^{2+} and Pb^{2+}, respectively, were achieved.

Li, Z. et al, 2006 assessed the biosorption of Cd^{2+} onto *Rhodotorula sp. Y11* yeast cells previously subjected to chemical modification. The chemical modification was accomplished by separately reacting the yeast cells with methanol and ethanolamine. The modified biosorbent was then used for the Cd^{2+} adsorption experiments from aqueous solution. An adsorption capacity of 11.38 mg/g of dry biomass was achieved. Xie, J. Z. et al, 1996 used bacterial (*E. coli*) biomass chemically pretreated for the removal of heavy metals from water. The chemical pre-treatment involved treating the bacterial biomass with CS_2, $POCl_3$, $HOCNH_2$, $NaCO_2CH_2Cl$ and Na_2SO_3. The biosorbents were evaluated under continuous flow conditions. Relatively high adsorption capacities were recorded for some of the bacterial cultures.

Tong, M. et al, 2007 investigated the grafting of baker's yeast with poly (amic acid) after initially cross-linking the yeast biomass with glutaraldehyde. The yeast crosslinking using the polymeric glutaraldehyde and the subsequent grafting with poly (amic acid) was achieved as shown in Scheme 2.1.
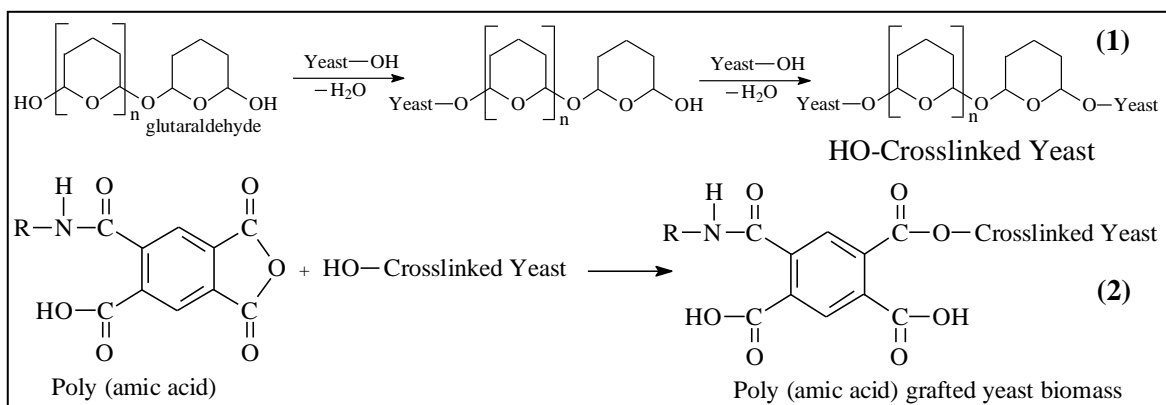
Scheme 2.1: Glutaradehyde crosslinking of yeast biomass and subsequent grafting with poly (amic acid).

The grafted yeast biomass was then evaluated for its adsorption properties by using Pb (II) and Ni (II) as model pollutants. The adsorption capacities of the modified grafted biomass were ten times those of the unmodified biomass. Yu, J. et al, 2007 investigated the grafting of poly (methacrylic acid) onto yeast biomass. They observed a marked improvement in the adsorption capacity of the grafted yeast biomass for Pb (II), Cd (II) and Cu (II) compared with the pristine biomass. The authors were also able to regenerate the heavy metal ion loaded adsorbent using ethylenediamine tetraacetic acid.

Having reviewed the adsorption of heavy metals from aqueous solution by lignocellulosic materials, the literature on the adsorption of organic pollutants by lignocellulosic was also reviewed. The next section gives a review on the adsorption of organic pollutants from aqueous solution onto lignocellulose based adsorbents.

2.4.2.2 Adsorption of organic pollutants

As stated in Section 1.3, the presence of organic dyes in the aquatic systems can cause a lot of problems including: formation of toxic or carcinogenic degradation products, imbalance of the aquatic ecosystem, as well as making the water less aesthetically pleasant. Other pollutants such as chlorinated organic compounds are suspected human carcinogens (Hanberg, A., 1996). This section reviews the literature on the adsorption of organic pollutants onto lignocellulosic material.

A review by Ahmaruzzaman, M., 2008 on the uptake of phenol by low-cost adsorbents like lignocellulosic material noted that these adsorbents have high removal capabilities for some phenolic compounds. In a study by Tahir, H. et al, 2008 marine algae biomass collected from the sea was used for the adsorption of methylene blue. The algae showed a dye removal efficiency of about 96%. Tarawou, T. et al, 2007 reported the adsorption of methyl red onto water hyacinth (*Eichornia*

crassipes) biomass from aqueous solution. The water hyacinth was found to have a Langmuir adsorption capacity of about 25 mg/g for methyl red.

Lignocellulose in the form of bark has been used for the adsorption of phenol. Vazquez, G. et al, 2006 used *P. pinaster* bark for the adsorption of phenol. Treatment with formaldehyde polymerized and immobilized water soluble phenols. Izadyar, S. et al, 2007 studied the adsorption of textile dyes onto wood sawdust. The authors used beechwood sawdust for the adsorption of three common textile dyes (acid green, acid orange and direct orange). Filipkowska, U. et al, 2008 compared the adsorption efficiencies of chitosan, sawdust and flyash for the adsorption of an organic dye, basic violet 10. The sawdust used here was treated with sulfuric acid before use. The chitosan was treated with 30% KOH solution. The sawdust and flyash were then immobilized on chitosan in a ratio of 1:1. The combination of chitosan and sawdust resulted in enhanced dye adsorption. The adsorption capacity was greater than that of chitosan and flyash (in combination), sawdust or chitosan alone. This demonstrated some synergy between the sawdust and the chitosan.

Batzias, F. A. et al, 2007 reported the adsorption of dyes onto acid hydrolysed beechwood sawdust. The mild acid hydrolysis of the sawdust was found to improve the uptake of the dyes from aqueous solution. They attributed the enhancement in adsorption to the removal of hemicellulose during acid hydrolysis which opened up the lignocellulosic structure. Elizalde-Gonzalez, M. P. et al, 2008 assessed the adsorption of methyl orange and arsenite onto maize cob biomass. The maize cob biomass was first chemically treated with phosphoric acid and different quaternary amines. It was observed that < 50% of dye was removed by the phosphoric acid treated biomass, while the samples treated with quaternary amines showed about 70% removal efficiency. The higher removal efficiency of the quaternary amine treated biomass than that of the acid-treated biomass was attributed to its low basicity, thus allowing for greater electrostatic interactions with the methyl orange anion.

Garg, V. K. et al, 2004 investigated the removal of malachite green dye from aqueous solution by adsorption onto formaldehyde- and sulfuric acid-treated saw dust. The adsorption efficiencies were comparable with activated carbon at low adsorbate concentration. However, at high concentration, activated carbon exhibited higher adsorption efficiencies relative to the chemically-modified sawdust. The adsorption of water soluble organic dyes onto ferrofluid-modified sawdust was investigated by Safarik, I. et al, 2007. The authors prepared a magnetically responsive composite material based on lignocellulose and magnetic nanoparticles. The spruce saw dust was modified by contact with magnetic fluid stabilized with perchloric acid. The modified biomass was assessed for the adsorption of acid green 25 and acid red 183.

Tang, J. et al, 2004 reported on the competitive sorption and desorption of chlorinated organic solvents (dense non-aqueous phase liquids) onto geosorbents (thermally aged natural organic matter). The authors used biomass including corn stalk, soybean stalks, oak leaves, red maple leaves, green ash leaves and pine bark. They investigated the sorption of trichloroethylene, tetrachloroethylene and 1,2-dichlorobenzene. They found that the thermally treated materials exhibited higher adsorption capacities than the untreated lignocellulose.

Aksu, Z. et al, 2001 investigated the adsorption and biosorption of monochlorinated phenols onto flyash and dried activated sludge. The activated sludge was found to have adsorption capacities of 281.1 mg/g for *o*-chlorophenol and 287.2 mg/g for *p*-chlorophenol. Activated sludge performed better than flyash which showed adsorption capacities of 98.7 and 118.6 mg/g for the respective adsorbates.

Lignocellulosic material also serve as a renewable source of activated carbon. Many reports appear in the literature on the derivation or preparation of activated carbon from many types of biomass. Jaguaribe, E. F. et al, 2005 investigated the use of activated carbon derived from sugarcane bagasse, babassu and coconut shells in the removal of residual chlorine from water. They reported that only sugarcane bagasse-activated carbon could remove 100% of the residual chlorine. Nethaji, S. et al, 2011 assessed the adsorption of amido black 10B dye onto lignocellulosic agricultural waste (palm flower) activated carbon. The palm flower waste biomass was treated for 48 h with concentrated H_2SO_4 in order to carbonize it. The authors reported an adsorption capacity of 3.68 mg/g.

The removal of basic dye by chemically activated *Pathernium* biomass was investigated by Lata, H. et al, 2008. The researchers treated the plant biomass with concentrated sulfuric acid (1:1.5% w/v) at 120 °C and the carbonized material was soaked in 1% sodium carbonate (Na_2CO_3) solution. The prepared adsorbent was found to have an adsorption capacity of 18.52 mg/g for the basic dye.

Agricultural waste biomass is widely available and can act as a source of lignocellulose. Senthilkumaar, S. et al, 2006 reported the adsorption of reactive red dye from aqueous solution onto activated carbon prepared from agricultural waste. They found adsorption capacities of 181.9 mg/g (coconut tree carbon) and 200 mg/g (jute fibre carbon) for the adsorption of the reactive dye onto the respective adsorbents. Santhi, T. et al, 2010 investigated the adsorption of methyl red from aqueous solution onto activated carbon prepared from *Annona squmosa* seed biomass. The authors found a removal efficiency of about 83% for methyl red adsorption onto the activated carbon.

Gong, R. et al, 2008 modified rice straw biomass with citric acid and used the modified biomass for methylene blue adsorption from aqueous solution. The modification of the rice straw biomass resulted in enhanced adsorption of methylene blue relative to the unmodified biomass. In another report,

Gong, R. et al, 2009 used wheat straw biomass modified with tartaric acid for the adsorption of methylene blue and crystal violet dyes. The modified wheat straw showed relatively high adsorption capacities for both dyes.

Cereal chaff (another agricultural waste) was evaluated for its methylene blue adsorption properties (Han, R. et al, 2006). The cereal chaff showed an adsorption capacity of 20.6 mg/g for methylene blue. Hameed, B. H. et al, 2008 studied the adsorption of malachite green dye onto char derived from rice straw. Relatively high adsorption capacities were recorded compared with other low-cost adsorbents.

Bulut, Y. et al, 2006 used untreated ground wheat shells for the adsorption of methylene blue dye. The wheat shells were just washed with distilled water until no colour was observed. The authors reported adsorption capacities ranging from 16.56 to 21.50 mg/g. Brás, I. et al, 2005 used unmodified pine bark biomass for the adsorption of pentachlorophenol from aqueous solution. Pineapple leaf powder was also used for the removal of dyes such as methylene blue (Weng, C. H. et al, 2009).

Mango tree leaf biomass was assessed as an adsorbent for a grey dye (Grey BL) from aqueous solution. The leaf biomass was washed with distilled water, dried, ground to powder and then used for adsorption experiments. Adsorption capacities of about 25 mg/g were obtained (Murugan, T. et al, 2010). Untreated banana stalk waste was used for the adsorption of methylene blue from aqueous solution (Hameed, B. H. et al, 2008). The banana stalk biomass was washed with water to remove all dirt and other water soluble compounds. The dry biomass was then powdered and used for adsorption experiments and an adsorption capacity of 243.90 mg/g for the methylene blue was obtained. Haris, M. R. H. M. et al, 2010 used modified banana trunk fibres for the adsorption of methyl red from aqueous solution. The investigators reported adsorption capacities of about 555 mg/g for the 5% NaOH-treated banana trunk fibre while acetylation, stearic acid and peroxide treatment of the banana fibres gave lower adsorption capacities.

Annadurai, G. et al, 2002 used orange and banana peels for the adsorption of methyl orange from aqueous solution. The orange and banana peel biomass was washed with distilled water, dried, crushed to powder and used for adsorption experiments. The authors reported adsorption capacities of 21.0 mg/g and 20.5 mg/g for methyl orange adsorption onto banana and orange peels biomass, respectively. Soya bean waste and bottom ash have been studied for their adsorption properties towards methyl orange. Mittal, A. et al, 2007 obtained adsorption capacities of 3.618 mg/g and 16.664 mg/g for methyl orange adsorption onto bottom ash and soya bean waste biomass, respectively. Elizalde-González, M. P. et al, 2008 investigated the adsorption of methyl orange onto chemically

modified maize cob waste. The maize cob waste-derived biomass was modified by quartenization and phosphorylation, with adsorption efficiencies of 68% and < 50% for the respective modifications.

It has been observed from the reviewed literature that lignocellulose materials can be used as low-cost adsorbents for both inorganic (heavy metals) and organic pollutants (dyes, chlorophenols, etc.) from aqueous solution in water treatment. There is quite a vast pool of different types of biomass from which the lignocellulosic material can be derived. The unmodified lignocellulosic materials show a relatively good uptake of both inorganic and organic pollutants from aqueous solution. Chemical modification of some lignocellulosic material was also observed to enhance the adsorption of some organic pollutants and heavy metals.

In this study, the lignocellulosic material (biopolymer) is to be modified with different monomers, as well as montmorillonite (nanoclay). The modification with nanoclay is expected to result in lignocellulose-montmorillonite nanocomposites in which the nanoclay is uniformly dispersed in the lignocellulose matrix and is also coupled or grafted to the lignocellulose covalently through a polymer. It is hoped that the resultant materials would show enhanced adsorption for both heavy metals and organic pollutants. As such, the following section will describe the methods of grafting of lignocellulose by different organic groups (especially polymers).

2.4.3 Chemical modification of lignocellulosic material (biomass)

The direct application of untreated plant waste as adsorbent can be accompanied by several problems such as low adsorption capacity, high chemical oxygen demand (COD) and biological chemical demand (BOD) as well as increase in total organic carbon (TOC) due to the release of soluble organic compounds contained in the plant material (Gaballah, L. et al., 1997). The increase of COD, BOD and TOC can cause depletion of oxygen content in water and can threaten aquatic life. Therefore, plant waste needs to be modified or treated before being applied for the decontamination of heavy metals.

The grafting of organic groups onto lignocellulose has been widely investigated in the literature. As shown from the lignocellulose structure, the lignin and cellulose structures (Figures 2.1, 2.2 and 2.3), the lignocellulose matrix possesses a lot of hydroxyl groups and it is these hydroxyl groups which act as reaction centres (active sites) in most of the grafting reactions (Hill, C. A. S. et al, 2000). The graft copolymerization method was used to attach new functional groups to the lignocellulosic material so as to increase its adsorption capacities for both heavy metals and dyes from aqueous solution. The graft polymerization may also improve the mechanical properties of the lignocellulose (Ye, J. H. et al, 2010).

The grafting of organic groups onto lignocellulose follows two mechanisms, i.e. condensation or free-radical (Gangopadhyay, R. et al, 2000) reaction depending on the reaction conditions and the type of organic group to be grafted. This section reviews the different types of modification with organic groups performed on lignocellulose for the purposes of enhancing its adsorption properties.

Wu, S. et al, 2009 reported grafting of methyl acrylate (MA) onto pullulan (PU) biomass. The polymerization initiator employed was cerium ammonium nitrate. Upon completion of the reaction, PU-g-MA was precipitated with ethanol. The investigators observed a decrease in water absorption of the grafted fibres with increase in the amount of polymer grafted. The grafting entailed the generation of a PU macroradical which then attacks the MA monomer, followed by polymer chain growth on the PU as follows:
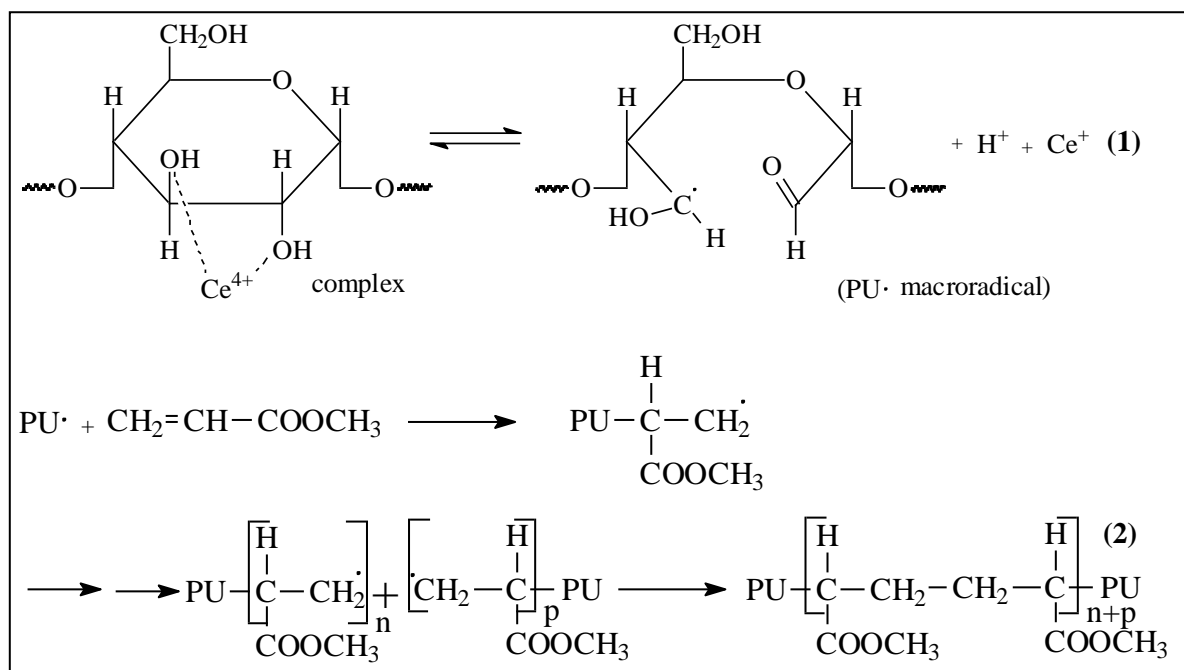
Scheme 2.2: Pullulan macroradical generation and subsequent grafting with poly (methacrylate) (Wu, S. et al, 2009).

Cellulose has also been modified for a number of applications. Ouajai, S., 2005 investigated the introduction of hydrophobic groups onto cellulose and the further modification to hydrophilic character after grafting. A solvent-free grafting system initiated by free radicals from azobisisobutyronitrile for grafting cellulose at low grafting levels was studied. The author modified natural cellulosic fibres in order to improve and increase consistency of their performance in biodegradable materials. Fibres were pretreated by solvent extraction and NaOH treatment in order to remove wax and lignin before grafting with acrylonitrile.

Cellulose was also modified with acrylonitrile through a free-radical graft polymerization reaction (Bianchi, E. et al, 1998). The cellulose was first modified with acryloyl chloride to produce cellulose-acrylate which was further reacted with acrylonitrile in the presence of azobisisobutyronitrile (initiator). The initiator decomposes to produce free radicals which then initiate the polymerization reaction by reacting with the double bonds on cellulose acrylate. The polymer chains grow from the cellulose backbone to give the poly (acrylonitrile)-grafted cellulose. Typical reactions are shown in Scheme 2.3.

Scheme 2.3: Grafting of cellulose with poly (acrylonitrile).

Hernández-Meléndez. O. et al, 2009 investigated the graft polymerisation of wood saw dust and peat with ethylene carbonate. The resulting material was used in the biofiltration of organic vapours. In this case the mechanism of graft polymerisation commences with the generation of kind of an alkoxide ion (on the substrate) which is then able to open the strained epoxide ring of the ethylene carbonate through an SN1 or SN2 reaction. Then the polymer chain grows from the lignocellulose backbone. This reaction is an example of anionic polymerisation.

Scheme 2.4: Grafting of sawdust with poly (ethylene carbonate).

Ye, J. H. et al, 2010 assessed the modification of sawdust lignocellulose with N-vinylpyrrolidone and its use in the adsorption of tea catechins from aqueous solution. The initiator, azobisisobutyronitrile, decomposed to free radicals which reacted with the lignocellulose to generate a macroradical from which the polymerisation of N-vinylpyrrolidone occurred (Scheme 2.5). The N-vinylpyrrolidone-grafted lignocellulose showed an improved uptake of tea catechins relative to the unmodified material.
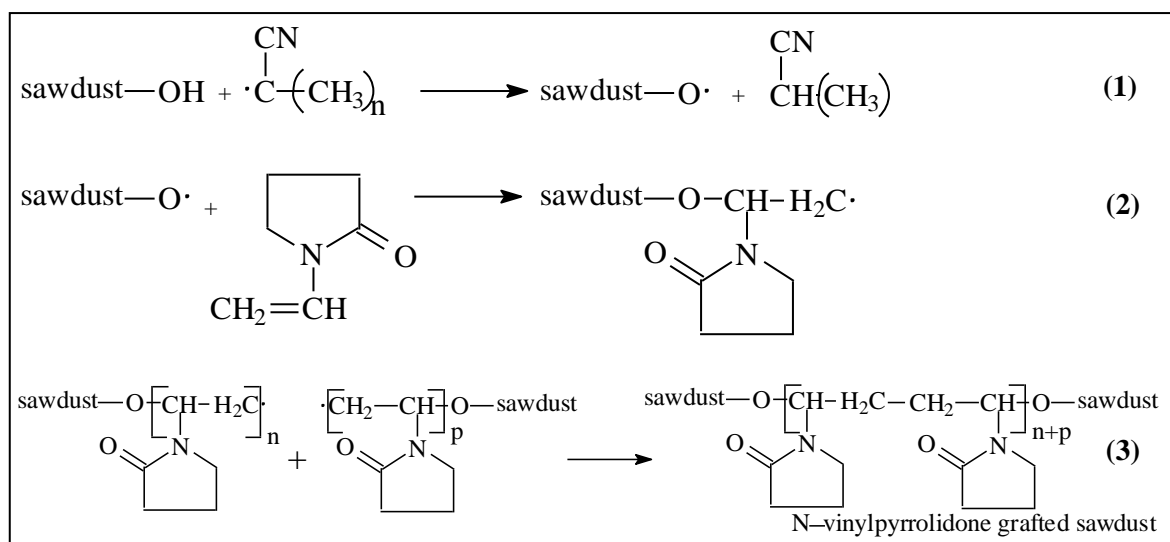
Scheme 2.5: Grafting of sawdust with poly (vinylpyrrolidone) (Ye, J. H. et al, 2010).

Alkoxysilanes are widely used as coupling agents in many applications. Salon, M. C. B. et al, 2005 investigated the grafting of organosilanes (γ-diethylenetriaminopropyl trimethoxysilane, aminopropyl trimethoxysilane and γ-methacryloxypropyl trimethoxysilane) onto cellulose fibres. The pristine and hydrolysed silanes were adsorbed to the cellulose fibres and then treated at 110 to 120 °C to allow the condensation of the silanes with the cellulose OH groups (forming covalent bonding). Typical reactions are displayed in Scheme 2.6.
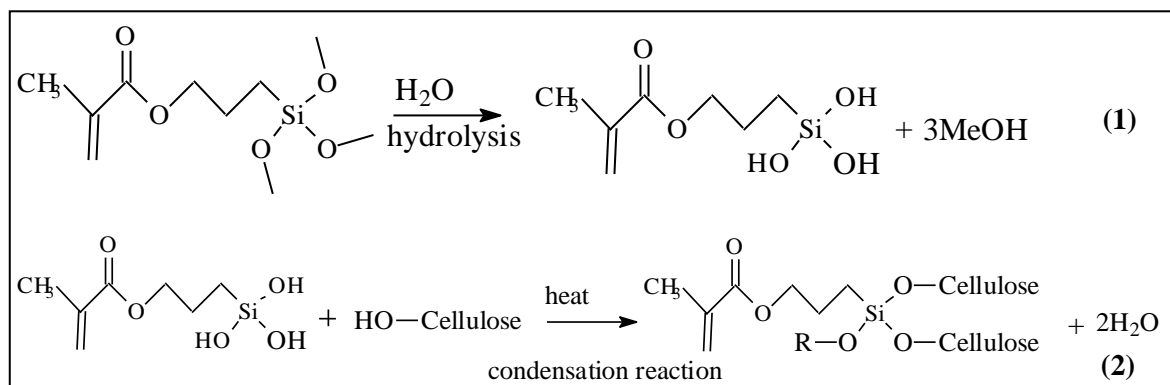
Scheme 2.6: Hydrolysis of methacryloxypropyl trimethoxysilane and grafting onto cellulose.

Abdelmouleh, M. et al, 2004 reported the modification of cellulosic fibres with functionalised silanes (γ-methacryloxypropyl trimethoxysilane, hexadecyltrimethoxysilane, aminopropyl trimethoxysilane and mercaptopropyl trimethoxysilane). The functionalised silanes were first hydrolysed and adsorbed onto the cellulosic fibres, which was then followed by subjecting the silane saturated fibres to heat treatment. The heat treatment allowed for the condensation of the silanes with the hydroxyl groups on the surface of the cellulosic fibres, as well as the self condensation of the silanol groups. The reactions were the same as illustrated in Scheme 2.6 above. Some of the adsorbents prepared in this study were prepared using the same procedure described here. To our understanding, there is no application of silane-grafted lignocellulose as a possible adsorbent for either organic or inorganic pollutants.

Castellano, M. et al, 2004 investigated the modification of cellulosic fibres with organosilanes (cyanoethyltrimethoxysilane and γ-methacryloxypropyltrimethoxysilane) under different conditions. Their study showed that the unhydrolysed silane did not react with cellulose even at high temperature, while it condensed with the phenolic OH of lignin. Condensation with cellulose OH groups only occurred in the presence of moisture which induced the hydrolysis of the silanes. Poly (methyl methacrylate) was then grafted onto the silane-modified cellulosic fibres. A similar procedure was employed in this study for the preparation of poly (methacrylic acid)-grafted lignocellulose, montmorillonite and a poly (methacrylic acid)-grafted lignocellulose-montmorillonite nanocomposite. The grafting process is further discussed in Sections 5.6.2.1 and 5.6.3.1.

Another study by Hill, C. A. S. et al, 2000 investigated the grafting of styrene onto wood flour. The wood flour was first modified with propionic acid, crotonic acid and methacrylic anhydride, then followed by a free-radical polymerization of styrene. Nada, A. M. L. et al, 2007 performed graft polymerization of acrylamide onto wood lignocellulose and used the grafted material for the adsorption of metal ions (Cu^{2+}, Cr^{3+}, Ni^{2+} and Pb^{2+}). The grafted wood pulp showed increased uptake of the metal ions from solution.

Gangopadhyay, R. et al, 2000 investigated the photografting of methyl methacrylate from photofunctionalised sisal fibre. The sisal fibres were first photofunctionalised by irradiating in a solution of oxalic acid (photoactive). The oxalic acid generates carboxyl free radicals which in turn lead to formation of cellulose macroradicals from which an incoming monomer polymerises. The polymer chain then grows on the surface of the fibres. The carboxyl free radicals can also initiate the homopolymerisation of the monomer, methyl methacrylate.

Meng, T. et al, 2009 also investigated the grafting of styrene and methyl methacrylate onto cellulose. The grafted cellulose was prepared by atom transfer radical polymerization (ATRP). Firstly, cellulose

2-bromoisobutyrylate (macro-initiator) was prepared. ATRP of the methyl methacrylate and styrene from the macro-initiator was then carried out. However, this method is rather expensive and besides, many steps are involved to get the final product. This will definitely increase the cost of production of such modified adsorbents, making it economically not viable.

Ojah, R. et al, 2006 investigated the graft polymerization of methyl methacrylate onto *Bombyx mori* fibre (natural silk) initiated by a semiconductor-based photocatalyst (CdS). The mechanism involved the generation of an electron/hole (e^-/h^+) pair under ultraviolet radiation by the semiconductor. The positively charged hole (h^+) transfers its charge to the silk fibre forming a silk macroradical and a proton (H^+). The initiation step involves the reaction of the monomer with the macroradical and the polymer chain grows 'from' the silk fibre backbone as more monomers react. The only difference is the initiator system involved. The grafted silk was found to have increased thermal stability and chemical resistance. The following scheme displays the typical reactions during the grafting process.
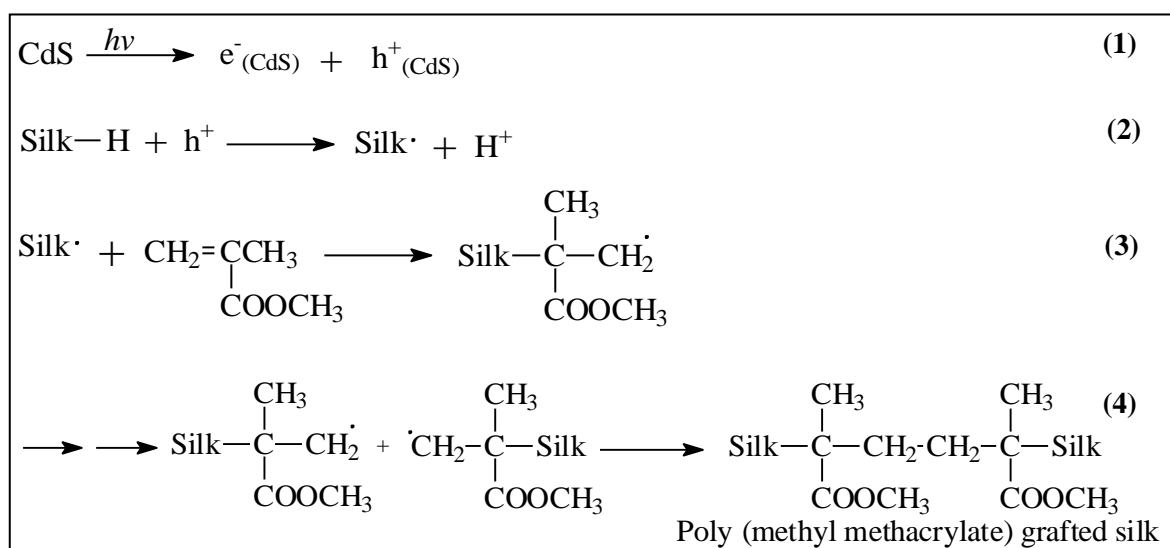
Scheme 2.7: Grafting of silk with poly (methyl methacrylate) under ultraviolet radiation.

This is an attractive method for the modification of lignocellulosic materials, however, the CdS used is known to be unstable and Cd^{2+} is known to be toxic.

Román-Aguirre, M. et al, 2004 investigated the graft copolymerization reaction of methyl methacrylate onto wood fibre. A typical grafting experiment was accomplished as follows: first, a mixture of woodfiber, water, sodium dodecyl benzene sulfonic acid, sodium metabisulfite was loaded in the reactor (mixed), followed by the addition of methyl methacrylate and potassium persulfate (initiator). The polymerization reaction was carried out under a nitrogen gas atmosphere. The authors gave a mechanism for the grafting reaction and this entailed the formation of the sulfate free radical species which then abstracts a hydrogen atom from the exposed lignocellulose hydroxyl groups to

form a macroradical (Gangopadhyay, R. et al, 2000). The macroradical then initiates the polymerization reaction of the monomer from the lignocellulose backbone. The graft polymerization reaction follows a 'grafting from' mechanism. Though methyl methacrylate has been widely applied in the modification of lignocellulosic materials, there is not a single study on the use of the poly (methyl methacrylate)-modified lignocellulose for adsorption purposes in water treatment. A similar procedure was used in this study to evaluate the grafting of methyl methacrylate onto both lignocellulose and montmorillonite clay, as well as in the preparation of some nanocomposites based on lignocellulose and montmorillonite clay.

Khan, F., 2004 assessed the graft copolymerization of methacrylic acid and acrylic acid onto jute fibre by pre-irradiating the fibres with ultraviolet radiation. 1-hydroxycyclohexyl-phenylketone was used as the photo-initiator and 2-methyl-2-propene 1-sulfonic acid (sodium salt) was added to suppress the formation of homopolymer and to facilitate the graft copolymerisation reaction. As highlighted above, poly (methacyrlic acid)-grafted yeast biomass was found to show high adsorption capacities for Cd^{2+}, Pb^{2+} and Cu^{2+} compared with the unmodified yeast biomass (Yu, J. et al, 2007). The yeast biomass was first cross-linked with glutaraldehyde followed by grafting with methacrylic acid. Potassium persulfate was used as the initiator and the mechanism followed more or less what has been discussed above for poly (methyl methacrylate). Methacrylic acid was also chosen in this study for the modification of both lignocellulose and montmorillonite, and also as a coupling agent in the preparation of lignocellulose-montmorillonite nanocomposites.

The following section describes some of the mineral based adsorbents currently being explored or already commercialized for water treatment.

2.5 Mineral adsorbents

Mineral adsorbents range from silica gels, activated alumina, activated carbon, oxides of metals, hydroxides of metals, zeolites, inorganic nanomaterials, porous clay heterostructures, clay minerals and pillared clays (Dabrowski, A., 2001). Activated alumina has been widely used for the removal of arsenic from water (Lin, T. S. et al, 2001; Singh, T. S. et al, 2004). Activated carbon is a porous carbonaceous material prepared through the carbonization and activation of organic substances, mainly of vegetable origin. Commercial activated carbon is mainly prepared from coal. The most commonly explored mineral adsorbents for water treatment and purification are zeolites and clay minerals. Many synthetic zeolites have been investigated for use as adsorbents in the treatment of contaminated water (Shevade, S. et al, 2004; Zhao, L. et al, 2010). In addition, natural zeolites like clinoptilolite have also attracted the attention of scientists because of their low cost and great potential

as adsorbents mainly for heavy metals (Sprynskyy, M. et al, 2006; Faghihian, H. et al, 2009; Chmielewská, E. et al, 2010). Perić, J. et al, 2004 investigated the adsorption of Cu^{2+}, Zn^{2+} and Pb^{2+} onto natural zeolite (clinoptilolite) from aqueous solution. Clinoptilolite showed a higher adsorption efficiency for Pb^{2+} than the other two heavy metals.

Clay minerals are now being widely researched for application in water treatment due to their potentially high adsorption capacity owing to their cation exchange capacity and nanoscale size and high surface area in the case of nanoclays. This study will focus on the use of pristine montmorillonite nanoclay and also metal-pillared montmorillonite nanoclay for the adsorption of pollutants (organic and inorganic) from aqueous solution.

The following section will look at the different types of clay minerals and their use as adsorbents in water treatment.

2.6 Clay minerals as adsorbents

Among the methods mentioned above, clays are widely used as adsorbents due to their high-specific surface area, high chemical and mechanical stabilities, a variety of structural properties and low cost (Bhattacharyya, K. G. et al, 2008; Cao, F. et al, 2008). Clays are abundant, have potentially high adsorption capacities and the potential for ion exchange and therefore, are good candidates for the development of adsorbents. Clay materials possess a layered structure and are considered as good host materials.

Different types of clays are available and they are classified according to the differences in their layered structures. However, a review by Bergaya, A. F., 2008 classifies the layered clay minerals into three broad classes based on their surface charge. The classes are: uncharged (kaolin, talc and pyrrophylite), negatively charged (paragonite, vermiculites, and smectites) and positively charged (layered double hydroxides).

Montmorillonite (MMT) clay is a widely studied 2:1 phylosilicate of the smectite clays due to its high cation exchange capacity (CEC) compared with other clays, and is reported to have the highest surface area (Ahmaruzzaman, M, 2008). A comparison of the adsorption properties of kaolinite and montmorillonite clays showed that montmorillonite had a higher adsorption capacity than kaolinite for the adsorption of cadmium (Bouchenafa-Saïb, N. et al, 2007). There has been an increasing interest to utilize clays for the adsorption of not only inorganic, but also organic molecules from aqueous solution (Ahmaruzzaman, M., 2008).

2.6.1 Montmorillonite clay: crystal structure

Montmorillonite (MMT) clay is a naturally occurring 2:1 phyllosilicate with other layered and crystalline clays such as talc and mica. The crystal lattice of MMT consists of octahedral alumina fused between two external tetrahedral silica sheets in such a way that the oxygens from the octahedral alumina sheets also belong to the silica tetrahedra (Lomakin, S. M. et al, 2003). The general formula of montmorillonite clay is $M_x(Al_{4-x}Mg_x)Si_8O_{20}(OH)_4$, where M is a monovalent cation and x is the degree of isomorphous substitution (Alexandre, M. et al, 2000). The crystal structure of 2:1 phyllosilicates is shown in Figure 2.6.

Isomorphic substitution in either the octahedral or tetrahedral layer by Mg^{2+} or Al^{3+} results in a net negative charge in each layer which is balanced by exchangeable hydrated cations in the interlayer space.
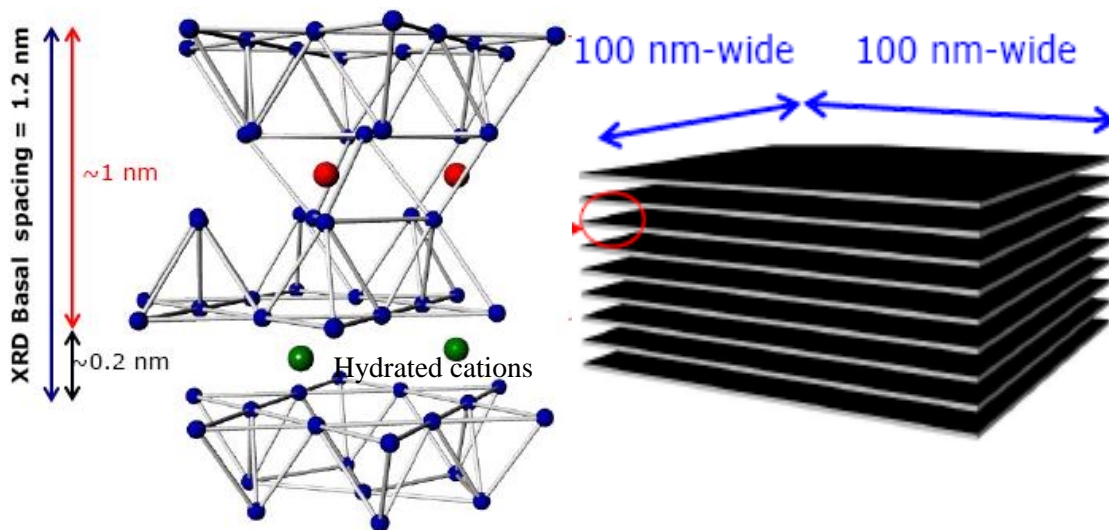
Figure 2.6: Crystal structure of MMT clay (Lin, J. J.).

The negative charge is defined through the cation exchange capacity (CEC), and for montmorillonite is typically 0.9 - 1.2 meq/gram depending on the mineral origin. These layers organize themselves in a parallel fashion to form stacks with a regular van de Waals gap in between them called the interlayer space or gallery. In their pristine form, the excess negative charge is balanced by cations (Na^+, Li^+, Ca^{2+}, K^+, etc.) which exist hydrated in the interlayer space. The MMT comes in a powder form with a mean particle size of 8 μm. Each powder contains thousands to more than a million thick platelets which have a much larger surface area (~750 m^2/g) and an aspect ratio of > 50 than conventional micro-sized fillers (Turng, L. S. et al, 2003). When completely delaminated, approximately 1 nm-thick platelets or clay sheets can be obtained.

The following section describes the use of montmorillonite and other clays for the adsorption of organic pollutants from aqueous solution.

2.6.1.1 Adsorption of heavy metals by montmorillonite

The practical applications of clay nanoparticles as adsorbents suffer from difficulties in solid-liquid separation in batch adsorption studies and packing complexity or high pressure drop for column processes. Montmorillonite clay has been used for the development of clay-filled composite membranes for use in cationic exchange process.

Montmorillonite clay adsorbs heavy metals via the physisorption mechanism which can be further divided into two categories, i.e. cation exchange in the interlayer spaces resulting from the interactions between metal ions and the permanent negative charge on the clay, and formation of inner-sphere complexes through Si–O$^-$ and Al–O$^-$ groups at the clay particle edges (Schindler P. W. et L, 1976; Mercier, L. et al, 1995). Takamatsu, R. et al, 2006 used EXAFS to probe the adsorption mechanism of Cd^{2+} onto montmorillonite. The investigators reported that there are two mechanisms observed, an outer sphere complexation and a surface precipitation mechanism. Scheme 2.8 illustrates the formation of innersphere and outersphere complexes during the adsorption of heavy metals onto montmorillonite clay.
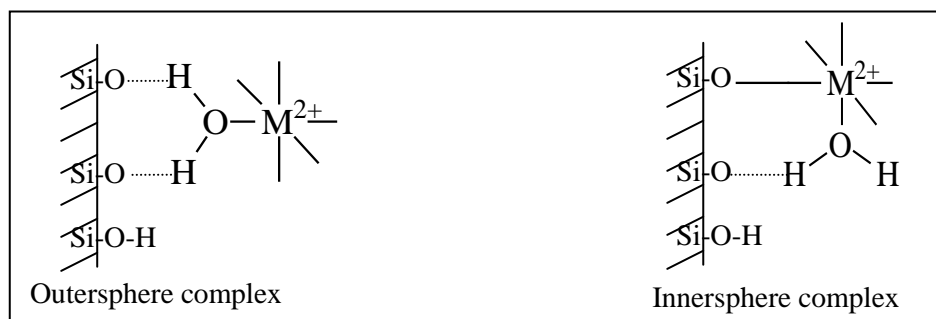
Scheme 2.8: Formation of innersphere and outersphere complexes during adsorption of heavy metals (M^{2+}) onto montmorillonite clay.

The two mechanisms are pH dependent because in acid conditions (pH 4) most silanol and aluminol groups are protonated. Therefore, in particular for the latter, acidification can lead to poor adsorption of heavy metals (Batchelor, B. et al, 1998). Gupta, N. et al, 2009 used pyrophyllite to assess the adsorption of heavy metals (Pb^{2+}, Cu^{2+} and Zn^{2+}) from aqueous solution. The adsorption of heavy metals was reported to follow an ion exchange mechanism (due to the permanent negative charge on the pyrophyllite structure) and a complexation mechanism (due to interaction with the surface groups, Si-O$^-$ and Al-O$^-$).

The amount of heavy metals adsorbed is a function of many other factors including: temperature, concentration, interaction between adsorbate and adsorbent, as well as internal and external surface area of the adsorbent. Kaya, A. et al, 2005 studied the adsorption of zinc onto bentonite clay. Bentonite clay is said to be 90% montmorillonite. The adsorption of Zn^{2+} from aqueous solution was found to be pH dependent with poor uptake at low pH. The main mechanism for the adsorption process was observed to be ion exchange, especially between pH 4 and 7. The authors also observed that the Na-exchanged bentonite was a better adsorbent than the pristine bentonite.

Bouchenafa-Saïb, N. et al, 2007 reported on the preparation and characterization of aluminum-pillared montmorillonite and its application in the adsorption of Cd^{2+} from aqueous solution. The authors used a Cr/Al pillaring solutions of varying Cr/Al ratios. They found that the clay pillared using a pure solution of Al_{13} showed greater affinity for Cd^{2+} than the mixed Cr/Al solutions. It is not clear whether the modification of the montmorillonite through Al-pillaring improved the uptake of Cd^{2+}. This study also sought to compare the performance of Al-pillared montmorillonite and the sodium-exchanged montmorillonite in the adsorption of Cd^{2+} as well as Pb^{2+}.

A detailed study on the adsorption of heavy metals by NaMMT clay was conducted by Abollino, O. et al, 2003. The NaMMT was also assessed for its heavy metal adsorption capabilities at different pH vlues as well as in the presence of different ligands. The authors found that pH greatly influences both the concentration of heavy metals in water as well as the amount of heavy metals adsorbed. As highlighted above, at low pH, there is the protonation of $Si\text{-}O^-$ and $Al\text{-}O^-$ groups and that results in low adsorption capacities for heavy metals.

Surface modification of clay minerals has received attention because it allows the creation of new materials and new applications. There have been various attempts to improve the quality and adsorption properties of the clays by modifying them with different techniques. Clays and clay minerals can be modified by several routes including adsorption, ion exchange with inorganic cations and organic cations, binding of inorganic and organic groups, grafting of organic compounds anions (mainly at the edges), reaction with acids, pillaring by different types of poly (hydroxo metal) cations, intraparticle and interparticle polymerization, dehydroxylation and calcination, delamination and reaggregation of smectites, and lyophilisation, ultrasound, and plasma (de Paiva, L. B. et al, 2008). Two of the common techniques in this regard are intercalation and pillaring, and acid activation.

Bhattacharyya, K. G. et al, 2008 published a review on the adsorption of heavy metals onto modified kaolinite and montmorillonite clays. The authors observed that the pillaring of the clays is commonly done using polyoxy cations of Zr^{4+}, Al^{3+}, Si^{4+}, Ti^{4+}, Fe^{3+}, Cr^{3+} or Ga^{3+}. From their review, it is clear that acid treatment of clays slightly boosts their adsorption capacities for heavy metals. In addition,

montmorillonite and its modified forms have much higher metal adsorption capacity compared to that of kaolinite and modified-kaolinite.

The treatment of clay minerals with mineral acids of high concentration and at high temperatures is referred to as acid activation. In such a process, the interlayer exchangeable cations are replaced by H^+. Al^{3+} and other cations escape out of the tetrahedral and octahedral layers leaving SiO_4 largely intact. An increase in surface area and acidity of the clay minerals is achieved through this process (Bhattachryya, K. G. et al, 2007). The process also affords the elimination of several mineral impurities and partial dissolution of external layers. The increase in surface area is attributed to the production of finely dispersed silicon dioxide particles from destruction of mineral structures, removal of octahedral Al or silica components, plugging surface pores or interlamellar spaces, formation of cracks and voids in the surface (Bhattachryya, K. G. et al, 2007).

Ayari, F. et al, 2007 reported the adsorption of Pb^{2+} onto bentonite clay ion exchanged to give Al- and Na-bentonites. The Al-exchanged bentonite showed greater adsorption than the Na-exchanged bentonite. The authors observed that the uptake of Pb^{2+} was through ion-exchange and surface adsorption. Barbier, F. et al, 2000 assessed the adsorption of Cd^{2+} and Pb^{2+} onto montmorillonite (MMT) from aqueous solution, and observed that Pb^{2+} adsorption was greater than that of Cd^{2+} to the same adsorbents. The authors also observed that the uptake of both Cd^{2+} and Pb^{2+} by the montmorillonite followed an ion-exchange mechanism (by MMT-Na sites) and surface hydroxyl groups (silanol, Si-OH and aluminol, Al-OH) were responsible for surface complexation.

Yun, L. et al, 2006 assessed the adsorption of Cu^{2+} and Pb^{2+} onto bentonite clay modified with 4`-methylbenzo-15-crown-5. The modified bentonite gave a higher adsorption capacity than the unmodified sodium bentonite for both Cu^{2+} and Pb^{2+}. Adsorption capacities of 21.73 mg/g (Cu^{2+}) and 98.325 mg/g (Pb^{2+}) were obtained for the modified bentonite compared with 17.67 mg/g (Cu^{2+}) and 64.79 mg/g (Pb^{2+}) for the unmodified bentonite. Vermiculite was used as an adsorbent for the uptake of heavy metals (cadmium, copper, lead, manganese, nickel, and zinc). The influence of organic ligands on uptake of the heavy metals was also investigated (Malndrino, M. et al, 2006). The presence of organic ligands was found to decrease the uptake of heavy metals by the vermiculite. Adsorption capacities of 64.10 mg/g (Pb^{2+}) and 37.71 mg/g (Cd^{2+}) were obtained for adsorption onto vermiculite.

Sodium dodecylsulfate-modified montmorillonite was assessed for the removal of Cu^{2+} and Zn^{2+} from aqueous solution (Lin, S. H. et al, 2002). It was not clear whether the surfactant-modified clay showed increased uptake of the two heavy metals from aqueous solution. The authors reported that more Cu^{2+} was adsorbed compared with Zn^{2+}. Oyanedel-Craver, V. A. et al, 2007 carried out competitive adsorption of benzene and heavy metals (Pb^{2+}, Cd^{2+}, Zn^{2+}, and Hg^{2+}) onto organoclays. The uptake of

all heavy metals was found to decrease in the presence of benzene. Altin, O. et al, 1998 investigated the adsorption of Pb^{2+} and Cd^{2+} onto calcium-saturated kaolinite and montmorillonite. The clays (unmodified and calcium saturated montmorillonite) showed a higher uptake of Pb^{2+} compared to Cd^{2+}.

Chen, Y. G. et al, 2010 assessed the adsorption of Cd^{2+} onto a Chinese bentonite. The author found an adsorption capacity of 3.16 mg/g for Cd^{2+} adsorption onto the bentonite. The adsorption mechanism was concluded to be complexation, electrostatic interaction and ion-exchange. Yan, L. et al, 2008 investigated the adsorption of Cd^{2+} onto Al_{13}-pillared acid activated montmorillonite ($Al_{13}PAAMMT$) from aqueous solution. The $Al_{13}PAAMMT$ showed a higher adsorption capacity for Cd^{2+} than NaMMT and Al_{13}-pillared MMT. Again, the adsorption properties of vermiculite were also assessed by Abate, G. et al, 2005, where the adsorption of Cd^{2+} and Pb^{2+} was investigated. The uptake of Pb^{2+} onto the vermiculite was much greater than the adsorption of Cd^{2+}. The authors also observed that vermiculite modified with humic acid showed increased uptake of both heavy metals compared with the unmodified vermiculite.

Sari, A. et al, 2007 reported the adsorption of Pb^{2+} and Cr^{3+} onto celtek clay from aqueous solution. The authors reported adsorption capacities of 18.08 mg/g (Pb^{2+}) and 21.55 mg/g (Cr^{3+}). Hefne, J. A. et al, 2010 assessed the adsorption of Ag^{+} ions onto sodium bentonite, and reported an adsorption capacity of about 100 mg/g. Yu, R. et al, 2008 investigated the adsorption of Cd^{2+} onto carbon modified Al-pillared montmorillonite from aqueous solution. They observed that the pillared clays showed increased uptake of Cd^{2+} compared with the unpillared montmorillonite. Section 2.6.1.2 describes the application of montmorillonite clay for the adsorption of organic pollutants.

2.6.1.2 Adsorption of organic pollutants by montmorillonite

Liu, P. et al, 2007 published a review on the adsorption of dyes onto natural clay nano-adsorbents. The authors highlighted that natural, acid activated, calcined and organophilic clays have been successfully used for the adsorption of dyes from aqueous solution. The investigators also observed that the benefits of the large surface area of these nanoadsorbent clays have not been fully realized.

Koumanoza, B. et al, 2002 investigated the adsorption of *p*-chlorophenol onto bentonite and perlite. The bentonite and perlite were used without further modification and the two showed adsorption capacities of 10.63 and 5.84 mg/g, respectively. Another study by Houari, M. et al, 2007 investigated the adsorption of phenol, nitrophenol, 2-chlorophenol and xylene onto geomaterial-modified montmorillonite. The adsorption capacities were 43.05, 44.70, 26.48 and 37.16 mg/g, for the respective adsorbates.

Pernyeszi, T. et al, 2006 evaluated the use on organoclay and an aquifer material for the adsorption of 2,4-dichlorophenol. The authors observed that clays have not been widely used because of their limited application under flow conditions. The treatment of clays with cationic surfactants may increase their adsorption capacity for organic pollutants of low water solubility and polarity. Organoclays have low permeability and wettability, thus making their direct application in column techniques difficult if not impossible. Li, F. et al, 2000, investigated the adsorption of cationic surfactants, unconventional Gemini surfactants and 4-chlorophenol onto montmorillonite clay. Adsorption capacity was highest for the C_{14}-gemini surfactant modified montmorillonite clay, 31.11 mg/g and lowest for C_{14}-tetramethylammonium bromide modified clay, 14.14 mg/g.

Jiang, J. Q. et al, 2003 investigated the possibility of the simultaneaous removal of both inorganic and organic contaminants from aqueous solution using a single adsorbent. Their study showed that inorganic contaminants are adsorbed more on the polymeric Fe/Al-pillared clays and organic pollutants on the surfactant modified clays due to specific surface properties introduced by the modification. Clays modified with both Fe/Al polycations and surfactants had the ability to adsorb both organic and inorganic contaminants. It was observed from the same study that the greater the d-spacing, the greater the adsorption of both phenol and Cu (II) from aqueous solution.

Lin, S. H. et al, 2004 reported the adsorption of amido black 10B onto pristine and acid-activated montmorillonite (activated with 6 M HCl) from aqueous solution. They observed that the adsorption of the dye was improved as a result of acid activation of the montmorillonite clay. Rytwo, G. et al, 2002 investigated the adsorption of divalent organic cations (paraquart and diquart) and methyl green onto sepiolite from aqueous solution. The sepiolite showed removal efficiencies of greater than 95% for the three adsorbates. Almeida, C. A. P. et al, 2009 assessed the adsorption of methylene blue onto montmorillonite clay from aqueous solution. The montmorillonite clay showed high removal efficiencies with adsorption capacities of about 300 mg/g being obtained. Awala, H. A. et al, 2011 reported the use of feldspar (tectosilicate mineral) for the adsorption of dyes (methyl red, fluoresceine and methlylene blue) from aqueous solution. Only methylene blue showed some adsorption (very low), while the other two dyes were not adsorbed at all.

A number of metals have been used for the pillaring of clays and these include Fe, Cr, Mn, etc (Mishra, T. et al, 1997). The clays pillared using these metals have been applied primarily in catalysis. Banat, F. A. et al, 2000 reported the adsorption of phenol by bentonite. The authors observed an increase in the uptake of phenol in the presence of cyclohexane. In addition, the use of cyclohexane was observed to destroy the crystal structure of the clay. Zielke, R. C. et al, 1988 investigated the adsorption of chlorinated phenols onto AlpMMT, Cr-pMMT and Al-delaminated laponite. Adsorption of chlorinated phenols onto Al-pMMT was found to increase with increase in hydrophobicity as well

as the number of chlorine atoms on the adsorbate. Al-delaminated laponite did not adsorb any chlorophenols.

Altunlu, M. et al, 2007 investigated the effect of OH/Al molar ratio and Al/clay (mmol/g) ratio on the adsorption properties of Al-pillared bentonites. They found that the amount of phenol adsorbed decreased with increase in OH/Al and Al/clay (mmol/g) molar ratios. The HDTMA-bentonite was found to adsorb more phenol than the Al-pillared bentonite.

Yilmaz, N. et al, 2004 investigated the adsorption properties of tetradecyl- and hexadecyl-ammonium salt modified bentonites for the removal of phenols from aqueous solution. The surface area of the bentonites was found to decrease after modification. Montmorillonite clay modified with hexadecyltrimethylammonium bromide at 100% CEC was found to have the highest adsorption capacity for phenol. Breen, C. et al, 1998 investigated the adsorption of benzene and *p*-nitrophenol (PNP) onto surfactant modified MMT clay and bentonites. The investigated clays were of different layer charges or charge densities. The amount of each pollutant adsorbed was found to be dependent upon the source and type of clay used. For PNP, the amount adsorbed also depended on the surfactant loading and also its size, being high at low surfactant loadings and decreased as the surfactant loadings increased. Sheng, G. et al, 2000 reported the adsorption of dichlorobenzene on hexadecyl trimethylammonium–exchanged clays (smectite and illite). Both clays were observed to adsorb *o*-, *m*-, *p*-dichlorobenzene from aqueous solution.

Rawajfih, Z. et al, 2006 assessed the adsorption of phenol and chlorinated phenols on surfactant modified bentonite clay. Sheng, G. et al, 2001 reported the adsorption of pesticides onto calcium- and potassium-saturated smectite clays. The authors concluded that these expandable clays have the potential of being used as adsorbents for certain pesticides. Torrents, A. et al, 1997 investigated the uptake of pesticides by Na-montmorillonite and Na-kaolinite. The authors found that the adsorption of pesticides onto Na-montmorillonite was higher than onto Na-kaolinite.

Wang, C. C. et al, 2004 reported the adsorption of basic green 5 and basic violet 10 dyes onto Ca-montmorillonite (Ca-MMT) and titanium-exchanged montmorillonite. They found that titanium-exchanged montmorillonite showed a lower adsorption capacity compared with Ca-MMT. Özcan, A. S. et al, 2004 assessed the adsorption of acid red (AR57) and acid blue (AB294) dyes from aqueous solution onto acid activated bentonite. The acid activated bentonite showed very high adsorption capacities for AR57 (416.3 mg/g) and AB294 (119.1 mg/g). Vinod, V. P. et al, 2003 used pillared clay coated with humic acid for the adsorption of basic dyes from aqueous solution. They reported removal efficiencies of about 99% (methylene blue), 97% (crystal violet) and 91% (rhodamin B) from aqueous solution.

Zhuannian, L. et al, 2009 investigated the adsorption of MetO onto ultrafine coal powder and found equilibrium adsorption capacities of about 6.0 mg/g for an initial methyl orange concentration of 100 ppm. Jeon, Y. S. et al, 2008 reported adsorption capacities of less than 0.3 mg/g for methyl orange adsorption onto alginate/polyaspartate hydrogels for an initial concentration of 10.0 mg/L. Teng, M. Y. et al, 2006 assessed the adsorption of methyl orange onto acid activated montmorillonite clay and reported an improvement of about eight times relative to the natural clay. Mittal, A. et al, 2007 reported adsorption capacities of 3.6 mg/g and 16.7 mg/g for methyl orange adsorption onto flyash and soya bean waste biomass, respectively. Anbia, M. et al, 2010 used modified nanoporous silica for the adsorption of anionic dyes including methyl orange, and reported an adsorption capacity of 357.1 mg/g. Chen, S. et al, 2010 found an adsorption capacity of about 50 mg/g for methyl orange adsorption onto powdered activated carbon at an initial concentration of 25 ppm. Their adsorption data were best described by the pseudo second-order kinetic model and the Langmuir isotherm. Yu, L. et al, 2011 reported an adsorption capacity of 36 mg/g for methyl orange adsorption onto anaerobic sludge. Haque, E. et al, 2011 found a capacity of 11.2 mg/g for methyl orange adsorption onto activated carbon.

The above reviewed literature has shown that there is a lot of research being undertaken on the use of clays (especially montmorillonite) as adsorbents for the removal of organic and inorganic pollutants from water. Apart from the use of montmorillonite clay as an adsorbent in water purification, it is also being used in other areas like gas purification, as well as in catalysis. The following section reviews some literature on the chemical modification of montmorillonite clay both through pillaring (with metal oxides and organic groups) and also through grafting (covalent bonding) of organic groups.

2.6.2 Chemically modified montmorillonite clays

Chemical modification can affect (either positively or negatively) the adsorption properties of montmorillonite. Different chemical modifications can enhance certain adsorption properties but can also suppress some of the properties. It can be seen from some of the reviewed work above (Section 2.6.1.2) that metal oxide-pillaring of montmorillonite can improve the uptake of heavy metals and some organics from aqueous solution. The pillaring of montmorillonite was also explored in this study, and the following section reviews the literature on the pillaring of montmorillonite with metals oxides and organic surfactants.

2.6.2.1 Intercalated and pillared clays

Pillared clays are materials prepared by the intercalation of metal oxide precursors between the silicate layers of the smectite type clays (Mahboub, R. et al, 2006). Upon heating, oxide pillars are formed, building a zeolite-like structure. According to Mahboub, R. et al, 2006, the dimensions and

the characteristics of the pores produced this way depend on a number of factors including: the nature, size and shape of the intercalated species and the precursor polymerization parameters (e.g. concentration of the metal ions, alkalinity, temperature of hydrolysis, time and temperature of aging) and to the chemical and crystallographic parameters of the clay (the magnitude of the layer charge, the location and the distribution of the charge and the nature of the octahedral sheet).

Pillared clays have a structure in which parallel two-dimensional silicate layers of the clay are supported with small particles of metal oxide with a dimension of nano- to subnano-meter size. Figure 2.7 shows a diagrammatic representation of the metal oxide-pillared clay.
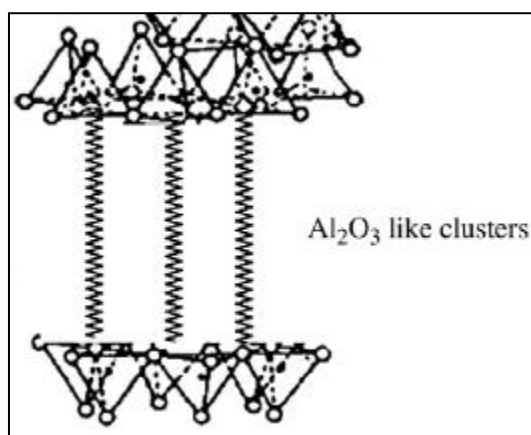
Figure 2.7: Graphic representation of metal oxide-pillared clay (Sivaiah, M. V. et al, 2010).

Microporous to mesoporous clay materials are formed. Pillared clays can provide large surface areas and pore volumes, which are beneficial for organic compounds and intermediates to reach and leave the active sites on the surface (Aouad, A. et al, 2005). The pillaring process increases the accessibility of the clay layers as well as stabilizes the metal oxide particles of nanometer dimension that prevent aggregation of the clay layers.

The surface groups exposed by these ultra-dispersed metal oxides play a key role in determining the catalytic and adsorptive properties of pillared clays. The pillared clays have a high thermal stability, intrinsic catalytic activity and a high surface area (Bhattacharyya, K. G. et al, 2008). Due to their potential applications as catalysts, supports, selective adsorbents, separating agents, and porous matrices for encapsulation of specific functional molecules, the design and synthesis of inorganic porous clay materials with a controlled pore structure have been of great interest.

Pillaring of clay with organic and inorganic pillaring agents is well known. These materials are usually prepared by ion-exchanging cations in the interlayer region of swelling clays with bulky

alkylammonium ions, polynuclear complex ions bearing inorganic ligands (hydroxo ligand, chloro ligand) or large metal complex ions bearing organic ligands.

The synthesis of metal-pillared clays entails the use of a dilute pillaring solution prepared from solutions of aluminium chloride and sodium hydroxide so that the Al/OH ration is at least 2.2. The key lies in controlling this ratio. Li, B. et al, 2009 prepared silica-pillared clay of mesoporous structure (pore sizes were in the nanometer range). The prepared pillared clays were found to have surface areas of between 590 -710 m^2/g, basal spacings of 4.76 - 5.62 nm and pore sizes of 3.75 - 4.51 nm. Mao, H. et al, 2009 also prepared silica-pillared clay with ordered mesoporous structure. The silica pillared clays had basal spacings of 3.7 - 4.3 nm and a uniform pore size of 2.5 - 3.2 nm. Surface areas of between 567 and 576 m^2/g were obtained for the pillared clays. Such silica-pillared clays have a lot of potential as adsorbents for the removal of toxic chemicals.

Salerno, P. et al, 2002 reported the preparation of Al-pillared clays (Al-PILC) from concentrated dispersions. The authors assessed the effect of varying the Al/clay ratio on the physicochemical properties of the resulting Al-PILC. The pillaring solution was an aluminum chloride with 47% of Al_2O_3 mainly as the Keggin cation which was added dropwise to 50% w/w natural clay suspension in acetone. The mixture then dialysed against distilled water until free of chloride ions. The product was dried and then calcined at 500 °C for 2 h. On heating, the intercalated inorganic species are converted to metal oxide clusters, generating a stable microporous structure with a high surface area (Sivaiah, M. V. et al, 2010). The surface area and microporosity was found to increase with the amount of Al_2O_3 in the pillared clays. Basal spacings of about 18.0 Å were obtained for all the Al-PILCs (Tichit, D. et al, 1988; Acemana, S. et al, 1999).

Schoonheydt, R. A. et al, 1993 investigated the preparation of Al-pillared clay using both dilute and concentrated Al_{13}-solutions. The clays investigated included the saponite, hectorite and laponite. Pillaring of these clays in concentrated Al-solutions resulted in Al-pillared clay of low thermal stability. The intercalated species are capable of preventing the collapse of the interlayer spaces, propping up the layers as pillars, and forming interlayer space.

Pires, J. et al, 1997 reported on the decomposition of the pillaring species in AlpMMT clays. They used differential scanning calorimetry (DSC) and thermogravimetric analysis (TGA) to follow the decomposition process. These two techniques can be used to follow the formation of Al_2O_3 pillars in the interlayer space of the clay. Pires, J. et al, 1997 prepared Al-PILC under the following conditions: the pillaring solution was aged for 2 h at 60 °C and had an OH/Al ratio of 2 and pH 6. The pillaring solution was added dropwise to a 0.5% clay suspension.

Montarges, E. et al, 1998 investigated the intercalation of polyethylene oxide (PEO) into montmorillonite clay and the use of the resultant lamellar solids as adsorbents for chlorinated phenol adsorption. The materials were also modified by pillaring with Al_{13} polyhydroxycations. The authors reported that the co-intercalation of PEO improves the hydrolytic stability of Al_{13} ions. In addition, the alumina-pillared clay derivatives obtained after calcining at 500 °C exhibited higher specific areas than those pillared in the absence of PEO. It was also observed that the surface area of the materials prepared only improved after pillaring with Al_{13} ions.

Chae, H. J. et al, 2001 pillared clays with other metal ions such as Ti, La, Y and Zr. There was a marked increase in the surface area and pore volume of the pillared clays regardless of the metal ion used for pillaring. Al-pillared and Zr-pillared clays exhibited higher microporosity than the Ti-pillared clay. The authors found that aluminum pillared clays prepared with an Al/clay ratio of above 10 mmol/g clay had a reduced surface area and thermal stability, which they attributed to the saturation of pillaring capacity by alumina. Calcination at 700 °C resulted in a decrease in the surface areas of the pillared clays due to the collapse or destruction of the micropores formed in the pore network of the clay. In the same study by Chae, H. et al, 2001, pillaring solutions of different OH/Al molar ratios (1.0 – 3.0) were prepared from 0.2 M NaOH and 0.2 M $AlCl_3$ solutions. After aging at room temperature for 24 h, the pillaring was carried out at different Al/clay ratios in the range from 3 to 20.

Manohar, D. M. et al, 2006 prepared aluminium-pillared bentonite clay (Al-PILC) using natural clay which contained almost 90% bentonite. The clay was converted into Na^+-MMT by washing several times, first with 1.0 M NaCl and then with deionised water. The washing process was then followed by drying the NaMMT properly before the pillaring process. The pillaring solution was prepared by titrating aqueous 0.5 M NaOH with aqueous 0.2 M $AlCl_3$·$6H_2O$ until the OH/Al ratio was equal to 2.4. It is reported by the authors (and many others) that at this hydrolysis ratio, Al_{13} is the major species in solution. After aging, the resulting solution was added to a 1% w/v aqueous suspension of Na-exchanged bentonite clay, keeping an Al/clay ratio at 20 mmol/g. An increase in the d-spacing, porosity and fluffiness of the clay after aluminum pillaring was observed. The authors reported that pillaring with oligomeric Al_{13} resulted in a more negative clay surface which helps in the adsorption of positively charged ions such as heavy metals through electrostatic interaction (Manohar, D. M. et al, 2006). The prepared Al-PILC was found to adsorb more Co (II) from aqueous solution compared with Na-bentonite. In fact, less Al-PILC was used to achieve a 100% removal of Co (II) than Na-bentonite.

During the pillaring process, the washing step is said to be necessary not only to remove anions from the clay, but also in the reorganization of the adsorbed or intercalated Al species and in the formation of the pillars (Storaro, L. et al, 1996). The more the number of washings, the more crystalline (the

sharper the basal reflection peak) the pillared clay becomes. The authors also observed that slow air drying below 60 °C before calcinations, removed most of the physisorbed water and leads to highly ordered materials. However, pillaring of the clay with an Al/Fe solution did not result in surface areas and porosities different from pillaring with pure Al_{13} solution.

De Carvalho, M. B. et al, 1996 characterized clays and aluminum-pillared clays by assessing the adsorption of probe molecules such as ethylene glycol, water, nitrogen, n-hexane, cyclohexane and triethylamine. The aluminum-pillared clays were prepared by first converting the raw clay to Na-form. The pillaring solution was prepared by adding 0.2 M NaOH solution to 0.2 M $AlCl_3$ solution. The authors then proceeded with the addition of the oligomer solution dropwise to a 0.5% aqueous suspension of clay at 80 °C under stirring. The solution was kept refluxing at 80 °C for 3 h and then at 25 °C overnight. The product was isolated by centrifuging and dialyzing. Calcination was then done at 350 °C. The clays were characterized by thermogravimetric analysis (TGA) and differential scanning calorimetry (DSC).

Tian, S. et al, 2009 investigated the adsorption of phosphate from water by lanthanum/aluminum pillared montmorillonite. Al-pillared clay (AlpMMT) was prepared by adding 1.0 M $NaCO_3$ solution dropwise to 0.5 M $AlCl_3.6H_2O$ solution at 60 °C and stirring for 2 h followed by aging the solution overnight at room temperature. Bentonite clay was then added under vigorous stirring at 60 °C. The mixture was stirred continuously for 5 h at 60 °C and then cooled to room temperature for the settling and separation of product. Lanthanum/aluminum pillared clay was prepared in more or less the same way and was found to adsorb 1.3 times more phosphate from aqueous solution than the aluminum pillared clay.

A study by Kloprogge, J. T. et al, 2002 assessed the preparation of Al-PILC from Australian smectites using $Al(NO_3)_3$ and NaOH as precursors for the pillaring solution. The pillaring solution had an OH/Al ratio of 2.2. An increase in the basal spacing and surface area of the smectites was observed after the pillaring process. Yuan, P. et al, 2006 investigated the synthesis and characterization of delaminated iron pillared clays with a meso-microporous structure. The pillaring solution was prepared from Na_2CO_3 and iron III nitrate and the OH/Fe molar ratio was varied during the pillaring process (in the range of 0.5-2.5). The iron pillaring solution was then added dropwise to a 2% clay suspension in water. The Fe/clay ratio was kept at 10 mmol/g of clay for all the samples. A large d-spacing of between 6.5 and 7.2 was obtained and the d-spacing was observed to increase with OH/Fe molar ratio. Also a significant increase in the surface area was observed for the pillared clays.

Mrad, I. et al, 1997 studied the optimum conditions for the preparation of aluminum pillared clays. Also assessed was the thermal stability and surface acidity of the pillared clays. The authors reported

obtaining samples of high surface area and thermal stability under the following conditions: OH/Al ratio of 2.0, pH 5.6 and an Al/clay ratio of 5 mmol/g of clay. Parameters such as amount of aluminum intercalated, surface area and porosity are said to depend on the presence of other aluminium Keggin ion species, the pH of the pillaring solution as well as on the Al/clay ratio.

Acemana, S. et al, 1999 used thermo-FTIR to investigate the changes that occur in clay after thermal treatment. KBr discs of the clay were gradually heated to 600 °C and the FTIR recorded after each 50 °C increment. The Keggin ion is reported to undergo dehydration, dehydroxylation and rearrangement which are observed from changes in the Al-O vibrations. At 550 °C, there is a condensation reaction of the dehydroxylated Keggin cation with Si-O-groups on the surface of the tetrahedral sheet, giving rise to new bands at 614 and 402 cm^{-1}. A similar study by Tichit, D. et al, 1988 came to the same conclusion of loss of hydration water through dehydroxylation with the preservation of the clay structure. The authors observed that microporosity as well as surface area decreased with calcination temperature.

The preparation of aluminium-pillared montmorillonite clay was also carried out in this study with the aim of producing high surface area Al-pillared clays with high adsorption capacities. Pillaring parameters such as pH, temperature, OH/Al molar ratio and Al/clay ratio were assessed. The procedure for the pillaring process and the results obtained from the characterisation of the Al-pillared samples are presented in Chapter 4.

Alkylammonium salts are also widely used for the modification of clays, thus making them hydrophobic or organocphilic. Organomodified clays are primarily essential in the development of polymer/clay nanocomposites. Organophilic clays are also used in other applications such as rheological control agents; paints; cosmetics; refractory varnish; thixotropic fluids and especially as adsorbents of organic pollutants in soil, water and air. Ion exchange with alkylammonium ions is widely known and is the preferential method for the preparation of organoclays.

The quaternary alkylammonium salts are cationic surfactants which are the most used organic compounds to prepare organoclays. They are synthesized by complete alkylation of ammonia or amines. For practical and industrial uses, quaternary alkylammonium ions are preferred to primary alkylammonium ions because hydrolysis (alkylammonium/alkylamine equilibrium) is absent, and desorption of free alkylamine is strongly reduced. A further advantage is that the large amount of organic material (30–40%) reduces the density of the dispersed particles (Favre, H. et al, 1991). This is an attractive property in the polymer industry where there is need to improve mechanical strength as well as maintain or if possible reduce the weight of the resultant nanocomposite.

Li, B. et al, 2009 prepared organophilic clays using a number of alkylammonium surfactants. Natural montmorillonite (MMT) was first suspended in 30 mL water. The alkylammonium salts were dissolved in pure alcohol, to which tetraethoxysilane (TEOS) had been added and the mixture was stirred for 0.5 h to get a clear solution. The prepared solution was added to the clay suspension dropwise. During this process, the TEOS and the cationic surfactants were intercalated into the interlayer regions simultaneously by ion exchange and solvation (Li, B. et al, 2009).

The organomodification of clays by alkyl ammonium surfactants for adsorption purposes may not be that attractive because of the danger of leaching of the surfactant molecules which can lead to secondary pollution problems. It would be more desirable to covalently or chemically attach the organic modifiers to the clays and avoid their leaching during application.

The following section describes the modification of clay minerals by using grafting reactions of organic groups.

2.6.2.2 Chemically-grafted montmorillonite clay

Only the 2:1 clay minerals (like montmorillonite) that provide the silanol and aluminol groups on the edge surface react with an organic agent through grafting reactions. Al and Si atoms exposed to the crystallite edges are partially hydrolyzed to silanol (SiOH) and aluminol (AlOH) groups. These unsaturated edge sites are much more reactive than the saturated basal sites (Bhattacharrya, K. G. et al, 2008). It can be said that more or less the same mechanisms described above for the chemical modification of lignocellulose through grafting also apply for the montmorillonite clay.

A lot of the grafting work reported in the literature used aminosilanes (Park, K. W. et al, 2004; Posthumus, W. et al, 2004; He, H. et al, 2005; Singh, R. P. et al, 2005; Dean, K. M. et al, 2007), isocyanates (Nishizawa, N. et al, 2005) and few articles report the use of polymers like poly (methyl) methacrylate and poly (methacrylic acid). A study by Park, K. W. et al, 2004 investigated the chemical modification of montmorillonite (MMT) clay by interlayer surface silylation using 3-aminopropyltriethoxysilane and dodecylamine in ethanol without a pre-swelling step. The authors also observed that layered materials with attached amine groups can be used as adsorbents of heavy metal ions, drug supports and photosensitive devices. They observed that the basal spacing of the modified MMT was observed to increase after silane grafting. The success of the grafting process was assessed by solid state ^{29}Si-CP-NMR spectroscopy.

Dean, K. M. et al, 2007 carried out a comparative study of ultraviolet-active silane grafted and ion-exchanged organoclay for application in photocurable urethane acrylate nano- and microcomposites. Daniel, L. M. et al, 2008 reported the grafting of dimethyl-octylmethoxysilane onto laponite clay. It

was observed that laponite possessed reactive hydroxyl groups on the edges in the form of Si-OH groups and within the interior of the clay sheets in the form of Mg-OH or Li-OH groups. The montmorillonite clay being used in this work also possesses these hydroxyl groups which serve as reaction centres during grafting with polymers or silanes.

He, H. et al, 2005 reported the grafting process of montmorillonite and a synthetic fluoro-hectorite with 3-aminopropyl trimethoxysilane (APS). After grafting, the basal spacings increased to 1.45 and 1.77 nm and indicated that the 3-aminopropyl triethoxysilane was intercalated. The silane molecules adopted a monolayer arrangement in the synthetic fluoro-hectorite and a bilayer arrangement in montmorillonite which demonstrates that the silylation reaction and the interlayer structure of the grafted products strongly depend on the clay mineral used. The grafting process was carried out in a mixture water/ethanol (25/75% v/v) solvent. The γ-APS was first introduced into a 1 L solvent mixture of water/ethanol and the temperature was kept at 80 °C. The clay was added into the above-mentioned solution and the grafting reaction was realized, under shearing, during five hours at 80 °C.

Herrera, N. N. et al, 2004 reported the grafting of laponite with monofunctional γ-methacryloxypropyl dimethyl methoxysilane and trifunctional γ-methacryloxypropyl trimethoxysilane (MPS) coupling agents. FTIR analysis showed evidence of covalent attachment of silane molecules to the hydroxyl groups. The tri-functional silane formed monolayer structure coverage at low concentrations and a multilayer structure at higher concentrations, while the monofunctional silane formed a monolayer.

MPS was also employed in the current study for the modification of montmorillonite and in the preparation of lignocellulose-montmorillonite nanocomposites.

Wang, L. et al, 2006 modified montmorillonite with γ-aminopropyl trimethoxysilane. The modified MMT was used for the preparation of epoxy nanocomposites. The authors observed a shift of the basal reflection peak to lower 2θ angles, which was attributed to the intercalation of the γ-aminopropyl trimethoxysilane and/or epoxy resin. The mechanism for the modification process is similar to that onto cellulose (Scheme 2.6).

Singh, R. P. et al, 2005 prepared silane-modified inorganic (Vycor glass) membranes. They assessed the effect of the silane layer structure on the gas separation properties of the resultant nanocomposite. Octadecyltricholorsilane membrane was found to be seven times more selective for *n*-butane over nitrogen than the dimethyloctadecylchlorosilane membrane. The authors also observed that the formation of an organosilane homopolymer layer on the inorganic supports can be avoided by carefully controlling the amount of water present in the reaction system or by using a mono-active silane. During their synthesis, the inorganic supports were dried overnight at 22 °C in a dessicator in

order to remove excess adsorbed water. The product was prepared in toluene (3% v/v of silane) and surface modification carried out at 22 °C for 3 h.

Posthumus, W. et al, 2004 investigated the grafting of 3-methacryloxypropyl trimethoxysilane (MPS) onto metal oxides. An aqueous dispersion (containing metal oxide), was mixed with a solvent mixture of methanol and water to ensure colloidal stability of both the modified and the unmodified particles. The required amount of MPS (ranging 1-20%) of the substrate was added after which the mixture was heated to reflux (approx 70 °C) for at least 4 h. The product was separated by centrifugation and washed with toluene to remove the homopolymers and unreacted MPS. Zhou, X. et al, 2009 reported the modification of silica particles with methacryloxypropyl trimethoxysilane. Silica was activated by heating at 150 ∘C for 12 h. MPS, activated silica and anhydrous toluene (250 mL) were reacted under reflux in an argon atmosphere. After 24 h of reflux, the MPS-treated silica was filtered off and extracted with dry toluene for 24 h to remove the unreacted MPS using a soxhlet apparatus. Then, the obtained MPS-functionalized silica was dried at 70 °C under vacuum overnight.

Sójka-Ledakowicz, J. et al, 2009 prepared alkoxysilane-grafted titanium dioxide for use in textiles. The surface modification of TiO_2 was conducted by using N-2-(aminoethyl)-3-aminopropyltrimethoxysilane or MPS. In order to avoid aging, the silanes were subjected to hydrolysis in a solution prepared directly before modification (methanol:water 4:1, v/v). The modification was performed in a specially constructed reactor in 1 h and the solvent was distilled off. Gultek, A. et al, 2001 also modified montmorillonite clay using MPS. The dried clay was suspended in a solution consisting of dried benzene and MPS. The mixture was stirred under dry N_2 at room temperature for 20 h and then refluxed under N_2 at 85°C by heating in an oil bath for another 24 h. The resulting mixture was distilled, the excess benzene and MPS were removed, and the resulting solid was extracted with methanol for 2 days. The remaining solid was dried under vacuum at room temperature for 16 h.

Arslan, G. et al, 2006 reported the surface modification of glass beads with an aminosilane monolayer. Prior to monolayer preparation, the glass beads were treated with boiling piranha solution (3:1 concentrated H_2SO_4:H_2O_2). The glass beads were rinsed with deionised water and dried followed by immersing in 1% (w/w) aminosilane (in anhydrous toluene) for 24 h with agitation. At the end of the coupling reaction, the glass beads were removed from the solution, followed by a sequence of two washes with anhydrous toluene, deionised water and ethanol were employed for the washing of the modified beads to remove any physisorbed aminosilane.

Many other researchers have reported the modification of clay minerals using some reactive organic groups (Nishizawa, N. et al, 2005; Wang, L. et al, 2006). The grafting of polymers, organic reactive

groups or silanes may follow different routes. During the grafting with silanes, it was suggested that the first stage entails the hydrolysis of the alkoxysilane which is then followed by a condensation reaction. The condensation reaction mechanism of the silane with the substrate is described Chapter 5. However, the grafting of organic polymers like poly (methacrylic acid) and poly (methyl methacrylate) follows a free-radical graft polymerization mechanism.

Ammonium and potassium persulfate are commonly used as free radical initiators in many graft polymerization reactions. It has been documented that the persulfate radical can attack the hydroxyl groups (-OH) on the surface of either lignocellulose or montmorillonite clay to generate what is called a macro-radical (Gangopadhyay, R. et al, 2000; Román-Aguirre, M. et al, 2004; Ojah, R. et al, 2006). The generation of the macroradical on the montmorillonite clay occurs as indicated in Equation 2.1. The grafting reaction is initiated by the macroradical and proceeds as illustrated for cellulose in Schemes 2.5 and 2.7.

$$ MMT{-}OH \; + \; SO_4^{-\cdot} \quad \longrightarrow \quad MMT{-}O^{\cdot} \; + \; HSO_4^{-} \qquad (2.1) $$
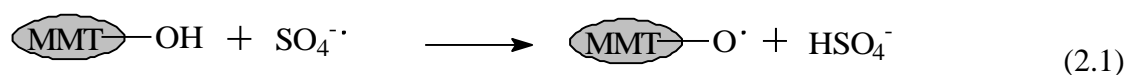
A more detailed mechanism for the generation of the macroradical and the subsequent graft polymerization of methyl methacrylate onto clay can be found in Section 5.6.1.1.

Poly (methyl methacrylate) (PMMA) graft polymerization onto montmorillonite was investigated by Atai, M. et al, 2008. The process involved emulsion polymerisation of MMA in the presence of NaMMT. After the grafting reaction, the authors extracted the homopolymer (pure PMMA) with tetrahydrofuran to give the PMMA-grafted MMT (Atai, M. et al, 2008). PMMA is the most widely researched and used polymer in aqueous solution. A study by Lin, R. Y. et al, 2009 reported the use of Na-MMT/polymethyl methacrylate (PMMA) ion exchange membranes for the adsorption of methyl violet dye. However, a low cation exchange capacity for the Na-MMT/PMMA nanocomposite membrane was obtained.

Liu, H. et al, 2008 reported the preparation and characterization of PMMA/flaky aluminium composite particle in the presence of MPS for use in aluminium pigments. The coupling of MPS onto aluminium particles was carried out at ambient temperature. The aluminium powder and MPS were dispersed in toluene through ultrasonication for about one hour. This was followed by the addition of hydroquinone and two drops of 2,6-dimethyl pyridine. The reaction mixture was refluxed under a N_2 atmosphere. The product was then soxhlet extracted with acetone for 72 h to remove the homopolymer and the ungrafted MPS. The MPS-modified aluminium was further reacted with methyl methacrylate in the presence of ammonium persulfate (as initiator) in order to graft the MMA to the

MPS-modified alumina. In this study, the preparation of PMMA-grafted lignocellulose, PMMA-grafted montmorillonite and PMMA-grafted lignocellulose-montmorillonite nanocomposite was successfully carried out in the absence of MPS.

Poly (methacrylic acid) (PMAA) was also used in this study for the modification of the montmorillonite and lignocellulose with the intention of improving their adsorption capacity for heavy metals. The PMAA, with its exposed –COOH groups, is expected to improve adsorption capacity relatively more compared with PMMA. MAA was grafted onto silica via a two-step grafting procedure, and the product was used for the adsorption of aniline from aqueous solution (An, F. et al, 2009). The first step involved the grafting of a reactive silane (MPS) onto the silica through a condensation reaction. After successfully grafting MPS onto the silica, a free-radical graft polymerization reaction of the MPS-modified silica and PMAA was carried out in the second step to give the PMAA-grafted silica particles. The PMAA-grafted silica was found to possess a high uptake of phenol. In another study, An, F. et al, 2010 assessed the adsorption of aniline onto the PMAA-grafted silica, and a high adsorption capacity was obtained.

Nanocomposites of PMAA and smectite clays have been reported by Singhal, R. et al, 2007. The nanocomposites of bentonite with PMAA were prepared for potential use in the absorption of toxic substances from waste water. However, such nanocomposites have not really demonstrated whether PMAA gets grafted covalently onto the clay structure or not. The nanocomposites were prepared by first modifying the bentonite with MPS, followed by the grafting of MAA. Chen, Y. et al, 2009 also used a similar two-step grafting process for the preparation of poly (acrylamide)-grafted palygorskite. The authors first modified the palygorskite with MPS, and then grafted the acrylamide onto the MPS-modified substrate.

Zhang, Z. et al, 2008 reported the preparation of α-alumina/poly (methacrylic acid) composite abrasive and its performance on a glass substrate. The alumina was first activated by grafting with MPS in toluene followed by graft polymerization with methacrylic acid in water using ammonium persulfate as an initiator. Another study by Wang, W., 2011 reported the grafting of PMAA onto silica and its use as an adsorbent for Cd^{2+} from aqueous solution. The authors employed more or less the same procedure as described by An, F. et al, 2010. A similar procedure as used by An, F. et al, 2010 and Wang, W., 2011 was used in the current study for the preparation of PMAA-grafted montmorillonite, PMAA-grafted lignocellulose and PMAA-grafted lignocellulose-montmorillonite nanocomposites reported in Sections 5.2.3, 5.3.3 and 5.4.3.

The following section describes the use of nanocomposite adsorbents in water treatment, preparation of nanocomposites and the different types (morphologies) of nanocomposites that can be obtained.

2.7 Nanocomposite adsorbents

It has already been highlighted in Chapter 1 that nanotechnology based methods are also being explored and applied in water treatment and purification. Nanotechnology based methods for water purification, if well developed, have the potential to produce highly purified water at low cost (Savage, N. et al, 2005).

Savage, N. et al, 2005 published a review on the application of nanomaterials in water treatment and purification, and also the challenges facing the widespread use of nanomaterials in the water treatment industry. The authors cited the development and use of many nanoadsorbents such as carbon nanotubes (for adsorbing Pb^{2+} and Cd^{2+}), zeolites (for adsorbing heavy metals from acid mine drainage), carbon nanotubes-supported cerium oxide (arsenate, As (V)) activated carbon fibres (benzenes), alginate/carbon nanotubes composites (dyes) and layered double hydroxides (chlorinated alkenes) in water treatment. Jin, S. et al, 2007 investigated the use of layered double hydroxide (LDH) nanocomposites for the removal of viruses and bacteria from water. The LDH nanocomposites had a viral and bacterial removal efficiency of greater than 99%.

Jeong, B. H. et al, 2007 reported the preparation of mixed matrix reverse osmosis membranes by interfacial polymerization of nanocomposite thin films in situ on porous polysulfone supports. The nanocomposite films contained zeolite NaA nanoparticles dispersed within polyamide films. The prepared nanocomposites had almost double pure water permeability and equal pollutant rejection levels compared with other reverse osmosis membranes.

Salipira, K. L. et al, 2007 reported the preparation and evaluation of cyclodextrin-carbon nanotubes nanocomposites for the removal of *p*-nitrophenol from aqueous solution. The nanocomposite adsorbent gave a removal efficiency of about 99%, which was greater than that obtained for the cyclodextrin polymer (58%) or activated carbon (47%) separately. The improvement might be due to a synergistic effect between the cyclodextrin and the carbon nanotubes. Salehi, R. et al, 2010 prepared a chitosan-ZnO biocompatible composite for the removal of dyes (direct blue 78 and acid black 26) from aqueous solution.

Khaydarov, R. A. et al, 2010 reported the preparation of nanocarbon-conjugated polymer nanocomposites using nanocarbon colloids and poly (ethylenimine) and their use in the removal of heavy metals from aqueous solution. The authors found removal efficiencies of greater than 99% for Cd^{2+}, Cu^{2+}, Ni^{2+}, Hg^{2+} and Zn^{2+}. Lin, Y. et al, 2006 prepared an electrically controllable ion-exchange

nanocomposite membrane based on poly (pyrrole) and carbon nanotubes and evaluated the nanocomposite membrane for the removal of perchlorate ions from aqueous solution.

Wang, L. et al, 2007 investigated the adsorption of Congo red dye onto chitosan/montmorillonite nanocomposite. The investigators observed that the nanocomposites had improved uptake of the dye than the montmorillonite or chitosan separately. This might mean a synergistic effect as a result of bringing the chitosan and the montmorillonite together.

In a study by Ake, C. L. et al, 2001, MMT clay was immobilized on activated carbon using an aqueous solution of hydroxycarboxymethyl cellulose. The composite material exhibited enhanced adsorption capacity for lead compared to activated carbon or MMT clay alone. In another study by Ake, C. L. et al, 2003, sand-immobilized cetylpyridinium-exchanged low pH montmorillonite (MMT) clay was used. This showed improved removal capacity of greater than 99% for naphthalene and pentachlorophenol.

It can be seen from the above cited literature and many other articles that nanocomposites hold the potential of giving highly treated and pure waste water effluents. The major hindrance in the widespread application of nanotechnology is the unavailability of a large quantity of nanomaterials at economically viable prices (Savage, N. et al, 2005). Therefore, the search for highly effective, efficient and low cost nanoadsorbent materials for water treatment and purification is an on-going challenge.

Lignocellulose and montmorillonite clay have been identified as low cost, and potentially effective and efficient adsorbents materials. This study seeks to prepare nanocomposites based on lignocellulose (biopolymer) and montmorillonite clay (nanoclay) and evaluate the same for the adsorption of both organic and inorganic pollutants from aqueous solution. The following section reviews the literature on both the preparation and application of lignocellulose-clay nanocomposites.

2.8 Lignocellulose-montmorillonite nanocomposites

It has been mentioned in Chapter 1 that lignocellulose-montmorillonite nanocomposites are widely researched for application in structural materials especially in the furniture industry as well as the packaging industry. However, there is no literature available thus far on the use of lignocellulose-clay nanocomposites as adsorbent materials for the removal of inorganic and organic pollutants from aqueous solution. Before reviewing some of the literature on the preparation and application of

lignocellulose-clay nanocomposites, the following section will describe the different types of nanocomposites or the different nanocomposite morphologies that can be obtained.

2.8.1 Types of nanocomposites

According to Alexandre, M. et al, 2000, there are three main types of composites that may be formed when a layered silicate is associated with a polymer. The type of composite formed mainly depends on the nature of the components used (i.e. layered silicate, organic cation, polymer) and also the method of preparation. Figure 2.8 below shows the different types of composites that can be formed from the interaction of layered silicates with polymers.
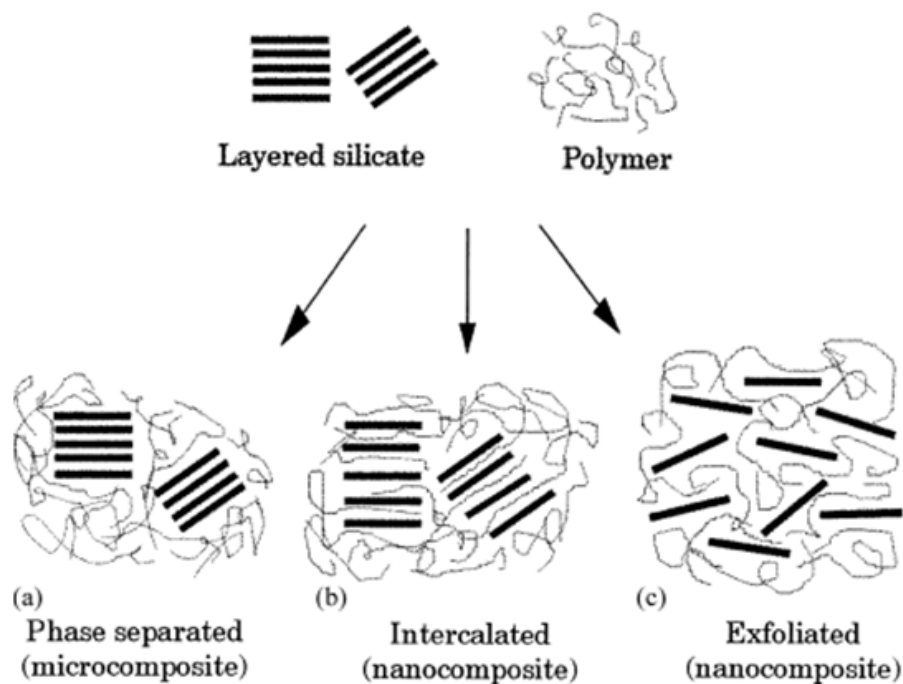

Figure 2.8: Schemes of different types of composites arising from the interaction of layered silicates and polymers (Alexandre, M. et al, 2000).

2.8.1.1 Microcomposites

When the polymer is unable to intercalate between the silicate layers, a phase separated composite is obtained (see Figure 2.8a above). The properties of a phase separated composite stay in the same range as traditional microcomposites (i.e. conventional composites). Di Gianni, A. et al, 2008 reported that conventional microcomposites are characterized by stakes of silicate layers dispersed at a microscale inside the polymer matrix. Beyond this classical family of composites, two types of nanocomposites are obtained, intercalated and exfoliated nanocomposites (Gilman, J. W. et al, 2000).

2.8.1.2 Intercalated nanocomposites

Intercalated nanocomposites are obtained when at least one polymer chain is intercalated between the silicate layers resulting in a well ordered multilayer morphology built up of alternating organic and inorganic layers (see Figure 2.8b above). According to Gilman, J. W. et al, 2000 intercalated structures are self-assembled, well-ordered multilayered structures where the extended polymer chains are inserted into the gallery space between parallel individual silicate layers separated by 2-3 nm. The long range order of silicate layers is maintained in intercalated nanocomposites (Di Gianni, A. et al, 2008).

2.8.1.3 Exfoliated or delaminated nanocomposite

As shown in Figure 2.8c, exfoliated nanocomposites are obtained when the silicate layers are completely and uniformly dispersed in a continuous polymer matrix (Alexandre, M. et al, 2000). The clay platelets are no longer ordered, but delaminated and distributed homogeneously throughout the polymer matrix. The best final properties are achieved when the clay mineral platelets are fully exfoliated and well dispersed in the polymer matrix (Di Gianni, A. et al, 2008).

2.8.2 Preparation of lignocellulose-clay nanocomposites

A review by Ray, S. S. et al, 2005 revealed that the commonly used techniques for the preparation of nanocomposites are: intercalative solution blending, *in situ* intercalative polymerization and melt intercalation method. A detailed description of these methods is given in the sections below.

2.8.2.1 Intercalative solution blending

This technique involves dissolving the polymer or dispersing the organically modified MMT in a suitable solvent, followed by addition of either the modified MMT or the polymer under high shear mixing or sonication. This is one of the approaches said to consistently give exfoliated materials, provided the clay organic treatment, suitable solvents and blending are used. Morgan, A. B. et al, 2004 synthesized exfoliated polystyrene-clay nanocomposites by the method of solvent blending with sonication. Gilman, J. W. et al, 2000 prepared poly (styrene)-layered silicate nanocomposite via solution blending and observed intercalated nanocomposites. This method was not employed in this study because of difficulties in getting a suitable solvent system for lignocellulose, with a low possibility of chemical bonding between the montmorillonite and the lignocellulose.

2.8.2.2 Melt intercalation

This is achieved by heating the mixture of polymer and silicate clay powder above the polymer glass transition or melt temperature. This results in sufficient polymer mobility thus allowing chains to diffuse into host layered silicate clay galleries. This produces an expanded polymer-silicate layer structure. Most reports in the literature on the preparation of lignocellulose-clay nanocomposites have

used the melt intercalation method. The technique was used by Fornes, T. D. et al, 2002 when they evaluated the effect of matrix molecular weight on nylon-6/clay nanocomposites. According to Chang, J. H. et al, 2003 melt intercalation is carried out by mixing a molten polymer matrix with the layered silicate clay. If the silicate surfaces are sufficiently compatible with the chosen polymer, then the polymer can enter the interlayer space and form an intercalated or exfoliated nanocomposite. The melt intercalation method has been shown to also give exfoliated nanocomposites depending on conditions such as polymer compatibility with the layered silicate, as well as the blending conditions.

Kord, B. et al, 2010 investigated the properties (mechanical, water absorbency, morphology, tensile strength, modulus) of poly (propylene)/wood flour/organophilic clay nanocomposites. The materials were prepared by melt blending. First, poly (propylene) was fed to the mixing chamber. After it was melted, the coupling agent and montmorillonite were added. After 5 min, wood flour (beech wood) was added and the total mixing time was 13 min. The compounded materials were then ground. Liao, H. T. et al, 2005 prepared poly (ethylene-octene) elastomer-clay-wood flour nanocomposites by melt blending. An improvement in the mechanical and tensile strength as well as the thermal stability of the resultant nanocomposites was observed. The nanocomposites were directed at structural materials like furniture boards and flooring materials.

Jiang, H. et al, 2004 published a review on poly (vinyl chloride)/wood composites. The authors observed that the use of poly (vinyl chloride)/wood nanocomposites is on the increase, with greater application in window or door profiles, decking, railings, etc. Poly [methylene-(polyphenyl isocyanate)], aminopropyltriethoxysilane, maleated polypropylene, and copper metallic complex have proved to be effective coupling agents for this composite system. The advantages of wood include low density, low equipment abrasiveness, relatively low cost, and good biodegradability. Zhao, Y. et al, 2006 described the preparation of poly (vinyl chloride)/wood flour/montmorillonite nanocomposites and assessed the effects of coupling agents and amount of layered silicate. The composites were prepared by melt blending the poly (vinyl chloride), silane modified wood flour and the layered silicate in a twin-screw extruder.

Melt blending has been the method of choice especially when preparing lignocellulose-clay nanocomposites. However, looking at the application of the lignocellulose-clay nanocomposites in this study, it would be important not to block or close up the adsorption sites of the lignocellulose and the interlayer galleries of the clay particles (especially when a polymer is used) in order to allow for maximum interaction with pollutant molecules after the coupling of the lignocellulose to the clay. It is also necessary to aim for covalent bonding of the polymer to both the lignocellulose and the clay to avoid leaching of the polymer (especially water soluble polymers like poly (methacrylic acid)) into solution which would cause secondary pollution problems. In view of the above highlighted concerns

and the inaccessibility of the melt blending equipment, this method could not be employed in this study.

2.8.2.3 In-situ intercalative polymerization

This technique (emulsion polymerization) involves clay organic treatments that have functional groups with which the polymer monomer can either co-polymerize with, or begin polymerization initiation at the organic treatment site (Morgan, A. B. et al, 2004). In situ intercalative polymerization relies on the swelling of the organoclay due to the monomer followed by in situ polymerization initiated thermally or by the addition of a suitable initiator. The polymer chain growth in the clay galleries triggers clay exfoliation and nanocomposite formation (Chang, J. H. A. et al, 2003).

The method employed in this study can be viewed as a modified in situ intercalative polymerization method. Monomers (polymers) where used as coupling agents, which served as bridges between the lignocellulose and the montmorillonite clay. In addition, in order to avoid the leaching of soluble polymeric units and to further clean the nanocomposite absorbents, the prepared nanocomposites were soxhlet-extracted with different solvents depending on the monomer used. It is postulated that MMT clay particles get covalently attached to lignocellulose to create some kind of a brush with the MMT particles sticking out for adsorption of pollutants from aqueous solution. The preparation of the lignocellulose-montmorillonite nanocomposites is described in Chapter 5.

2.9 Conclusion

Lignocellulose and montmorillonite clay can serve as low cost adsorbent materials for the removal of both heavy metals and organic pollutants from water. Different modifications can be performed on both lignocellulose and montmorillonite in order to enhance their adsorption properties. Metal oxide pillaring of montmorillonite can potentially improve its adsorption capacity for both inorganic and organic pollutants. The grafting of organic groups to both lignocellulose and montmorillonite was found to influence their adsorption properties towards different pollutants. One way of possibly improving the adsorption properties of these materials is to prepare composites of the same in which the nanoclay (montmorillonite) is uniformly dispersed and covalently bonded in the lignocellulosic (biopolymer) matrix.

Chapter 3 gives an overview of the experimental procedures employed in the preparation of the adsorbents evaluated in this study. Also presented are the analytical techniques used in the characterization of all the adsorbents prepared.

2.10 References

1. Abate, G.; Masini, J. C. Influence of pH, ionic strength and humic acid on adsorption of Cd(II) and Pb(II) onto vermiculite. *Colloids and Surfaces A: Physicochemical Engineering Aspects*, **2005**, *262*, 33–39.

2. Abdelmouleh, M.; Boufi, S.; Belgacemb, M. N.; Duarte, A. P. Ben Salah, A.; Gandini, A. Modification of cellulosic fibres with functionalised silanes:development of surface properties. *International Journal of Adhesion & Adhesives*, **2004**, *24*, 43–54.

3. Abollino, O.; Aceto, M.; Malandrino, M.; Sarzanini, C.; Mentasti, E. Adsorption of heavy metals on Na-montmorillonite: Effect of pH and organic substances. *Water Research*, **2003**, *37*, 1619–1627.

4. Acemana, S.; Lahava, N.; Yarivb, S. A thermo-FTIR-spectroscopy analysis of Al-pillared smectites differing in source of charge, in KBr disks. *Thermochimica Acta*, **1999**, *340-341*, 349-366.

5. Ahmad, A.; Rafatullah, M.; Sulaiman, O.; Ibrahim, M. H.; Chii, Y. Y.; Siddique, B. M. Removal of Cu(II) and Pb(II) ions from aqueous solutions by adsorption on sawdust of *Meranti* wood. *Desalination*, **2009**, *250*, 300-310.

6. Ahmaruzzaman, M. Adsorption of phenolic compounds on low-cost adsorbents: A review. *Advances in Colloid and Interface Science*, **2008**, *143*, 48–67.

7. Ake, C. L.; Mayura, K.; Huebner, H. J.; Bratton, G. R.; Phillips, T. D. Development of clay-based composites for the sorption of lead from water. *Journal of Toxicology and Environmental Health Part A*, **2001**, *63*, 459–475.

8. Ake, C. L.; Wiles, M. C.; Huebner, H. J.; MacDonald, T. J.; Cosgriff, D.; Richardson, M. B.; Donelly, K. C.; Phillips, T. D.; *Chemosphere*, **2003**, *51*, 835-844

9. Aksu, Z.; Yener, J. A comparative adsorption/biosorption study of mono-chlorinated phenols onto various sorbents. *Waste Management*, **2001**, *21* (8), 695-702.

10. Alexandre, M.; Dubois, P. Polymer-layered silicate nanocomposites: preparation, properties and uses of a new class of materials. *Materials Sciences and Engineering*, **2000**, *28*, 1-63.

11. Alexandre, M.; Dubois, P. Polymer-layered Silicate Nanocomposites: Preparation, Properties and Uses of a New Class of Materials. *Materials Sciences and Engineering*, **2000**, *28*, 1-63.

12. Almeida, C. A. P.; Debacher, N. A.; Downs, A. J.; Cottet, L.; Mello, C. A. D. Removal of methylene blue from colored effluents by adsorption on montmorillonite clay. *Journal of Colloid and Interface Science*, **2009**, *332*, 46–53.

13. Altin, O.; Özbelge, H. Ö.; Doğu, T. Use of general purpose adsorption isotherms for heavy metal–clay mineral interactions. *Journal of Colloid and Interface Science*, **1998**, *198*, 130–140.

14. Altunlu, M.; Yapar, S. Effect of OH^-/Al^{3+} and Al^{3+}/clay ratios on the adsorption properties of Al-pillared bentonites. *Colloids and Surfaces A: Physicochemical and Engineering Aspects,* **2007***, 306,* 88-94.

15. An, F.; Feng, X.; Gao, B. Adsorption property and mechanism of composite adsorbent $PMAA/SiO_2$ for aniline. *Journal of Hazardous Materials*, **2010**, *178*, 499–504.

16. An, F.; Gao, B.; Feng, X. Adsorption mechanism and property of novel composite material $PMAA/SiO_2$ towards phenol. *Chemical Engineering Journal*, **2009**, *153*, 108–113.

17. Anbia, M.; Hariri, S. A.; Ashrafizadeh, S. N. Adsorptive removal of anionic dyes by modified nanoporous silica SBA-3. *Applied Surface Science*, **2010**, *256*, 3228–3233.

18. Annabi-Bergaya, F. Layered clay minerals: Basic research and innovative composite applications. *Microporous and Mesoporous Materials*, **2008**, *107*, 141–148.

19. Annadurai, G.; Juang, R. S.; Lee, D. J. Use of cellulose-based wastes for adsorption of dyes from aqueous solutions. *Journal of Hazardous Materials*, **2002**, *B92*, 263–274.

20. Antizar-Ladislao, B.; Galil, N. I. Biosorption of phenol and chlorophenols by acclimated residential biomass under bioremediation conditions in a sandy aquifer. *Water Research*, **2004**, *38*, 267–276.

21. Aouad, A..; Mandalia, T.; Bergaya, F.; A novel method of Al-pillared montmorillonite preparation for potential industrial up-scaling. *Applied Clay Science,* **2005**, *28,* 175–182.

22. Arief, V. O.; Trilestari, K.; Sunarso, J.; Indraswati, N.; Ismadji, S. Recent Progress on biosorption of Heavy Metals from Liquids Using Low Cost Biosorbents: Characterization, Biosorption Parameters and Mechanism Studies. *Clean*, **2008**, *36* (12), 937 – 962.

23. Arslan, G.; Özmen, M.; Gündüz, B.; Zhang, X.; Ersöz, M. Surface Modication of Glass Beads with an Aminosilane Monolayer. *Turkish Journal of Chemistry*, **2006**, *30*, 203-210.

24. Atai, M.; Solhi, L.; Nodehi, A.; Mirabedini, S. M.; Kasraei, S.; Akbari, K.; Babanzadeh, S. PMMA-grafted nanoclay as novel filler for dental adhesives. *Dental Materials*, **2009**, *25*, 339–347.

25. Awala, H. A.; El Jamal, M. M. Equilibrium and kinetics study of adsorption of some dyes onto feldspar, *Journal of the University of Chemical Technology and Metallurgy,* **2011**, *46* (1)*,* 45-52.

26. Ayari, F.; Srasra, E.; Trabelsi-Ayadi, M. Retention of lead from aqueous solution by bentonite as an adsorbent for reducing leaching from industrial effluents. *Desalination*, **2007**, *206*, 270-278.

27. Baig, T. H.; Garcia, A. E.; Tiemann, K. J.; Gardea-Torresdey, J. L. Adsorption of heavy metal ions by the biomass of *Solanum Elaeagnifolium* (silverleaf nightshade). *Proceedings of the 1999 Conference on Hazardous Waste Research.*

28. Bajpai, S. K.; Rohit, V. K. Cation exchanger saw dust (cesd) as an effective sorbent for removal of Cu (II) from aqueous solution. *Electronic Journal of Environmental, Agricultural and Food Chemistry*, **2007**, *6* (5), 2053-2055.

29. Banat, F. A.; Al-Bashir, B.; Al-Asheh, S.; Hayajneh, O. Adsorption of phenol by bentonite. *Environmental Pollution*, **2000**, *107*, 391-398.

30. Baral, S. S.; Das, S. N.; Rath, P. Hexavalent chromium removal from aqueous solution by adsorption onto treated sawdust. *Biochemical Engineering Journal*, **2006**, *31* (3), 216-222.

31. Barbier, F.; Duc, G.; Petit-Ramel, M. Adsorption of lead and cadmium ions from aqueous solution to the montmorillonite/water interface. *Colloids and Surfaces A: Physicochemical and Engineering Aspects*, **2000**, *166*, 153–159.

32. Batchelor, B. Leach models for contaminants immobilized by pH dependent mechanisms. *Environmental Science and Technology*, **1998**, *32* (11), 1721–1726.

33. Batzias, F. A.; Sidiras, D.K. Dye adsorption by prehydrolysed beech sawdust in batch and fixed-bed systems. *Bioresource Technology*, **2007**, *98*, 1208–1217.

34. Bello, O. S.; Oladipo, M. A.; Olatunde, A. M. Sorption studies of lead ions onto activated carbon produced from oil-palm fruit fibre. *Stem Cell*, **2010**, *1* (1), 15-30.

35. Bhatnagar, A.; Sillanpaa, M. Utilization of agro-industrial and municipal waste materials as potential adsorbents for water treatment - A review. *Chemical Engineering Journal*, **2010**, *157*, 277–296.

36. Bhattacharyya, K. G., Gupta, S. S. Influence of acid activation of kaolinite and montmorillonite on adsorptive removal of Cd (II) from water. *Industrial & Engineering Chemistry Research*, **2007**, *46,* 3734-3742.

37. Bhattacharyya, K. G.; Gupta, S. S. Adsorption of a few heavy metals on natural and modified kaolinite and montmorillonite: A review. *Advances in Colloid and Interface Science*, **2008**, *140*, 114–131.

38. Bianchi, E.; Marsano, E.; Ricco, L.; Russo, S. Free radical grafting onto cellulose in homogeneous conditions 1. Modified cellulose–acrylonitrile system. *Carbohydrate Polymers*, **1998**, *36*, 313–318.

39. Bouchenafa-Saïb, N.; Khouli, K.; Mohammedi, O. Preparation and characterization of pillared montmorillonite: application in adsorption of cadmium. *Desalination,* **2007**, *217*, 282–289.

40. Breen, C.; Watson, R. Polycation-Exchanged Clays as Sorbents for Organic Pollutants: Influence of Layer Charge on Pollutant Sorption Capacity. *Journal of Colloid and Interface Science*, **1998**, *208*, 2 (15), 422-429.

41. Bulut, Y.; Aydin, H. A kinetics and thermodynamics study of methylene blue adsorption on wheat shells. *Desalination*, **2006**, *194* (1-3), 259-267.

42. Cao, F.; Bai, P.; Li, H.; Ma, Y.; Deng, X.; Zhao, C. Preparation of polyethersulfone–organophilic montmorillonite hybrid particles for the removal of bisphenol A. *Journal of Hazardous Materials*, **2009**, *162*, 791-798.

43. Castellano, M; Gandini, A.; Fabbri, P.; Belgacem, M. N.; Modification of cellulose fibres with organosilanes: Under what conditions does coupling occur? *Journal of Colloid and Interface Science*, **2004**, *273*, 505–511.

44. Chae, H. J.; Nam, I.-S.; Ham, S. W.; Hong, S. B. Physicochemical characteristics of pillared interlayered clays. *Catalysis Today*, **2001**, *68,* 31-40.

45. Chang, J. H. A.; Y. U.; Kim, S. J.; Im, S.; Poly(butylene terephthalate)/organoclay nanocomposites prepared by in situ interlayer polymerization and its fiber (II). *Polymer*, **2003**, *44*, 5655-5661.

46. Chen, S.; Zhang, J.; Zhang, C.; Yue, Q.; Li, Y.; Li, C. Equilibrium and kinetic studies of methyl orange and methyl violet adsorption on activated carbon derived from *Phragmites australis*. *Desalination*, **2010**, *252*, 149–156.

47. Chen, Y. G.; Ye, W. M.; Yang, X. M.; Deng, F. Y.; He, Y. Effect of contact time, pH, and ionic strength on Cd(II) adsorption from aqueous solution onto bentonite from Gaomiaozi, China. *Environmental and Earth Science,* 2010, 1-8. DOI 10.1007/s12665-010-0850-6.

48. Chen, Y.; Zhao, Y.; Zhou, S.; Chu, X.; Yang, L.; Xing, W. Preparation and characterization of polyacrylamide/palygorskite. *Applied Clay Science*, **2009**, *46*, 148–152.

49. Chmielewská, E.; Gáplovská, K.; Molnár, D.; Polakovičová, G.; Nagyová, S. Validity of adsorption efficiency of new combined zeolite based adsorbents towards petroleum, azodyes and some oxyanionic pollutants. *Petroleum & Coal*, **2010**, *52* (1), 25-30.

50. Crini, G. Recent developments in polysaccharide-based materials used as adsorbents in wastewater treatment. *Progress in Polymer Science*, **2005**, *30*, 38–70.

51. Dabrowski, A. Adsorption - from theory to practice. *Advances in Colloid and Interface Science*, **2001**, 93, 135-224.

52. Daniel, L. M.; Frost, R. L.; Zhu, H. Y. Edge-modification of laponite with dimethyl-octylmethoxysilane. *Journal of Colloidal & Interface Science*, **2008**, *321* (2), 302-309.

53. De Carvalho, M. B.; Pires, J.; Carvalho, A. P. Characterisation of clays and aluminium pillared clays by adsorption of probe molecules. *Microporous Materials*, **1996**, *6* (2), 65-77.

54. de Paiva, L. B.; Morales, A. R.; Valenzuela-Díaz, F. R. Organoclays: Properties, preparation and applications. *Applied Clay Science*, **2008,** *42*, 8-24.

55. Dean, K. M.; Bateman, S. A.; Simons, R. A comparative study of UV active silane-grafted and ion-exchanged organo-clay for application in photocurable urethane acrylate nano- and micro-composites. *Polymer*, **2007**, *48*, 2231-2240.

56. Denizli, A.; Cihangir, N.; Tüzmen, N.; Alsancak, G. Removal of chlorophenols from aquatic systems using the dried and dead fungus *Pleurotus sajor caju*. *Bioresource Technology*, **2005**, *96*, 59–62.

57. Di Gianni, A.; Amerio, E.; Monticelli, O.; Bongiovanni, R. Preparation of polymer/clay mineral nanocomposites via dispersion of silylated montmorillonite in a UV curable epoxy matrix. *Applied Clay Science*, **2008**, *42*, 116–124.

58. Duncan, J. R.; Stoll, A.; Wilhelmi, B.; Zhao, M. and van Hille, R. *Department of Biochemistry and Microbiology, Rhodes University, South Africa*. (**2003**) (WRC Report No. 616/1/03).

59. Elizalde-González, M. P.; Mattusch, J.; Wennrich, R. Chemically modified maize cobs waste with enhanced adsorption properties upon methyl orange and arsenic. *Bioresource Technology*, **2008**, *99*, 5134–5139.

60. Faghihian, H.; Nejati-Yazdinejad, M. A comparative study of the sorption of Cd(II) and Pb(II) ions from aqueous solution by local bentonite and clinoptilolite. *Adsorption Science & Technology*, **2009**, *27* (1)*, 107-115.*

61. Favre, H.; Lagaly, G. Organo-bentonites with quaternary alkylammonium ions. *Clay Minerals*, **1991**, *26*, 19-32.

62. FitzPatrick, M.; Champagne, P.; Cunningham, M. F.; Whitney, R. A. A biorefinery processing perspective: Treatment of lignocellulosic materials for the production of value-added products. *Bioresource Technology*, **2010**, *101*, 8915–8922.

63. Fornes, T. D.; Yoon, P. J.; Hunter, D. L., Keskkula, H.; Paul, D. R. Effect of organoclay structure on nylon 6 nanocomposite morphology and properties. *Polymer*, **2002**, *43* (22), 5915-5933.

64. Gaballah, I.; Kilbertus, G. Recovery of heavy metal ions through decontamination of synthetic solutions and industrial effluents using modified barks. *Journal of Geochemical Exploration*, **1998**, *62* (1-3), 241-286.

65. Gangopadhyay, R.; Ghosh, P. Uncatalysed photografting of poly(methyl methacylate) from photofunctionalised sisal fibre. *European Polymer Journal*, **2000**, *36*, 1597-1606.

66. Garg, V. K.; Kumar, R.; Gupta, R. Removal of malachite green dye from aqueous solution by adsorption using agro-industry waste: a case study of *Prosopis cineraria*. *Dyes and Pigments*, **2004**, *62*, 1–10.

67. Gilman, J. W.; Jackson, C. L.; Morgan, A. B.; Harris, R. (Jr); Manias, E.; Giannelis, E. P.; Wuthenow, M.; Hilton, D.; Phillips, S. H. Flammability properties of polymer-layered-silicate nanocomposites. Polypropylene and polystyrene nanocomposites. *Chemical Materials.* **2000**, *12,* 1866-1873.

68. Gong, R. Liu, Y.; Jiang, Y.; Li, C. Isothermal, kinetic and thermodynamic studies on basic dye sorption onto tartaric acid esterified wheat straw. *African Journal of Biotechnology*, **2009**, *8* (24), 7138-7147.

69. Gong, R.; Zhong, K.; Hu, Y.; Chen, J.; Zhu, G. Thermochemical esterifying citric acid onto lignocellulose for enhancing methylene blue sorption capacity of rice straw. *Journal of Environmental Management*, **2008**, *88*, 875–880.

70. Gultek, A.; Seckin, T.; Onal, Y.; Icduygu, M. G. Preparation and phenol captivating properties of polyvinylpyrrolidone-montmorillonite hybrid materials. *Journal of Applied Polymer Science*, **2001**, *81*, 512–519.

71. Gupta, N.; Prasad, M.; Singhal, N.; Kumar, V. Modeling the adsorption kinetics of divalent metal ions onto pyrophyllite using the integral method. *Industrial Engineering and Chemical Research*, **2009**, *48,* 2125–2128.

72. Halttunen, T.; Salminen, S.; Tahvonen, R. Rapid removal of lead and cadmium from water by specific lactic acid bacteria. *International Journal of Food Microbiology*, **2007**, *114*, 30–35.

73. Hameed, B. H.; Mahmoud, D. K.; Ahmad, A. L. Sorption equilibrium and kinetics of basic dye from aqueous solution using banana stalk waste. *Journal of Hazardous Materials*, **2008**, *158*, 499–506.

74. Han, R.; Wang, Y.; Han, P.; Shi, J.; Yang, J.; Lu, Y. Removal of methylene blue from aqueous solution by chaff in batch mode. *Journal of Hazardous Materials*, **2006**, *B137*, 550–557.

75. Han, R.; Zhang, J.; Zou, W.; Shi, J.; Liu, H. Equilibrium biosorption isotherm for lead ion on chaff. *Journal of Hazardous Materials*, **2005**, *B125*, 266–271.

76. Hanberg, A. Toxicology of environmentally persistent chlorinated organic compounds. *Pure and Applied Chemistry*, **1996**, *68* (9), 1791-1799.

77. Haque, E.; Jun, J. W.; Jhung, S. H. Adsorptive removal of methyl orange and methylene blue from aqueous solution with a metal-organic framework material, iron terephthalate (MOF-235). *Journal of Hazardous Materials*, **2011**, *185*, 507–511.

78. Haris, M. R. H. M.; Sathasivam, K. The Removal of methyl red from aqueous solutions using modified banana trunk fibers. *Archives of Applied Science Research*, **2010**, *2* (5), 209-216.

79. He, H.; Duchet, J.; Galy, J.; Gerard, J. F. Grafting of Swelling Clay Materials with 3-aminopropyltriethoxysilane. *Journal of Colloid and Interface Science,* **2005**, *288* (1), 171-176.

80. Hefne, J. A.; Mekhemer, W. K.; Alandis, N. M.; Aldayel, O. A.; Alajyan, T.. Kinetic and thermodynamic study of the adsorption of Pb (II) from aqueous solution to the natural and treated bentonite. *International Journal of Physical Sciences*, **2008**, *3* (11), 281-288.

81. Hernández-Meléndez, O.; Peydecastaing, J.; Bárzana, E.; Vaca-Garcia, C.; Hernández-Luna, M.; Borredon, M. E. Graft polymerization of wood sawdust and peat with ethylene

carbonate. A novel method for the preparation of supports with enhanced mechanical properties to be used in biofiltration of organic vapors. *Bioresource Technology*, **2009**, *100*, 737–743.

82. Herrera, N. N.; Letoffe, J. M.; Reymond, J. P.; Bourgeat-Lami, E. Silylation of laponite clay particles with monofunctional and trifunctional vinyl alkoxysilanes. *Journal of Materials Chemistry*, **2005**, *15*, 863–871.

83. Hill, C. A. S.; Cetin, N. S. Surface activation of wood for graft polymerisation. *International Journal of Adhesion and Adhesives*, **2000**, *20*, 71-76.

84. Houari, M.; Hamdi, B.; Brendle, J.; Bouras, O.; Bollinger, J.C.; Baudu, M. Dynamic sorption of ionizable organic compounds (IOCs) and xylene from water using geomaterial-modified montmorillonite. *Journal of Hazardous Materials*, **2007**, *147* (3), 738-745.

85. Howard R. L.; Abotsi E.; van Rensburg E. L. J.; Howard S. Lignocellulose biotechnology: issues of bioconversion and enzyme production. *African Journal of Biotechnology*, **2003**, *2* (12), 602-619.

86. http://www.doitpoms.ac.uk/tlplib/wood/structure (Accessed - 07/10/2011).

87. Izadyar, S.; Rahimi, M. Use of beech wood sawdust for adsorption of textile dyes. *Pakistan Journal of Biological Sciences*, **2007**, *10* (2), 287-293.

88. Jaguaribe, E. F.; Medeiros, L. L.; Barreto, M. C. S.; Araujo, L. P. The performance of activated carbons from sugarcane bagasse, babassu, and coconut shells in removing residual chlorine. *Brazilian Journal of Chemical Engineering*, **2005**, *22* (1), 41-47.

89. Jeong, B. H.; Hoek, E. M. V.; Yan, Y.; Subramani, A.; Huang, X.; Hurwitz, G.; Ghosh, A. K.; Jawor, J. Interfacial polymerization of thin film nanocomposites: A new concept for reverse osmosis membranes. *Journal of Membrane Science*, **2007**, *294*, 1–7.

90. Jiang, H.; Kamdem, D. P. Development of poly (vinyl chloride)/wood composites.A literature review. *Journal of Vinyl & Additive Technology,* **2004***, 10* (2), 59-69.

91. Jiang, J. Q.; Zeng, Z. Comparison of modified montmorillonite adsorbents Part II: The effects of the type of raw clays and modification conditions on the adsorption performance. *Chemosphere*, **2003**, *53*, 53–62.

92. Jin, S.; Fallgren, P. H.; Morris, J. F.; Chen, Q. Removal of bacteria and viruses from waters using layered double hydroxide nanocomposites. *Science and Technology of Advanced Materials*, **2007**, *8*, 67–70.

93. Kaya, A.; Ören, A. H. Adsorption of zinc from aqueous solutions to bentonite. *Journal of Hazardous Materials*, **2005**, *B125*, 183–189.

94. Khan, F. Photoinduced graft-copolymer synthesis and characterization of methacrylic acid onto natural biodegradable lignocellulose fiber. *Biomacromolecules*, **2004**, *5* (3), 1078-1088.

95. Khaydarov, R. A.; Khaydarov, R. R.; Gapurova, O. Water purification from metal ions using carbon nanoparticle-conjugated polymer nanocomposites. *Water Research*, **2010**, *44*, 1927 – 1933.

96. King, P.; Rakesh, N.; Beenalahari, S.; Kumar, Y. P.; Prasad, V. S. R. K. Removal of lead from aqueous solution using *Syzygium cumini* L.: Equilibrium and kinetic studies. *Journal of Hazardous Materials*, **2007**, *142* (1-2), 340-347.

97. Kirk, T. K.; Farell, R. L. Enzymatic combustion: the microbial degradation of lignin. *Annual Review of Microbiology*, **1987**, *41*, 465-505.

98. Kloprogge, J. T.; Evans, R.; Hickey, L.; Frost, R.; Characterisation and Al-pillaring of smectites from Miles, Queensland (Australia). *Applied Clay Science*, **2002**, *20*, 157–163.

99. Koumanova, B.; Peeva-Antova, P. Adsorption of p-chlorophenol from aqueous solutions on bentonite and perlite. *Journal of Hazardous Materials*, **2002**, *A90*, 229–234.

100. Krishnani, K. K.; Meng, X.; Dupont, L. Metal ions binding onto lignocellulosic biosorbent. *Journal of Environmental Science and Health Part A,* **2009**, *44*, 688–699.

101. Kumar, U.; Bandyopadhyay, M. Sorption of cadmium from aqueous solution using pretreatedrice husk. *Bioresource Technology*, **2006**, *97*, 104–109.

102. Laine, C. Structures of hemicelluloses and pectins in wood and pulp. *PhD Dissertation, Department of Chemical Technology, Helsinki University of Technology*, **2005**.

103. Lata, H.; Garg, V. K.; Gupta, R. K. Adsorptive removal of basic dye by chemically activated Parthenium biomass: equilibrium and kinetic modelling. *Desalination*, **2008**, *219*, 250–261.

104. Li, B.; Mao, H.; Li, X.; Ma, W.; Liu, Z. Synthesis of mesoporous silica-pillared clay by intragallery ammonia-catalyzed hydrolysis of tetraethoxysilane using quaternary ammonium surfactants as gallery templates, *Journal of Colloid and Interface Science*, **2009**, *336*, 244–249.

105. Li, F.; Rosen, M. J. Adsorption of gemini and conventional cationic surfactants onto montmorillonite and the removal of some pollutants by the clay. *Journal of Colloid and Interface Science*, **2000**, *224* (2), 265-271.

106. Li, Y. H.; Ding, J.; Luan, Z.; Di, Z.; Zhu, Y.; Xu, C.; Wu, D.; Wei, B. Competitive adsorption of Pb, Cu and Cd ions from aqueous solutions by multiwalled carbon nanotubes. *Carbon*, **2003**, *41*, 2787–2792.

107. Li, Y. H.; Wang, S.; Luan, Z.; Ding, J.; Xu, C.; Wu, D. A dsorption of cadmium (II) from aqueous solution by surface oxidized carbon nanotubes. *Carbon*, **2003**, *41*, 1057–1062.

108. Li, Z.; Yuan, H. Characterization of cadmium removal by *Rhodotorula sp. Y11*. *Applied Microbiology and Biotechnology*, **2006**, *73*, 458–463.

109.   Liao, H. T.; Wu, C. S. Preparation of poly(ethylene-octene) elastomer/clay/wood flour nanocomposites by a melting method. *Macromolecular Material Engineering*, **2005**, *290*, 695–703.

110.   Lin, J. J., *www.rocktone.com.tw*, (Accessed – 11/01/2011).

111.   Lin, J. X.; Zhan, S. L.; Fang, M. H.; Qian, X. Q.; Yang, H. Adsorption of basic dye from aqueous solution onto fly ash. *Journal of Environmental Management*, **2008**, *87*, 193–200.

112.   Lin, R. Y.; Chen, B. S.; Chen, G. L.; Wu, J. Y.; Chiu, H. C.; Suen, S. Y. Preparation of porous PMMA/Na$^+$–montmorillonite cation-exchange membranes for cationic dye adsorption. *Journal of Membrane Science*, **2009**, *326*, 117-129

113.   Lin, S. H.; Juang, R. S. Heavy metal removal from water by sorption using surfactant-modified montmorillonite. *Journal of Hazardous Materials*, **2002**, *B92*, 315–326.

114.   Lin, S. H.; Juang, R. S.; Wang, Y. H. Adsorption of acid dye from water onto pristine and acid-activated clays in fixed beds. *Journal of Hazardous Materials*, **2004**, *B113*, 195–200.

115.   Lin, T. S.; Wu, J. K. Adsorption of arsenite and arsenate within activated alumina grains: equilibrium and kinetics. *Water Research*, **2001**, *35* (8), 2049–2057.

116.   Lin, Y.; Cui, X.; Bontha, J. Electrically controlled anion exchange based on polypyrrole and carbon nanotubes nanocomposite for perchlorate removal. *Environmental Science and Technology*, **2006**, *40* (12), 4004-4009.

117.   Lin, Y.; Cui, X.; Bontha, J. Electrically controlled anion exchange based on polypyrrole and carbon nanotubes nanocomposite for perchlorate removal. *Environmental Science Technology*, **2006**, *40*, 4004-4009.

118.   Liu, H.; Ye, H.; Zhang, Y. Preparation and characterization of PMMA/flaky aluminum composite particle in the presence of MPS. *Colloids and Surfaces A: Physicochemical and Engineering Aspects*, **2008**, *315* (1-3), 1-6.

119.   Liu, P.; Zhang, L. Adsorption of dyes from aqueous solutions or suspensions with clay nano-adsorbents. *Separation and Purification Technology*, **2007**, *58*, 32–39.

120.   Lomakin, S. M.; Zaikov, G. E. New concepts in polymer science: Modern polymer flame retardance. books.google.co.za/books?isbn=9067643904, **2003**; *1-6*, 200-259.

121.   Mahboub, R.; Mouzdahir, Y. E.; Elmchaouri, A.; Carvalho, A.; Pinto, M.; Pires, J. Characterization of a delaminated clay and pillared clays by adsorption of probe molecules. *Colloids and Surfaces A: Physicochem. Eng. Aspects*, **2006**, *280*, 81–87.

122.   Malndrino, M.; Abollino, O.; Giacomino, A.; Aceto, M.; Mentasti, E. Adsorption of heavy metals on vermiculite: Influence of pH and organic ligands. *Journal of Colloid and Interface Science*, **2006**, *299* (2), 537-546.

123.   Manohar, D. M.; Noeline, B. F.; Anirudhan, T. S. Adsorption performance of Al-pillared bentonite clay for the removal of cobalt(II) from aqueous phase. *Applied Clay Science*, **2006**, *31*, 194-206.

124.   Mao, H.; Li, B.; Li, X.; Liu, Z.; Ma, W. Synthesis of silica-pillared clay (SPC) with ordered mesoporous structure by one-step method without preswelling process. *Applied Surface Science*, **2009,** *255,* 4787–4791.

125.   Meena, A. K.; Kadirvelu, K.; Mishra, G. K.; Rajagopal, C.; Nagar, P. N. Adsorptive removal of heavy metals from aqueous solution by treated sawdust (*Acacia arabica*). *Journal of Hazardous Materials*, **2008**, *150*, 604–611.

126.   Meng, T.; Gao, X.; Zhang, J.; Yuan, J.; Zhang, Y.; He, J. Graft copolymers prepared by atom transfer radical polymerization (ATRP) from cellulose. *Polymer*, **2009**, *50*, 447–454.

127.   Mercier, L.; Detellier C. Preparation, characterization, and applications as heavy metals sorbents of covalently grafted thiol functionalities on the interlamellar surface of montmorillonite. *Environmental Science and Technology*, **1995**, *29* (5), 1318–1323.

128.   Mishra, T.; Parida, K. M. Transition metal pillared clay: A para selective catalyst for nitration of chlorobenzene. *Journal of Molecular Catalysis A: Chemical*, **1997**, *121* (1), 91-96.

129.   Mittal, A.; Malviya, A.; Kaur, D.; Mittal, J.; Kurup, L. Studies on the adsorption kinetics and isotherms for the removal and recovery of methyl orange from wastewaters using waste materials. *Journal of Hazardous Materials*, **2007**, *148*, 229–240.

130.   Mobasherpour, I.; Salahi, E.; Pazouki, M. Comparative of the removal of Pb^{2+}, Cd^{2+} and Ni^{2+} by nano crystallite hydroxyapatite from aqueous solutions: Adsorption isotherm study. *Arabian Journal of Chemistry*, **2011**, http://dx.doi.org/10.1016/j.arabjc.2010.12.022.

131.   Montarges, E.; Moreau, A.; Michot, L. J. Removing of organic toxicants from water by Al –pluronic modified clay. *Applied Clay Science*, **1998**, *13*, 165–185.

132.   Morgan, A. B.; Harris, J. D. Exfoliated polystyrene-clay nanocomposites synthesized by solvent blending with sonication. *Polymer*, **2004**, *45*, 8695-8703.

133.   Mrad, I.; Ghorbel, A.; Tichit, D.; Lambert, J. F. Optimisation of the preparation of an Al-pillared clay: thermal stability and surface acidity. *Applied Clay Science*, **1997**, *12* (4), 349-364.

134.   Muhammad, N.; Parr, J.; Smith, M. D.; Wheatley, A. D. Adsorption of heavy metals in slow sand filters. *24th WEDC Conference*. Islamabad, Pakistan, **1998**.

135.   Murugan, T.; Ganapathi, A.; Valliappan, R. Removal of dyes from aqueous solution by adsorption on biomass of mango (*mangifera indica*) leaves. *E-Journal of Chemistry*, **2010**, *7* (3), 669-676. (http://www.e-journals.net).

136.   Nada, A. M. A.; Alkady, M. Y.; Ferkry, H. M. Synthesis and characterisation of grafted cellulose for use in water and metal ions sorption. *Bioresources*, **2007**, *3* (1), 46-59.

137.   Namasivayam, C.; Sureshkumar, M. V. Removal of chromium (VI) from water and wastewater using surfactant modified coconut coir pith as a biosorbent. *Bioresource Technology*, **2008**, *99*, 2218–2225.

138.   Nameni, M.; Moghadam, M. R. A.; Arami, M. Adsorption of hexavalent chromium from aqueous solutions by wheat bran. *International Journal of Environmental Science and Technology*, **2008**, *5* (2), 161-168.

139.   Nethaji, S.; Sivasamy, A. Adsorptive removal of an acid dye by lignocellulosic waste biomass activated carbon: Equilibrium and kinetic studies. *Chemosphere*, **2011**, *82*, 1367–1372.

140.   Ngah, W. S. W.; Hanafiah, M. A. K. M. Removal of heavy metal ions from wastewater by chemically modified plant wastes as adsorbents: A review. *Bioresource Technology,* **2008**, *99*, 3935–3948.

141.   Ngah, W. S. W.; Teong, L.C.; Hanafiah, M. A. K. M. Adsorption of dyes and heavy metal ions by chitosan composites: A review. *Carbohydrate Polymers*, **2011**, *83*, 1446–1456.

142.   Nigam, P.; Banat, I. M.; Singh, D.; Marchant, R. Microbial process for the decolorization of textile effluent containing azo, diazo and reactive dyes. *Process Biochemistry*, **1996**, *31*, (5), 435-442.

143.   Nishizawa, N.; Nishimura, J.; Saitoh, H.; Fujiki, K.; Tsubokawa, N. Grafting of branched polymers onto nano-sized silica surface: Postgrafting of polymers with pendant isocyanate groups of polymer chain grafted onto nano-sized silica surface. *Progress in Organic Coatings*, **2005**, *53* (4), 306-311.

144.   Oboh, I.; Aluyor, E.; Audu, T. Biosorption of heavy metal ions from aqueous solutions using a biomaterial. *Leonardo Journal of Sciences*, **2009**, *14*, 58-65.

145.   Office of Water Washington, D.C., United States Environmental Protection Agency. Wastewater Technology Fact Sheet Chemical Precipitation. EPA 832-F-00-018, September **2000**.

146.   Ojah, R.; Dolui, S. K. Graft polymerization of methyl methacrylate onto *Bombyx mori* initiated by semiconductor-based catalyst. *Bioresource Technology*, **2006**, *97*, 1529-1535.

147.   Ouajai, S., RMIT University, **2005,** Biopolymer composite based on natural and derived hemp cellulose fibreshttp://researchbank.rmit.edu.au/eserv/rmit:9575/Ouajai.pdf (Accessed – 29/08/2011).

148.   Oyanedel-Craver, V. A.; Fuller, M.; Smith, J. A. Simultaneous sorption of benzene and heavy metals onto two organoclays. *Journal of Colloid and Interface Science*, **2007**, 309, 485–492.

149.   Özcan, A. S.; Özcan, A. Adsorption of acid dyes from aqueous solutions onto acid-activated bentonite. *Journal of Colloid and Interface Science*, **2004**, *276*, 39–46.

150.   Park, K.W.; Kwon, O. Y. Interlamellar silylation of montmorillonite with 3-aminopropyl-triethoxysilane. *Bulletin of the Korean Chemical Society*, **2004**, *25* (7), 965-968.

151.   Pavasant, P.; Apiratikul, R.; Sungkhum, V.; Suthiparinyanont, P.; Wattanachira, S.; Marhaba, T. F. Biosorption of Cu^{2+}, Cd^{2+}, Pb^{2+}, and Zn^{2+} using dried marine green macroalga Caulerpa lentillifera. *Bioresource Technology*, **2006**; *97*, 2321–2329.

152.   Peric, J.; Trgo, M.; Medvidovic N. V. Removal of zinc, copper and lead bynatural zeolite - a comparison of adsorption isotherms. *Water Research*, **2004**, *38*, 1893–1899.

153.   Pernyeszi, T.; Kasteel, R.; Witthuhn, B.; Klahre, P.; Vereecken, H.; Klumpp, E. Organoclays for soil remediation: Adsorption of 2,4-dichlorophenol on organoclay/aquifer material mixtures studied under static and flow conditions. *Applied Clay Science*, **2006**, *32* (3-4), 179-189.

154.   Pires, J.; de Carvalho, M. B.; Carvalho, A. P. Aluminum-pillared clays: Decomposition of the intercalating species and textural properties. *Zeolites*, **1997**, *19*, 107-113.

155.   Posthumus, W.; Magusin, P. C. M. M.; Brokken-Zijp, J. C. M.; Tinnemans, A. H. A.; van der Linde, R. Surface modification of oxidic nanoparticles using 3-methacryloxypropyltrimethoxysilane. *Journal of Colloid and Interface Science*, **2004**, *269*, 109–116.

156.   Rawajfih, Z.; Nsour, N. Characteristics of phenol and chlorinated phenols sorption onto surfactant-modified bentonite. *Journal of Colloid and Interface Science*, **2006**, *298*. 39–49.

157.   Ray, S. S.; Bousmina, M. Biodegradable polymers and their layered silicate nanocomposites: In greening the 21st century materials world. *Progress in Materials Science*, **2005**, *50*, 962-1079.

158.   Ritter, S. K. Lignocellulose: A complex biomaterial. *Plant Biochemistry*, **2008**, *86* (49), 15.

159.   Robinson, T.; McMullan, G.; Marchant, R.; Nigam, P. Remediation of dyes in textile effluent: a critical review on current treatment technologies with a proposed alternative. *Bioresource Technology*, **2001**, *77*, 247-255.

160.   Román-Aguirre, M.; Márquez-Lucero, A.; Zaragoza-Contreras, E. A. Elucidating the graft copolymerization of methyl methacrylate onto wood-fiber. *Carbohydrate Polymers,* **2004**, *55*, 201-210.

161.   Rytwo, G.; Tropp, D.; Serban, C. Adsorption of diquat, paraquat and methyl green on sepiolite: experimental results and model calculations. *Applied Clay Science*, **2002**, *20*, 273–282.

162.   Safarik, I.; Lunackova, P.; Mosiniewicz-Szablewska, E.; Weyda, F.; Safarikova, M. *Holzforschung*, **2007**, *61* (3), 247-253.

163.   Salerno, P.; Mendioroz, S. Preparation of Al-pillared montmorillonite from concentrated dispersions. *Applied Clay Science*, **2002**, *22*, 115– 123

164.   Salipira, K. L.; Mamba, B. B.; Krause, R. W.; Malefetse, T. J.; Durbach, S. H. Carbon nanotubes and cyclodextrin polymers for removing organic pollutants from water. *Environmental Chemical Letters*, **2007**, *5*, 13–17.

165.   Salipira, K. L.; Mamba, B. B.; Krause, R. W.; Malefetse, T. J.; Durbach, S. H. Carbon nanotubes and cyclodextrin polymers for removing organic pollutants from water. *Environmental Chemical Letters*, **2007**, *5*, 13–17.

166.   Salon, M. C. B.; Abdelmouleh, M.; Boufi, S.; Belgacem, M. N.; Gandini, M. Silane adsorption onto cellulose fibers: Hydrolysis and condensation reactions. *Journal of Colloid and Interface Science*, **2005**, 289, 249–261.

167.   Santhi, T.; Manonmani, S.; Smitha, T. Removal of methyl red from aqueous solution by activated carbon prepared from the *annona squmosa* seed by adsorption. *Chemical Engineering Research Bulletin*, **2010**, *14*, 11-18.

168.   Sari, A.; Tuzen, M.; Soylak, M. Adsorption of Pb(II) and Cr(III) from aqueous solution on Celtek clay. *Journal of Hazardous Materials*, **2007**, *144*, 41–46.

169.   Savage, N.; Diallo, M. S. Nanomaterials and water purification: opportunities and challenges. *Journal of Nanoparticle Research*, **2005**, *7*, 331–342.

170.   Schindler, P. W.; Furst, B.; Dick, R.; Wolf, P. U. Ligand properties of surface silanol groups. I. Surface complex formation with Fe^{3+}, Cu^{2+}, Cd^{2+}, and Pb^{2+}. *Journal of Colloids and Interface Science*, **1976**, *55* (2), 469–475.

171.   Schoonheydt, R. A.; van Den Eynde, J.; Tubbax, H.; Leeman, H.; Stuyckens, M.; Lenotte, I.; Stone, W. E. E. The A1 pillaring of clays. Part I. Pillaring with dilute and concentrated A1 solutions. *Clays and Clay Minerals,* **1993**, *41* (5), 598-607.

172.   Senthilkumaar, S. Senthilkumaar, S.; Kalaamani, P.; Porkodi, K.; Varadarajan, P. R.; Subburaam, C. V. Adsorption of dissolved reactive red dye from aqueous phase onto activated carbon prepared from agricultural waste. *Bioresource Technology*, **2006**, *97* (14), 1618-1625.

173.   Sheng, G.; Boyd, S. A. Polarity effect on dichlorobenzene sorption by hexadecyltrimethylammonium-exchanged clays. *Clays and Clay Minerals,* **2000**, *48* (1), 43–50.

174.   Shevade, S.; Ford, R. G. Use of synthetic zeolites for arsenate removal from pollutant water. *Water Research*, **2004**, *38*, 3197–3204.

175.   Shin, E. W.; Rowell, R. M. Cadmium ion sorption onto lignocellulosic biosorbent modified by sulfonation: the origin of sorption capacity improvement. *Chemosphere*, **2005**, *60*, 1054–1061.

176.   Singh, R. P.; Way, J. D.; Dec, S. F. Silane modified inorganic membranes: effects of silane surface structure, *Journal of Membrane Science*, **2005**, *259* (1–2), 34–46.

177.   Singh, T. S.; Pant, K. K. Equilibrium, kinetics and thermodynamic studies for adsorption of As(III) on activated alumina. *Separation and Purification Technology*, **2004**, 36, 139–147.

178.   Singhal, R.; Datta, M. Development of nanocomposites of bentonite with polyaniline and poly (methacrylic acid). *Journal of Applied Polymer Science*, **2007**, *103*, 3299–3306.

179.   Sivaiah, M. V.; Petit, S.; Brendlé, J.; Patrier, P. Rapid synthesis of aluminium polycations by microwave assisted hydrolysis of aluminium via decomposition of urea and preparation of Al-pillared montmorillonite. *Applied Clay Science*, **2010**, *48*, 138–145.

180.   Sójka-Ledakowicz, J.; Lewartowska, J.; Kudzin, M.; Leonowicz, M.; Jesionowski, T.; Siwinśka-Stefanśka, K.; Krysztafkiewicz, A. Functionalization of textile materials by alkoxysilane-grafted titanium dioxide. *Journal of Material Science,* **2009,** *44*, 3852–3860.

181.   Sprynskyy, M.; Buszewski, B.; Terzyk, A. P.; Namieśnik, J. Study of the selection mechanism of heavy metal (Pb^{2+}, Cu^{2+}, Ni^{2+}, and Cd^{2+}) adsorption on clinoptilolite. *Journal of Colloid and Interface Science*, **2006**, 304, 21–28.

182.   Storaro, L.; Lenarda, M.; Gazerla, R.; Rinaldi, A. Preparation of hydroxy Al and Al/Fe pillared bentonites from concentrated clay suspensions. *Microporous Materials*, **1996**, *6*, 55-63.

183.   Taherzadeh, M. J.; Karimi, K. Pre-treatment of Lignocellulosic Wastes to Improve Ethanol and Biogas Production: A Review. *International Journal of Molecular Science,* **2008**, *9*, 1621-1651.

184.   Tahir, H.; Sultan, M.; Jahanzeb, Q. Removal of basic dye methylene blue by using bioabsorbents *Ulva lactuca* and *Sargassum. African Journal of Biotechnology*, **2008**, *7* (15), 2649-2655.

185.   Takamatsu, R.; Asakura, K.; Chun, W. J.; Miyazaki, T.; Nakano, M. EXAFS Studies about the sorption of cadmium ions on montmorillonite. *Chemistry Letters*, **2006**, *35* (2)

186.   Tang, J.; Weber, W. J. (Jr). Competitive sorption and desorption of chlorinated organic solvents (dnapls) in engineered natural organic matter. *227th American Chemical Society Meeting, Anaheim,* CA (US), **2004**, 497-500.

187.   Tarawou, T.; Horsfall, M. (Jr); Vicente, J. L. Adsorption of methyl red by water-hyacinth (*Eichornia crassipes*) biomass. *Chemistry & Biodiversity*, **2007**, *4*, 2236-2245.

188.   Teng, M. Y.; Lin, S. H. Removal of methyl orange dye from water onto raw and acid activated montmorillonite in fixed beds. *Desalination*, **2006**, *201*, 71–81.

189.   Tian, S.; Jiang, P.; Ning, P.; Su, Y. Enhanced adsorption removal of phosphate from water by mixed lanthanum/aluminum pillared montmorillonite. *Chemical Engineering Journal*, **2009**, *151* (1-3) 141–148.

190.   Tichit, D.; Fajula, F.;Figueras, F.; Ducourant, B.; Mascherpa, G.; Gueguen, C.; Bousquet, J. Sintering of montomorillonites pillared by hydroxy-aluminum species, *Clays and Clay Minerals,* **1988**, *36* (4), 369-375.

191.   Tobin, J. M.; Cooper, D. G.; Neufeld, R. J. Uptake of metal ions by rhizopus arrhizus biomass. *Applied and Environmental Microbiology*, **1984**, 821-824.

192.   Tong, M.; Yu, J.; Sun, X.; Li, B. Polymer modified biomass of baker's yeast for treating simulated wastewater containing nickel and lead. *Polymers for Advanced Technologies*, **2007**, *18*, 829–834.

193.   Torrents, A.; Jayasundera, S. The sorption of nonionic pesticides onto clays and the influence of natural organic carbon. *Chemosphere,* **1997**, *35* (7), 1549-1565.

194.   Turng, L.-S.; Yuan, M.; Kharbas, H.; Winata, H.; Caulfield, D. F. Applications of nanocomposites and woodfiber plastics for microcellular injection molding. *The Seventh International Conference on Woodfiber-Plastic Composites*, Wisconsin, USA, **2003**, 217.

195.   Vazquez, G.; Alonso, R.; Freire, S.; González- Álvarez, J.; Antorrena, G. Uptake of phenol from aqueous solutions by adsorption in a *Pinus pinaster* bark packed bed. *Journal of Hazardous Materials*, **2006**, *B133*, 61–67.

196.   Vinod, V. P.; Anirudhan, T. S. Adsorption behaviour of basic dyes on the humic acid immobilized pillared clay. *Water, Air, and Soil Pollution*, **2003**, *150*, 193–217.

197.   Wang, C. C.; Juang, L. C.; Hsu, T. C.; Lee, C. K.; Lee, J. F.; Huang, F. C. Adsorption of basic dyes onto montmorillonite. *Journal of Colloid and Interface Science*, **2004**, *273*, 80–86.

198.   Wang, L.; Wang, A. Adsorption characteristics of Congo red onto the chitosan/montmorillonite nanocomposite. *Journal of Hazardous Materials*, **2007**, *147*, 979–985.

199.   Wang, L.; Wang, K.; Chen, L.; Zhang, Y.; He, C. Preparation, morphology and thermal/mechanical properties of epoxy/nanoclay composite. *Composites Part A: Applied Science and Manufacturing*, **2006**, *37* (11), 1890-1896.

200.   Wang, W. Chelating adsorption properties of Cd (II) on the $PMAA/SiO_2$. *Process Safety and Environmental Protection*, **2011**, *89* (2), 127–132.

201.   Weng, C. H.; Lin, Y. T.; Tzeng, T. W. Removal of methylene blue from aqueous solution by adsorption onto pineapple leaf powder. *Journal of Hazardous Materials*, **2009**, *170*, 417–424.

202.   Wilke, A.; Buchholz, R.; Bunke, G. Selective biosorption of heavy metals by algae. *Environmental Biotechnology*, **2006**, *2* (2), 47-56.

203.   Wong, K. K.; Lee, C. K.; Low, K. S.; Haron, M. J. Removal of Cu^{2+} and Pb^{2+} by tartaric acid modified rice husk from aqueous solutions. *Chemosphere*, **2003**, *50*, 23–28.

204.   Wu, S.; Jin, Z.; Kim, J. M.; Tong, Q.; Chen, H. Graft copolymerization of methyl acrylate onto pullulan using ceric ammonium nitrate as initiator; Elsevi*er: Oxf*ord**,** ROYAUME-UNI, **2009**.

205.   Xie, J. Z.; Chang, H. L.; Kilbane, J. J. Removal and recovery of metai, ions from wastewater using biosorbents and chemically modified biosorbents. *Bioresource Technology*, **1996**, *57*, 127-136.

206.   Xuan, Z.; Tang, Y.; Li, X.; Liu, Y.; Luo, F. Study on the equilibrium, kinetics and isotherm of biosorption of lead ions onto pretreated chemically modified orange peel. *Biochemical Engineering Journal*, **2006**, *31* (2), 160-164.

207.   Yan, L.; Shan, X.; Wen, B.; Owens, G. Adsorption of cadmium onto Al_{13}-pillared acid-activated montmorillonite. *Journal of Hazardous Materials*, **2008**, *156*, 499–508.

208.   Ye, J. H.; Dong, J. J.; Lu, J. L.; Zheng, X. Q.; Jin, J.; Chena, H.; Liang, Y. Effect of graft copolymerization of fir sawdust lignocellulose with N-vinylpyrrolidone on adsorption capacity to tea catechins. *Carbohydrate Polymers*, **2010**, *81*, 441–447.

209.   Yilmaz, N.; Yapar, S. Adsorption properties of tetradecyl- and hexadecyltrimethylammonium bentonites. *Applied Clay Science*, **2004**, *27*, 223–228.

210.   Yu, J.; Tong, M.; Sun, X.; Li, B. Poly (methacrylic acid) modified biomass for enhancement adsorption of Pb^{2+}, Cd^{2+} and Cu^{2+}. *Journal of Chemical Technology Biotechnology*, **2007**, *82*, 558-565.

211.   Yu, J.; Tong, M.; Sun, X.; Li, B. Poly (methacrylic acid) modified biomass for enhancement adsorption of Pb^{2+}, Cd^{2+} and Cu^{2+}. *Journal of Chemical Technology and Biotechnology*, **2007**, *82*, 558–565.

212.   Yu, L.; Li, W. W.; Lam, M. H. W.; Yu, H. Q. Adsorption and decolorization kinetics of methyl orange by anaerobic sludge. *Applied Microbiology Biotechnology*, **2011**, *90* (3), 1119-1127.

213.   Yu, R.; Wang, S.; Wang, D.; Ke, J.; Xing, X.; Kumada, N.; Kinomura, N. Removal of Cd^{2+} from aqueous solution with carbon modified aluminum-pillared montmorillonite. *Catalysis Today*, **2008**, *139*, 135–139.

214.   Yuan, P.; He, H.; Bergaya, F. A.; Wu, D.; Zhou, Q.; Zhu, J. Synthesis and characterization of delaminated iron-pillared clay with meso–microporous structure. *Microporous and Mesoporous Materials*, **2006**, *88*, 8–15.

215.   Yun, L.; Xing, S.; Qiming, X.; Haidong, C.; Huixian, Z.; Shixiang, G. Adsorption of copper and lead in aqueous solution onto bentonite modified by 4-methylbenzo-15-crown-5. *Journal of Hazardous Materials*, **2006**, *B137*, 1149–1155.

216.   Zhang, G.; Li, X.; Li, Y.; Wu, T.; Sun, D.; Lu, F. Removal of anionic dyes from aqueous solution by leaching solutions of white mud. *Desalination*, **2011**, *274* (1-3), 255–261.

217.   Zhang, Z.; Lei, H. Preparation of a-alumina/polymethacrylic acid composite abrasive and its CMP performance on glass substrate. *Microelectronic Engineering*, **2008**, *85*, 714–720.

218.   Zhao, L.; Zou, W.; Zou, L.; He, X.; Song, J.; Han, R. Adsorption of methylene blue and methyl orange from aqueous solution by iron oxide-coated zeolite in fixed bed column: predicted curves. *Desalination and Water Treatment*, **2010**, *22*, 258–264.

219.   Zhao, Y.; Wang, K.; Zhu, F.; Xue, P.; Jia, M. Properties of poly (vinyl chloride)/wood flour/montmorillonite composites: Effects of coupling agents and layered silicate. *Polymer Degradation and Stability*, **2006**, *91*, 2874-2883.

220.   Zhou, X.; Wu, T.; Hu, B.; Jiang, T.; Han, B. Ruthenium nanoparticles stabilized by poly (N-vinyl-2-pyrrolidone) grafted onto silica: Very active and stable catalysts for hydrogenation of aromatics. *Journal of Molecular Catalysis A: Chemical*, **2009**, *306*, 143–148.

221.   Zhuannian, L.; Anning, Z.; Guirong, W.; Xiaoguang, Z. Adsorption behavior of methyl orange onto modified ultrafine coal powder. *Chinese Journal of Chemical Engineering*, **2009**, *17* (6), 942-948.

222.   Zielke, R. C.; Pinnavaia, T. J. Modified clays for the adsorption of environmental toxicants: binding of chlorophenols to pillared, delaminated, and hydroxy-interlayered smectites. *Clays and Clay Minerals,* **1988**, *36* (5), 403-408.

Chapter 3

Experimental: Materials and General Procedures

3.0 Introduction

This chapter gives the details of the materials and reagents used in order to achieve the aims and objectives of this study. It also gives an overview of the methods used for the pre-treatment of the precursors (lignocellulose, montmorillonite, methyl methacrylate, methacryloxypropyl trimethoxysilane and methacrylic acid). Also included is a general description (summary) of the procedures followed in the synthesis of the polymer-grafted lignocellulose and montmorillonite adsorbents. A detailed description of each method used for the preparation of each adsorbent is given in Chapter 5.

3.1 Materials and chemical reagents

Platanus x hispanica (London plane) tree leaves were used as the source of lignocellulose (biopolymer). The tree leaves were collected from the University of Fort Hare grounds, Alice Campus and dried. Montmorillonite clay was purchased from BaoBio Holdings (Pty) Ltd, South Africa.

Methyl methacrylate (MMA, 99%) and methyl orange were purchased from SAARCHEM (Pty) Ltd, South Africa. Methyl methacrylate was distilled before use and methyl orange was used as received. Methacrylic acid (MAA, 99%) and dibutyl tin dilaurate (DBTDL, 95%) from Aldrich Chemicals, South Africa were used as received. Methacryloxypropyl trimethoxysilane (MPS, 99%) from Sigma-Aldrich (Pty) Ltd (South Africa) was used as received, ammonium persulfate (AMPS, 98%) and aluminium chloride hexahydrate (99%) were from Associated Chemical Enterprises, South Africa. Dodecylbenzylsulfonic acid (DBS) and sodium metabisulfite (SMBS, 95%) were from BDH Chemicals (England) and sodium chloride salt (99.5%) was from MET-U-ED CC, South Africa. Lead nitrate (99.5%) was from SAARCHEM (Pty) Ltd (South Africa), cadmium nitrate tetrahydrate (100%) was from Riedel-de Haën, Germany. Lead nitrate, $Pb(NO_3)_2$ and cadmium nitrate tetrahydrate, $Cd(NO_3)_2.4H_2O$ for the synthetic water were used as received.

Methyl orange, neutral red, lead nitrate ($Pb(NO_3)_2$) and cadmium nitrate tetrahydrate ($Cd(NO_3)_2.4H_2O$) were used as model pollutants in the evaluation of the prepared adsorbent materials.

The lignocellulose and montmorillonite clay were pretreated first before use in the synthesis of the nanocomposite adsorbents. The following section describes the pre-treatments performed on the lignocellulose and montmorillonite.

3.2 Pre-treatment of precursors: lignocellulose and montmorillonite

The lignocellulose and montmorillonite (MMT) used for the preparation of the nanocomposites were first pre-treated as summarized in Figure 3.1. The detailed pre-treatment of each material is also presented after the schematic.
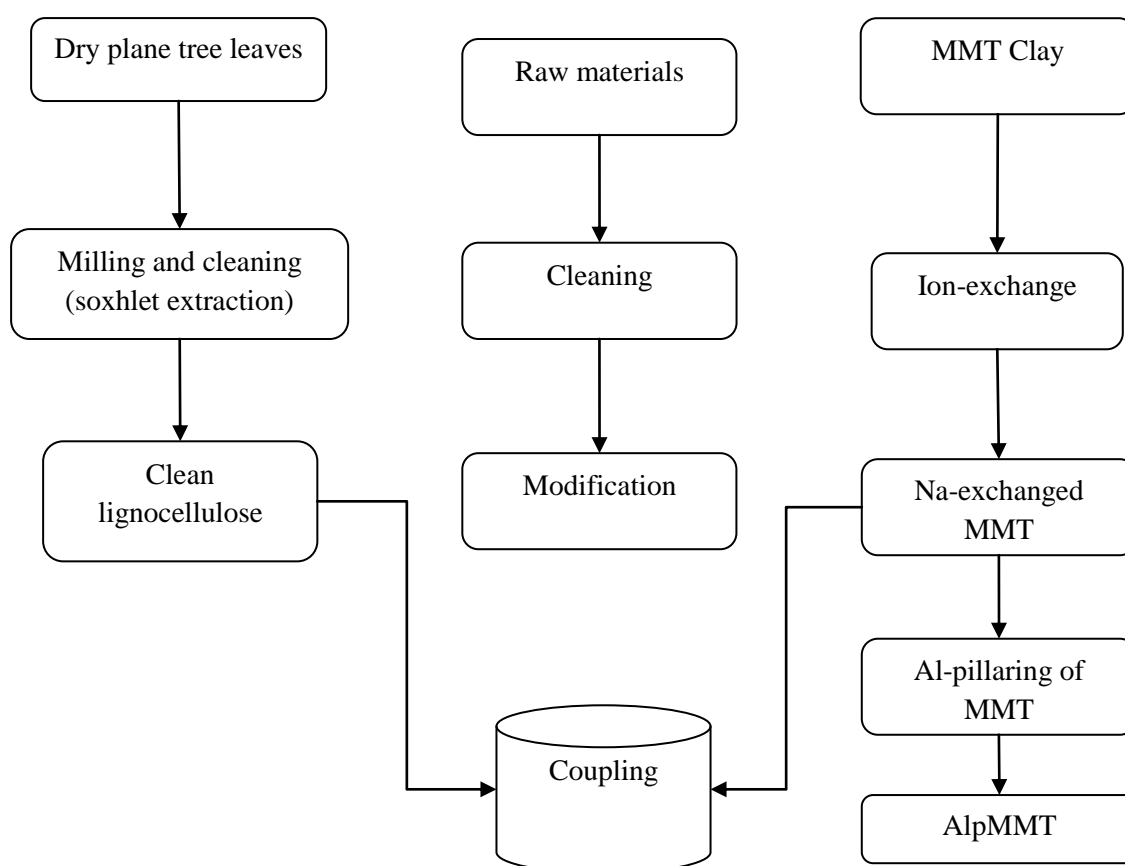
Figure 3.1: Schematic of the pre-treatment of montmorillonite and lignocellulose.

3.2.1 Pre-treatment of biomass

The leaves were first dried in a ventilated oven at a temperature of 105 °C for 24 h until they were completely dry. The dry leaves were then reduced to powder using a food blender and sieved through a 170 mesh sieve. It was necessary to remove impurities and some water soluble organic compounds which could taint the water during the adsorption experiments. The leaf biomass was initially soxhlet-extracted with acetone (Zhao, Y. et al, 2006), but it was observed that there were still pigments

leaching from the lignocellulose after dispersing the acetone-extracted leaf biomass in water. The sieved leaf powder (10 g) was then soxhlet extracted using a 1:1 v/v ethanol (EtOH): water (H_2O) solvent mixture (250 mL of solvent was used in each case) for 48 h, and that removed the pigments. The soxhlet-extracted lignocellulose powder was then dried in a ventilated oven at 50 °C for 48 h after which it was placed in a dessicator to prevent moisture absorption.

3.2.2 Purification of montmorillonite clay

Montmorillonite clay is normally purified first before use in the preparation of nanocomposites or being used as an adsorbent. The purification is necessary in order to remove natural organic matter, hydroxides and carbonates whose presence would otherwise compromise the performance of the montmorillonite. The purification of clay entails the removal of organic matter, hydroxides and carbonates. It is standard procedure to convert the purified MMT to the mono-ionic sodium form (NaMMT) by ion exchange (Carrado, K. A. et al, 2006).

However, because of the added product cost and the labour intensiveness in the above purification procedure, it was imperative to find a simple and cheap method for the purification of the MMT clay. The other method commonly used for clays was developed by van Olephen, H., 1965. The purification of clay is accomplished through the replacement of exchangeable cations by Na^+ followed by washing with distilled water. The washing removes excess salts and also affords the removal of fine impurities from the clay. The section below describes this simple method for clay purification.

3.2.2.1 Preparation of NaMMT via the van Olephen method

Raw clays from identified geological deposits may be purified without removing the carbonates, hydroxides or organic matter (Carrado, K. A. et al, 2006). The quality of the clay is said to be quite acceptable for most applications including nanocomposite synthesis.

The method used for the preparation of NaMMT in this study was adapted from the work done by Manohar, D. M. et al, 2006 but with minor modifications. The raw clay was carefully dispersed in 1.0 M NaCl solution by shaking for about 12 h, then separating by centrifugation. This procedure was repeated at least two times. The sediment of the Na^+-exchanged clay mineral (NaMMT) was washed with deionised water. As long as the clay minerals could be separated by centrifugation, the visually clear supernatant was decanted and fresh water added. The procedure was repeated until no Cl^- ions could be detected by the $AgNO_3$ test. The residual water in the sodium-exchanged montmorillonite clay was evaporated in a ventilated oven and the NaMMT dried at 50 °C for 48 h. This procedure can produce highly purified clay without significant alterations to the initial crystal structure of the clay.

The cation exchange capacity of the clay was determined using the procedure described in Section 3.3.2.2.

3.2.2.2 Determination of the cation exchange capacity of montmorillonite

Cation exchange capacity (CEC) refers to the quantity of negative charges existing on the surfaces of clay and organic matter (present in the clay). The negative charges attract positively charged ions, or cations, hence the name 'cation exchange capacity'. Some authors report that the cation exchange capacity of clays is related to the adsorption capacity (Blachier, C. et al, 2009) especially with respect to heavy metals (Matthes, W. et al, 1999). The following procedure was used for the determination of the CEC of the montmorillonite clay.

The method used for the determination of CEC of the montmorillonite (MMT) was adapted from the work carried out by Barton, C. D. et al, 1997. A portion (5.0 g) of oven-dried clay was weighed into a 125 mL conical flask, barium chloride solution (50 mL of 0.5 M) was added and the flask placed on a rotary shaker for 30 min. A control was also included during the analysis. After shaking for 30 min, the MMT clay suspension was vacuum-filtered through Whatman No. 1 filter paper. The MMT was leached with 100 mL of 1.0 M $BaCl_2$ solution. The excess $BaCl_2$ was rinsed from the clay sample in the Buchner funnel by leaching with an equal volume of ethanol. This leachate was discarded and a clean, dry vacuum flask was connected.

It was important to gently fill the funnel to remove all excess Ba^{2+} ions and allow it to drain until only damp clay remained. Ethanol (200 mL) was added to the mixture in the same manner. A clean 500 mL vacuum flask was then used and the clay sample leached with 225 mL of ammonium acetate to replace the exchangeable Ba^{2+} ions. The leachate was diluted to a 250 mL volume in a volumetric flask using deionised water .The concentration of Ba^{2+} in the final leachate was determined using atomic absorption spectroscopy (AAS) using the external standard calibration method.

The CEC was computed using the following formula (Ross, D. S. et al, 1995; Skinner, M. F. et al, 2001) and the CEC value reported was the average of three replicates.

$$CEC \text{ in meq per 100 g of clay} = \frac{mg}{L} \; Ba^{2+} \text{ in leachate} \times \frac{0.25}{69} \times \frac{100}{sample\ size\ (g)}$$

The cation exchange capacity of the montmorillonite was found to be 91.42 meq per 100 g of clay (Ross, D. S. et al, 1995; Adamis, Z. et al, 2005).

3.2.2.3 Preparation of aluminium-pillared montmorillonite clay

As a way of modifying the Na-exchanged montmorillonite clay, metal pillaring was carried out in an attempt to increase the adsorption capacity of MMT for both heavy metals and organic pollutants. The pillaring of clays by metal oxides has been reported to result in increased surface area (Yuan, P. et al, 2006), microporosity and enhanced adsorption properties (Maes, N. et al, 1997; Cao, F. et al, 2009). Aluminium-pillaring of the montmorillonite was assessed in this study, and the Al-pillared MMT was evaluated in adsorption properties for both organic and inorganic pollutants. The preparation of Al-pillared montmorillonite is presented in more detail in Chapter 4. The results of the adsorption of heavy metals as well as organics pollutants onto the Al-pillared MMT are reported in Chapter 6.

3.3 Preparation of polymer-grafted lignocellulose-montmorillonite nanocomposite adsorbents
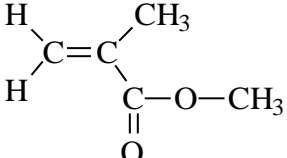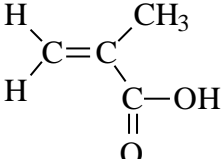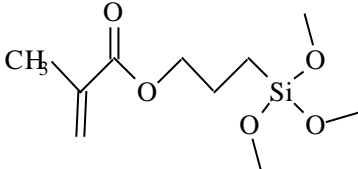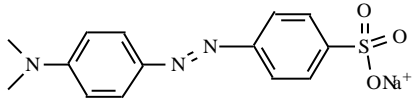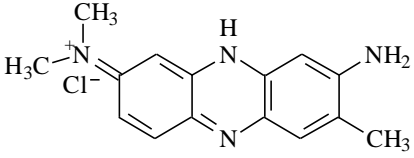
Three monomers were chosen for the preparation of polymer-grafted lignocellulose-montmorillonite adsorbents. The monomers are: methyl methacrylate, methacryloxypropyl trimethoxysilane and methacrylic acid. The structures, formulae and molecular masses of the three are displayed in Table 3.1. Also included in the table are the details of methyl orange which was used as a model organic pollutant.

Homopolymers of the three respective monomers were prepared separately and characterized accordingly. The homopolymers were used in the comparison of data after various modifications of the lignocellulose and montmorillonite using the three monomers. In the preparation of the adsorbent materials, Na-exchanged montmorillonite clay (NaMMT) and the soxhlet-extracted lignocellulose were first grafted separately or individually with each of the three monomers shown in Table 3.1. This was carried out in order to determine the optimum conditions for the synthesis of the lignocellulose-montmorillonite nanocomposites.

Polymer-grafted or coupled lignocellulose-montmorillonite nanocomposites were then prepared after establishing the optimum preparation conditions. The three monomers (methyl methacrylate, methacrylic acid and methacryloxypropyl trimethoxysilane) listed in the table were used as couplers or bridges linking the lignocellulose and the montmorillonite together. A free-radical graft polymerization reaction was used for the preparation of adsorbents based on methacrylic acid and methyl methacrylate. However, for the grafting of MPS, a condensation type of reaction was employed.   All nanocomposites were prepared using the sodium-exchanged montmorillonite (NaMMT).

Table 3.1: Chemical names, formulae, molecular structures and molecular masses of the monomers, methyl orange and neutral red.

Chemical Name	Molecular mass (g/mol)	Molecular formular	Chemical structure
Methyl methacrylate	100.12	$CH_3CH_2CCOOCH_3$	
Methacrylic acid	86.09	CH_3CH_2CCOOH	
Methacryloxy propyl trimethoxy silane	248.35	$CH_3CCOO(CH_2)_3Si(OCH_3)_4$	
Methyl orange	327.34	$C_{14}H_{14}N_3O_3NaS$	
Neutral red	288.78	$C_{15}H_{17}ClN_4$	

3.4 Characterization techniques

This section describes the analytical techniques that were used for the characterization of adsorbents prepared. The different samples were characterized using a number of techniques including: Fourier transform infrared spectroscopy (FTIR), thermogravimetric analysis (TGA), X-ray diffraction (XRD) analysis, scanning electron microscopy (SEM), transmission electron microscopy (TEM) and Brunauer-Emmet-Teller (BET) surface area analysis. Also described in this section are the techniques used for the quantitative analysis of heavy metals and dyes during adsorption studies.

3.4.1 Fourier Transform Infra-red spectroscopy

Fourier transform infra-red (FTIR) technique is based on the excitation of molecular vibrations by light absorption. It is widely used in the determination of structure and identification of both organic and inorganic compounds. It is mainly used in the identification of functional groups present in a given sample.

In infrared spectroscopy, infrared radiation is passed through a sample. Some of the infrared radiation is absorbed by the sample and some is transmitted. The resulting spectrum represents the molecular absorption and transmission, creating a molecular fingerprint of the sample. Like a fingerprint, no two unique molecular structures produce the same infrared spectrum. This makes FTIR spectroscopy useful for several types of analyses, including: identification of an unknown material, quality control of samples and the determination of amounts of components in a mixture.

The sample analysis process entails the emission of infrared radiation from a black body source. The beam of radiation passes through an aperture which controls the amount of energy presented to the sample and ultimately to the detector. The beam enters the interferometer where the 'spectral encoding' takes place. The resulting interferogram signal then exits the interferometer. The beam enters the sample compartment where it is transmitted through or reflected off the surface of the sample, depending on the type of analysis being carried out. This is where specific frequencies of energy, uniquely characteristic of the sample, are absorbed. The beam finally passes through to the detector for final measurement. The detectors used are specially designed to measure the special interferogram signal (Kellener, R. et al, 1998; Pavia, D. L. et al, 2001). FTIR spectroscopy was employed in this study for the analysis of raw clay and lignocellulose samples as well as the analysis of the various adsorbent materials prepared in this work.

3.4.2 Thermogravimetric analysis

Thermogravimetric analysis (TGA) measures the amount and rate of change in the weight of a material as a function of temperature or time (isothermal conditions) in a controlled atmosphere. Measurements are used to primarily determine the composition of material and to predict their thermal stability. The technique can characterise materials that exhibit weight loss or gain due to decomposition, oxidation or dehydration. The breaking and formation of chemical bonds at elevated temperatures leads to changes in the weight of the sample which is monitored by a very sensitive analytical balance.

In TGA, the weight of a sample is continuously recorded as the temperature is increased. Samples are placed in a crucible that is positioned in a furnace on a quartz beam attached to an automatic

recording balance. The horizontal quartz beam is maintained in the null position by the current flowing through the transducer coil of an electromagnetic balance. A pair of photosensitive diodes acts as a position sensor to determine the movement of the beam. Any change in the weight of the sample causes a deflection of the beam, which is sensed by one of the photodiodes. The beam is then restored to the original null position by a feedback current sent from the photodiodes to the coil of the balance. The feedback current is proportional to the change in weight of the sample (Willard, H. H. et al, 1988).

TGA has been used to characterise a wide range of materials, including nanocomposites and clays. The thermal stability of polymer/clay nanocomposites, the amount of clay incorporated per given amount of polymer, as well as the formation of metal oxide pillars can be determined by TGA (Kloprogge, J. T. et al, 1994; Chae, H. J. et al, 2001).

3.4.3 X-ray powder diffraction

In this method, X-rays are diffracted from the planes of a crystal (diffraction analysis). This method depends on the wave character of the X-rays and the regular spacing of the planes in a crystal. Although diffraction methods can be used for quantitative analysis, they are most widely used for qualitative identification of crystalline phases.

X-ray powder diffraction analysis is a powerful method by which X-rays of a known wavelength are passed through a sample. X-ray diffraction techniques are based on the elastic scattering of X-rays from structures that have long-range order. The wave nature of the X-rays means that they are diffracted by the lattice of the crystal to give a unique pattern of peaks of 'reflections' at differing angles and of different intensity, just as light can be diffracted by a grating of suitably spaced lines. The diffracted beams from atoms in successive planes cancel unless they are in phase, and the condition for this is given by the Bragg relationship:

$$n\lambda = 2dSin\theta \qquad (3.2)$$

where, λ is the wavelength of the X-rays, d is the distance between different plane of atoms in the crystal lattice, θ is the angle of diffraction and n is a constant. The X-ray detector moves around the sample and measures the intensity of these peaks and the position of these peaks (diffraction angle 2θ). The highest peak is defined as the 100% peak and the intensity of all the other peaks are measured as a percentage of the 100% peak (http://www.plasma-biotal.com/xraydif1.html).

Materials that do not have long range order may also be studied by scattering methods that rely on elastic scattering of monochromatic X-rays. The X-ray techniques that can be employed include: X-ray reflectivity, wide-angle and small-angle X-ray scattering (WAXS and SAXS, respectively).

SAXS is a small-angle scattering technique where the elastic scattering of X-rays (0.1... 0.2 nm) by a sample which has inhomogeneities in the nanometer range is recorded at very low angles (typically 0.1 - 10°). This angular range contains information about the shape and size of macromolecules, characteristic distances of partially ordered materials, pore sizes, and other data. SAXS is capable of delivering structural information of macromolecules between 5 and 25 nm, of repeat distances in partially ordered systems of up to 150 nm (Fischer, E. W., 1971; Whiston, C., 1987).

3.4.4 Scanning electron microscopy

Scanning electron microscopy (SEM) is a type of electron microscopy that images the sample surface by scanning it with a high energy beam of electrons in a *raster* scan pattern. The electrons interact with the atoms that make up the sample producing signals that contain information about the sample's surface topography, composition and other properties such as electrical conductivity.

SEM requires that the samples be conductive for the electron beam to scan the surface and that the electrons have a path to ground. Non-conductive solid samples are coated with a layer of conductive material (such as gold, gold/palladium alloy, platinum, tungsten or graphite). An ultrathin layer of coating is deposited on the sample either by low vacuum sputter-coating or high vacuum evaporation.

The imaging mode can be based on the detection of secondary electrons or detection of back-scattered electrons. X-rays are also produced by the interaction of electrons with the sample and these can be detected in SEM instruments equipped for energy- or wavelength-dispersive X-ray spectroscopy (Goldstein, J. et al, 2003).

3.4.5 Transmission electron microscopy

In transmission electron microscopy, a beam of electrons is transmitted through an ultrathin (100 nm) sample or specimen. The beam of electrons interacts with the sample as it passes through it. An image is formed from the transmitted electrons, magnified and focussed by an objective lense and appears on an imaging screen. A fluorescent screen is used in most TEM instruments.

Just like scanning electron microscopy, to avoid charge build-up on the surface, tissue samples are normally coated with a conductive thin layer of material such as carbon. Differences in the electron densities of the sample are detected, developing an enlarged image of the focussed area. The samples

can also be stained in order to improve contrast and resolution, thus revealing minute details of biological samples (http://cimewww.epfl.ch/people/cayron/Fichiers/thesebook-chap3.pdf).

3.4.6 BET surface area analysis

This technique was named after S. Brunauer, P. H. Emmet and E. Teller (BET). The three developed the method in 1938 as they were working on ammonia catalysts. It is the first method developed to measure the specific surface area of finely divided and porous solids. The method is applied in the analysis of pharmaceuticals, catalysts, projectile propellants, medical implants, filters, cements and adsorbents. The BET method is based on the adsorption of gas on a surface. Adsorption is a consequence of surface energy change. The energy is minimized in the bulk when every atom or molecule is surrounded by neighbours. The amount of gas adsorbed at a given pressure allows for the determination of surface area.

In a gas sorption experiment, the material is heated and degassed by vacuum force or inert gas purging to remove adsorbed foreign molecules. Controlled doses of an inert gas, such as nitrogen, krypton, or argon, are introduced and the gas is adsorbed, or alternatively, withdrawn and desorbed. The sample material is placed in a vacuum chamber at a constant and very low temperature, usually at the temperature of liquid nitrogen (-195.6 °C), and subjected to a wide range of pressures, to generate adsorption and desorption isotherms. The amounts of gas molecules adsorbed or desorbed are determined by the pressure variations due to the adsorption or desorption of the gas molecules by the material (the adsorbent). Various amounts of gas molecules will be adsorbed or desorbed at different doses of the gas (the adsorbate). Knowing the area occupied by one adsorbate molecule, σ (for example, $\sigma = 16.2$ Å^2 for nitrogen), and using an adsorption model, the total surface area of the material can be determined (Mahboub, R. et al, 2006).

The concept of the theory is an extension of the Langmuir theory (a theory for monolayer molecular adsorption) to multilayer adsorption. The BET theory assumes that: gas molecules physically adsorb on the surface of a solid in layers infinitely, there is no interaction between each adsorption layer, and the Langmuir equation can be applied to each of the layers. The resulting BET equation is expressed by:

$$\frac{P}{n(P_0 - P)} = \frac{1}{cn_m} + \frac{(c-1).P}{cn_m.P_0} \qquad (3.3)$$

where P, P_0, c, n, n_m are the adsorption pressure, the saturation vapour pressure, a constant, the amount adsorbed (moles per gram of adsorbent) at the relative pressure P/P_0, and the monolayer capacity (moles of molecules needed to make a monolayer coverage on the surface of one gram of

adsorbent), respectively. Through the slope and intercept of a plot of $P/[n(P_0\text{-}P)]$ against (P/P_0), n_m can be determined. The specific surface area, S, can then be derived using the following equation:

$$S = N_A n_m \sigma \qquad (3.4)$$

N_A is Avogadro's number and σ is the area occupied by the adsorbed species. The specific surface area that can be determined by gas sorption ranges from 0.01 to over 2000 m^2/g. Determination of pore volume and pore size distribution of porous materials can be made from the N_2 gas adsorption/desorption isotherm using an assessment model, suitable for the shape and structure of the pores. The range of pore sizes that can be measured using gas sorption is from a few Ångstroms up to about half a micron (Sing. K. S. W. et al, 1985).

3.4.7 Ultra-violet/visible spectroscopy

An ultraviolet-visible (UV/Vis) spectrophotometer consists of three components: the source, the dispersive system (combined in a monochromator) and a detector. These components are typically integrated into the same instrument to make spectrophotometers for chemical analysis. The sample can be placed in the optical path before or after the dispersive system and recorded spectra can be treated by using a number of different computer algorithms.

The light sources commonly used in this spectral domain are of two types. An incandescent lamp made from a tungsten filament housed in a glass envelope is used for the visible portion of the spectrum, for wavelengths longer than 350 nm. For the UV portion (wavelengths shorter than 350 nm), a medium pressure deuterium arc lamp is used. Detectors are again of two types: photomultiplier tubes and semiconductors (e.g. silicone photodiodes and charge transfer devices).

Double-beam spectrophotometers allow differential measurements to be made between the sample and the analytical blank. UV-Vis spectroscopy uses light in the visible and near ultraviolet as well as near infra-red ranges. Absorption in the visible region results in molecules undergoing electronic transitions. The absorbance is measured and the concentration of the analyte is related to the signal by the Beer-Lambert law. The Beer-Lambert equation is expressed as follows:

$$A = \epsilon bc \qquad (3.5)$$

where A, ϵ, b and c are the absorption, molar absorptivity (a constant which is characteristic of the absorbing species at a specific wavelength), pathlength of the sample and the concentration,

respectively. The absorption is therefore directly proportional to concentration for a given set of instrumental conditions (Pavia, D. L. et al, 2001).

3.4.8 Flame atomic absorption spectroscopy

Quantitative analysis using flame atomic absorption spectroscopy (FAAS) is also based on the Beer-Lambert law. In quantitative determinations using FAAS, combustion flames provide a means of converting analytes in solution to atoms in the vapour phase freed of their chemical surroundings. These free atoms are then transformed into excited electronic states by absorption of radiant energy from an external source. The flame that contains the free atoms serves as a sample cell. The free atoms absorb radiation focussed on the cell from an external source to the flame. The incident radiation absorbed by the free atoms in moving from the ground state to an excited state provides the analytical data (Beaty, R. D. et al, 1993).

The sample is introduced as an aerosol into the flame, where the analyte ions are converted into free atoms. Once formed, the free atoms absorb radiation of a specific wavelength from an external source (hollow cathode lamp) and the amount of radiation absorbed is detected and determined by FAAS.

As the number of atoms in the light path increases, the amount of light absorbed increases in a predictable way. Measuring the amount of light absorbed allows a quantitative determination of the amount of analyte element present in solution. The ease and speed at which precise and accurate measurements can be made with this technique have made FAAS one of the most popular methods for the determination of metals.

The work on the adsorption of heavy metals carried out in this study during the evaluation of the various adsorbents prepared has employed atomic absorption spectroscopy. The results from the adsorption experiments are presented in Chapter 6.

3.5 References

1. Adamis, Z.; Williams, R. B. Bentonite, kaolin, and selected clay minerals. *Environmental Health Criteria 231, World Health Organisation*, Geneva, **2005**.

2. Barton, C. D.; Karathanasis A. D. Measuring cation exchange capacity and total exchangeable bases in batch and flow experiments. *Soil Technology*, **1997**, *11*, 153-162.

3. Beaty, R. D.; Kerber, J. D.; Concepts: Instrumentation and Techniques in Atomic absorption spectrophometry, 2nd edition, **1993**, *The Perkin Elmer Corporation*.

4. Blachier, C.; Michot, L.; Bihannic, I.; Barrès, O.; Jacquet, A.; Mosquet, M. Adsorption of polyamine on clay minerals. *Journal of Colloid and Interface Science*, **2009**, *336*, 599–606.

5. Cao, F.; Bai, P.; Li, H.; Ma, Y.; Deng, X.; Zhao, C. Preparation of polyethersulfone–organophilic montmorillonite hybrid particles for the removal of bisphenol A. *Journal of Hazardous Materials*, **2009**, *162*, 791-798.

6. Carrado, K. A.; Decarreu, A.; Petit, S.; Bergaya, F.; Lagaly, G. Synthetic clay minerals and purification of natural clays. *Handbook of Clay Science*, **2006**, *1*, 115-139. Elsevier, Ltd.

7. Chae, H. J.; Nam, I. S.; Ham, S. W.; Hong, S. B. Physicochemical characteristics of pillared interlayered clays. *Catalysis Today*, **2001**, *68*, 31–40.

8. Fischer, E. W. Small angle x-ray scattering studies of phase transitions in polymeric and oligomeric systems. *Pure and Applied Chemistry*, **1971**, *26* (3-4), 385-422.

9. Goldstein, J.; Newbury, D.; Joy, D.; Lyman, C.; Echlin, P.; Lifshin, E.; Sawyer, L.; Michael, J. Scanning electron microscopy and X-ray microanalysis. *Plenum Press, New York,* **2003**, 3rd edition, pp. 1-9.

10. http://cimewww.epfl.ch/people/cayron/Fichiers/thesebook-chap3.pdf (Accessed – 08/09/2011)

11. http://www.plasma-biotal.com/xraydif1.html (Accessed - 31/08/2011).

12. Kellner, R.; Mermet, J. M.; Otto, M.; Widmer, H. M. Analytical Chemistry, *Wiley-VCH, New York*, **1998**, pp. 541-546, 691-700.

13. Kloprogge, J. T.; Booy, E.; Jansen, J. B. H.; Geus, J. W. The effect of thermal treatment on the properties of hydroxy-Al and hydroxy-Ga pillared montmorillonite and beidellite. *Clay Minerals*, **1994**, *29*, 153-167.

14. Maes, N.; Heylen, I.; Cool, P.; Vansant, E. F. The relation between the synthesis of pillared clays and their resulting porosity. *Applied Clay Science*, **1997**, *12*, 43-60.

15. Mahboub, R.; Mouzdahir, Y. E.; Elmchaouri, A.; Carvalho, A.; Pinto, M.; Pires, J. Characterization of a delaminated clay and pillared clays by adsorption of probe molecules. *Colloids and Surfaces A: Physicochem. Eng. Aspects*, **2006**, *280*, 81–87.

16. Manohar, D. M.; Noeline, B. F.; Anirudhan, T. S. Adsorption performance of Al-pillared bentonite clay for the removal of cobalt (II) from aqueous phase. *Applied Clay Science*, **2006**, *31*, 194–206.

17. Matthes, W.; Madsen, F. W.; Kahr, G. Sorption of heavy-metal cationsby Al and Zr-hydroxyintercalated and pillared bentonite. *Clays and Clay Minerals,* **1999**, *47* (5), 617-629.

18. Pavia, D. L.; Lampman, G. M.; Kriz, G. S. Introduction to spectroscopy: A guide for for students of organic chemistry. *Thomson Learning, Inc*, **2001**, 3rd edition, 14-24, 353-358.

19. Ross, D. S.; Ketterings, Q. Recommended Methods for Determining Soil Cation Exchange Capacity. *Recommended soil testing procedures for the North-eastern America:Cooperative Bulletin No. 493,* pp 62-69 (http://ag.udel.edu/extension/Soil_Testing/INTRO.pdf).

20. Sing. K. S. W.; Haul, R. A. W.; Pierotti, R. A.; Siemieniewska, T. Reporting physisorption data for gas/solid systems with special reference to the determination of surface area and porosity. *Pure & Applied Chemistry*, **1985**, *57* (4), 603-619.

21. Skinner, M. F.; Zabowski, D.; Harrison, R.; Lowe, A.; Xue, D. Measuring the cation exchange capacity of forest soils. *Communications in Soil Science and Plant Analysis*, **2001**, *32* (11&12), 1751–1764.

22. van Olephen, H. Thermodynamics of interlayer adsorption of water in clays. I.—Sodium vermiculite. *Journal of Colloid Science*, **1965**, *20* (8), 822-837.

23. Whiston, C. X-ray methods (Analytical chemistry by open learning). *John Wiley & Sons*, **1987**, pp. 1-225.

24. Willard, H. H.; Merrit, L. L. (Jr); Dean, J. A.; Settle, F. A. (Jr). Instrumental Methods of Analysis, **1988**, 7th edition, pp. 321-338, 767-769, *Warsdworth Publishing Company*, Belmont, California.

25. Yuan, P.; He, H.; Bergaya, F. A.; Wu, D.; Zhou, Q.; Zhu, J. Synthesis and characterization of delaminated iron-pillared clay with meso–microporous structure. *Microporous and Mesoporous Materials*, **2006**, *88*, 8–15.

26. Zhao, Y.; Wang, K.; Zhu, F.; Xue, P.; Jia, M. Properties of poly (vinyl chloride)/wood flour/montmorillonite composites: Effects of coupling agents and layered silicate. *Polymer Degradation and Stability*, **2006**, *91*, 2874-2883.

Chapter 4

Preparation and Characterization of Aluminium-pillared Montmorillonite Clay

4.0 Introduction

This chapter is about the preparation of aluminium-pillared montmorillonite (AlpMMT). In an attempt to enhance the adsorption properties toward both heavy metals and organic pollutants, montmorillonite clay was modified through aluminium pillaring.

A number of pillaring parameters were varied in order to achieve high d-spacing, high surface area, and hence, high adsorption capacity. Such parameters included: pillaring temperature, pH, hydroxide ions to aluminium cations (OH/Al) molar ratio and Al/clay ratio as these are known to have an effect on the microporosity and surface acidity of Al-pillared clays (Hutson, N. D. et al, 1999). The Al-pillared materials were characterized using a number of techniques and the results are presented in Section 4.4.

To the best of our knowledge, there is no reported systematic study showing how the properties of clay depend on Al/clay ratio, OH/Al molar ratio, temperature and pH. In addition, there is no assessment or evaluation reported on how the adsorption of heavy metals onto Al-pillared MMT depends on the OH/Al molar ratio.

4.1 Experimental Details

4.1.1 Preparation of aluminum-pillared montmorillonite

The process of pillaring entails the following: intercalation and fixation (by a thermal treatment) of bulky molecules (which act as pillars or props) separating the layers apart, creating a permanent porosity (Bouchenafa-Saïb, N. et al, 2007). The achieved porosity is very versatile which makes the pillared clays very attractive for adsorption purposes (Maes, N. et al, 1997).

A review of the work done on aluminum-pillared clays (AlpMMT) as well as their preparation and application has been given in Chapter 2. From literature, the preparation of AlpMMT generally entails these steps i.e. the preparation of a dilute pillaring solution, preparation of a dilute aqueous clay suspension, followed by the addition of the pillaring solution to the clay suspension, settling, washing,

drying and calcination (Manohar, D. M. et al, 2006). The calcination stage leads to the formation of the aluminum oxide pillars. The procedure followed in this work is described in the sections that follow.

4.1.1.1 Preparation of pillaring solution

The procedure used for the pillaring was similar to the one reported previously in the literature (Tichit, D. et al, 1988; Khalaf, H. et al, 1997; Danis, T. G. et al, 1998; Manohar, D. M. et al, 2006). In this study, 0.2 M $AlCl_3.6H_2O$ solution (200 mL) was added to a 1000 mL beaker followed by the addition of 184 mL of 0.5 M NaOH solution dropwise using a burette. This gave a pillaring solution with an OH/Al ratio of 2.3. At this hydrolysis ratio, Al_{13} is the major species in solution. The resulting pillaring solution was then aged overnight before use in the pillaring process. A clear pillaring solution resulted after overnight aging under constant magnetic stirring.

4.1.1.2 Pillaring process

About 4.0 g of NaMMT was slowly dispersed in 400 mL of deionised water under high speed magnetic stirring to give a 1% w/v NaMMT suspension, as was done in a reported procedure (Pires, J. et al, 1997). Stirring continued for 2 h until all the NaMMT was uniformly dispersed in the distilled water. This was followed by the dropwise addition of the aged pillaring solution to the dispersed NaMMT at room temperature. Vigorous magnetic stirring was maintained throughout the addition process. The mixture was stirred for a further 3 h after addition of all the pillaring solution. The slurry was then poured into a 1-L measuring cylinder and allowed to settle overnight. The Al-pillared MMT clay was isolated via centrifugation and washed several times with distilled water until no more Cl^- ions could be detected with a 0.1 M $AgNO_3$ solution. The chloride-free AlpMMT was then dried at 50 °C overnight in a ventilated oven. It is reported that rapid drying of the AlpMMT clay at higher temperatures results in a very hard product that is difficult to grind to powder (Storaro, L. et al, 1996; Matthes, W. et al, 1999).

4.1.1.3 Calcination of Al-pillared montmorillonite samples.

Calcination was carried out in order to form and permanently fix the aluminium oxide pillars between clay sheets ((Bouchenafa-Saïb, N. et al, 2007). Calcination was performed to prevent aluminium species from leaching into water during the adsorption process. The dry AlpMMT samples were ground into a fine powder by using mortar and pestle. To facilitate calcination, a ceramic (porcelain) dish containing a fine powder of AlpMMT was placed in an oven and the temperature was subsequently raised from ambient to 400 °C at a rate of 13.3 °C/min. The temperature of the oven was held at 400 °C for 4 h. The AlpMMT samples were then characterized using FTIR, TGA, XRD and BET surface area analysis. The following section describes the preparation of AlpMMT under

different conditions; variation of pH (2 – 5.7), temperature (25 – 80 °C), Al/NaMMT and OH/Al molar ratios (0.5 – 2.6).

4.1.2 Optimization of the pillaring process

It has been reported that a number of factors affect the porosity and surface area of the metal pillared clays. Such factors include: the Al/NaMMT, OH/Al molar ratios, pH and temperature. It was therefore, important to optimize the pillaring process to establish the ideal conditions for the pillaring of clay with polyhydroxyaluminum (Al_{13}) cations.

4.1.2.1 Variation of Al/NaMMT ratio

The Al/clay ratio is another parameter reported to affect the porosity, surface area and acidity of the aluminum pillared clays (Katdare, S. P. et al, 2000). Samples of aluminum pillared clays were prepared at varying Al/clay ratios. The Al/clay ratio varied as follows: 5, 10, 15 and 20 mmol/g (of clay). The amount of NaMMT dispersed in water for pillaring was maintained constant and the volumes of the pillaring solutions were varied. The pH values of the pillaring solutions were about 4.3 and that of the NaMMT clay suspension was 4.0. The washing of the pillared clay to remove Cl^- ions, and the isolation of the AlpMMT samples was the same as reported for other pillared samples described earlier. The product was then dried at 50 °C for 24 h before calcinations at 350 °C for 3 h. The AlpMMT samples were labelled AlpMMT-5, AlpMMT-10, AlpMMT-15 and AlpMMT-20. Characterisation was achieved by FTIR, TGA, BET surface area analysis and XRD. The results are presented later in Section 4.4.6.

4.1.2.2 Variation of OH/Al molar ratio

Pillaring solutions were prepared at various OH/Al molar ratios using solutions of concentration 0.2 M $AlCl_3.6H_2O$ and 0.5 M NaOH. The pillaring solutions were in OH/Al molar ratios of 0.5, 1.0, 1.5, 2.0, 2.2, 2.3, 2.4, 2.5 and 2.6. Different volumes of 0.2 M $AlCl_3.6H_2O$ and 0.5 M NaOH solutions were used for the preparation of the pillaring solutions.

Suspensions of NaMMT (1%w/v) were then pillared using these solutions at room temperature (25 °C) and the pillared clay samples were dried at 50 °C in a ventilated oven. The dry samples were then calcined at 400 °C for 4 h. The calcined aluminum-pillared MMT samples were labelled AlpMMT-0.5, AlpMMT-OH/Al-1.0, AlpMMT-OH/Al-1.5, AlpMMT-OH/Al-2.0, AlpMMT-OH/Al-2.2, AlpMMT-OH/Al-2.3, AlpMMT-OH/Al-2.4, AlpMMT-OH/Al-2.5 and AlpMMT-OH/Al-2.6. The samples were characterized by TGA, FTIR, BET surface area analysis and XRD. The results are presented in Section 4.4.7.

4.1.2.3 Variation of pH

Mrad, I. et al, 1997 prepared pillared clays at various pH values and Al/clay ratios. The authors obtained the best results at a pH of 5.6 and an Al/clay ratio of 5 mmol/g of clay. Pires, J. et al, 1997 reported that they adjusted the pH of their pillaring solutions to 6 though they did not disclose what the initial pH values had been and what acid or base they used to adjust the values.

Aluminum pillared clays were also prepared at three different pH values i.e. 2.0, 4.0 and 5.7. The pH of the pillaring solution was adjusted using 0.1 M HCl and 3.0 M NH_4OH solutions, as necessary. It was quite a challenge to adjust the pH of the pillaring solutions to 6, as precipitation of colloidal $Al(OH)_3$ was observed at that pH and the solution did not clarify even after stirring for several hours. Attempts were made in vain to redissolve the colloidal $Al(OH)_3$ by heating to 50 °C.

The pH of the 1% w/v NaMMT suspensions was determined to be 8.73 and was also adjusted independently to the respective pH using 0.1 M HCl before the addition of the pillaring solutions. The aluminum-pillared MMT samples were then isolated by centrifuging and washing, followed by drying in an oven at 50 °C overnight. The samples were labelled AlpMMT-pH 2.0, AlpMMT-pH 4.0 and AlpMMT-pH 5.6, and were calcined at 400 °C for 4 h. Characterisation of the samples was carried out using FTIR, TGA, BET surface area analysis and XRD. The results for the variation of pH are discussed in Section 4.4.8.

4.1.2.4 Variation of temperature

Pillaring of MMT clay was conducted at three different temperatures (25, 50 and 80°C) with the OH/Al molar ratio, the Al/NaMMT ratio and pH values fixed at 2.3, 10 mmol/g and 4.3, respectively. The pillaring solutions were prepared and aged overnight at room temperature and then heated to 25, 50 or 80 °C just before being added to the clay suspension. The NaMMT suspensions (1% w/v) were heated to the different respective temperatures and then the hot pillaring solutions added dropwise using a burette under high-speed magnetic stirring. After all the pillaring solution was added, the mixture was kept at the respective temperature for a further 3 h applying magnetic stirring. The mixtures were then cooled to room temperature and allowed to settle. The pillared clay was then isolated by centrifuging and washing several times with distilled water until no Cl⁻ ions could be detected when tested with $AgNO_3$.

The respective AlpMMT samples were labelled AlpMMT-25 °C, AlpMMT-50 °C and AlpMMT-80 °C. Characterisation of the samples was carried out by FTIR, TGA, BET surface area analysis and XRD. The results of the variation of temperature with porosity, surface area and d-spacing are reported and discussed in Section 4.4.9. The procedure followed in this study is the same as was

reported by de Carvalho, M. B. et al, 1996. Section 4.3 gives details about the characterization of the clay samples using different techniques.

4.1.3 Characterisation of AlpMMT clay

A PerkinElmer System 2000 FTIR was used to record the infrared spectra of the NaMMT and AlpMMT. About 2.0 mg of sample was properly mixed with 200 mg of KBr and then ground thoroughly using mortar and pestle. An appropriate amount of the ground sample was pelletized using a SPECAC bolt and nut pelletizer to give a transparent pellet. The samples were run against an air background. Each sample was analysed at 24 scans in the wavenumber range 4000 cm^{-1} to 370 cm^{-1} with a resolution of 4 cm^{-1}. A PerkinElmer thermogravimetric analyzer (TGA7) fitted with a thermal analysis controller (TAC7/DX) was used for thermogravimetric analysis. The machine was operated under a nitrogen gas atmosphere and the samples were heated from 20 °C to 900 °C at a heating rate of 15 °C/minute. About 10 mg of sample was weighed into the pan and run accordingly.

Micrographs of the AlpMMT and NaMMT samples were obtained by SEM on a SEM JEOL JSM-6390 LV instrument. Surface area measurements were carried out on a TriStar II 3020 V1.02 BET instrument from Micromeritics Instrument Corporation. BET surface area analysis was carried out at the Council for Scientific and Industrial Research (CSIR) in Pretoria. The pillared clay materials (0.20 g) were heated and degassed by vacuum force to remove adsorbed foreign molecules. Controlled doses of nitrogen were introduced for adsorption and desorption cycles. The sample was placed in a vacuum chamber under liquid nitrogen at-195.6 °C and subjected to a wide range of pressures to generate adsorption and desorption isotherms. The amount of gas molecules adsorbed or desorbed was determined by the pressure variations due to the adsorption or desorption of the gas molecules by the montmorillonite clay materials. Various amounts of gas molecules are adsorbed or desorbed at different doses of the N_2 gas (the adsorbate). Knowing the area occupied by one adsorbate molecule, σ (for example, σ = 16.2 Å^2 for nitrogen), and using an adsorption model, the total surface area of the material could be determined. X-ray diffraction analysis was carried out in locked couple mode with a Bruker AXS D8 Advance diffractometer (Cu Kα radiation with λ = 1.5406 Å, 40 kV, 40 mA, equipped with a PSD Lynx-Eye Si-strip detector (with 196 channels), at room temperature.

4.2 Results and Discussion

4.2.1 Theory of the pillaring process

Equation 4.1 describes the formation of the pillaring agent, the Keggin ion (Pires, J. et al, 1997). The Keggin ion is said to be the dominant species in solution at an OH/Al molar ratio of about 2.

$$13[Al(H_2O)_6]^{3+} + 24OH^- \rightarrow [Al_{13}O_4(OH)_{24}(H_2O)_{12}]^{7+} + 62H_2O \quad + 8H^+ \qquad (4.1)$$
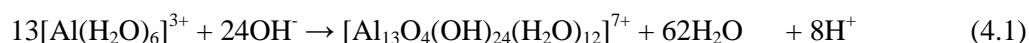
During the pillaring process, the Keggin ion gets intercalated between clay sheets. Upon calcinations of the clay, the Keggin ion decomposes (via dehydration and dehydroxylation) to form the Al_2O_3 pillars in between the clay sheets or layers. Equation 4.2 describes the formation of Al_2O_3 pillars upon calcination of the Keggin ion intercalated clay to form the Al-pillared clay (Pires, J. et al, 1997; Ohtsuka, K., 1997).

$$2[Al_{13}O_4(OH)_{24}(H_2O)_{12}]^{7+} \rightarrow 13Al_2O_3 + 14H^+ + 41H_2O \qquad (4.2)$$
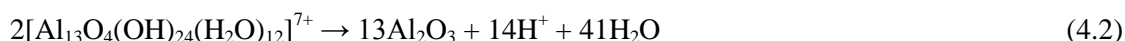
During calcination, there is loss of water and Al_2O_3 pillars are formed. The Al_2O_3 pillars prop up the clay sheets creating galleries which can act as adsorption sites for both organic molecules and heavy metals.

4.2.2 FTIR analysis of NaMMT and AlpMMT

FTIR was used to probe any changes that would occur to the clay structure as a result of Al-pillaring. Figure 4.1 below shows the spectra of NaMMT and AlpMMT (before and after calcination). The peaks labeled in the spectra of the three samples can be ascribed to structural –OH stretching vibration (3624 cm^{-1}), adsorbed water OH stretching (3431 cm^{-1}), H-O-H bending of interlayer water (1642 cm^{-1}), Si-O-Si stretching (1049 cm^{-1}), Al-OH-Al bending or deformation (920 cm^{-1}), Fe-OH-Al deformation (880 cm^{-1}), Al-OH-Mg deformation (840 cm^{-1}), O-Si-O asymmetric stretch (800 cm^{-1}), AlO_4 asymmetric stretching (780 cm^{-1}), Al-O-Si deformation (520 cm^{-1}) and Si-O-Si deformation (470 cm^{-1}) according to Manohar, D. M. et al, 2006 and Bhattacharyya, K. G. et al, 2009.

The FTIR spectra of the uncalcined NaMMT and AlpMMT did not show any major differences as seen in Figure 4.1. Kloprogge, J. T. et al, 1999 reported that the pillaring of clay with Al_{13} results in new peaks at 3682 and 3538 cm^{-1}. These new vibration bands are attributed to the Al-OH and Al-H_2O stretching of the Al_{13} complex, respectively. The authors further stated that the interlayer water (H-O-H) stretching band shifted to 3200 cm^{-1}.
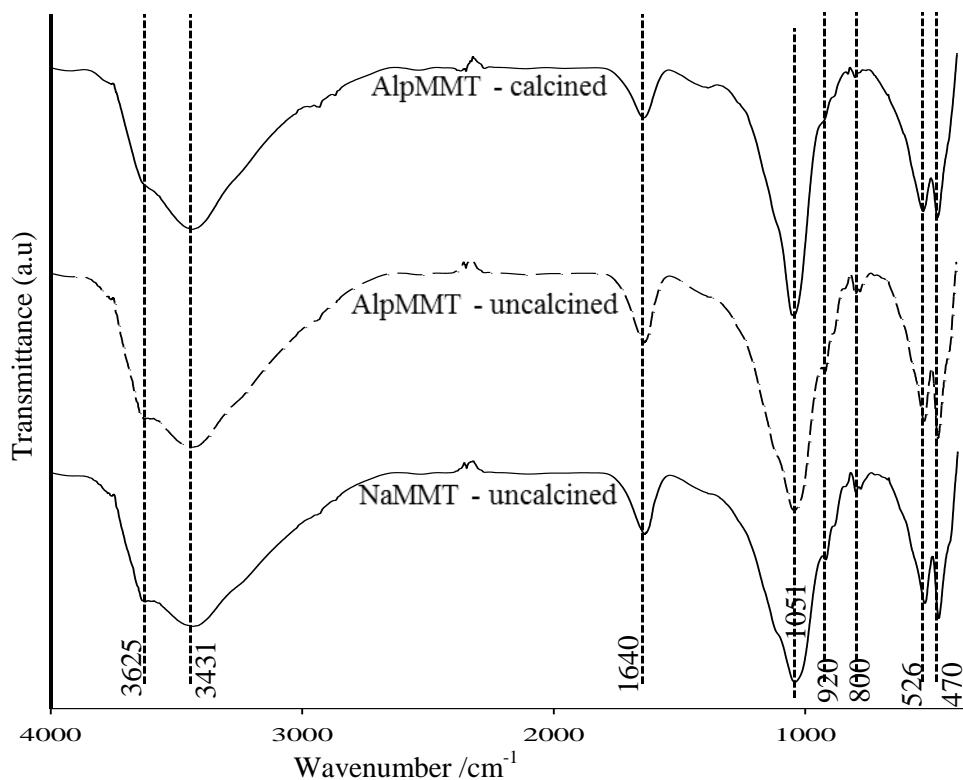
Figure 4.1: FTIR spectra of NaMMT, AlpMMT (uncalcined) and AlpMMT (calcined).

However, in all the pillared clay samples analysed in this work, such peaks have not been detected or observed. Kloprogge, J. T. et al, 1999 also observed a decrease in intensity of the interlayer water bending vibration (1642 cm^{-1}) after pillaring with Al_{13}, and attributed it to the replacement of water molecules by the incoming Al_{13} Keggin ion. In another investigation, Kloprogge, J. T. et al, 2002 synthesised Al-pillared MMT clay and reported observing a small band at about 670 cm^{-1} which again was attributed to the intercalated Al_{13} complex or oligomer. This band was ascribed to the Al-O bond of tetrahedrally coordinated Al atoms in the centre of the Al_{13} oligomer. After calcination at 400 °C, differences were observed for vibrational peaks at 3631, 920, 880 and 840 cm^{-1}.

However, the retention of all peaks as in the parent montmorillonite framework clearly shows that the basic clay layer structure remains unaffected on pillaring as well as on calcination at 400 °C. The absence of additional peaks suggests that no bond formation occurred between the Al_2O_3 pillars and the montmorillonite structure (Kurian, M. et al, 2005).

4.2.3 Thermogravimetric analysis of NaMMT and AlpMMT

The clay samples were subjected to TGA analysis in the temperature range 20 – 900 °C. Figure 4.2 shows thermograms (TGA) and differential thermograms (DTG) of uncalcined NaMMT and

AlpMMT. The TGA thermograms show two major steps, and the respective DTG thermograms (dW/dT) showed two peaks corresponding to these steps.
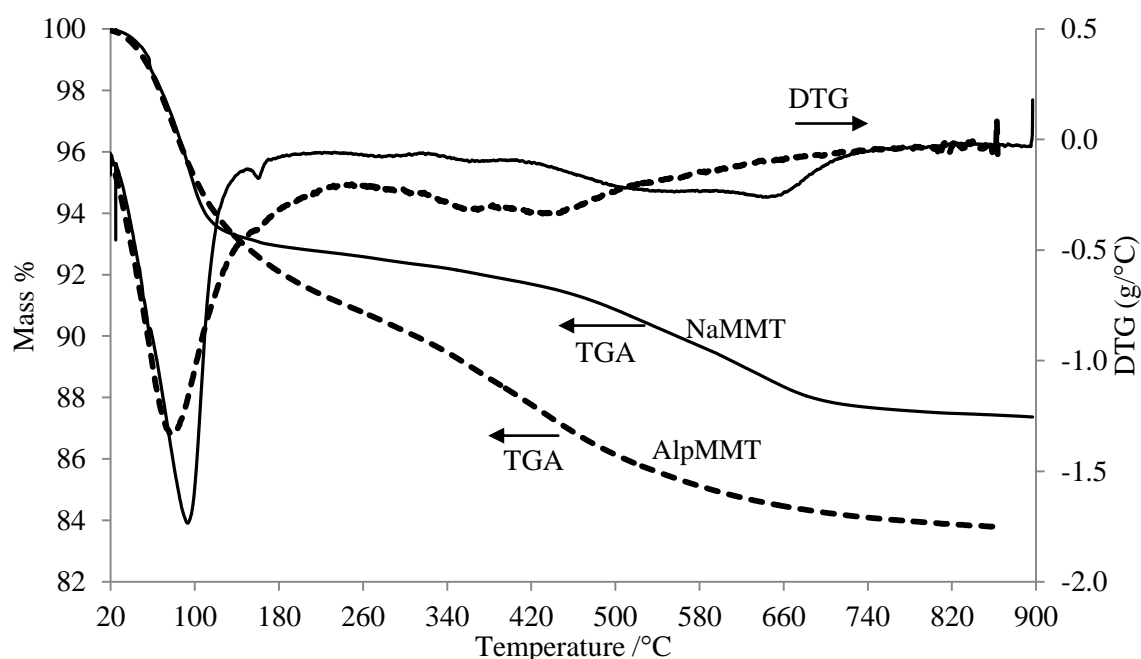
Figure 4.2: Thermograms and differential thermograms of uncalcined NaMMT and uncalcined AlpMMT.

In both AlpMMT and NaMMT the first mass loss step (or peak) is found below 120 °C which can be attributed to the removal of adsorbed water. The second mass loss step (or peak) for NaMMT, which is broad can be observed within the temperature range 500-700 °C. This peak is due to the removal of interlayer water (dehydroxylation) of the montmorillonite clay. The second peak for AlpMMT in the temperature range 320-520 °C can be ascribed to the dehydroxylation of the Al_{13} pillars, as well as the removal of interlayer water. The peak is again broad as observed for NaMMT. The different temperature ranges for the dehydroxylation process can be explained by the fact that the clay sheets are relatively closely packed in the NaMMT than in AlpMMT. The intercalation of the polymeric Keggin ion (Al_{13}) species into the clay layers forces the clay sheets further apart, thus resulting in easy diffusion (removal) of water associated with the Keggin ion pillars upon heating. The formation of metal oxide pillars in the interlayer space also occurs in this temperature region (Acemana, S. et al, 1999). In the closed structure of the NaMMT clay, the cation hydration water cannot easily escape upon heating. Similar results were reported by Kurian, M. et al, 2005 but on iron-pillared montmorillonite clay.

In addition, there was a greater mass loss for the AlpMMT than the NaMMT. This can be explained in terms of the dehydroxylation of the intercalated Al_{13} oligomer as well as the clay structure, whereas in

the NaMMT, there is only the dehydroxylation of the clay structure (Pires, J. et al, 1997; Manohar, D. M. et al, 2006). Otherwise, there were no other major changes observed in the thermograms. The samples were further analysed by BET surface area analysis.

4.2.4 BET surface area analysis of NaMMT and AlpMMT

The BET method is based on the adsorption of gas on a surface. The theory of BET surface area analysis has been presented in Section 3.5.6 of Chapter 3 together with the classification of different gas adsorption-desorption isotherms. Figure 4.3 shows the N_2 adsorption-desorption isotherms for calcined NaMMT and AlpMMT. The adsorption isotherms can be classified as Type IV for both NaMMT and AlpMMT. Characteristic features of the Type IV isotherm are its hysteresis loop (which is associated with capillary condensation taking place in mesopores) and the limiting uptake over a range of high relative pressure. The initial part of the Type IV isotherm is attributed to monolayer-multilayer adsorption since it follows the same path as the corresponding part of a Type II isotherm obtained with a given gaseous adsorbate on the same surface area of the adsorbent in a non-porous form. Type IV isotherms are given by many mesoporous industrial adsorbents (Sing, K. S. W. et al, 1985).

Adsorption hysteresis arises when the adsorption and desorption curves do not concide. The quantity adsorbed is different when gas is being added than it is when being removed. The specific causes of adsorption hysteresis are still an active area of research, but it is linked to differences in the nucleation and evaporation mechanisms inside mesopores. These mechanisms are further complicated by effects such as cavitation and pore blocking. In physical adsorption, hysteresis is evidence of mesoporosity. (Sing, K. S. W. et al, 1985).
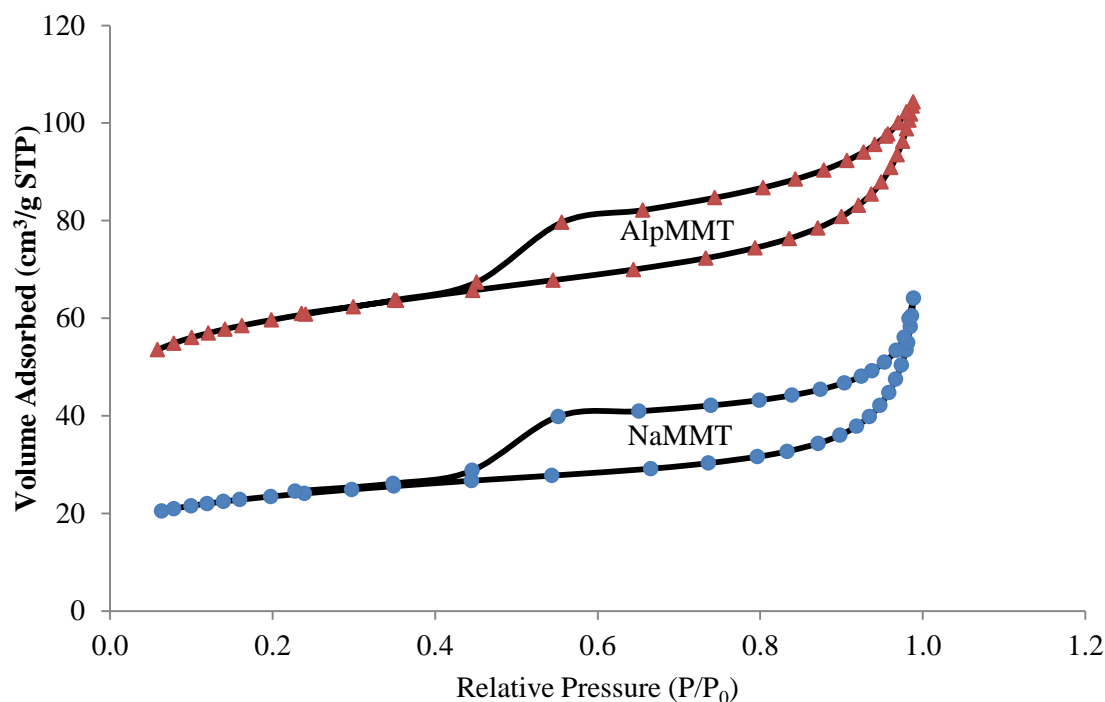
Figure 4.3: N_2 adsorption-desorption isotherms for NaMMT and AlpMMT.

Both the unpillared and pillared MMT samples showed a hysteresis loop. The presence of a hysteresis in the N_2 adsorption-desorption isotherms is an indication of mesoporosity (Sing, K. S. W. et al, 1985; Mahboub, R. et al, 2006). Physisorption in mesopores is said to take place in two more or less distinct stages (monolayer-multilayer adsorption and capillary condensation). In monolayer adsorption all the adsorbed molecules are in contact with the surface layer of the adsorbent. In multilayer adsorption the adsorption space accommodates more than one layer of molecules so that not all adsorbed molecules are in direct contact with the surface layer of the adsorbent. In capillary condensation the residual pore space which remains after multilayer adsorption has occurred is filled with condensate separated from the gas phase by menisci. Capillary condensation is often accompanied by hysteresis. (Sing. K. S. W. et al, 1985).

A feature common to many hysteresis loops is that the steep region of the desorption branch leading to the lower closure point occurs (for a given adsorbate at a given temperature) at a relative pressure which is almost independent of the nature of the porous adsorbent but depends mainly on the nature of the adsorbate (e.g. for nitrogen at its boiling point at $p/p° \approx 0.42$). The hysteresis loops observed in the two samples can be classified as H4 which are known to be associated with narrow slit-like pores (Sing. K. S. W. et al, 1985; Salerno, P. et al, 2002). The N_2 adsorption-desorption isotherms of the two samples show that more N_2 adsorption occurs onto AlpMMT than NaMMT.

Park, H. M. et al, 2006 prepared nickel-intercalated montmorillonite clay. The authors detected a hysteresis in the pressure region of $p/p_0 > 0.5$ for the nickel-pillared samples. This was attributed to the formation of a mesoporous structure originating from the "house-of-card" stacking of the clay crystallites. This type of stacking of clay is also referred to as clay delamination. The N_2 adsorption-desorption isotherms of their nickel-pillared clay were found to follow the BDDT type I and IV shape, along with H4-type hysteresis loop according to the IUPAC classification. Such a type of isotherm underlines the presence of the open slit-shaped capillaries with very wide bodies and narrow short necks (Park, H. M. et al, 2006).

4.2.5 SEM analysis of NaMMT and AlpMMT

The Al-pillared and sodium-exchanged montmorillonite (NaMMT) clay samples were anaylsed by using scanning electron microscopy in order to assess the changes in morphology after pillaring. Figure 4.4 displays the scanning electron micrographs of the unpillared NaMMT and AlpMMT.
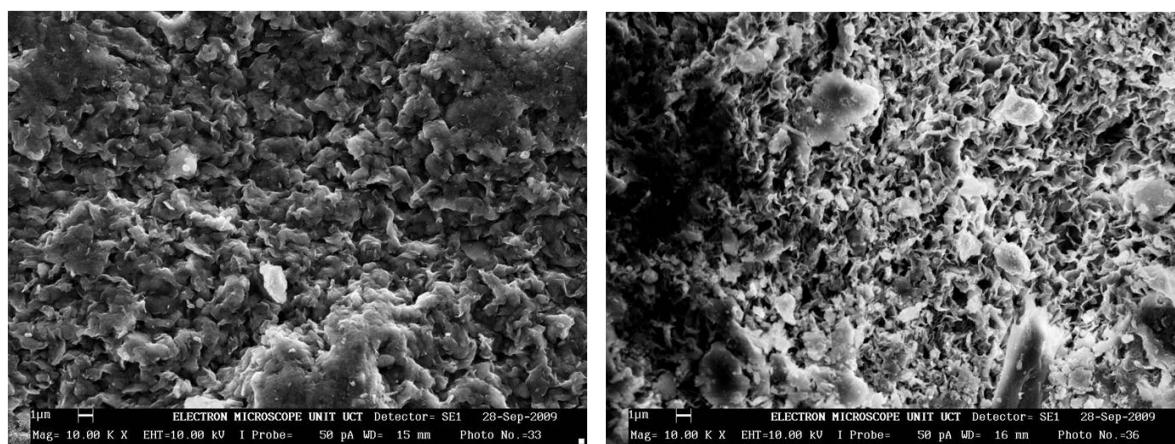
Figure 4.4: SEM images of NaMMT and AlpMMT at a Magnification of 10 000X.

It is evident from the two micrographs that the pillared and unpillared MMT samples display different morphologies. Al-pillared MMT showed a more open, porous structure compared with the unmodified NaMMT sample. The SEM images suggest that pillaring resulted in the delamination of the clay sheets and the creation of cavities which may serve as adsorption sites for both organic and inorganic pollutants. The Al-pillared samples are expected to have improved surface areas as a result of the delamination of the clay sheets.

As mentioned in Section 4.2, a number of parameters were varied to assess their effect of the physicochemical properties of the Al-pillared MMT samples. The following sections discuss the results obtained from the characterization of AlpMMT samples prepared at different conditions of pH, temperature, Al/clay ratio and OH/Al molar ratio.

4.2.6 Effect of variation of Al/NaMMT ratio

As mentioned above, a number of parameters were varied in order to optimize the pillaring process. The Al/clay ratio is one of the parameters assessed, and the following section presents the FTIR results.

4.2.6.1 FTIR analysis of AlpMMT-n samples

Figure 4.5 shows the FTIR spectra of AlpMMT samples prepared at different Al/NaMMT clay ratios ranging from 5 to 20 mmol/g. The number written after AlpMMT- represents the Al/NaMMT ratio (in mmol/g). The change in the Al/clay ratio did not affect the clay framework structure. The same vibrational peaks as discussed in Section 4.2.2 were observed.
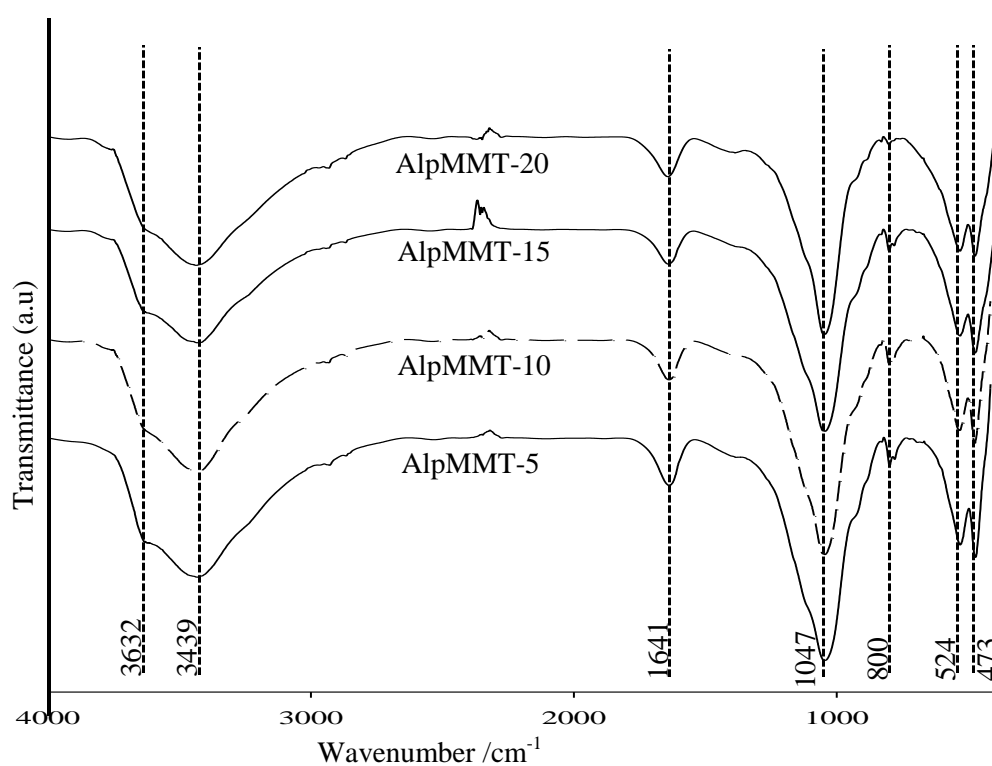
Figure 4.5: FTIR spectra of AlpMMT samples prepared at different Al/NaMMT clay ratios (mmol Al/g of NaMMT).

4.2.6.2 Thermogravimetric analysis of AlpMMT-n samples

Figure 4.6 displays the thermograms of AlpMMT samples prepared at different Al/clay ratios. There was no trend that could be deduced from the thermograms. High intercalation of the Al_{13} species was expected to result in an increased % mass loss of the pillared clays as discussed in Section 4.4.3. The NaMMT showed the least % mass loss while AlpMMT-20 gave the highest. The high % mass loss in AlpMMT-20 can be speculated to be due to increased intercalation of the Al_{13} ion (Manohar, D. M. et al, 2006) as described in Section 4.4.3 above.
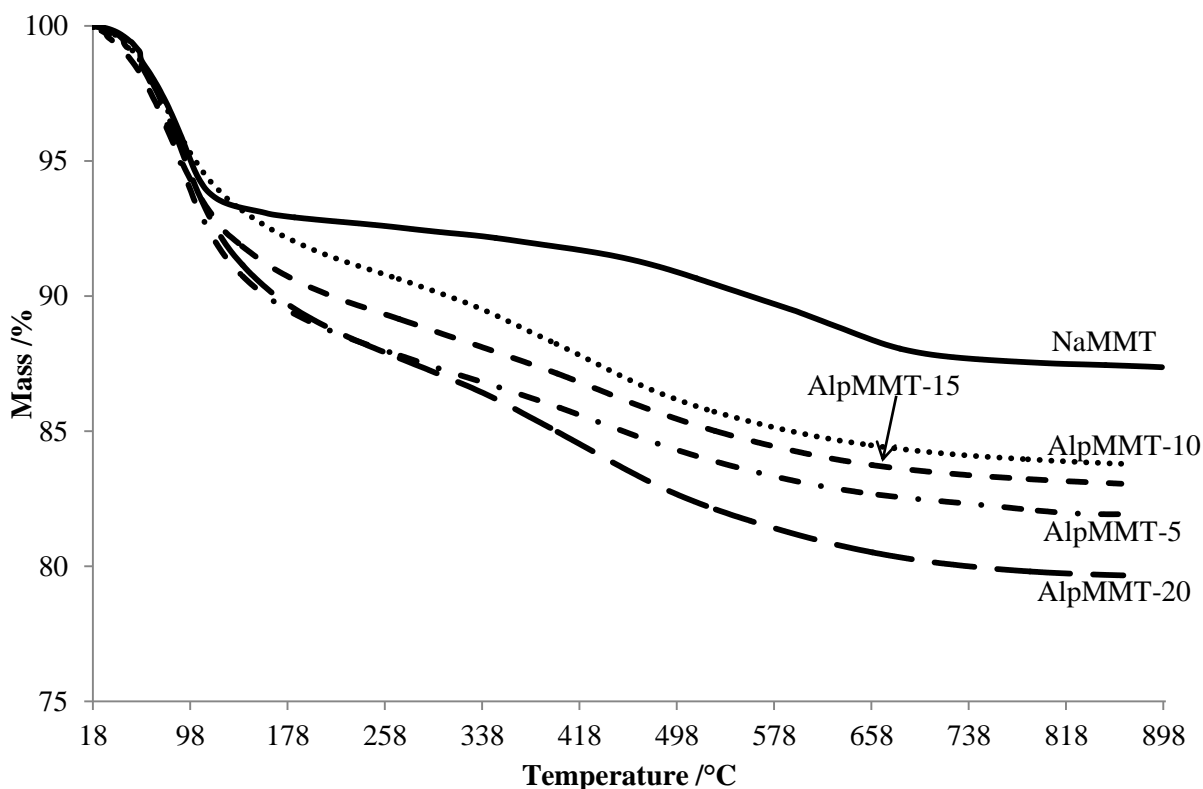
Figure 4.6: Thermograms of AlpMMT samples prepared at different Al/clay ratios.

4.2.6.3 BET surface area analysis of AlpMMT-n samples

Table 4.1 shows the BET surface areas and pore sizes of Al-pillared samples prepared at different Al/clay ratios. The respective N_2 adsorption-desorption curves can be found in Figures A-1 to A-5. The surface area was observed to increase with increase in the Al/clay ratio, reaching a maximum at 10 mmol/g. Above 10 mmol/g, there was a decrease in the surface areas of the samples. However, the pore sizes did not show the same trend as seen with the surface areas. The best Al/clay ratio for pillaring can be said to be 10 mmol/g since it registered the highest surface area even though it had the smallest pore size.

Table 4.1: BET surface area results for the variation of Al/NaMMT clay ratio.

Sample	BET surface area (m^2/g)	Pore sizes (nm)
NaMMT	82	4.17
AlpMMT-5	164	2.99
AlpMMT-10	214	2.65
AlpMMT-15	194	3.36
AlpMMT-20	195	3.14

Chae, H. J. et al, 2001 varied the Al/NaMMT clay ratio in their preparation of interlayered clays. The samples were calcined at 300 °C. Their BET results showed that the surface area of the Al-pillared samples increased with increase in Al/NaMMT clay ratio (from 3 mmol/g to 5 mmol/g, reaching a maximum at 10 mmol/g). Their respective surface areas in increasing order were 188, 208, 220 and 205 m^2/g for Al/clay ratios of 3, 5, 10 and 20 mmol/g, respectively. Their results were similar to what was found in this study with the highest surface area being recorded at an Al/clay ratio of 10 mmol/g. The samples were also analysed by XRD and the results are discussed in the next section.

4.2.6.4 X-ray diffraction analysis of AlpMMT-n samples
Figure 4.7 shows the XRD patterns of AlpMMT samples prepared by varying the Al/clay ratio. The diffractogram of NaMMT showed that its basal reflection peak occurred at a 2θ angle of around 6.22° corresponding a d-spacing of 14.2 Å (see Figure 4.10).
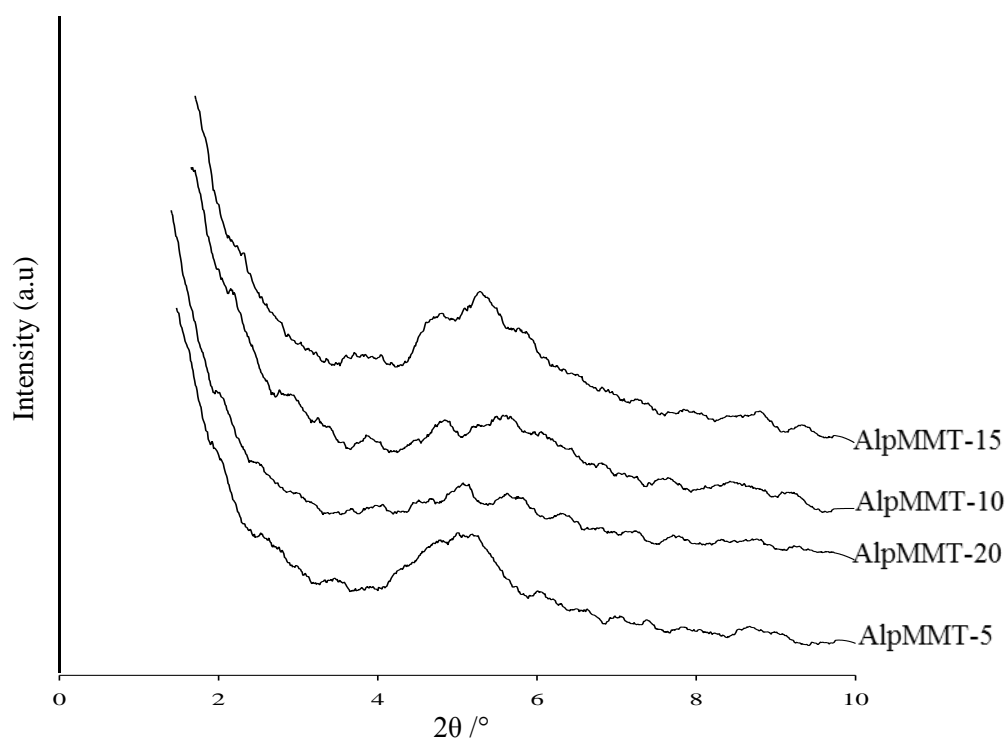
Figure 4.7: XRD patterns for AlpMMT samples prepared at varying Al/NaMMT clay ratios.

Table 4.2 displays results of the d-spacing of AlpMMT samples prepared at different Al/NaMMT clay ratios. The AlpMMT samples were prepared at a pH of 4.3 and OH/Al molar ratio of 2.3. The basal spacings (d-spacing) of the NaMMT and AlpMMT samples were computed using Braggs equation:

$$n\lambda = 2dSin\theta \qquad\qquad (4.5)$$

107

Table 4.2: Variation of d-spacing of AlpMMT samples with Al/NaMMT clay ratio.

Sample	2θ /°	d-spacing /Å	Δ(d-spacing) /Å
NaMMT	6.22	14.2	-
AlpMMT-5	4.92	18.0	3.8
AlpMMT-10	4.92	18.0	3.8
AlpMMT-15	5.16	16.9	2.7
AlpMMT-20	5.02	17.6	3.4

The d-spacing appeared to decrease with increase in the Al/NaMMT clay ratio. The same d-spacing value was obtained for AlpMMT-5 and AlpMMT-10 which were prepared at an Al/NaMMT clay ratio of 5 and 10 mmol/g, respectively. It appears the change in Al/NaMMT clay ratio did not have a direct effect on the d-spacing.

Mishra, T. et al, 1997 prepared manganese-pillared clay at varying OH/Mn molar ratio. Their results showed a direct correlation between the d-spacing and the surface areas obtained. These two parameters had their maxima at the highest amount of metal ion incorporated. In this study, an Al/clay ratio of 10 mmol/g was chosen for further investigation. An investigation by Kloprogge, J. T. et al, 1994 found an increase in the d-spacing of Al-pillared clays (16.7 to 17.7 Å) with increase in the Al/clay ratio from 3.0 to 5.5 mmol/g. The d-spacing then decreased to 17.4 Å on increasing the Al/clay ratio to 20 mmol/g. According to the XRD results, the Al-pillaring of NaMMT can be carried out at an Al/clay ratio of between 5 and 10.

Khalaf, H. et al, 1997 prepared Al-pillared clays under different conditions. They varied the drying temperature, aging period for the pillaring solution, OH/Al molar ratio and Al/clay ratio. The authors did not observe any major differences in the d-spacing of pillared samples when they varied the Al/clay ratio. Sun-Kou, M. R. et al, 1998 prepared zirconium-pillared montmorillonite at different Zr/clay ratios and also under different mixing conditions. The surface areas of the pillared samples increased with increase in the Zr/clay ratio which was attributed to an increase in the amount of Zr in the pillared samples with increase in the Zr/clay ratio. The d-spacing was also observed to increase with increase in the amount of intercalated Zr.

4.2.7 Effect of variation of OH/Al molar ratio

4.2.7.1 FTIR analysis of AlpMMT-OH/Al-n samples

The OH/Al molar ratio of the pillaring solutions was varied from 0.5 to 2.6. Figure 4.8 displays the FTIR spectra of the different AlpMMT samples prepared at different OH/Al molar ratios and these are

labelled accordingly, with the number representing the OH/Al molar ratio. As observed above for the pillared samples prepared at different Al/clay ratios, the effects of varying the OH/Al molar ratio were not detectable by FTIR or there were no changes to the framework bonding of the clay structure.
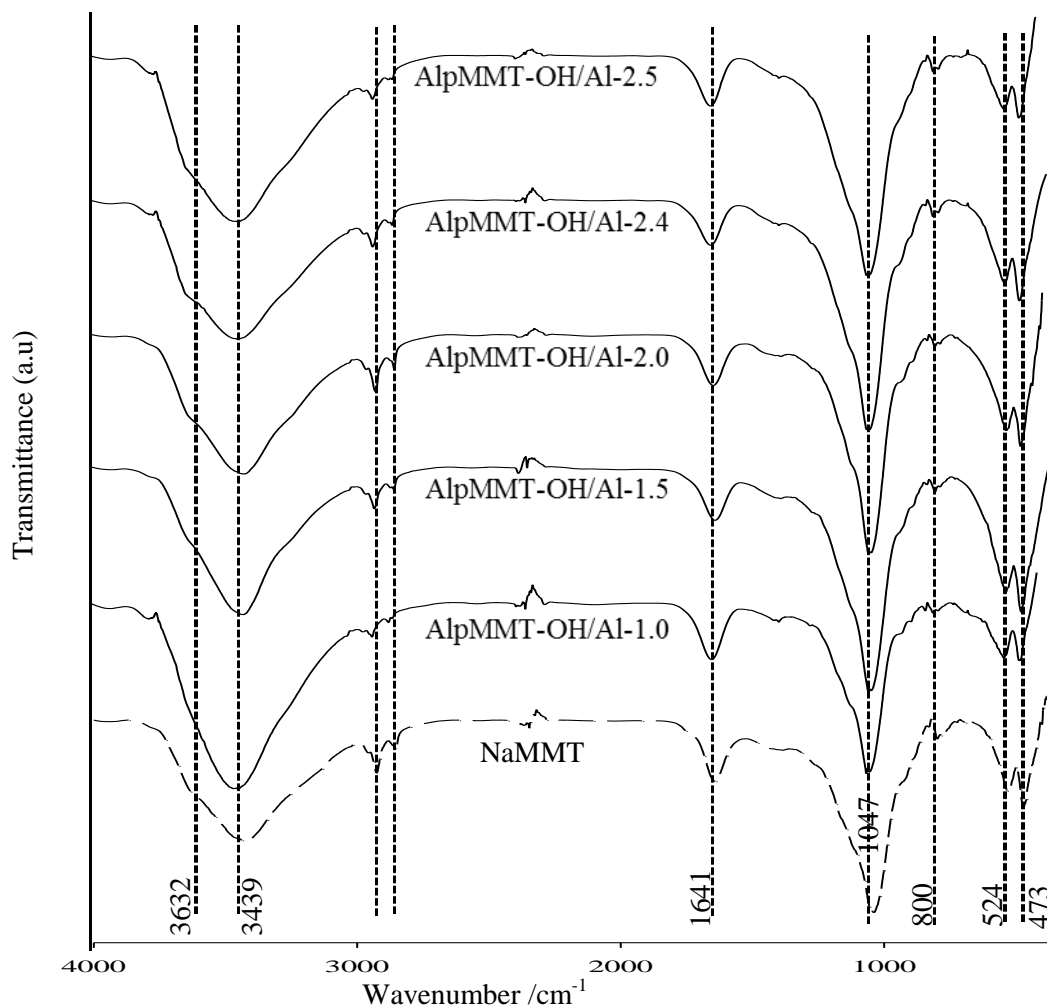
Figure 4.8: FTIR spectra for AlpMMT prepared at different OH/Al molar ratios.

Almost the same FTIR spectra were observed for all the AlpMMT clay samples prepared at different OH/Al molar ratios. The samples were further analysed by thermogravimetric analysis and the results are discussed in the following section.

4.2.7.2 Thermogravimetric analysis of AlpMMT-OH/Al-n samples

The thermograms of the different samples are displayed in Figure 4.9. The mass loss of the pillared samples decreased with an increase in the OH/Al molar ratio, at least for the samples pillared at OH/Al ratio of 1.5, 2.0, 2.4 and 2.6, respectively. The decreasing mass loss was attributed to possibly the decreasing degree of intercalation as the OH/Al molar ratio increased.
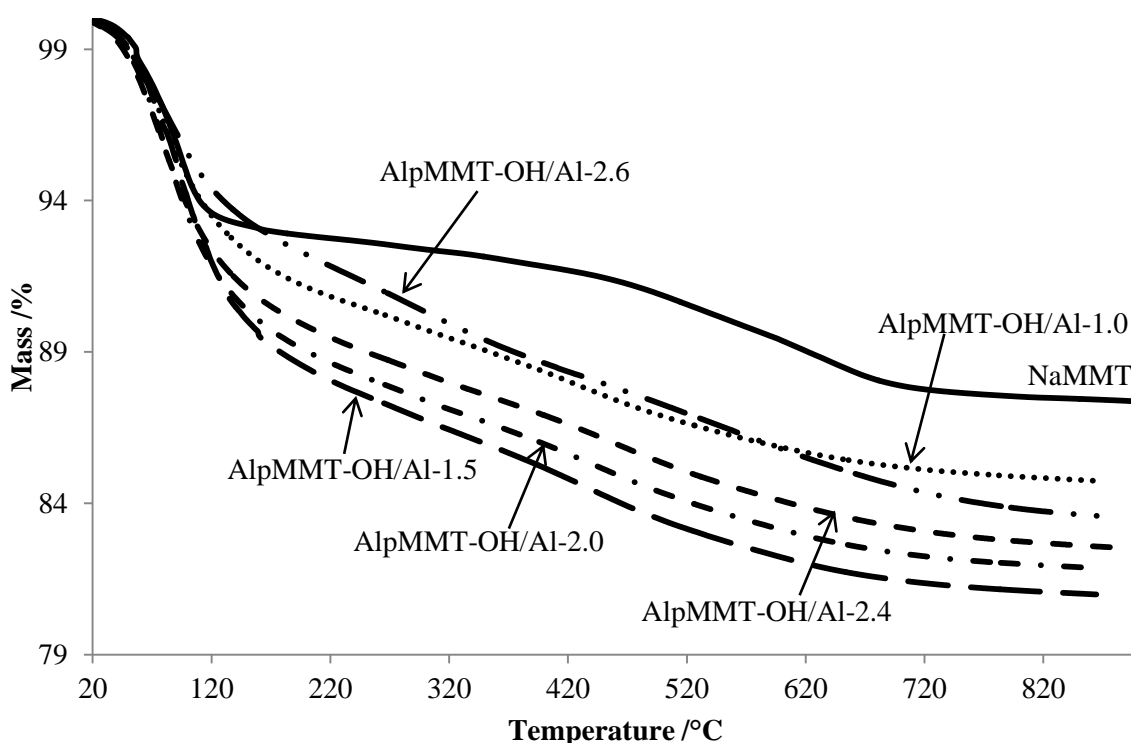
Figure 4.9: Thermograms of AlpMMT samples prepared at different OH/Al molar ratios.

During the preparation of the pillaring solutions, it was observed that starting from an OH/Al molar ratio of 2.4, there was formation of colloidal Al(OH)$_3$ which took time to redissolve. At higher OH/Al molar ratios (2.5 and 2.6), the Al(OH)$_3$ remained suspended in the pillaring solution without dissolving. The formation of colloidal Al(OH)$_3$ caused a reduction of the concentration of the intercalating agent, the Keggin ion species, hence little Al(OH)$_3$ was intercalated. Also, the Al$_{13}$ ion species concentration might have been much lower at an OH/Al molar ratio of 1.0, hence, poor intercalation and the low mass losses recorded for 1.0, 2.5 and 2.6 (Bergaya, F. et al, 2006). The following section presents the results from BET surface area analysis.

4.4.7.3 BET surface area analysis of AlpMMT-OH/Al-n samples

BET surface analysis was employed in this study to determine the surface areas of the different AlpMMT samples prepared and also the NaMMT. The total surface areas of the AlpMMT samples prepared under different conditions were determined and a comparison carried out in order to establish the favourable conditions for the pillaring process.

Table 4.3 below summarises the BET surface area analysis data, i.e. surface areas and pore sizes of AlpMMT samples prepared at different OH/Al molar ratios and NaMMT. Some of the N$_2$ adsorption-desorption curves can be found in Figures A-6 to A-11. It was observed that the pillaring of clays with

Al$_{13}$-oligomer resulted in an increase in the surface area of the pillared clays relative to the NaMMT. The increase was attributed to an increase in the microporosity of the clay (Sychev, M. et al, 1997).

Table 4.3: BET surface areas and pore sizes of AlpMMT samples prepared at different OH/Al molar ratios.

Sample	BET Surface Area (m^2/g)	Pore size /nm
MMT	75.5	6.63
NaMMT	81.6	4.17
AlpMMT-OH/Al-0.0	98.4	4.05
AlpMMT-OH/Al-1.0	127.1	2.88
AlpMMT-OH/Al-1.5	248.8	2.56
AlpMMT-OH/Al-2.0	190.7	2.72
AlpMMT-OH/Al-2.3	214.0	2.65
AlpMMT-OH/Al-2.4	197.0	2.92
AlpMMT-OH/Al-2.6	194.7	2.78

From Table 4.3 above, it can be seen that the ion-exchange of MMT to NaMMT resulted in an increase in the surface area and a decrease in the pore size. After Al-pillaring, the results showed that there was an initial increase for the surface areas with OH/Al molar ratio up to a molar ratio of 1.5, followed by a decrease from 2.3 to 2.6. At low OH/Al molar ratios, (0.5 and 1.0), it can be assumed that the concentration of the pillaring species (Keggin ion) was very low and therefore, resulted in poor intercalation or ion-exchange of the clay mineral by the Keggin ion. It appears that most of the clay remained largely intact (no intercalation) at low OH/Al molar ratios. Figueras, F. et al, 1990 carried out competitive ion exchange for intercalation of montmorillonite with hydroxyl-Al$_{13}$ species. They found that the surface areas increased with increase in the amount of Al incorporated in the clays. In this study, the results of the variation of surface area with OH/Al molar ratio might imply that the maximum amount of Al incorporated in the clay structures occurred at an OH/Al molar ratio of 1.5.

For Fe-pillared MMT clay, Yuan, P. et al, 2006 found an increase in the surface area with OH/Fe molar ratio which had a maximum at an OH/Fe molar ratio of 1.0. The authors did not find a direct relationship between the surface areas obtained with the d-spacing of the clay layers. In this study, the largest surface area was obtained at an OH/Al molar ratio of 1.5.

Also shown in Table 4.3 are the pore sizes of the clays. Pore size is defined by the IUPAC as the distance between two opposite walls of the pore (diameter of cylindrical pores, width of slit-shaped

pores). It can be seen from Table 4.3 that the pore sizes changed after the pillaring process. The pore sizes also decrease in like manner as observed for the surface areas. According to Sing, K. S. W. et al, 1985, pore widths of less than 2 nm are associated with microporosity. The pore sizes showed a shift towards the microporous region after pillaring with the Al_{13}-oligomer. NaMMT showed the largest pore sizes and the smallest surface area and AlpMMT prepared at an OH/Al molar ratio of 1.5 has the least pore size and the largest surface area. Nevertheless, the samples pillared at an OH/Al molar ratio of 2.0, 2.4 and 2.6 did not quite follow the same inverse proportionality. The pore widths of the clays initially seem to decrease with increase in the OH/Al molar ratio and the trend discontinues at molar ratios of 2.0, 2.4 and 2.6.

4.2.7.4 X-ray diffraction analysis of AlpMMT-OH/Al-n samples

This section presents the XRD results of the samples prepared at different OH/Al molar ratios. The XRD patterns of NaMMT and AlpMMT samples prepared at different OH/Al molar ratios are shown in Figure 4.10. The XRD pattern for NaMMT showed a basal reflection at a 2θ angle of 6.22°. The peak was relatively more intense and sharper than those of the pillared clay samples whose basal reflection peaks were centered around a $2\theta°$ angle of 5.0°.
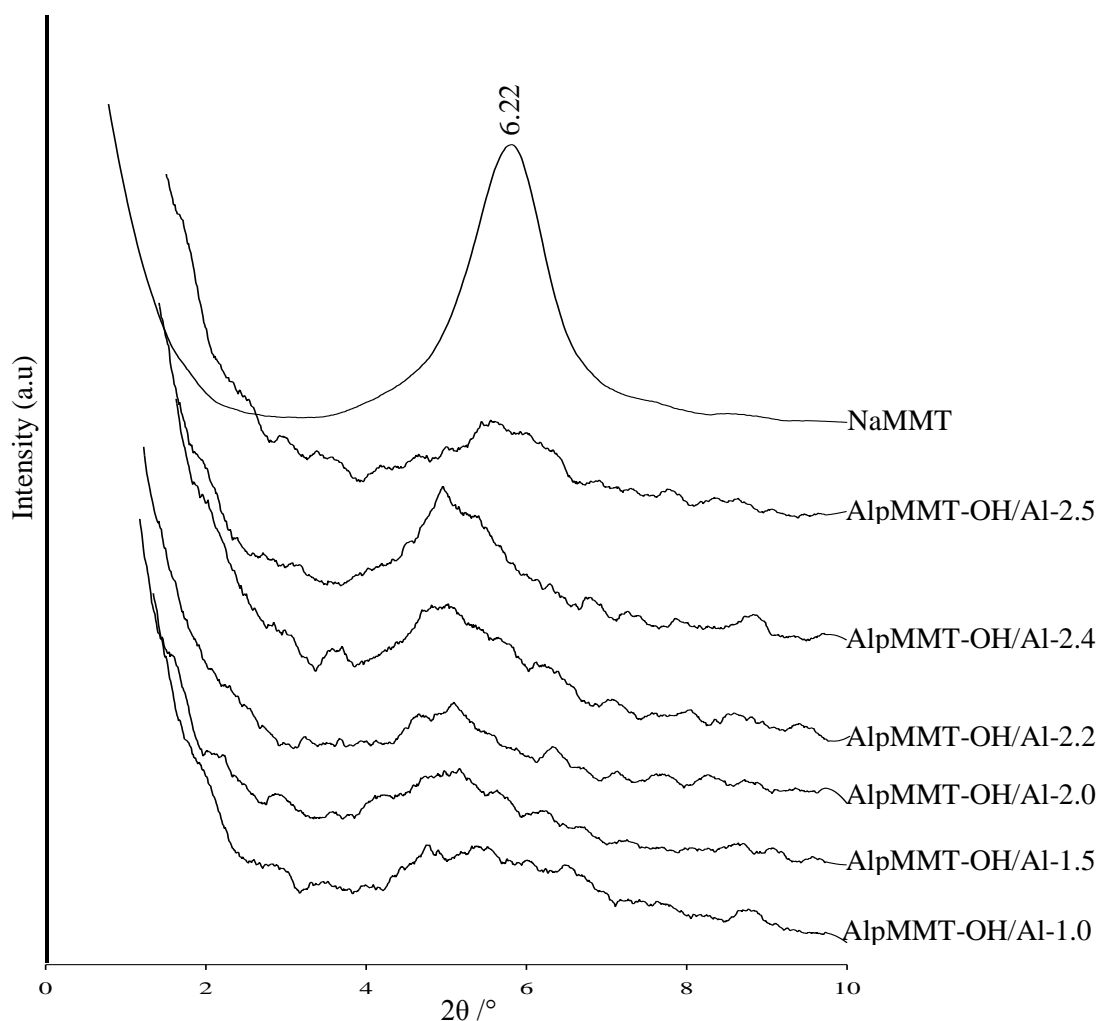
Figure 4.10: XRD patterns of AlpMMT samples prepared at different OH/Al molar ratios.

The less intense and broader peaks for the pillared samples may suggest that a fraction of the clay remained unpillared and/or delamination occurred (Altunlu, M. et al, 2007). Similar, less intense and broad peaks were obtained by Kurian, M. et al, 2005 when they investigated acid-base properties of pillared montmorillonite clays. The broad basal reflection peaks obtained for the metal-pillared clays were attributed to the destruction of crystallinity resulting in an amorphous product.

The d-spacing values are displayed in Table 4.4 together with the molar ratios of the pillared clays. NaMMT showed a d-spacing of 14.20 Å. This value was comparable with some values reported in the literature for NaMMT (Yuan, P. et al, 2006). Kricsi, I. et al, 1997 reported a d-spacing of 14.60 Å and BET surface area of 90 m^2/g for NaMMT which compare well with the values obtained in this study. It can be seen that the pillaring of the MMT resulted in a shift of the basal reflection peak to lower 2θ angles and hence, an increase in the d-spacing. This generally agrees with what has been discussed earlier regarding BET surface areas which increased after Al-pillaring.

Table 4.4: Variation of the d-spacing with OH/Al molar ratio

OH/Al^{3+}	2θ /°	d-spacing /Å	Δ(d-spacing) /Å
NaMMT	6.22	14.20	-
AlpMMT-OH/Al-1.0	4.73	18.67	4.47
AlpMMT-OH/Al-1.5	5.10	17.31	3.11
AlpMMT-OH/Al-2.0	5.07	17.42	3.22
AlpMMT-OH/Al-2.3	4.92	17.95	3.75
AlpMMT-OH/Al-2.4	4.88	18.09	3.89
AlpMMT-OH/Al-2.6	4.75	18.59	4.39

The d-spacing of the AlpMMT samples increased with increase in the OH/Al molar ratio. This is with the exception of the sample pillared at a molar ratio of 1.0. This is further confirmed by the amount of change in the d-spacing relative to the unpillared sample (see far right column of Table 4.4).

Khalaf, H. et al, 1997 prepared Al-pillared clays under different conditions. They varied the drying temperature, aging period for the pillaring solution, OH/Al molar ratio and Al/clay ratio. Their pillared clays had increased d-spacings ranging from 14 Å to 18 Å. They concluded that the optimal OH/Al molar ratio for the preparation of pillared clays was 1.8. However, a close look at their data does not show much variation in the d-spacing of the pillared samples.

Altunlu, M. et al, 2007 investigated the effect of OH/Al and Al/NaMMT clay molar ratio on the adsorption properties of Al-pillared bentonites. Results of XRD analysis of their pillared samples showed an increase in d-spacing with OH/Al molar ratio. The d-spacing increased from an OH/Al molar ratio of 1.44 and reached a peak at a molar ratio of 2.0. The d-spacing then dropped at the molar ratio of 2.5. The results obtained in our study show an increase in the d-spacing with increase in the OH/Al molar ratio, reaching a maximum at a molar ratio of 2.6. Although molar ratios of 2.4 - 2.6 had the highest increase in the d-spacing, there were challenges in the preparation of the pillaring solution as highlighted in the experimental section. There was formation of colloidal $Al(OH)_3$ which precipitated out of solution, and this $Al(OH)_3$ could not be redissolved once precipitated even after heating the solution further for 1 h. In addition, the BET surface areas of AlpMMT samples prepared at OH/Al molar ratios of 2.4 and 2.6 were relatively low compared with the one at 1.5.

The pH for the pillaring process was also varied to investigate its influence on the textural properties of the metal oxide-pillared clays. The influence of pH on the textural and structural properties of the pillared clay is discussed in Section 4.4.8.

4.2.8 Effect of variation of pillaring pH

The pillaring of NaMMT was also assessed by varying the pH of both the pillaring solution and the 1% w/v NaMMT aqueous suspension. The pillaring solutions and the clay suspensions were adjusted to the required pH by using 0.1 M HCl or 3.0 M NH₄OH as described in Section 4.2.2.

4.2.8.1 FTIR analysis of AlpMMT-pHn samples

Figure 4.11 displays the FTIR spectra of AlpMMT samples prepared at different pH values. The AlpMMT sample prepared at pH 4.0 and 5.7 showed much sharper bands at 1046 cm^{-1} compared with the broad peak observed for the sample pillared at pH 2.0. This suggests that there was a loss of crystallinity in the clay prepared at pH 2.0.
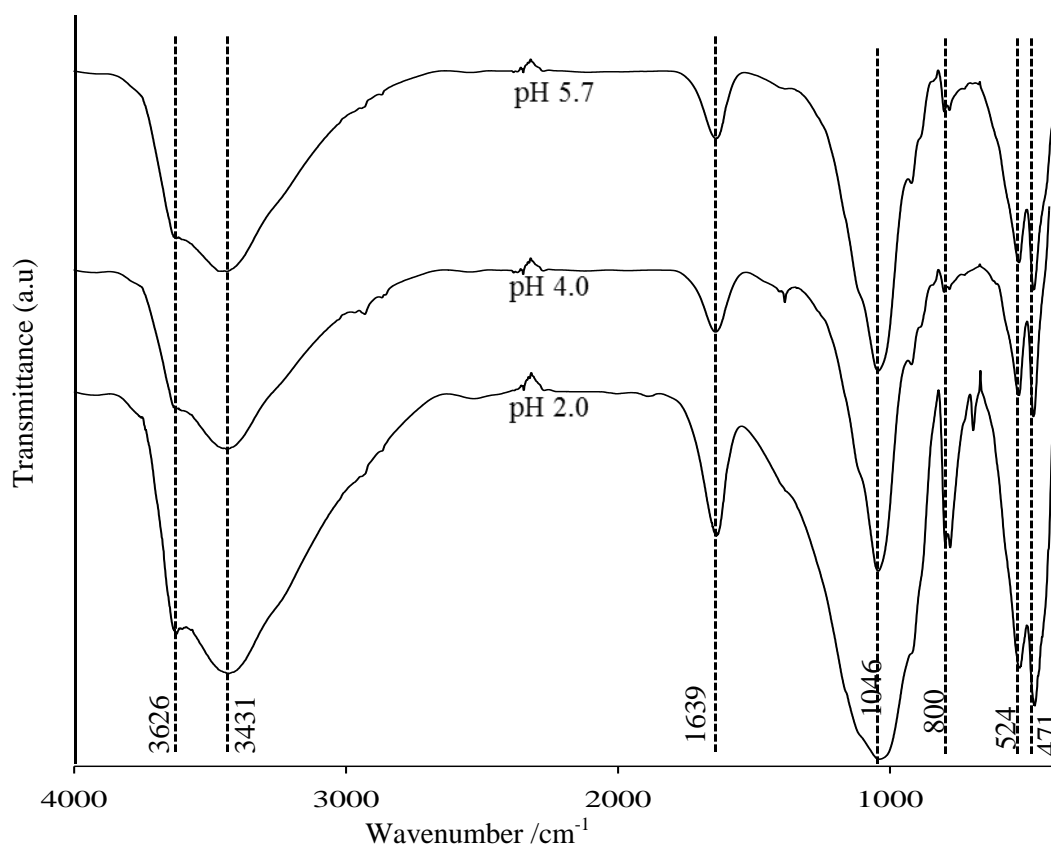
Figure 4.11: FTIR spectra of AlpMMT samples prepared at different pHs.

It is documented that acid treatment of montmorillonite clay results in the destruction of the crystal structure of the clay sheets, resulting in an amorphous material (Bhattacharyya, K. G. et al, 2007 and 2008). There was an increase in the intensity of peak at 780 cm^{-1} relative to the peak at 799 cm^{-1}. The overall intensity of these two peaks for the pH 2.0 sample is relatively greater than what was observed for the same peaks in the pH 4.0 and 5.7 samples. This increased intensity of the vibration band

around 780 cm^{-1} can be attributed to the presence of more free SiO$_2$ liberated from the tetrahedral region of the clay structure as a result of acid attack (Yildiz, N et al, 2004).

A new vibration band at 695 cm^{-1} also appeared in the sample pillared at pH 2. This can be attributed to asymmetric bending mode of O-Si-O (Manohar, D. M. et al, 2006). All the other spectral regions showed no significant differences.

4.2.8.2 Thermogravimetric analysis of AlpMMT-pHn samples
The thermograms of AlpMMT samples pillared at different pH are shown in Figure 4.12. It was observed that as the pH increased, there was also a progressive increase in the mass loss. The AlpMMT sample prepared at a pH of 2.0 had the lowest mass loss. The highest mass loss was recorded for AlpMMT pillared at a pH of 5.7. This can be attributed to the possible increased concentration of the Keggin ion (Al$_{13}$ species) at higher pH, and hence increased intercalation compared with pillaring at low pH. It can be said that the greater the amount of the Al$_{13}$ species intercalated, the greater the mass loss due to thermal decomposition.
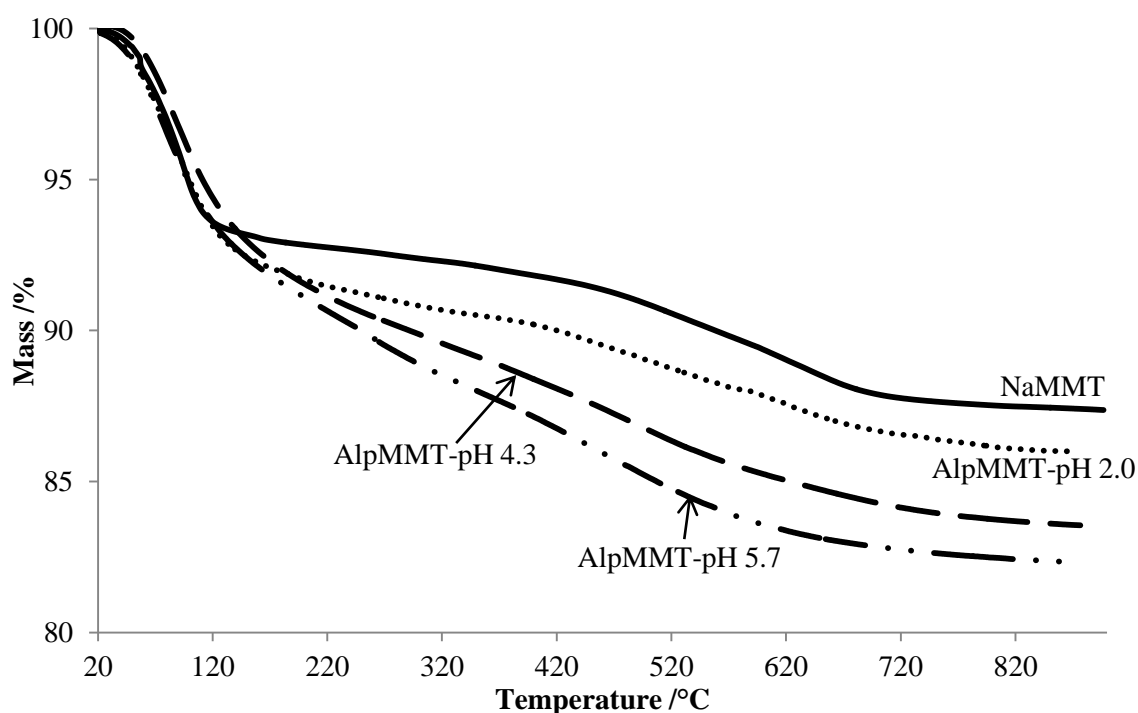
Figure 4.12: Thermograms of NaMMT and AlpMMT prepared at pH 2.0, 4.3 and 5.7.

4.2.8.3 BET surface area analysis of AlpMMT-pHn samples
Table 4.5 shows the BET surface area analysis data for the AlpMMT samples prepared at different pH values. Also included in the same table are the pore sizes data for the respective samples. The respective N$_2$ adsorption-desorption curves can be found in Figures A-12 to A-14. The sample

116

prepared at pH 2.0 had the smallest surface area and largest pore size. At pH 4.0 and 5.7, the samples had relatively high surface areas which were nearly 3 times that observed for the sample prepared at pH 2.0. This result agrees with the the findings by Yildiz, N. et al, 2004 who observed a decrease in the surface areas of montmorillonite clay activated using strong H_2SO_4 acid.

Table 4.5: BET surface area analysis data for AlpMMT samples prepared at different pH.

Sample	BET surface area (m^2/g)	Pore size /nm
NaMMT	81.62	4.17
AlpMMT-pH 2.0	72.06	4.73
AlpMMT-pH 4.0	209.01	2.65
AlpMMT-pH 5.7	205.29	3.03

The pore sizes of the AlpMMT samples were observed to increase in the order, pH 4.0 < 5.7 < 2.0. The values of the surface areas were observed to increase in the same order as follows: pH 2.0 < 5.7 < 4.0. The low surface area obtained for the AlpMMT pillared at pH 2.0 could be due to the collapse of the clay sheets upon each other as discussed is Section 4.4.8.1. The surface area of AlpMMT pillared (72.06 m^2/g) at pH 2.0 dropped below that of NaMMT (81.62 m^2/g) and the pore size increased to 4.73 nm (greater than for NaMMT). These results show that pillared should ideally be carried out at pH between 4 and 5.7.

XRD was used to further analyse the AlpMMT samples prepared at different pH values and the results are presented in the following section.

4.2.8.4 X-ray diffraction analysis of AlpMMT-pHn samples

Figure 4.13 displays the XRD patterns of AlpMMT samples prepared at different pH. The samples prepared at pH 4.0 and 5.7 do not show much differences from each other. The basal reflection peak occurred at the same 2θ° angle. However, a marked difference was observed for the sample pillared at a pH of 2.0. The basal reflection peak appeared at a higher 2θ° angle (giving a d-spacing of 10.0 Å) for the pH 2.0 sample whereas the d-spacing values were 17.7 Å and 17.8 Å for AlpMMT samples pillared at pH 5.7 and pH 4.0, respectively.
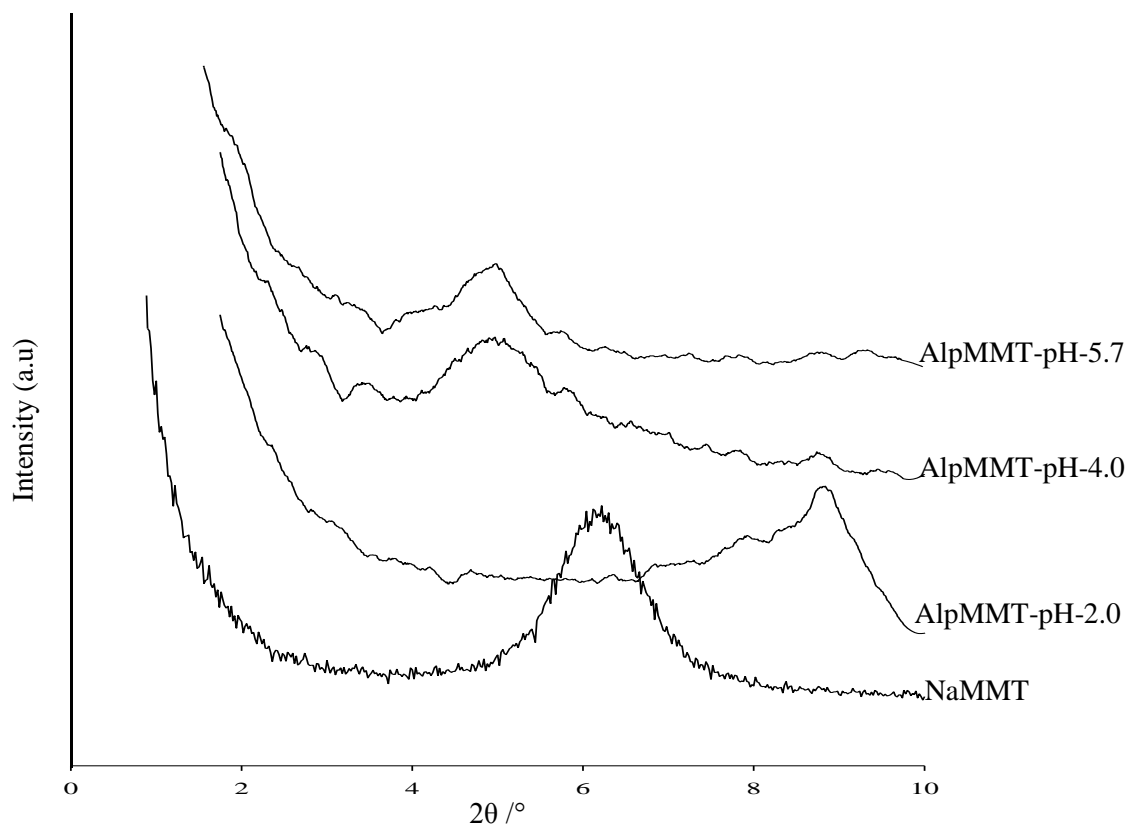
Figure 4.13: XRD patterns for AlpMMT samples prepared at different pH values.

The results observed here agree very well with the FTIR, TGA and BET results discussed above which indicated a loss of crystallinity and decrease of surface area of the material under acidic conditions at which the pillaring was carried out. This suggests that at pH 2.0, no pillaring occurred at all and/or that treatment under acidic conditions resulted in the collapsing of the clay sheets upon each other. Table 4.6 summarises the XRD results for samples pillared at different pH values.

Table 4.6: XRD data for AlpMMT samples prepared at different temperatures.

Sample	2θ /°	d-spacing /Å	Δ(d-spacing) /Å
NaMMT	6.22	14.2	0
AlpMMT-pH 2.0	8.80	10.0	-4.16
AlpMMT-pH 4.0	4.95	17.8	3.63
AlpMMT-pH 5.7	4.98	17.7	3.53

4.2.9 Effects of variation of pillaring temperature

AlpMMT samples were prepared at different temperatures in order to assess the effect of pillaring temperature on the structural and textural properties of the pillared samples. The following section discusses the FTIR data for the characterization of AlpMMT samples prepared at different temperatures.

118

4.2.9.1 FTIR analysis of AlpMMT - x °C samples

Figure 4.14 shows the FTIR spectra of AlpMMT pillared at temperatures 25, 50 and 80 °C. The spectra looked more or less the same for all temperatures, there were no additional peaks observed in all the spectra or any change of the shape of the vibration bands. This suggests that pillaring temperature did not affect the crystal structure of the clay mineral or the structural changes (if any) were not detectable by FTIR.

The pillared clay samples were further characterized by thermal gravimetric analysis and the results are presented in the following section.
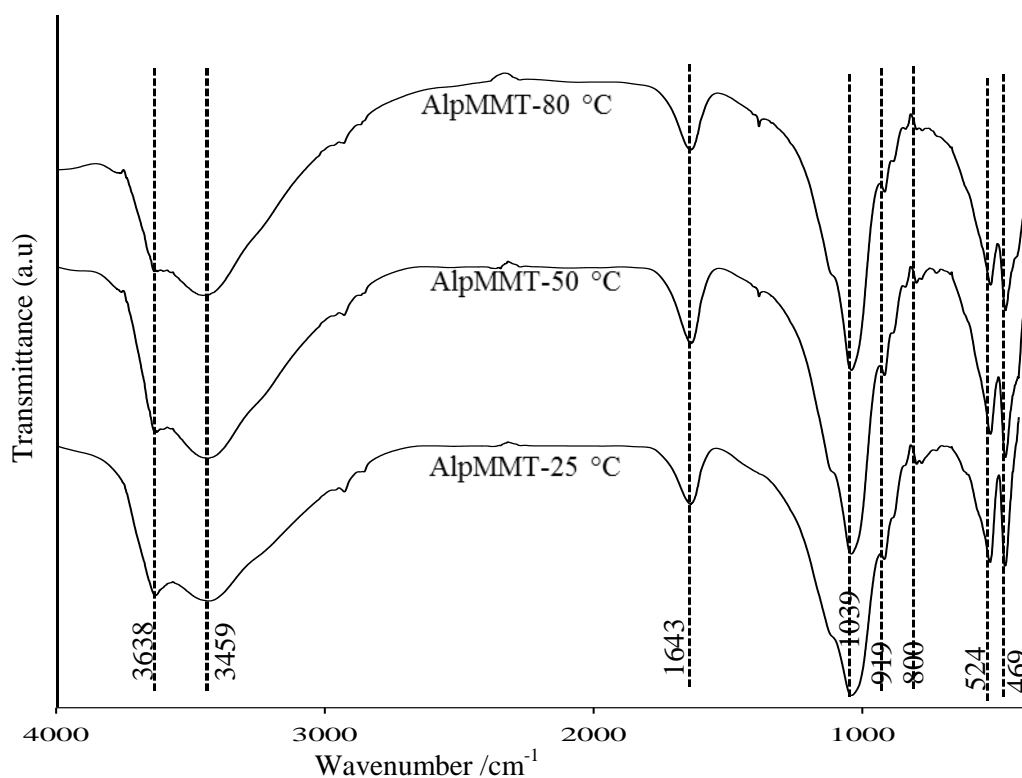
Figure 4.14: FTIR spectra for AlpMMT prepared at different temperatures.

4.2.9.2 Thermal gravimetric analysis of AlpMMT – x °C samples

Figure 4.15 below shows the thermograms of the AlpMMT samples prepared at different temperatures. The sample pillared at 50 °C showed the greatest mass loss, possibly due to more intercalated Al_{13} which then thermally decomposed resulting in increased mass loss.
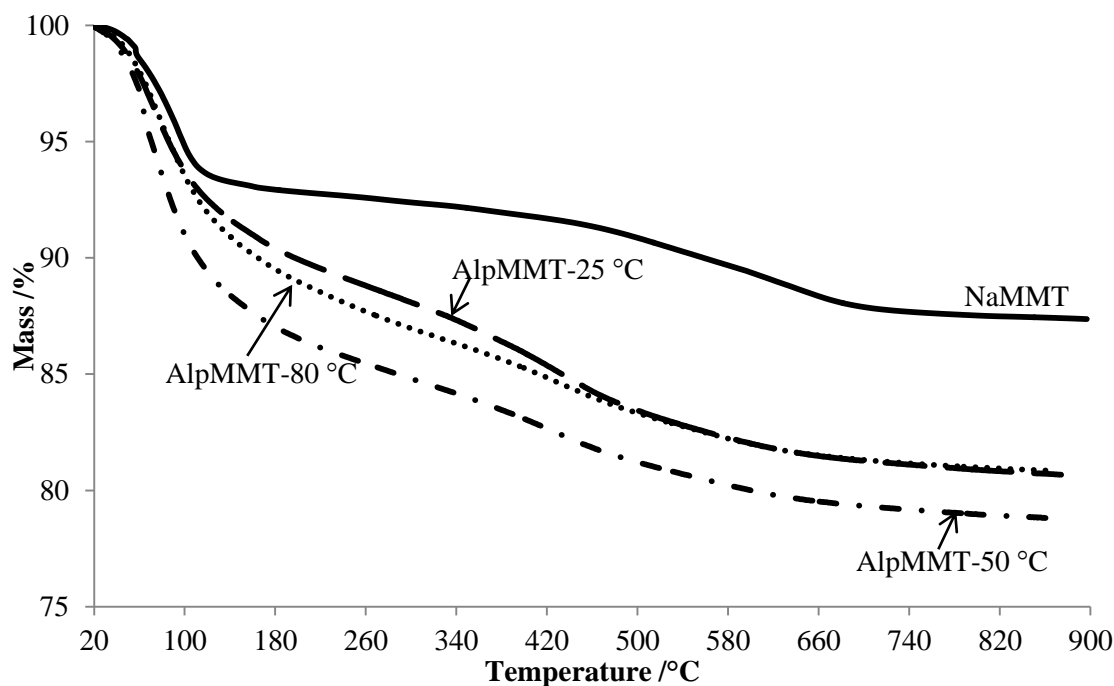
Figure 4.15: Thermograms of AlpMMT samples prepared at different temperatures.

The AlpMMT samples prepared at 25 °C and 80 °C gave more or less the same thermograms with slightly higher thermal stability than the one pillared at 50 °C.

Further analysis of the samples was carried out by BET surface area analysis and Section 4.4.9.3 presents the results.

4.4.9.3 BET surface area analysis of AlpMMT – x °C samples

Table 4.8 below summarises the results of surface areas and pore sizes obtained from BET analysis. The respective N_2 adsorption-desorption curves can be found in Figures A-15 to A-16. It can be seen that the increase in pillaring temperature from 25 to 80 °C resulted in an increase in the surface area.

Table 4.8: BET surface area analysis data for AlpMMT samples prepared at different pH.

Sample	BET surface area (m^2/g)	Pore size /nm
AlpMMT-25 °C	226	2.40
AlpMMT-50 °C	253	2.42
AlpMMT-80 °C	252	2.28

However, further increase in pillaring temperature from 50 to 80 °C did not cause a further increase in the surface area but a slight decrease in surface area was recorded instead. The pore sizes seemed to

follow more or less the same trend as the surface areas, with a slight increase from 2.40 nm (25 °C) to 2.42 nm (50 °C) and a relatively significant decrease to 2.28 nm (80 °C). Judging from the results of surface areas, 50 °C appeared to be ideal temperature for the pillaring process since it gave the highest surface area.

4.2.9.4 X-ray diffraction analysis of AlpMMT – x °C samples
This section presents the XRD results of AlpMMT samples prepared at different temperatures. Figure 4.16 displays the XRD patterns for AlpMMT samples prepared at different temperatures. The variation of the pillaring temperature did not result in any major differences in XRD patterns. The basal reflection peak for all three samples occurred at around the same 2θ° angle.
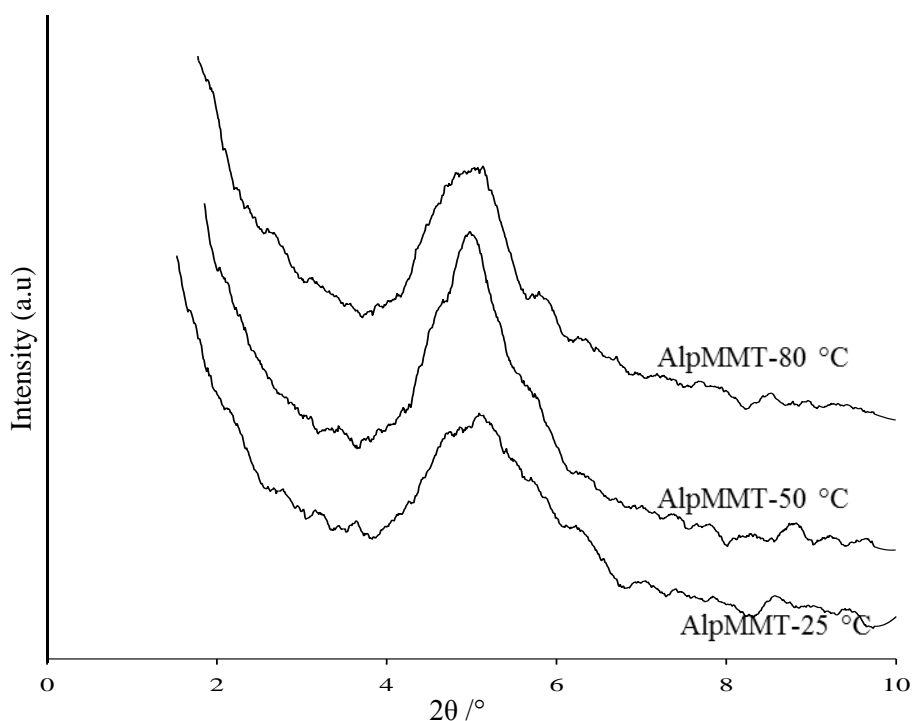
Figure 4.16: XRD patterns for AlpMMT samples prepared at different temperatures.

However, the sample prepared at 50 °C showed a relatively sharper peak compared with the other two. This might mean higher crystallinity in the AlpMMT sample prepared at 50 °C than those at 25 and 80 °C.

Table 4.9 summarizes the XRD data for the samples prepared at different temperatures. The highest d-spacing was achieved at a temperature of 50 °C. This can be taken as the optimum temperature for the pillaring process.

Table 2: XRD data for AlpMMT samples prepared at different temperatures

Sample	2θ /°	d-spacing /Å	Δ(d-spacing) /Å
NaMMT	5.88	14.2	0
AlpMMT-25 °C	5.06	17.5	3.25
AlpMMT-50 °C	4.92	18.0	3.75
AlpMMT-80 °C	5.08	17.4	3.18

Many researchers have aged their pillaring solutions at relatively high temperatures (about 60 - 90 °C), in order to facilitate the formation of the Keggin ion (de Carvalho, M. B. et al, 1996; Pires, J. et al, 1997; Manohar, D. M. et al, 2006). However, d-spacing values higher than 17.95 Å were achieved at 25 °C in this study, but at higher molar ratios (2.4 and 2.6) as discussed in Section 4.4.7.4.

Section 4.4.10 further discusses the data from BET surface area analysis, specifically the variation of surface area with pore size.

4.2.10 Variation of surface area with pore size

The surface areas were generally found to decrease with increase in pore sizes. However, there were some irregularities observed with some samples not following this general trend. Generally, the smaller the pore sizes the greater the surface area. This has been shown to be the case (to some extent) in this study. The surface areas obtained in this study were similar to what was previously reported for Al-pillared montmorillonite (Konstantinou, I. K. et al, 2000; Manohar, D. M. et al, 2006; Salerno, P. et al, 2002).
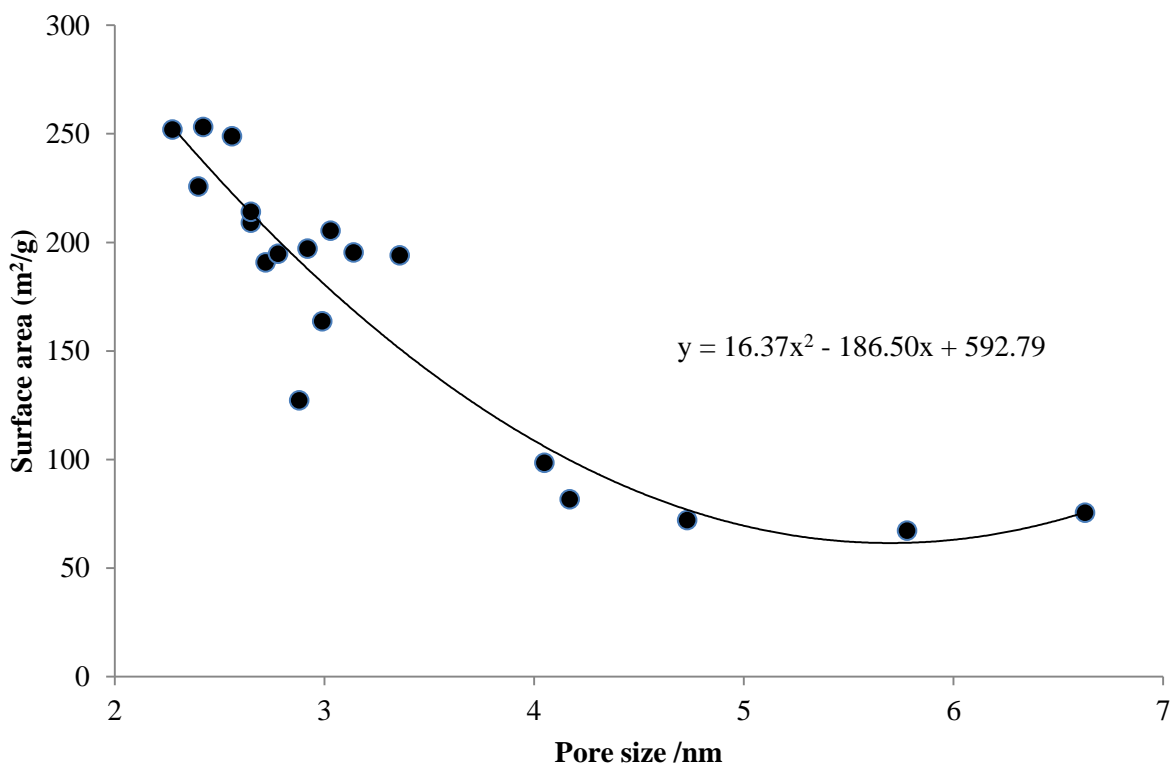
Figure 4.17: Variation of surface area with pore size.

4.3 Conclusion

This study provided a detailed assessment of the Al-pillaring of montmorillonite clay. Al-pillaring of montmorillonite clay resulted in an increase in surface area and a shift of the texture of the pillared clays to micro-porosity. The basal spacings of the pillared clays were higher than that obtained for NaMMT. The basal spacings were found to increase with increase in the OH/Al molar ratio. According to the XRD results, the optimum OH/Al molar ratio was found to be 2.6 since it had the highest d-spacing. However, according to BET surface area analysis, the optimum OH/Al molar ratio was 1.5. Pillaring at pH 2 resulted in a decrease of surface area, probably due to the collapse of clay sheets upon each other as evidenced by a lower d-spacing than the original NaMMT. Ideally, the pillaring pH should be at least 4.0 and not more than 5.7. Optimum pillaring temperature was found to be 50 °C since the AlpMMT sample pillared at this temperature had the highest surface area and also a relatively high d-spacing. However, there was no relationship found between the d-spacing of pillared clays with surface area and pore size. The surface area was generally dependent upon porosity (pore sizes). The greater the pore size the greater the surface area. Microporous to mesoporous materials were successfully prepared. Pore sizes were found to generally decrease with increase in the OH/Al molar ratio. From the FTIR, TGA, XRD and BET surface area analysis, it can be concluded

that the ideal conditions for the Al-pillaring of montmorillonite clay were: pH 4.3, temperature − 50 °C, OH/Al molar ratio − 2.3 and Al/clay ratio − 10 mmol/g.

4.4 References

1. Acemanaa, S.; Lahava, N.; Yarivb, S. A thermo-FTIR-spectroscopy analysis of Al-pillared smectites differing in source of charge, in KBr disks. *Thermochimica Acta*, **1999**, *340-341*, 349-366.

2. Altunlu, M.; Yapar, S. Effect of OH^-/Al^{3+} and Al^{3+}/clay ratios on the adsorption properties of Al-pillared bentonites. *Colloids and Surfaces A: Physicochemical and Engineering Aspects,* **2007***, 306,* 88-94.

3. Bergaya, F.; Aouad, O.; Mandalia, T. Pillared clays and clay minerals. *Handbook of Clay Science, Developments in Clay Science*, **2006**, *1*, 393-421.

4. Bhattacharyya, K. G.; Gupta, S. S. Adsorption of a few heavy metals on natural and modified kaolinite and montmorillonite: A review. *Advances in Colloid and Interface Science*, **2008**, *140*, 114–131.

5. Bhattacharyya, K. G.; Gupta, S. S. Calcined tetrabutylammonium kaolinite and montmorillonite and adsorption of Fe(II), Co(II) and Ni(II) from solution. *Applied Clay Science*, **2009**, *46*, 216–221.

6. Bhattacharyya, K. G.; Gupta, S. S. Influence of Acid Activation of Kaolinite and Montmorillonite on adsorptive removal of Cd(II) from water. *Industrial Engineering and Chemical Research*, **2007**, *46,* 3734-3742.

7. Bouchenafa-Saïb, N.; Khouli, K.; Mohammedi, O. Preparation and characterization of pillared montmorillonite: application in adsorption of cadmium. *Desalination,* **2007**, *217*, 282–289.

8. Chae, H. J.; Nam, I. S.; Ham, S. W.; Hong, S. B. Physicochemical characteristics of pillared interlayered clays. *Catalysis Today*, **2001**, *68*, 31–40.

9. Danis, T. G.; Albanis, T. A.; Petrakis, D. E.; Pomonis, P. J. Removal of chlorinated phenols from aqueous solutions by adsorption on alumina pillared clays and mesoporous alumina aluminum phosphates. *Water Research*, **1998**, *32* (2), 295-302.

10. De Carvalho, M. B. Pires, J.; Carvalho, A. P. Characterisation of clays and aluminium pillared clays by adsorption of probe molecules. *Microporous Materials*, **1996**, *6* (2), 65-77.

11. Figueras, F.; Klapyta, Z.; Massiani, P.; Mountassir, Z.; Tichit, D.; Fajula, F. Use of competitive ion exchange for intercalation of montmorillonite with hydroxy-aluminum species**.** *Clays and Clay Minerals*, **1990**, 38 (3), 257-264.

12. Hutson. N. D.; Hoekstra, M. J.; Yang, R. T. Control of microporosity of Al_2O_3-pillared clays: effect of pH, calcination temperature and clay cation exchange capacity. *Microporous and Mesoporous Materials*, **1999**, *28,* 447–459.

13. Katdare, S. P.; Ramaswamy, V.; Ramaswamy, A.V. Factors affecting the preparation of alumina pillared montmorillonite employing ultrasonics. *Microporous and Mesoporous Materials*, **2000**, *37*, 329–336.

14. Khalaf, H.; Bouras, O.; Perrichon, V. Synthesis and characterization of Al-pillared and cationic surfactant-modified Al-pillared Algerian bentonite. *Microporous Materials*, **1997**, *8*, 141-150.

15. Kircsi, I.; Molnár, Á.; Pálinkó, I.;, Fudala, Á.; Nagy. J. B. Nanoscale redox catalysts: Cr- and Cr, Al-pillared layer clays: Characterization and catalytic activity. *Solid State Ionics*, **1997**, *101-103*, 793-797.

16. Kloprogge, J. T.; Booy, E.; Jansen, J. B. H.; Geus, J. W. The effect of thermal treatment on the properties of hydroxy-Al and hydroxy-Ga pillared montmorillonite and beidellite. *Clay Minerals*, **1994**, *29*, 153-167.

17. Kloprogge, J. T.; Evans, R.; Hickey, L.; Frost, R. Characterisation and Al-pillaring of smectites from Miles, Queensland (Australia). *Applied Clay Science*, **2002**, *20*, 157–163.

18. Kloprogge, J. T.; Frost, R. L.; Fry, R. Infrared emission study of the thermal transformation mechanism of Al_{13}-pillared clay. *Analyst*, **1999**, *124*, 381–384

19. Konstantinou, I. K.; Albanis, T. A.; Petrakis, D. E.; Pomonis, P. J. Removal of herbicides from aqueous solutions by adsorption on al-pillared clays, Fe-Al pillared clays and mesoporous alumina aluminum phosphates. *Water Research,* **2000**, *34* (12), 3123-3136.

20. Kurian, M.; Sugunan S. Characterisation of the acid–base properties of pillared montmorillonites. *Microporous and Mesoporous Materials*, **2005**, *83*, 25–34.

21. Maes, N.; Heylen, I.; Cool, P.; Vansant, E. F. The relation between the synthesis of pillared clays and their resulting porosity. *Applied Clay Science*, **1997**, *12*, 43-60.

22. Manohar, D. M.; Noeline, B. F.; Anirudhan, T. S. Adsorption performance of Al-pillared bentonite clay for the removal of cobalt(II) from aqueous phase. *Applied Clay Science*, **2006**, *31*, 194-206.

23. Mishra, T.; Parida, K. Transition metal oxide pillared clays. *Journal of Material Chemistry*, **1997**, *7* (1), 147–152.

24. Mrad, I.; Ghorbel, A.; Tichit, D.; Lambert, J. F. Optimisation of the preparation of an Al-pillared clay: thermal stability and surface acidity. *Applied Clay Science*, **1997**, *12* (4), 349-364.

25. Ohtsuka, K. Preparation and properties of two-dimensional microporous pillared interlayered solids. *Chemistry of Materials*, **1997**, *9*, 2039-2050.

26. Park, H. M.; Kim, T. W.; Hwang, S. J.; Choy, J. H. Chemical bonding nature and mesoporous structure of nickel intercalated montmorillonite clay. *Bulletin of the Korean Chemical. Society*, **2006**, *27* (9), 1323-1328.

27. Pires, J.; de Carvalho, M. B.; Carvalho, A. P. Aluminum-pillared clays: Decomposition of the intercalating species and textural properties. *Zeolites*, **1997**, *19*, 107-113.

28. Salerno, P.; Mendioroz, S. Preparation of Al-pillared montmorillonite from concentrated dispersions. *Applied Clay Science*, **2002**, *22*, 115–123.

29. Sing. K. S. W.; Haul, R. A. W.; Pierotti, R. A.; Siemieniewska, T. Reporting physisorption data for gas/solid systems with special reference to the determination of surface area and porosity. *Pure & Applied Chemistry*, **1985**, *57* (4), 603-619.

30. Sun-Koi, M. R.; Mendioroz, S.; Guijarro, M. I. A thermal study of Zr-pillared montmorillonite. *Thermochimica Acta*, **1998**, *323*, 145-157.

31. Sychev, M.; San de Beer, V. H. J.; Kodentsov, A.; van Oers, E. M.; van Santen, R. A. Chromia-and chromium sulfide-pillared clays: preparation, characterization, and catalytic activity for thiophene hydrodesulfurization. *Journal of Catalysis*, **1997**, *168*, 245–254.

32. Tichit, D.; Fajula, F.; Figueras, F.; Ducourant, B.; Mascherpa, G.; Gueguen, C.; Bousquet, J. Sintering of montomorillonites pillared by hydroxy-aluminum species. *Clays and Clay Minerals,* **1988**, *36* (4), 369-375.

33. Yildiz, N.; Aktas, Z.; Calimli, A. Sulfuric acid activation of a calcium bentonite. *Particulate Science and Technology*, **2004**, *22*, 21–33.

34. Yuan, P.; He, H.; Bergaya, F.; Wu, D.; Zhou, Q.; Zhu, J. Synthesis and characterization of delaminated iron-pillared clay with meso–microporous structure, *Microporous and Mesoporous Materials*, **2006**, *88*, 8–15.

Chapter 5

Preparation of Polymer-grafted Lignocellulose and Montmorillonite Clay Adsorbents

5.0 Introduction

This chapter describes the procedures followed in the synthesis of polymer-grafted (coupled) lignocellulose-montmorillonite clay nanocomposites. The detailed methods for the separate modification of both the lignocellulose and montmorillonite through grafting of organic groups are also presented together with the preparation of the homopolymers from the monomers used for the modification. The homopolymers were used as control samples. The characterization of the prepared materials was carried out using FTIR, TGA, SEM, TEM and XRD and the results for the characterization are reported in Section 5.6.

5.1 Synthesis of homopolymers

5.1.1 Preparation of poly (methyl methacrylate)

The emulsion polymerization of methyl methacrylate (MMA) was carried out in a 250 mL three neck round-bottom flask with magnetic stirring and a thermometer. Deionised water (100 mL), 0.0145 g (4.4×10^{-5} mol) sodium dodecyl benzene sulfonic acid (DBS) and 0.0072 g (3.8×10^{-5} mol) sodium metabisulfite (SMBS) were loaded in the reactor and stirred for 30 min. Afterwards, MMA (3.5 g, 3.5×10^{-2} mol) was added in order to form the emulsion. This was then followed by the addition of the initiator, ammonium persulfate, AMPS (0.0306 g, 1.3×10^{-4} mol) dissolved in 10 mL distilled water. Nitrogen gas was bubbled into the reaction flask for 30 min to evacuate dissolved oxygen with constant stirring. The nitrogen gas atmosphere was maintained and the mixture was heated at 60 °C for 4 h after which the mixture was cooled to room temperature. The product was isolated by filtration through MN615 filter papers and washed with distilled water. The poly (methyl methacrylate) was then dried in a ventilated oven for 24 h at 50 °C. The PMMA homopolymer was then characterized using FTIR and TGA.

5.1.2 Preparation of poly (methacrylic acid)

Pure poly (methacrylic acid) (PMAA) was prepared using the following procedure: Methacrylic acid, MAA (5.0 g, 5.8×10^{-2} mol) was pipetted into 150 mL of a 1:1 (v/v) EtOH/H_2O solvent mixture in a 250 mL round flask. The mixture was stirred for 30 min, followed by the addition of ammonium

persulfate (0.05, 2.2 x 10^{-4} mol), dissolved in 10 mL of deionized water. Nitrogen gas was bubbled into the reaction flask to drive out oxygen and the mixture was heated at 70 °C for 4 h.

The PMAA was precipitated by adding acetonitrile to the reaction mixture. The solvent was poured out and the PMAA left to dry in the fume hood for 24 h. In order to purify the PMAA, it was redissolved in a 1:1 (v/v) EtOH:H$_2$O solvent mixture and then precipitated using diethyl ether. The PMAA was dried in a ventilated oven at 50 °C for 48 h, and was characterized using FTIR and TGA.

5.1.3 Polymerisation of poly (methacryloxypropyl trimethoxy silane)

Methacryloxypropyl trimethoxy silane, MPS (15.0 g, 6.0 x 10^{-2} mol) was added to 200 mL of a 1:1 v/v EtOH:H$_2$O solvent mixture and mixed for 10 min under magnetic stirring. Dibutyltin dilaurate, DBTDL (0.21 g, 3.4 x 10^{-4} mol) was added and the mixture stirred for another 10 min. The mixture was then heated to 70 °C and left to react at this temperature for 24 h. After 24 h, the mixture was cooled to room temperature and the product isolated by filtration. The product was washed with EtOH to remove any MPS monomer and then dried in a ventilated oven at 50 °C for 24 h. The poly (methacryloxypropyl trimethoxysilane) (PMPS) was characterized by FTIR and TGA and the results are discussed in Section 5.6.2.

5.2 Synthesis of polymer-grafted montmorillonite adsorbents

5.2.1 Preparation of poly (methyl methacrylate)-grafted montmorillonite

The procedure for the grafting of methyl methacrylate to montmorillonite clay was adapted from an article by Atai, M. et al, 2009. The graft polymerization reaction was carried out in a 250 mL three neck round-bottom flask with magnetic stirring and a thermometer. Sodium-exchanged montmorillonite clay (NaMMT), 5.1 g was slowly added to deionised water (100 mL) under high-speed stirring. The vigorous stirring was maintained until all the NaMMT was completely dispersed in the water. DBS (0.0152 g, 4.7 x 10^{-5} mol) and SMBS (0.0075 g, 3.9 x 10^{-5} mol) were added to the mixture and stirred for 30 min. Methyl methacrylate (MMA) was then added and mixed for 30 min in order to form the emulsion. The initiator, AMPS (0.0301 g, 1.3 x 10^{-4} mol) was first dissolved in 10 mL deionised water and then added to the flask. The system was purged with nitrogen gas for 30 min to remove dissolved oxygen. The nitrogen gas flow was maintained and the mixture was refluxed at 60 °C for 4 h after which the mixture was cooled to room temperature. The product was isolated by filtration, washed with distilled water and then dried in a ventilated oven for 24 h at 50 °C. In order to remove PMMA homopolymer, the PMMA-grafted MMT (PMMAgMMT) was soxhlet extracted with tetrahydrofuran (THF) for 24 h and then dried at 50 °C.

The PMMAgMMT was characterized by FTIR, TGA, SEM and XRD, and used for adsorption studies. The characterization results are reported in Section 5.6.1 and the adsorption experiments reported in Chapter 6.

5.2.2 Preparation of methacryloxypropyl trimethoxy silane–grafted montmorillonite

The method employed in the preparation of MPS-grafted montmorillonite was adapted from previous works (An, F. et al, 2010 and Wang, W., 2010) where MPS was grafted onto SiO_2 particles. However, the substrate in this study was montmorillonite clay. NaMMT (5.0 g) was dispersed in 200 mL of a 1:1 v/v $EtOH:H_2O$ solvent mixture under high speed magnetic stirring for 1 h or until all the NaMMT was homogeneously dispersed. Methacryloxypropyl trimethoxysilane (MPS), (3.5 g, 1.4×10^{-2} mol), was added to the clay dispersion and mixed for 10 min. Dibutyltin dilaurate, DBTDL (0.21 g, 3.4×10^{-4} mol) was added and the mixture stirred for another 10 min. The mixture was then heated to 70 °C and reacted at this temperature for 24 h.

After 24 h, the mixture was cooled to room temperature and the product isolated by filtration. The product was washed with 50 mL of EtOH to remove unreacted MPS and then dried in a ventilated oven for 24 h at 50 °C. Tetrahydrofuran (THF) was used for soxhlet extraction (24 h) in order to remove the free MPS as well as the homopolymerised silane together with the catalyst. The product was dried at 50 °C for 24 h and then characterised by FTIR, TGA and XRD, and the results are presented in Section 5.6.2. The MPS-grafted MMT (MPSgMMT) was further modified with poly (methacrylic acid) to give the poly (methacrylic acid)-grafted MMT as described below.

5.2.3 Preparation of poly (methacrylic acid)-grafted montmorillonite

Though poly (methacrylic acid) (PMAA) has been applied widely in water treatment, it is said to be unstable under shear. It is also reported to contain toxic residual monomers which could cause severe secondary environmental pollution problems (An, F. et al, 2010). Therefore, it is necessary that the PMAA be covalently attached to the NaMMT backbone so that there is no leaching of toxic materials into the water. The direct grafting of methacrylic acid (MAA) onto MMT was assessed in this study, and proved to be quite difficult. A two-step grafting procedure (as described by Liu, P. et al, 2007) was eventually used for the grafting of PMAA onto NaMMT as described below.

The procedure used for the preparation of poly (methacrylic acid)-grafted MMT (PMAAgMMT) was adapted from the work by An, F. et al, 2010 and Wang, W., 2010. Sodium dodecyl benzene sulfonic acid, DBS (0.0152 g, 4.7×10^{-5} mol) was first dissolved in 150 mL of deionized water in order to aid the dispersion process. Methacryloxypropyl trimethoxysilane-grafted montmorillonite, MPSgMMT (5.0 g) was dispersed under high speed stirring in the solution above for 1 h. Ethanol was added to

improve the wetting properties of MPSgMMT. Methacrylic acid (3.5 g, 4.1 x 10^{-2} mol) was measured and added into the dispersion above and mixed for 30 min. Ammonium persulfate, AMPS (0.0746 g, 8.7 x 10^{-4} mol) was dissolved in 10 mL of deionised water and added to the mixture. Nitrogen gas was bubbled into the reaction flask to provide an inert environment. The mixture was heated at 70 °C for 24 h to effect the reaction of the MAA with the alkene groups of the covalently attached MPS groups. The product was isolated by filtration, washed with EtOH to remove the PMAA homopolymer and unreacted monomer. The PMAAgMMT was further washed with 0.01 M NaOH until the pH of filtrate was about 5. The product was dried at 50 °C for 24 h and characterized by FTIR, TGA and XRD.

5.3 Synthesis of polymer-grafted lignocellulose adsorbents

5.3.1 Preparation of poly (methyl methacrylate)-grafted lignocellulose

The procedure followed in the grafting of MMA onto lignocellulose was adapted from the work by Román-Aguirre, M. et al, 2004. Sodium metabisulfite, SMBS (0.0087 g, 4.6 x 10^{-5} mol) and DBS (0.0152 g, 4.7 x 10^{-5} mol) were dissolved in deionised water (100 mL) in a three-neck round-bottom flask equipped with a magnetic stirrer. The EtOH:H_2O soxhlet-extracted lignocellulose (5.2 g) was then added slowly to the mixture at high speed magnetic stirring. The mixture was stirred for 1 h or until all the lignocellulose was homogeneously dispersed followed by the addition of MMA (3.5 g, 3.5 x 10^{-2} mol) to form an emulsion. Nitrogen gas was purged through the system to evacuate oxygen and the inert atmosphere was maintained till the end of the reaction. After mixing for another 30 min, AMPS (0.0346 g, 1.5 x 10^{-4} mol) dissolved in 10 mL of deionised water was added to the mixture and stirred for 30 min before heating the mixture at 60 °C under nitrogen gas for 4 h.

After 4 h, the mixture was cooled to room temperature, and the product isolated by filtration. The PMMA-grafted lignocellulose (PMMAgLig) was purified by solvent extraction with 250 mL of THF to remove PMMA homopolymer and dried at 50 °C for 24 h. The product was characterized by FTIR, SEM and TGA and the results reported in Section 5.6.4.

5.3.2 Preparation of methacryloxypropyl trimethoxysilane–grafted lignocellulose

Castellano, M. et al, 2004 investigated the grafting of organosilanes to cellulose and lignin. Their study showed that the grafting of the organosilanes onto cellulose occurred only in the presence of moisture, whereas grafting onto lignin occurred even in the absence of moisture. As such, a solvent mixture of 1:1 v/v EtOH:H_2O was chosen as reported by An, F. et al, 2010. The soxhlet-extracted lignocellulose (10.0 g) was dispersed in 300 mL of a 1:1 v/v EtOH:H_2O solvent mixture under high speed magnetic stirring for 1 h in a 500 mL 3-neck round flask. Methacryloxypropyl

trimethoxysilane, MPS (7.5 g, 3.0 x 10^{-2} mol) was added to the lignocellulose dispersion and mixed for 10 min. A catalyst, DBTDL (0.2 g, 4.1 x 10^{-4} mol) was added and the dispersion stirred for another 10 min. The mixture was then heated to 70 °C and left to react at this temperature for 24 h.

After 24 h, the mixture was cooled to room temperature and the product isolated by filtration, followed by drying in a ventilated oven for 24 h. THF was used for soxhlet extraction (24 h) in order to remove the free MPS, homopolymerised silane, as well as the catalyst. The MPS-grafted lignocellulose (PMPSgLig) was dried at 50 °C for 24 h and then characterized by FTIR and TGA, and the results are presented in Section 5.6.5. The PMPSgLig was used for the preparation of poly (methacrylic acid)-grafted lignocellulose (PMAAgLig) as described below.

5.3.3 Preparation of poly (methacrylic acid)-grafted lignocellulose

MPS-grafted lignocellulose (5.0 g) was dispersed under high speed stirring in deionised water for 1 h. Methacylic acid, MAA (3.5 g, 4.1 x 10^{-2} mol) was measured into the dispersion above and mixed for 30 min. Ammonium persulfate (0.083g, 3.6 x 10^{-4} mol) was dissolved in 10 mL of deionised water and added to the mixture. Nitrogen gas was bubbled into the reaction flask to provide an inert environment and the mixture was heated to 70 °C. The mixture was left to react at 70 °C for 24 h to effect the reaction of the methacrylic acid on the C=C double bonds of the MPS already grafted to the lignocellulose.

The mixture was cooled to room temperature and the product isolated by filtration, washed with 0.01 M NaOH until the pH of the filtrate was about 5. It was further washed by soxhlet extraction (using EtOH) to remove the homopolymer and free monomer followed by drying at 50 °C for 24 h. The PMAA-grafted lignocellulose (PMAAgLig) was characterized by FTIR and TGA.

5.4 Synthesis of polymer-grafted lignocellulose-montmorillonite composite adsorbents

5.4.1 Preparation of poly (methyl methacrylate)-grafted lignocellulose-montmorillonite nanocomposite

Nanocomposites of MMT and lignocellulose were prepared as follows: SMBS and DBS were dissolved in deionised water in a three-neck round bottom flask equipped with a magnetic stirrer. Soxhlet-extracted lignocellulose was then added slowly to the mixture under high speed magnetic stirring then followed by the slow addition of NaMMT. The mixture was stirred for 1 h to completely disperse the solids followed by the addition of MMA to form the emulsion. Nitrogen gas was bubbled into the system to remove oxygen and was maintained till the end of the reaction. After mixing for

another 30 min, AMPS (dissolved in 10 mL of deionised water) was added to the mixture and stirred for 30 min before refluxing the mixture at 60 °C under nitrogen gas for 4 h.

The mixture was cooled to room temperature, and the product (PMMAgLig-NaMMT) was isolated by filtration. The product was purified by solvent extraction with 250 mL of THF to remove PMMA homopolymer and dried at 50 °C for 24 h. The nanocomposites were prepared at different compositions of montmorillonite ranging from 10% to 50% w/w. The amounts of both lignocellulose and NaMMT were varied as displayed in Table 5.6.

Table 5.6: Materials used for the preparation of nanocomposites of different clay loadings.

*Sample	Mass /g		Amount /mol			
	NaMMT	Lignocellulose	SMBS	DBS	MMA	AMPS
Nano-10	0.6091	5.4011	4.3×10^{-5}	4.5×10^{-5}	3.5×10^{-2}	1.4×10^{-4}
Nano-20	1.2065	4.8100	4.2×10^{-5}	5.6×10^{-5}	3.5×10^{-2}	1.4×10^{-4}
Nano-30	1.8079	4.2034	4.7×10^{-5}	5.1×10^{-5}	3.5×10^{-2}	1.4×10^{-4}
Nano-40	2.4018	3.6002	4.1×10^{-5}	4.6×10^{-5}	3.5×10^{-2}	1.5×10^{-4}
Nano-50	3.0109	3.1030	5.0×10^{-5}	4.6×10^{-5}	3.5×10^{-2}	1.4×10^{-4}

*The number after Nano- represents the percentage amount of MMT in the respective sample.

The samples were analysed by FTIR, TGA, XRD and TEM, and the results are presented in Section 5.6.7.

5.4.2 Preparation of methacryloxypropyl trimethoxy silane–coupled lignocellulose-montmorillonite nanocomposite

Soxhlet-extracted lignocellulose (3.0 g) and NaMMT (3.0 g) were dispersed in 150 mL of a 1:1 v/v EtOH:H_2O solvent mixture under high speed magnetic stirring for 1 hour. Methacryloxypropyl trimethoxysilane (MPS), about 1.4×10^{-2} mol, was added to the lignocellulose-NaMMT dispersion and mixed for 10 min. A catalyst, dibutyl tin dilaurate (2.1×10^{-4} mol) was added and the mixture stirred for 10 min. The mixture was then heated to 70 °C and left to react at this temperature for 24 h.

After 24 h, the mixture was cooled to room temperature and the MPS-coupled lignocellulose-montmorillonite (PMPSgLig-NaMMT) nanocomposite was isolated by filtration. THF was used as solvent in soxhlet extraction for 24 h in order to remove the free MPS monomer, the

homopolymerised silane and the catalyst. The MPSgLig-NaMMT nanocomposite was dried at 50 °C for 24 h and then characterized by FTIR, TGA, XRD and TEM.

5.4.3 Preparation of poly (methacrylic acid)-grafted lignocellulose-montmorillonite nanocomposites

PMAA-grafted lignocellulose-montmorillonite (PMAAgLig-NaMMT) nanocomposites were prepared at different montmorillonite clay loadings. The required amount of MPS-grafted lignocellulose was slowly dispersed in 150 mL of deionized water to which 5 mL EtOH had been added. The EtOH was added to improve the dispersion of both the MPS-grafted lignocellulose and PMPSgMMT in the water. After all the solids had been homogeneously dispersed in the water (about 1 hour), MAA was added and mixed for 30 min, followed by the addition of AMPS. The AMPS was first dissolved in 10 mL of deionized water before adding to the mixture. Nitrogen gas was used to purge the system to provide an inert atmosphere. The system was heated to 70 °C to initiate the graft polymerization reaction, and the temperature was maintained for 24 h, after which the mixture was cooled to room temperature and the product (PMAAgLig-NaMMT) was isolated by filtration. The product was washed with 0.01 M NaOH solution and then deionized water until the pH of the filtrate was about 5. The product was further soxhlet extracted with EtOH for 24 h in order to remove all PMAA homopolymer and then dried at 50 °C for 24 h.

The amounts of the different reactants used in the synthesis of the nanocomposites are shown in Table 5.7 below. The nanocomposites were characterized by FTIR, TGA, XRD and TEM.

Table 5.7: Materials used for the preparation of nanocomposites of different clay loadings.

*Sample	Mass /g		Amount /mol	
	PMPSgMMT	PMPSgLig	MAA	AMPS
Nano-10	0.6091	5.4012	4.1×10^{-2}	3.6×10^{-4}
Nano-20	1.2128	4.8193	4.1×10^{-2}	3.6×10^{-4}
Nano-30	1.8000	4.2102	4.2×10^{-2}	3.7×10^{-4}
Nano-40	2.0113	3.1433	4.1×10^{-2}	3.7×10^{-4}
Nano-50	3.0119	3.0173	4.1×10^{-2}	3.7×10^{-4}

*The number after Nano- represents the percentage amount of MMT in the respective sample.

5.5 Characterisation of adsorbents

The samples prepared in this study were characterized by FTIR, TGA, SEM and XRD. In order to determine the morphology of nanocomposites, they were further analysed by transmission electron microscopy (TEM). TEM analysis was performed at the University of Cape Town. TEM was used to visualize the morphology of the polymer-grafted or coupled lignocellulose-NaMMT nanocomposites. The TEM images were recorded on a JEM 200CX transmission electron microscope (JEOL, Tokyo, Japan) at an accelerating voltage of 120 kV. Prior to analysis, the nanocomposites were stained with OsO_4, then embedded in epoxy resin and cured for 24 h at 60 °C. The embedded samples were then ultra-microtomed with a diamond knife on a Reichert Ultracut S ultra-microtome at room temperature to give sections of about 100 nm thick. The sections were transferred from water at room temperature to 300-mesh copper grids, which were then transferred to the TEM instrument.

The following section describes the results obtained from the characterisation of all the materials prepared in this study as described above.

5.6 Results and discussion

5.6.1 Poly (methyl methacrylate)-grafted montmorillonite

The following section describes the possible mechanism for the direct grafting of PMMA onto a substrate, either NaMMT or lignocellulose. A sodium metabisulfite/ammonium persulfate redox system was used as the initiator for the free-radical polymerization reaction.

5.6.1.1 Suggested mechanism for the grafting of methyl methacrylate to a substrate

Equation 1 describes the free radical generation mechanism of the sodium metabisulfite/ammonium persulfate system.

$$H_2O + HSO_3^- + 2S_2O_8^{2-} \rightarrow 3HSO_4^- + 2SO_4^{\cdot -} \qquad (1)$$
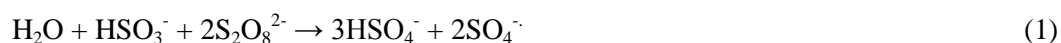
The sulfate radical essentially generates a macro-radical onto which an incoming MMA monomer attaches itself (Román-Aguirre, M. et al, 2004). Chain propagation then occurs with more monomers getting attached to the growing polymer chain as shown in the following schematic:
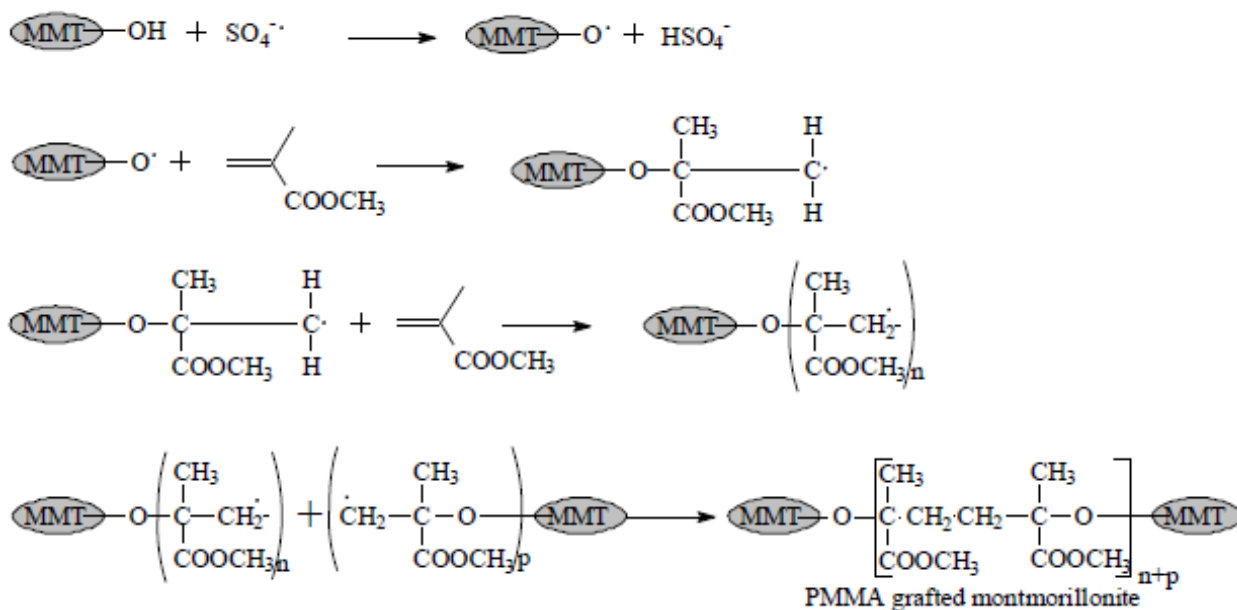
Scheme 5.1: Graft polymerisation of MMA onto a substrate.

A similar mechanism was expected for the grafting of methacrylic acid onto the different substrates, but as already stated, the direct grafting of PMAA was unsuccessful as shown by analysis of some of the prepared samples with FTIR and TGA.

5.6.1.2 FTIR analysis of PMMAgMMT

Figure 5.1 displays the FTIR spectra of poly (methyl methacrylate)-grafted montmorillonite (PMMAgMMT). In the FTIR spectrum, the NaMMT showed stretching vibrations at 467, 527, 801, 843, 886, 919, 1045, 1639, 2927, 3436 and 3636 cm^{-1}. These frequencies were attributed to Si-O-Si bending, Si-O-Al bending, O-Si-O asymmetric stretching, Al-OH-Mg deformation, Al-OH-Fe deformation, OH bending (Al_2OH), Si-O stretching, H-O-H deformation (interlayer H_2O), -CH$_3$ asymmetric stretching, H-O-H stretching (adsorbed H_2O) and structural O-H stretching vibrations, respectively (Yuan, P. et al, 2006).

The IR spectrum of grafted MMT showed a stretching vibration at 1733 cm^{-1} and 1436 cm^{-1} in addition to the bands listed above. To check if the PMMA was covalently attached to the MMT, the grafted MMT was extracted with THF for 48 h before analysis with FTIR. This procedure should remove free PMMA homopolymer that formed during the grafting reaction.
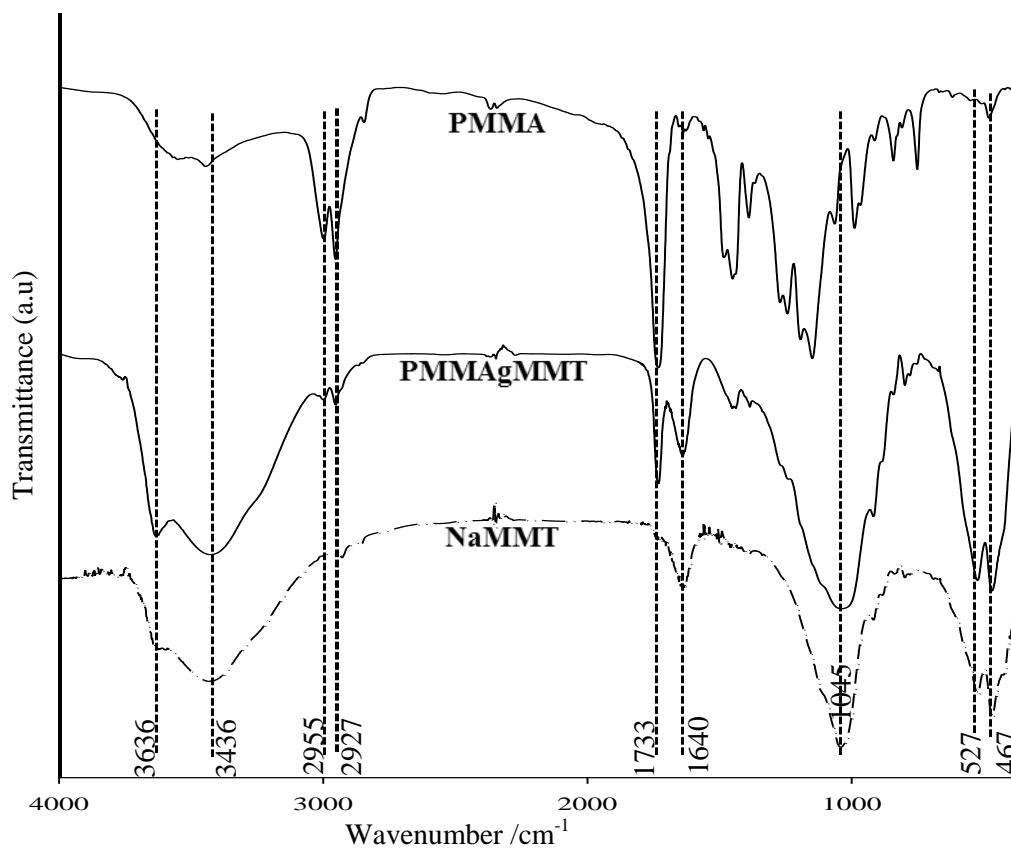
Figure 5.1: FTIR spectra of NaMMT, PMMA and PMMAgMMT.

The persistence of the stretching vibrations at 1733 cm^{-1} (C=O stretching vibration) and 1453 cm^{-1} (-O-CH$_3$ asymmetric deformation) in the THF extracted product confirmed that methyl methacrylate groups were covalently attached to MMT during the grafting process (Rajendran, S. et al, 2001).

5.6.1.3 Scanning electron micrscopy of PMMAgMMT

Scanning electron microscopy showed marked differences in morphology between the NaMMT and PMMA-grafted MMT as displayed in Figure 5.2.
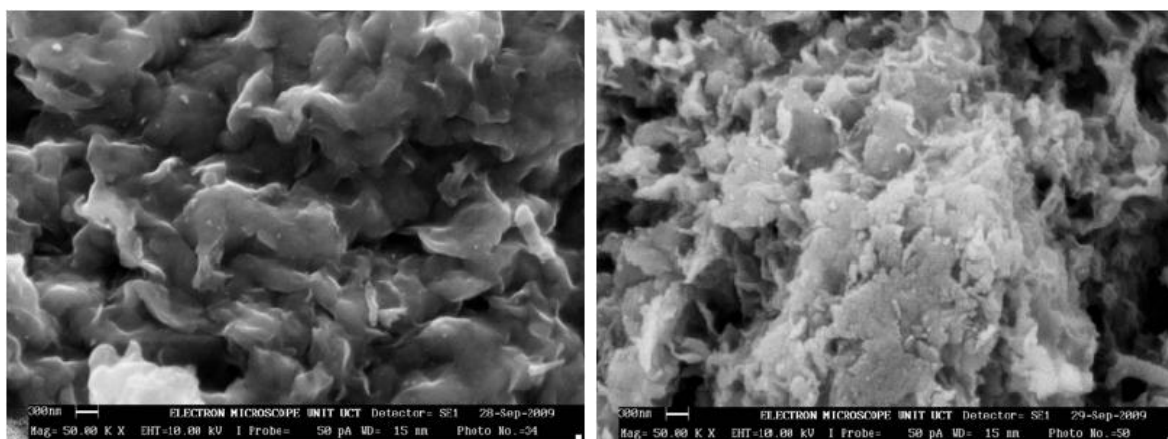
Figure 5.2: SEM micrographs for NaMMT (left) and PMMAgMMT (right) at a magnification of 50000X.

The ungrafted NaMMT sample showed a relatively smooth surface, whereas the soxhlet extracted PMMAgMMT had rough surfaces (with cavities) which must have been due to the attached PMMA particles (see Figure 5.2).

5.6.1.4 Thermogravimetric analysis of PMMAgMMT

Figure 5.3 displays the thermograms of PMMA, NaMMT and PMMAgMMT. The thermogram of PMMA indicated that the decomposition started at 250 °C and continued up to about 420 °C (Figure 5.3). Above 430 °C, all the PMMA was completely decomposed. The thermogram of NaMMT showed a two step degradation process, at 60-120 °C (loss of adsorbed water) and 370-670 °C (dehydroxylation of the clay structure) (Binitha, N. N. et al, 2006). The greater mass loss between 270 and 400 °C for the PMMAgMMT than the NaMMT was due to the decomposition of the grafted PMMA. The grafting efficiency was estimated from the mass loss at temperatures between 270 and 390 °C. This calculation indicated that PMMAgMMT contained about 9.0 mass % PMMA.
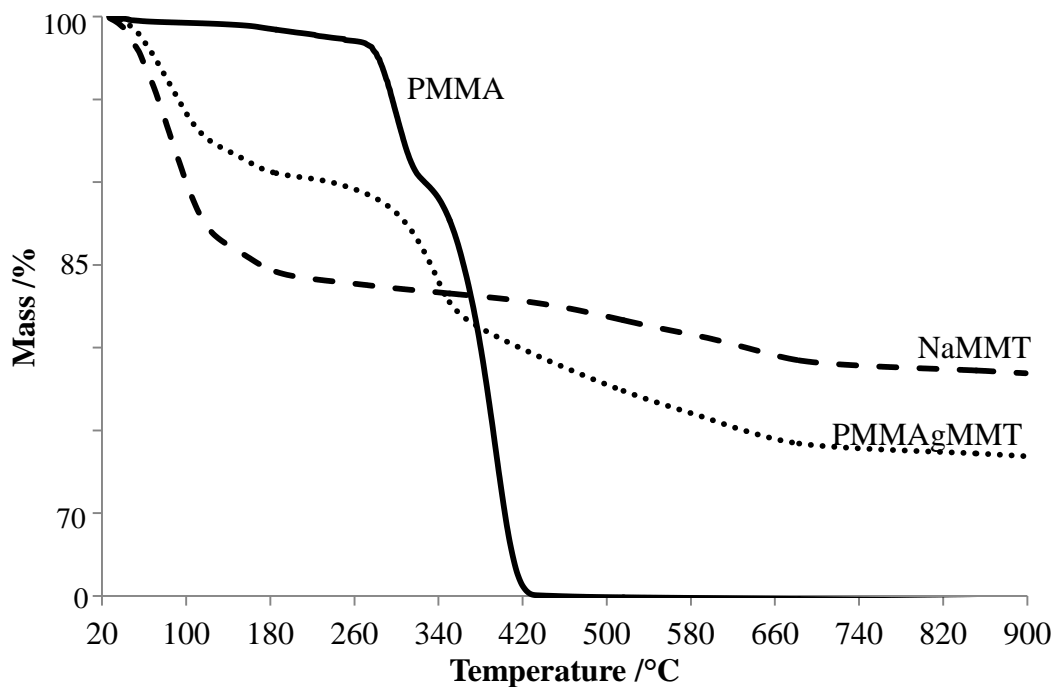
Figure 5.3: Thermograms of PMMA, NaMMT and PMMAgMMT.

5.6.1.5 X-ray diffraction analysis of PMMAgMMT

Figure 5.4 shows the XRD patterns for the NaMMT and the PMMAgMMT. The characteristic basal reflection peak of NaMMT occurred at $2\theta = 6.22$ ° (basal spacing = 14.2 Å) while that of PMMAgMMT occurred at $2\theta = 5.88°$ (basal spacing = 15.0 Å).
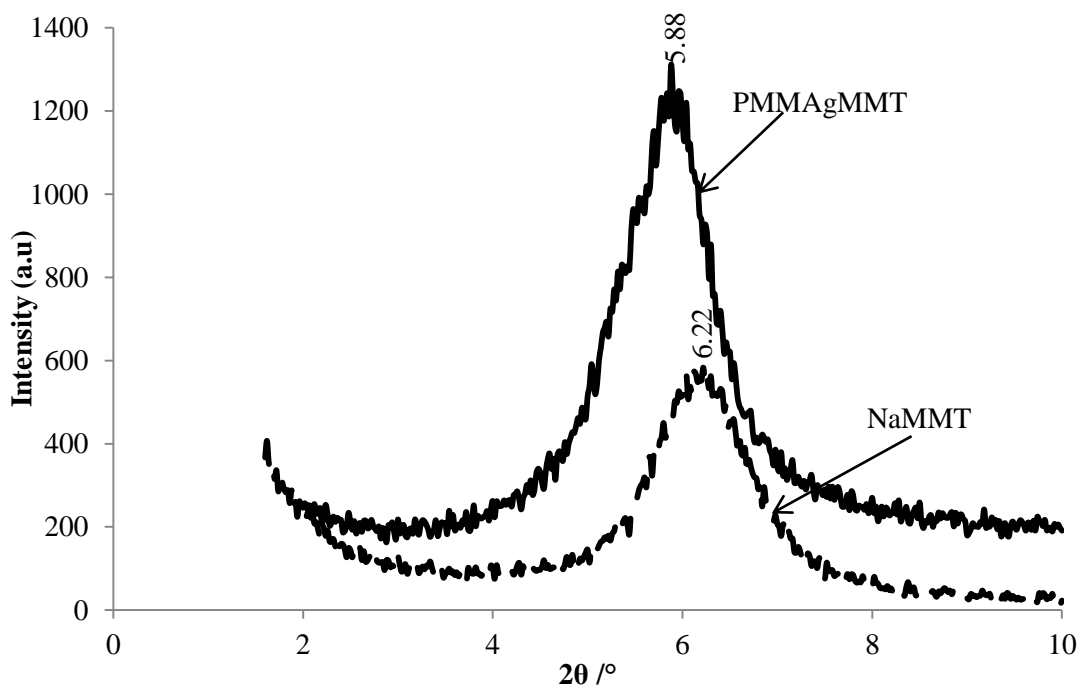
Figure 5.4: XRD patterns of NaMMT and PMMAgMMT.

There was a shift of the peak to lower 2θ angles (an increase in the basal spacing) after modification with PMMA. This suggested that PMMA was partially intercalated and polymerized within the interlayer space of the NaMMT.

5.6.2 Methacryloxypropyl trimethoxysilane-grafted montmorillonite

The mechanism for the grafting of MPS onto a substrate is described in Section 5.6.2.1. Unlike the mechanism described above for the grafting of PMMA, the reaction here followed a condensation mechanism.

5.6.2.1 Suggested mechanism for the grafting of MPS onto NaMMT substrate

The grafting process entails the in-situ hydrolysis of the MPS and then the condensation reaction of the silanol (MPSi(OH)$_3$) with the silanol or aluminol groups on the surface of the MMT. The reaction can be summarised as shown in Scheme 5.2:
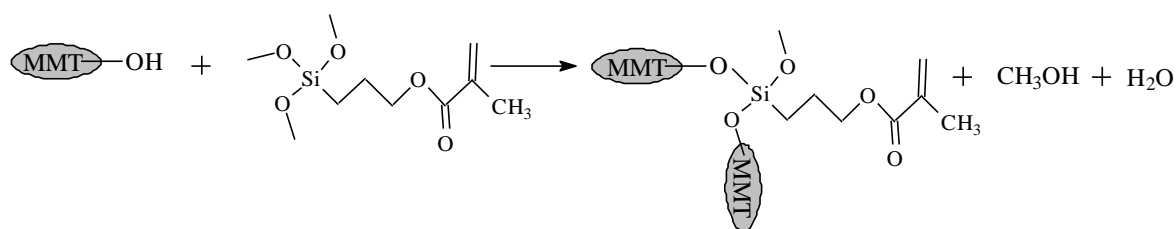
Scheme 5.2: Grafting of MPS onto montmorillonite clay by condensation.

5.6.2.2 FTIR analysis of PMPSgMMT

Figure 5.5 shows the FTIR spectra of NaMMT, poly (methacryloxypropyl trimethoxysilane), PMPS and PMPSgMMT. The vibrational peaks for NaMMT have already been discussed in Section 5.6.1.2. For the PMPSgMMT spectrum, the vibrational peak at 2959 cm^{-1} was assigned as the methyl (CH$_3$-) asymmetric stretching and the vibrational peak at 2887 cm^{-1} was ascribed to the symmetric stretching of the same peak (Costa, R. O. R. et al, 2002). Peaks due to the asymmetric and symmetric bending vibrations of the methyl (CH$_3$-) groups were observed at 1468 and 1394 cm^{-1}, respectively (Costa, R. O. R. et al, 2002).
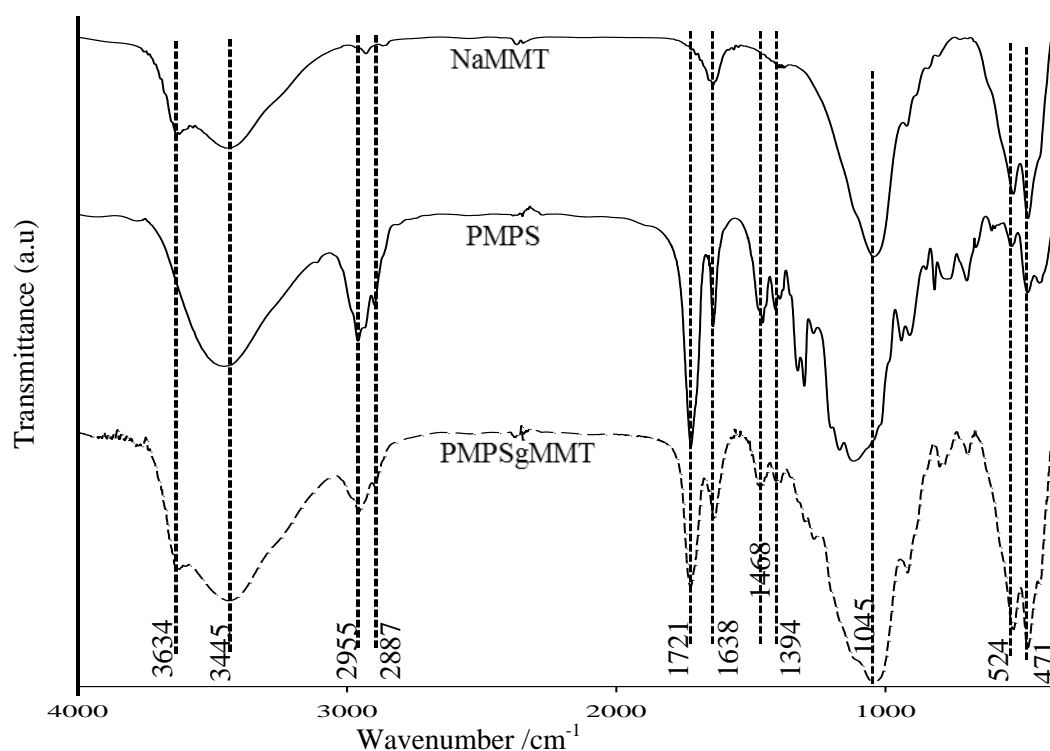
Figure 5.5: FTIR spectra of NaMMT, poly (methacryloxypropyl trimethoxy silane) and PMPSgMMT.

The alkenyl (C=C) stretching vibration was superimposed over the bending vibration of the H-O-H around 1638 cm^{-1} (Günzler, H. et al, 2002). The peak at 1721 cm^{-1} was attributable to the carbonyl (C=O) stretching vibration of the ester group of the grafted MPS (Costa, R. O. R. et al, 2002). The presence of this functional group (after soxhlet extraction of the sample with THF) indicated that the graft polymerisation of MPS onto the NaMMT structure was successful. The grafting of MPS onto MMT was further assessed by TGA.

5.6.2.3 Thermogravimetric analysis of PMPSgMMT

Figure 5.6 displays the TGA thermograms of NaMMT, PMPS and PMPSgMMT. PMPS showed only a single decomposition step centred at 450 °C. The decomposition started at about 300 °C until a charcoal-like residue was obtained at 615 °C. Its decomposition under N$_2$ did not result in ash as observed with lignocellulose and the other polymers, rather, a charcoal black solid was observed, and that explains the approximately 55% mass loss registered in the thermogram after heating to 900 °C. Tiwari, A. et al, 2004 found similar results for the degradation of poly (methylphenyl siloxane).

NaMMT showed two decomposition steps as explained earlier while PMPSgMMT displayed three decomposition steps in the temperature regions: 50-120, 200-460 and 490-730 °C. The first mass loss (59 °C) was attributed to the removal of volatile organics as well as adsorbed water. The second mass

loss (418 °C) was ascribed to the thermal decomposition of grafted PMPS from the NaMMT. The third step (674 °C) was attributed to the loss of interlayer water, the dehydroxylation of the clay structure, as well as the decomposition of residual PMPS compounds.
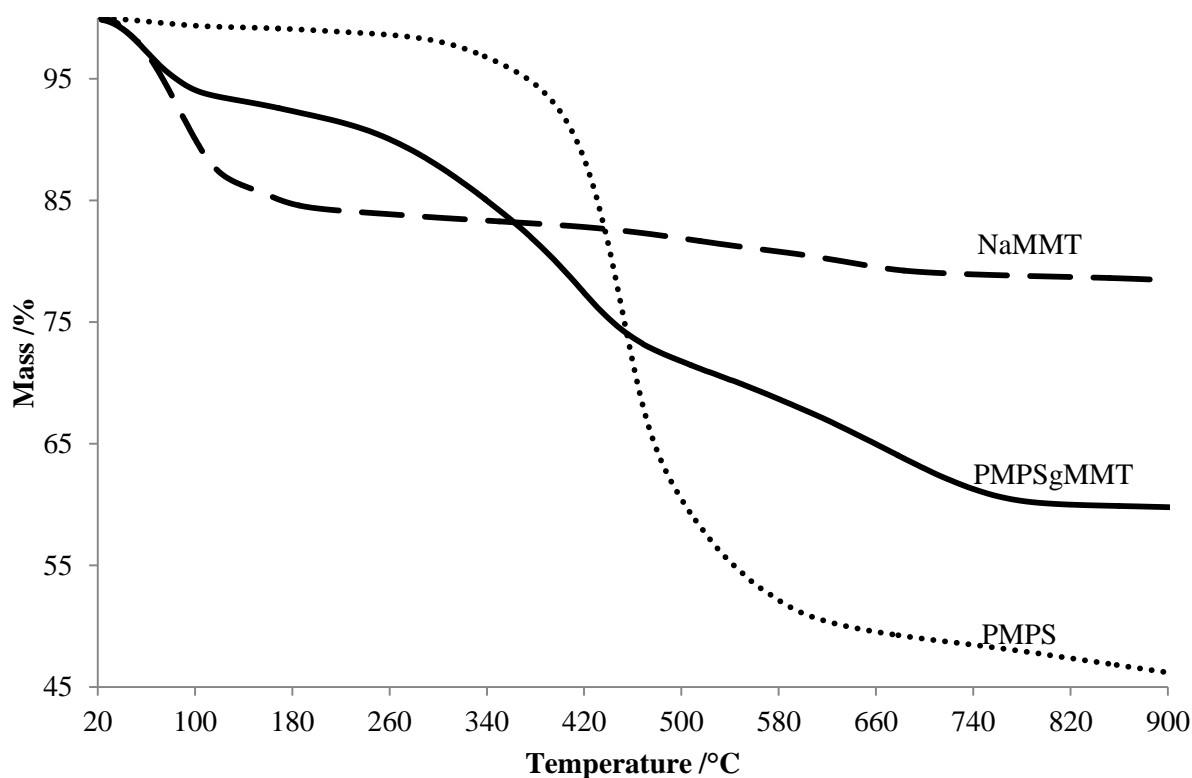
Figure 5.6: TGA thermograms of NaMMT, PMPS and PMPSgMMT.

The amount of PMPS grafted to the NaMMT was determined from the mass loss of the PMPSgMMT in the temperature range of 200 to 430 °C. The mass loss for the NaMMT in the same temperature region was subtracted from the mass loss of the PMPSgMMT in order to get the actual mass of PMPS grafted. The amount of PMPS grafted was found to be about 16% assuming no physical or chemical interaction between the PMPS and NaMMT. The samples were further analysed by XRD.

5.6.2.4 X-ray diffraction analysis PMPSgMMT

The XRD patterns of NaMMT and PMPSgMMT are shown in Figure 5.7. There was no change in the position of the basal reflection peak of montmorillonite after modifying the NaMMT with PMPS. This might imply that the PMPS did not intercalate the interlayer space of the clay, rather, it was grafted on the surface or edges of the clay sheets. However, the basal reflection peak just broadened after modification with PMPS which might suggest a reduction in crystallinity. Piscitelli, F. et al, 2010 observed a shift to lower 2θ angles of the basal reflection peak after silylation of NaMMT. Differences can be attributed to the different experimental conditions used in the studies.
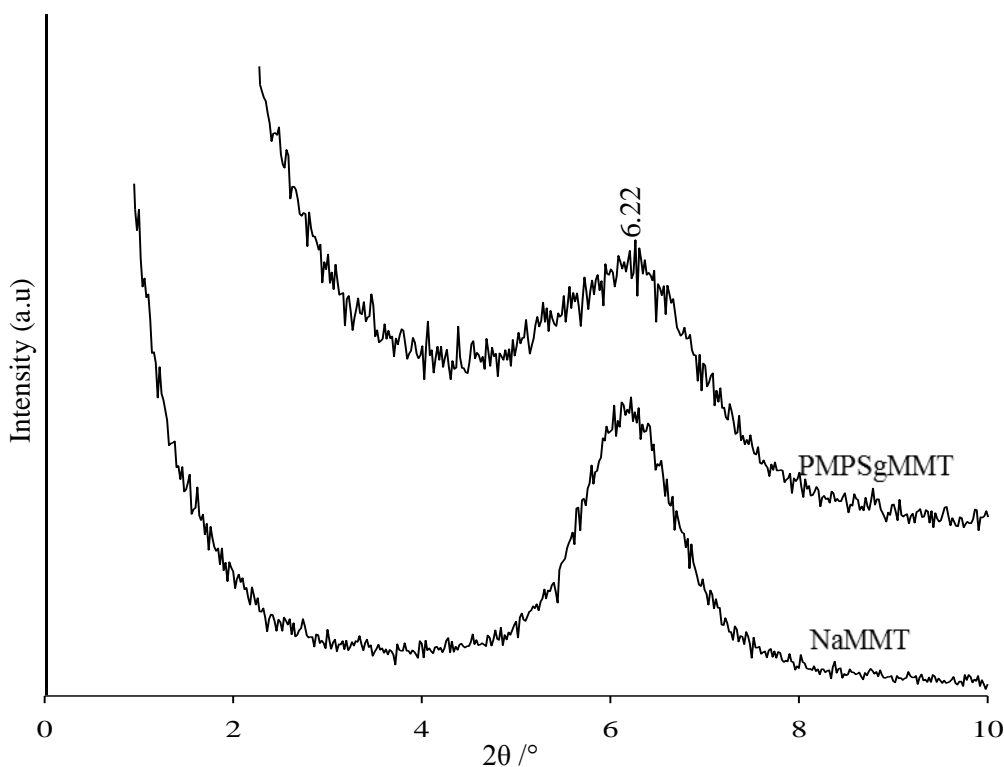
Figure 5.7: XRD patterns of NaMMT and PMPSgMMT.

5.6.3 Poly (methacrylic acid)-grafted montmorillonite

NaMMT was first grafted with PMPS which has a reactive group (C=C bond). MAA was then covalently attached onto the PMPS molecules already grafted onto the NaMMT via the C=C bonds. The mechanism for the grafting of PMPS to a substrate has been described above. The next section describes the mechanism for the grafting of PMAA onto PMPS-modified NaMMT.

5.6.3.1 Suggested mechanism for the grafting of methacrylic acid to PMPSgMMT

The grafting of PMAA to PMPS-grated NaMMT probably followed a free-radical mechanism, and was carried out under aqueous conditions. The generation of the sulphate radical is more or less the same as described above in Section 5.6.1.1. The generated sulphate radical can initiate reaction on the C=C bonds of the grafted PMPS or the C=C bond on the MAA units. The following schematic summarises the grafting of MAA onto PMPS-grafted NaMMT.
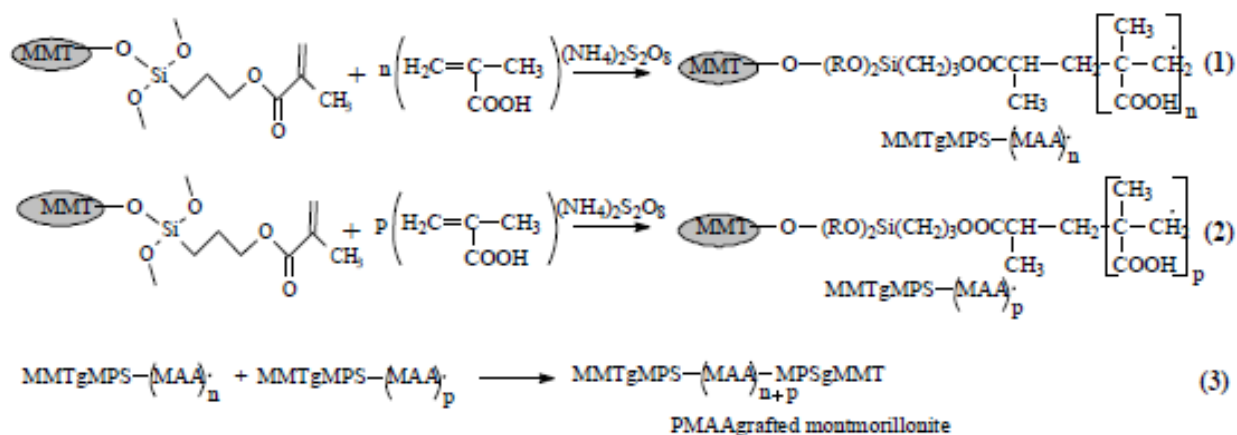
Scheme 5.3: Grafting of PMAA to PMPSgMMT.

5.6.3.2 FTIR analysis of PMAAgMMT

Figure 5.8 displays the FTIR spectra of PMAA, PMPSgMMT and PMAAgMMT. The spectra of PMAA and PMPSgMMT were included for comparison purposes.
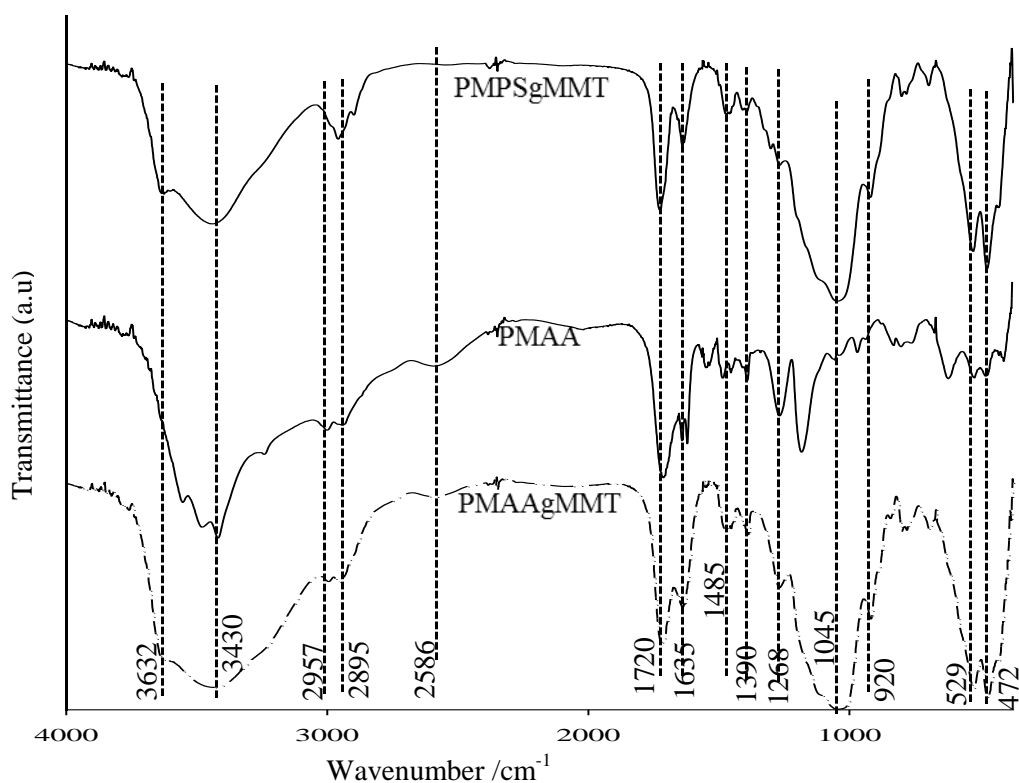
Figure 5.8: FTIR spectra of PMAA, PMPSgMMT and PMAAgMMT.

The FTIR spectrum for PMPSgMMT has been discussed in Section 5.6.2.2. The PMAA spectrum showed a broad peak spanning from 2700 to 3300 cm^{-1} which is attributable to the OH stretching vibration. The broadness is due to the hydrogen bonding common in carboxylic acids and possible

overlap with the peak of the C-H stretching vibration. The spectrum of PMAAgMMT showed a strong band at 1720 cm^{-1} ascribed to the C=O stretching vibration of either a carboxylic group (from PMAA) and/or ester linkage (from PMPS). The ester C=O vibration (PMPS) could be overlapping with the carboxyl C=O vibration. The band at 1268 cm^{-1} (relatively low intensity compared with that of PMAA) was ascribed to the C-O stretching vibration coupled with O-H in-plane bending, associated with the acid dimer of the (-COOH group) from the grafted PMAA (McNeill, I. C. et al, 1995; Dong, J. et al, 1997; Polacco, G. et al, 2000). The assignment of peaks for PMAA and PMAAgMMT spectra is summarised in Table 5.8.

Table 5.8: FTIR peak assignment for the PMAA and PMAAgMMT.

Wavenumber /cm^{-1}	Assignment	Reference
3436	OH stretching vibration of water molecules associated with the COOH	(Polacco, G. et al, 2000)
3248	OH stretching vibration of the COOH	Günzler, H. et al, 2002
2959	CH$_2$ or CH stretching	Dong, J. et al, 1997; Tang, E. et al, 2006
2585	O-H stretching vibration carboxylic acid dimmers	Erhardt, R. et al, 2003; Günzler, H. et al, 2002
1711	C=O stretching vibration of saturated dimeric carboxylic group	Günzler, H. et al, 2002
1640	possibly H-O-H bending or C=C stretching vibration from residual MAA	Günzler, H. et al, 2002; Costa, R. O. R. et al, 2002
1547	Anti-symmetric deformation vibration of C=O in COOH	Tang, E. et al, 2006
1479	C-O stretching coupled with O-H in-plane bending	Günzler, H. et al, 2002
1387 - 1453	Symmetric deformation vibration of C=O in COOH	Tang, E. et al, 2006; Günzler, H. et al, 2002; Kurt, A. et al, 2009
1268	C-O stretching vibration	Günzler, H. et al, 2002

The peak at 1268 cm^{-1} (PMAAgMMT) was not present in the PMPSgMMT spectrum. The broad band at 2584 cm^{-1} (associated with the carboxyl O-H stretching vibration) was found to be present in both PMAA and PMAA-g-MMT but not in PMPSgMMT. These findings show that the grafting of PMAA onto PMPSgMMT was carried out successfully.

5.6.3.3 Thermogravimetric analysis of PMAAgMMT

Figure 5.9 shows the TGA thermograms of PMAA, PMPSgMMT and PMAAgMMT. Both thermograms of PMAAgMMT and PMPSgMMT showed three degradation steps. For PMAAgMMT, the degradation steps occurred at temperatures 68, 395, and 626 °C while for PMPSgMMT, the degradation steps occurred at temperatures 63, 419 and 678 °C. The composite PMPSgMMT displayed a relatively higher thermal stability compared with PMAAgMMT. The thermogram of PMAAgMMT showed a greater mass loss compared with the PMPSgMMT. The amount of PMAA that was grafted could be calculated from the mass loss in the temperature region 200 to 430 °C, and was found to be about 8%. This again showed that the grafting of PMAA onto PMPSgMMT had been carried out successfully. The increased mass loss recorded in the thermogram of PMAAgMMT was attributed to the presence of grafted PMAA.
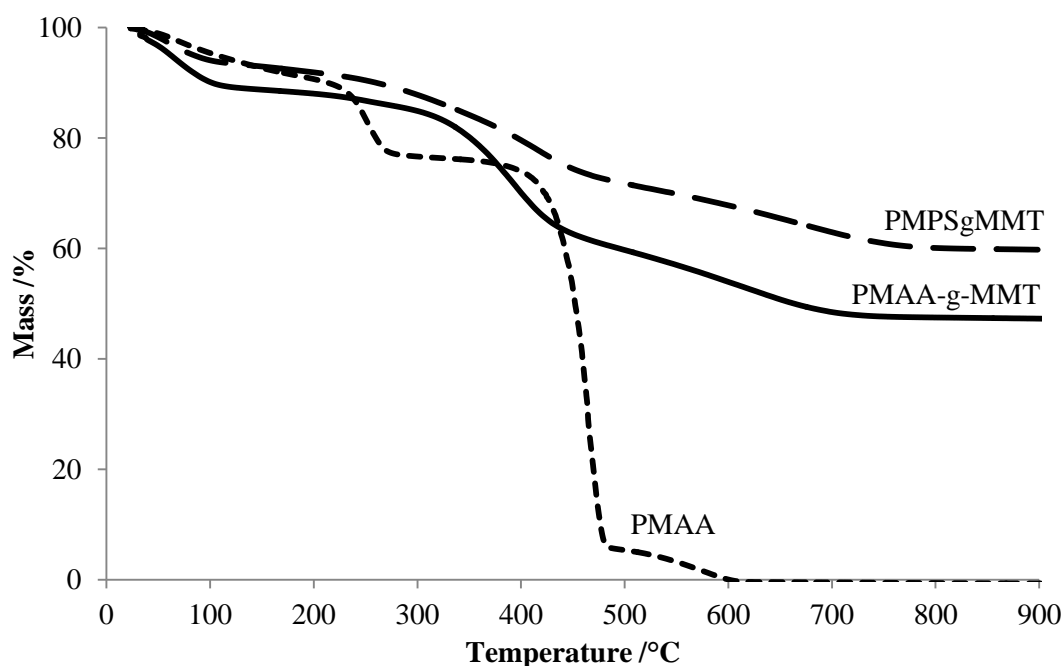
Figure 5.9: TGA thermograms of PMAA, PMPSgMMT and PMAA-g-MMT.

5.6.3.4 X-ray diffraction analysis PMAAgMMT

The PMAAgMMT was further analysed by XRD and the diffractograms are shown in Figure 5.10.
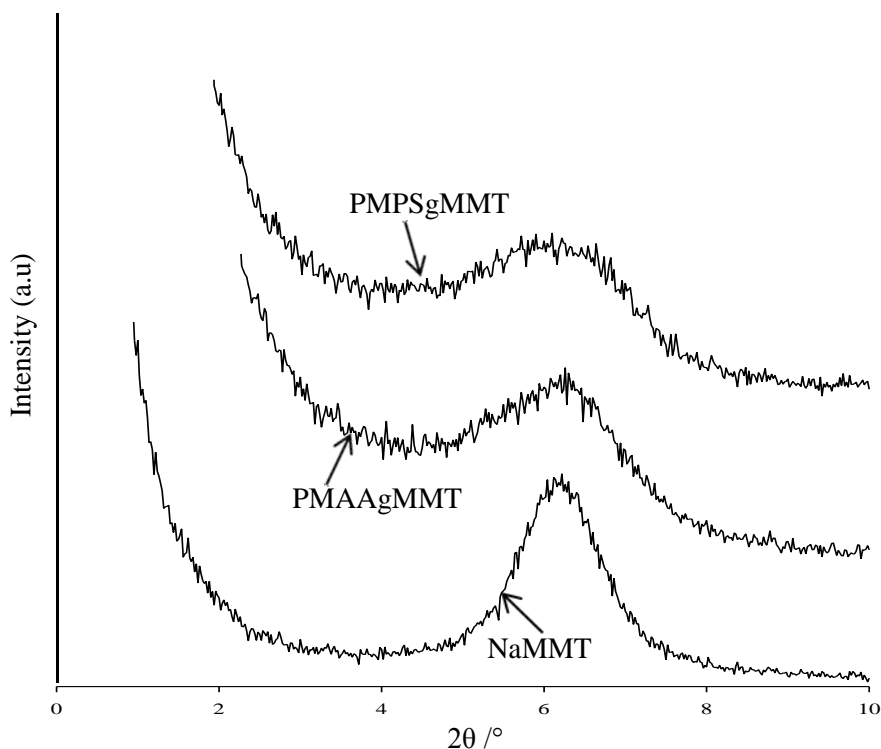
Figure 5.10: XRD patterns of NaMMT, PMPSgMMT and PMAAgMMT.

The grafting of PMAA onto PMPSgMMT did not result in a change in the position of the basal reflection peak of montmorillonite. The XRD patterns of PMPSgMMT and PMAAgMMT looked almost the same (see Figure 5.10). This suggests that grafting occurred onto the edges of the NaMMT clay, there was no intercalation.

5.6.4 Poly (methyl methacrylate)-grafted lignocellulose

The grafting of polymers was expected to occur on the OH groups of the lignocellulose (Hill, C. A. S. et al, 2000) via the mechanism described in Section 5.6.1.1.

5.6.4.1 FTIR analysis of PMMAgLig

Figure 5.11 displays the FTIR spectra of PMMA, lignocellulose and PMMA-grafted lignocellulose. The spectrum of the raw lignocellulose showed stretching vibrations at 1065 cm^{-1}, 1387 cm^{-1}, 1621 cm^{-1}, 2955 cm^{-1} and 3435 cm^{-1}. These are attributed to C-O-C skeletal vibration, O-H bending, H-O-H bending (absorbed water), C-H stretching and hydroxyl stretching, respectively.

The soxhlet extracted PMMA-grafted lignocellulose showed the above-highlighted peaks for raw lignocellulose as well as two extra peaks at 755 cm^{-1} and 1732 cm^{-1}. These peaks are characteristic of PMMA. It can also be observed that the O-H bending peak at 1387 cm^{-1} is relatively more intense for the lignocellulose blank sample than for the PMMA-grafted lignocellulose. This can be attributed to

the bonding of the MMA monomer to some of the OH groups during the free radical polymerization reaction leaving fewer OH groups exposed in the grafted lignocellulose, hence the reduced O-H intensity in the grafted lignocellulose. FTIR results show that PMMA was grafted onto lignocellulose.
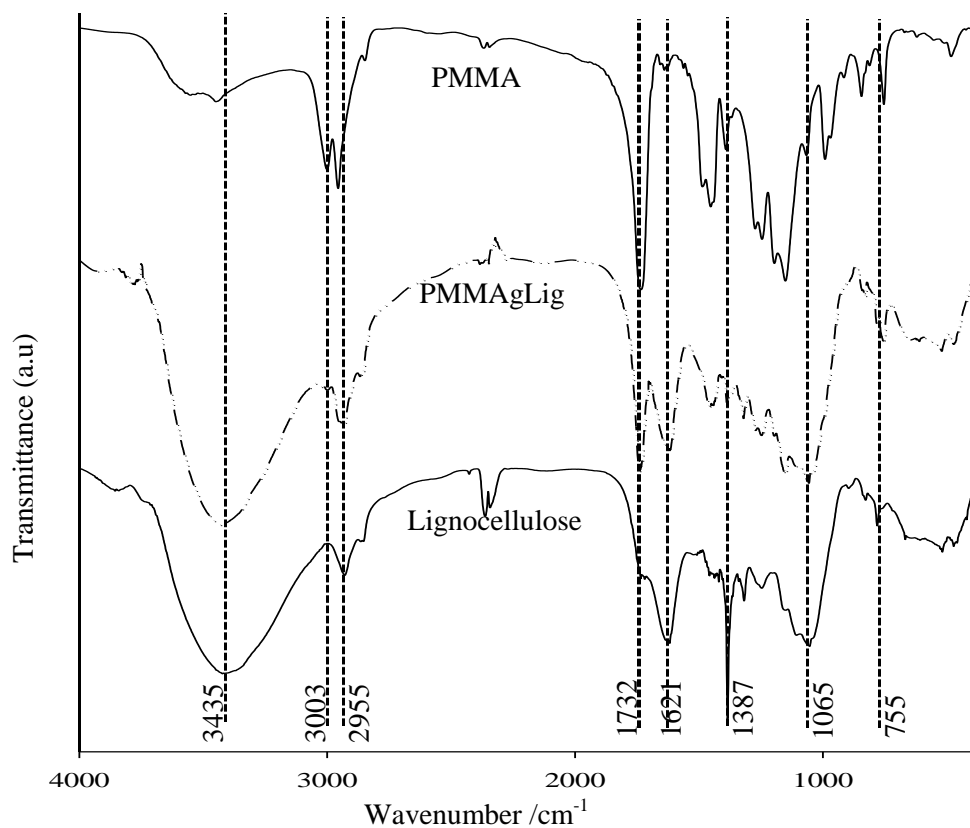
Figure 5.11: FTIR spectra of lignocellulose, PMMA and PMMAgLig.

5.6.4.2 Scanning electron microscopy of PMMAgLig

The grafting of PMMA to lignocellulose was also assessed using scanning electron microscopy and Figure 5.12 shows the micrographs of unmodified and PMMA-modified lignocellulose samples. The micrographs of the unmodified and modified lignocellulose showed different morphologies. The PMMA particles attached to the lignocellulose can be seen in the modified lignocellulose sample.

147
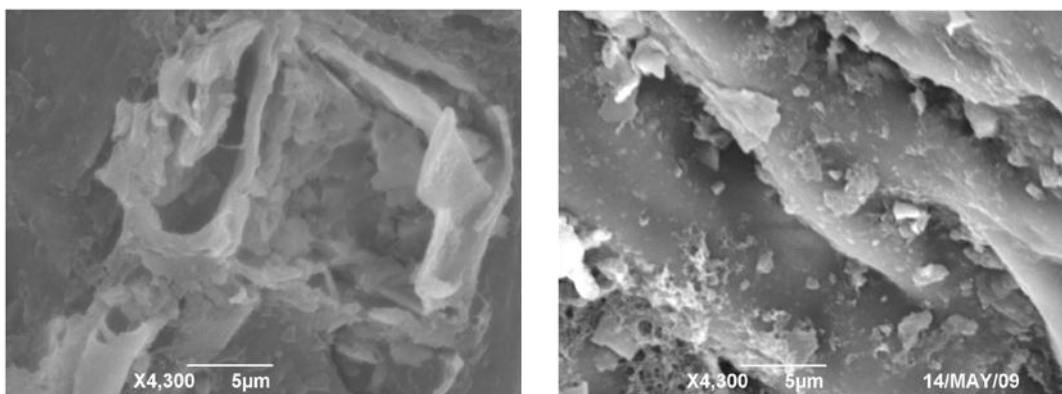
Figure 5.12: SEM micrographs for raw lignocellulose (left) and PMMA-grafted lignocellulose (right). Magnification 4300X.

SEM was employed in the assessment of the grafting of polymers to lignocellulose in the past. Such studies include the work by Gangopadhyay, R. et al, 2000; Román-Aguirre, M. et al, 2000 and Ojah, R. et al, 2006 in which they observed similar changes in the morphologies of lignocellulose and silk after modification.

5.6.4.3 Thermogravimetric analysis of PMMAgLig

The grafting of PMMA onto the lignocellulose was also assessed by TGA. A number of authors (Gangopadhyay, R. et al, 2000; Román-Aguirre, M. et al, 2004 and Ojah, R. et al, 2006) have used thermogravimetric analysis as a tool to assess the grafting of polymers onto lignocellulose. Figure 5.13 shows the thermograms of pure PMMA, raw lignocellulose and the PMMA-grafted lignocellulose.

It was observed that PMMA thermally degraded in the same temperature region as both the unmodified and the PMMA-grafted lignocellulose. However, all the PMMA was completely degraded at a temperature of about 420 °C. The unmodified lignocellulose showed a similar degradation thermogram to that of the PMMA-grafted lignocelluloses although the unmodified lignocellulose showed slightly higher thermal stability than the grafted lignocellulose. Gangopadhyay, R. et al, 2000 and Ojah, R. et al, 2006 reported an increase in the thermal stability of lignocellulose following grafting with PMMA. Román-Aguirre, M. et al, 2004 also found that the grafting of lignocellulose with PMMA resulted in a reduced thermal stability. The reduced thermal stability was attributed to the strong oxidative activity of potassium persulfate. Ojah, R et al, 2006 used a CdS photocatalyst (which might be not as oxidizing as potassium persulfate or ammonium persufate) for the grafting process, and that might explain why they observed an increased thermal stability of their polymer-grafted silk material.
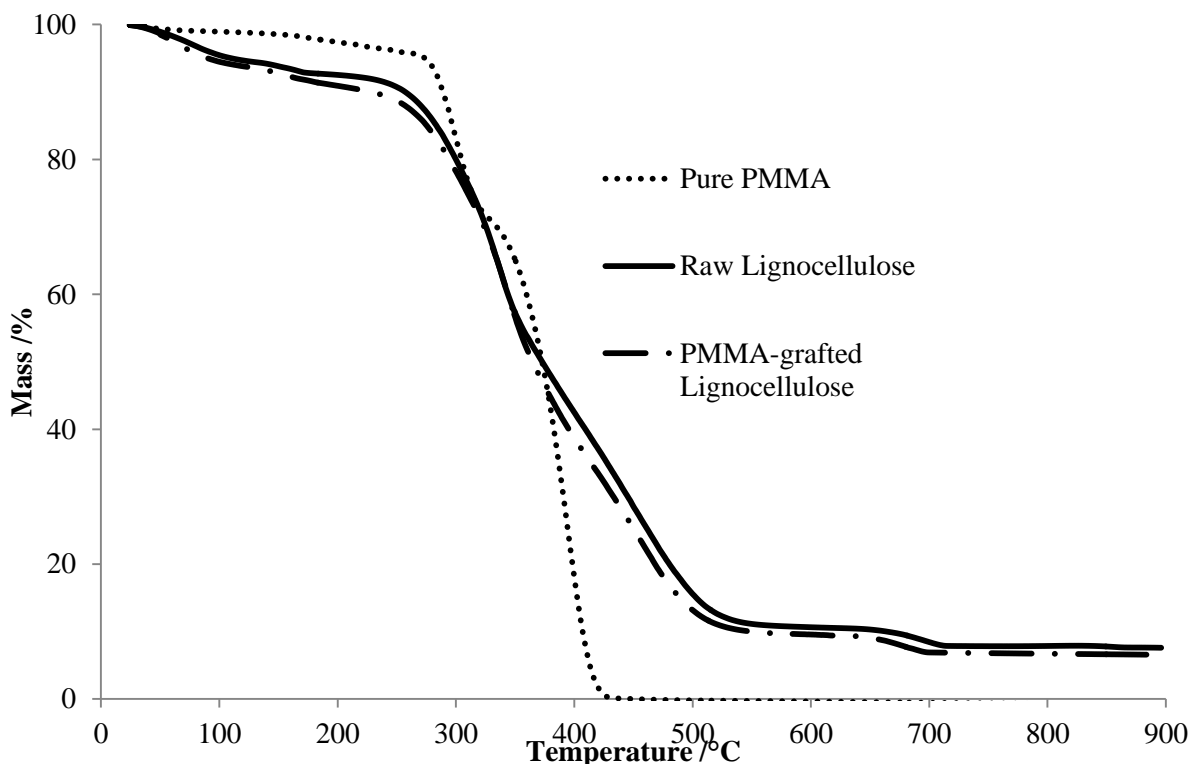
Figure 5.13: Thermograms of pure PMMA, lignocellulose and PMMA-grafted lignocellulose.

Gangopadhyay, R. et al, 2000 carried out photo-grafting of PMMA to sisal fibres using oxalic acid. In this study, ammonium persulfate was used as an initiator for the grafting reaction. The reduced thermal stability observed in the grafted lignocelluloses prepared in this study can be attributed to the effect of the ammonium persulfate. The grafting efficiency was determined by gravimetric analysis and the efficiency achieved under the conditions reported in this study was about 17%.

5.6.5 Methacryloxypropyl trimethoxysilane-grafted lignocellulose

The mechanism for the grafting of MPS onto lignocellulose is the same as described for the preparation of PMPSgMMT (see Section 5.6.2.2). The only difference is the substrate.

5.6.5.1 FTIR analysis of PMPSgLig

Figure 5.14 below shows the FTIR spectra of lignocellulose and MPS-grafted lignocellulose. The peak at 1720 cm^{-1} in the PMPS-grafted lignocellulose was ascribed to the C=O (unsaturated ester) stretching vibration of the grafted MPS. The peak at 1620 cm^{-1} was ascribed to the C=C stretching vibration which overlapped with that of the H-O-H bending vibration (1638 cm^{-1}).

The -CH$_2$- asymmetric stretching vibration can be observed at 2932 cm^{-1} and the symmetric stretching vibration of the same at 2855 cm^{-1}. The stretching vibration of the Si-O-C group can be observed at 1055 cm^{-1} and this overlapped with the C-O-C stretching vibration from the lignocellulose. The

149

presence of the C=O stretching vibration (of the conjugated ester group) in the tetrahydrofuran-extracted MPS-grafted lignocellulose sample showed that the grafting of MPS had been carried out successfully.
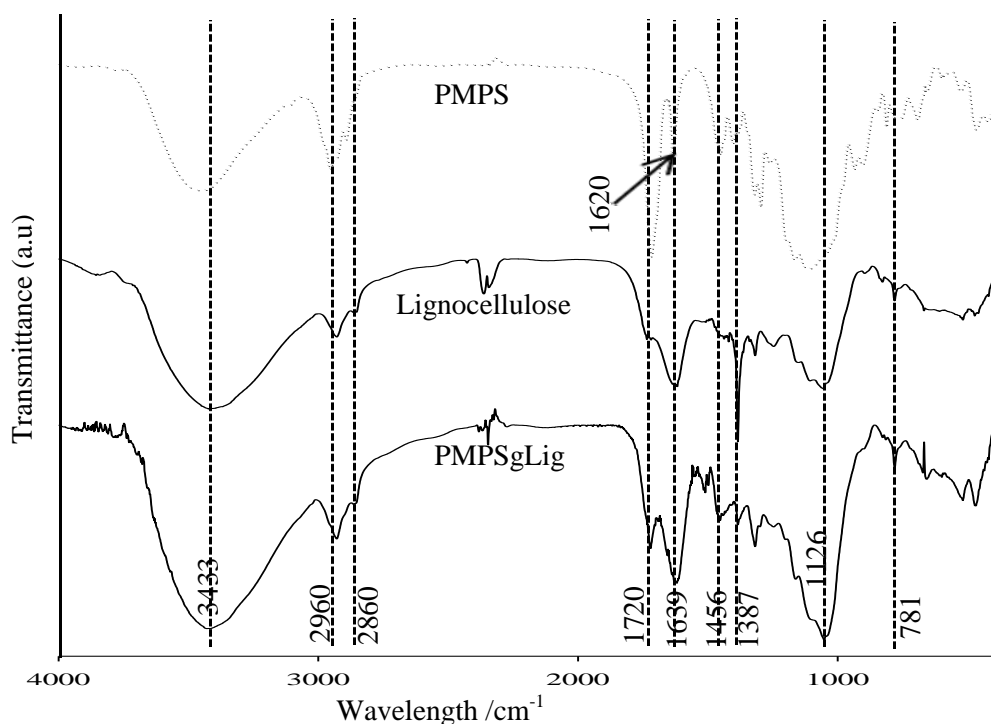
Figure 5.14: FTIR spectra of lignocellulose, PMPS and PMPSgLig.

5.6.5.2 Thermogravimetric analysis of PMPSgLig

MPS-grafted lignocellulose was also analysed by TGA and the thermograms are displayed in Figure 5.15. The thermogram of pure poly (methacryloxypropyl trimethoxysilane) has been discussed in Section 5.6.2.3. There was no significant difference in the thermal stabilities of the raw lignocellulose and the MPS-grafted lignocellulose. The slight increase in the thermal stability of the MPS-grafted lignocellulose could be due to single MPS units grafted on the lignocellulose, whereas the higher thermal stability of the MPS is due to the formation of silicon carbides or oxides.
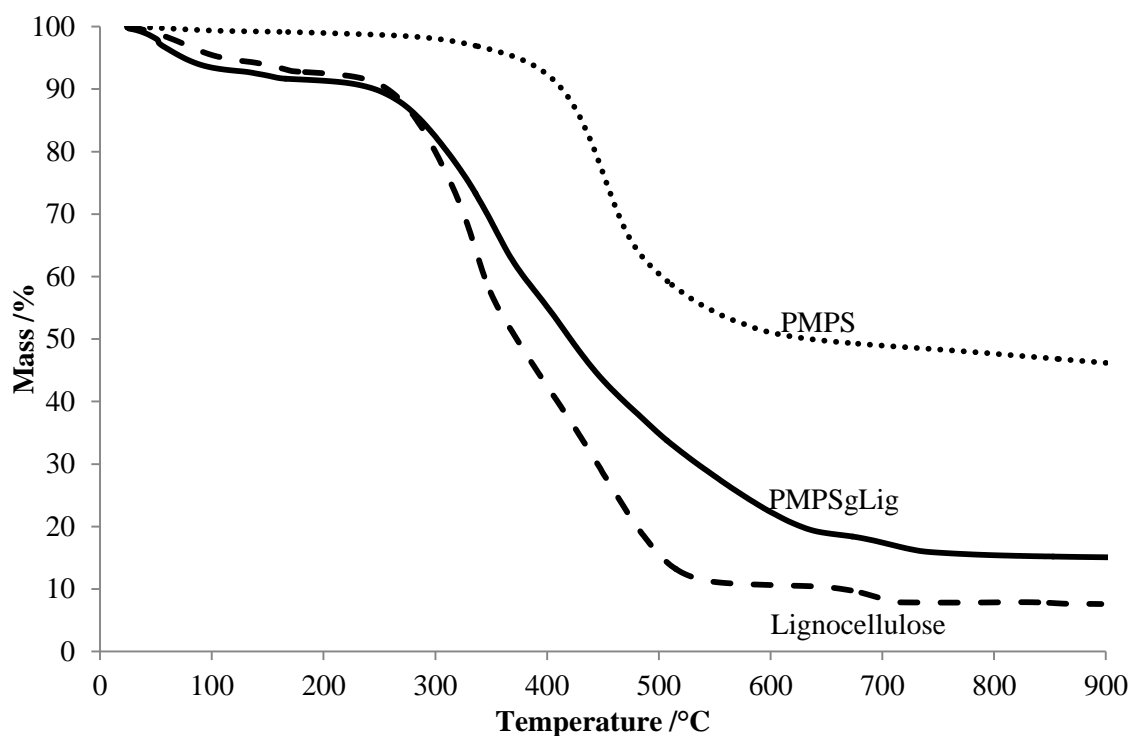
Figure 5.15: Thermograms of lignocellulose, PMPS and PMPSgLig.

The results obtained from TGA again suggested that the grafting of lignocellulose with MPS was carried out successfully. This is different from what was observed for the grafting of PMMA to lignocellulose were the thermograms showed higher stability for the raw lignocellulose than the PMMA-grafted lignocellulose.

5.6.6 Poly (methacrylic acid)-grafted lignocellulose

Poly (methacrylic acid)-grafted lignocellulose was prepared via a possible free-radical graft polymerisation reaction. The mechanism for the grafting of MAA onto MPS-grafted lignocellulose is the same as that described in Section 5.6.3.1 for the grafting of the same to PMPSgMMT.

5.6.6.1 FTIR analysis of PMAAgLig

Figure 5.16 displays the FTIR spectra of the raw lignocellulose, PMAA and PMAA-grafted lignocellulose. The spectra of PMAA and raw lignocellulose were included for ease of comparison and assignment of peaks.
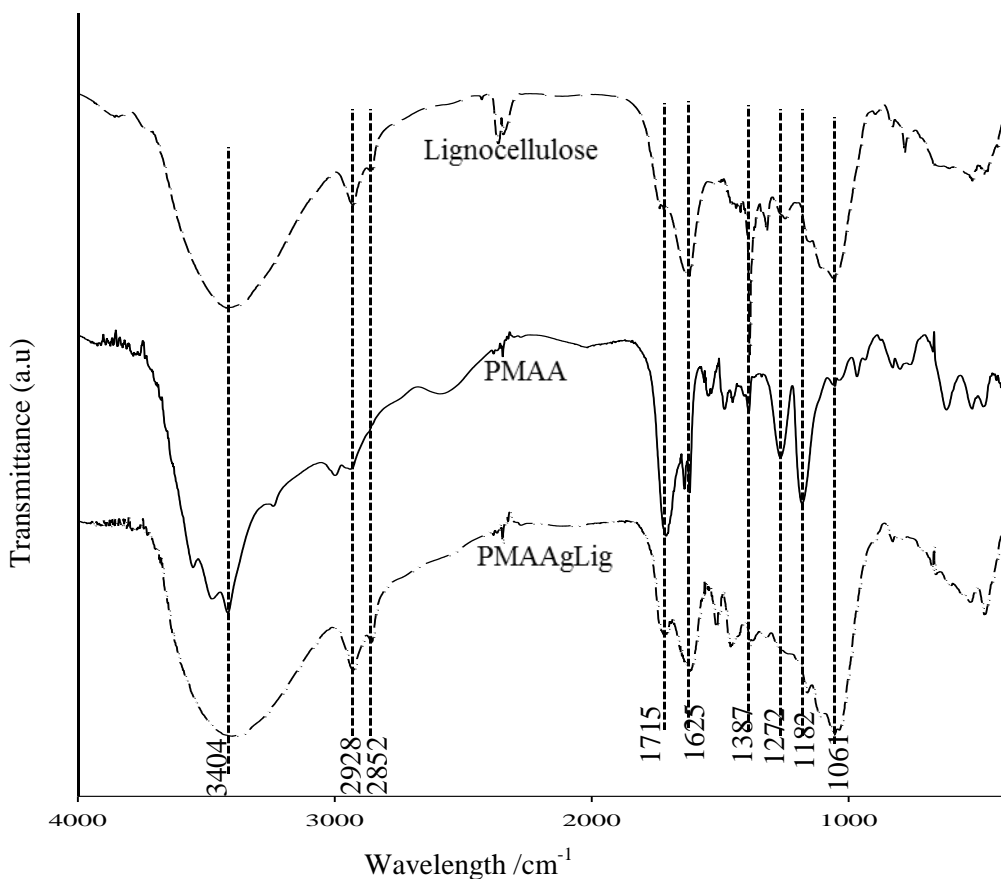
Figure 5.16: FTIR spectra of lignocellulose, PMAA and PMAAgLig.

For the PMAA-grafted lignocellulose, the peak at 1717 cm^{-1} can be attributed to the C=O stretching vibration of the carboxyl groups from the grafted PMAA (Tong, M. et al, 2007). The band at 1182 cm^{-1} was assigned to the C-O symmetric stretching vibration. The band at 1061 cm^{-1} was ascribed to C-O-C stretching vibration (Wang, L. et al, 2007). The presence of the carboxylate C=O stretching vibration peak at 1717 cm^{-1} in the PMAA-grafted lignocellulose sample showed that the grafting of PMAA onto MPS-grafted lignocellulose was carried out successfully.

5.6.6.2 Thermogravimetric analysis of PMAAgLig

The PMAA-grafted lignocellulose was further analysed by TGA and the thermograms of raw lignocellulose, PMPSgLig and PMAA-grafted lignocellulose are shown in Figure 5.17.

152
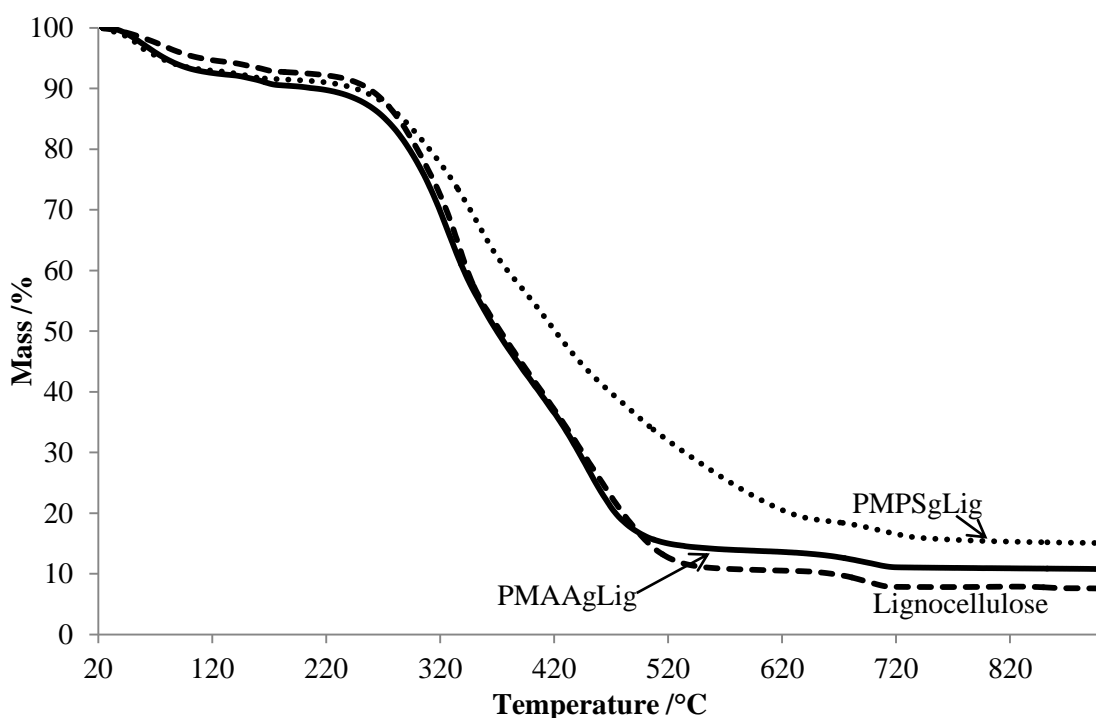
Figure 5.17: TGA thermograms of lignocellulose, PMPSgLig and PMAAgLig.

PMAA-grafted lignocellulose thermogram also showed three decomposition steps which were assigned as follows: 60 °C (loss of adsorbed water), 322 °C (possibly due to the decomposition of PMAA-grafted lignocellulose and also of lignocellulose material) and 440 °C (decomposition of lignocellulose char). The only difference is that PMAA-grafted lignocellulose gave slightly more residue (more thermal stability) compared with the raw lignocellulose. PMAA-grafted lignocellulose showed poor thermal stability relative to the MPS-grafted lignocellulose. The poor thermal stability of the PMAA-grafted lignocellulose compared with MPS-grafted lignocellulose can possibly be explained in terms of the oxidative effect of ammonium persulfate on the MPS-modified lignocellulose fibres during the grafting with MAA (Román-Aguirre, M. et al, 2004). However, the oxidative activity did not occur to the same extent as on the raw lignocellulose as described in Section 5.6.4.3 for the grafting of methyl methacrylate. The presence of the grafted MPS on the lignocellulose offered some kind of stabilizing effect.

The TGA results further confirm that the grafting of PMAA onto lignocellulose was carried out successfully. Both FTIR and TGA results showed that PMAA was covalently attached to the lignocellulose backbone.

5.6.7 Poly (methyl methacrylate)-grafted montmorillonite-lignocellulose nanocomposite

5.6.7.1 Suggested mechanism for the coupling of lignocellulose with NaMMT

After the successful grafting of PMMA onto both montmorillonite and lignocellulose separately, nanocomposites based on these materials were then prepared. The coupling process of the lignocellulose and montmorillonite is summarized in Scheme 5.4.
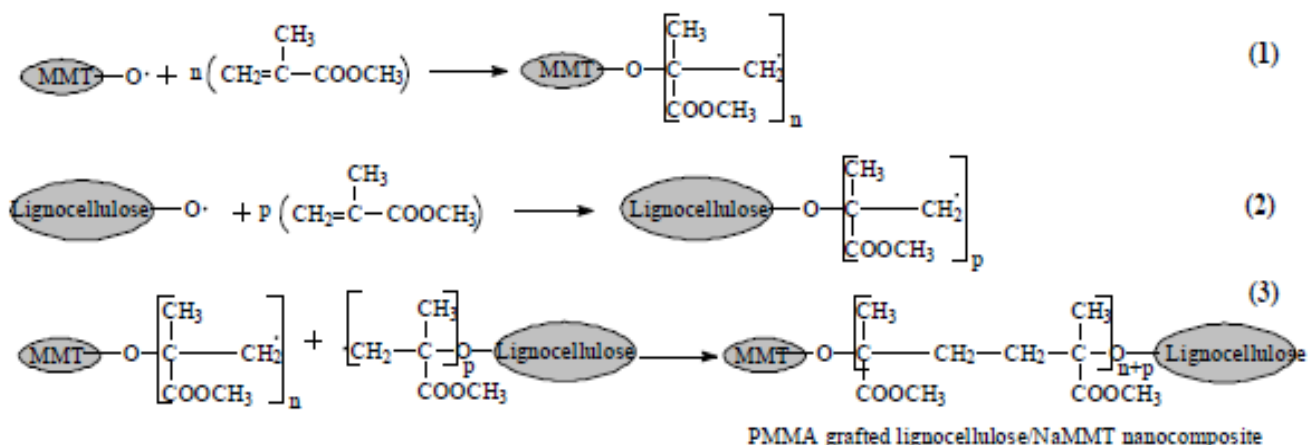
Scheme 5.4: Coupling of NaMMT and lignocellulose with PMMA to form a nanocomposite.

The generation of macroradical species has been described in Section 5.6.1.1. It is worth noting that a range of species can be present and these include: lignocellulose-PMMA-lignocellulose, montmorillonite-PMMA-montmorillonite, PMMA-grafted lignocellulose, ungrafted lignocellulose and ungrafted montmorillonite and PMMA-grafted montmorillonite. The PMMA was expected to act as a bridge linking the lignocellulose to the NaMMT as depicted in Scheme 5.4.

5.6.7.2 FTIR analysis of PMMAgLig-NaMMT

Figure 5.18 shows the FTIR spectrum of raw lignocellulose, NaMMT and a representative nanocomposite. The FTIR spectra of the different nanocomposites (at different clay loadings) did not show major differences from each other. In addition, there were no new peaks observed apart from what has already been discussed for the PMMA-grafted MMT and PMMA-grafted lignocellulose. The presence of the peak at 1734 cm^{-1} (C=O of the ester linkage of PMMA) after soxhlet extraction of the sample using tetrahydrofuran showed that the grafting reaction had been successful (Castellano, M. et al, 2004). The presence of the NaMMT in the nanocomposite was shown by the presence of the peaks at 468 cm^{-1} and 530 cm^{-1} which were ascribed to Si-O-Si and Al-O-Si, respectively. The soxhlet extraction was necessary in order to open up the spaces in the nanocomposite which would act as adsorption sites for both heavy metals and organic pollutants.
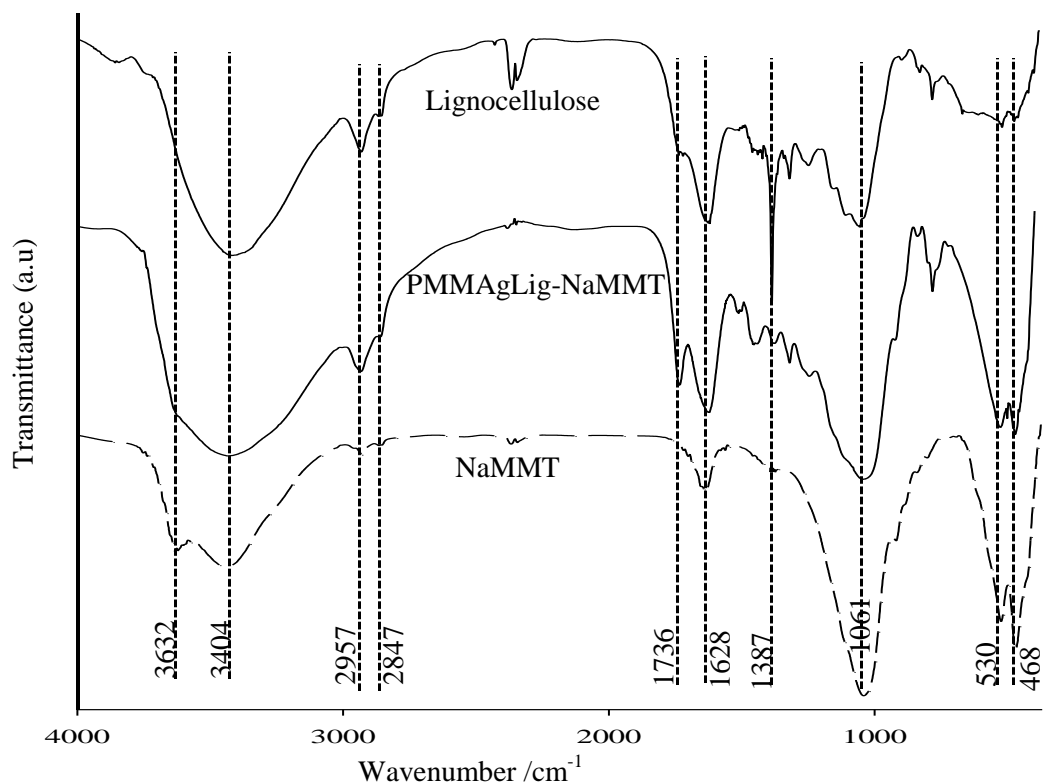
Figure 5.18: FTIR spectra of raw lignocellulose, NaMMT and PMMAgLig -NaMMT nanocomposite.

5.6.7.3 Thermogravimetric analysis of PMMAgLig-NaMMT

The nanocomposites were also analysed by TGA and the thermograms are shown in Figure 5.19. It can be seen that the presence of NaMMT in the lignocellulose matrix resulted in an increased thermal stability of the nanocomposites. The more the amount of NaMMT, the greater was the thermal stability of the nanocomposites.

The raw lignocellulose showed a degradation temperature of about 344 °C whereas the nanocomposite showed a decomposition of temperature of about 375 °C. In addition, a greater mass loss was observed for the raw lignocellulose than was recorded for the nanocomposites. The mass loss decreased with increase in amount of NaMMT in the nanocomposites. Only one nanocomposite thermogram is shown in Figure 5.19, and this is the nanocomposite prepared at 40%. The amount of NaMMT in the nanocomposites could also be determined from the ash that remained after heating the samples to 900 °C, and this roughly corresponded with the theoretical amount of NaMMT in the nanocomposite.
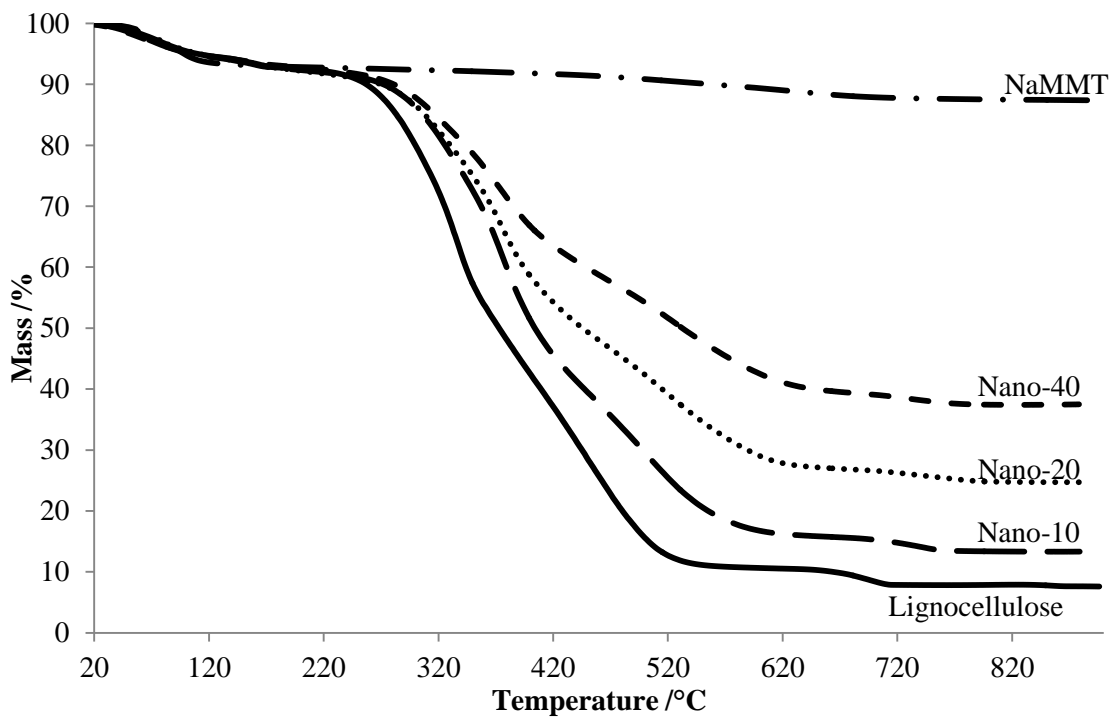
Figure 5.19: TGA thermograms of NaMMT, raw lignocellulose and PMMAgLig-NaMMT nanocomposites (Nano-10, Nano-20 and Nano-40).

5.6.7.4 X-ray diffraction analysis

Figure 5.20 below shows the XRD patterns of NaMMT and PMMA-grafted lignocellulose-montmorillonite nanocomposite.
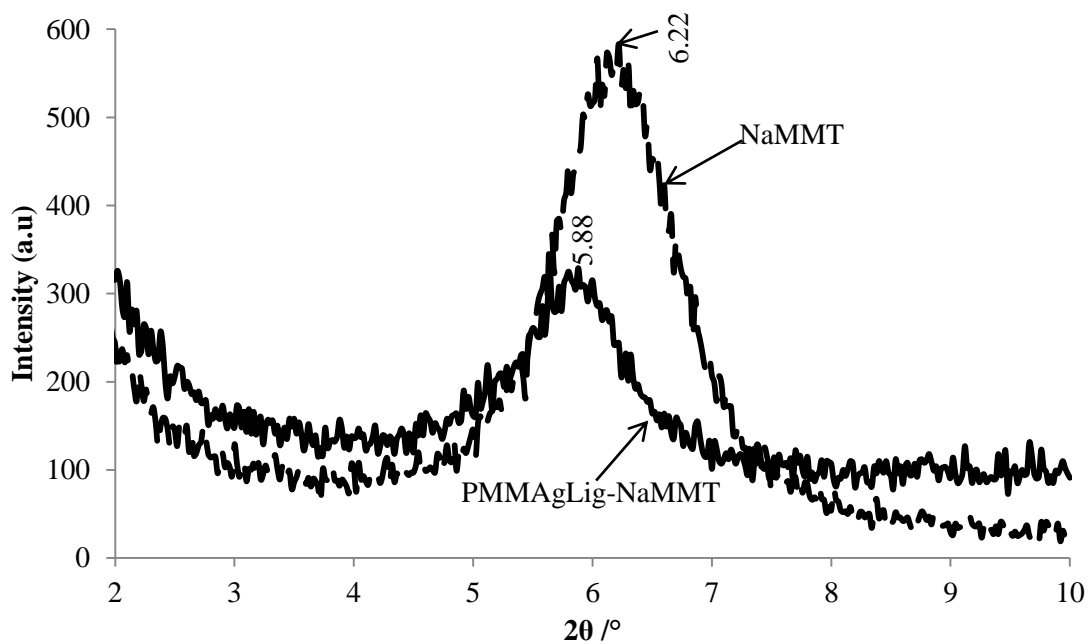
Figure 5.20: XRD pattern of NaMMT and PMMA-grafted lignocellulose-montmorillonite nanocomposite.

5.6.7.5 Transmission electron microscopy of PMMAgLig-NaMMT

The nanocomposite was further analysed by transmission electron microscopy (TEM). Figure 5.21 shows the TEM micrograph for PMMAgLig-NaMMT nanocomposite. The micrograph showed that the NaMMT was dispersed in the lignocellulose matrix at nanoscale. However, the clay sheets are still quite ordered, confirming the findings from the XRD data already been discussed above. It can be suggested that the product formed was an intercalated nanocomposite.
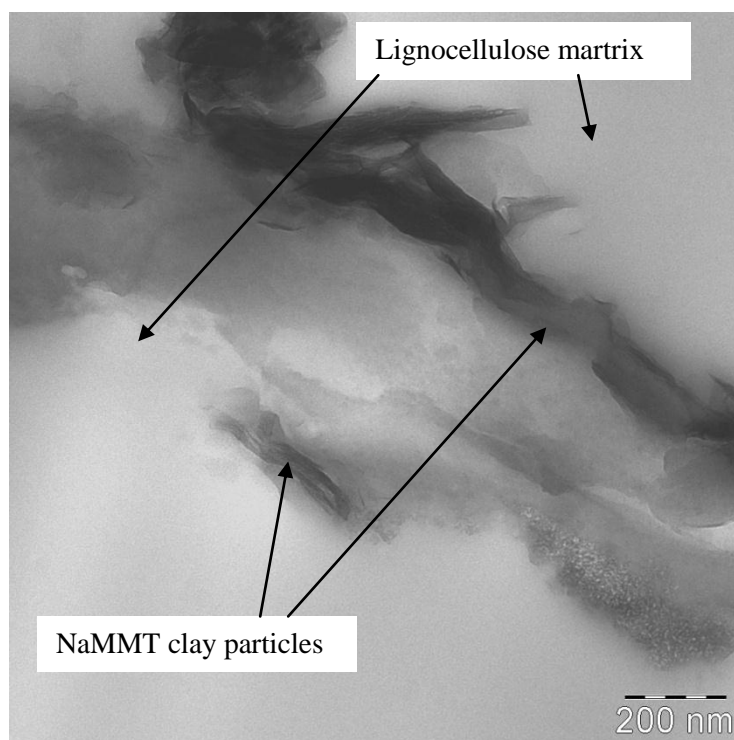
Figure 5.21: Transmission electron micrograph of PMMAgLig-NaMMT nanocomposite.

The basal reflection peak of montmorillonite shifted from 6.22° (NaMMT) to 5.88° for the PMMA-grafted nanocomposite. This corresponded to a d-spacing of 15.02° for the nanocomposite from 14.20° (NaMMT). It can be speculated that there was some partial intercalation of the poly (methyl methacrylate) into the interlayer space of the clay sheets.

5.6.8 Poly (methacrylic acid)-coupled lignocellulose-clay nanocomposites

5.6.8.1 Suggested mechanism for the coupling of MPS-modified NaMMT and lignocellulose using MAA

After demonstrating that methacrylic acid can be grafted to both PMPSgMMT and MPS-grafted lignocellulose, a nanocomposite based on the modified lignocellulose and montmorillonite coupled via the poly (methacrylic acid) was prepared by in-situ graft polymerization. The same free-radical polymerization process as described earlier was expected to occur during the coupling of the clay to

the lignocellulose. The following scheme illustrates the proposed coupling process to give the nanocomposite product. Again, a number of species is expected to be present other than the desired PMAA-grafted lignocellulose-montmorillonite nanocomposite.
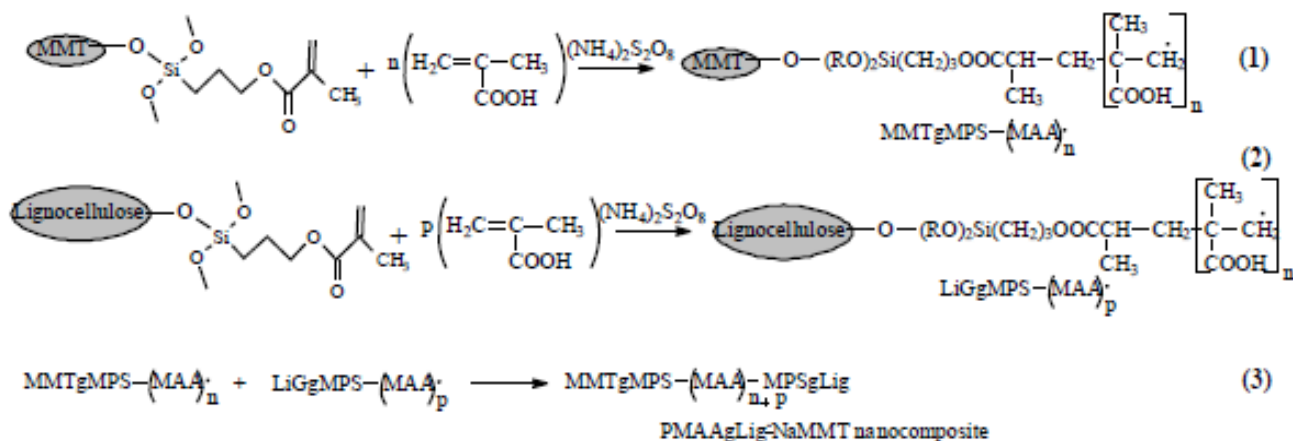
Scheme 5.5: Coupling of PMPSgLig-NaMMT to PMPSgLig through PMAA.

5.6.8.2 FTIR analysis of PMAAgLig-NaMMT

Figure 5.22 displays the FTIR spectra of PMAA, MPS-grafted lignocellulose and PMAA-grafted lignocellulose-montmorillonite nanocomposite. The PMAA-grafted nanocomposite showed an additional peak at 1268 cm^{-1} which was assigned to C-O stretching vibration coupled with O-H in-plane bending, associated with the -COOH dimer (McNeill, I. C. et al, 1995; Dong, J. et al, 1997 and Polacco, G. et al, 2000). This peak can also be clearly seen in the spectrum of PMAA. Another peak associated with the presence of the PMAA in the nanocomposite can be seen at 2576 cm^{-1} (O-H stretching vibration carboxylic acid dimers (Erhardt, R. et al, 2003)) from the grafted PMAA. There was a slight shift of the C=O stretching vibration peak to higher frequencies in the nanocomposite. This might be a result of the loss of C=C bonds as MAA units reacted with the C=C groups of the grafted MPS, resulting in a saturated ester linkage.

The structural OH stretching vibration (3646 cm^{-1}) of the MMT was not very visible in the nanocomposite possibly because of the presence of hydrogen bonded OH groups from the lignocellulose. FTIR showed that the preparation of PMAA-grafted lignocellulose-montmorillonite clay nanocomposite was successful.
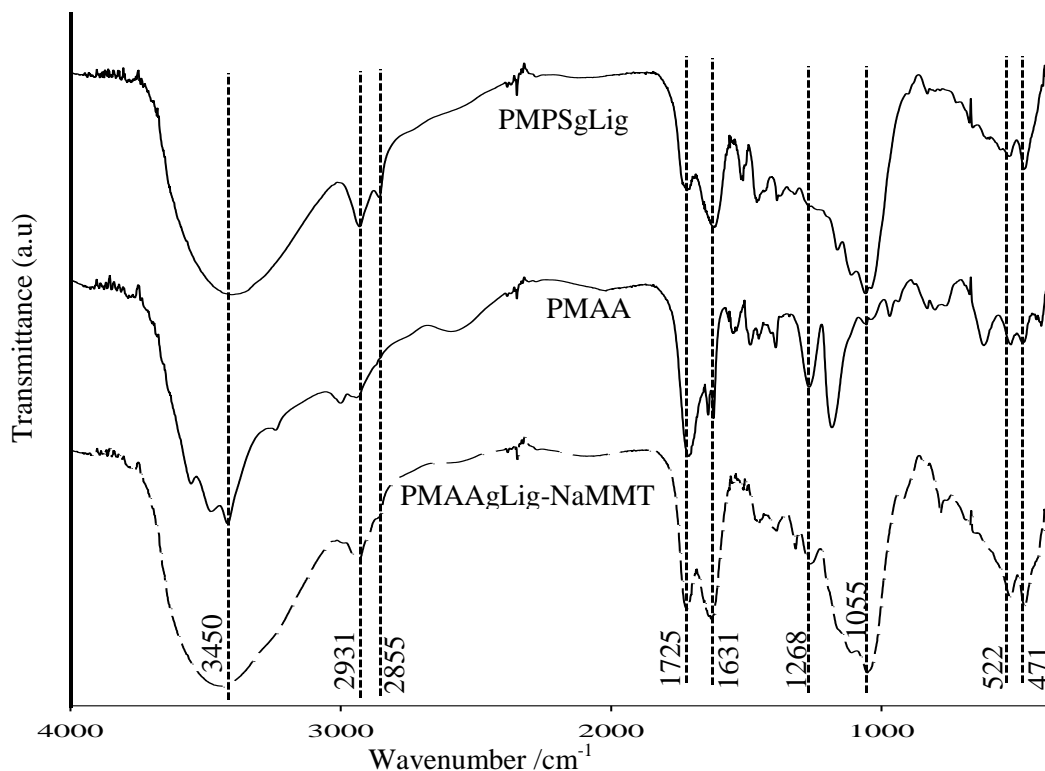
Figure 5.22: FTIR spectra of PMAA, PMPSgLig and PMAAgLig-NaMMT nanocomposite.

5.6.8.3 Thermogravimetric analysis of PMAAgLig-NaMMT

The nanocomposites were further analysed by TGA. Figure 5.23 displays the thermograms of PMPSgMMT, PMPSgLig and PMAA-grafted lignocellulose-montmorillonite clay nanocomposite. The thermograms of PMPSgMMT and PMPSgLig were included for comparison purposes.

The % mass loss for PMAA-grafted lignocellulose-montmorillonite nanocomposite was intermediate relative to that of PMPSgMMT and PMPSgLig. Three decomposition steps could be observed at temperatures: 30-120 °C, 220-420 °C and 420-650 °C. The decomposition steps corresponded to: loss of water, decomposition of lignocellulose together with the grafted polymers to form char and decomposition of the solid residue (char), respectively. A greater thermal stability was recorded for the nanocomposite compared to the PMPSgLig. The higher thermal stability shown by the nanocomposite can be attributed to the presence of NaMMT dispersed in the lignocellulose matrix.

159
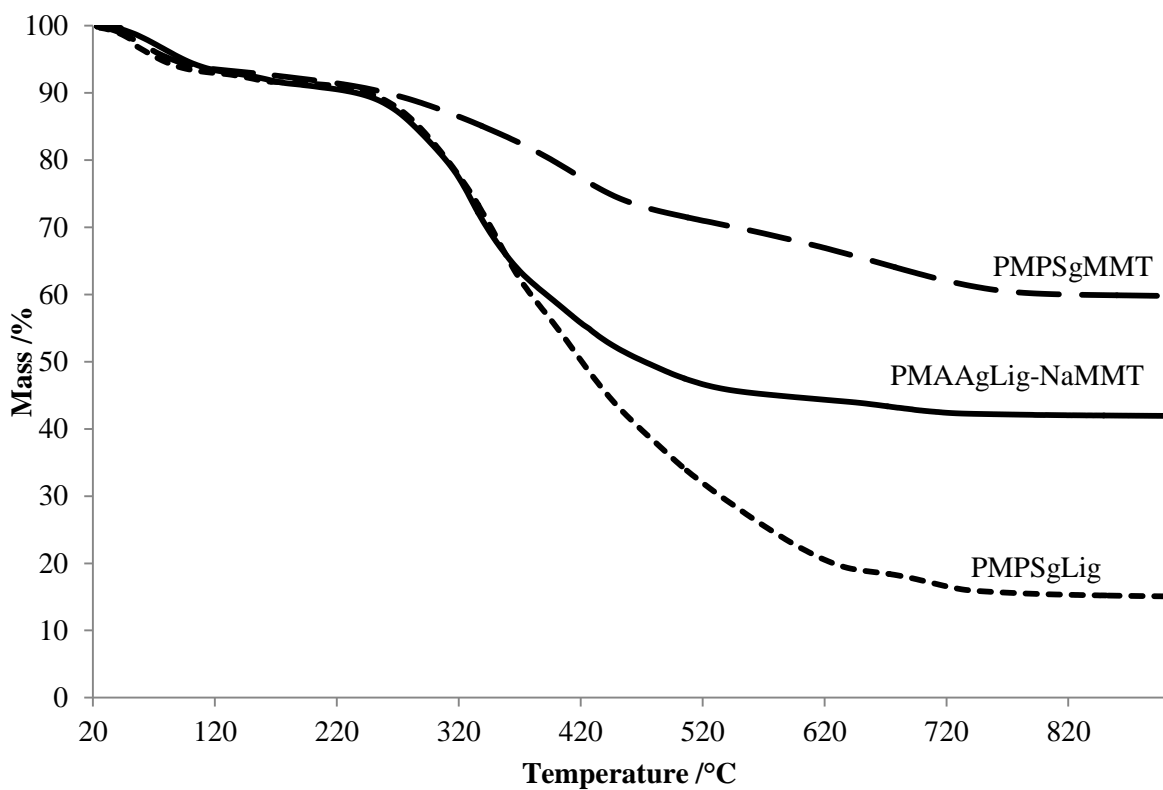
Figure 5.23: TGA thermograms of PMPSgMMT, PMPSgLig and PMAAgLig-NaMMT nanocomposite.

5.6.8.4 X-ray diffraction analysis

The X-ray diffractograms of NaMMT and PMAAgLig-NaMMT nanocomposite are displayed in Figure 5.24. A slight shift of the basal reflection peak to lower 2θ angles (an increase in the d-spacing) was observed. This observation was more or less similar to what was discussed above for PMMAgLig-NaMMT.
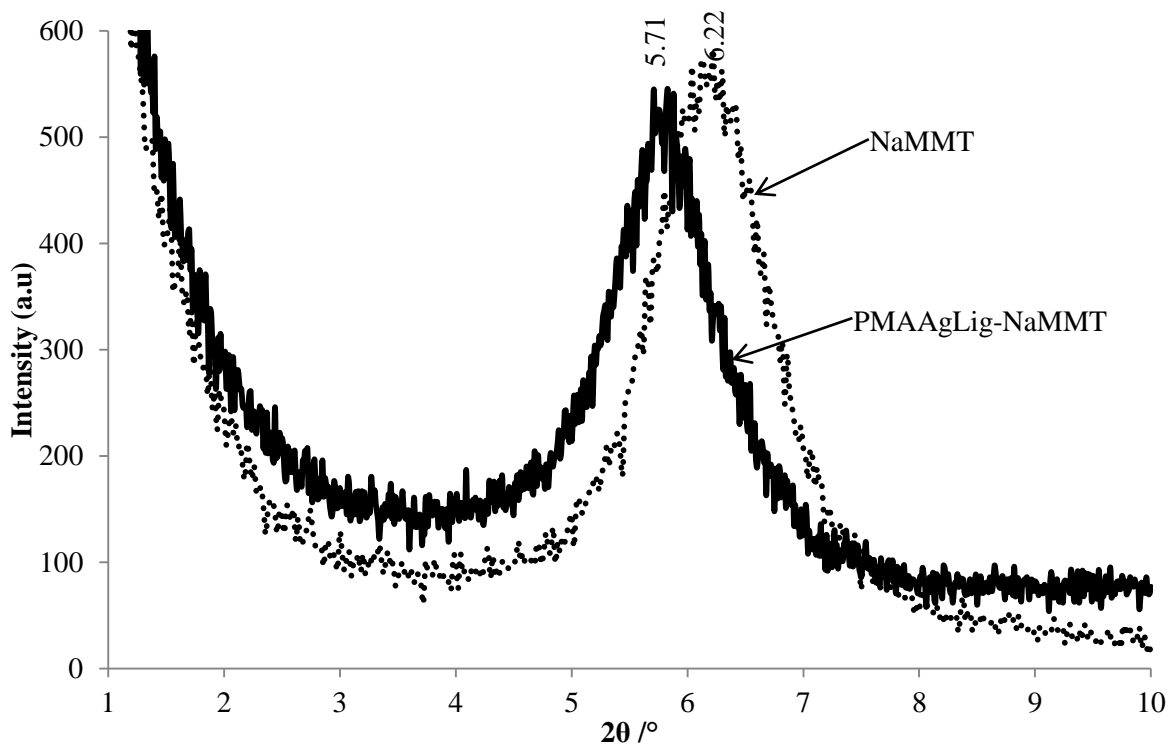
Figure 5.24: XRD patterns of NaMMT and PMAAgLig-NaMMT.

5.6.8.5 Transmission electron microscopy of PMAAgLig-NaMMT

Figure 5.25 shows the TEM micrograph of PMAAgLig-NaMMT nanocomposite. The micrograph showed the NaMMT still fairly ordered within the lignocellulose matrix. The PMAAgLig-NaMMT morphology was comparable with that of PMMAgLig-NaMMT discussed above. However, relatively poor clay dispersion was observed for the PMAAgLig-NaMMT nanocomposite.
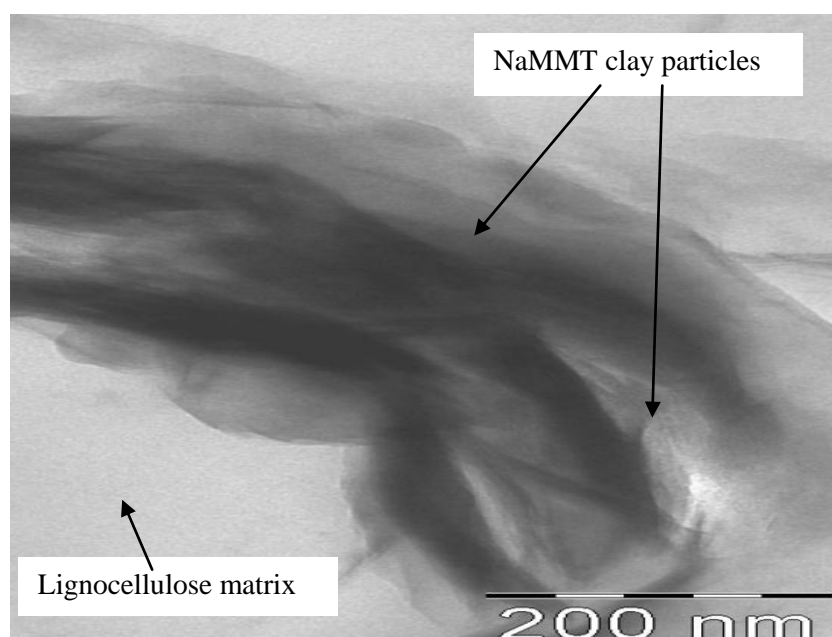
Figure 5.25: Transmission electron micrograph of PMAAgLig-NaMMT nanocomposite.

161

The TEM results confirm the observations made from the XRD results which also showed a highly ordered, partially intercalated clay structure in the nanocomposite. It can also be seen that the clay particles displayed some long-range order, indicating the presence of strong van der Waals forces between the clay sheets.

5.6.9 Methacryloxypropyl trimethoxy silane-coupled lignocellulose-montmorillonite nanocomposites

5.6.9.1 Suggested mechanism for the coupling of lignocellulose to NaMMT with MPS

The following schematic shows the proposed mechanism for the formation of MPS-grafted lignocellulose-montmorillonite nanocomposite. The MPS is shown as the already hydrolysed silanol species which undergoes a condensation reaction with the OH groups on both the lignocellulose and the NaMMT. The carbonyl (C=O) and alkene (C=C) groups would act as possible π-π adsorption sites for organic pollutants such as chlorophenols, benzenes and dyes like methyl orange.

MPS grafted lignocellulose/MMT nanocomposite
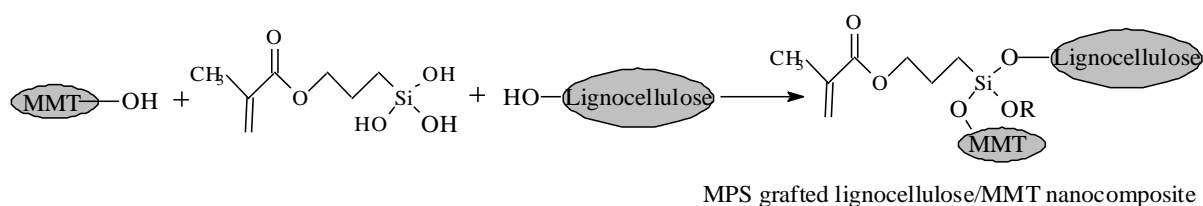
Scheme 5.6: Coupling of lignocellulose and NaMMT through MPS.

5.6.9.2 FTIR analysis of PMPSgLig-NaMMT

Figure 5.26 below shows the FTIR spectra of PMPS and PMPS-grafted lignocellulose-NaMMT nanocomposite. The C=C stretching vibration peak of the nanocomposite was superimposed over that of the H-O-H bending vibration (1635 cm^{-1}) of adsorbed water molecules. The peaks at 2960 and 2930 cm^{-1} in the nanocomposite were ascribed to methylene –CH$_2$- asymmetric and symmetric stretching vibrations, respectively. The other bands present in the two spectra have been discussed in Sections 5.6.2.2 and 5.6.5.1. The presence of the band at 1724 cm^{-1} (C=O stretching vibration of the ester group) in the nanocomposite after soxhlet extraction with THF showed that the grafting and/or coupling of lignocellulose and NaMMT was successful.

162
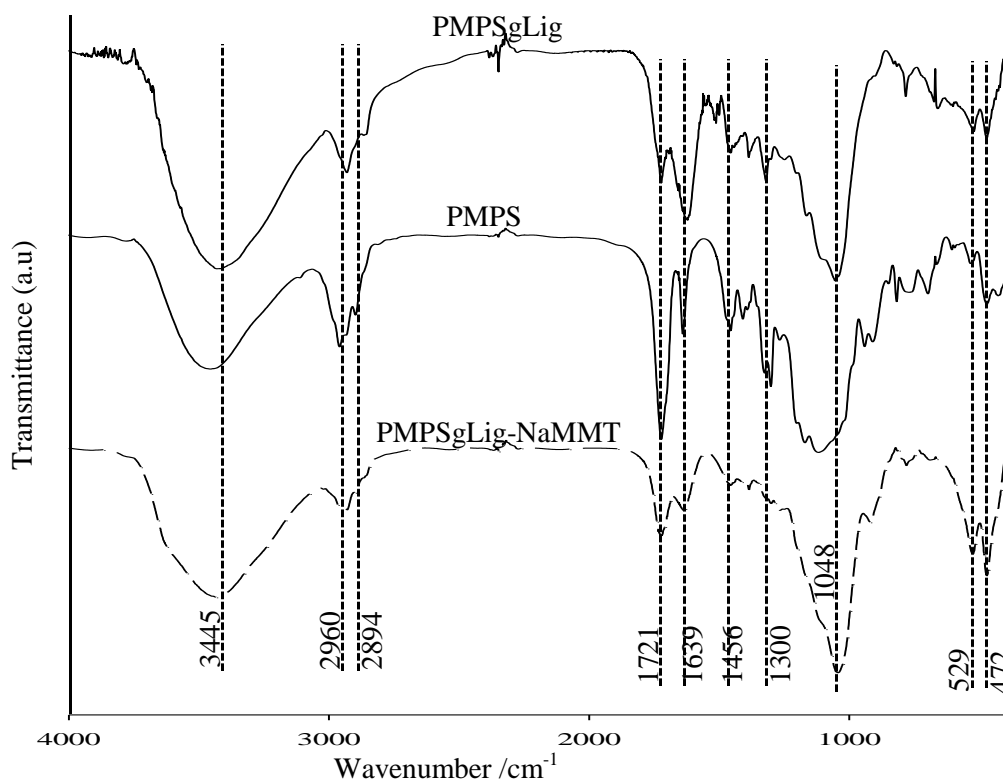
Figure 5.26: FTIR spectra of PMPS and PMPSgLig-NaMMT nanocomposite.

The nanocomposite was further characterised by TGA and the results are presented in the next section.

5.6.9.3 Thermogravimetric analysis of PMPSgLig-NaMMT

The TGA thermograms of NaMMT, raw lignocellulose and PMPS-grafted lignocellulose-montmorillonite nanocomposite are shown in Figure 5.27. It was observed that the nanocomposite was more thermally stable compared with the raw lignocellulose, but less stable relative to the NaMMT. The nanocomposite showed a degradation temperature of 425 °C compared with 343 °C for the lignocellulose. The increased thermal stability can be attributed to the presence of NaMMT in the lignocellulose matrix. The TGA thermogram and the FTIR spectrum of the MPS-grafted lignocellulose-montmorillonite nanocomposite show that NaMMT was incorporated into the lignocellulose matrix. It was observed that more residue was recorded for NaMMT followed by PMPSgLig-NaMMT nanocomposite and the least amount of residue was recorded for lignocellulose. This further demonstrates the relative thermal stabilities of the respective samples.
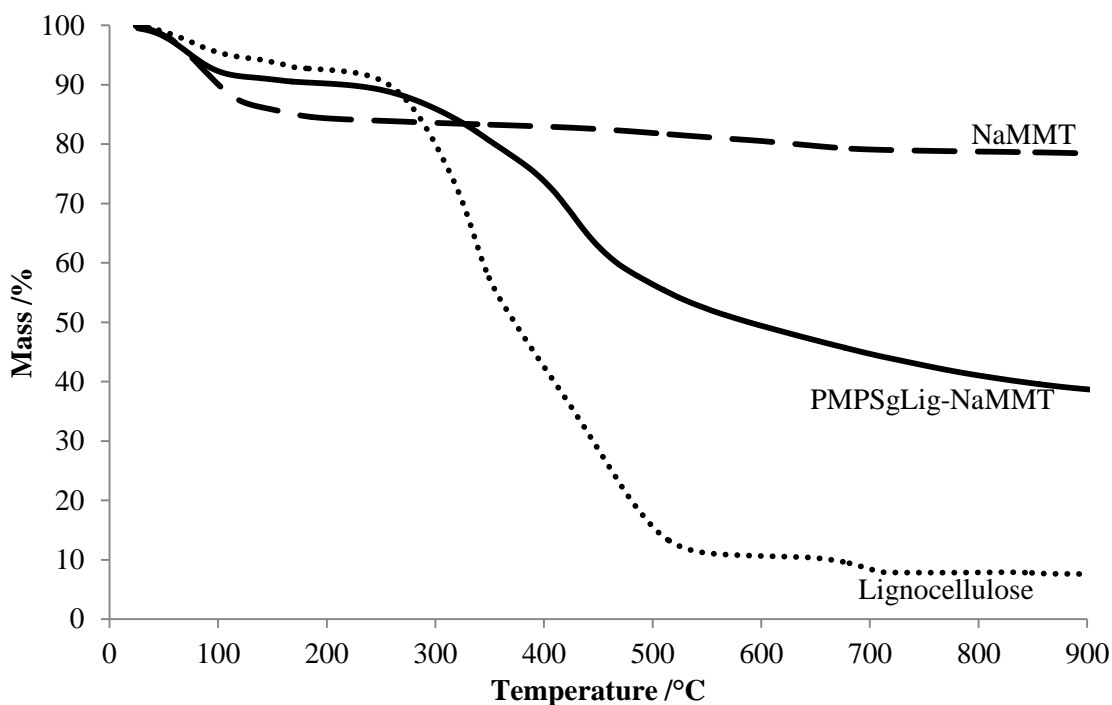
Figure 5.27: Thermograms of raw lignocellulose, NaMMT and PMPS-grafted lignocellulose-montmorillonite nanocomposite.

5.6.9.4 X-ray powder diffraction analysis PMPSgLig-NaMMT

Figure 5.28 displays the XRD patterns of NaMMT and PMPSgLig-NaMMT nanocomposite. There was a slight shift in the montmorillonite basal reflection peak towards lower 2θ angles for the PMPS-grafted nanocomposite.
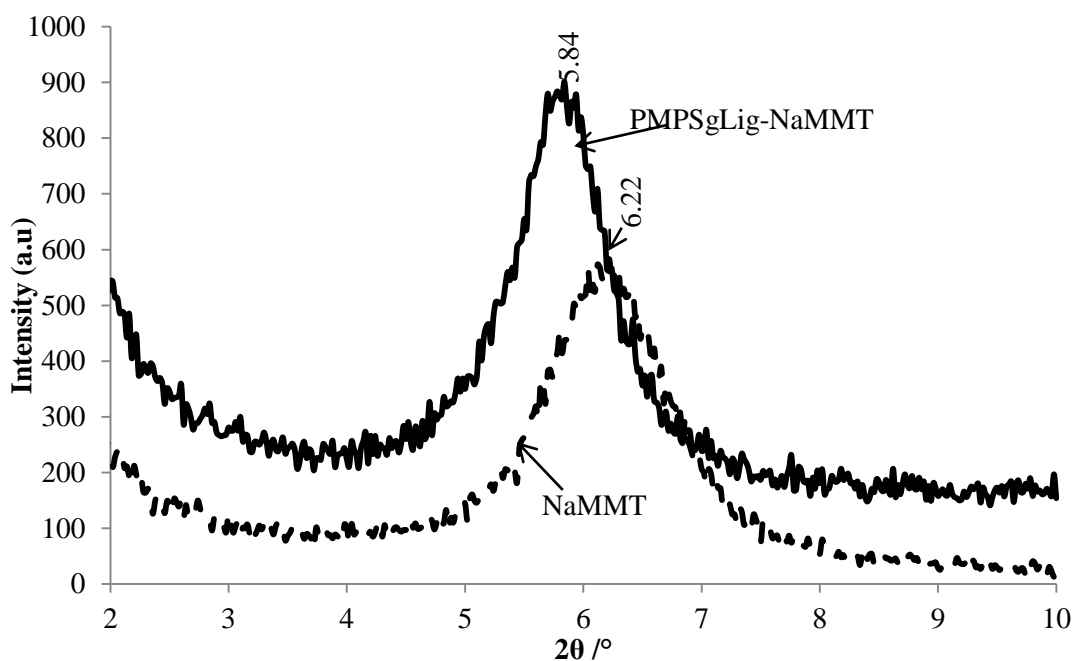
Figure 5.28: XRD patterns of NaMMT and PMPSgLig-NaMMT nanocomposite.

164

This shift might be as a result of partial intercalation and polymerization of the MPS in the interlayer galleries of the NaMMT. The d-spacing increased from 14.20 Å (NaMMT) to 15.12 Å for the nanocomposite. The XRD patterns show that the NaMMT clay sheets are still quite ordered in the nanocomposite as judged from the intensity of the basal reflection peak as well as the d-spacing. This might suggest an intercalated nanocomposite or a microcomposite (phase-separated).

5.6.9.5 Transmission electron microscopy of PMPSgLig-NaMMT

The nanocomposite was further analysed by transmission electron microscopy and Figure 5.29 displays the micrograph obtained. The micrograph of PMPSgLig-NaMMT (Figure 5.29) shows some clay aggregates, as well as nanometer-sized clay particles dispersed in the lignocellulose matrix. This might suggest that the dispersion of the clay particles was not homogeneous, thus giving a phase-separated composite.
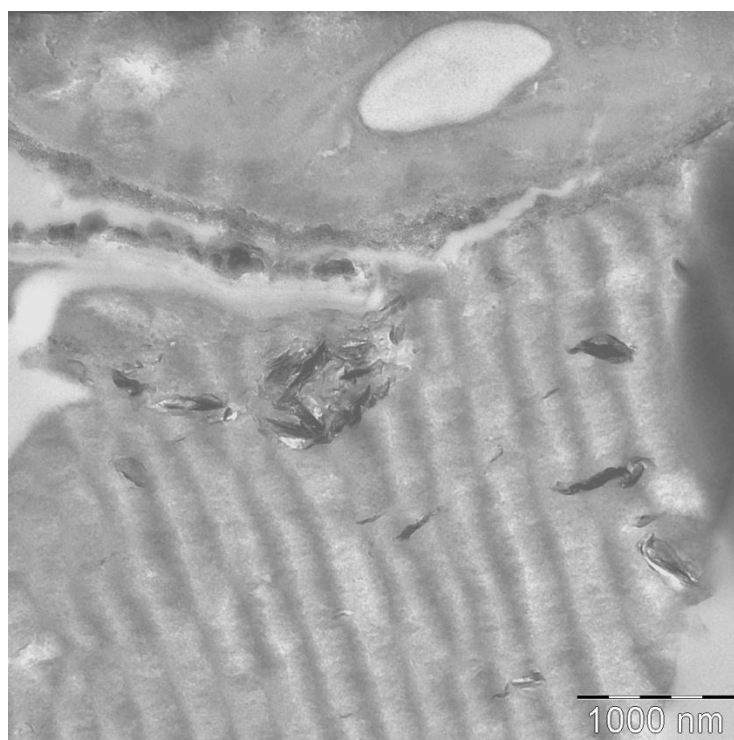
Figure 5.29: Transmission electron micrograph of PMPSgLig-NaMMT nanocomposite.

5.7 Conclusion

Novel adsorbent materials (PMMAgLig-MMT nanocomposite, PMAAgMMT, PMAAgLig, PMPSgLig-MMT and PMAAgLig-MMT nanocomposite) were prepared through condensation as well as free-radical graft polymerization reactions. The intended modification of the lignocellulose and MMT separately was achieved as confirmed by FTIR, TGA and XRD. XRD showed some partial intercalation of MMA into the interlayer space of the clay sheets. The same can be said for the

nanocomposite adsorbents, which also showed a slight increase in the basal spacing of the MMT clay sheets. Intercalated nanocomposite adsorbent materials were successfully prepared as shown by FTIR, TGA and XRD. Modification of lignocellulose with MPS resulted in improved thermal stability. All the nanocomposites prepared also showed an increase in thermal stability, which was attributed to the presence of clay in the lignocellulose matrix. However, modification of lignocellulose with PMMA resulted in a slight reduction in thermal stability.

5.8 References

1. An, F.; Feng, X.; Gao, B. Adsorption property and mechanism of composite adsorbent PMAA/SiO$_2$ for aniline. *Journal of Hazardous Materials*, **2010**, *178*, 499–504.

2. An, F.; Gao, B.; Feng, X. Adsorption mechanism and property of novel composite material PMAA/SiO$_2$ towards phenol. *Chemical Engineering Journal*, **2009**, *153*, 108–113.

3. Atai, M.; Solhi, L.; Nodehi, A.; Mirabedini, S. M.; Kasraei, S.; Akbari, K.; Babanzadeh, S. PMMA-grafted nanoclay as novel filler for dental adhesives. *Dental Materials*, **2009**, *25*, 339–347.

4. Binithat, N. N.; Sugunan, S. Preparation and characterisation and catalytic activity of titania-pillared montmorillonite clays. *Microporous and Mesoporous Materials*, **2006**, *93*, 82-89.

5. Castellano, M.; Gandini, A.; Fabbri, P.; Belgacem, M. N.; Modification of cellulose fibres with organosilanes: Under what conditions does coupling occur? *Journal of Colloid and Interface Science*, **2004**, *273*, 505–511.

6. Costa, R. O. R.; Vasconcelos, W. L. Structural modification of poly(2-hydroxyethylmethacrylate)–silica hybrids utilizing 3-methacryloxypropyltrimethoxysilane. *Journal of Non-Crystalline Solids*, **2002**, *304*, 84–91.

7. Dong, J.; Ozaki, Y.; Nakashima, K. FTIR studies of conformational energies of poly (acrylic acid) in cast films. *John Wiley & Sons, Inc.*, **1997**, pp. 507-515, CCC 0887-6266/97/030507-09.

8. Erhardt, R.; Zhang, M.; Böker, A.; Zettl, H.; Abetz, C.; Frederik, P.; Krausch, G.; Abetz, V.; Müller, A. H. E. Amphiphilic janus micelles with polystyrene and poly(methacrylic acid) hemispheres. *Journal of American Chemical Society*, **2003**, *125*, 3260-3267.

9. Gangopadhyay, R.; Ghosh, P. Uncatalysed photografting of poly (methyl methacylate) from photofunctionalised sisal fibre. *European Polymer Journal*, **2000**, *36*, 1597-1606.

10. Günzler, H.; Gremlich, H. U. IR Spectroscopy: An introduction. *Wiley-VCH Verlag GmbH, 69469 Weinheim, Germany*, **2002**, 171-229.

11. Hill, C. A. S.; Cetin, N. S. Surface activation of wood for graft polymerisation. *International Journal of Adhesion and Adhesives*, **2000**, *20*, 71-76.

12. Kurt, A.; Demirelli, K. Thermal degradation of block copolymers of ethyl methacrylate with styrene synthesized by atom transfer radical polymerization method. *Turkish Journal of Science & Technology*, **2009**, *4* (1), 65-72.

13. Liu, P. Polymer modified clay minerals: A review. *Applied Clay Science*, **2007**, *38*, 64–76.

14. McNeill, I. C.; Ahmed, S.; Memetea, L. Thermal degradation of vinyl acetatemethacrylic acid copolymer and homopolymers: An FTIR spectroscopic investigation of structural changes in the degrading material. *Polymer Degradation and Stability*, **1995**, *47*, 423-433.

15. Ojah, R.; Dolui, S. K. Graft polymerization of methyl methacrylate onto *Bombyx mori* initiated by semiconductor-based catalyst. *Bioresource Technology*, **2006**, *97*, 1529-1535.

16. Piscitelli, F.; Posocco, P.; Toth, R.; Fermeglia, M.; Pricl, S.; Mensitieri, G.; Lavorgna, M. Sodium montmorillonite silylation: unexpected effect of the aminosilane chain length. *Journal of Colloid and Interface Science*, **2010,** *351*, 108–115.

17. Polacco, G.; Cascone, M. G.; Petarca, L.; Peretti, A. Thermal behaviour of poly (methacrylic acid)/poly(N-vinyl-2-pyrrolidone) complexes. *European Polymer Journal*, **2000**, *36*, 2541-2544.

18. Rajendran. S.; Kannan, R.; Mahendran, O. An electrochemical investigation on PMMA/PVdF blend-based polymer electrolytes. *Materials Letters*, **2001**, *49*, 172–179.

19. Román-Aguirre, M.; Márquez-Lucero, A.; Zaragoza-Contreras, E. A. Elucidating the graft copolymerization of methyl methacrylate onto wood-fiber. *Carbohydrate Polymers,* **2004**, *55*, 201-210.

20. Singhal, R.; Datta, M. Development of nanocomposites of bentonitewith polyaniline and poly (methacrylic acid). *Journal of Applied Polymer Science*, **2007**, *103*, 3299–3306.

21. Tang, E.; Cheng, G.; Ma, X.; Pang, X.; Zhao, Q. Surface modification of zinc oxide nanoparticle by PMAA and its dispersion in aqueous system. *Applied Surface Science*, **2006**, *252*, 5227–5232.

22. Tiwari, A.; Nema, A. K.; Das, C. K.; Nema, S. K. Thermal analysis of polysiloxanes, aromatic polyimide and their blends. *Thermochimica Acta*, **2004**, *417*, 133–142.

23. Tong, M.; Yu, J.; Sun, X.; Li, B. Polymer modified biomass of baker's yeast for treating simulated wastewater containing nickel and lead. *Polymers for Advanced Technologies*, **2007**, *18*, 829–834.

24. Wang, L.; Dong, W.; Xu, Y. Synthesis and characterization of hydroxypropyl methylcellulose and ethyl acrylate graft copolymers. *Carbohydrate Polymers*, **2007**, *68*, 626–636.

25. Wang, W. Chelating adsorption properties of Cd (II) on the PMAA/SiO$_2$. *Process Safety and Environmental Protection*, **2011**, *89* (2), 127–132.

26. Yuan, P.; He, H.; Bergaya, F. A.; Wu, D.; Zhou, Q.; Zhu, J. Synthesis and characterization of delaminated iron-pillared clay with meso–microporous structure. *Microporous and Mesoporous Materials*, **2006**, *88*, 8–15.

Chapter 6

Adsorption of heavy metals (Cd^{2+} and Pb^{2+}) onto the polymer-grafted lignocellulose-montmorillonite adsorbents

6.0 Introduction

The previous three chapters have dealt with the preparation and characterization of the adsorbent materials (modified lignocellulose, modified montmorillonite and the polymer-grafted nanocomposites) evaluated in this study. This chapter details the procedures used in the evaluation of the adsorbent materials. The results obtained from the adsorption experiments are presented together with a discussion, and a conclusion.

The prepared materials were evaluated for their adsorption properties using synthetic solutions of heavy metals and organic compounds as pollutants. The heavy metals used in the evaluation are lead (Pb^{2+}) and cadmium (Cd^{2+}) and the organic pollutants are methyl orange and neutral red.

The samples evaluated in the adsorption studies are: sodium-exchanged montmorillonite (NaMMT), aluminum-pillared montmorillonite (AlpMMT), poly (methyl methacrylate)-grafted montmorillonite (PMMAgMMT), poly (methyacrylic acid)-grafted montmorillonite (PMAAgMMT), methacryloxypropyl trimethoxysilane-grafted montmorillonite (PMPSgMMT), lignocellulose, poly (methyl methacrylate)-grafted lignocellulose (PMMAgLig), poly (methacrylic acid)-grafted lignocellulose (PMAAgLig), methacryloxypropyl trimethoxysilane-grafted lignocellulose (PMPSgLig), PMMA-grafted lignocellulose-montmorillonite (PMMAgLig-NaMMT), PMAA-grafted lignocellulose-montmorillonite (PMAAgLig-NaMMT) and PMPS-grafted lignocellulose-montmorillonite (PMPSgLig-NaMMT) nanocomposites.

The adsorption experiments were carried out so as to generate adsorption isotherms and adsorption kinetics data. The adsorption capacity of each adsorbent was computed from adsorption isotherms and the kinetic models.

6.1 Batch adsorption experiments

All adsorption experiments were carried out in 250 mL conical flasks by agitating a given dose of each adsorbent in the synthetic solution of each model pollutant in deionized water. A mass of 0.10 g

of adsorbent was dispersed in 80 mL of the synthetic solution at 25 °C. The mixtures were placed on a rotary shaker and agitated at 200 rpm for six hours. Aliquots of sample solutions were withdrawn at set time intervals. The adsorbent was separated by filtering through Acrodisc syringe filters (0.45 µm Supor Membrane) of low protein binding, and the concentration of each heavy metal ion in the filtrate determined by atomic absorption spectroscopy (AAS). All assays were carried out in triplicate and the average values taken. A Thermo Scientific iCE 3000 Series AA Spectrometer was used for the determination of the concentrations of Cd (II) and Pb (II) in the test solutions.

6.1.1 Adsorption isotherms

The conditions used to generate adsorption isotherms were as follows: adsorbent dosage was 1.25 g adsorbent per litre of solution; metal ion concentration ranges were 10 to 50 ppm for both Cd^{2+} and Pb^{2+}; the pH was 5.0 for all the adsorption experiments; the shaking time was 6 h. Aliquots were taken after six hours for measurement with AAS. The adsorption isotherm studies were carried out separately for each heavy metal ion. In order to get the concentration of Cd^{2+} in the samples within the calibration range of 2 to 10 ppm, it was necessary to dilute the sample 10-fold. The adsorption experiments were carried out a temperature of 25 °C.

6.1.2 Adsorption kinetics

In order to assess the rate of the adsorption for both Cd^{2+} and Pb^{2+}, experiments were carried out under the following conditions: amount of adsorbent used was 1.25 g per 1.0 L of solution; the initial metal concentration for both Cd^{2+} and Pb^{2+} was 50 ppm; the pH was 5.0 and the shaking time was six hours. Aliquots of sample solutions were withdrawn at set time intervals and the concentration of each heavy metal was determined by AAS. The adsorption kinetic studies were carried out separately for each heavy metal ion. The temperature of the mixtures was maintained at 25 °C.

6.1.3 Effect of OH/Al molar ratio on the adsorption of Cd^{2+} and Pb^{2+}

This section is concerned with aluminium-pillared montmorillonite (AlpMMT). This type of clay has been widely reported, and is promoted as a potentially effective and efficient adsorbent (Altunlu, M. et al, 2007). However, there is no published study of the effect of the OH/Al molar ratio on the adsorption of heavy metals onto AlpMMT. As presented in Section 4.2.3, AlpMMT samples were prepared at different OH/Al molar ratios, and the samples were evaluated for their adsorption properties in relation to the ratios.

To assess the effect of OH/Al molar ratio on the extent of heavy metals adsorption, about 0.1 g of AlpMMT of different OH/Al molar ratios was added to a 250 mL conical flask. A volume of 80 mL of either Cd (II) or Pb (II) solution (10 ppm) was added and the mixture placed on a rotary shaker for

six hours at 25 °C and a pH of 5.0. After six hours, the mixture was filtered through Acrodisc syringe filters (0.45 μm Supor Membrane) of low protein binding. The concentration of heavy metals in the filtrate was determined by AAS.

6.1.4 Competitive adsorption studies of Cd^{2+} and Pb^{2+}

In most cases, waste water contains a lot of other pollutants and the presence of other pollutants will affect the uptake or removal of a specific pollutant through adsorption. Waste waters from the different industries may also contain more than one metal ion (it is usually a mixture of a number of metal ions together with organic dyes or solvents). This section outlines and assesses the influence of the presence of Cd^{2+} (in a synthetic solution) on the adsorption of Pb^{2+} from aqueous solution. Selected adsorbents were used to assess the competitive adsorption of Cd^{2+} and Pb^{2+} from aqueous solution.

Synthetic solutions containing a mixture of Cd^{2+} and Pb^{2+} with concentrations of each metal ion ranging from 10 to 50 ppm were prepared. The adsorption experiments were carried out as already described in Sections 6.1.1 and 6.1.2 where 80 mL of the synthetic solutions were added to 0.10 g of adsorbent in 250 mL conical flasks. The mixtures were placed on a rotary shaker and left to agitate for six hours. Sample aliquots were withdrawn at set time intervals and analysed by AAS. For the analysis of Cd^{2+}, the samples had to be diluted 10-fold.

Adsorption isotherms and adsorption kinetics data were generated as described in Sections 6.1.1 and 6.1.2 for each heavy metal ion in the mixture. The data were processed accordingly. The temperature was kept at 25 °C and the pH of the mixtures was 5.0.

6.1.5 Determination of concentration of heavy metals in solution by atomic absorption spectroscopy

The AAS instrument was operated under the following conditions: flame – air/acetylene, background correction – deuterium lamp, bandpass – 0.5 nm, burner height – 7.0 mm, fuel flow – 1.2 mL/min. The heavy metals were determined at the following wavelengths: Cd^{2+} (228.8 nm) and Pb^{2+} (217.0 nm).

The determination of heavy metal ions in solution before and after adsorption was carried out by using the external standard calibration method. Calibration curves were generated for each metal ion and the concentrations of the calibration standards ranged from 10 to 50 ppm for Pb^{2+} and 2 to 10 ppm for Cd^{2+}. The instrument was calibrated first before each analysis. The initial concentrations of the test solutions were determined. Before analysis with AAS, the solutions were filtered through Acrodisc

syringe filters (0.45 µm Supor Membrane) of low protein binding to remove solid particles. The adsorption data was processed or analysed according to the procedure presented in Section 6.2.

6.2 Analysis of adsorption data

The data generated from the experiments detailed in Section 6.1 were analysed in order to get the adsorbed amount of heavy metals which is presented in Section 6.2.1. The data were fitted to different models depending on whether one was dealing with adsorption isotherms or kinetics. The same data analysis procedure was applied to all the pollutants assessed in this study.

6.2.1 Calculation of the adsorbed amount of solute (Cd^{2+} and Pb^{2+})

The data obtained from the adsorption experiments as described in the Sections 6.1.1 to 6.1.5 were processed as detailed in this section. The adsorbed amount of Cd (II) and Pb (II) was computed using Equation 6.1 (Musapatika, E. T. et al, 2010).

$$Q_t = \frac{(C_0 - C_t) \times V}{m} \tag{6.1}$$

where Q_t is the adsorbed amount of heavy metal ions at time t; C_0 is the initial concentration of heavy metal ions; C_t is the concentration of heavy metal ions in solution at time t; m is the mass of adsorbent and V is the volume of heavy metal ions solution used in L. The results reported in this study are the averages of at least two replicates.

6.2.2 Adsorption isotherms

An adsorption isotherm is a curve describing the retention of a substance (at various concentrations) on a solid at constant temperature, and is an important tool used to describe and predict the mobility of pollutants in the environment. Adsorption isotherms are useful for describing the adsorption capacity to facilitate evaluation of the feasibility of a process for a given application, for selection of the most appropriate sorbent and for preliminary determination of sorbent dosage requirements. The isotherm also plays an important role in the predictive modeling procedures for analysis and design of sorption systems (Kumar, U. et al, 2006).

Giles, C. H. et al, 1960 proposed a system for the classification of adsorption isotherms. Adsorption isotherms are classified into four major classes based on the slope of the initial portion of the curve of the equilibrium adsorbed amount (Q_e, mg/g) versus equilibrium adsorbate concentration (C_e, mg/L) and thereafter into subgroups. Q_e can be calculated according to Equation 6.1. The classification

system proposed by Giles, C. H. et al, 1960 was further explained by Hinz, C., 2001 and the different classes of the adsorption isotherms according to Giles and Hinz are shown in Figure 6.1. This was one of the methods used in the analysis of adsorption data in this study.
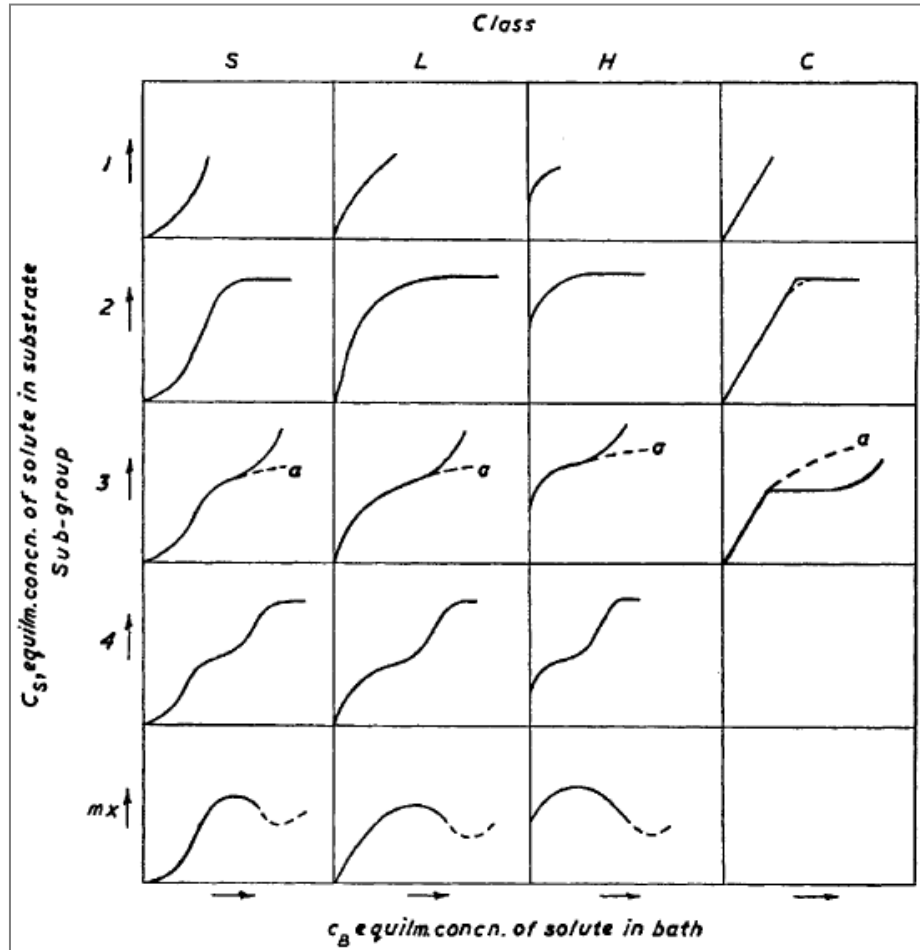
Figure 6.1: System of isotherm classification (Giles, C. H. et al, 1960).

The four major classes shown in Figure 6.1 are: *S*-shaped curve, *L*-shaped (Langmuir type), *H*-type (high affinity) and *C*-type (constant partition). The relevant isotherm types are discussed in Section 6.3.

The second method also commonly used in the processing of adsorption data is the use of adsorption isotherm models or equations. The method of visual inspection of isotherms as proposed by Giles, C. H. et al, 1960 and described above complements the use of isotherm models. The adsorption data were also fitted to the two commonly used adsorption equations, the Langmuir and the Freundlich models.

6.2.2.1 Langmuir model

The linear Langmuir equation is normally expressed as follows:

Langmuir equation:
$$\frac{C_e}{Q_e} = \frac{1}{Q_0 . b} + \frac{C_e}{Q_0} \qquad (6.2)$$

where C_e is the equilibrium amount of adsorbate in solution (mg/L); Q_e is the equilibrium adsorbed amount of adsorbate per unit mass of adsorbent (mg/g); Q_0 (mg/g) and b (L/mg) are the Langmuir constants related to the adsorption capacity (mg/g) and the rate of adsorption, respectively [Kumar, D. et al, 2008]. A plot of C_e/Q_e against C_e should give a straight line if the adsorption data conform to the Langmuir isotherm.

The Langmuir adsorption model assumes that the solid adsorbent has a limited adsorption capacity (a fixed number of adsorption sites), all adsorption sites are identical, each site retains one molecule of the given species and that all sites are energetically and sterically independent of the adsorbed amount (Limousin, G. et al, 2007).

The second model considered and applied in the analysis of data in this study is the Freundlich model.

6.2.2.2 Freundlich model

The Freundlich model describes multilayer adsorption onto heterogeneous surfaces (Annadurai, G. et al, 2002) as opposed to monolayer adsorption onto homogeneous surfaces according to the Langmuir model. It can be viewed as an extension of the Langmuir model in that it assumes uptake of solute onto different classes of adsorption sites on a solid, with the adsorption on each class of adsorption sites following the Langmuir isotherm. The empirical form of the Freundlich equation is given by

$$Q = K_f C^n \qquad (6.3)$$

Q (mg/g) is the adsorbed amount; C (mg/L) the remaining solute concentration and K_f (L kg^{-1}) and n (dimensionless) are constants. The linearised form of the Freundlich equation is normally expressed as follows:

$$log\ Q_e = log\ K_f + \frac{1}{n} log\ C_e \qquad (6.4)$$

where Q_e is the equilibrium adsorbed amount (mg/g); C_e is the equilibrium concentration of the adsorbate (mg/L); K_f and n are the Freundlich constants related to the adsorption capacity and the rate of adsorption respectively (Namane, A. et al, 2005; Rawajfih, Z. et al, 2006; Kumar, D. et al, 2008;

Wang, S. et al, 2009; Kul, A. R. et al, 2010). The units of K_f are mg.g^{-1}(Lmg^{-1})^n. A plot of Log Qe against Log Ce should yield a straight line if the adsorption data conform to the Freundlich model. K_f and n can be determined from the intercept and the slope (n>1), respectively (Limousine, G. et al, 2007).

According to Rawajfih, Z. et al, 2006, a high value of n (>1) means that adsorption is good over the entire concentration range studied while a small value of n (<1) indicates that adsorption is good at high concentrations and poor at low solute concentrations. The uptake of the heavy metals was also monitored with time to generate kinetics data.

6.2.3 Adsorption kinetics

Chemical kinetics studies are closely related to the development of an understanding of reaction mechanisms (Laidler, K. J., 1987). The study of sorption kinetics in waste water treatment provides an insight into the reaction pathways and the mechanism of the sorption process. Such information is necessary in the design of appropriate sorption water treatment plants. The prediction of sorption kinetics is also necessary for the design of industrial sorption columns. Ho, Y. S. et al, 1999 carried out a literature review on three sorption kinetic models for the adsorption of organics or heavy metals onto biosorbents. The investigators reported that the highest correlation coefficients for many sorption systems were observed for the pseudo second-order model compared with the pseudo first-order correlation coefficients.

The experimental adsorption data were fitted to the two commonly used adsorption kinetic models: the pseudo first-order and pseudo second-order models.

6.2.3.1 Pseudo first-order kinetics model

The Lagergren linear pseudo first-order equation is generally expressed as follows:

$$Log\ (Q_e - Q_t) =\ Log\ Qe - \frac{k_1}{2.303}t \qquad (6.5)$$

where Q_e is the amount of solute adsorbed at equilibrium per unit mass of adsorbent (mg/g); Q_t is the amount of solute adsorbed (mg/g) at time t, and k_1 is the pseudo first-order rate constant in min^{-1}.

In order to fit experimental data to the pseudo first-order equation, the equilibrium sorption capacity, Q_e must be known. However, in many cases, Q_e is unknown because chemisorption tends to be immeasurably slow and the amount adsorbed is significantly smaller than the equilibrium amount (King, P. et al, 2007). In this study, Q_e was taken as the amount of solute adsorbed after 6 h. If the

pseudo first-order is the best fit for the adsorption data, a plot of *Log* (Q_e-Q_t) against time (*t*) should yield a straight line.

6.2.3.2 Pseudo second-order kinetics model

The pseudo second-order equation is written as:

$$\frac{t}{Q_t} = \frac{1}{k_2 Q_e^2} + \frac{t}{Q_e}$$

(6.6)

where Q_e is the amount of solute adsorbed at equilibrium per unit mass of adsorbent (mg/g); Q_t is the amount of solute adsorbed (mg/g) at time *t*; k_2 is the pseudo second-order rate constant with units of gmg^{-1}min^{-1}. If the linear pseudo second-order equation is applicable, a plot of *t/Q_t* versus time *t*, should give a straight line (Delval, F. et al, 2002; Kumar, K. V., 2006). The pseudo second-order model assumes chemisorption and can be used to describe the adsorption mechanism for the whole sorption process.

The following section presents the results obtained from the adsorption experiments whose procedure was detailed in Section 6.1 together with a discussion of the adsorption results.

6.3 Results and discussion

The first part of this section will discuss the results of the adsorbent materials prepared from the modification of NaMMT clay only. This will be followed by the adsorption results of the adsorbents based on lignocellulose and then the results of the polymer-grafted lignocellulose-montmorillonite nanocomposites will be presented. As mentioned in Section 6.2, the adsorption data were analysed and fitted to adsorption isotherms and kinetic models.

6.3.1 Adsorption of Pb^{2+} onto montmorillonite based adsorbents

6.3.1.1 Adsorption isotherms

According to Hinz, C., 2001 a Langmuir type adsorption model is when the initial part of the curve is concave (Figure 6.1), whereas when it is convex, that shows an *S*-shaped curve (multilayer adsorption). Figure 6.2 displays the isotherms for Pb^{2+} adsorption onto montmorillonite based adsorbents. The isotherms are labelled accordingly. It can be seen that all the isotherms show a concave shape at low concentrations (C$_e$, mg/L), showing conformity to the Langmuir adsorption model. The isotherms can all be classified as Langmuir type 2 (L$_2$). The isotherm for adsorption onto AlpMMT showed a clear plateau at higher Pb^{2+} concentrations (the adsorbent showed a limited adsorption capacity). It must be noted that the initial concentrations of solutions used for all the

adsorbents displayed in Figure 6.2 ranged from 10 to 50 ppm. Due to the different extent of adsorption of Pb^{2+} onto the adsorbents, different C_e values were recorded with AlpMMT showing the least uptake and the highest C_e values.
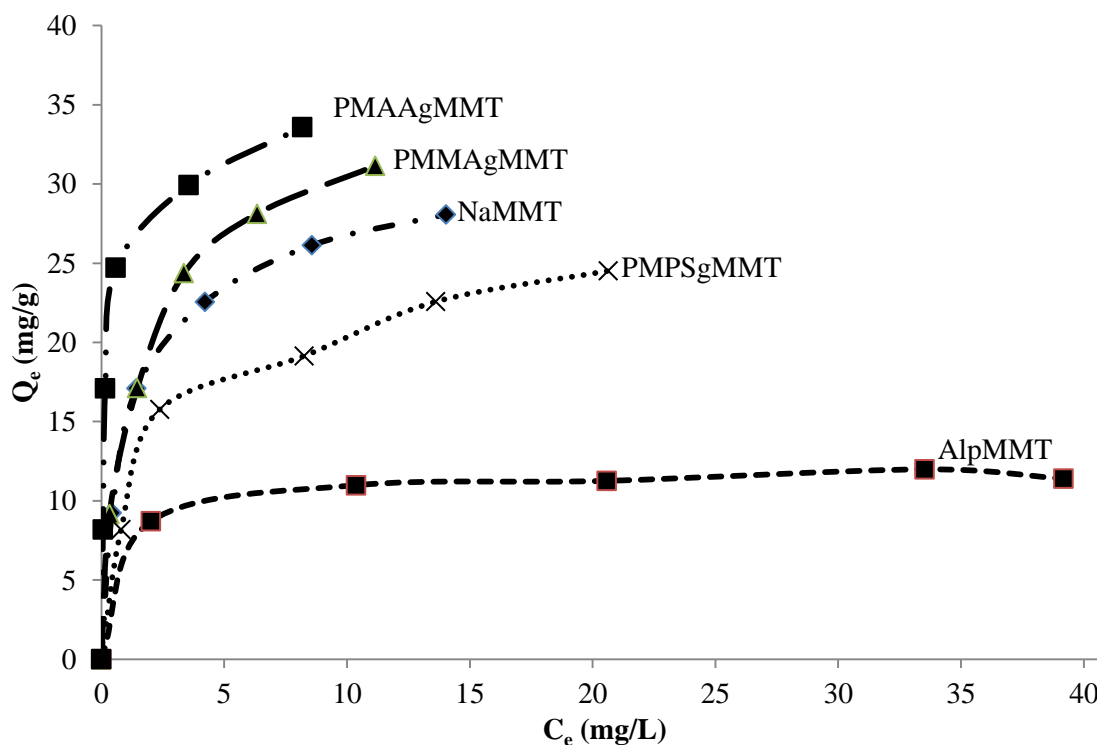
Figure 6.2: Isotherms for the adsorption of Pb^{2+} onto montmorillonite based adsorbents.

For the other adsorbents, it can also be seen that as the equilibrium concentration of Pb^{2+} increased, the isotherms approached a plateau, but did not show a pronounced plateau. The plateau was not that observed in these isotherms (PMAAgMMT, PMMAgMMT, NaMMT and PMPSgMMT) possibly because of a higher adsorption capacity (Limuosin, G. e al, 2007). The plateau length also indicates the orientation of the adsorbate. A less pronounced plateau shows that the exposed adsorbate surface can readily attract more solute and a more pronounced plateau that it tends to repel solute. The differences observed in the isotherms (and the scale) were a result of the different extents of adsorption onto each adsorbent. It can be seen from Figure 6.2 that PMAAgMMT had the highest adsorption capacity and AlpMMT had the least.

The initial curvature in all the isotherms showed that as more sites in the adsorbent were occupied, it became increasingly difficult for a colliding Pb^{2+} ion to find a vacant site available on the adsorbent surface (Giles, C. H. et al, 1960; Hinz, C., 2001; Okada, T., 2004). The type of curves obtained fit the Langmuir isotherm (Giles, C. H. et al, 1960; Hinz, C., 2001; Okada, T., 2004).

The experimental data were then fitted to the commonly used linear Langmuir and Freundlich equations as described in Sections 6.2.2.1 and 6.2.2.1. Figures 6.3 and 6.4 display the Langmuir and Freundlich plots, respectively for the adsorption of Pb^{2+} onto montmorillonite based adsorbents. The plot for each adsorbent is labeled accordingly.
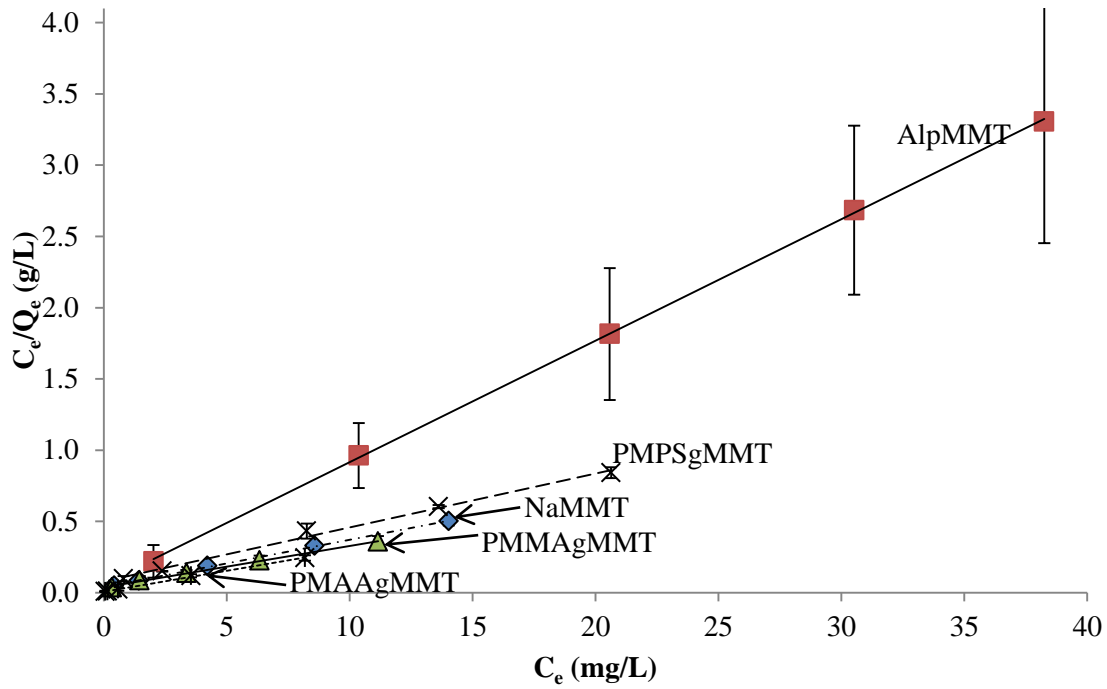
Figure 6.3: Langmuir plots for the adsorption of Pb^{2+} onto montmorillonite based adsorbents.

The practice has been to assess and compare the correlation coefficients (R^2) of the Freundlich and Langmuir plots. Depending on which one of the models has a greater correlation coefficient, one can conclude that the adsorption process best fits that particular model (Annadurai, G. et al, 2002; Benmaarmar, Z. et al, 2007).
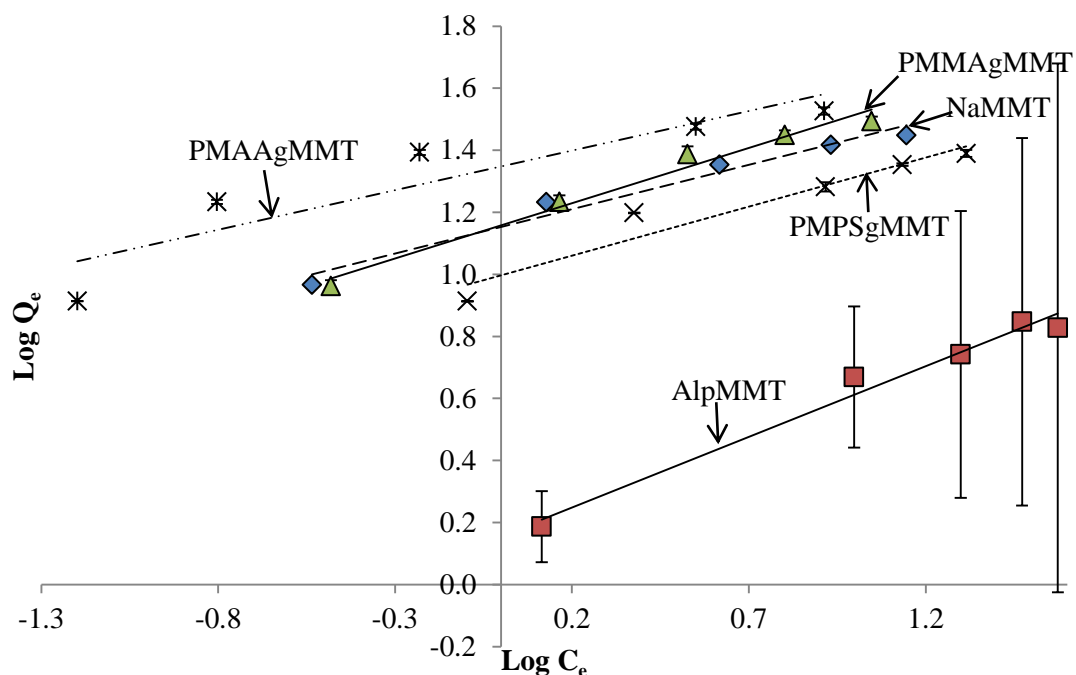
Figure 6.4: Freundlich plots for the adsorption of Pb^{2+} onto montmorillonite based adsorbents.

The respective Freundlich and Langmuir parameters and the correlation coefficients for the adsorption of Pb (II) onto the different montmorillonite based adsorbents are shown in Table 6.1. The Langmuir adsorption capacity (Q_0) can be determined from the slope and the adsorption intensity parameter b is determined from the intercept.

Table 6.1: Freundlich and Langmuir parameters for the adsorption of Pb (II).

Adsorbent	Isotherm	Slope	R^2	Q_0/K_f	Intercept	n/b
PMPSgMMT	Langmuir	0.0379	0.9937	26.39	0.0787	0.4816
	Freundlich	0.3162	0.9299	9.922	0.9966	3.1626
PMAAgMMT	Langmuir	0.0293	0.9982	34.13	0.0071	4.1268
	Freundlich	0.2554	0.8419	22.27	1.3477	3.9154
AlpMMT	Langmuir	0.0853	0.9998	11.72	0.0620	1.3758
	Freundlich	0.4559	0.9784	1.435	0.1568	2.1935
PMMAgMMT	Langmuir	0.0292	0.9972	34.25	0.0364	0.8022
	Freundlich	0.3566	0.9783	14.39	1.1581	2.8043
NaMMT	Langmuir	0.0328	0.9978	30.03	0.0429	0.8627
	Freundlich	0.3214	0.9687	14.35	1.1159	3.4965

A comparison of the correlation coefficient values of the Freundlich and the Langmuir model showed greater values for the Langmuir model. The Langmuir correlation coefficients were all greater than 0.9900, showing that the adsorption process of Pb^{2+} onto the montmorillonite based adsorbents can best be described by the Langmuir isotherm (Jaynes, W. F. et al, 1991; Rawajfih, Z. et al, 2006). The adsorption capacity of each adsorbent was calculated using the Langmuir equation and the values are shown in bold in Table 6.1.

The Freundlich correlation coefficients were significantly greater than 0.8900, except for adsorption onto PMAAgMMT which implies that the Freundlich model is also applicable (Jaynes, W. F. et al, 1991; Rawajfih, Z. et al, 2006) in describing the adsorption process of Pb (II) onto the adsorbents in Table 6.1 except PMAAgMMT. Since the Freundlich model describes adsorption onto heterogeneous surfaces, the relatively high Freundlich R^2 values obtained for the adsorbents, NaMMT, AlpMMT, PMMAgMMT and PMPSgMMT might suggest some surface heterogeneity in these adsorbents.

As defined in Section 6.2.2.2, *n* (Freundlich affinity constant) is related to the rate of adsorption and can be determined from the slope of the Freundlich plot. A Freundlich affinity constant (*n*) of >1 would also indicate conformity of the data to multilayer formation at the adsorbent surface (Rawajfih, Z. et al, 2006). It is also reported that if the slope ranges between 0 and 1 (n>1), this is indicative of chemisorption, whereas a value of slope > 1 (n < 1) indicates cooperative adsorption (Foo, K. Y. et al, 2010).

In this study, the values of *n* were found to range between 2.0 and 3.5 for all the montmorillonite based adsorbents. These values were significantly >1 which suggested conformity of experimental data to multilayer adsorption. The experimental adsorption data can be said to conform to both Langmuir and Freundlich models for the adsorption of Pb (II) onto the montmorillonite adsorbents. However, the Langmuir is a better fitting model than the Freundlich. Figure 6.5 displays the Langmuir adsorption capacities of the montmorillonite based adsorbents in the form of bar graphs for ease of comparison.

Langmuir adsorption capacities of 30.03, 34.25, 34.13, 26.39 and 11.72 mg/g were found for the adsorption of Pb^{2+} onto NaMMT, PMMAgMMT, PMAAgMMT, PMPSgMMT and AlpMMT, respectively. Donat, R. et al, 2005 assessed the adsorption of Pb^{2+} and Ni^{2+} onto natural bentonite from aqueous solution and obtained an adsorption capacity of 14.49 mg/g for Pb^{2+} for a concentration range of 50 - 500 ppm. The modification of NaMMT with PMMA and PMAA resulted in an increase in the adsorption capacity for the uptake of Pb^{2+} from aqueous solution.
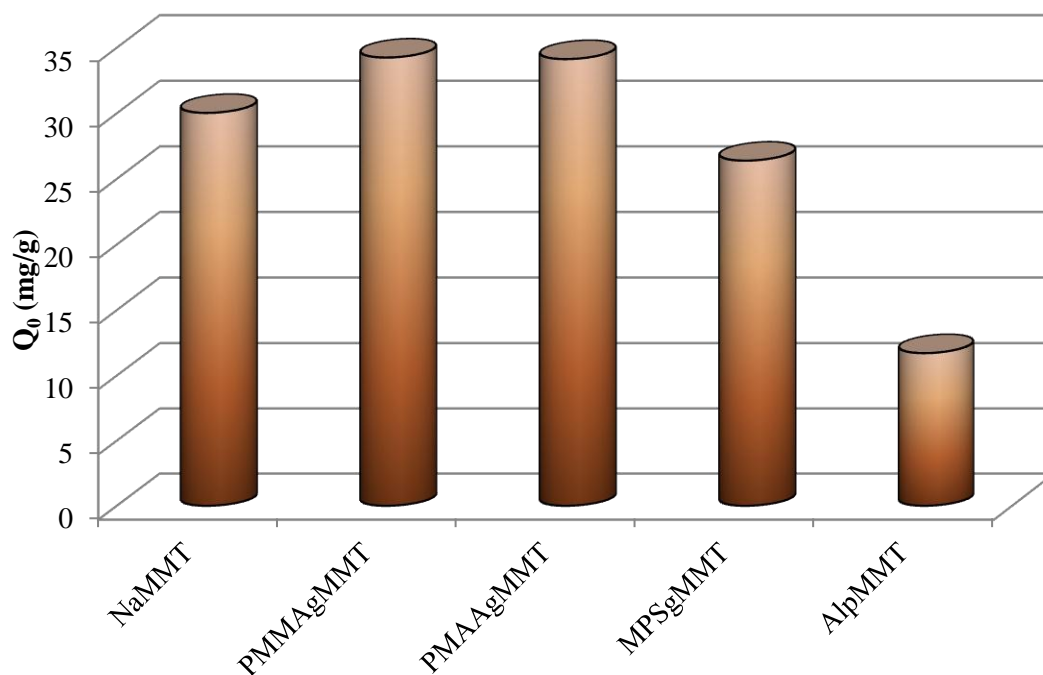
Figure 6.5: Adsorption capacities (according to the Langmuir model) of montmorillonite based adsorbents for Pb^{2+}.

The grafting of NaMMT using MPS resulted in a slight decrease in the uptake of Pb^{2+}. The different results obtained for PMMAgMMT and PMPSgMMT can probably be explained in terms of the chain lengths of the monomers attached to the NaMMT. Since MPS has a large organic component compared with MMA (see Chapter 3 for the structures of each), there is poor interaction of the PMPSgMMT with the Pb^{2+} ions. There is poor solubility of the Pb^{2+} in the essentially hydrophobic film on the PMPSgMMT clay surface. Sprynskyy, M. et al, 2006 reported a capacity of 26.81 mg/g for Pb^{2+} adsorption onto clinoptilolite. Sari, A. et al, 2007 assessed the adsorption of Cu^{2+} and Pb^{2+} onto expanded perlite from aqueous solution and reported an adsorption capacity of 13.39 mg/g. The adsorption capacities found in this study are comparable with those reported in the literature.

However, after further grafting PMAA to the PMPSgMMT to give PMAAgMMT, the adsorption capacity increased to more or less the same level as what was obtained for PMMAgMMT. An even higher adsorption capacity was expected for the PMAAgMMT since it now had carboxylate groups attached on the surface which acted as adsorption sites for Pb^{2+}. The presence of the MPS might have exerted some influence on the interaction of the surface groups with Pb^{2+} thus affecting the adsorption process.

Modification of NaMMT through Al-pillaring resulted in a drastic loss of the adsorption capacity. The uptake of Pb^{2+} dropped to about a third of what was obtained with the unmodified clay (NaMMT).

The results obtained for AlpMMT were contrary to what is reported in the literature (Lottenbach, B., 1996; Matthes, W. et al, 1999; Cooper, C. et al, 2002; Manohar, D. M. et al, 2006) and the expectations of this study. It can be said that the pillaring of montmorillonite with Al_2O_3 caused a lot of the adsorption sites to be blocked, thus becoming inaccessible to the colliding metal ions. However, Sampieri, A. et al, 2006 also found similar results when they investigated the adsorption of cobalt to silica-pillared montmorillonite clay. The authors found a decrease (of about 40%) in the uptake of Co (II) after calcining the Si-pillared montmorillonite.

Some authors reported a decrease in the cation exchange capacity (CEC) of the clay as a result of metal-pillaring (Keren, R. 1986; Kloprogge, J. T., 1998). According to Cooper, C. et al, 2002, the aluminium polymers compensate part of the permanent negative charge of the clay minerals so that the adsorption of heavy metals by cation exchange is less than on the untreated montmorillonite. The authors further say that the loss of cation exchange sites is however, more than offset by the formation of surface hydroxyl groups at the surface of the interlayer hydroxyl-Al polymer (Cooper, C. et al, 2002). In this study, it can be said that the loss of CEC was greater than the gains made in increasing the number of oxygen atoms (from the Al_2O_3 pillars) and the surface area of the clays through Al-pillaring. It also brings about the point that a large surface area on adsorbents does not necessarily translate into high adsorption capacity for heavy metals.

The adsorption of metal ions (including Pb^{2+}) was further investigated by carrying out adsorption experiments onto AlpMMT of different OH/Al molar ratio and also relating the adsorbed amount to the amount of Al in the AlpMMT samples. The results are reported in Section 6.3.6.

The following section discusses the adsorption kinetics results for the adsorption of Pb^{2+} onto the five montmorillonite based adsorbents.

6.3.1.2 Adsorption kinetics
Figure 6.6 shows the graphs of the amount (mg/g) of Pb^{2+} adsorbed onto the five montmorillonite based adsorbents plotted against time (min).
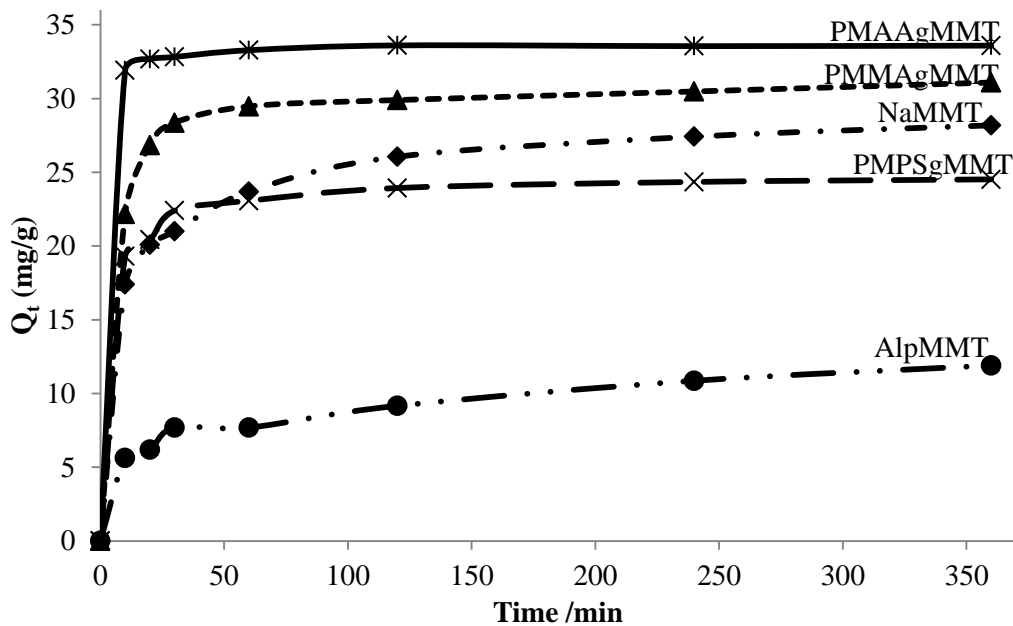
Figure 6.6: Plots of adsorbed amount (mg/g) of Pb^{2+} onto montmorillonite based adsorbents against time (min).

It can be seen that the amount of Pb (II) adsorbed increased with time, rapid adsorption occurring in the first hour for all systems. This rapid initial uptake was attributable to the availability of a large number of adsorption sites. As the sites were gradually filled up, adsorption became slow and the kinetics more dependent on the rate at which the Pb^{2+} was transported from the bulk solution to the actual adsorption sites (Yu, R. *et al*, 2008). After 3 h, the adsorption process of Pb (II) onto the different adsorbents had reached equilibrium. At equilibrium, there is no change in the amount of Pb^{2+} in solution or adsorbed since the rate of adsorption is equal to the rate of desorption. After equilibrium had been established, there was no change in the amount of Pb^{2+} adsorbed, implying that the adsorbent had taken the maximum amount of adsorbate it could accommodate. It was at this time (after equilibrium had been established) that data for adsorption isotherms were collected or generated.

However, though equilibrium was established within 3 h, the mixtures were left to shake until six hours had expired then the solutions were filtered and taken for AAS analysis for the generation of adsorption data. For AlpMMT, equilibrium state was achieved rather slowly (after 4 h) compared with the other adsorbents. From Figure 6.6, it can also be seen that AlpMMT adsorbed the least amount of Pb^{2+} compared with the other four adsorbents.

The experimental adsorption data were fitted to the two commonly used adsorption kinetic models: the pseudo first- and second-order models as discussed in Sections 6.2.3.1 and 6.2.3.2. Figures 6.7 and

6.8 display the pseudo first- and second-order plots for the adsorption of Pb^{2+} onto the montmorillonite based adsorbents.
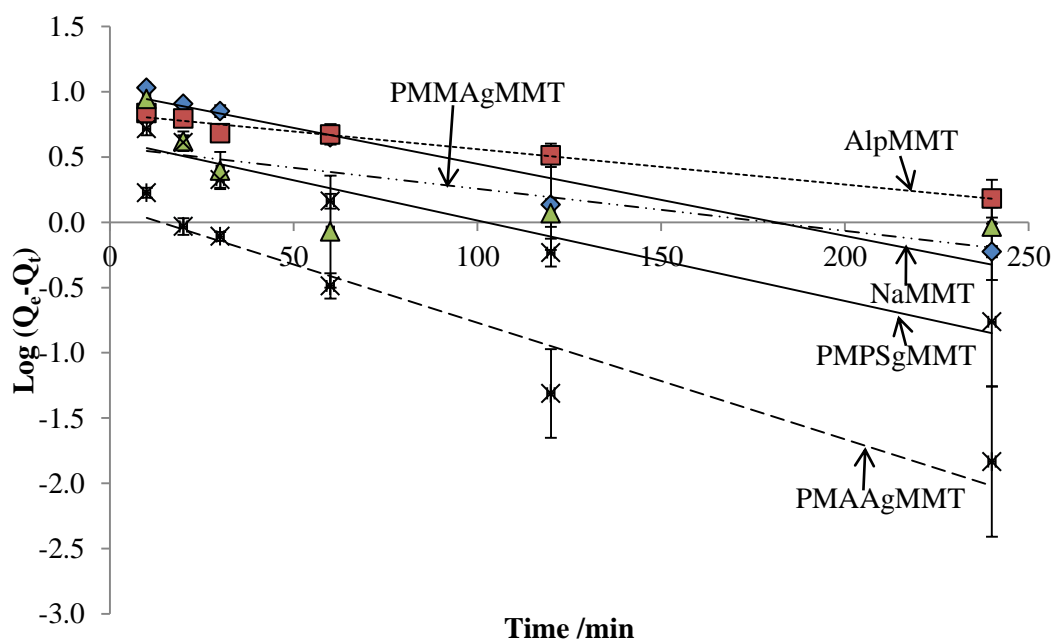
Figure 6.7: Pseudo first-order plots for the adsorption of Pb^{2+} onto montmorillonite based adsorbents.

A mere inspection of the plots in Figures 6.7 and 6.8 shows higher linearity or correlation for the pseudo second-order data than the pseudo first-order data.
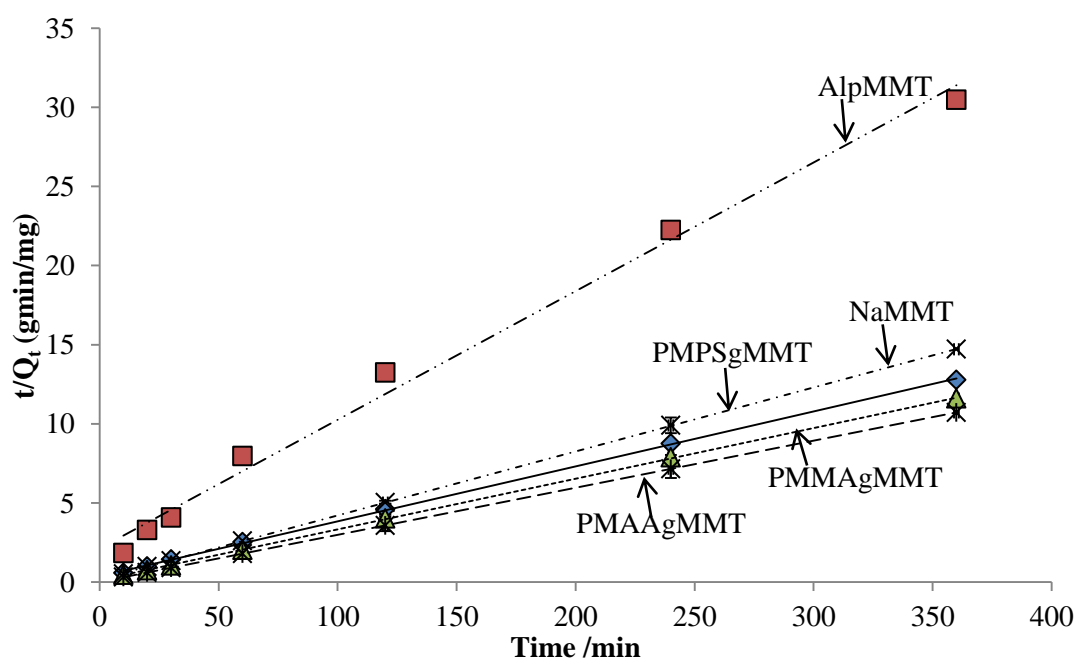
Figure 6.8: Pseudo second-order plots for the adsorption of Pb^{2+} onto montmorillonite based adsorbents.

Table 6.2 summarises the data of the adsorption parameters of the pseudo first- and second-order models for the adsorption of Pb (II) onto the five montmorillonite based adsorbents.

Table 6.2: Pseudo first- and second-order parameters for the adsorption of Pb^{2+} onto the different adsorbents based on montmorillonite only.

Adsorbent	Model	Slope	R^2	Intercept	k_1/k_2	Q_e (mg/g)
NaMMT	1st	-0.0055	0.9521	1.0005	0.0127	10.01
	2nd	0.0347	0.9996	0.3586	0.0034	28.81
PMMAgMMT	1st	-0.0032	0.4843	0.5798	0.0074	3.800
	2nd	0.0320	0.9999	01291	0.0079	31.25
PMAAgMMT	1st	-0.0089	0.9359	0.1233	0.0205	1.328
	2nd	0.0297	1.000	0.0169	0.0522	33.67
PMPSgMMT	1st	-0.0062	0.9485	0.1589	0.0143	4.264
	2nd	0.0405	1.000	0.1589	0.0103	24.69
AlpMMT	1st	-0.0027	0.9797	0.8310	0.0062	6.78
	2nd	0.0813	0.9919	2.1179	0.0031	12.30

The pseudo first- and second order rate constants (k_1 and k_2), and the correlation coefficients (R^2) of each model are also given for each adsorbent.

From Table 6.2, it can be seen that the pseudo second-order model gave the highest R^2 values compared with the pseudo first-order model as seen from the respective plots. The R^2 values for the pseudo second-order model were greater than 0.99 for all the adsorbents. AlpMMT had the least pseudo second-order R^2 value while the other four adsorbents had R^2 values close to 1.000. The high R^2 values obtained for the pseudo second-order model support the assumption behind the model that the adsorption process is due to chemisorption (King, P. et al, 2007). The pseudo second-order model is reported to give the highest R^2 values for most sorption systems (Ho, Y. S. et al, 1999 and 2006).

The equilibrium adsorbed amount (Q_e) for each adsorbent was determined from the pseudo second-order model since higher R^2 were obtained using this model than with the pseudo first-order model. The Q_e (mg/g) values were plotted against the adsorption capacities (Q_0, mg/g) determined from the Langmuir isotherm and the graph is shown in Figure 6.9. It can be seen that there was a very good

correlation between the kinetics Qe values and the isotherms Q_0 values. This suggests that the pseudo second-order model can be used to predict the adsorption capacity of these adsorbents for Pb^{2+}. The good correlation seen here also means that the adsorption data is quite reliable.
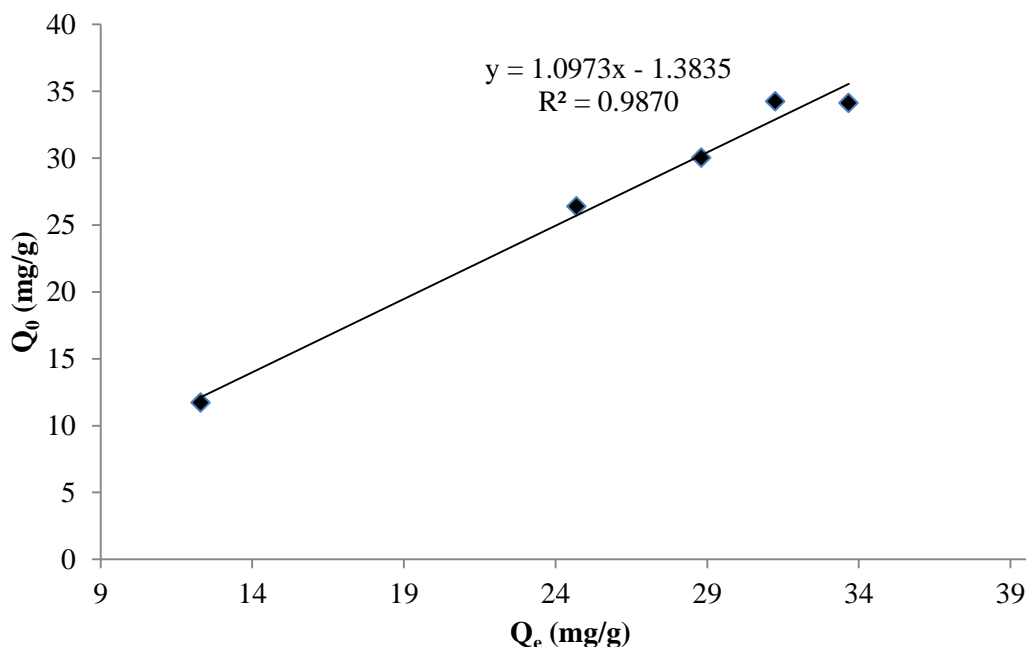
Figure 6.9: Correlation between Q_0 (mg/g) and Q_e (mg/g) values for the adsorption of Pb^{2+} onto montmorillonite based adsorbents.

Lignocellulose is a naturally occurring, abundant material being widely investigated as an adsorbent for the removal of both heavy metals and organic pollutants from water. Lignocellulose from plane tree leaves was assessed in this study for its possible use (before and after modification) for the adsorption of Pb^{2+} from aqueous solution. The following section presents the results obtained from the adsorption of Pb^{2+} onto lignocellulose based adsorbents.

6.3.2 Adsorption of Pb^{2+} onto lignocellulose based adsorbents

The adsorption data onto the lignocellulose based adsorbents were processed according to the procedure detailed in Section 6.2.

6.3.2.1 Adsorption isotherms

Figure 6.10 shows the isotherms for the adsorption of Pb^{2+} onto lignocellulose based adsorbents. Due to the different extents of adsorption of Pb^{2+} onto the lignocellulose based adsorbents, different C_e values were recorded as shown in Figure 6.10. The isotherms of PMMAgLig and PMAAgLig displayed a concave shape at the early stages and then a levelling off while for PMPSgLig and lignocellulose, the levelling off was not that pronounced. The isotherm for the adsorption of Pb^{2+} onto

PMPSgLig can be classified as a Langmuir type 3 because of the point of inflection which is evident in the graph (Giles, C. H., 1960 and 1974; Hinz, C., 2001). The other three isotherms can be safely classified as Langmuir type 2 (Limousin, G. et al, 2007). The maximum amount of Pb^{2+} adsorbed can be extrapolated from the region where the isotherms have leveled off.
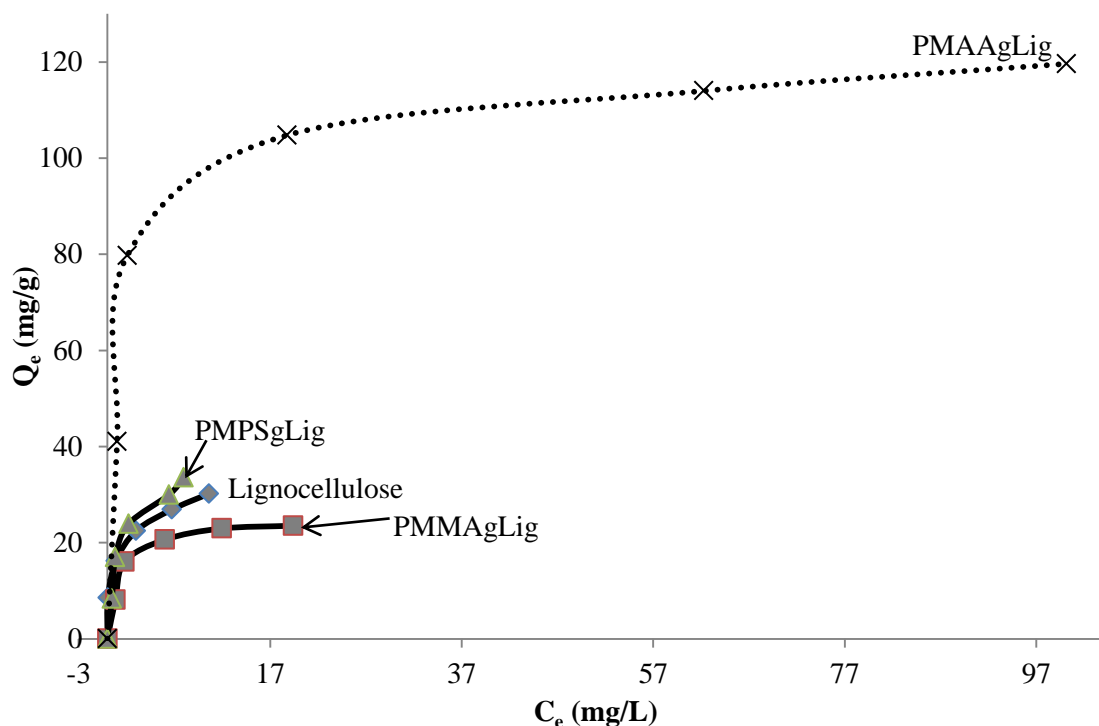
Figure 6.10: Isotherms for the adsorption of Pb^{2+} onto lignocellulose based adsorbents.

As mentioned for Pb^{2+} adsorption onto montmorillonite based adsorbents, the initial curvature in all the isotherms showed that as more sites in the adsorbent were occupied, it became increasingly difficult for a colliding Pb^{2+} ion to find a vacant site available on the adsorbent surface (Giles, C. H. et al, 1960; Hinz, C., 2001; Okada, T., 2004). A look at the isotherms shows that PMAAgLig adsorbed the highest amount of Pb^{2+} from solution and this was followed by PMPSgLig, then lignocellulose and lastly PMMAgLig.

The experimental data were again fitted to the linear Langmuir and Freundlich equations as described in Section 6.2.2. Figure 6.11 displays the Langmuir plots (C_e/Q_e vs C_e) for the adsorption of Pb^{2+} onto the lignocellulose based adsorbents.

186
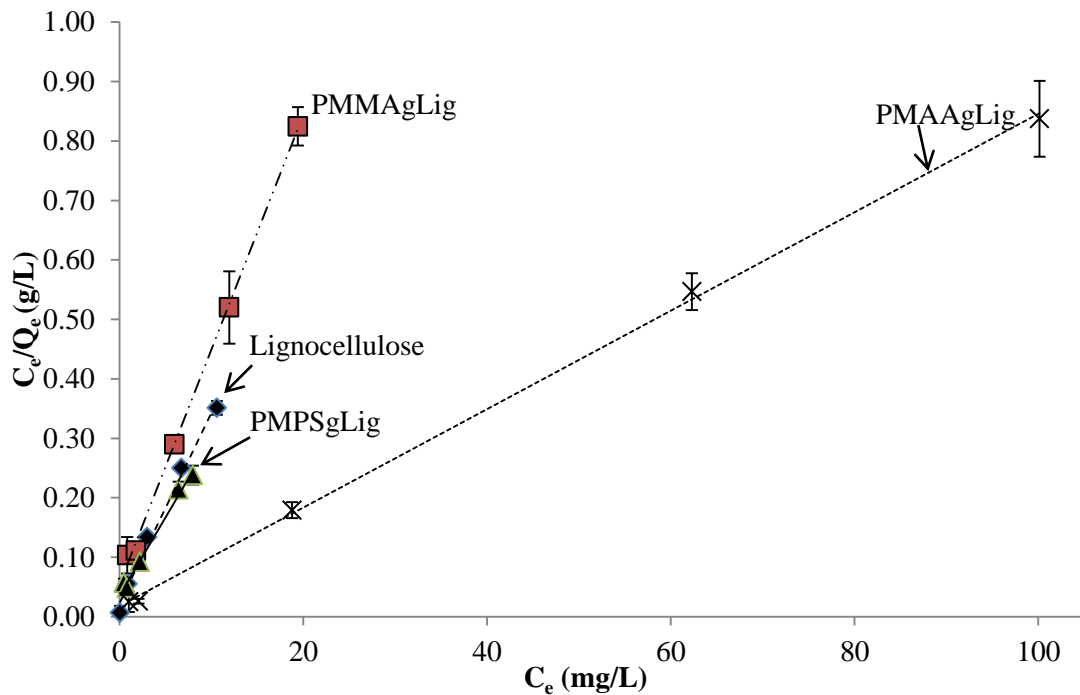
Figure 6.11: Langmuir plots for the adsorption of Pb^{2+} onto lignocellulose based adsorbents.

The respective Freundlich plots (Log Q_e vs Log C_e) for Pb^{2+} adsorption onto the lignocellulose based adsorbents are displayed in Figures 6.12.
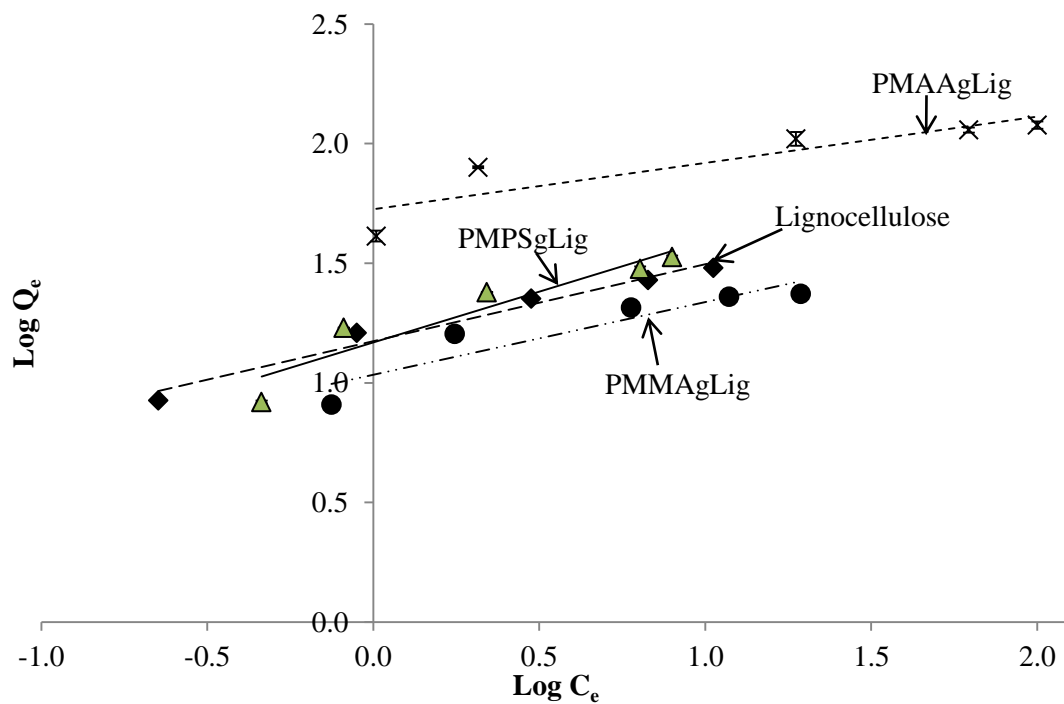
Figure 6.12: Freundlich plots for the adsorption of Pb^{2+} onto lignocellulose based adsorbents.

The respective Langmuir parameters for the adsorption of Pb (II) onto the lignocellulose based adsorbents are shown in Table 6.3. The Freundlich constant K_f, is determined from the intercept of the Freundlich plot while the Freundlich affinity index, n, is computed from the slope.

Table 6.3: Freundlich and Langmuir parameters for the adsorption of Pb^{2+} to lignocellulose based adsorbents.

Adsorbent	Isotherm	Slope	R^2	Q_0/K_f	Intercept	n/b
Lignocellulose	Langmuir	0.0320	0.9898	31.25	0.0229	1.3974
	Freundlich	0.3226	0.9724	14.93	1.1741	3.0998
PMMAgLig	Langmuir	0.0394	0.9987	25.38	0.0546	4.1268
	Freundlich	0.3038	0.8538	10.82	1.0343	3.2916
PMPSgLig	Langmuir	0.0261	0.9913	38.31	0.0364	0.7170
	Freundlich	0.4246	0.8864	14.74	1.1685	2.3551
PMAAgLig	Langmuir	0.0083	0.9993	120.48	0.0177	0.4689
	Freundlich	0.1936	0.7963	53.11	1.7252	5.1653

Again, as observed for the adsorption of Pb^{2+} onto montmorillonite based adsorbents, the Langmuir isotherm showed higher R^2 values than the Freundlich isotherm (Table 6.3). Except for lignocellulose, the Freundlich R^2 values for the adsorption of Pb (II) onto the other three adsorbents were significantly low (< 0.8900). Although the values of the Freundlich affinity constant, n, are significantly greater than 1, multilayer adsorption cannot be said to be significant in the adsorption of Pb^{2+} to the lignocellulose adsorbents since the R^2 values are less than 0.8900.

The calculated Langmuir adsorption capacities followed the same trend as described above for the isotherms (Figure 6.10) of the lignocellulose based adsorbents. PMAAgLig gave the highest adsorption capacity followed by PMPSgLig, then raw lignocellulose and lastly PMMAgLig. The trend was not the same as observed for the montmorillonite based adsorbents after modifying with the respective organic monomers, except for PMAAgMMT.

Modification of NaMMT with MPS resulted in a decrease in the adsorption capacity, while modification of the same with MMA gave a higher adsorption capacity. However, for lignocellulose, modification with MPS gave a higher adsorption capacity (38.31 mg/g) relative to the raw lignocellulose (31.25 mg/g), whereas modification with MMA resulted in a slightly lower adsorption capacity (25.38 mg/g). It was also noted that the adsorption capacity for the lignocellulose (31.25 mg/g) was almost the same as that for the NaMMT (30.03 mg/g).

For ease of comparison, the Langmuir adsorption capacities were plotted as shown in Figure 6.13. PMAAgLig gave a much higher adsorption capacity (120.48 mg/g) than recorded for all the other adsorbents discussed so far. The adsorption of Pb^{2+} onto raw silkworm chrysalides was found to follow the Langmuir model (Paulino, A. T. et al, 2006). The authors reported an adsorption capacity of 46.94 mg/g. The same authors also found an adsorption capacity of 87.97 mg/g for Pb^{2+} adsorption onto chitosan. Yu, J. et al, 2007 found an adsorption capacity of 45.87 mg/g for the adsorption of Pb^{2+} onto cystine-modified fungi biomass.
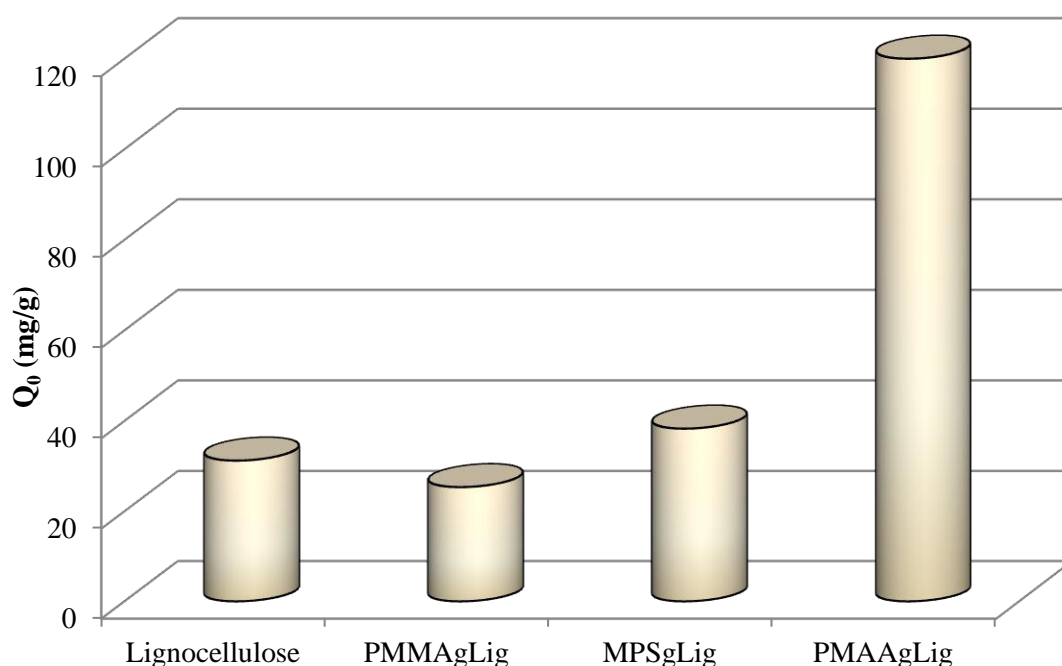
Figure 6.13: Adsorption capacities of lignocellulose based adsorbents for Pb^{2+}.

Pavasant, P. et al, 2006 reported an adsorption capacity of 28.70 mg/g for Pb^{2+} adsorption onto marine green macroalgae (*Caulerpa lentillifera*). Yu, J. et al, 2009 found an adsorption capacity of 243.9 mg/g for Pb^{2+} adsorption onto poly (methacrylic acid)-modified baker's yeast biomass. Differences in adsorption capacity can be attributed to the type of biomass used and possibly different conditions of adsorption used. Haltunnen, T. et al, 2007 reported an adsorption capacity of about 176 mg/g for Pb^{2+} adsorption onto lactic acid bacteria. Farag, S. et al, 2009 assessed the adsorption of Pb^{2+} onto salsola green plant bark and leaf biomass, and found adsorption capacities of about 26 mg/g. Wong, K. K. et al, 2003 reported a capacity of 108 mg/g for the adsorption of Pb^{2+} onto tartaric acid modified rice husk. Different types of chemical modifications have been carried out on cellulose giving different adsorption capacities as reviewed by O'Connell, D. W. et al, 2008. NaOH treated sawdust gave an adsorption capacity of 52.38 mg/g for Pb^{2+} (Meena, A. K. et al, 2008). The adsorption capacities obtained in this study were comparable to those reported in the literature for similar adsorbents.

The kinetics for the adsorption of Pb^{2+} onto the lignocellulose based adsorbents are presented in the next section.

6.3.2.2 Adsorption kinetics

Figure 6.14 displays the plots for the adsorbed amount (mg/g) of Pb^{2+} onto the different lignocellulose based adsorbents. All the four systems appeared to reach equilibrium in about 3 h just like for adsorption onto montmorillonite adsorbents. There was also a rapid increase in the amount of Pb^{2+} adsorbed onto the lignocellulose adsorbents within the first 1 h. After 1 h, there was not much change in the amount of Pb^{2+} adsorbed for all the systems probably due to a reduced number of adsorption sites available on the surface of the adsorbents as suggested in Section 6.3.1.2. It became increasingly difficult for the colliding Pb^{2+} ions to find a vacant site on the solid surface. PMAAgLig showed the highest equilibrium adsorbed amount of Pb^{2+} with the least amount being recorded for PMMAgLig, just as observed from the isotherms.
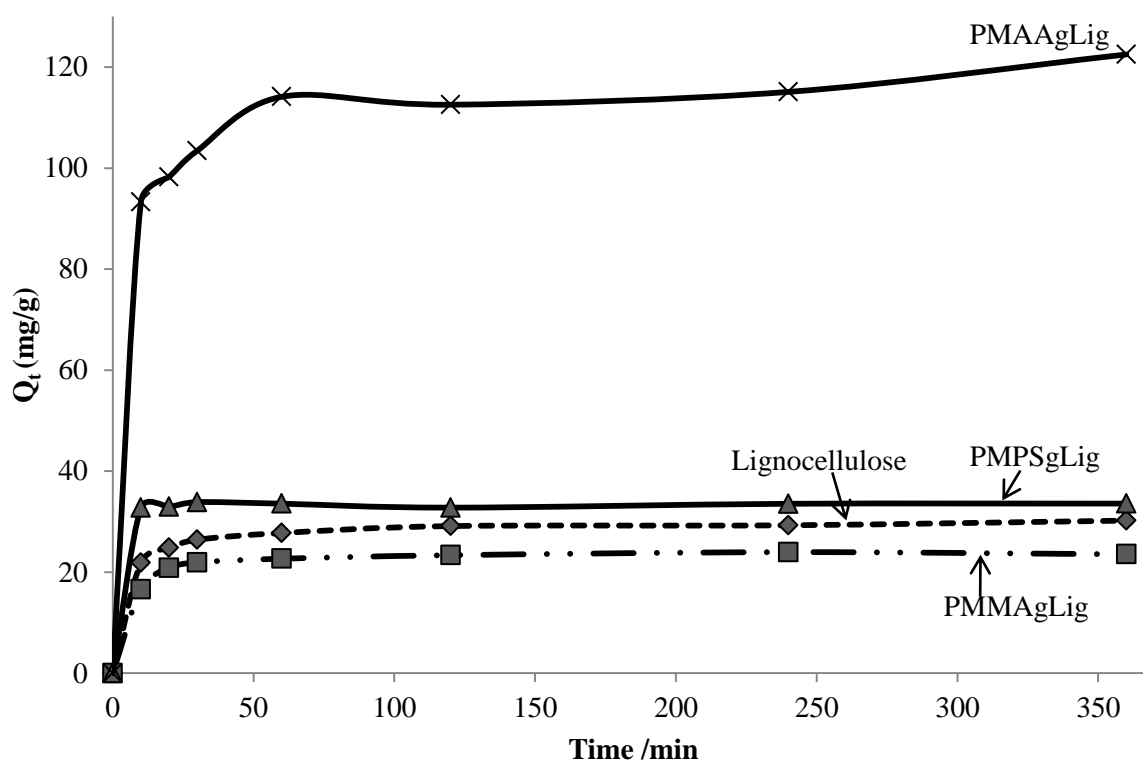
Figure 6.14: Plots for the adsorbed amount (mg/g) of Pb^{2+} onto lignocellulose based adsorbents against time (min).

The experimental adsorption data was analysed using the pseudo first-order and pseudo second-order equations. Figure 6.15 presents the pseudo first-order and the pseudo second-order plots for the adsorption of Pb^{2+} to the lignocellulose based adsorbents. The equilibrium adsorbed amount (Q_e,

mg/g) and k_1 (pseudo first-order rate constant) were determined from the intercept and the slope of the plots, respectively.

 A quick inspection of the plots shows that there was a poor correlation for the pseudo first-order data compared with the pseudo second-order data. Data points appear widely scattered for the pseudo first-order data. According to the pseudo first-order model, the rate constant, k_1 and the equilibrium adsorbed amount, Q_e are determined from the slope and the intercept, respectively.
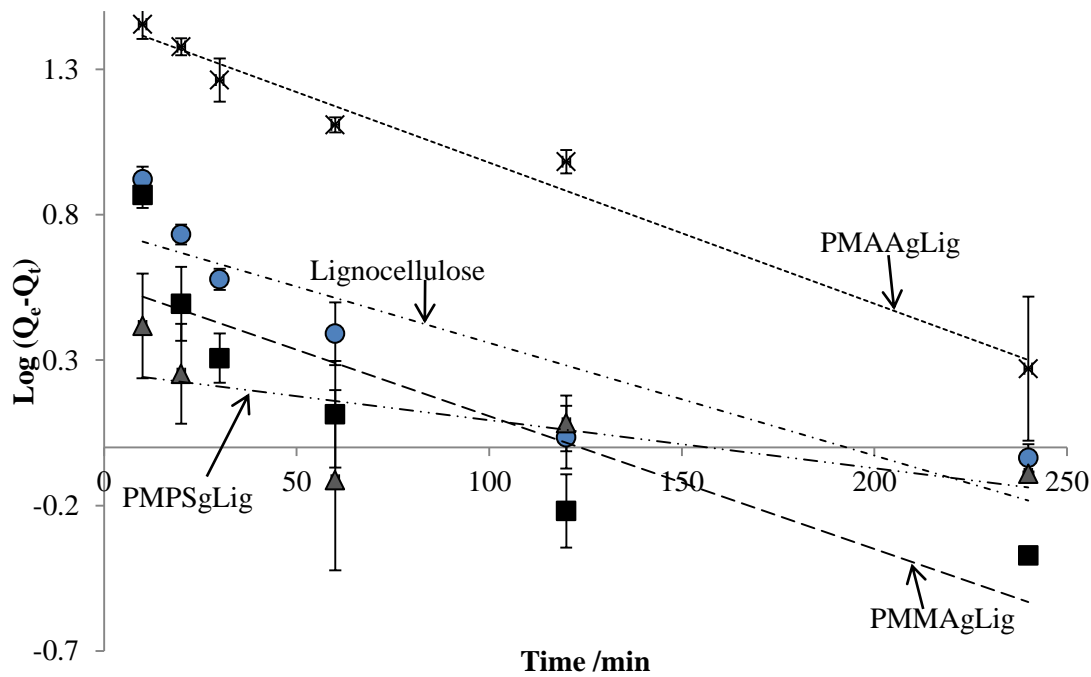
Figure 6.15: Pseudo first-order plots for the adsorption of Pb^{2+} onto lignocellulose based adsorbents.

The pseudo second-order plots are shown in Figure 6.16. According to the pseudo second-order model, the equilibrium adsorbed amount (Q_e, mg/g) and the pseudo second-order rate constant, k_2 are determined from the slope and the intercept, respectively.
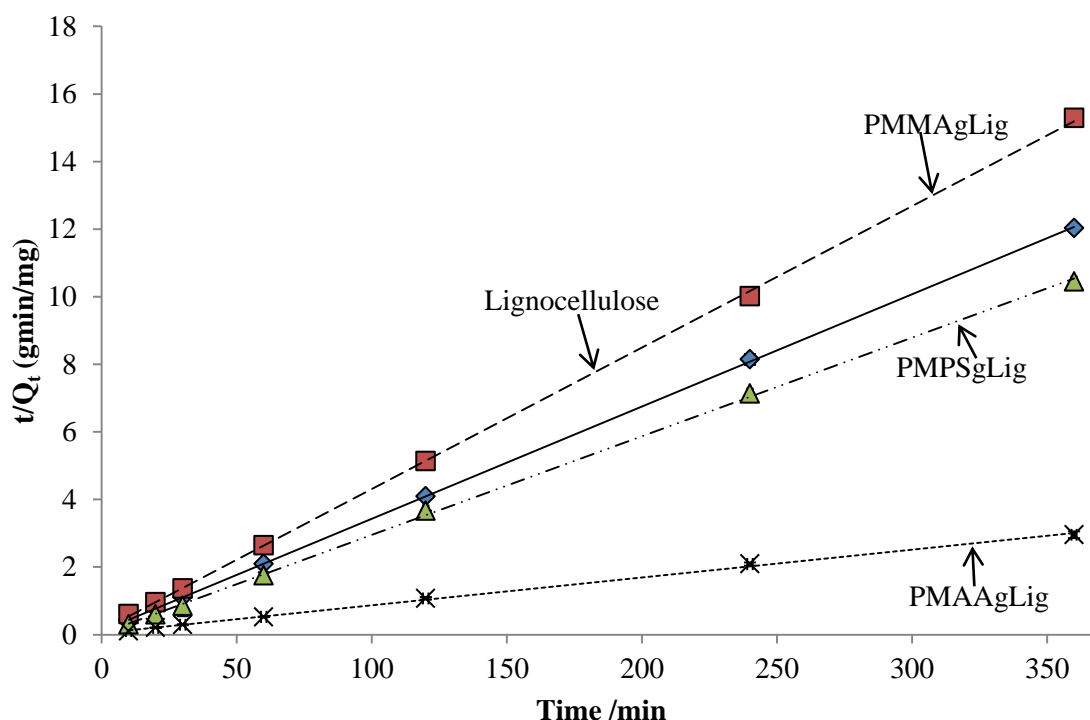
Figure 6.16: Pseudo second-order plots for the adsorption of Pb^{2+} onto lignocellulose based adsorbents.

The pseudo first-order and pseudo second-order parameters for the adsorption of Pb^{2+} onto the lignocellulose adsorbents are displayed in Table 6.4 below. As observed above for the adsorption of Pb^{2+} onto montmorillonite based adsorbents, the pseudo second-order model showed the highest correlation coefficients (R^2). The pseudo first-order R^2 values for Pb^{2+} adsorption onto lignocellulose, PMMAgLig and PMAAgLig were all less than 0.8900, suggesting that this model cannot be adequately used to describe the adsorption mechanism of Pb^{2+} onto these adsorbents.

Table 6.4: Pseudo first-order and pseudo second order kinetic parameters for the adsorption of Pb^{2+} onto lignocellulose based adsorbents.

Adsorbent	Model	Slope	R^2	Intercept	k_1/k_2	Q_e (mg/g)
Lignocellulose	1st	-0.0039	0.7938	0.7469	0.008982	5.583
	2nd	0.0332	1.0000	0.1130	0.009754	30.12
PMMAgLig	1st	-0.0046	0.7638	0.5642	0.01059	3.666
	2nd	0.0418	0.9998	01238	0.01411	23.92
PMPSgLig	1st	-0.0049	0.9787	1.4647	0.003915	1.8147
	2nd	0.0292	0.9995	0.0169	0.02493	34.25
PMAAgLig	1st	-0.0017	0.4730	0.2588	0.01129	29.15
	2nd	0.0082	0.9986	0.0502	0.001339	121.95

The pseudo first-order R^2 value for the adsorption of Pb^{2+} onto PMPSgLig was 0.9787 which was significantly higher than 0.8900, but still less that the pseudo second-order R^2 value of 0.9998. This might mean that both models can be used to describe the mechanism of adsorption of Pb^{2+} onto PMPSgLig. The equilibrium adsorbed amounts, Q_e (mg/g) values were compared with the Langmuir adsorption capacities, Q_0 (mg/g).

Figure 6.17 shows a plot for the correlation between Q_0 against Q_e (mg/g) for the adsorption of Pb^{2+} onto lignocellulose based adsorbents. An R^2 value of 0.9990 was obtained, again showing a good correlation between these two parameters.
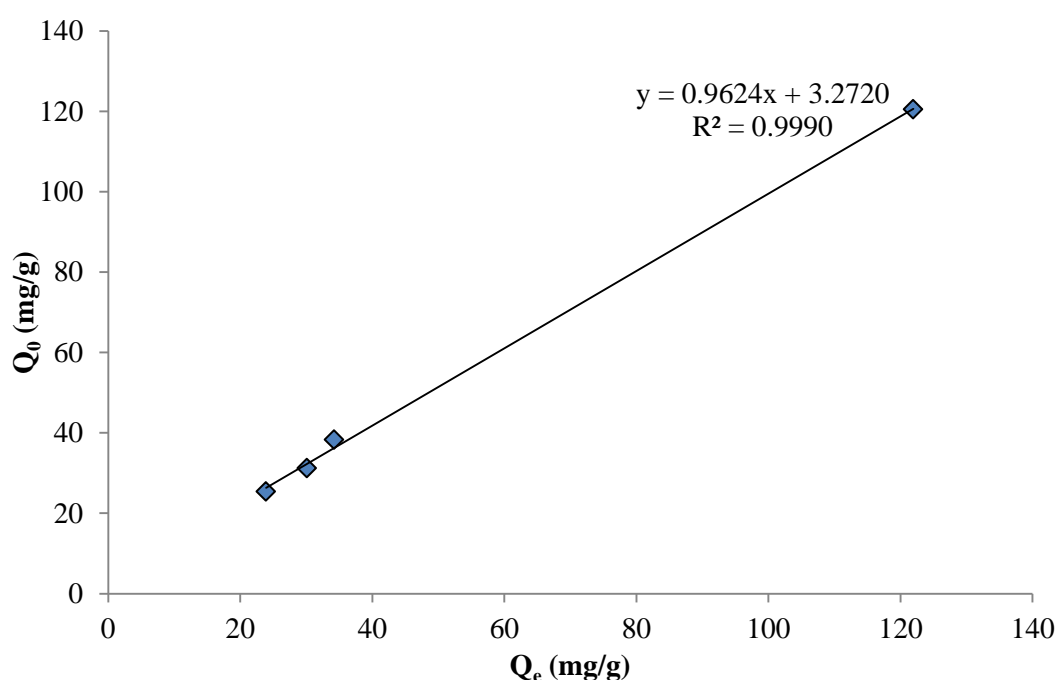
Figure 6.17: Correlation between Q_0 and Q_e values for the adsorption of Pb^{2+} onto lignocellulose-based adsorbents.

Another metal ion, Cd^{2+} was also assessed for its adsorption onto both the lignocellulose based and montmorillonite based adsorbents. Section 6.3.3 discusses the results obtained from the adsorption of Cd^{2+} onto montmorillonite based adsorbents.

6.3.3 Adsorption of Cd^{2+} onto montmorillonite based adsorbents

6.3.3.1 Adsorption isotherms

The system proposed by Giles, C. H. et al, 1960 and 1974 and further expounded by Hinz, C., 2001 for the classification of adsorption isotherms was again applied here to analyse data from the

adsorption of Cd^{2+} onto montmorillonite adsorbents. The isotherms for the adsorption of Cd^{2+} onto the different adsorbents are shown in Figure 6.18.

Unlike what was observed for the adsorption of Pb^{2+} onto the same adsorbents, the isotherms of Cd^{2+} were not as straightforward to assign or classify. Based on the concave nature of the isotherms at the initial stages, it can be suggested that the adsorption process fits the Langmuir model for all the adsorbents. AlpMMT isotherm showed a clear leveling off while the same was not observed for the other four isotherms. The isotherms can be classified into subgroups as follows: NaMMT (L_2), AlpMMT (L_2), PMAAgMMT (L_3), PMPSgMMT (L_4) and PMMAgMMT (L_{mx}) according to Giles, C. H. et al, 1960.
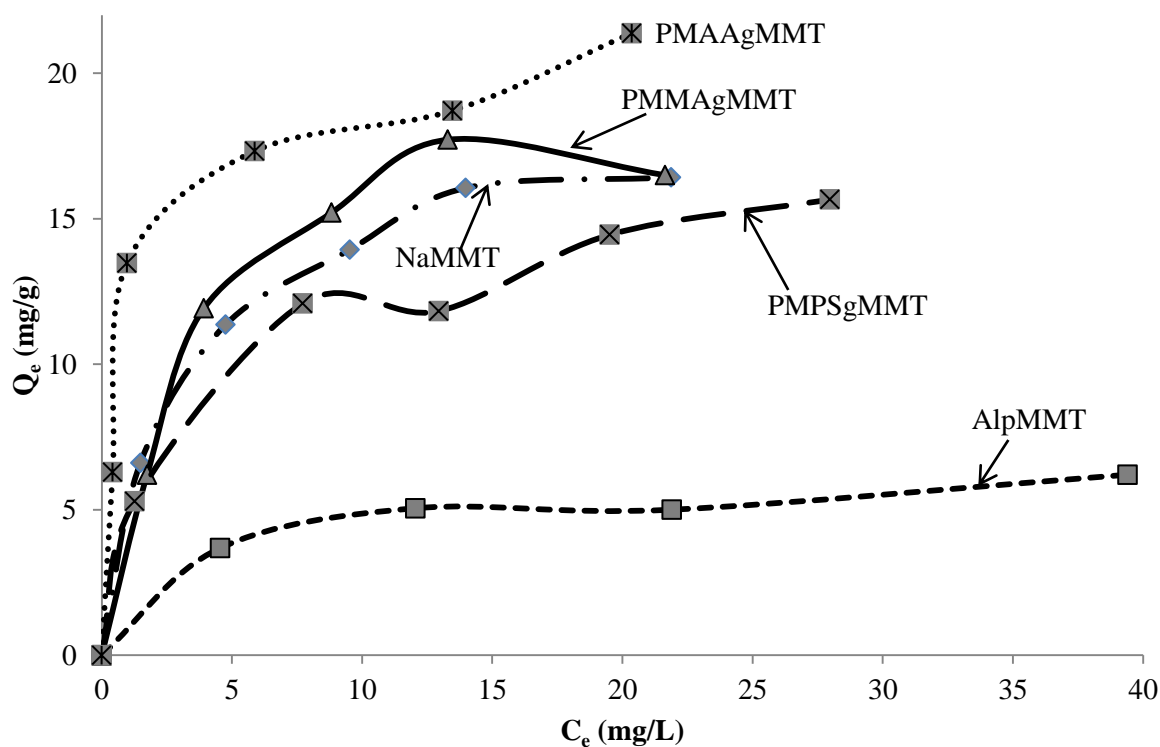
Figure 6.18: Isotherms for the adsorption of Cd^{2+} onto montmorillonite based adsorbents.

According to the isotherms in Figure 6.18, the adsorbents can be ordered as follows from the one with the highest uptake of Cd^{2+} to the least: PMAAgMMT > PMMAgMMT > NaMMT > PMPSgMMT > AlpMMT. This same trend was observed for the adsorption of Pb^{2+} onto the same adsorbents.

The experimental data were also analysed using the Langmuir and Freundlich equations (see Section 6.2.2). For the Langmuir isotherm C_e (mg/L) data are plotted against C_e/Q_e (g/L) data and a straight line should be generated if the data is best described by the Langmuir model. For the Freundlich

isotherm, Log C_e data are plotted against Log Q_e data and a straight line is generated if this model best fits the adsorption data.

Figures 6.19 and 6.20 display the Langmuir plots and the Freundlich plots for the adsorption of Cd^{2+} onto the different montmorillonite based adsorbents. The Langmuir plots for NaMMT and PMMAgMMT were nearly superimposed over each other, making it difficult to separate them. It can be also seen from Figure 6.20 (Freundlich plots) that the data points showed poor correlation compared with the Langmuir plots.
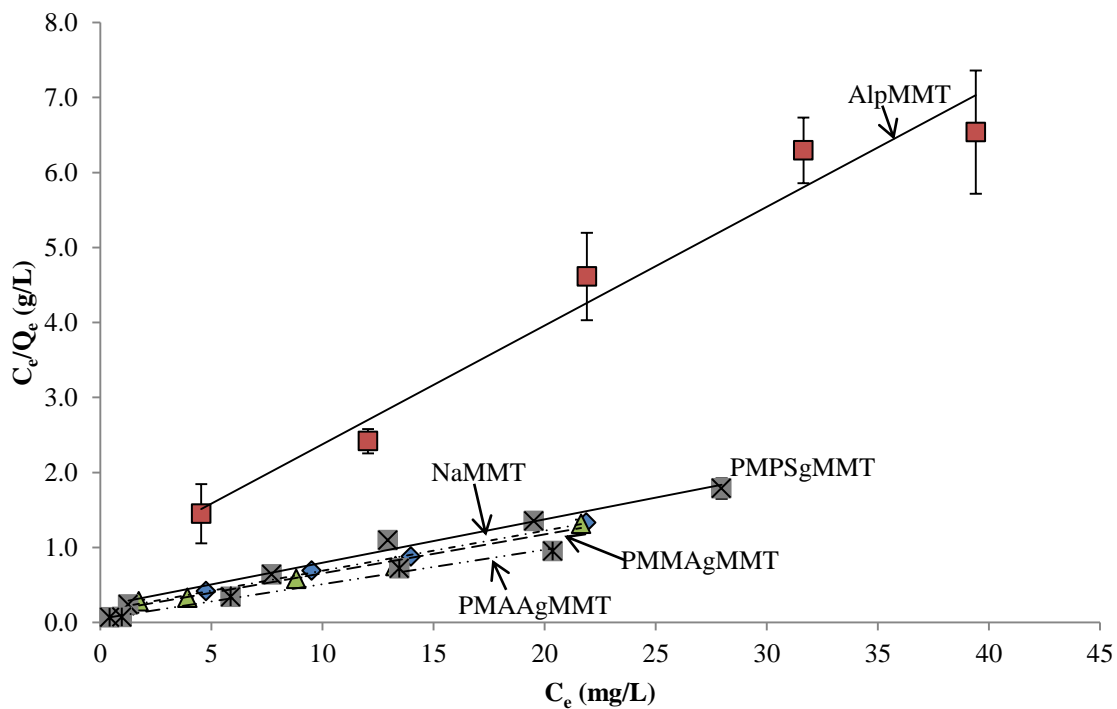
Figure 6.19: Langmuir plots for the adsorption of Cd^{2+} onto montmorillonite based adsorbents.
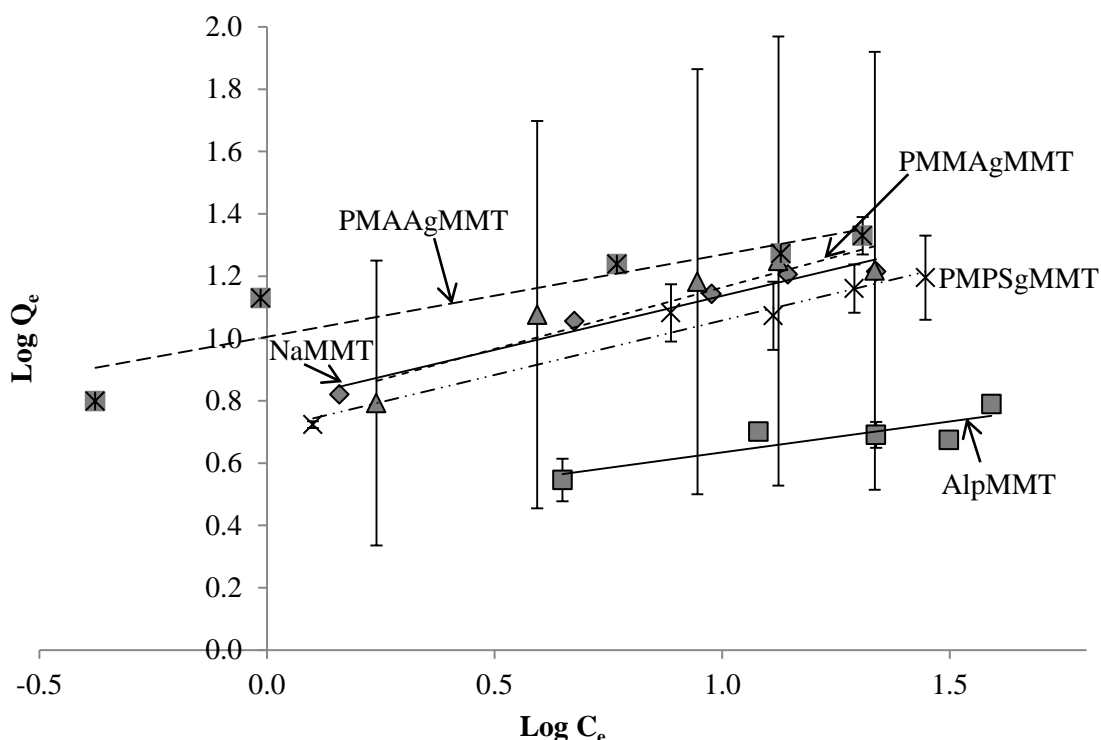
Figure 6.20: Freundlich plots for the adsorption of Cd^{2+} onto montmorillonite based adsorbents.

The Freundlich and Langmuir isotherm parameters, together with the correlation coefficients (R^2) are shown in Table 6.5. As observed above for the adsorption Pb^{2+} and what has been discussed above for Cd^{2+} isotherms in Figure 6.18, the Langmuir model showed higher correlation coefficients than the Freundlich model. This essentially means that the adsorption data of Cd^{2+} can be best described by the Langmuir model which assumes monolayer adsorption.

Table 6.5: Freundlich and Langmuir parameters for the adsorption of Cd^{2+} onto montmorillonite based adsorbents.

Adsorbent	Isotherm	Slope	R^2	Q_0/K_f	Intercept	n/b
NaMMT	Langmuir	0.0534	0.9979	18.73	0.1567	0.3408
	Freundlich	0.3468	0.9654	6.162	0.7897	2.883
AlpMMT	Langmuir	0.1583	0.9665	6.317	0.7948	0.1992
	Freundlich	0.1983	0.7423	2.729	0.4360	5.0428
PMMAgMMT	Langmuir	0.0519	0.9831	19.27	0.1376	0.3772
	Freundlich	0.3952	0.8594	5.865	0.7683	2.530
PMPSgMMT	Langmuir	0.0579	0.9847	17.27	0.2181	0.2655
	Freundlich	0.3494	0.9617	5.112	0.7086	2.862
PMAAgMMT	Langmuir	0.0460	0.9927	21.74	0.0523	0.8795
	Freundlich	0.2641	0.8318	10.11	1.005	3.786

Relatively high Freundlich R^2 values were also obtained for the adsorption of Cd^{2+} onto NaMMT (0.9654) and PMPSgMMT (0.9617). These R^2 values were significantly greater than 0.8900, meaning the adsorption process can also be described by the Freundlich model for these two adsorbents. As described earlier, the Freundlich model assumes multilayer adsorption onto heterogeneous surfaces. The values of n (Freundlich affinity constant) were significantly higher than 1 and the values of $1/n$ ranged between 0.2 and 0.4, indicating favourable adsorption of heavy metals (Kumar, U. et al, 2006).

The adsorption capacities (Q_0) of the montmorillonite based adsorbents were then computed using the Langmuir equation since it had the higher R^2 values of the two models. The values are shown in Table 6.5 and are highlighted in bold. The adsorption capacities are presented in the form of a bar graph as shown in Figure 6.21. It was observed that grafting of NaMMT with PMMA resulted in a slight increase in the adsorption capacity (19.27 mg/g), and relatively more Cd^{2+} was adsorbed after grafting the NaMMT with PMAA (21.74 mg/g). A decrease in the uptake of Cd^{2+} was recorded for PMPSgMMT (17.27 mg/g) and AlpMMT (6.32 mg/g) just as observed for the adsorption of Pb^{2+}. The adsorption capacities followed more or less the same trend for both Cd^{2+} and Pb^{2+} adsorption onto the montmorillonite based adsorbents.
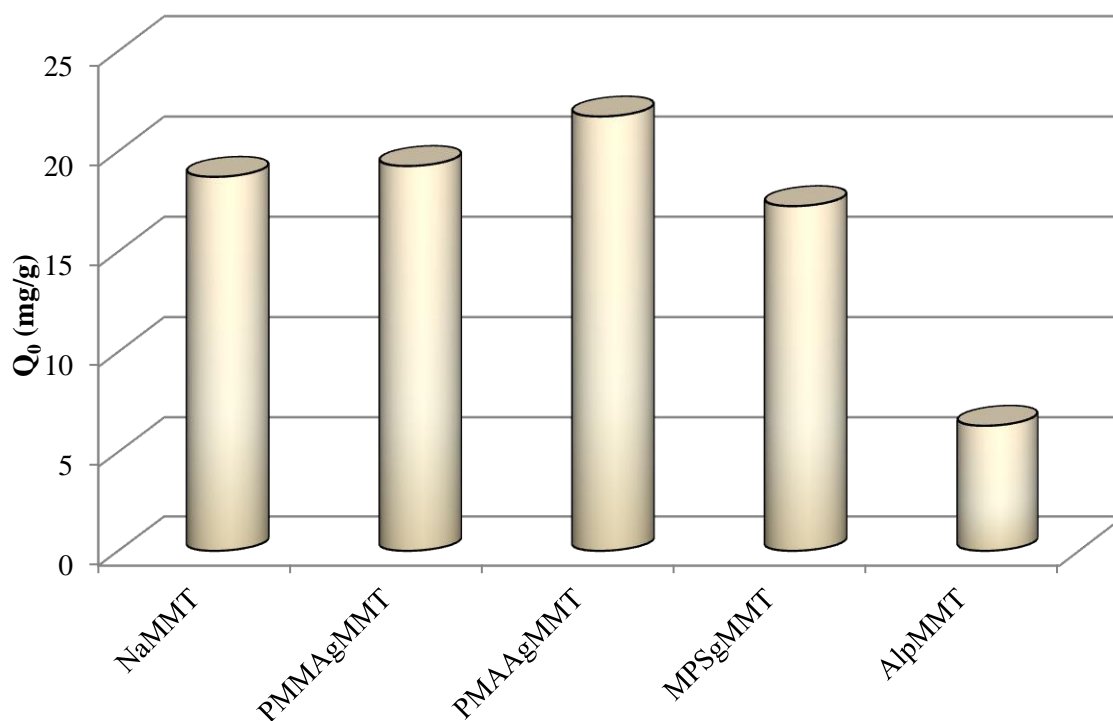
Figure 6.21: Adsorption capacities of montmorillonite based adsorbents for Cd^{2+}.

The drastic decrease in the amount of Cd^{2+} and Pb^{2+} adsorbed after modifying the NaMMT through Al-pillaring suggests that metal-pillaring of montmorillonite for the purposes of adsorbing metals from aqueous solution is not appropriate. Since lower adsorption capacities were recorded for the adsorption of Cd^{2+} than Pb^{2+} onto montmorillonite based adsorbents, it means that Cd^{2+} has a lower affinity for these adsorbents than Pb^{2+}.

Lee, B. et al, 2001 found a capacity of 28 mg/g for Cd^{2+} adsorption onto 3-mercaptopropyl trimethoxysilane modified silica. Wang, W., 2010 reported an adsorption capacity of 42.6 mg/g for Cd^{2+} adsorption onto PMAA-grafted silica particles. However, the investigators used an initial concentration of 1000 ppm for their adsorption studies. Li, Y. H. et al, 2003 found an adsorption capacity of 11.0 mg/g for Cd^{2+} adsorption onto chemically oxidized carbon nanotubes. Abollino, O. et al, 2003 obtained an adsorption capacity of 5.30 mg/g for the adsorption of Cd (II) onto Na-montmorillonite. Yu, R. et al, 2008 found equilibrium adsorption capacities of about 30 mg/g for Cd^{2+} adsorption onto carbon modified Al-pillared bentonite. The adsorption capacities found for the adsorption of Cd^{2+} onto montmorillonite based adsorbents are comparable to those reported in the literature for similar adsorbents.

6.3.3.2 Adsorption kinetics

Figure 6.22 shows the plots for the adsorbed amount (mg/g) of Cd^{2+} against time (min) for adsorption onto the montmorillonite based adsorbents. Equilibrium state was achieved within the first three hours, as shown by the leveling off of all the plots at this stage. It can also be seen that the highest amount of Cd^{2+} was adsorbed onto PMAAgMMT and the least onto AlpMMT. As observed for the adsorption of Pb^{2+} to the montmorillonite based adsorbents, most of the adsorption occurs within the first 1 h. After 1 h, there was not much observable change.

However, the plot for the adsorption onto NaMMT showed an increase in the amount adsorbed up to 60 min, followed by a drop at 2 h (possibly due to desorption). Desorption could have been due to the instability of the adsorbent-adsorbate complex formed during the initial stages of the adsorption process or the presence of another competing reaction like complexation.
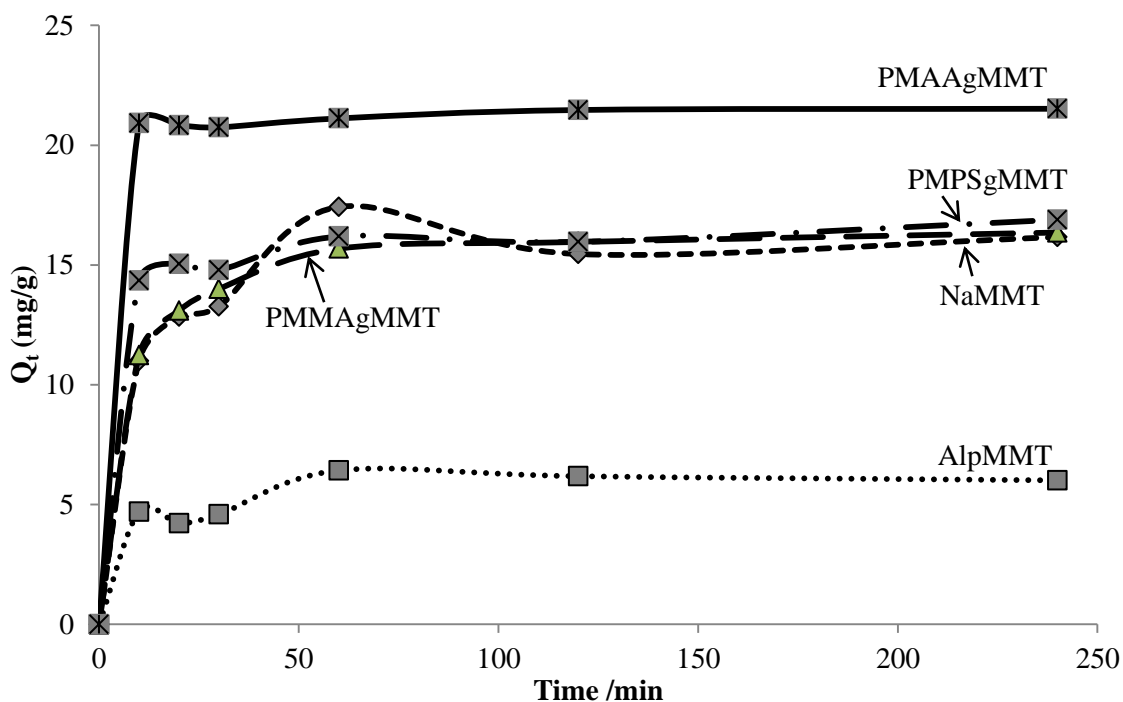
Figure 6.22: Plots for the adsorbed amount (mg/g) of Cd^{2+} onto montmorillonite based adsorbents against time (min).

The experimental data were then fitted to the pseudo first- and second-order equations in order to assess the mechanism of the adsorption process. Both the pseudo first- and second-order equations have been given above in Section 6.2.3. For pseudo first-order plot, Log (Q_e-Q_t) data are plotted against time (min). A straight line is obtained if the data fits well to the pseudo first-order model. The pseudo second-order graph is obtained by plotting t/Q_t (gmin/mg) data against time (min). Again, if the data fits to the pseudo second-order, a straight line is obtained.

Figures 6.23 and 6.24 display the pseudo first-order and pseudo second-order plots for the adsorption of Cd^{2+} onto the montmorillonite based adsorbents. The parameters of the pseudo first-order and pseudo second-order models were then compiled into a table for ease of comparison.
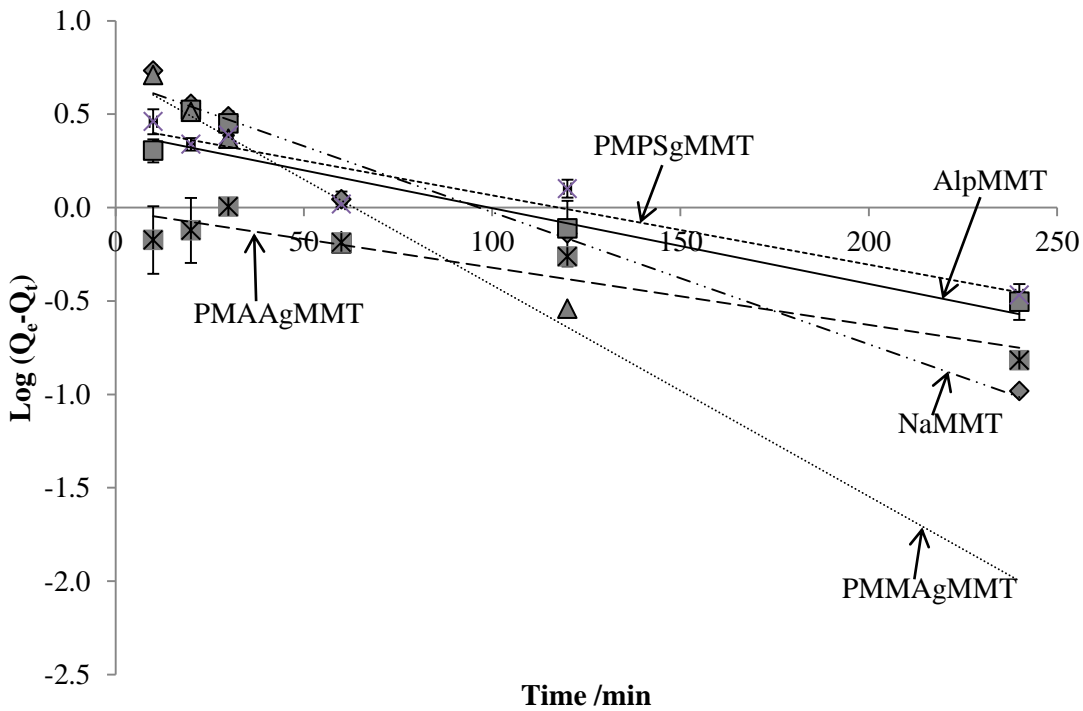
Figure 6.23: Pseudo first-order plots for the adsorption of Cd^{2+} to montmorillonite based adsorbents.
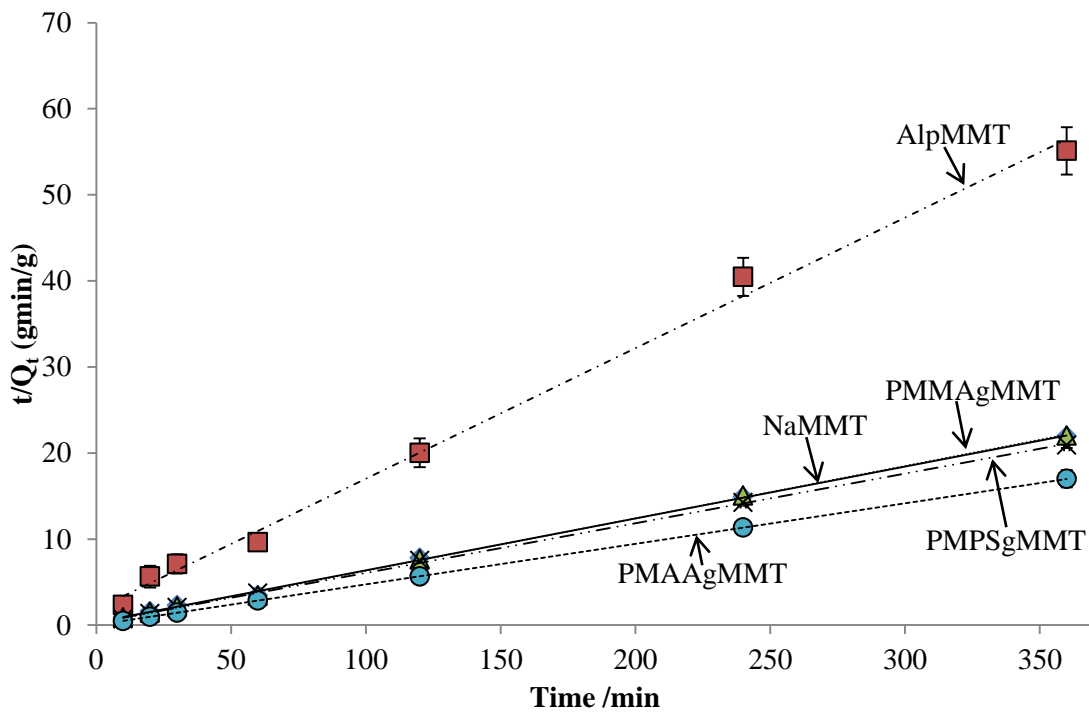
Figure 6.24: Pseudo second-order plots for the adsorption of Cd^{2+} onto montmorillonite based adsorbents.

The values of the different parameters of the two kinetic models for each adsorbent are shown in Table 6.6, together with their correlation coefficients (R^2). The pseudo second-order kinetic model

showed higher correlation coefficients (close to 1.00) than the pseudo first-order model for all the adsorbents.

Table 6.6: Pseudo first-order and pseudo second-order kinetic parameters for the adsorption of Cd^{2+} onto the montmorillonite based adsorbents.

Adsorbent	Model	Slope	R^2	Intercept	k_1/k_2	Q_e (mg/g)
NaMMT	1st	-0.0071	0.9683	0.6817	0.0164	4.805
	2nd	0.0603	0.9991	0.3303	0.0110	16.58
AlpMMT	1st	-0.0041	0.7597	0.4021	0.0094	2.524
	2nd	0.1516	0.9957	1.8512	0.0124	6.596
PMMAgMMT	1st	-0.0113	0.9361	0.7157	0.0260	5.196
	2nd	0.0609	0.9992	0.2258	0.0164	16.42
PMPSgMMT	1st	-0.0037	0.9003	0.4358	0.0085	2.728
	2nd	0.0578	0.9995	0.2775	0.0120	17.30
PMAAgMMT	1st	-0.0031	0.8792	-0.0150	0.007139	0.966
	2nd	0.0471	1.0000	0.0242	0.09167	21.23

This implies that the adsorption mechanism can best be described by the pseudo second-order model. However, NaMMT, PMPSgMMT and PMMAgMMT had pseudo first-order correlation coefficients (R^2) greater than 0.8900. It therefore, means that the pseudo first-order model can (to some extent) also be used to describe the mechanism for the adsorption of Cd^{2+} onto these three adsorbents. The pseudo first-order R^2 values for the other two adsorbents were less than 0.8900, i.e. PMAA (0.8792) and AlpMMT (0.7597). The pseudo first-order model is therefore, not applicable to describe the mechanism of adsorption onto these two adsorbents.

A comparison of the kinetics Q_e values and the isotherm Q_0 values showed a relatively good correlation, but not as what was obtained for the adsorption of Pb^{2+} to the same adsorbents. For the adsorption of Cd^{2+} onto AlpMMT, PMPSgMMT and PMAAgMMT, there was a good correlation between the Q_e and Q_0 values. Much lower Q_e values were obtained for Cd^{2+} adsorption onto NaMMT and PMMAgMMT than the respective Q_0 values from the Langmuir isotherm (Tables 6.5 and 6.6). In addition, the uptake of Cd^{2+} onto these adsorbents was relatively low compared with the uptake of Pb^{2+} to the same adsorbents. This shows a higher affinity of Pb^{2+} for these adsorbents than Cd^{2+}.

The adsorption of Cd^{2+} onto lignocellulose based adsorbents was also assessed. Section 6.4.4 presents the results obtained from the adsorption of Cd^{2+} onto the lignocellulose based adsorbents. The

adsorption of Cd^{2+} was carried out onto raw lignocellulose and modified lignocellulose just as presented for Pb^{2+}.

6.3.4 Adsorption of Cd^{2+} on lignocellulose based adsorbents

6.3.4.1 Adsorption isotherms

The data for the adsorption of Cd^{2+} onto the lignocellulose based adsorbents were analysed using the Giles classification system as discussed in Sections 6.2.2 and 6.3.3.1. Figure 6.25 shows the isotherms for the adsorption of Cd^{2+} onto the lignocellulose based adsorbents. As already stated for Pb^{2+}, due to the different extents of adsorption of Cd^{2+} onto the lignocellulose based adsorbents, different C_e values were recorded.
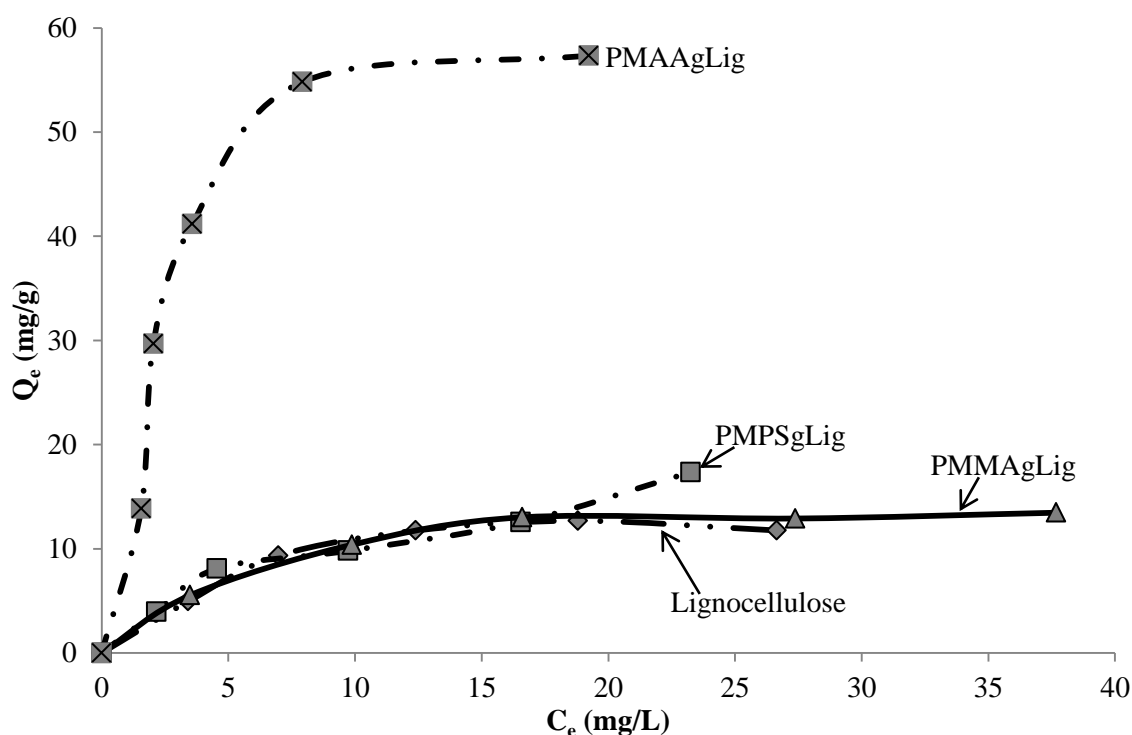
Figure 6.25: Isotherms for the adsorption of Cd^{2+} onto lignocellulose based adsorbents.

The isotherms for the adsorption of Cd^{2+} onto lignocellulose, PMAAgLig, PMMAgLig and PMPSgLig can be classified as Langmuir type 2, type 2, type 2 and type 3, respectively. The isotherm for Cd^{2+} adsorption onto PMAAgLig has some bias towards an H isotherm. The uptake of Cd^{2+} onto the four adsorbents can be expected to be in the following order: PMAAgLig > PMPSgLig > PMMAgLig > lignocellulose, as observed from the respective adsorption isotherms (see Figure 6.25).

The adsorption data were fitted to the Langmuir and Freundlich equations, and Figures 6.26 and 6.27 display the Langmuir and Freundlich plots, respectively.
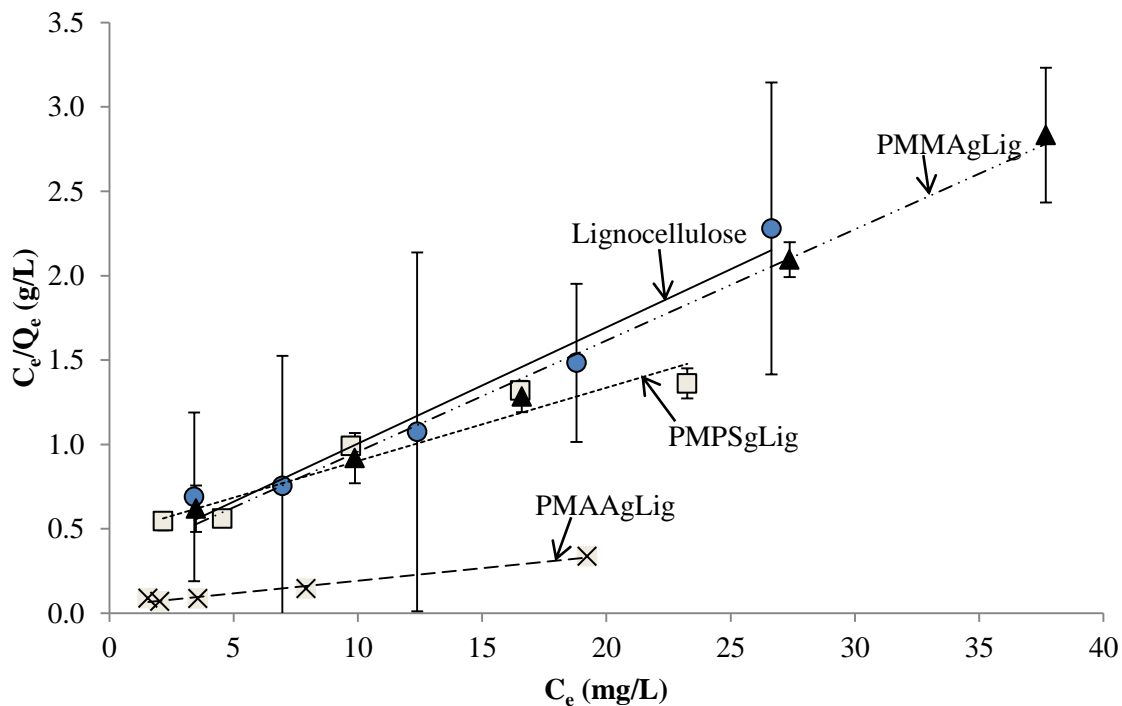
Figure 6.26: Langmuir plots for the adsorption of Cd^{2+} onto lignocellulose based adsorbents.
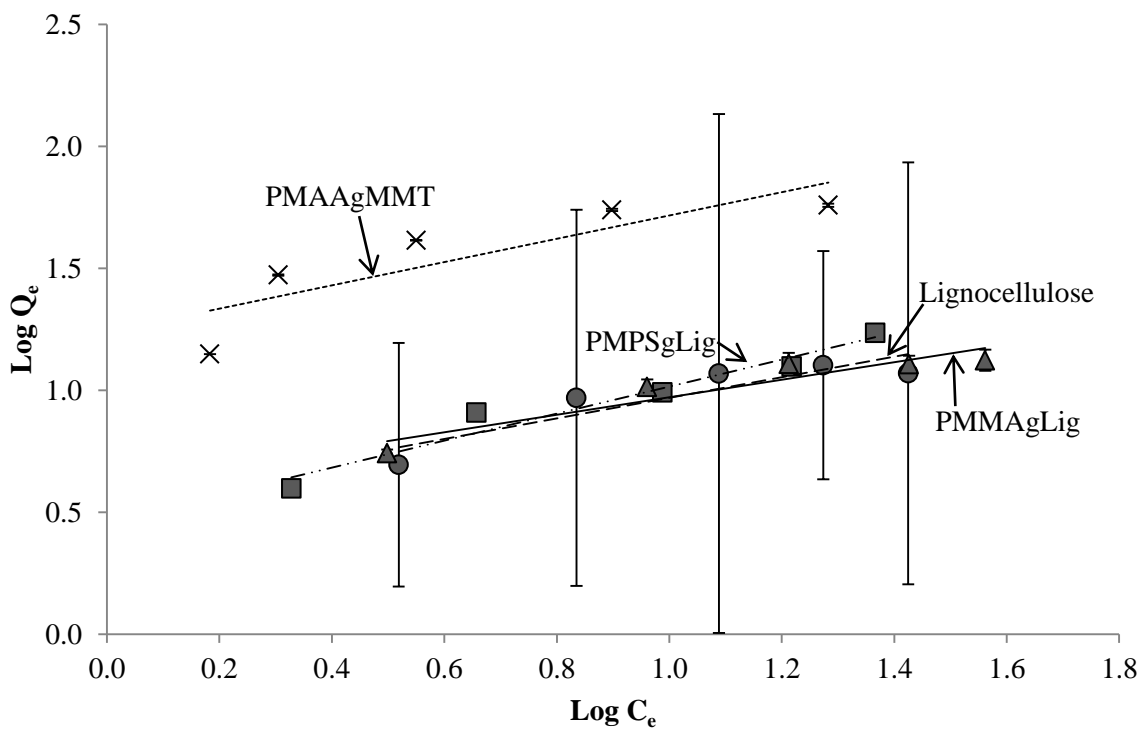
Figure 6.27: Freundlich plots for the adsorption of Cd^{2+} to lignocellulose based adsorbents.

The Langmuir and Freundlich parameters for the adsorption of Cd^{2+} onto the lignocellulose based adsorbents are shown in Table 6.7.

Table 6.7: Freundlich and Langmuir parameters for the adsorption of Cd^{2+} onto lignocellulose based adsorbents.

Adsorbent	Isotherm	Slope	R^2	Q_0/K_f	Intercept	n/b
Lignocellulose	Langmuir	0.0689	0.9898	14.51	0.3170	0.2174
	Freundlich	0.4218	0.8188	3.528	0.5475	2.371
PMMAgLig	Langmuir	0.0659	0.9928	15.17	0.2969	0.2220
	Freundlich	0.3583	0.8839	4.101	0.6129	2.791
PMPSgLig	Langmuir	0.0435	0.9158	22.99	0.4669	0.0932
	Freundlich	0.5535	0.9524	2.895	0.4616	1.807
PMAAgLig	Langmuir	0.0149	0.9822	67.11	0.0423	0.3522
	Freundlich	0.4779	0.7370	17.33	1.2388	2.0925

The Langmuir model gave relatively higher R^2 values than the Freundlich model (see Table 6.7). However, this was with the exception of PMPSgLig which gave a higher R^2 value for the Freundlich model. Since the Langmuir R^2 value found is > 0.8900, it can be said that the process for Cd^{2+} adsorption onto PMPSgLig can be described by both the Langmuir and Freundlich models. The findings here agree with what has been discussed on the adsorption isotherm onto PMPSgMMT (Figure 6.25). Freundlich correlation coefficients of < 0.8900 were obtained for the adsorption of Cd^{2+} onto lignocellulose, PMMAgLig and PMAAgLig. The low R^2 values suggest that the Freundlich model cannot adequately describe the adsorption process of Cd^{2+} onto these adsorbents though Unnithan, M. R. et al, 2002 and Kumar, U. et al, 2006 reported that values of $0.1 < 1/n < 1.0$ indicate favourable adsorption. In this study the slope ($1/n$) ranged from 0.36 to about 0.56.

The Langmuir model was used to determine the adsorption capacities of the lignocellulose based adsorbents and Figure 6.28 illustrates the adsorption capacity of each adsorbent in the form of a bar graph. It can be seen that PMAAgLig (67.11 mg/g) displayed the highest uptake of Cd^{2+} followed by PMPSgLig (22.99 mg/g), then PMMAgLig (15.17 g/g) and lastly the lignocellulose (14.51 mg/g). The increased uptake of Cd^{2+} onto PMPSgLig and PMAAgLig agrees with what was observed for Pb^{2+} adsorption (Section 6.4.2). There was no significant change in the adsorption of Cd^{2+} onto PMMA-grafted lignocellulose. Kumar, U. et al, 2006 investigated the adsorption of Cd^{2+} onto NaOH and sodium bicarbonate modified rice husk and found an increase in the adsorption capacity from about 8 mg/g to about 20 mg/g. Yu, J. et al, 2007 investigated the adsorption of Cd^{2+} and Pb^{2+} onto cysteine-modified fungi biomass and found an adsorption capacity of 11.63 mg/g for the adsorption of Cd^{2+}. Pavasant, P. et al, 2006 reported an adsorption capacity of 4.70 mg/g for Cd^{2+} adsorption onto marine green macroalgae (*Caulerpa lentillifera*).
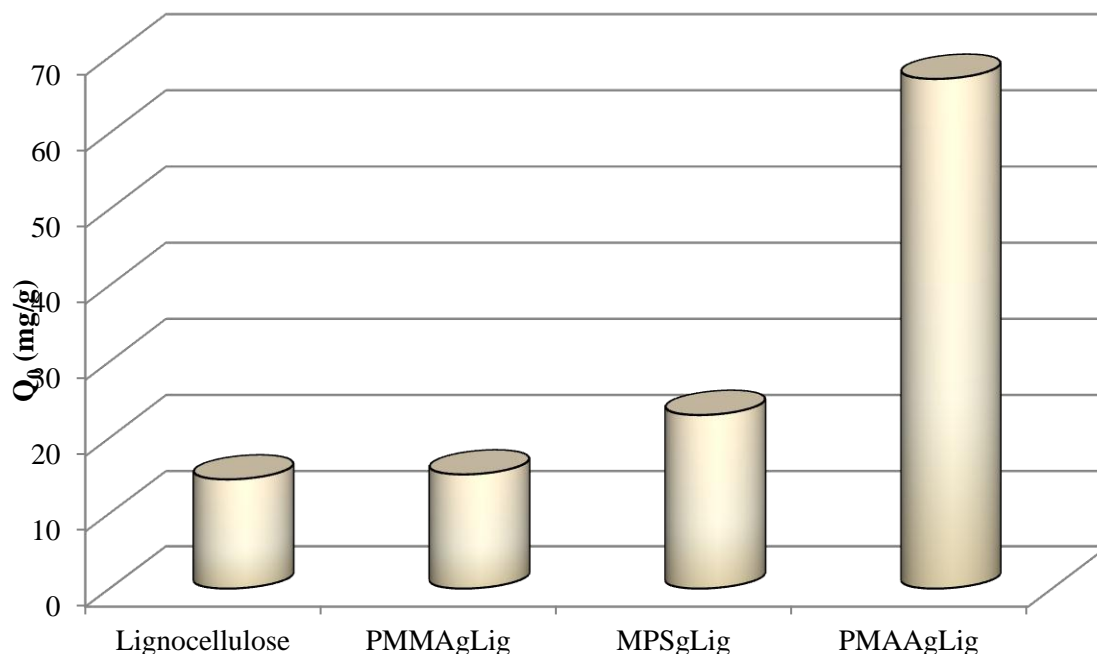
Figure 6.28: Adsorption capacities of lignocellulose based adsorbents for Cd^{2+}.

Sawalha, M. F. et al, 2006 reported a capacity of 2.24 for Cd^{2+} adsorption onto saltbush (*Atriplex canescens)* biomass. Li, Z. et al, 2006 found a capacity of 11.38 mg/g for Cd^{2+} adsorption onto heat treated yeast (*Rhodotorula* sp. Y11) biomass. Halttunen, T. et al, 2007 reported adsorption capacities ranging from 12.0 mg/g to 55.0 mg/g for Cd^{2+} onto lactic acid bacteria. Poly (methacrylic acid)-modified baker's yeast biomass showed an adsorption capacity of about 110 mg/g for Cd^{2+} (Yu, J. et al, 2007) whereas PMAAgLig gave about 67 mg/g. The differences can be attributed to the type of biomass and also adsorption conditions. The adsorption capacities found in this study are comparable with what has been previously reported in the literature for similar adsorbents.

6.3.4.2 Adsorption kinetics

Figure 6.29 displays the plots of adsorbed amount (mg/g) of Cd^{2+} onto the lignocellulose based adsorbents against time. It can be seen in Figure 6.28 that rapid adsorption of Cd^{2+} occurred within the first hour such that there was no observable change in the amount of Cd^{2+} adsorbed after the first 60 min. As explained above, the rapid adsorption in the first hour was attributed to the availability of a large number of adsorption sites on the adsorbent. As the sites were gradually filled up, adsorption became slow and the kinetics more dependent on the rate at which the adsorbate was transported from the bulk solution to the actual adsorption sites (Yu, R. et al, 2008). The plots in Figure 6.29 show that equilibrium was achieved within 3 h for all adsorbents.
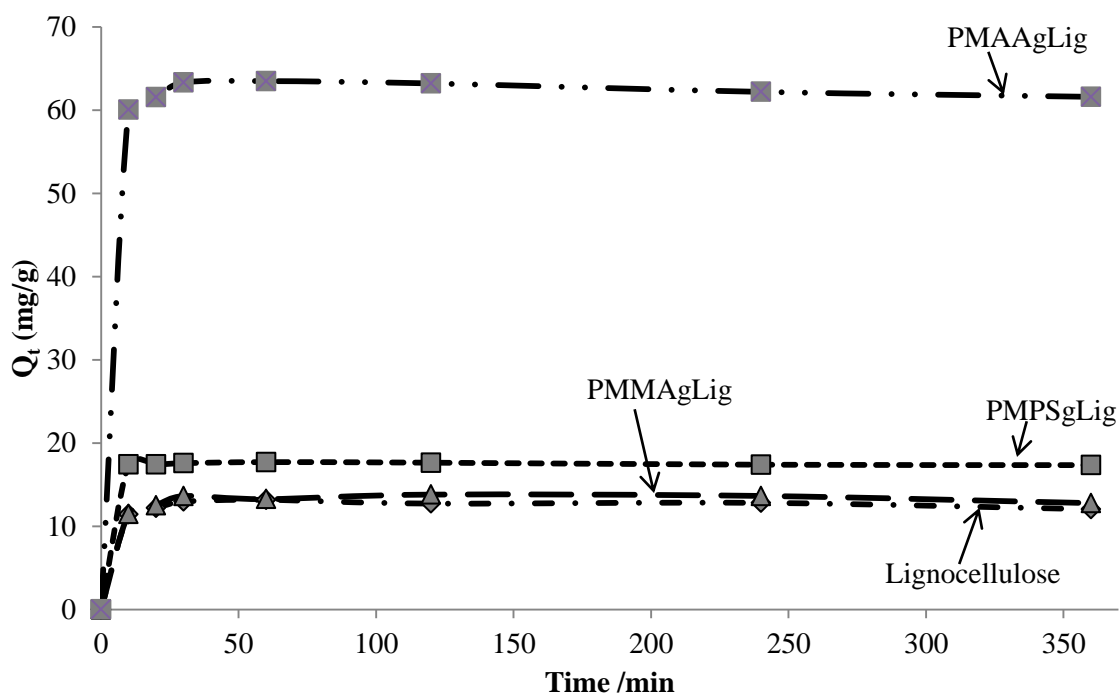
Figure 6.29: Plots of adsorbed amount (mg/g) of Cd^{2+} onto lignocellulose based adsorbents against time (min).

The experimental adsorption data were fitted to the two kinetic models, pseudo first-order and pseudo second-order models. Kinetic models are used to try and describe the mechanism of adsorption. Figure 6.30 displays the pseudo first-order plots for the adsorption of Cd^{2+} onto lignocellulose based adsorbents.

It can be seen that the data points of the pseudo first-order plots (Figure 6.30) are scattered compared with the pseudo second-order plots (Figure 6.31). This shows poor correlation between $Log\ (Q_e\text{-}Q_t)$ data and time for the pseudo first-order plots.
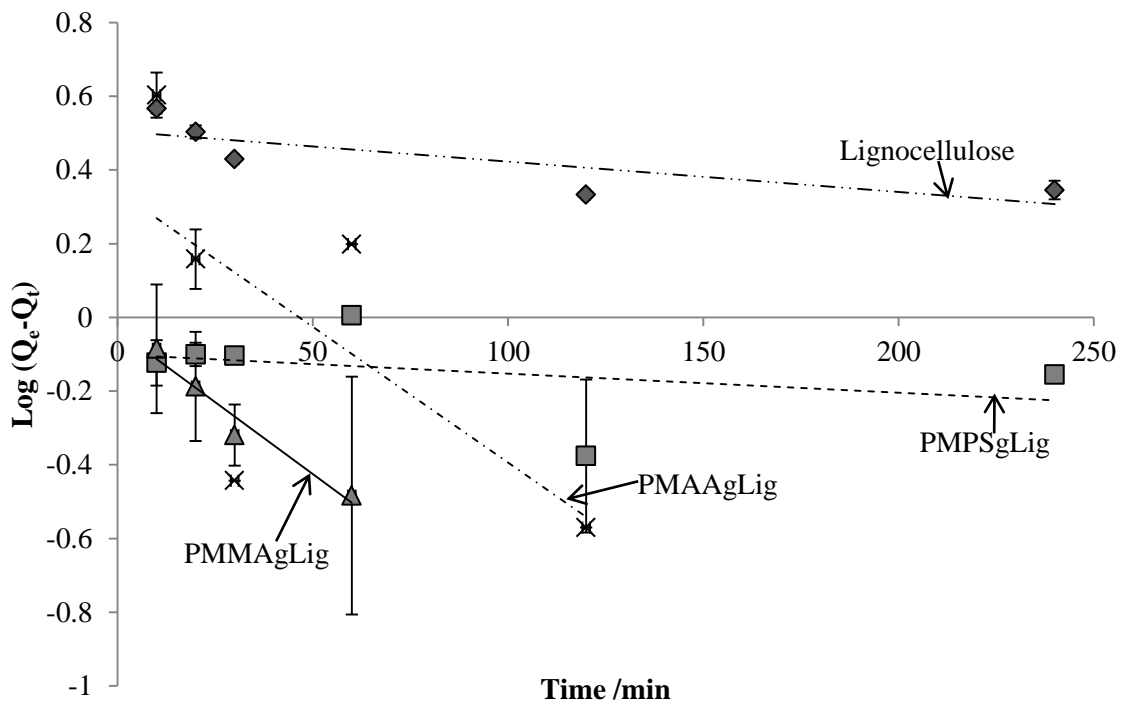
Figure 6.30: Pseudo first-order plots for the adsorption of Cd^{2+} onto lignocellulose based adsorbents.

Figures 6.31 shows the pseudo second-order plots for the adsorption of Cd^{2+} onto lignocellulose based adsorbents. The data points are not as scattered as observed for the pseudo first-order plots.
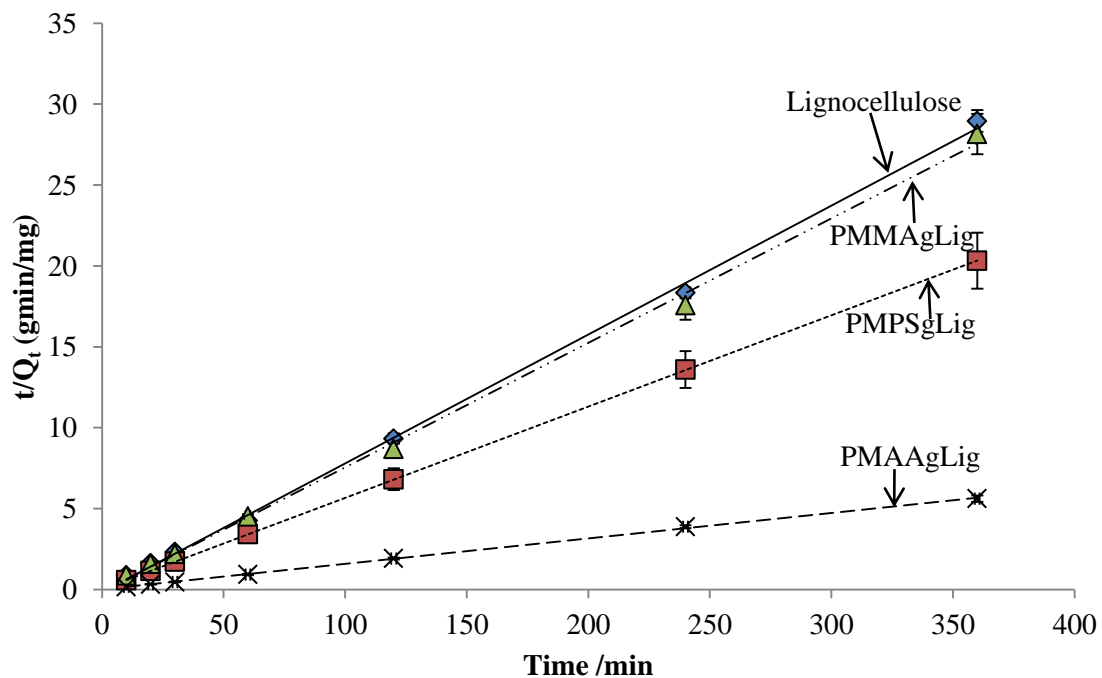
Figure 6.31: Pseudo second-order plots for the adsorption of Cd^{2+} onto lignocellulose based adsorbents.

The pseudo first-order and pseudo second-order parameters and the corresponding correlation coefficients (R^2) are shown in Table 6.8. The pseudo second-order model displayed quite high R^2 values (> 0.9900) compared with pseudo first-order model. This agrees well with what has been discussed for the adsorption of Cd^{2+} onto montmorillonite based adsorbents and also for the adsorption of Pb^{2+} onto both lignocellulose and montmorillonite based adsorbents.

Table 6.8: Pseudo first- and second-order parameters for the adsorption of Cd^{2+} onto lignocellulose based adsorbents.

Adsorbent	Model	Slope	R^2	Intercept	k_1/k_2	Q_e (mg/g)
Lignocellulose	1st	-0.0008	0.6425	0.5047	0.00184	3.197
	2nd	0.0796	0.9988	-0.1647	-0.03847	12.56
PMMAgLig	1st	-0.0078	0.9580	-0.0347	0.01796	0.923
	2nd	0.0769	0.9981	-0.1467	-0.0403	13.00
MPSgLig	1st	-0.0005	0.1300	-0.1007	0.00115	0.7930
	2nd	0.0564	1.0000	0.0337	0.0944	17.73
PMAAgLig	1st	-0.0074	0.4505	0.3427	0.01704	2.201
	2nd	0.0157	0.9995	0.0149	0.01654	63.69

The pseudo first-order R^2 values for the adsorption of Cd^{2+} onto lignocellulose (0.6425), PMPSgLig (0.1300) and PMAAgLig (0.4505) were very low, suggesting that the adsorption mechanism cannot be described by this model at all. Although the pseudo second-order model gave the highest R^2 values, negative rate constants (k_2) were obtained for Cd^{2+} adsorption onto lignocellulose and PMMAgLig, which might suggest a lack of conformity of the data to the pseudo second-order model for these adsorbents. A comparison of the kinetics Q_e values and the adsorption capacities (Q_0) from the isotherms showed that the Q_e values obtained were slightly lower than the Q_0 values.

The adsorption capacities obtained for Cd^{2+} uptake onto the lignocellulose adsorbents again showed lower uptake of Cd^{2+} compared with Pb^{2+}. Mobasherpour, I. et al, 2011 found a similar trend for the adsorption of Cd^{2+} and Pb^{2+} onto nano-crystallite hydroxyapatite from aqueous solution. The higher affinity of Pb^{2+} for the adsorbent was attributed to the smaller hydrated radius of Pb^{2+} and its low hydration energy (Pb^{2+} = -1481 kJ/mol) relative to the Cd^{2+} (-2106 kJ/mol). Pavasant, P. et al, 2006 also observed the same trend for Zn^{2+}, Cu^{2+}, Cd^{2+} and Pb^{2+} adsorption onto marine green macroalgae.

The next section presents the results obtained from the adsorption of both Cd^{2+} and Pb^{2+} onto polymer-grafted or coupled lignocellulose-montmorillonite nanocomposites. Four types of nanocomposites were prepared and these were: PMPS-grafted, PMMA-grafted, PMAA-grafted

nanocomposite and a physical mixture of lignocellulose and NaMMT. The physical mixture was prepared in the same way as the other polymer-grafted nanocomposites but without addition of any polymer.

6.3.5 Adsorption of Cd^{2+} and Pb^{2+} onto polymer-grafted lignocellulose-montmorillonite nanocomposites

It was hoped that the composites would display improved adsorption capacities compared with the raw starting materials (lignocellulose and montmorillonite) as well as the separately modified materials. The adsorption results of the separately modified materials (lignocellulose and montmorillonite) have already been discussed in Sections 6.3.1, 6.3.2, 6.3.3 and 6.3.4. A synergistic effect was observed for the composites of montmorillonite and granulated activated carbon as reported by Ake, C. L. et al, 2001. It was also expected that the lignocellulose-montmorillonite nanocomposites would show enhanced adsorption of organic pollutants from water as a result of similar synergy.

6.3.5.1 Adsorption isotherms of Pb^{2+} onto the lignocellulose-montmorillonite nanocomposites

Figure 6.32 displays the isotherms of Pb^{2+} adsorption onto the different polymer-grafted or coupled lignocellulose-montmorillonite nanocomposites. Due to the different extents of adsorption of Pb^{2+} onto the nanocomposite adsorbents, different C_e values were recorded.
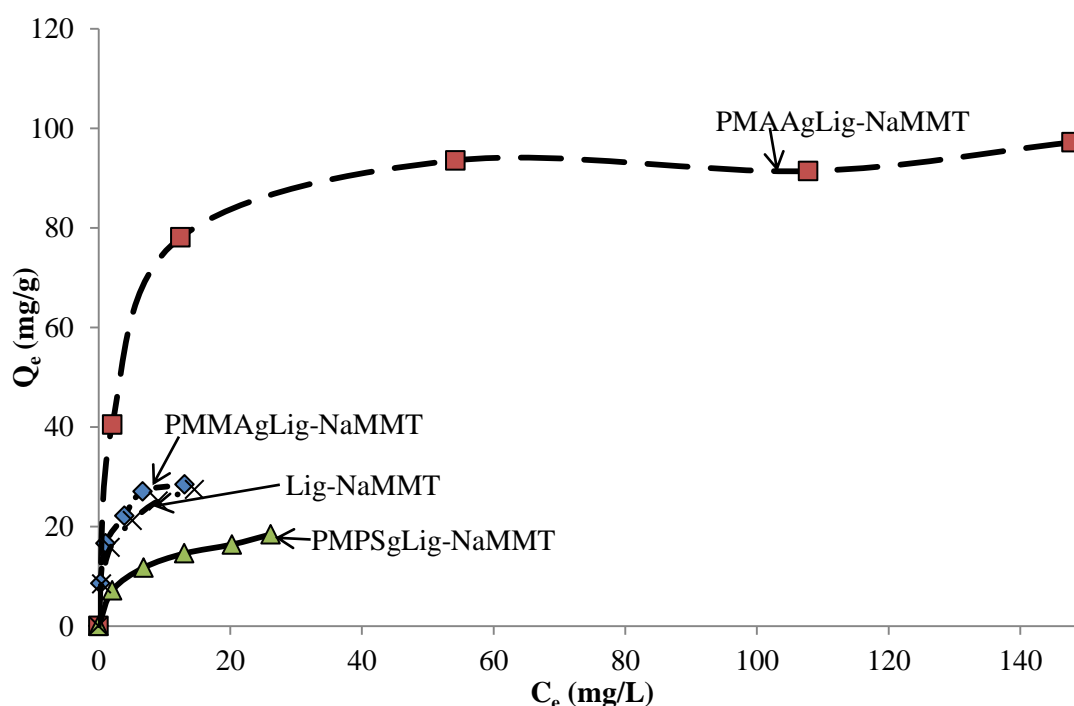
Figure 6.32: Isotherms of Pb^{2+} adsorption onto lignocellulose-montmorillonite nanocomposites.

The results in Section 6.3.4 showed that those materials modified with poly (methacrylic acid) gave the greatest improvement in the adsorption of heavy metals. The isotherms in Figure 6.32 also show that the highest amount of Pb^{2+} was adsorbed onto the PMAAgLig-NaMMT adsorbent.

PMPSgLig-NaMMT nanocomposite showed the least equilibrium amount of Pb^{2+} adsorbed. The amount of Pb^{2+} adsorbed onto LigNaMMT and PMMAgLig-NaMMT was more or less comparable. Again, using the classification system proposed by Giles, C. H. et al, 1960 and 1974; Hinz, C., 2001, all the isotherms can be said to follow the Langmuir model because of the concave shape of the isotherm at the beginning. The isotherms were classified into subgroups as follows: PMAAgLig-NaMMT (L_2), PMMAgLig-NaMMT (L_2), Lig-NaMMT (L_2) and PMPSgLig-NaMMT (L_3).

The adsorption data were processed further by fitting to the Langmuir and Freundlich equations discussed in Section 6.3.2. Figure 6.33 shows the Langmuir plots for the adsorption of Pb^{2+} onto the four nanocomposite adsorbents. The Freundlich plots are displayed in Figure 6.34.
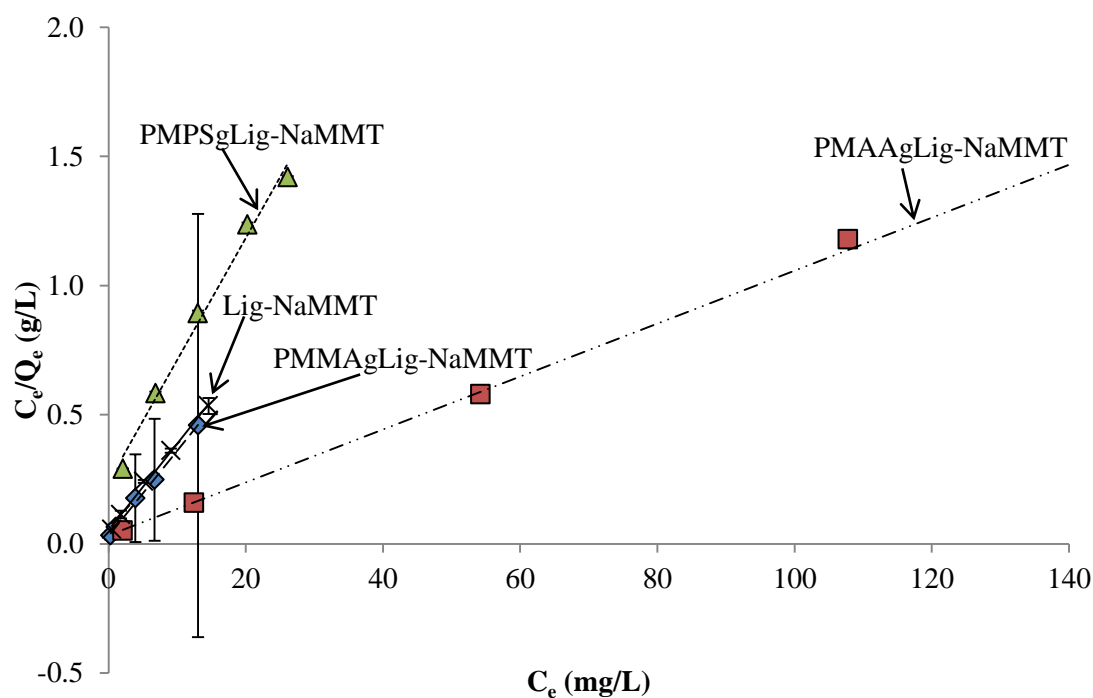
Figure 6.33: Langmuir plots for the adsorption of Pb^{2+} onto lignocellulose-montmorillonite nanocomposite adsorbents.
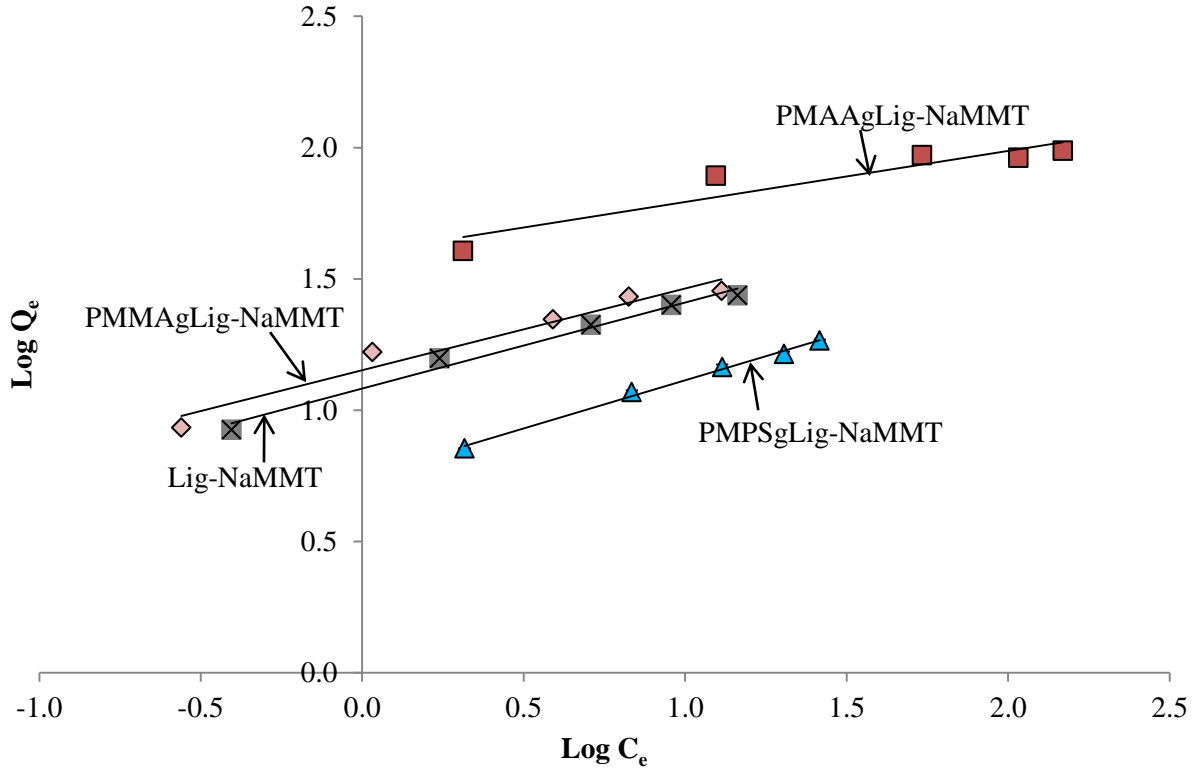
Figure 6.34: Freundlich plots for the adsorption of Pb^{2+} onto lignocellulose-montmorillonite nanocomposite adsorbents.

The Freundlich and Langmuir parameters and the correlation coefficients (R^2) are displayed in Table 6.9. The Langmuir R^2 values were greater than the Freundlich R^2 values for all the nanocomposite adsorbents except PMPSgLig-NaMMT.

Table 6.9: Freundlich and Langmuir parameters for the adsorption of Pb^{2+} onto lignocellulose-montmorillonite nanocomposite adsorbents.

Adsorbent	Isotherm	Slope	R^2	Q_0/K_f	Intercept	n/b
Lig-NaMMT	Langmuir	0.0335	0.9964	29.85	0.0537	0.6238
	Freundlich	0.3274	0.9842	12.09	1.0825	3.0544
PMMAgLig-NaMMT	Langmuir	0.0330	0.9969	30.30	0.0311	1.0611
	Freundlich	0.3116	0.9558	14.20	1.1524	3.2092
PMPSgLig-NaMMT	Langmuir	0.0471	0.9898	21.23	0.2401	0.1962
	Freundlich	0.3670	0.9948	5.585	0.7470	2.7248
PMAAgLig-NaMMT	Langmuir	0.0102	0.9985	98.04	0.0335	0.3045
	Freundlich	0.1937	0.8741	39.76	1.5994	5.1626

PMPSgLig-NaMMT nanocomposite showed a greater Freundlich R^2 value than was obtained for the Langmuir model. This might mean that the combination of lignocellulose, MPS and NaMMT had an

effect on the adsorption process in the PMPSgLig-NaMMT nanocomposite. The relatively high Langmuir and Freundlich R^2 values obtained for the adsorption of Pb^{2+} onto Lig-NaMMT, PMMAgLig-NaMMT and PMPSgLig-NaMMT nanocomposites might suggest that both models can be used to describe the adsorption process onto these adsorbents.

The Langmuir adsorption capacities were found to be 29.85 mg/g (Lig-NaMMT), 30.30 mg/g (PMMAgLig-NaMMT), 21.23 mg/g (PMPSgLig-NaMMT) and 98.04 mg/g (PMAAgLig-NaMMT). A look at the adsorption capacities obtained for the unmodified starting materials (lignocellulose – 31.25 mg/g and NaMMT – 30.03 mg/g) reveals that there was no improvement in the adsorption capacities found for the Lig-NaMMT and PMMAgLig-NaMMT nanocomposites. A decrease in the uptake of Pb^{2+} was recorded for the PMPSgLig-NaMMT nanocomposite. The higher adsorption capacity recorded for the PMAAgLig-NaMMT nanocomposite than either lignocellulose or NaMMT was attributed to the presence of grafted PMAA as observed with PMAAgLig and PMAAgMMT. It is not clear what caused the decrease recorded in the uptake of Pb^{2+} onto the PMPSgLig-NaMMT nanocomposite. PMPSgLig had an improved uptake of both Pb^{2+} and Cd^{2+} whereas PMPSgMMT had a reduced uptake of the same.

6.3.5.2 Adsorption kinetics of Pb^{2+} onto the lignocellulose-montmorillonite nanocomposites
Figure 6.35 displays the plots for the adsorbed amount (mg/g) of Pb^{2+} onto the lignocellulose-montmorillonite nanocomposites against time (min). The early stage of the adsorption process was characterized by a rapid uptake of Pb^{2+} onto all the nanocomposite adsorbents. There was no observable change in the adsorbed amount of Pb^{2+} from about an hour until 6 h for Lig-NaMMT, PMMAgLig-NaMMT and PMPSgLig-NaMMT nanocomposites. These systems reached equilibrium in about 3 h.

However, PMAAgLig showed a slight surge in the amount of Pb^{2+} adsorbed at 4 h which dropped to a relatively constant level. This can be attributed to the presence of other competing reactions in the vessel.
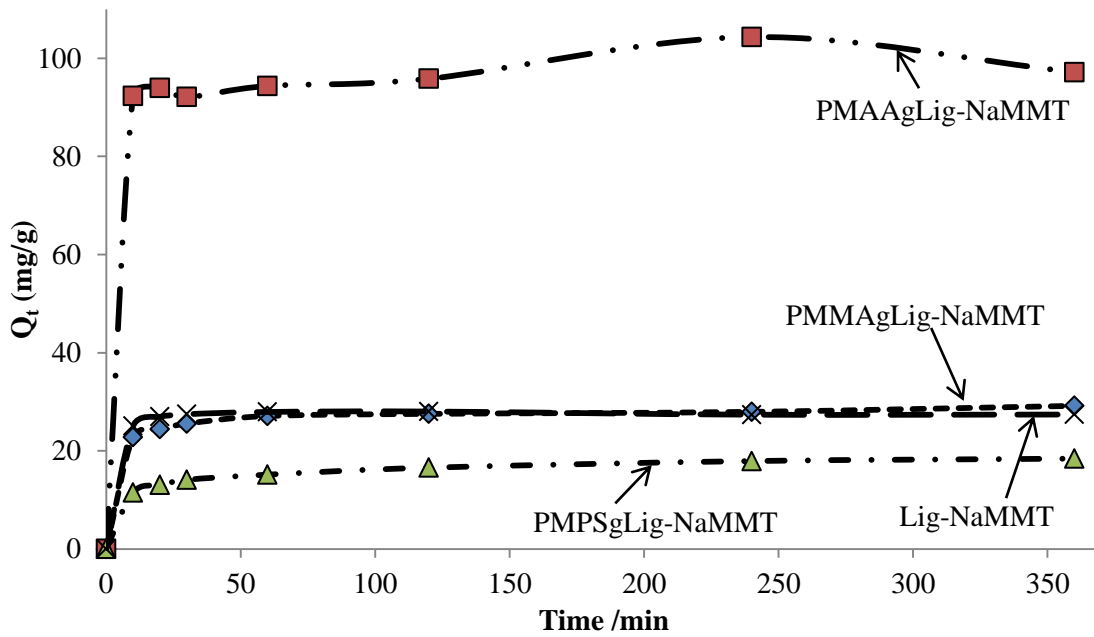
Figure 6.35: Plots of adsorbed amount (mg/g) of Pb^{2+} onto lignocellulose-montmorillonite nanocomposites.

The adsorption data was analysed by means of kinetic models, the pseudo first-order and pseudo second order models and Figure 6.36 shows the pseudo first-order plots.
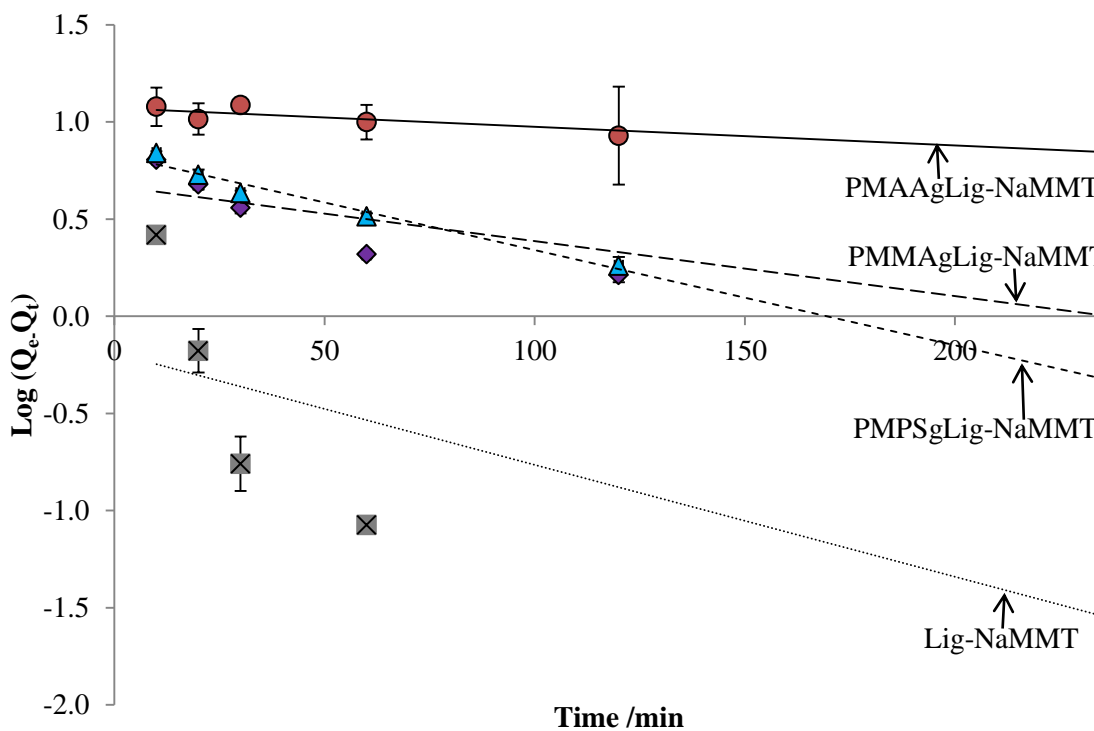
Figure 6.36: Pseudo first-order plots for the adsorption of Pb^{2+} onto lignocellulose-montmorillonite nanocomposites.

213

The plots of the pseudo second-order model for the adsorption of Pb^{2+} onto the nanocomposites are shown in Figure 6.37.
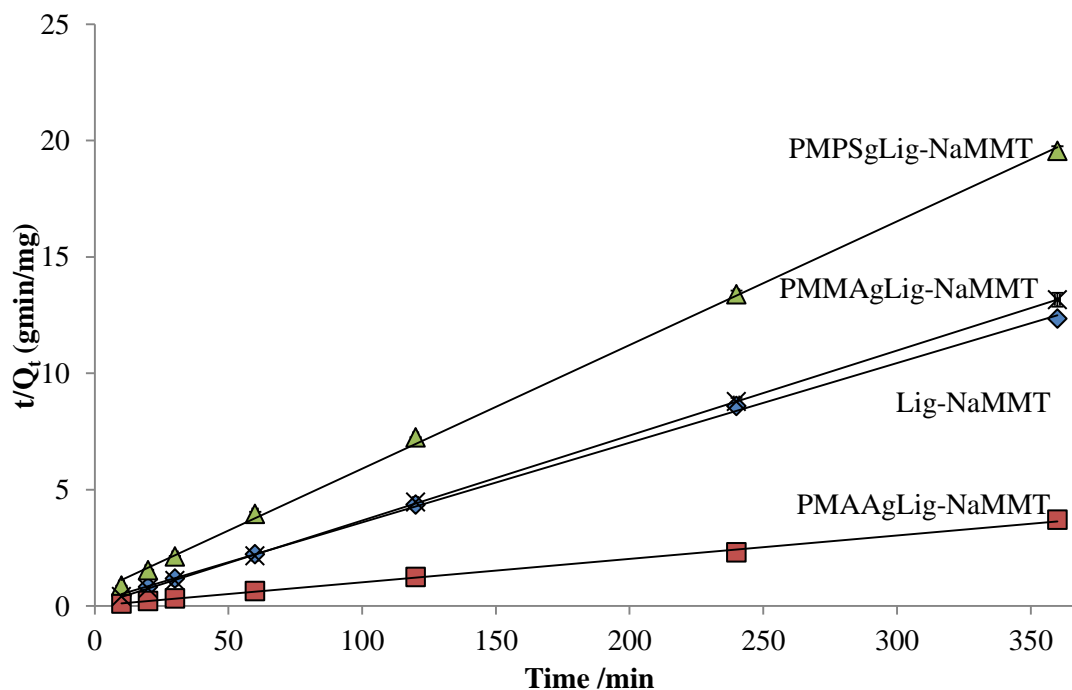
Figure 6.37: Pseudo second-order plot for the adsorption of lignocellulose-montmorillonite nanocomposites.

The parameters of the pseudo first-order model and the pseudo second-order model as well as the correlation coefficients are listed in Table 6.10.

Table 6.10: Pseudo first-order and pseudo second-order parameters for the adsorption of Pb^{2+} onto the lignocellulose-montmorillonite nanocomposites.

Adsorbent	Model	Slope	R^2	Intercept	k_1/k_2	Q_e (mg/g)
Lig-NaMMT	1st	-0.0058	0.5670	-0.1887	0.0134	0.6476
	2nd	0.0365	0.9999	0.0149	0.0894	27.40
PMMAgLig-NaMMT	1st	-0.0028	0.7788	0.6694	0.0064	4.671
	2nd	0.0343	0.9994	0.1680	0.0070	29.15
PMPSgLig-NaMMT	1st	-0.0049	0.9661	0.8315	0.0113	6.784
	2nd	0.0531	0.9993	0.5791	0.0049	18.83
PMAAgLig-NaMMT	1st	-0.0010	0.8809	1.0702	0.0023	11.75
	2nd	-0.0101	0.9979	0.0126	0.0081	99.01

As has been observed for the other adsorbents evaluated earlier, the pseudo second-order showed greater R^2 values than the pseudo first-order model. This means the adsorption mechanism for Pb^{2+} uptake onto the lignocellulose-montmorillonite adsorbents is best represented by the pseudo second-order model. PMPSgLig-NaMMT had also a relatively high pseudo first-order R^2 value (0.9661) and this means that this model can also be applied to describe the adsorption mechanism of Pb^{2+} onto this nanocomposite.

There was a relatively good agreement between the equilibrium adsorption capacities (Q_e) and Q_0 values from the Langmuir isotherm. This can be clearly seen in the plot of Q_e (mg/g) against Q_0 (mg/g) shown in Figure 6.38.
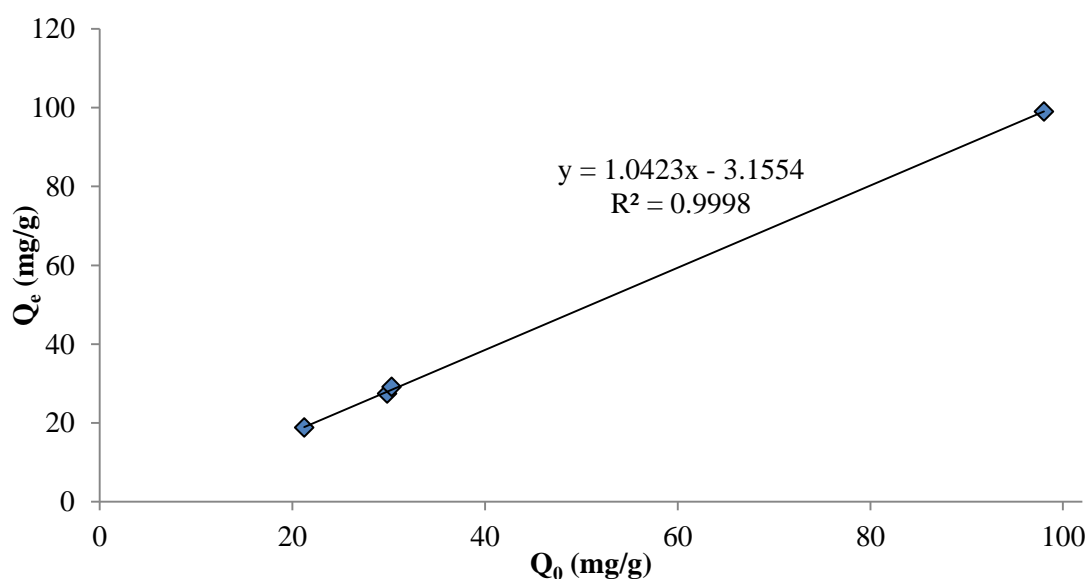
Figure 6.38: Correlation between Q_0 and Q_e values for the adsorption of Pb^{2+} onto lignocellulose-montmorillonite nanocomposites.

6.3.5.3 Adsorption isotherms of Cd^{2+} onto the lignocellulose-montmorillonite nanocomposites

The adsorption properties of the lignocellulose-montmorillonite nanocomposites were also evaluated using Cd^{2+} as a model pollutant. This section presents the results obtained from the adsorption of Cd^{2+} onto the lignocellulose-montmorillonite nanocomposite adsorbents. Figure 6.39 shows the isotherms for the adsorption of Cd^{2+} onto the lignocellulose-montmorillonite nanocomposites. Again, different C_e values were recorded for Cd^{2+} adsorption onto the nanocomposite adsorbents because of the different extents of adsorption of Cd^{2+} onto each adsorbent.

The isotherm for Cd^{2+} adsorption onto PMAAgLig-NaMMT can be classified as H-type of subgroup *mx* (H_{mx}) according to Giles, C. H. et al, 1960. The H-type isotherm is a special case of the Langmuir

type curve. The solute has a high affinity for the adsorbent such that in dilute solutions, it is completely adsorbed or there is a negligible amount of the solute remaining in solution.
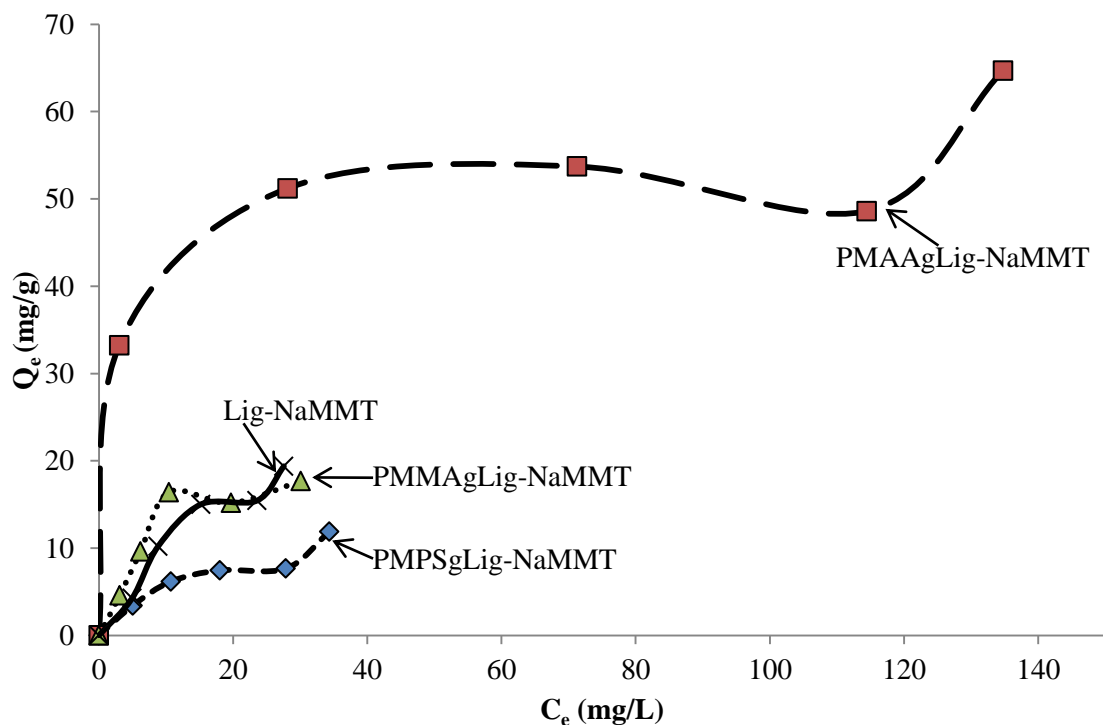
Figure 6.39: Isotherms of Cd^{2+} adsorption onto lignocellulose-montmorillonite nanocomposites.

Isotherms for Cd^{2+} adsorption onto PMMAgLig-NaMMT, Lig-NaMMT and PMPSgLig-NaMMT can all be classified as S curves of subgroup 3 (S_3). The initial curvature of this isotherm shows that adsorption becomes easier as the concentration rises. The S curve appears only when the solute is mono-functional, has moderate intermolecular attraction and meets strong competition for adsorption sites due to presence of impurities (Giles, C. H. et al, 1960 and 1974). It is difficult to imagine the presence of intermolecular attraction among the positively charged Cd^{2+} ions. The other two conditions are conceivable, most likely the third condition which can be a result of the presence of residual Na^+ from NaOH used to adjust the pH of the nanocomposite. However, it also begs the question why this was not observed with the adsorption of Pb^{2+}.

The data for the adsorption of Cd^{2+} onto the lignocellulose-montmorillonite nanocomposites were fitted to the Langmuir and Freundlich equations, the respective plots are shown in Figures 6.40 and 6.41.
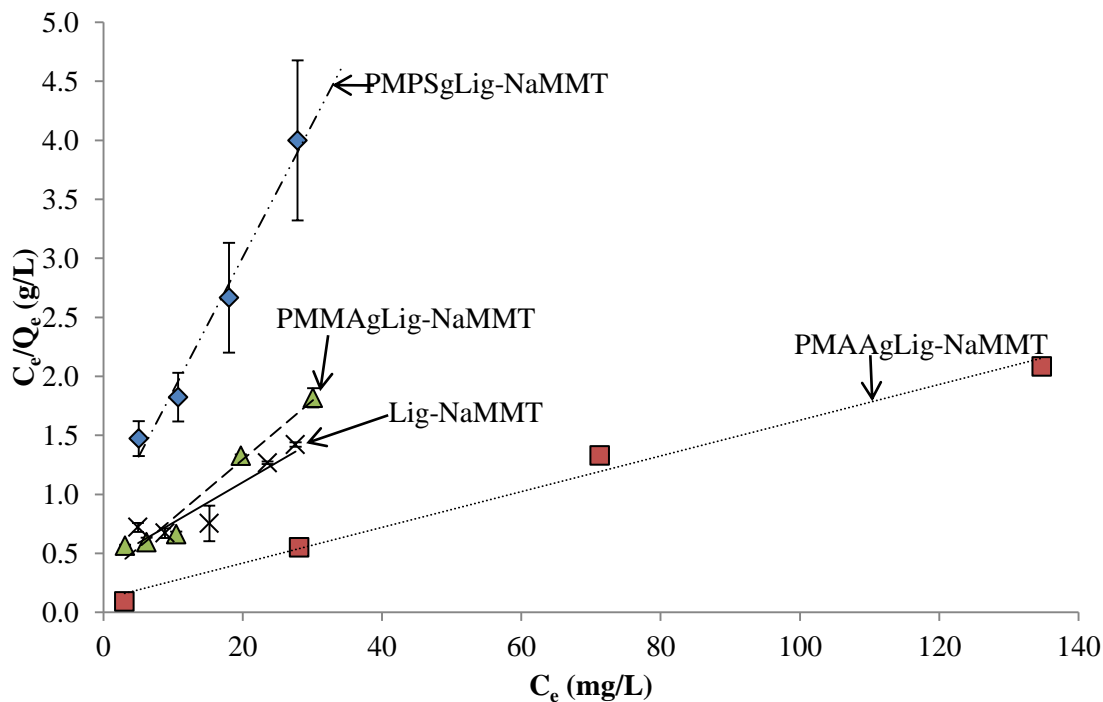
Figure 6.40: Langmuir plots for Cd^{2+} adsorption to lignocellulose-montmorillonite nanocomposites.
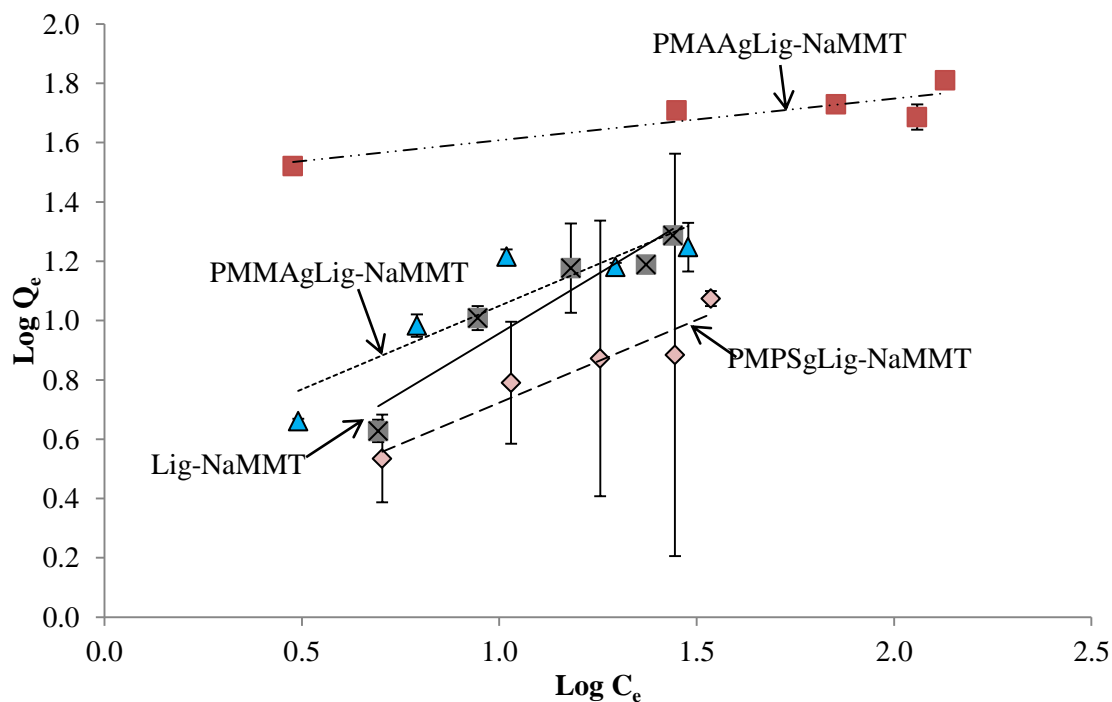
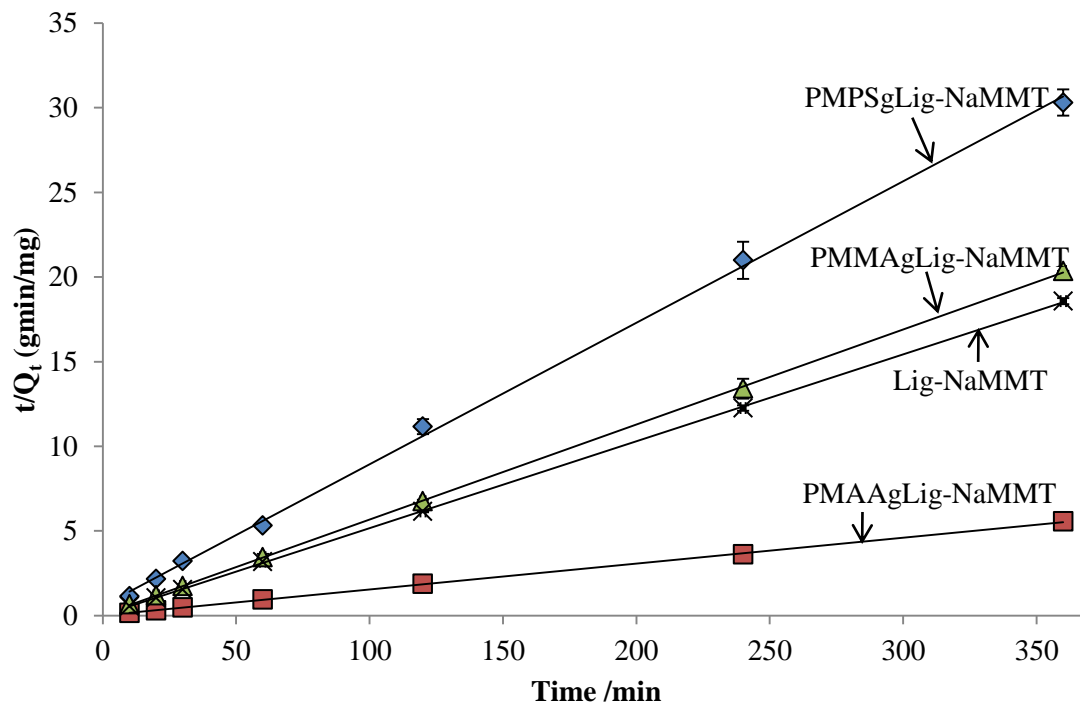Figure 6.41: Freundlich plots for Cd^{2+} adsorption to lignocellulose-montmorillonite nanocomposites.

The parameters and the correlation coefficients (R^2) of the Freundlich and Langmuir models are displayed in Table 6.11. The Langmuir R^2 values for the adsorbents, PMMAgLig-NaMMT (0.9679), PMPSgLig-NaMMT (0.9825) and PMAAgLig-NaMMT (0.9880) were greater than those of the Freundlich model. This showed that the adsorption data can best be represented by the Langmuir

model. The R^2 values were, however, relatively smaller than those obtained for Pb^{2+} adsorption onto the same adsorbents. The data for Cd^{2+} adsorption onto PMPSgLig-NaMMT can be represented by both the Freundlich and Langmuir models since the respective R^2 values are all > 0.8900.

Table 6.11: Freundlich and Langmuir parameters for Cd^{2+} adsorption onto lignocellulose-montmorillonite nanocomposites.

Adsorbent	Isotherm	Slope	R^2	Intercept	Q_0/K_f	n/b
Lig-NaMMT	Langmuir	0.0344	0.8786	0.4166	29.07	0.0826
	Freundlich	0.8001	0.9023	0.1563	1.433	1.250
PMMAgLig-NaMMT	Langmuir	0.0499	0.9679	0.2992	20.04	0.1668
	Freundlich	0.5632	0.8184	0.4860	3.062	1.776
PMPSgLig-NaMMT	Langmuir	0.1130	0.9825	0.7489	8.850	0.1509
	Freundlich	0.5568	0.9124	0.1664	1.467	1.796
PMAAgLig-NaMMT	Langmuir	0.0151	0.9880	0.1160	66.23	0.1302
	Freundlich	0.1409	0.8111	1.4671	29.32	7.097

For Cd^{2+} adsorption onto Lig-NaMMT, the Langmuir R^2 value (0.8786) was less than the Freundlich R^2 value (0.9023). The adsorption process here could best be described by the Freundlich model, which assumes multilayer adsorption onto a heterogeneous surface. The Langmuir capacity for Lig-NaMMT (29.07 mg/g) was much greater than found for lignocellulose (14.51 mg/g) and for NaMMT (18.73 mg/g) separately but since its Langmuir R^2 value was poor, the value could not be regarded as reliable. A decrease was observed in the uptake of Cd^{2+} onto PMPSgLig-NaMMT compared with lignocellulose and NaMMT. This agrees with what has been discussed above for Pb^{2+} adsorption onto PMPSgLig-NaMMT. The uptake of Cd^{2+} onto PMAAgLig-NaMMT (66.23 mg/g) was comparable to the uptake onto PMAAgLig (67.11 mg/g) and was much higher than uptake onto both lignocellulose and NaMMT. As discussed earlier, the high uptake can be ascribed to the presence of grafted PMAA in the two adsorbents. Overall, there was no improvement in Cd^{2+} adsorption onto the nanocomposites.

The following section presents the results for the kinetic studies of Cd^{2+} adsorption onto the lignocellulose-montmorillonite adsorbents.

6.3.5.4 Adsorption kinetics of Cd^{2+} onto the lignocellulose-montmorillonite nanocomposites
Figure 6.42 shows the plots of the adsorbed amount (mg/g) of Cd^{2+} onto the lignocellulose-montmorillonite adsorbents against time. The adsorption of Cd^{2+} onto PMAAgLig-NaMMT was characterized by rapid adsorption in the first 20 min, which was followed by desorption and the

adsorbed amount of Cd^{2+} remained relatively constant until 3 h. At 4 h, a slightly increased amount of Cd^{2+} was recorded followed by desorption to give a reduced amount of adsorbed Cd^{2+} at six hours. The same trend was observed for Pb^{2+} adsorption onto the same nanocomposite adsorbent (Figure 6.35).
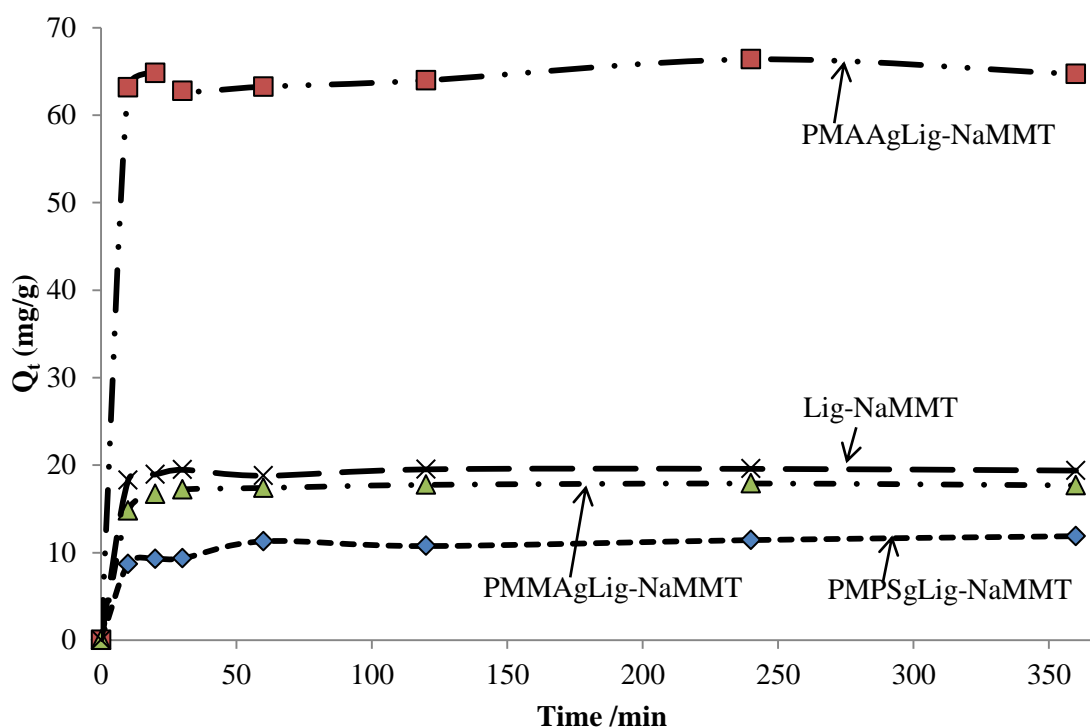
Figure 6.42: Plot of adsorbed amount (mg/g) of Cd^{2+} onto lignocellulose-montmorillonite nanocomposites against time (min).

Adsorption onto the other three nanocomposites was fairly straightforward with all systems reaching equilibrium in about three hours. According to the plots in Figure 6.42, the highest amount of Cd^{2+} was adsorbed onto PMAAgLig-NaMMT and the least onto PMPSgLig-NaMMT which agrees with what has been discussed in Section 6.3.5.3.

The adsorption data were fitted to the pseudo first order and pseudo second-order kinetic models. Figure 6.43 displays the pseudo first-order plots for Cd^{2+} adsorption onto lignocellulose-montmorillonite nanocomposites. The pseudo second-order plots are shown in Figure 6.44.
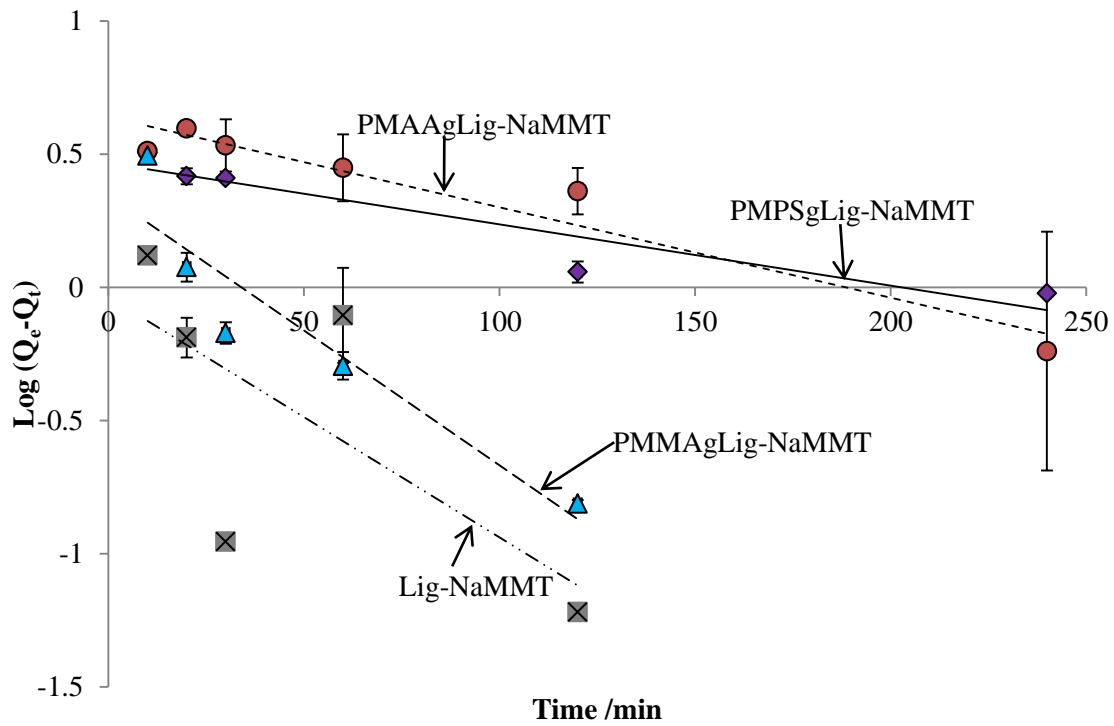
Figure 6.43: Pseudo first-order plots for Cd^{2+} adsorption onto lignocellulose-montmorillonite nanocomposites.

Figure 6.44: Pseudo second-order plots for Cd^{2+} adsorption onto lignocellulose-montmorillonite nanocomposites.

The pseudo first-order and pseudo second-order parameters and their correlation coefficients (R^2) values are displayed in Table 6.12. As can be seen from the table, the pseudo second-order R^2 values were greater than pseudo first-order R^2 values for all the adsorbents. Therefore, the mechanism of Cd^{2+} adsorption onto the lignocellulose-montmorillonite nanocomposites is best described by the pseudo second-order model. The adsorption of Cd^{2+} onto PMAAgLig-NaMMT could also be described by the pseudo first-order model since the R^2 value is > 0.8900.

Table 6.12: Pseudo first-order and pseudo second order parameters for Cd^{2+} adsorption onto lignocellulose-montmorillonite nanocomposites.

Adsorbent	Model	Slope	R^2	Intercept	k_1/k_2	Q_e (mg/g)
Lig-NaMMT	1st	-0.0090	0.4730	-0.0366	0.0207	0.9192
	2nd	0.0514	0.9999	0.0260	0.1016	19.46
PMMAgLig-NaMMT	1st	-0.0101	0.8736	0.3443	0.0233	2.210
	2nd	0.0561	0.9999	0.0654	0.0481	17.83
PMPSgLig-NaMMT	1st	-0.0023	0.8875	0.4665	0.0053	2.928
	2nd	0.0836	0.9990	0.5837	0.0120	11.96
PMAAgLig-NaMMT	1st	-0.0034	0.9355	0.6399	0.0078	4.364
	2nd	0.0153	0.9997	0.0112	0.0209	65.36

There was poor correlation between the equilibrium Q_e values (Table 6.12) and the Langmuir Q_0 values (Table 6.11) for Lig-NaMMT and PMPSgLig-NaMMT. A relatively good agreement was observed between the Q_e and Q_0 values for Cd^{2+} adsorption to PMAAgLig-NaMMT and PMMAgLig-NaMMT.

As mentioned earlier, Pb^{2+} showed higher adsorption capacities for the lignocellulose-montmorillonite nanocomposite adsorbents. This showed a higher affinity of Pb^{2+} for the nanocomposite adsorbents than Cd^{2+}. Lazarević, S. et al, 2007 found that higher metal electronegativity and hydrolysis constant lead to a higher tendency of the ion for specific adsorption. The metal electronegativities are 1.8 (Pb^{2+}) > 1.7 (Cd^{2+}), and the hydrolysis constants are 1.6×10^{-8} (Pb^{2+}) > 6.7×10^{-10} (Cd^{2+}). Therefore, Cd^{2+} is relatively more stable in solution and hence might show less affinity for specific adsorption onto solid surfaces. Similar results showing a high affinity of Pb^{2+} for solid adsorbents were reported by Holm, T. R. et al, 1994.

The next section presents the adsorption results for the uptake of both Cd^{2+} and Pb^{2+} onto AlpMMT prepared at different molar ratios.

6.3.6 Effect of OH/Al molar ratio on the adsorption of Cd^{2+} and Pb^{2+}

The variation of the adsorbed amount of both Cd (II) and Pb (II) onto AlpMMT samples of different OH/Al molar ratios was assessed according to the procedure in Section 6.1.3. Figure 6.45 displays the plots of the adsorbed amount of heavy metals against the OH/Al molar ratio of the Al-pillared clay. It was observed that the adsorbed amount of Cd^{2+} and Pb^{2+} gradually decreased with increase in the OH/Al molar ratio, with a rapid decline above a molar ratio of 2.0.
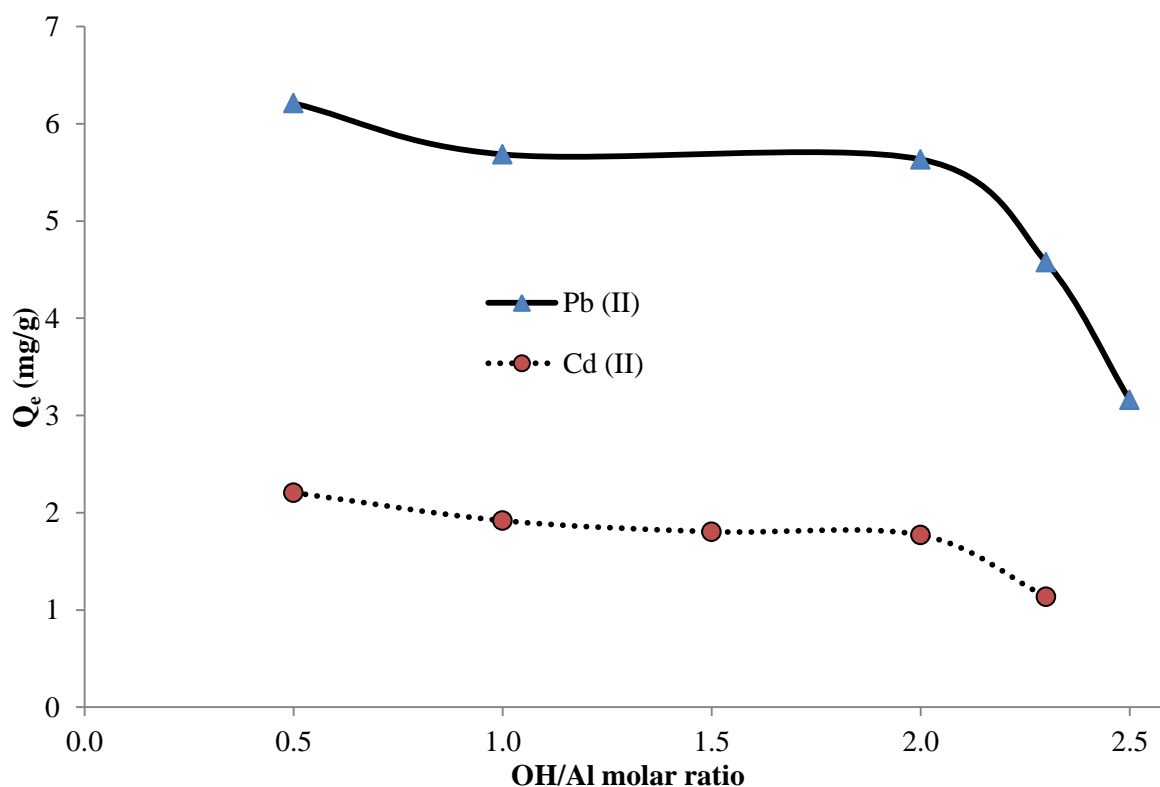
Figure 6.45: Variation of equilibrium adsorbed amount of Pb^{2+} and Cd^{2+} (mg/g) onto AlpMMT of different OH/Al molar ratio.

Elemental analysis of the Al-pillared samples was carried out using SEM-EDX in order to assess whether the amount of heavy metals adsorbed was related to the amount of Al incorporated into the clay structure as Al_2O_3 pillars. It was observed that as the amount of Al (%) incorporated increased and the amount of heavy metals adsorbed decreased.

To the best of our knowledge, we have not found any literature dealing with the assessment of adsorbed amount of heavy metals onto metal-pillared clay of different OH/M^{n+} ratio. The fact that the amount of heavy metals adsorbed decreased with increase in OH/Al^{3+} molar ratio, and that NaMMT had a higher adsorption capacity than AlpMMT might mean that metal-pillaring of clays for heavy metal adsorption purposes (from aqueous solution) is not a good method of choice.

The following section gives a brief discussion on the effect of chemical modification of the lignocellulose and montmorillonite based adsorbents on the amount of heavy metals adsorbed.

6.3.7 Effect of chemical modification on the adsorption of Cd^{2+} and Pb^{2+}

From the results presented thus far, it was seen that the modification of both lignocellulose and montmorillonite clay using methacrylic acid resulted in improved adsorption of both Cd^{2+} and Pb^{2+}. Modification of montmorillonite with MPS resulted in reduced uptake of both Cd^{2+} and Pb^{2+}. However, modification of lignocellulose with MPS improved the adsorption of both heavy metals, Cd^{2+} and Pb^{2+}. Grafting of MMA to montmorillonite resulted in improved adsorption of both Cd^{2+} and Pb^{2+} from aqueous solution. The modification of lignocellulose with MMA gave mixed results, with a slight improvement being recorded for the adsorption of Cd^{2+} and a decrease being recorded for Pb^{2+}.

The adsorbents, PMPSgLig, PMPSgMMT, PMAAgMMT, PMMAgLig and PMMAgMMT have not been reported before as possible adsorbents for both Cd^{2+} and Pb^{2+}. Studies in the literature related to the use of PMAA, MPS and MMT for adsorption are very few. One such study was by Wang, W. (2010) on the grafting of MPS-modified SiO_2 with PMAA and its use for the adsorption of Cd^{2+} from aqueous solution. Another study was by An, F. et al, 2009 and 2010 on the adsorption of phenol and aniline, respectively onto PMAA-grafted MPS-modified SiO_2. The adsorbent powders prepared in this study could be handled easily and their separation through filtration was found to be much easier compared with the NaMMT. There was also no problem with the clogging of membrane filters as observed with NaMMT.

The following section presents the results obtained from the competitive adsorption of both Pb^{2+} and Cd^{2+} onto PMMAgMMT. The procedure used for the competitive adsorption experiments has already been described in Section 6.1.4.

6.3.8 Competitive adsorption studies of Cd^{2+} and Pb^{2+} onto NaMMT and PMMAgMMT

The isotherms (Langmuir and Freundlich) and the kinetics plots (pseudo first-order and pseudo second-order) of both Cd^{2+} and Pb^{2+} adsorption onto NaMMT and PMMAgMMT from a Cd^{2+}-Pb^{2+} combined solution were generated.

6.3.8.1 Adsorption isotherms

Figure 6.46 displays the isotherms of Cd^{2+} adsorption onto both NaMMT and PMMAgMMT, as well as the isotherms for the adsorption of Pb^{2+} onto the same adsorbents. The isotherms for Cd^{2+} adsorption onto both NaMMT and PMMAgMMT were classified as Langmuir type 2. The isotherm

for Pb^{2+} adsorption onto PMMAgMMT was classified as Langmuir type 4 (L_4), while the isotherm for Pb^{2+} adsorption onto NaMMT was classified as Langmuir type *mx* (L_{mx}).
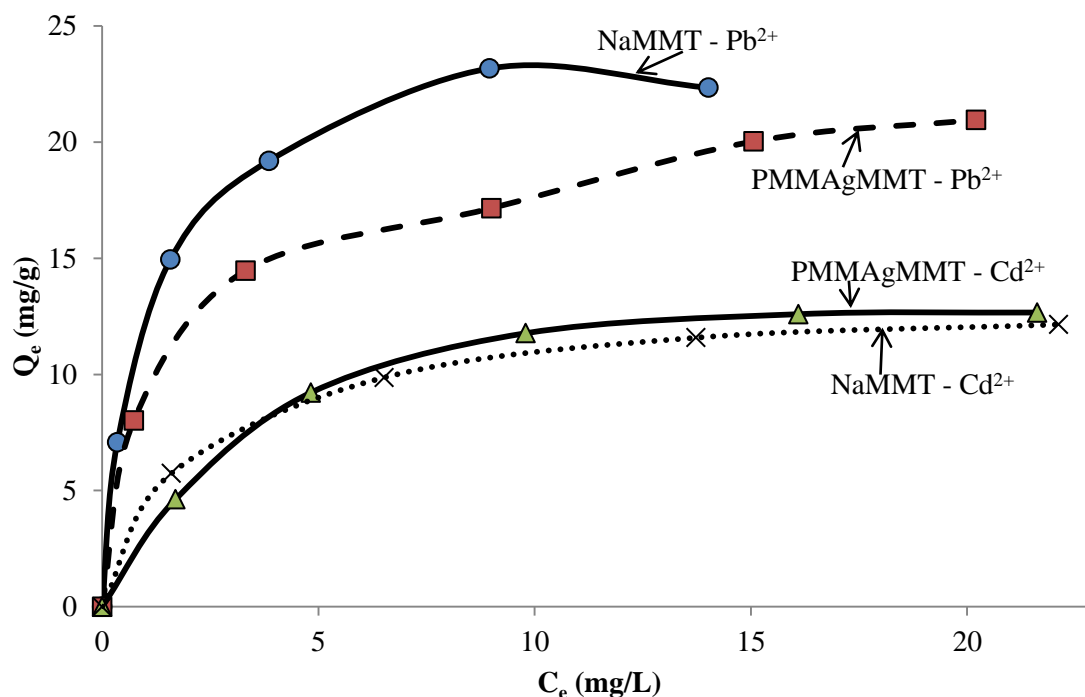
Figure 6.46: Isotherms for Cd^{2+} and Pb^{2+} adsorption onto NaMMT and PMMAgMMT from a Cd^{2+}-Pb^{2+} mixture.

From the isotherms in Figure 6.46, it can be seen that Pb^{2+} showed a higher adsorbed equilibrium amount (Q_e) onto both NaMMT and PMMAgMMT for the binary mixture. This agrees with what has been discussed above that Pb^{2+} has greater affinity for the adsorbents prepared in this study than Cd^{2+}. The presence of both heavy metals in solution did not significantly affect the adsorption process of each heavy metal from solution.

The adsorption data were fitted to the Langmuir equation and the Freundlich equation and the plots are presented in Figures 6.47 and 6.48, respectively. Figure 6.47 presents the Langmuir plots for Cd^{2+} and Pb^{2+} adsorption onto both NaMMT and PMMAgMMT from a Cd^{2+}-Pb^{2+} mixture.
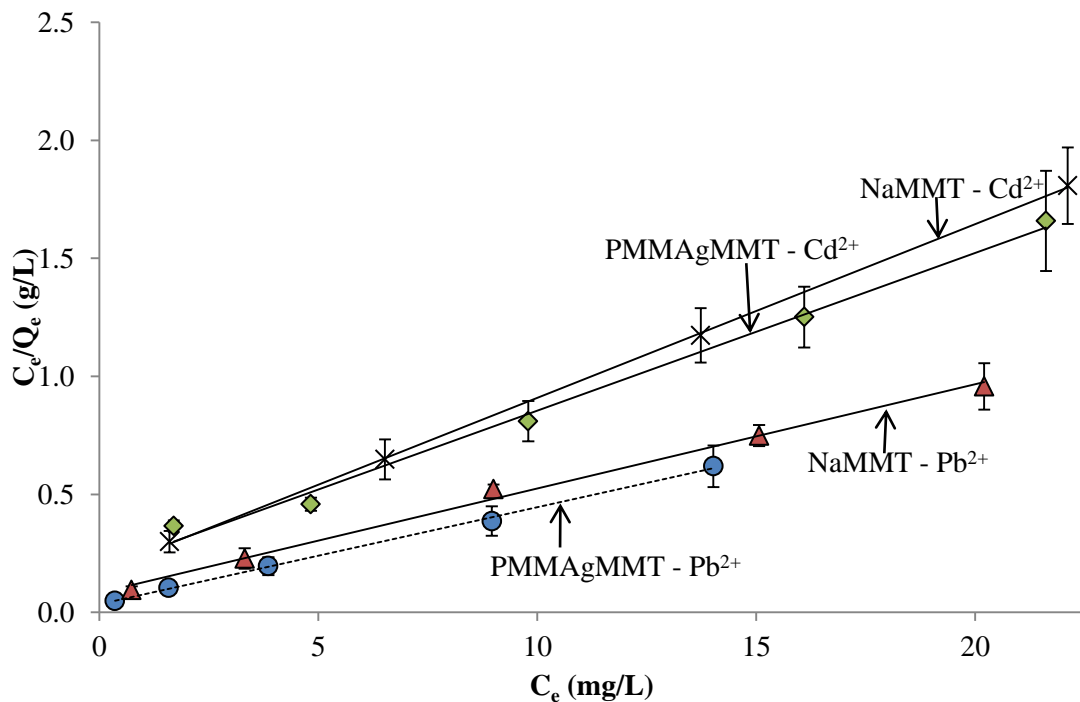
Figure 6.47: Langmuir plots for the adsorption of Cd^{2+} and Pb^{2+} onto NaMMT and PMMAgMMT from a Cd^{2+}-Pb^{2+} mixture.

Figure 6.48 presents the Freundlich plots for Cd^{2+} and Pb^{2+} adsorption onto both NaMMT and PMMAgMMT from a Cd^{2+}-Pb^{2+} mixture.
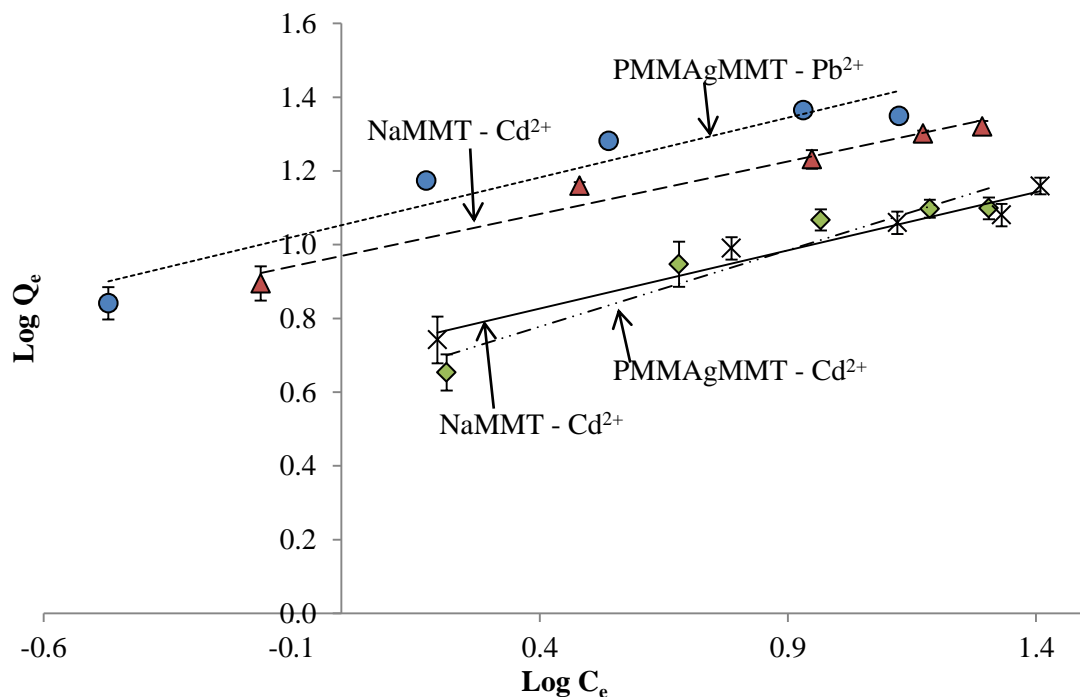
Figure 6.48: Freundlich plots for the adsorption of Cd^{2+} and Pb^{2+} to NaMMT and PMMAgMMT from a Cd^{2+}-Pb^{2+} mixture.

The Freundlich and Langmuir parameters for Cd^{2+} and Pb^{2+} adsorption onto NaMMT and PMMAgMMT from a Cd^{2+}-Pb^{2+} mixture are displayed in Table 6.13. The Langmuir model gave higher correlation coefficients (R^2) than the Freundlich model. From the Langmuir adsorption capacities, it was observed that slightly less Cd^{2+} was adsorbed onto PMMAgMMT than on NaMMT. This is contrary to what was observed for the adsorption of Cd^{2+} alone onto the same adsorbents, which gave a slightly higher adsorbed amount of Cd^{2+} for PMMAgMMT than NaMMT (Table 6.5). For Pb^{2+} adsorption, the trend observed for the adsorption of Pb^{2+} alone was maintained (Table 6.1).

Table 6.13: Freundlich and Langmuir parameters for the adsorption of Cd^{2+} and Pb^{2+} onto NaMMT and PMMAgMMT from a Cd^{2+}-Pb^{2+} mixture.

Adsorbent	Isotherm	Slope	R^2	Intercept	n/b	Q_0/K_f
			Cd (II)			
PMMAgMMT	Langmuir	0.0668	0.9927	0.1869	0.357	14.97
	Freundlich	0.4147	0.9237	0.6117	2.411	4.09
NaMMT	Langmuir	0.0637	0.9736	0.2455	0.259	15.70
	Freundlich	0.3161	0.9613	0.7001	3.164	5.01
			Pb (II)			
PMMAgMMT	Langmuir	0.0410	0.9984	0.0348	1.18	24.39
	Freundlich	0.3242	0.9161	1.0531	3.08	11.30
NaMMT	Langmuir	0.0441	0.9950	0.0836	0.53	22.67
	Freundlich	0.2846	0.9658	0.9692	3.51	9.32

It was observed that the amounts of each heavy metal adsorbed to both NaMMT and PMMAgMMT decreased when the two metals coexisted in solution. This reduction was attributed to the competition for the same adsorption sites by the two heavy metals. However, the adsorption capacities found for each heavy metal were still significant, thus making the nanocomposite material suitable for use in the treatment of heavy metals contaminated water.

6.3.8.2 Adsorption kinetics

Figure 6.49 shows the plots of adsorbed amount (mg/g) of Cd^{2+} and Pb^{2+} onto NaMMT and PMMAgMMT against time (min) from a combined solution. As was observed for similar plots discussed above, the systems reached equilibrium within 3 h. Again, the uptake of Pb^{2+} was clearly higher than the uptake of Cd^{2+} to both adsorbents.
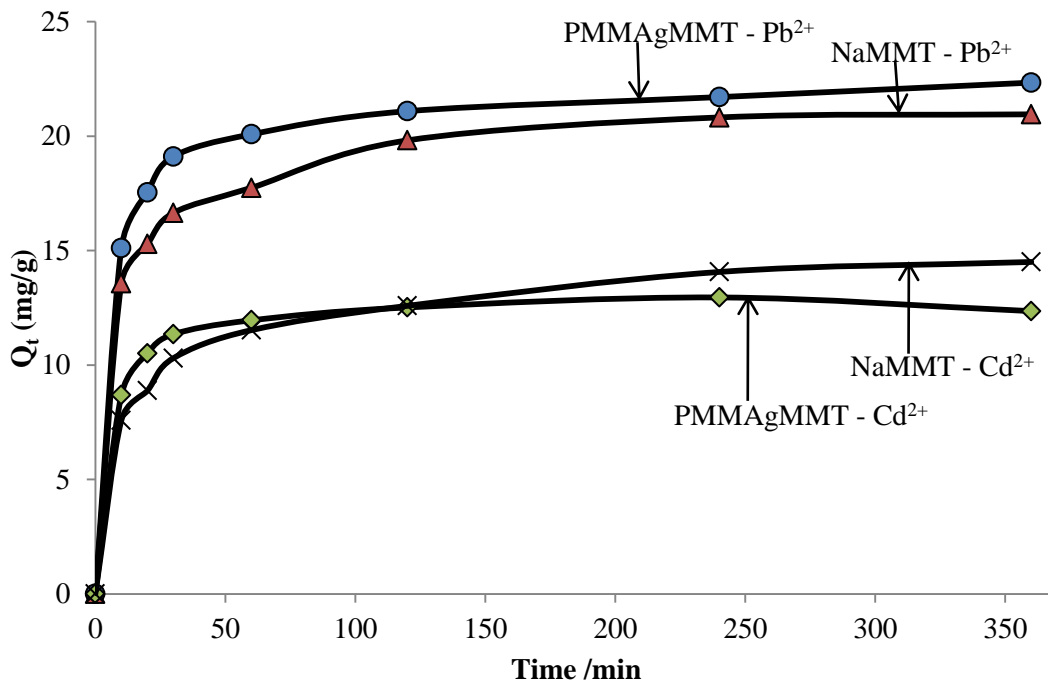
Figure 6.49: Plots of adsorbed amount (mg/g) of Cd^{2+} and Pb^{2+} onto NaMMT and PMMAgMMT from a combined Cd^{2+}-Pb^{2+} mixture against time (min).

The adsorption data were fitted to the pseudo first-order and pseudo second-order equations. The pseudo first-order and pseudo second-order plots are shown in Figures 6.50 and 6.51.
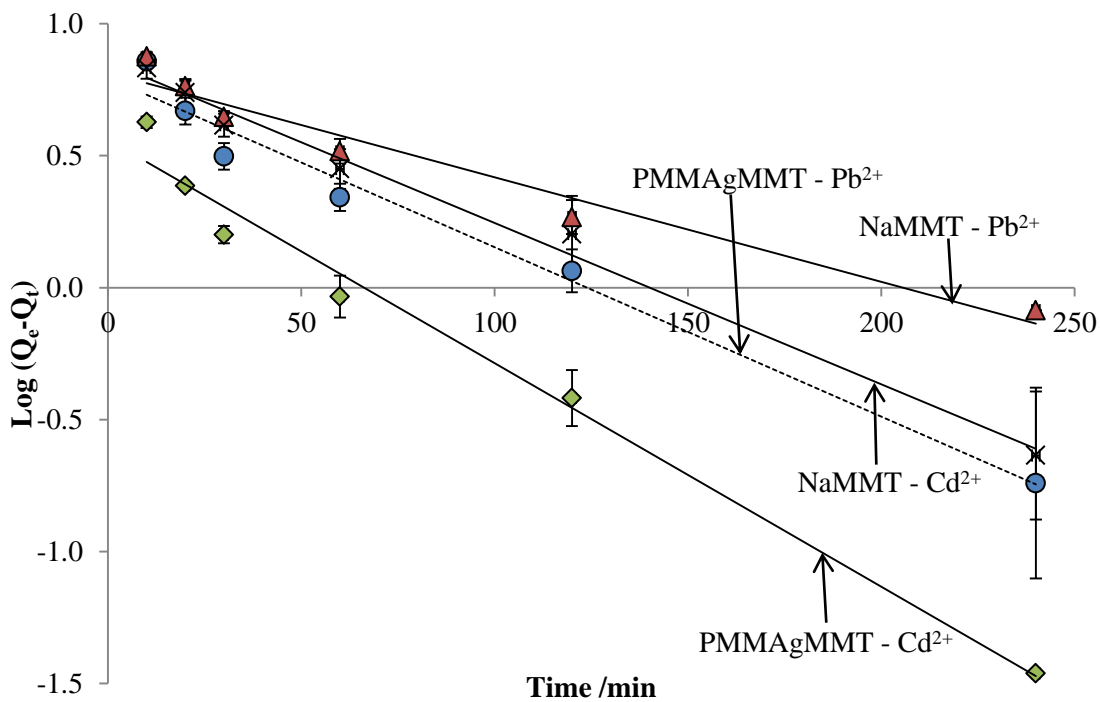
Figure 6.50: Pseudo first-order plots for Cd^{2+} and Pb^{2+} adsorption onto NaMMT and PMMAgMMT from a Cd^{2+}-Pb^{2+} mixture.
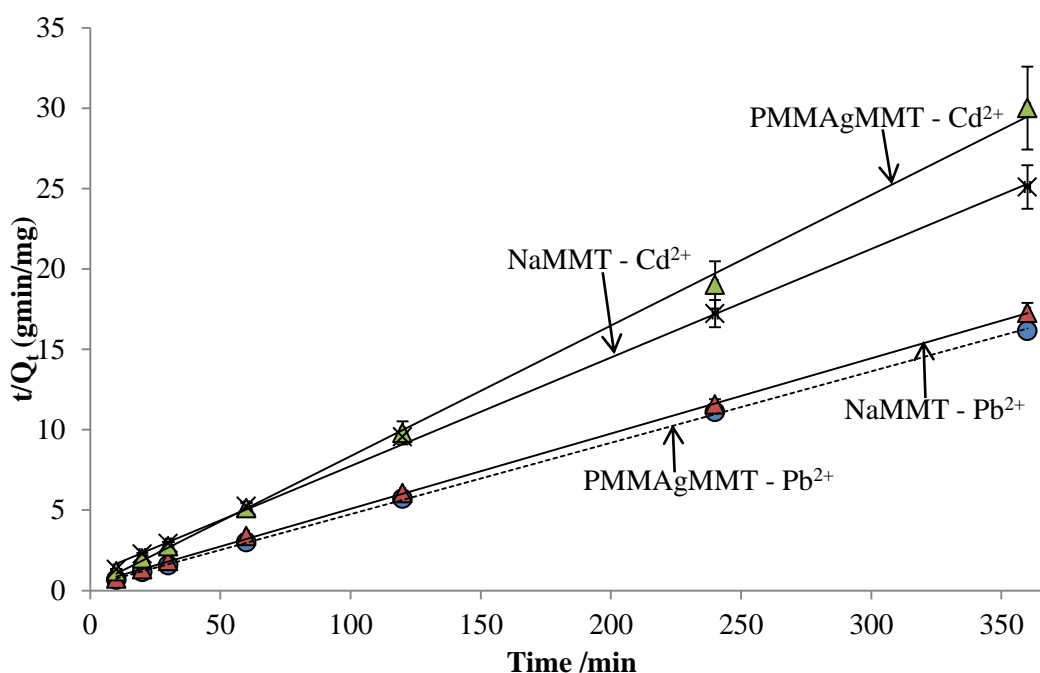
Figure 6.51: Pseudo second-order plots for Cd^{2+} and Pb^{2+} adsorption onto NaMMT and PMMAgMMT from a Cd^{2+}-Pb^{2+} mixture.

The parameters for the pseudo first-order and pseudo second-order models are displayed in Table 6.14. The pseudo second-order model had the highest R^2 values for both metal ions. However, the pseudo first-order R^2 were relatively high (> 0.9600) showing that the data can be described by both models.

Table 6.14: Pseudo first-order and pseudo secong-order parameters for the competitive adsorption of Cd^{2+} and Pb^{2+} onto NaMMT and PMMAgMMT from a Cd^{2+}-Pb^{2+} mixture.

Adsorbate	Adsorbent	Slope	R^2	Intercept	k_1/k_2	Q_e (mg/g)
			Pb (II)			
NaMMT	1st	-0.0040	0.9608	0.8139	0.009212	6.24
	2nd	0.0468	0.9998	0.4087	0.005359	21.37
PMMAgMMT	1st	-0.0064	0.9796	0.7950	0.01474	6.24
	2nd	0.0444	0.9997	0.2983	0.00661	22.52
			Cd (II)			
NaMMT	1st	-0.0061	0.9908	0.8561	0.014048	7.18
	2nd	0.0675	0.9991	0.9911	0.004597	14.81
PMMAgMMT	1st	-0.0085	0.9847	0.5609	0.01958	3.34
	2nd	0.0813	0.9988	0.2331	0.028356	12.30

As discussed in Section 6.3.8.1, a lower adsorption capacity was obtained for Cd^{2+} adsorption onto PMMAgMMT than for NaMMT. Both the Q_e and Q_0 values obtained from kinetics and isotherms, respectively, confirm this. However, for the adsorption of Pb (II), PMMAgMMT still showed a relatively higher adsorption capacity than NaMMT. The equilibrium adsorbed amount of Pb (II) calculated from the kinetics and isotherms support this deduction.

6.3.9 Desorption studies

Figure 6.52 displays the plots for Cd^{2+} and Pb^{2+} adsorbed onto PMMAgMMT against the number of regeneration cycles. The regeneration was carried out with 80 mL of 0.1 M HNO_3 and the adsorbent washed repeatedly with water until the pH of the filtrate or washings was about 5.0. It was observed that the amount of both Cd^{2+} and Pb^{2+} adsorbed (mg/g) decreased with increase in the number of regeneration cycles. Pb^{2+} uptake decreased by about 27% while Cd^{2+} uptake decreased by about 23% after three regeneration cycles.
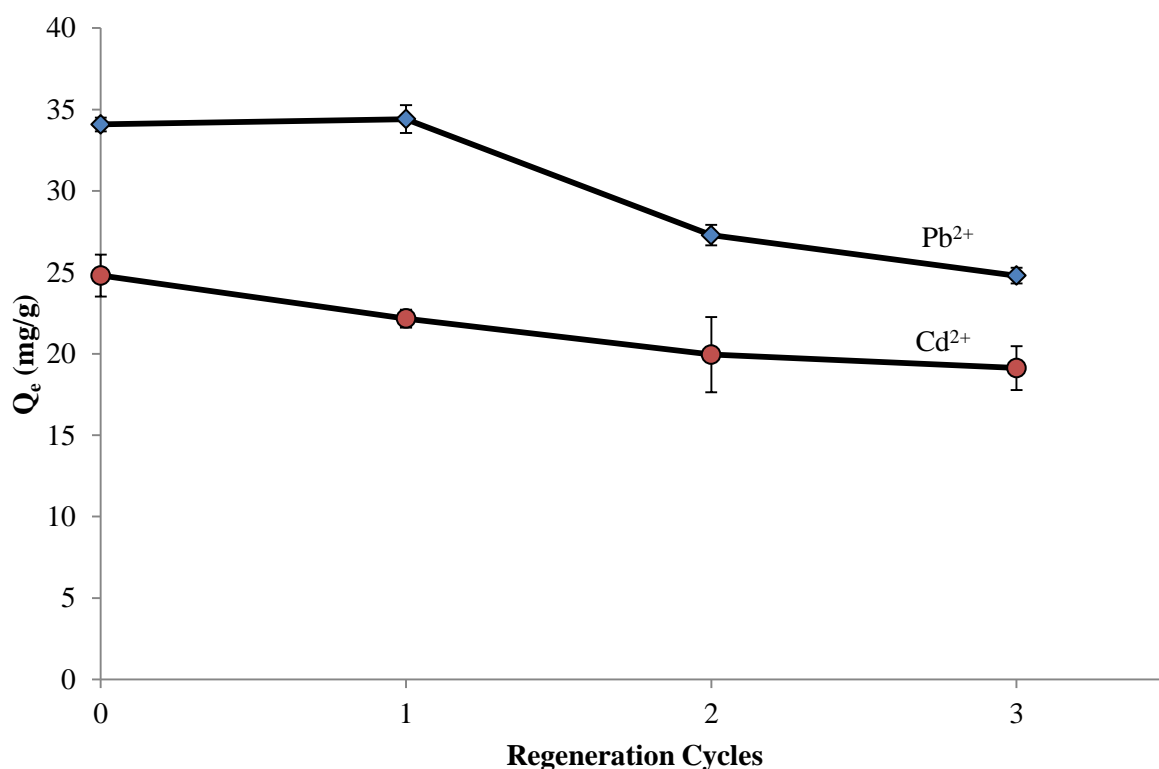
Figure 6.52: Plots of Cd^{2+} and Pb^{2+} adsorbed onto PMMAgMMT against the number of regeneration cycles.

The slight decrease in the uptake of the two heavy metals might suggest that PMMAgMMT can be used repeatedly for a couple of regeneration cycles without a significant loss in the adsorption capacity, which was one of the objectives of the study. The desorption experiments of Pb^{2+} from

229

PMMAgMMT showed that up to 96% of the adsorbed amount could be desorbed by using 80 mL of 0.1 M HNO$_3$, while 100% of Cd^{2+} could be desorbed. The differences may be due to the differences in the affinity of the metal ions for the adsorbent.

6.4 Conclusion

The grafting of montmorillonite clay with methyl methacrylate (MMA) and methacrylic acid (MAA) resulted in enhanced adsorption of both Cd^{2+} and Pb^{2+} from solution. Modification with MPS caused a decrease in the adsorption capacity for both Cd^{2+} and Pb^{2+}. The modification of NaMMT through aluminium-pillaring caused a drastic decrease in the adsorption capacity of the clay, showing that this type of clay modification is not suitable for the adsorption of heavy metals. Modification of lignocellulose with methacryloxypropyl trimethoxysilane and methacrylic acid resulted in improved uptake of both heavy metals from solution. The grafting of lignocellulose with methyl methacrylate did not result in enhanced adsorption.

The nanocomposites did not show improved adsorption capacity for both Cd^{2+} and Pb^{2+} except for PMAAgLig-NaMMT. The amount of Cd^{2+} and Pb^{2+} adsorbed onto the other nanocomposites was comparable with that of the separately modified adsorbents. The compounding of lignocellulose and montmorillonite did not show the expected synergy in the adsorption of heavy metals. The improvement observed in the adsorption capacity of the PMAAgLig-NaMMT nanocomposite relative to the raw lignocellulose and NaMMT was due to the presence of attached PMAA groups.

Pb^{2+} was observed to have a higher affinity for most of the adsorbents prepared and evaluated in this study. Relatively higher correlation coefficients (isotherms and kinetic models) were obtained for Pb^{2+} adsorption onto almost all the adsorbents than were obtained for Cd^{2+} adsorption. The higher affinity of Pb^{2+} than Cd^{2+} for the adsorbents was attributed to the differences in their hydration energies as well as the radii of their hydrated ions.

The Langmuir model showed higher correlation coefficients than the Freundlich model for most adsorbents evaluated in this study. The adsorption process of Cd^{2+} and Pb^{2+} from aqueous solution onto the prepared adsorbents could best be described by the Langmuir model. As such, the adsorption capacities of all the adsorbents reported in this chapter were computed using the Langmuir equation. The pseudo second-order model gave consistently high R^2 values for all the adsorbents, and there was a good correlation between the Langmuir adsorption capacities and the pseudo second-order equilibrium adsorbed amount (Q_e). Therefore, Q_e values derived from the pseudo second-order could be used to compute adsorption capacities for all the adsorbents evaluated in this study.

Competitive adsorption results showed a decrease in the uptake of both heavy metals due to competition for the same adsorption sites (the number of which is fixed). The co-adsorption of Cd^{2+} and Pb^{2+} from solution did not significantly affect the adsorption process of each and the mechanism of adsorption. The data from the competitive adsorption studies still could be best represented by the Langmuir model (isotherms) and pseudo second-order model (kinetics).

The adsorption capacities found for most of the adsorbents evaluated in this study for the adsorption on Cd^{2+} and Pb^{2+} were comparable to those reported in the literature. Desorption studies showed that some of the adsorbents could be regenerated by using 0.1 M HNO_3 without significant loss in the adsorption capacity.

6.5 References

1. Abollino, O.; Aceto, M.; Malandrino, M.; Sazarnini, C.; Mentasti, E. Adsorption of heavy metals onto Na-montmorillonite: Effect of pH and organic substances. *Water Research*, **2003**, *37*, 1619–1627.

2. Ake, C. L.; Mayura, K.; Huebner, H.; Bratton, G. R.; Phillips, T. D. Development of porous clay-based composites for the sorption of lead from water. *Journal of Toxicology and Environmental Health, Part A*, **2001**, *63*, 459–475.

3. Altunlu, M.; Yapar, S. Effect of OH^-/Al^{3+} and Al^{3+}/clay ratios on the adsorption properties of Al-pillared bentonites. *Colloids and Surfaces A: Physicochemical and Engineering Aspects,* **2007**, *306,* 88-94.

4. An, F.; Feng, X.; Gao, B. Adsorption property and mechanism of composite adsorbent $PMAA/SiO_2$ for aniline. *Journal of Hazardous Materials*, **2010**, *178*, 499–504.

5. An, F.; Gao, B.; Feng, X. Adsorption mechanism and property of novel composite material $PMAA/SiO_2$ towards phenol. *Chemical Engineering Journal*, **2009**, *153*, 108–113.

6. Annadurai, G.; Juang, R. S.; Lee, D. J. Use of cellulose-based wastes for adsorption of dyes from aqueous solutions. *Journal of Hazardous Materials*, **2002**, *B92*, 263–274.

7. Benmaarmar, Z.; Bengueddach, A. Correlation with different models for adsorption isotherms of m-xylene and toluene on zeolites. *Journal for Applied Sciences in Environmental Sanitation*, **2007**, *2* (2), 43-56.

8. Cooper, C.; Jiang, J. Q.;_Ouki, S. Preliminary evaluation of polymeric Fe- and Al-modified clays as adsorbents for heavy metal removal in water treatment. *Journal of Chemical Technology and Biotechnology*, **2002**, *77*, 546-551.

9. Delval, F.; Crini, G.; Morinc, N.; Vebrel, J.; Bertini, S.; Torri, G. The sorption of several types of dye on crosslinked polysaccharides derivatives. *Dyes and Pigments*, **2002**, *53*, 79–92.

10. Donat, R.; Akdogan, A.; Erdem, E.; Cetisli, H. Thermodynamics of Pb^{2+} and Ni^{2+} adsorption onto natural bentonite from aqueous solutions. *Journal of Colloid and Interface Science*, **2005**, *286*, 43–52.

11. Farag, S.; Kareem, S. S. A. A. Different natural biomasses for lead cation removal. *Carbohydrate Polymers*, **2009**, *78* (2), 263-267.

12. Foo, K. Y.; Hameed, B. H. Insights into the modeling of adsorption isotherm systems. *Chemical Engineering Journal*, **2010**, *156*, 2–10.

13. Giles, C. H.; D'silva, A. P.; Easton, I. A. A General Treatment and Classification of the Solute Adsorption Isotherm Part II. Experimental Interpretation. *Journal of Colloid and Interface Science,* **1974**, *47* (3), 766-778.

14. Giles, C. H.; Macewans, T. H.; Nakhwa, N.; Smith, D. Studies in adsorption Part XI. A system of classification of solution adsorption isotherms, and its use in diagnosis of adsorption mechanisms and in measurement of specific surface areas of solids. *Journal of Chemical Society*, **1960**, *111*, 3973-3993.

15. Halttunen, T.; Salminen, S.; Tahvonen, R. Rapid removal of lead and cadmium from water by specific lactic acid bacteria. *International Journal of Food Microbiology*, **2007**, *114*, 30–35.

16. Hinz, C. Description of sorption data with isotherm Equations. *Geoderma*, **2001**, *99*, 225–243.

17. Ho, Y. S.; Ofomaja, A. E. Pseudo-second-order model for lead ion sorption from aqueous solutions onto palm kernel fiber. *Journal of Hazardous Materials,* **2006**, *B129*, 137–142.

18. Ho, Y.S.; McKay, G. Pseudo-second order model for sorption processes. *Process Biochemistry*, **1999**, *34*, 451–465.

19. Holm, T. R.; Zhu, X.-F. Sorption by kaolinite of Cd^{2+}, Pb^{2+} and Cu^{2+} from landfill leachate-contaminated groundwater. *Journal of Contaminant Hydrology*, **1994**, *16*, 271-287.

20. Jaynes, W. F.; Boyd, S. A. Hydrophobicity of siloxane surfaces in smectites as revealed by aromatic hydrocarbon adsorption from water. *Clays and Clay Minerals,* **1991**, *39* (4), 428-436.

21. Keren, R. Reduction of the cation-exchange capacity of montmorillonite by take-up of hydroxy-a1 polymers. *Clays and Clay Minerals,* **1986**, *34* (5), 534-538.

22. King, P.; Rakesh, N.; Beenalahari S.; Kumar, Y. P.; Prasad, V. S. R. K. Removal of lead from aqueous solution using *Syzygium cumini* L.: Equilibrium and kinetic studies. *Journal of Hazardous Materials*, **2007**, *142* (1-2), 340-347.

23. Kloprogge, J. T. Synthesis of smectites and porous pillared clay catalysts: A review. *Journal of Porous Materials*, **1998**, *5*, 5–41.

24. Kul, A. R.; Koyuncu, H. Adsorption of Pb(II) ions from aqueous solution by native and activated bentonite: kinetic, equilibrium and thermodynamic study. *Journal of Hazardous Materials*, **2010**, *179*, 332–339.

25. Kumar, D.; Singh, A.; Gaur, J. P. Mono-component versus binary isotherm models for Cu(II) and Pb(II) sorption from binary metal solution by the green alga Pithophora oedogonia. *Bioresource Technology*, **2008**, *99*, 8280–8287.

26. Kumar, K. V.; Sivanesan, S. Pseudo second order kinetic models for safranin onto rice husk: Comparison of linear and non-linear regression analysis. *Process Biochemistry*, **2006**, *41*, 1198–1202.

27. Kumar, U.; Bandyopadhyay, M. Sorption of cadmium from aqueous solution using pretreatedrice husk. *Bioresource Technology*, **2006**, *97*, 104–109.

28. Laidler, K. J. Chemical kinetics. *Harper and Row Publishers, Inc*, **1987**, *3ʳᵈ edition*, pp 1-10.

29. Lazarević, S.; Janković-Častvan, I.; Jovanović, D.; Milonjić, S.; Janaćković, D.; Petrović, R. Adsorption of Pb^{2+}, Cd^{2+} and Sr^{2+} ions onto natural and acid-activated sepiolites. *Applied Clay Science*, **2007**, *37*, 47–57.

30. Lee, B.; Kim, Y.; Lee, H.; Yi, J. Synthesis of functionalized porous silica via templating method as heavy metal adsorbents: the introduction of surface hydrophilicity onto the surface of adsorbents. *Microporous and Mesoporous Materials*, **2001**, *50*, 77-90.

31. Li, Y. H.; Wang, S.; Luan, Z.; Ding, J.; Xu, C.; Wu, D. A dsorption of cadmium (II) from aqueous solution by surface oxidized carbon nanotubes. *Carbon*, **2003**, *41*, 1057–1062.

32. Li, Z.; Yuan, H. Characterization of cadmium removal by *Rhodotorula sp. Y11*. Applied Microbiology & Biotechnology, **2006**, *73*, 458–463.

33. Limousin, G.; Gaudet, J.-P.; Charlet, L.; Szenknect, S.; Barthès, V.; Krimissa, M. Sorption isotherms: A review on physical bases, modelling and measurement: Review. *Applied Geochemistry*, **2007**, *22*, 249–275.

34. Lottenbach, B. Gentle soil remediation: Immobilisation of heavy metals by Aluminium and montmorillonite compounds. *Swiss Federal Institute of Technology*, Zurich. PhD Thesis, **1996**.

35. Manohar, D. M.; Noeline, B. F.; Anirudhan, T. S. Adsorption performance of Al-pillared bentonite clay for the removal of cobalt (II) from aqueous phase. *Applied Clay Science*, **2006**, *31*, 194–206.

36. Matthes, W.; Madsen, F. W.; Kahr, G. Sorption of heavy-metal cationsby Al and Zr-hydroxyinetrcalated and pillared bentonite. *Clays and Clay Minerals,* **1999**, *47* (5), 617-629.

37. Meena, A. K.; Kadirvelu, K.; Mishra, G. K.; Rajagopal, C.; Nagar, P. N. Adsorptive removal of heavy metals from aqueous solution by treated sawdust (*Acacia arabica*). *Journal of Hazardous Materials*, **2008**, *150*, 604–611.

38. Mobasherpour, I.; Salahi, E.; Pazouki, M. Comparative of the removal of Pb^{2+}, Cd^{2+} and Ni^{2+} by nano crystallite hydroxyapatite from aqueous solutions: Adsorption isotherm study. *Arabian Journal of Chemistry*, **2011**, http://dx.doi.org/10.1016/j.arabjc.2010.12.022.

39. Musapatika, E. T.; Onyango, M. S.; Aoyi, O. Cobalt(II) removal from syntheticwastewater by adsorption on South African coal fly ash *South African Journal of Science*, **2010**, *106*, 1-7.

40. Namane, A.; Mekarzia, A.; Benrachedi, K.; Belhaneche-Bensemra, N.; Hellal, A. Determination of the adsorption capacity of activated carbon made from coffee grounds by chemical activation with $ZnCl_2$ and H_3PO_4. *Journal of Hazardous Materials*, **2005**, *B119*, 189–194.

41. O'Connell, D. W.; Birkinshaw, C.; O'Dwyer, T. F. Heavy metal adsorbents prepared from the modification of cellulose: A review. *Bioresource Technology*, **2008**, *99*, 6709–6724.

42. Okada T. Adsorption properties of smectites modified with various cationic species PhD Thesis, *Waseda Univeristy*, *Department of Earth Sciences*, **2004**.

43. Paulino, A. T.; Minasse, F. A. S.; Guilherme, M. R.; Reis, A. V.; Muniz, E. C.; Nozaki, J. Novel adsorbent based on silkworm chrysalides for removal of heavy metals from wastewaters. *Journal of Colloid and Interface Science*, **2006**, *301*, 479–487.

44. Pavasant, P.; Apiratikul, R.; Sungkhum, V.; Suthiparinyanont, P.; Wattanachira, S.; Marhaba, T. F. Biosorption of Cu^{2+}, Cd^{2+}, Pb^{2+}, and Zn^{2+} using dried marine green macroalga Caulerpa lentillifera. *Bioresource Technology*, **2006**; *97*, 2321–2329.

45. Rawajfih, Z..; Nsour, N. Characteristics of phenol and chlorinated phenols sorption onto surfactant-modified bentonite. *Journal of Colloid and Interface Science*, **2006**, *298*, *39–49.*

46. Sampieri, A.; Fetter, G.; Bosch, P.; Bulbulian, S. Cobalt sorption in silica-pillared clays. *Langmuir*, **2006**, *22,* 385-388.

47. Sawalha, M. F.; Peralta-Videa, J. R.; Romero-González, J.; Gardea-Torresdey, J. L. Biosorption of Cd(II), Cr(III), and Cr(VI) by saltbush (*Atriplex canescens*) biomass: Thermodynamic and isotherm studies. *Journal of Colloid and Interface Science*, **2006**, *300*, 100–104.

48. Sprynskyy, M.; Buszewski, B.; Terzyk, A. T.; Namiésnik, J. Study of the selection mechanism of heavy metal (Pb^{2+}, Cu^{2+}, Ni^{2+}, and Cd^{2+}) adsorption on clinoptilolite. *Journal of Colloid and Interface Science*, **2006**, *304*, 21–28.

49. Unnithan, M. R.; Vinod, V. P.; Anirudhan, T. S. Ability of iron(III)-loaded carboxylated polyacrylamide-grafted sawdust to remove phosphate ions from aqueous solution and fertilizer industry wastewater: Adsorption kinetics and isotherm studies. *Journal of Applied Polymer Science*, **2002**, *84* (13), 2541-2553.

50. Wang, S.; Dong, Y.; He, M.; Chen, L.; Yu, X. Characterization of GMZ bentonite and its application in the adsorption of Pb(II) from aqueous solutions. *Applied Clay Science*, **2009**, *43*, 164-171.

51. Wang, W. Chelating adsorption properties of Cd (II) on the PMAA/SiO$_2$. *Process Safety and Environmental Protection*, **2011**, *89* (2), 127–132.

52. Wong, K. K.; Lee, C. K.; Low, K. S.; Haron, M. J. Removal of Cu^{2+} and Pb^{2+} by tartaric acid modified rice husk from aqueous solutions. *Chemosphere*, **2003**, *50*, 23–28.

53. Yu, J.; Tong, M.; Sun, X.; Li, B. Cystine-modified biomass for Cd(II) and Pb(II) biosorption. *Journal of Hazardous Materials*, **2007**, *143*, 277–284.

54. Yu, J.; Tong, M.; Sun, X.; Li, B. Poly (methacrylic acid) modified biomass for enhancement adsorption of Pb^{2+}, Cd^{2+} and Cu$^{2+.}$ *Journal of Chemical Technology and Biotechnology,* **2007,** *82,* 558–565.

55. Yu. R.; Wang, S.; Wang, D.; Ke, J.; Xing, X.; Kumada, N.; Kinomura, N. Removal of Cd^{2+} from aqueous solution with carbon modified aluminium-pillared bentonite. *Catalysis Today*, **2008**, *139*, 135–139.

Chapter 7

Adsorption of methyl orange and neutral red onto lignocellulose and montmorillonite based adsorbents

7.0 Introduction

The previous chapter presented the procedures followed in carrying out experiments for the adsorption of heavy metals onto all the adsorbents prepared in this study, together with a discussion of the adsorption results. This chapter presents the experimental details for the adsorption of organic pollutants (methyl orange and neutral red) onto the same adsorbents (lignocellulose based, montmorillonite based and lignocellulose-montmorillonite nanocomposite adsorbents) as listed in Section 6.0. The adsorption experiments are described, the results and discussion on the adsorption of methyl orange and neutral red are given, followed by a conclusion.

7.1 Batch adsorption experiments

All adsorption experiments were carried out in 250 mL conical flasks by agitating a given dose of each adsorbent in the synthetic solution of methyl orange or neutral red in deionized water. A known mass of the adsorbent was dispersed in 80 mL of the synthetic solution at 25 °C. The mixtures were placed on a rotary shaker and agitated at 200 rpm. Aliquots of sample solutions were withdrawn at set time intervals. The adsorbent was separated by filtering through Acrodisc syringe filters (0.45 µm Supor Membrane) of low protein binding, and the concentration of each pollutant in the filtrate was determined by ultraviolet-visible (UV/Vis) spectroscopy. All assays were carried out in replicates of at least two and the average values are presented. A PerkinElmer Lambda 25 UV/Vis Spectrophotometer was used for the determination of methyl orange and neutral red concentrations in the test solutions. The experiments were carried out so as to generate isotherms and kinetics data.

7.1.1. Adsorption isotherms

The conditions used to generate adsorption isotherms were as follows: adsorbent dosage was 1.25 g of adsorbent per 1 L of solution; methyl orange concentrations ranged from 2 to 10 ppm; neutral red concentrations ranged from 10 to 50 ppm; the pH was 5.0 for all the adsorption experiments; the shaking time was six hours. Aliquots were taken after six hours, filtered through Acrodisc syringe filters (0.45 µm Supor Membrane) of low protein binding and the filtrate taken for measurement by UV/Vis spectrophotometry to determine the remaining amount of methyl orange or neutral red. The

solutions of neutral red were first diluted 5-fold before analysis. Solutions were left for 24 h but there was no significant change in the adsorbed amount of methyl orange or neutral red so the results up to six hours of shaking are reported.

7.1.2 Adsorption kinetics

In order to assess the rate of the adsorption of methyl orange (MetO) and neutral red (NeuR), the adsorption experiments were carried out under the following conditions: amount of adsorbent used was 1.25 g per 1.0 L of solution; the initial concentration was 10 ppm for MetO and 50 ppm for NeuR; the shaking time was up to six hours. Aliquots of sample solutions were withdrawn at set time intervals up to six hours and filtered through Acrodisc syringe filters (0.45 μm Supor Membrane) of low protein binding. The remaining concentration of MetO or NeuR (in the filtrate) was determined by UV/Vis spectrophotometry. The temperature of the mixtures was 25 °C and the pH was 5.0.

7.1.3 Effect of OH/Al molar ratio on the adsorption of dyes to AlpMMT

As described in Chapter 4, AlpMMT samples were prepared at different OH/Al molar ratios. The adsorption of methyl orange or neutral red onto AlpMMT samples of different OH/Al molar ratios was determined. A study by Altunlu, M. et al, 2007 on the adsorption of phenol onto AlpMMT prepared at different OH/Al molar ratios showed a decrease in the amount of phenol adsorbed with increase in the OH/Al molar ratio.

To assess the effect of OH/Al molar ratio on the amount of methyl orange or neutral red adsorbed, about 0.10 g of AlpMMT of different OH/Al molar ratios was added to 250 mL conical flasks. Methyl orange (80 mL, 10 ppm) or neutral red (80 mL, 50 ppm) was added and the mixture placed on a rotary shaker for six hours at 25 °C and a pH of 5.0. After six hours, the mixtures were filtered through Acrodisc syringe filters (0.45 μm Supor Membrane) of low protein binding. The concentration of methyl orange or neutral red in the filtrate was determined by UV/Vis spectrophotometry.

7.1.4 Competitive adsorption studies of methyl orange in the presence of Cd^{2+} or Pb^{2+}

Synthetic solutions containing a binary mixture of either methyl orange and Cd^{2+} or methyl orange and Pb^{2+} were prepared in deionized water. The concentrations of methyl orange ranged from 2 to 10 ppm and each metal ion concentration range was from 10 to 50 ppm. The adsorption experiments were carried out as already described above in which 0.10 g of adsorbent was dispersed in 80 mL of the synthetic solutions in 250 mL conical flasks. The mixtures were placed on a rotary shaker and left to agitate for six hours. Sample aliquots were withdrawn at set time intervals and the solutions were filtered through Acrodisc syringe filters (0.45 μm Supor Membrane) of low protein binding and the remaining MetO was determined by UV/Vis spectrophotometry. The determination of heavy metals in

the solutions was carried out by AAS. For the analysis of Cd^{2+}, the samples had to be diluted 10-fold in order to reduce the concentration of Cd^{2+} in sample solutions into the calibration range (2 – 10 ppm). The competitive adsorption experiments were carried out in such a way as to generate data for both adsorption isotherms and adsorption kinetics.

7.1.5 Determination of concentration of methyl orange and neutral red in solution by ultraviolet-visible spectrophotometry

The procedure used for the determination of heavy metal ions in solution before and after adsorption has already been described in Section 6.1.5. The amounts of methyl orange (MetO) and neutral red (NeuR) before and after adsorption were determined by using the external standard calibration method. Calibration curves were generated for both MetO and NeuR, the concentrations of the calibration standards ranged from 2 to 10 ppm for both dyes. The instrument was calibrated first before each analysis. The initial concentrations of the test solutions were determined and these were used in the calculation of the adsorbed amounts of MetO and NeuR. The determination of the concentrations of MetO and NeuR in the solutions was carried out on a PerkinElmer Lambda 25 UV/Vis spectrophotometer at a wavelength of 465 and 530 nm, respectively. Before analysis with UV/Vis spectrophotometry, the solutions were filtered through Acrodisc syringe filters (0.45 µm Supor Membrane) of low protein binding to remove solid particles. The solutions were analysed using a matched pair of quartz cells of 1 cm pathlength. The adsorption data were processed or analysed according to the procedure presented in Section 7.2.

7.1.6 Desorption studies

Desorption studies were carried out to assess the reusability of the some of the nanocomposite adsorbents prepared. Both neutral red and methyl orange were used in the desorption studies. A number of solvents were assessed for the desorption of methyl orange and neutral red from the selected adsorbents. The solvents tried include: deionized water, ethanol, methanol, NaOH and HNO_3. The complete desorption of MetO was achieved by using 80 mL of the 0.01 M NaOH solution. Neutral red was difficult to desorb but eventually, it was desorbed by first washing with 40 mL of methanol followed by 40 mL of 0.1 M HNO_3.

A mass of 0.200 g of adsorbent was added to 80 mL of dye solution. The concentrations of the dyes were as follows: methyl orange - 10 ppm and neutral red - 50 ppm. The mixtures were left to shake and equilibrate for six hours followed by filtration through Whatman N° 1 filter papers. All the dye-laden adsorbent was quantitatively transferred to the filter paper. Methyl orange was then desorbed by 80 mL of 0.01 M NaOH solution. The 80 mL of NaOH solution was added to the filter paper with adsorbent in small volumes in order to completely desorb the dye. The adsorbent was then washed

with water and 0.1 M HNO$_3$ until the pH of the filtrate or washings was 5.0, followed by drying at 60 °C for 12 h. Neutral red was desorbed by slowly adding 40 mL of methanol followed by 40 mL of 0.1 M HNO$_3$. The adsorbent was then washed with water and a small amount of 0.01 M NaOH until the pH of the washings was 5.0. However, it must be mentioned that still neutral red could not be completely desorbed using the selected solvent system. The adsorption-desorption cycles were carried out three times.

7.2 Analysis of adsorption data

The raw data generated from the experiments detailed above were analysed as presented in Section 7.2.1. The data were fitted to different models depending on whether one was dealing with adsorption isotherms or kinetics.

7.2.1 Calculation of the adsorbed amount of solute

The adsorption data obtained from the adsorption experiments as described in Sections 7.1.1 to 7.1.2 were processed so as to determine the adsorbed amount of methyl orange and neutral red. The adsorbed amount of MetO and NeuR was computed using Equation 6.1.

The data were processed in order to generate adsorption isotherms and adsorption kinetic plots as presented in Sections 7.2.2 and 7.2.3.

7.2.2 Adsorption isotherms

Again, as presented in Chapter 6 for the heavy metals, the adsorption data were analysed by plotting equilibrium adsorbed amount (Q_e, mg/g) versus equilibrium adsorbate concentration (C_e, mg/L) to generate isotherms. Then the isotherms were inspected and classified according to the system proposed by Giles, C. H. et al, 1960 and 1974. The classification entailed assessing the slope of the initial portion of this curve of Q_e (mg/g) versus C_e (mg/L) followed by assigning a class after comparing with the curves shown in Figure 6.1. This was one of the methods used in the analysis of data for both methyl orange and neutral red adsorption onto the different adsorbents prepared and evaluated in this study.

The adsorption data were also fitted to the two commonly used adsorption isotherm equations, the Langmuir and the Freundlich models. A detailed description of each of these models has been presented in Section 6.2.2.

7.2.3 Adsorption kinetics

The rate of uptake of methyl orange or neutral red onto the prepared adsorbents was assessed as described in Section 7.1.2. The amount of methyl orange or neutral red adsorbed (mg/g) was plotted against time (min), to see how the uptake varied with time. The experimental adsorption data were also fitted to the commonly used kinetic models, the pseudo first-order and pseudo second-order equations. The details of these two models have already been presented in Section 6.2.3.

Section 7.3 presents the results obtained from the adsorption experiments and a discussion of the adsorption results.

7.3 Results and discussion

This section presents the results obtained from the adsorption of methyl orange and neutral red onto the different adsorbents prepared in this study. The adsorption of MetO and NeuR onto montmorillonite based adsorbents, lignocellulose based adsorbents and the lignocellulose-montmorillonite nanocomposite adsorbents was carried out. As highlighted in Section 7.1.4, the adsorption of MetO was also assessed in the presence of heavy metals onto selected adsorbents. The results for MetO adsorption are presented first followed by results for NeuR adsorption.

7.3.1 Adsorption of methyl orange onto montmorillonite based adsorbents

7.3.1.1 Adsorption isotherms

The equilibrium adsorbed amount (Q_e, mg/g) was plotted against the equilibrium pollutant concentration (C_e, mg/L) in solution to generate the isotherms. Figure 7.1 displays the isotherms for the adsorption of methyl orange to the montmorillonite based adsorbents. The isotherms were not as easy to assign as those discussed above for the adsorption of Cd^{2+} and Pb^{2+} onto the same adsorbents. It can be seen that the adsorption of methyl orange onto the montmorillonite adsorbents was not large, as can be judged from the equilibrium adsorbed amounts (Q_e values). According to the isotherms, the amount of methyl orange adsorbed at equilibrium decreased in the following order: AlpMMT > NaMMT > PMPSgMMT > PMMAgMMT > PMAAgMMT.
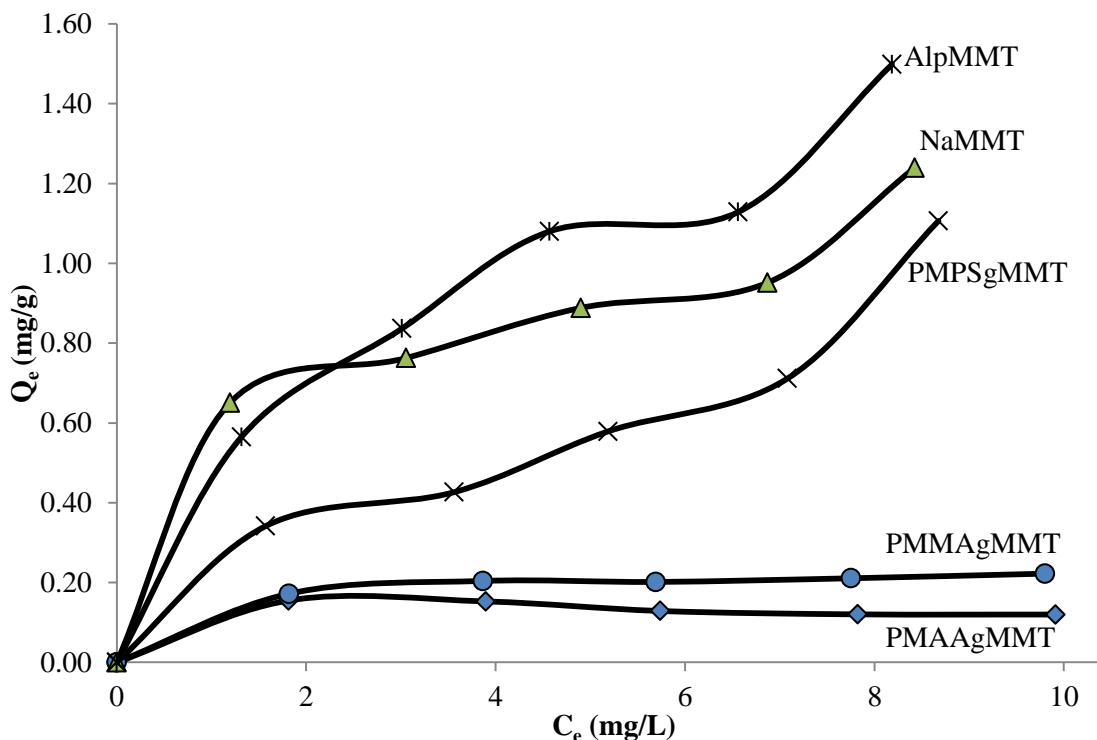
Figure 7.1: Isotherms for the adsorption of methyl orange onto montmorillonite based adsorbents.

Using the classification system proposed by Giles, C. H. et al, 1960 and 1974, the isotherms can be classified as follows: PMMAgMMT and PMAAgMMT (Langmuir type 2, L_2), NaMMT, AlpMMT and PMPSgMMT (Langmuir type 3, L_3). The initial curvature of the PMAAgMMT and PMMAgMMT isotherms shows that as more sites are filled on the substrate, it becomes increasingly difficult for the incoming methyl orange molecule to find a vacant site. According to Giles, C. H. et al, 1974, this might also imply that the adsorbed molecules are horizontally oriented (flat). The long plateau shown by PMMAgMMT and PMAAgMMT suggested that the exposed adsorbate surface tends to repel solute (Giles, C. H. et al, 1974).

The latter parts of the isotherms for MetO adsorption onto NaMMT, AlpMMT and PMPSgMMT suggested that adsorption became easy as the concentration of MetO increased. The L_3 class shows that a second layer can form readily, whereby the hydrophobic end of methyl orange forms a new surface on which a second layer of methyl orange molecules can deposit. One system that showed this type of isotherm is phenol adsorption onto alumina (Giles, C. H. et al, 1974).

The data were fitted to the Freundlich and Langmuir equations. Figures 7.2 shows the Langmuir plots for the adsorption of methyl orange onto the montmorillonite based adsorbents. The Langmuir plots were generated by plotting the equilibrium partition coefficient, C_e/Q_e (g/L) against equilibrium solution concentration, C_e (mg/L).
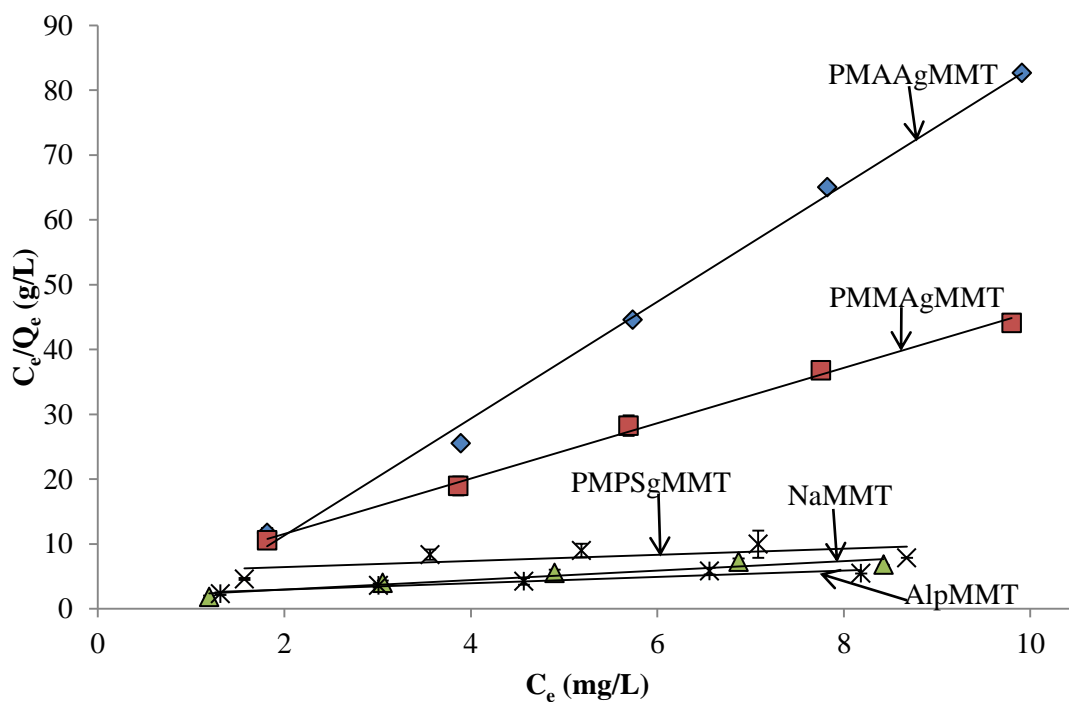
Figure 7.2: Langmuir plots for methyl orange adsorption onto montmorillonite based adsorbents.

The Freundlich plots for methyl orange adsorption onto the montmorillonite based adsorbents are displayed in Figure 7.3. In order to generate the Freundlich plots, *Log Q_e* was plotted against *Log C_e*.
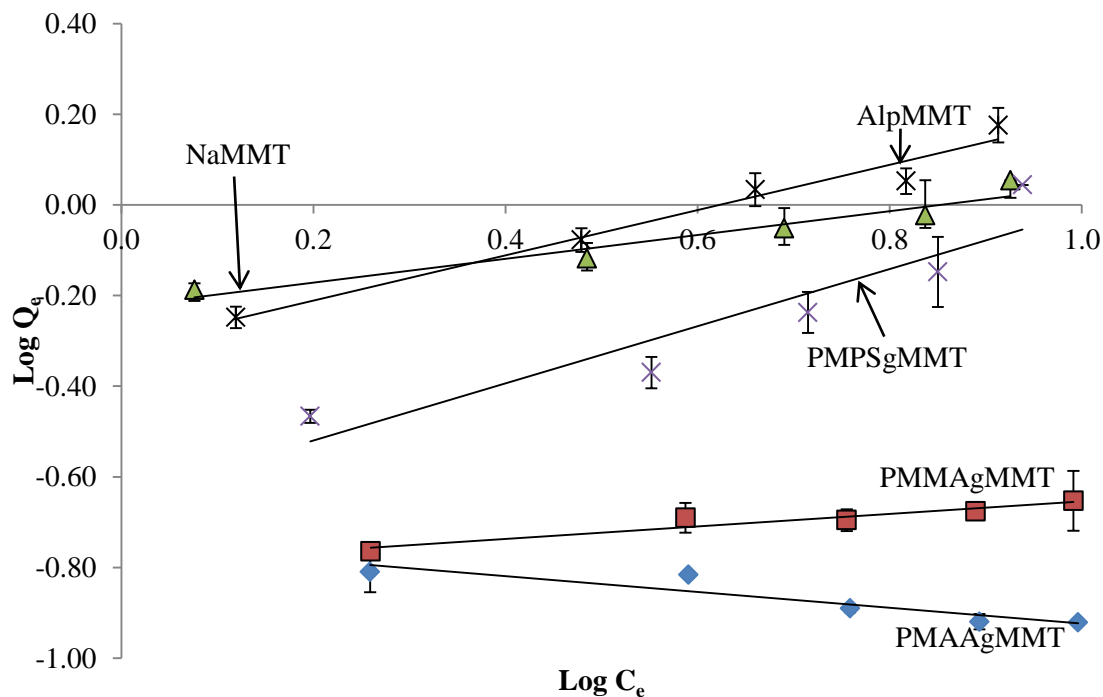
Figure 7.3: Freundlich plots for methyl orange adsorption onto montmorillonite based adsorbents.

The Freundlich and Langmuir parameters and the correlation coefficients (R^2) for methyl orange adsorption onto the montmorillonite based adsorbents are listed in Table 7.1. The Langmuir R^2 values for methyl orange adsorption onto NaMMT, PMPSgMMT and AlpMMT were found to be relatively low compared with the corresponding Freundlich R^2 values. This implies that the adsorption process conformed more to the Freundlich model than the Langmuir model. Both models could be used to describe the adsorption process onto NaMMT, AlpMMT and PMMAgMMT.

Table 7.1: Freundlich and Langmuir parameters for the adsorption of methyl orange onto montmorillonite based adsorbents.

Adsorbent	Isotherm	Slope	R^2	Intercept	Q_0/K_f	n/b
NaMMT	Langmuir	0.7258	0.9082	1.5273	1.3778	0.4752
	Freundlich	0.2628	0.9301	-0.2239	0.5972	3.8052
AlpMMT	Langmuir	0.4923	0.9041	1.9601	2.0313	0.2511
	Freundlich	0.4992	0.9686	-0.3112	0.4884	2.0032
PMPSgMMT	Langmuir	0.4726	0.4279	5.4790	2.1160	0.0863
	Freundlich	0.6301	0.8655	-0.6455	0.2262	1.5871
PMAAgMMT	Langmuir	9.0133	0.9957	-6.7099	0.1109	-1.343
	Freundlich	-0.1745	0.8486	-0.7493	0.1781	-5.731
PMMAgMMT	Langmuir	4.2700	0.9968	3.0220	0.2342	1.4130
	Freundlich	0.1388	0.9123	-0.7927	0.1612	7.2046

For methyl orange adsorption onto PMAAgMMT, both the Freundlich and Langmuir models were not applicable since the Freundlich (*n*) and Langmuir (*b*) affinity constants were found to be negative. It can be suggested that the adsorption process of MetO onto PMAAgMMT was not favourable. The washing of the PMAAgMMT with NaOH (Section 5.2.3) probably generated some negatively charged carboxylate groups on the surface which could have caused repulsions with the negatively charged methyl orange molecules. The adsorption capacities of the adsorbents for methyl orange were very low just as seen from the isotherms shown in Figure 7.1. The equilibrium adsorption capacities of the montmorillonite based adsorbents were computed using the kinetic models reported in Section 7.3.1.2.

Atmani, F. et al, 2009 reported adsorption capacities of 20.24 mg/g and 31.94 mg/g for methyl orange adsorption onto natural and treated almond skins, respectively. Their data conformed more to the Freundlich isotherm than the Langmuir isotherm. The adsorption of methyl orange onto modified ultrafine coal powder was found to follow both the Langmuir and the Freundlich models (Zhuannuan, L. et al, 2009).

The following section discusses the results for the change in the amount of methyl orange adsorbed onto the montmorillonite adsorbents with time.

7.3.1.2 Adsorption kinetics

The adsorbed amount of methyl orange (Q_t, mg/g) onto the montmorillonite based adsorbents was plotted against time (min) to generate the plots shown in Figure 7.4. The plots showed that equilibrium state was achieved in about 4 h for all the adsorbents except AlpMMT and PMPSgMMT which appeared to take slightly longer to reach equilibrium. The rate of adsorption of methyl orange onto AlpMMT was painstakingly slow considering the amount adsorbed in six hours of shaking and yet the system had not yet reached equilibrium state. The system was monitored for about 24 h but the change in the amount adsorbed was insignificant.
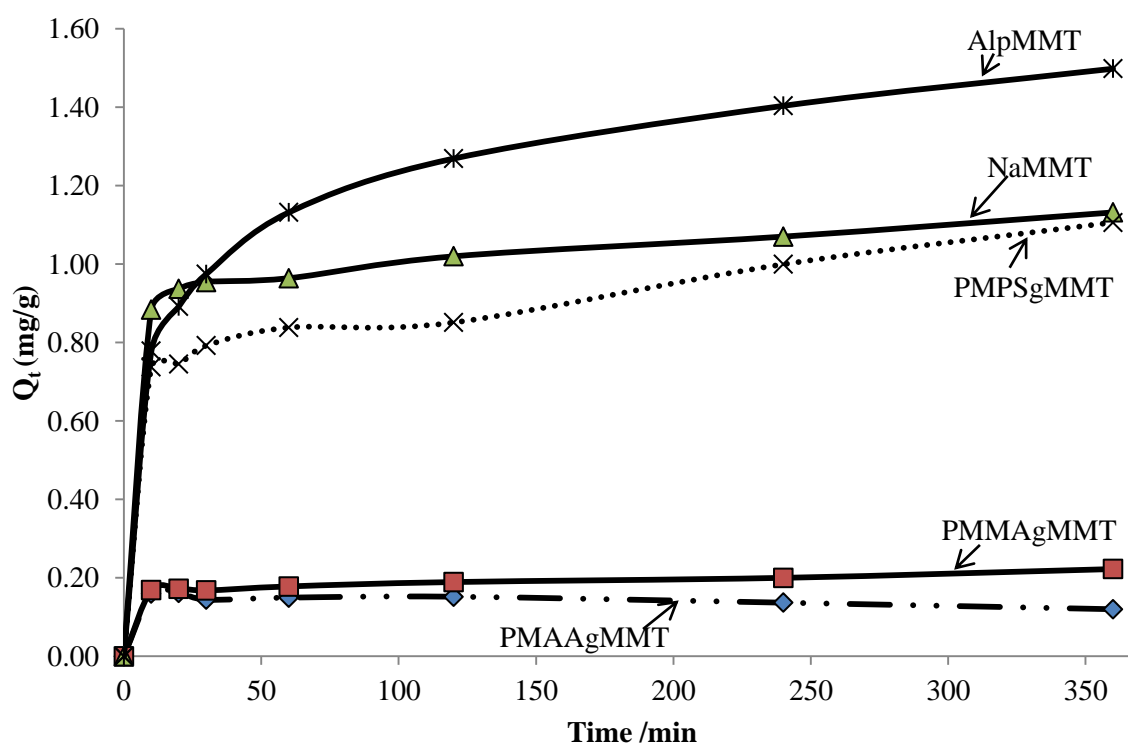
Figure 7.4: Plots of adsorbed amount (mg/g) of methyl orange onto montmorillonite based adsorbents versus time (min).

The experimental data for the adsorbed amount (mg/g) of methyl orange for the whole adsorption period onto the montmorillonite based adsorbents were fitted to the pseudo first-order and pseudo second-order kinetic models. It was observed in Chapter 6 that the pseudo second-order equation can be used to predict the equilibrium adsorption capacity and there was a relatively good correlation between the Langmuir adsorption capacities (Q_0) and the kinetics equilibrium adsorption capacities

(Q_e). Therefore, the pseudo second-order kinetic model was employed in the determination of the equilibrium adsorption capacity of each adsorbent.

Figures 7.5 displays the pseudo first-order plots for the adsorption of methyl orange onto the montmorillonite based adsorbents. The plots were generated by plotting *Log* (Q_e-Q_t) against time (min). The pseudo first-order plot for the adsorption of methyl orange onto PMAAgMMT was not included in Figure 7.5 because the data could not be fitted to the pseudo first-order equation. As can be seen from the plots in Figure 7.4, the amount of methyl orange adsorbed onto PMAAgMMT decreased with time (instead of increasing), thus making it difficult to estimate the value of Q_e. As highlighted in Section 6.2.3.1, in order to fit the adsorption data to the pseudo first-order model, the value of Q_e must be known first. In this study, Q_e was assumed to be the amount of solute adsorbed after six hours, which in this case was less than the amount initially adsorbed.
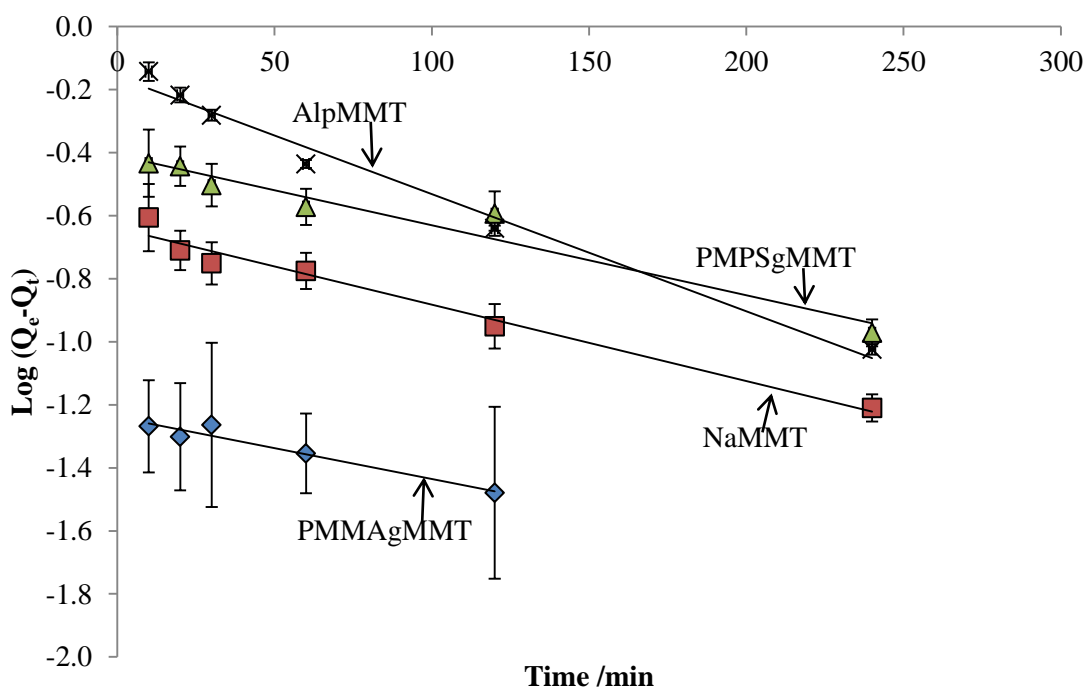
Figure 7.5: Pseudo first-order plots for methyl orange adsorption onto montmorillonite based adsorbents.

The pseudo second-order plots for MetO adsorption onto the montmorillonite adsorbents are displayed in Figure 7.6. The plots were generated by plotting t/Q_t (gmin/mg) against time (min).
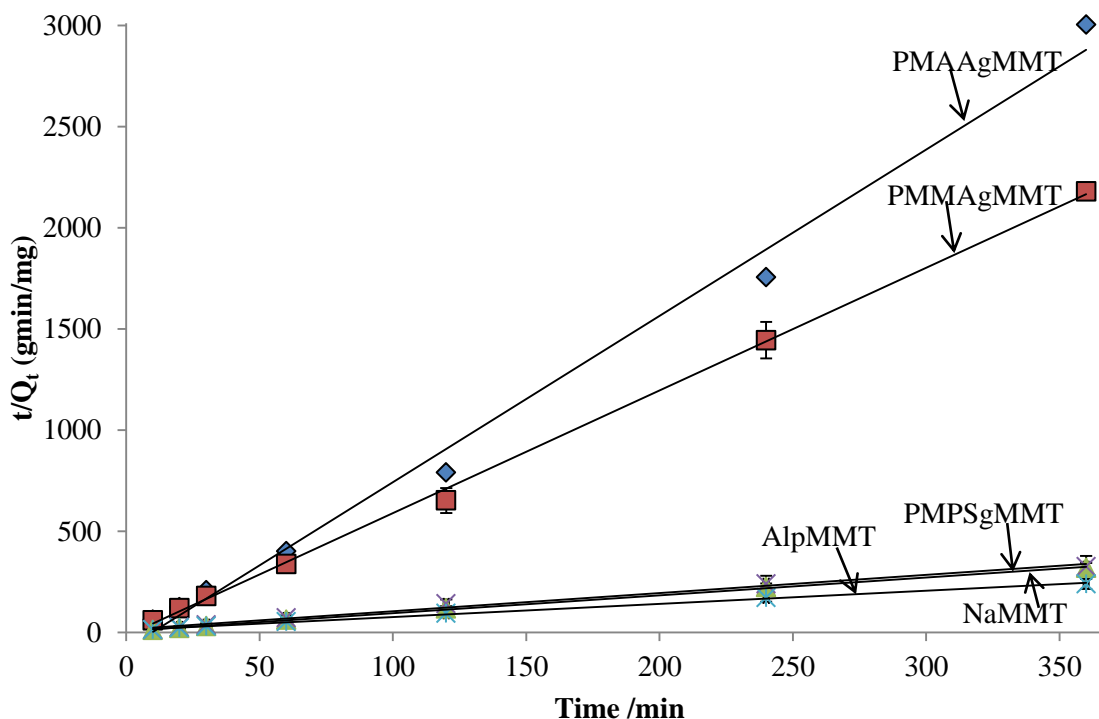
Figure 7.6: Pseudo second-order plots for methyl orange adsorption onto montmorillonite based adsorbents.

The challenge was to know the value of the equilibrium adsorbed amount (Q_e) of solute prior to processing the kinetics data as required for the pseudo first-order model. This is not required when fitting the adsorption data to the pseudo second-order model (Section 6.2.3.2). The parameters and the correlation coefficients (R^2) for the pseudo first-order and pseudo second-order kinetic models are shown in Table 7.2.

As observed and discussed for the adsorption of Cd^{2+} and Pb^{2+} onto most of the adsorbents evaluated in this study, the pseudo second-order R^2 values were greater than the pseudo first-order R^2 values. However, relatively high pseudo first-order R^2 values were obtained though they were lower than the pseudo second-order R^2 values. The pseudo second-order model was found to fit most sorption systems and can describe the adsorption mechanism for the whole sorption process (Ho, Y. S., 2006; Ho, Y. S., 2006). Atmani, F. et al, 2009 reported that their data were best represented by the pseudo second-order model. Zhuannian, L. et al, 2009 found that their data for methyl orange adsorption onto ultrafine coal powder could best be represented by the pseudo first-order model, though the pseudo second-order model also gave relatively high R^2 values. Methyl orange adsorption onto Lapindo volcanic mud was found to conform to the pseudo second-order model (Jalil, A. A. et al, 2010).

Table 7.2: Pseudo first-order and pseudo second-order parameters for methyl orange adsorption onto montmorillonite based adsorbents.

Adsorbent	Model	Slope	R^2	Intercept	Q_e (mg/g)	k_1/k_2
NaMMT	1st	-0.0024	0.9743	-0.6401	0.2290	0.0055
	2nd	0.882	0.9984	6.5033	1.1338	0.1196
AlpMMT	1st	-0.0037	0.9851	-0.1591	0.6933	0.0085
	2nd	0.6482	0.9977	11.489	1.5427	0.0366
PMPSgMMT	1st	-0.0022	0.9530	-0.4083	0.3906	0.0051
	2nd	0.8983	0.9912	14.489	1.1132	0.0555
PMAAgMMT	1st	NA				
	2nd	8.2169	0.9924	-79.617	0.1217	-3.442
PMMAgMMT	1st	-0.0020	0.9434	-1.2396	0.0576	0.0046
	2nd	6.0613	0.9989	-17.007	0.1650	-2.160

Therefore, the mechanism for methyl orange adsorption onto the adsorbents shown in Table 7.2 can be described by both kinetic models, but is more favourably described by the pseudo second-order model since it showed higher R^2 values than the pseudo first-order model. As predicted from the isotherms in Figure 7.1 and the plots in Figure 7.4, the data in Table 7.2 shows that the adsorbents can be placed in order of decreasing adsorption capacity as follows: AlpMMT > NaMMT > PMPSgMMT > PMMAgMMT > PMAAgMMT. The modification of NaMMT with organic groups, PMMA, PMAA and MPS was expected to significantly enhance the adsorption of methyl orange through greater hydrophobic, π-π and van der Waals interactions. However, the results shown in Table 7.2 do not show any improvement, instead, a decrease in the uptake of methyl orange was observed for PMAAgMMT and PMMAgMMT. The presence of the organic groups might have possibly blocked some of the adsorption sites of the montmorillonite, thus, resulting in low uptake.

Since AlpMMT showed the highest MetO uptake, it can be said that Al-pillaring of NaMMT improved the uptake of methyl orange. Zhuannian, L. et al, 2009 investigated the adsorption of MetO onto ultrafine coal powder and found equilibrium adsorption capacities of about 6.0 mg/g for an initial methyl orange concentration of 100 ppm. Jeon, Y. S. et al, 2008 reported an adsorption capacities of less than 0.3 mg/g for methyl orange adsorption onto alginate/polyaspartate hydrogels for an initial concentration of 10.0 mg/L. Teng, M.-Y. et al, 2006 assessed the adsorption of methyl orange onto acid activated montmorillonite clay and reported an improvement of about eight times relative to the natural clay. Mittal, A. et al, 2007 reported adsorption capacities of 3.6 and 16.7 mg/g for methyl

orange adsorption onto flyash and soya bean waste biomass, respectively. Anbia, M. et al, 2010 used modified nanoporous silica for the adsorption of anionic dyes including methyl orange, and reported an adsorption capacity of 357.1 mg/g. Chen, S. et al, 2010 found an adsorption capacity of about 50 mg/g for methyl orange adsorption onto powdered activated carbon at an initial concentration of 25 ppm. Their adsorption data were best described by the pseudo second-order kinetic model and the Langmuir isotherm. Yu, L. et al, 2011 reported an adsorption capacity of 36 mg/g for methyl orange adsorption onto anaerobic sludge. Haque, E. et al 2011, found a capacity of 11.2 mg/g for methyl orange adsorption onto activated carbon. The adsorption capacities found in this study for methyl orange adsorption to montmorillonite based adsorbents can be said to be comparable with those reported in the literature.

The following section presents results obtained from the adsorption of methyl orange onto lignocellulose based adsorbents. It was expected that a relatively high uptake of methyl orange (organic molecule) would occur onto the lignocellulose based adsorbents given that the lignocellulose itself is a biopolymer with a lot of organic functional groups (see Figures 2.2, 2.3 and 2.4 of Chapter 2 for structure).

7.3.2 Adsorption of methyl orange onto lignocellulose based adsorbents

The adsorption of methyl orange was carried out onto lignocellulose based adsorbents of different modifications. The procedure used has been presented in Section 7.1.

7.3.2.1 Adsorption isotherms

Again, the equilibrium adsorbed amount (Q_e, mg/g) of methyl orange was plotted against the equilibrium solution concentration (C_e, mg/L) as mentioned above. Figure 7.7 displays the isotherms for the adsorption of MetO onto lignocellulose based adsorbents. The uptake of methyl orange onto the lignocellulose adsorbents was also relatively low (< 1.0 mg/g).
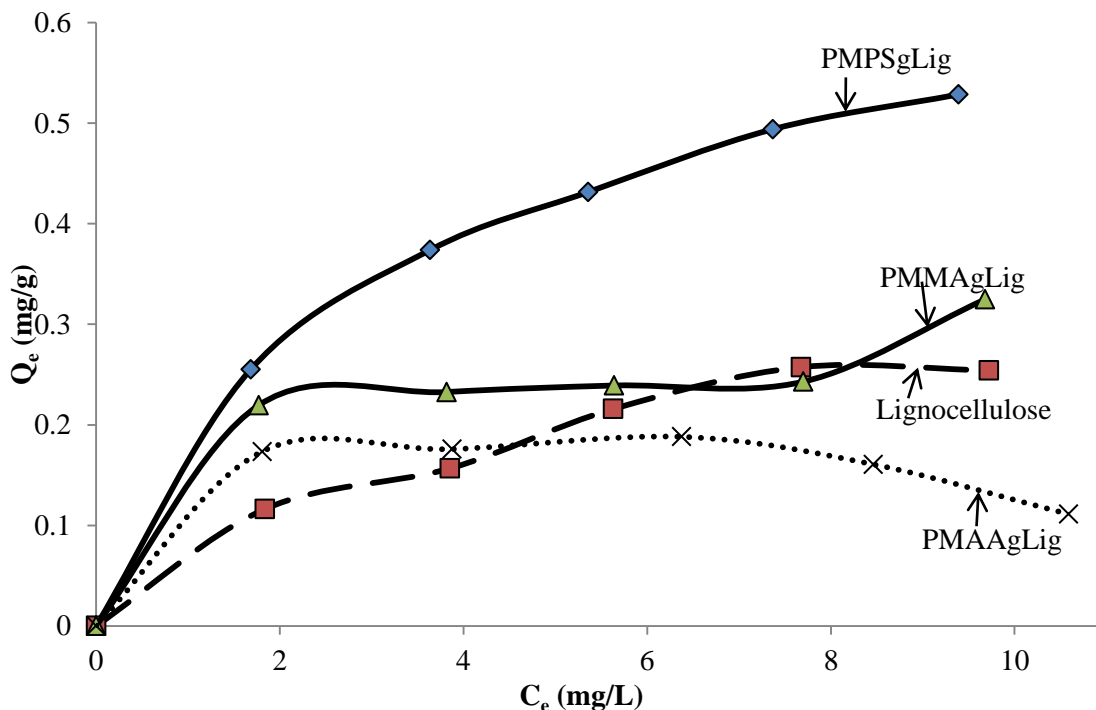
Figure 7.7: Isotherms for methyl orange uptake onto lignocellulose based adsorbents.

The isotherms can be classified as follows: PMPSgLig (Langmuir type 1, L_1), lignocellulose (Langmuir type 4, L_4), PMMAgLig (Langmuir type 3, L_3) and PMAAgLig (Langmuir type mx, L_{mx}). The isotherm for methyl orange adsorption onto PMAAgLig shows that adsorption becomes difficult as the solute concentration increases. This can be seen from the decreasing uptake of methyl orange at high concentrations. Similar results were obtained by Li, F. et al, 2000 for the adsorption of 4-chlorophenol onto Gemini surfactant-modified montmorillonite clay.

The adsorption data were fitted to the Freundlich model and the Langmuir model. The Langmuir plots for methyl orange adsorption onto the lignocellulose based adsorbent are shown in Figures 7.8. For the Langmuir isotherms, C_e/Q_e (g/L) was plotted against C_e (mg/L).
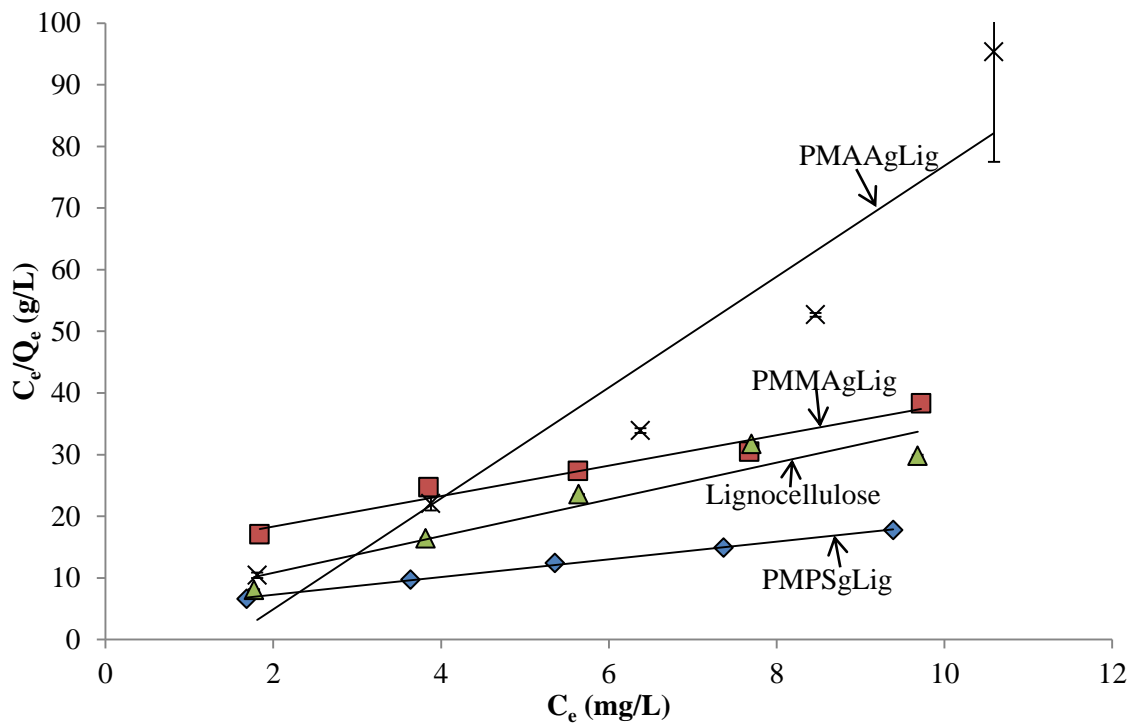
Figure 7.8: Langmuir plots for methyl orange adsorption onto lignocellulose based adsorbents.

The Freundlich plots for methyl orange adsorption onto the lignocellulose based adsorbents are shown in Figure 7.9.
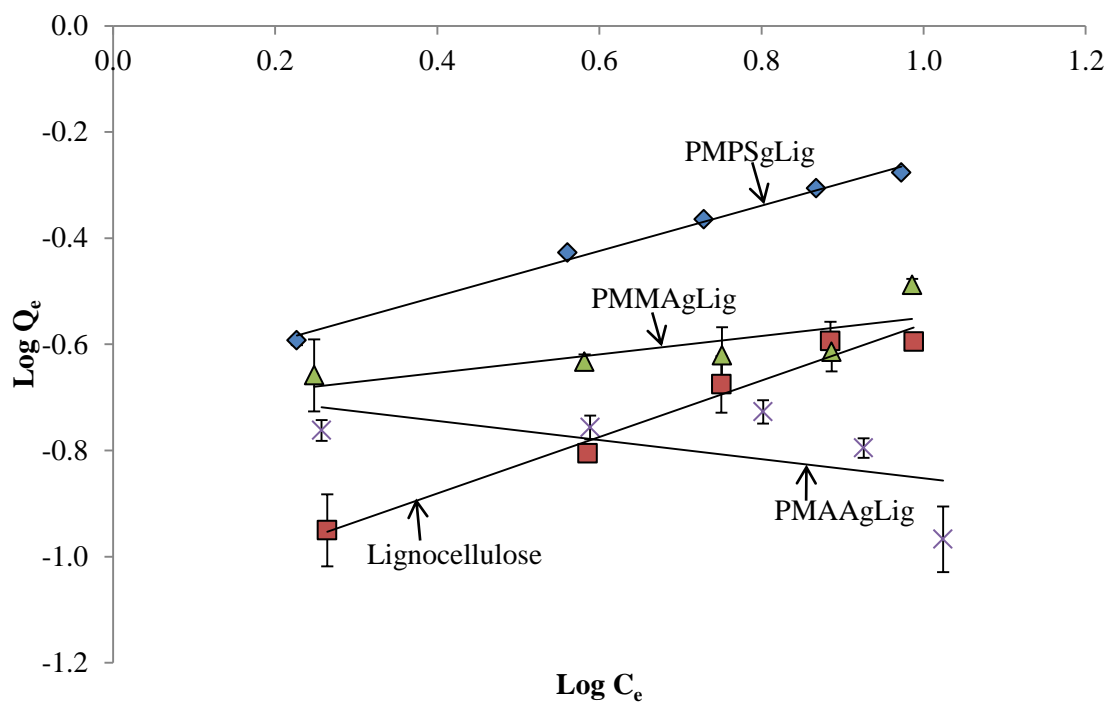
Figure 7.9: Freundlich plots for methyl orange adsorption onto lignocellulose based adsorbents.

The Freundlich and Langmuir parameters for methyl orange adsorption onto lignocellulose based adsorbents are displayed in Table 7.3. The Langmuir R^2 values were all > 0.8900 showing that the adsorption process fits the Langmuir model. The methyl orange molecules can be said to form a monolayer on the surface of the lignocellulose adsorbents. This agrees to some extent with the classification of the respective isotherms shown in Figure 7.7.

Table 7.3: Freundlich and Langmuir parameters for methyl orange adsorption onto lignocellulose based adsorbents.

Adsorbent	Isotherm	Slope	R^2	Intercept	Q_0/K_f	n/b
Lignocellulose	Langmuir	2.4690	0.9660	13.409	0.4050	0.1841
	Freundlich	0.5320	0.9735	-1.0938	0.0806	1.8797
PMMAgLig	Langmuir	2.9774	0.8997	4.8758	0.3359	0.6106
	Freundlich	0.1735	0.5746	-0.7231	0.1892	5.7637
PMPSgLig	Langmuir	1.4359	0.9976	4.4053	0.6964	0.3259
	Freundlich	0.4273	0.9929	-0.6805	0.2087	2.3403
PMAAgLig	Langmuir	8.9941	0.9003	-13.098	0.1112	-0.687
	Freundlich	-0.1798	0.3299	-0.6724	4.7032	-5.562

The adsorption data onto lignocellulose and PMPSgLig could also be described by the Freundlich isotherm since relatively high correlation coefficient values of 0.9735 and 0.9929, respectively were obtained. Annadurai, G. et al, 2002 reported that their adsorption data (MetO onto cellulose based adsorbents) could be described by both the Freundlich and Langmuir isotherms, though the Freundlich had slightly higher R^2 values.

The Langmuir adsorption capacities in decreasing order were as follows: PMPSgLig (0.696 mg/g), lignocellulose (0.405 mg/g), PMMAgLig (0.336 mg/g) and PMAAgLig (0.111 mg/g). Grafting of lignocellulose resulted in a slight improvement in the uptake of methyl orange from aqueous solution. Grafting with PMMA caused a slight decrease in the amount adsorbed, whereas PMAA caused a marked drop in the amount of methyl orange adsorbed. The poor performance of PMAAgLig can be ascribed to the presence of negatively charged carboxylate groups (from washing with 0.01 M NaOH) which possibly caused repulsion of the negatively charged anionic methyl orange molecules, thus hindering adsorption. The same behavior was observed for PMAAgMMT discussed above.

A lot of literature is available on the adsorption of MetO onto lignocellulosic materials. Annadurai, et al, 2002 reported adsorption capacities of 21.0 mg/g (banana peel) and 20.5 mg/g (orange peel). Ai, L. et al, 2010 investigated the adsorption of methyl orange onto poly (aniline) microspheres and found

an adsorption capacity of about 48.0 mg/g. Their adsorption data fitted well to the pseudo second-order kinetic model as well as to the Freundlich isotherm. Morais, W. A. et al, 2008 assessed the adsorption of MetO onto chitosan spheres and found an adsorption capacity of about 8 mg/g. The adsorption capacities found in this study were lower than those reported in the literature for similar adsorbent materials.

7.3.2.2 Adsorption kinetics

The amount of methyl orange adsorbed was monitored against time for each of the lignocellulose based adsorbents. Figure 7.10 shows the plots of adsorbed amount (Q_t, mg/g) of methyl orange onto the lignocellulose based adsorbents against time (min).

The first 30 min were characterised by rapid adsorption (possibly in the first 10 min) and then desorption up to 30 min. The amount adsorbed then increased at 1 h and remained constant until 2 h. Desorption was observed after 2 h for lignocellulose, PMAAgLig and PMMAgLig, but not for PMPSgLig. The desorption was attributed to the formation of an unstable solute-adsorbent complex which may have easily dissociated due to the presence of other competing reactions.
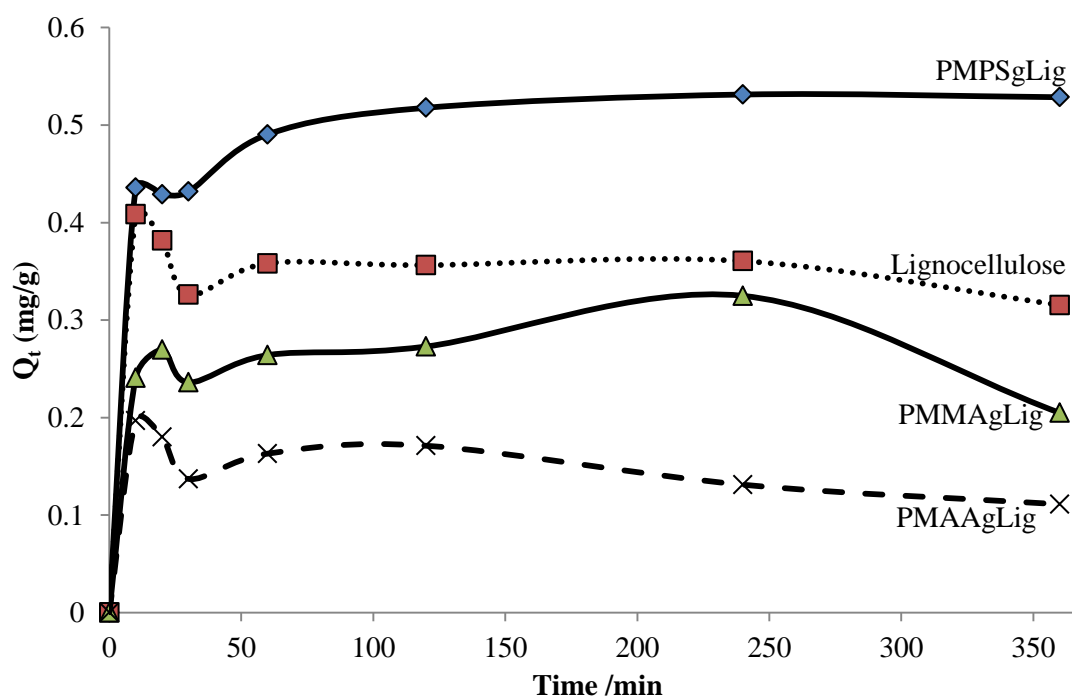
Figure 7.10: Plots of adsorbed amount (mg/g) of methyl orange onto lignocellulose based adsorbents against time (min).

The experimental data were fitted to the pseudo first-order and pseudo second-order equations. The pseudo first-order plots for methyl orange adsorption onto the lignocellulose based adsorbents are shown in Figure 7.11, except for lignocellulose.
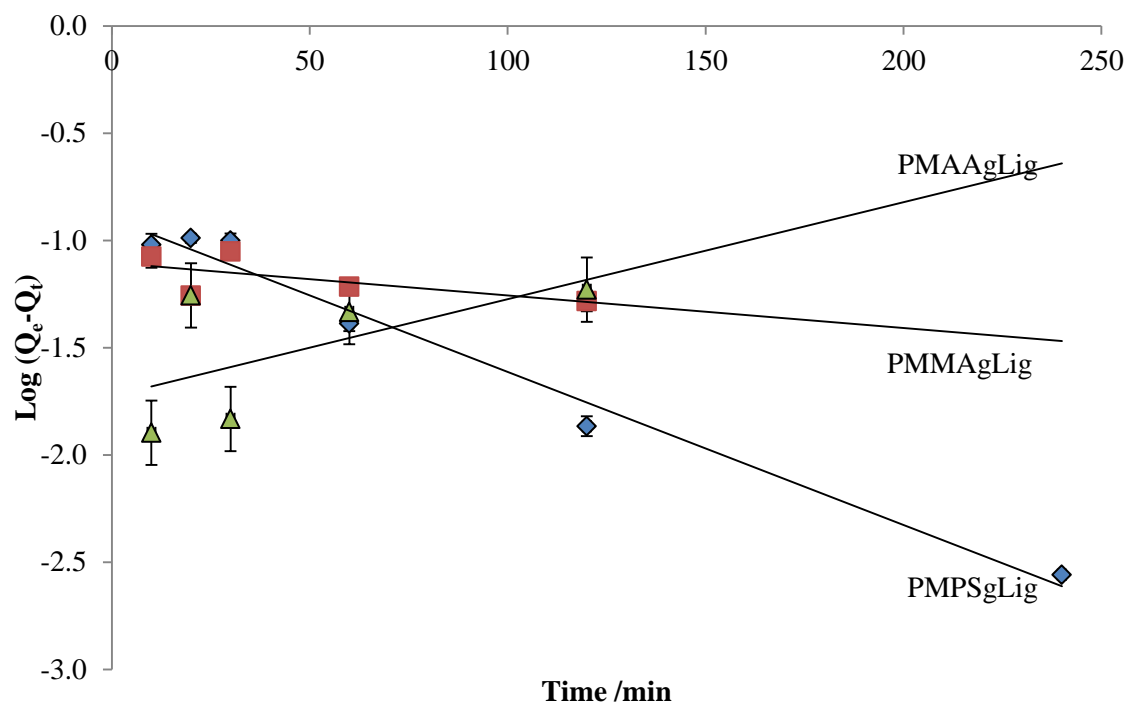
Figure 7.11: Pseudo first-order plots for methyl orange adsorption onto lignocellulose adsorbents.

Adsorption data for lignocellulose could not be processed using the pseudo first-order equation for the same reasons discussed earlier for PMAAgMMT in Section 7.3.1.2. Figure 7.12 displays the pseudo second-order plots for methyl orange adsorption onto the lignocellulose based adsorbents.
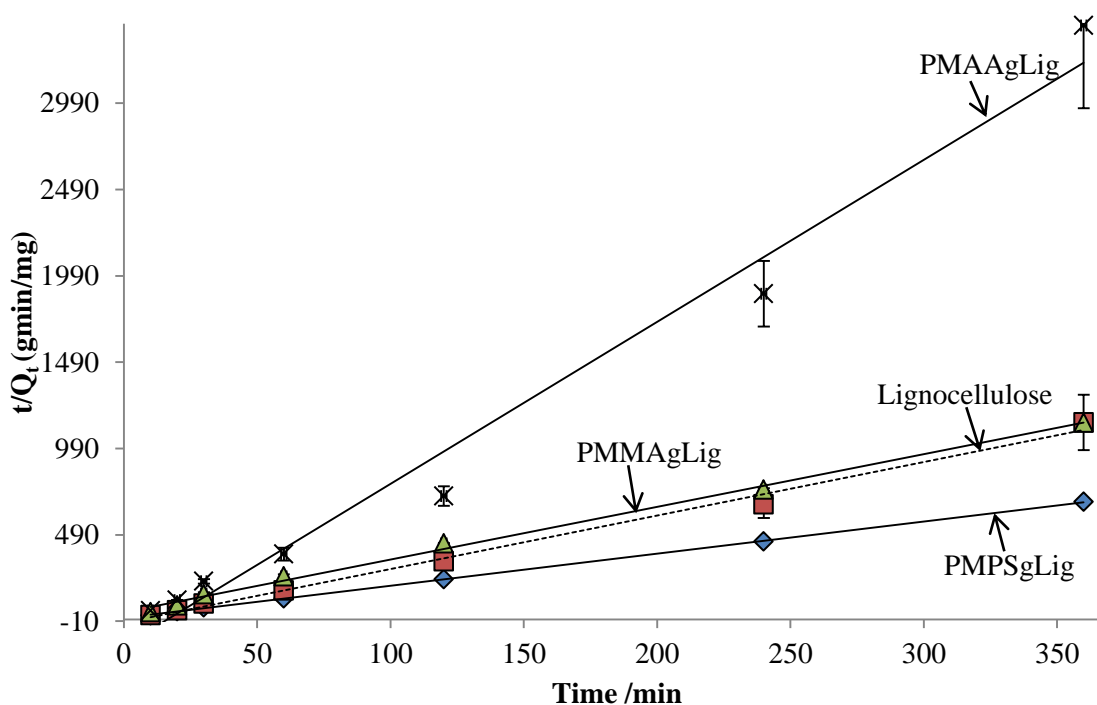
Figure 7.12: Pseudo second-order plots for methyl orange adsorption onto lignocellulose based adsorbents.

The parameters for the pseudo first-order and pseudo second-order models are displayed in Table 7.4 together with their respective correlation coefficients (R^2). Relatively high pseudo second-order R^2 values (> 0.8900) were recorded for all adsorbents compared with the pseudo first-order R^2 values.

Table 7.4: Pseudo first-order and second-order parameters for methyl orange adsorption onto lignocellulose based adsorbents.

Adsorbent	Model	Slope	R^2	Intercept	Q_e	k_1/k_2
Lignocellulose	1st	NA				
	2nd	3.0954	0.9938	-17.173	0.3231	-0.5579
PMMAgLig	1st	-0.0015	0.4020	-1.1039	0.0787	0.0035
	2nd	3.0522	0.9898	40.936	0.3276	0.2276
PMPSgLig	1st	-0.0071	0.9818	-0.8999	0.1259	0.01635
	2nd	1.8608	0.9998	8.9751	0.5374	0.3858
PMAAgLig	1st	0.0045	0.3774	-1.7267	0.0188	-0.0104
	2nd	9.3815	0.9804	-153.99	0.1066	-0.5716

The mechanism of MetO adsorption onto PMPSgLig and PMMAgLig could best be described by the pseudo second-order model. The pseudo second-order rate constants (k_2) found for lignocellulose and PMAAgLig were, however, negative which might mean that the adsorption process onto these

adsorbents is highly unfavourable. This would be a logical assumption since very little (if not negligible) adsorption of methyl orange occurred with these adsorbents.

Vinoth, M. et al, 2010 assessed the adsorption of MetO onto yam plant leaf biomass. The leaf biomass was pretreated by boiling with water followed by drying. The FTIR spectra of their leaf biomass and the leaf biomass used in this study were compared and showed the presence of more or less the same functional groups. However, Vinoth, M. et al, 2010 reported an adsorption capacity of about 80 mg/g (initial concentration of 100 ppm and at pH 3) for the uptake of methyl orange onto the yam plant leaf biomass. The poor uptake of methyl orange by the lignocellulose based adsorbents evaluated in this study means that there was poor interaction between the functional groups on the lignocellulose with the MetO. The differences observed can also be explained in terms of the initial concentration of MetO, adsorbent dosage and adsorption pH (pH was not adjusted in this study).

A number of articles reported the adsorption of methyl orange onto biomass materials (Seyis, I. et al, 2008; Samarghandi, M. R. et al, 2009; Subasioglu, T. et al, 2009). However, a direct comparison of the data obtained is difficult since different approaches were employed.

The following section describes the results obtained from methyl orange adsorption onto the lignocellulose-montmorillonite nanocomposite adsorbents.

7.3.3 Adsorption of methyl orange onto lignocellulose-montmorillonite nanocomposite adsorbents

The adsorption of methyl orange onto the nanocomposites (Lig-NaMMT, PMMAgLig-NaMMT, PMAAgLig-NaMMT and PMPSgLig-NaMMT) was expected to be improved relative to the raw materials and the separately modified lignocellulose based and montmorillonite based adsorbents. A synergistic effect was expected to be at play in the nanocomposite adsorbents which would combine the adsorption properties of lignocellulose and montmorillonite in one material. The isotherms for methyl orange adsorption onto four nanocomposite adsorbents are presented in the following section.

7.3.3.1 Adsorption isotherms

The isotherms for the adsorption of methyl orange onto the lignocellulose-montmorillonite adsorbents are displayed in Figure 7.13. In order to generate the isotherms, Q_e was plotted against C_e. It was observed from the isotherms that the equilibrium adsorbed amounts of methyl orange onto Lig-NaMMT, PMMAgLig-NaMMT and PMAAgLig-NaMMT were much lower than was adsorbed onto PMPSgLig-NaMMT. The least amount of methyl orange was adsorbed onto PMAAgLig-NaMMT.
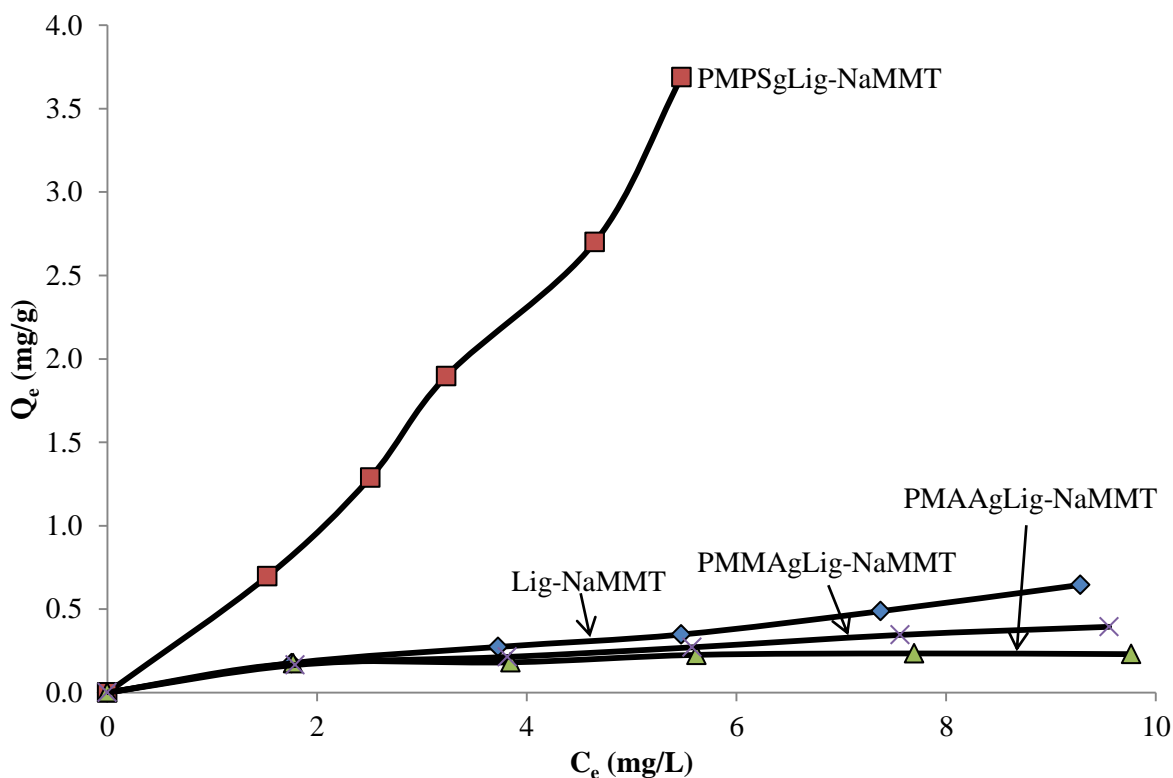
Figure 7.13: Isotherms for methyl orange adsorption onto lignocellulose-montmorillonite adsorbents.

The isotherms were classified as follows: L_3 (Lig-NaMMT), L_4 (PMMAgLig-NaMMT), L_1 (PMAAgLig-NaMMT) and S_3 (PMPSgLig-NaMMT) (Giles, C. H. et al, 1960 and 1974; Hinz, C., 2001).The Langmuir type isotherm has been discussed at length in Section 6.3.1.1.

The *S*-type isotherm is said to arise when the activation energy for desorption of the solute is concentration dependent or is markedly reduced by large negative contributions of the solvent or a second solute (Giles, C. H. et al, 1974). For the initial part of the *S*-curves, the more solute there is already adsorbed, the easier it is for additional amounts to become fixed. This may imply a side-by-side association between adsorbed molecules, helping to hold them to the surface, a behavior called 'cooperative adsorption' (Giles, C. H. et al, 1960). The MetO can be said to be monofunctional in its attraction towards polar surfaces because the attraction arises from its sulfonic group. The MetO units can be visualized as packed vertically in a regular array in the adsorbed layer. Similar isotherms have been reported for the adsorption of monohydric phenols and many monosulfonated dyes onto a polar substrate from a polar solvent like water (Giles, C. H. et al, 1960). Jaoui, M. et al, 1998 also reported similar isotherms for the adsorption of phenol and 4-chlorophenol onto petroleum asphaltenes.

The equilibrium adsorption data were analysed by fitting the data to the Freundlich and Langmuir models, and the respective plots are shown in Figures 7.14 and 7.15.
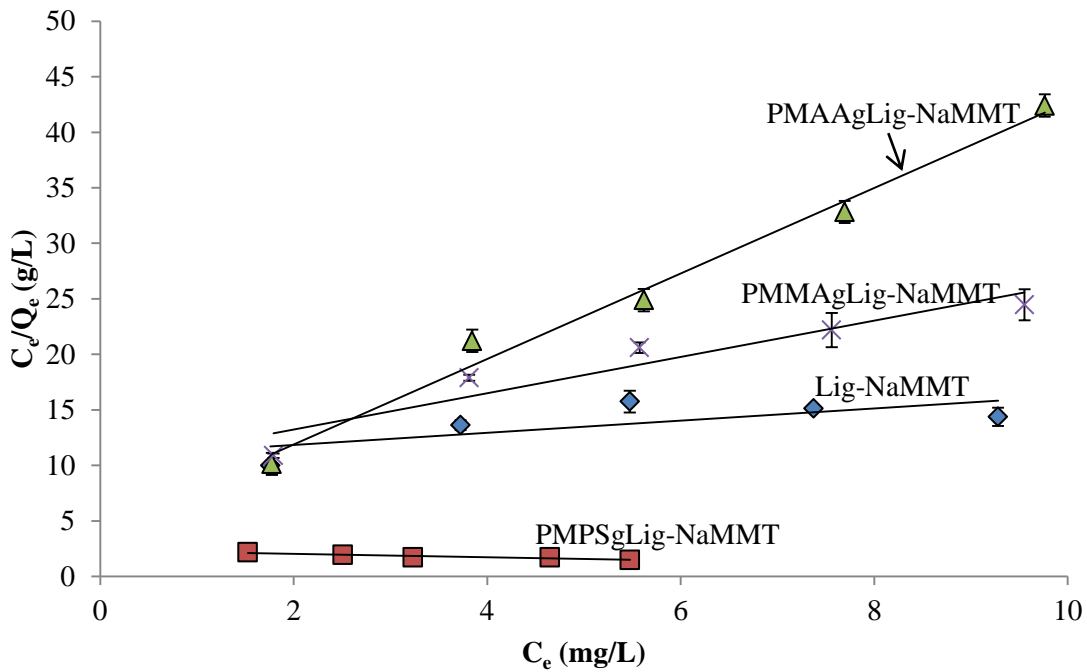
Figure 7.14: Langmuir plots for methyl orange adsorption to lignocellulose-montmorillonite composite adsorbents.
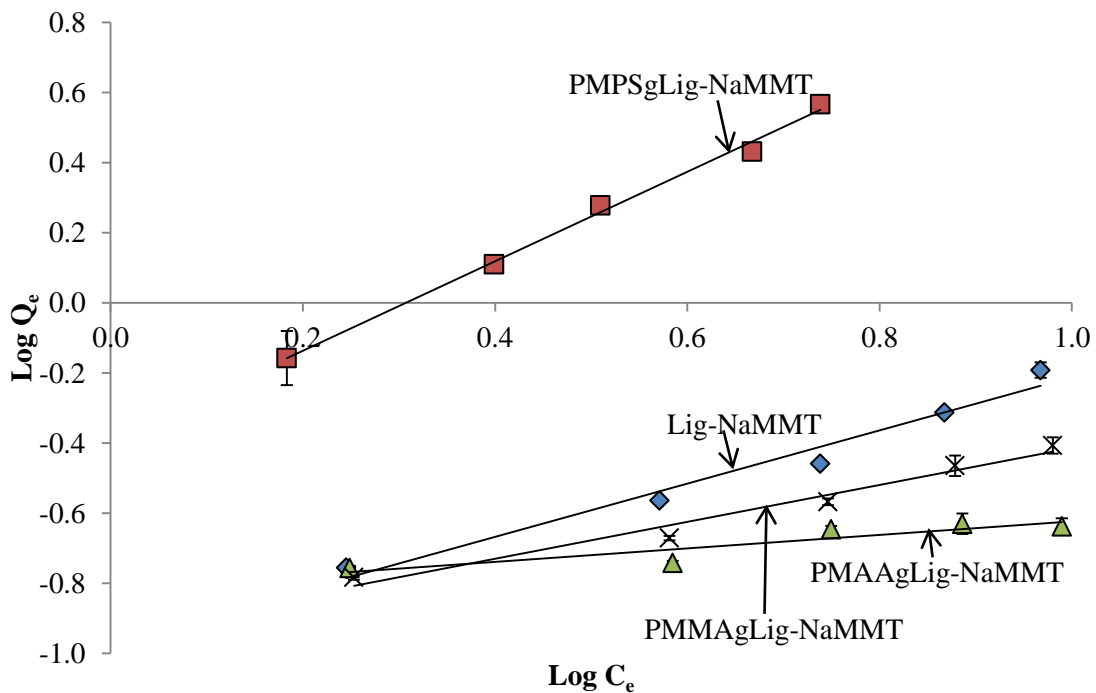
Figure 7.15: Freundlich plots for methyl orange adsorption to lignocellulose-montmorillonite composite adsorbents.

The Freundlich and Langmuir parameters and the correlation coefficients (R^2) for MetO adsorption onto the lignocellulose-montmorillonite nanocomposite adsorbents are listed in Table 7.5. The Freundlich R^2 values were greater than the Langmuir R^2 values for all the nanocomposite adsorbents

except PMAAgLig-NaMMT. The high Freundlich R^2 values suggested a multilayer adsorption process.

Table 7.5: Freundlich and Langmuir parameters for methyl orange adsorption onto the lignocellulose-montmorillonite nanocomposite adsorbents.

Adsorbent	Isotherm	Slope	R^2	Intercept	Q_0/K_f	n/b
Lig-NaMMT	Langmuir	0.5478	0.5158	10.749	1.8255	0.0510
	Freundlich	0.7595	0.9693	-0.9712	0.1069	1.3166
PMMAgLig-NaMMT	Langmuir	1.6338	0.9043	9.9537	0.6121	0.1641
	Freundlich	0.5267	0.9697	-0.9406	0.1147	1.8986
PMPSgLig-NaMMT	Langmuir	-0.1573	0.8752	2.3562	-6.357	-0.067
	Freundlich	1.2753	0.9952	-0.3912	0.4063	0.7841
PMAAgLig-NaMMT	Langmuir	3.8504	0.9845	4.1945	0.2597	0.9180
	Freundlich	-0.1920	0.8248	-0.8154	0.1495	5.2083

The adsorption process of methyl orange onto PMMAgLig-NaMMT can also be described by the Langmuir equation since the R^2 value is > 0.8900. The Langmuir model best fits the data for methyl adsorption onto PMAAgLig-NaMMT. Both the Freundlich R^2 and the isotherm plot of PMPSgLig-NaMMT (Figure 7.13) suggest strong multilayer adsorption. Since the Langmuir R^2 values were found to be relatively low, the adsorption capacities of each of the nanocomposite adsorbents were taken as the equilibrium adsorbed amount determined from the pseudo second-order equation. The next section presents the kinetics data for the adsorption of MetO onto the lignocellulose-montmorillonite nanocomposites adsorbents.

7.3.3.2 Adsorption kinetics

Figure 7.16 shows the plots of the adsorbed amount (mg/g) of methyl orange onto the lignocellulose-montmorillonite nanocomposite adsorbents. The plots in Figure 7.16 show that PMPSgLig-NaMMT had an improved (about five times more) uptake of methyl orange compared with the other nanocomposites and the other adsorbents reported so far. In addition, the other nanocomposites appear to have reached equilibrium in about 2 h, whereas for PMPSgLig-NaMMT still had not quite reached equilibrium even after 6 h of shaking. The uptake of methyl orange by the nanocomposite adsorbents in the following order: PMPSgLig-MMT > Lig-NaMMT > PMMAgLig-NaMMT > PMAAgLig-NaMMT.
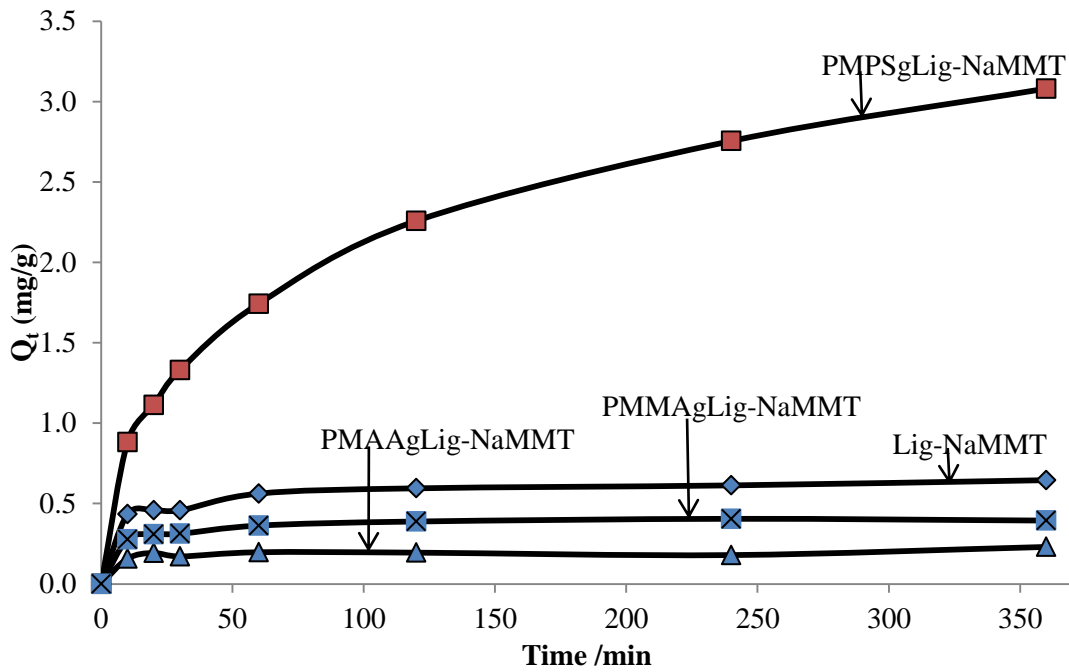
Figure 7.16: Plots of adsorbed amount (mg/g) of methyl orange onto lignocellulose-montmorillonite nanocomposite adsorbents.

The adsorption data were fitted to the pseudo first-order and pseudo second-order kinetic models. Figure 7.17 and 7.18 display the pseudo first-order and pseudo second-order (respectively) plots for MetO adsorption onto the lignocellulose-montmorillonite nanocomposite adsorbents.
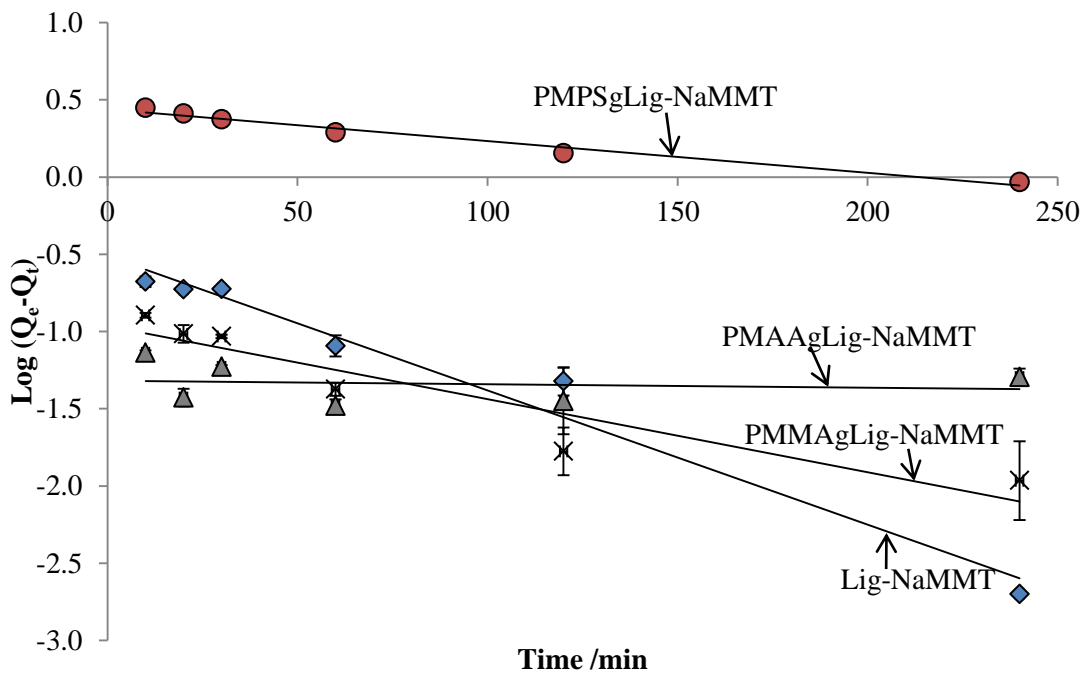
Figure 7.17: Pseudo first-order plots for methyl orange adsorption onto lignocellulose-montmorillonite adsorbents.

259
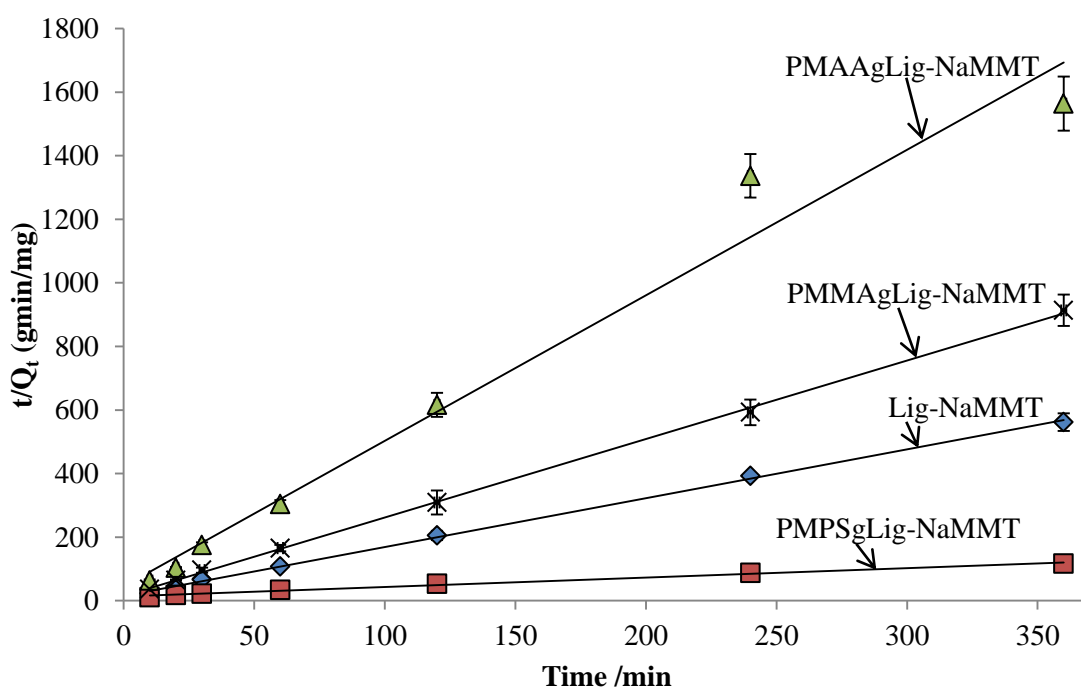
Figure 7.18: Pseudo second-order plots for methyl orange adsorption onto lignocellulose-montmorillonite nanocomposite adsorbents.

The pseudo first-order and pseudo second-order parameters and the correlation coefficients (R^2) are listed in Table 7.6. The pseudo second-order R^2 values were higher than the pseudo first-order R^2 values for all the adsorbents except PMAAgLig-NaMMT.

Table 7.6: Pseudo first-order and pseudo second-order parameters for methyl orange adsorption onto lignocellulose-montmorillonite nanocomposite adsorbents.

Adsorbent	Model	Slope	R^2	Intercept	Q_e (mg/g)	k_1/k_2
Lig-NaMMT	1st	-0.0087	0.9739	-0.5119	0.3077	0.0200
	2nd	1.5363	0.9991	15.623	0.1511	0.6509
PMMAgLig-NaMMT	1st	-0.0047	0.8831	-0.9641	0.1086	0.0108
	2nd	2.4697	0.9994	14.698	0.4049	0.4150
PMPSgLig-NaMMT	1st	-0.0021	0.9777	0.4384	2.7441	0.0048
	2nd	0.2964	0.9923	13.485	3.3738	0.0065
PMAAgLig-NaMMT	1st	-0.0021	0.9777	0.4384	0.0481	0.00046
	2nd	4.5769	0.9752	45.477	0.2185	0.4606

The mechanism for the adsorption of methyl orange onto Lig-NaMMT, PMMAgLig-NaMMT and PMPSgLig-NaMMT could best be described by the pseudo second-order model. Given the relatively

high and comparable pseudo first-order and pseudo second-order R^2 values, both models could be used to represent the adsorption mechanism onto Lig-NaMMT and PMAAgLig-NaMMT. The equilibrium adsorption capacity of PMPSgLig-NaMMT (3.374 mg/g) was relatively high compared with what was obtained for AlpMMT (1.543 mg/g), NaMMT (1.134 mg/g) and lignocellulose (0.405 mg/g).

Given that the starting materials (NaMMT and lignocellulose) and the physical mixture (Lig-NaMMT) had lower adsorption capacities than PMPSgLig-NaMMT, the improvement observed in the uptake of methyl orange by PMPSgLig-NaMMT seems to be attributable to some synergy between lignocellulose and NaMMT as aimed for in this study. This is the first study that has produced synergy in the adsorption of dyes onto a nanocomposite of lignocellulose and NaMMT. The separately grafted materials (PMPSgMMT and PMPSgLig) did not show that much uptake of methyl orange. A slight improvement was observed for PMPSgLig (0.537 mg/g) compared with lignocellulose, whereas PMPSgMMT (1.113 mg/g) showed more or less the same uptake of methyl orange as NaMMT. Also improved uptake could have been due to some synergy contributed by the presence of the three materials (MPS, NaMMT and lignocellulose) in the composite material.

Igwe, J. C. et al, 2007 reported adsorption capacities of about 10 mg/g for the adsorption of methyl orange onto Great millet waste biomass. The reason for the relatively higher uptake reported by Igwe, J. C. et al, 2007 was possibly due to the higher concentration of methyl orange (100 ppm) they used than was used in this study (10 ppm). Saha, T. K. et al, 2010 used chitosan for the adsorption of methyl orange and reported an adsorption capacity of about 10 mg/g. Their adsorption data were best represented by the pseudo second-order and the Langmuir models as shown by the high R^2 values obtained. Kumar, K. V., 2006 investigated the sorption kinetics of methylene blue onto activated. They reported that their sorption process followed both the pseudo first-order and pseudo second-order models. In another study, Kumar, K. V. et al, 2008 assessed the adsorption of Auramin O onto activated carbon and found that the adsorption mechanism followed the pseudo second-order model. The findings here agree with what has been reported in the literature.

It has already been reported in Sections 7.3.3.1 and 7.3.3.2 that adsorption of MetO onto the other nanocomposite adsorbents (PMAAglig-NaMMT and PMMAgLig-NaMMT) was relatively low (< 0.700 mg/g).

The following section discusses the results obtained from the adsorption of MetO onto AlpMMT samples of different OH/Al molar ratio.

7.3.4 Effect of OH/Al molar ratio on the adsorption of methyl orange

Figure 7.19 shows the plot of the variation of adsorbed amount (mg/g/ of MetO against the OH/Al molar ratio. It was observed that the equilibrium adsorbed amount of MetO decreased with increase in the OH/Al molar ratio. Methyl orange (anionic form) is said to interact with clay via cationic bridges, whereas the cationic form is weakly adsorbed by a cation-exchange mechanism (Saunyama, P. et al, 2001; Ökte, A. N. et al, 2009). It is not yet clear why the uptake of MetO should decrease with increase in the OH/Al molar ratio. It was highlighted in Chapter 6 that the amount of aluminium incorporated into the pillared clays increased with increase in the OH/Al molar ratio. One would have expected an increase in the amount of MetO adsorbed with increase in the amount of aluminium incorporated in the clay, since there will be more aluminium cationic species which should interact with the sulfonic group of the MetO.
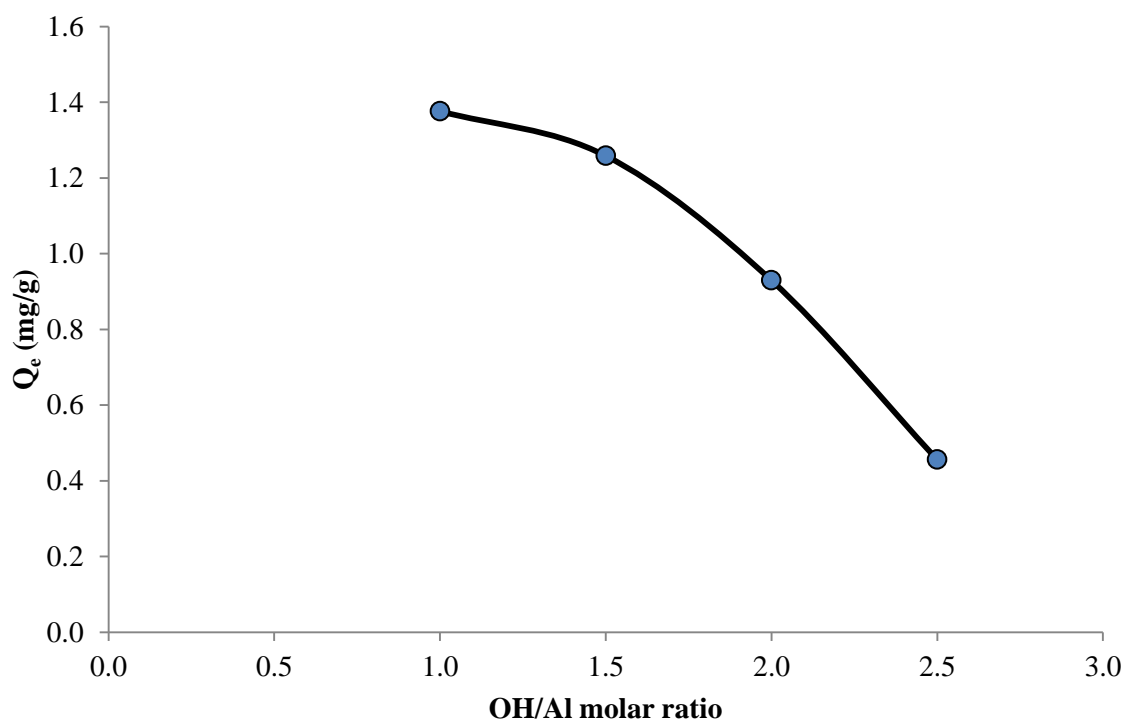
Figure 7.19: Variation of adsorbed amount (mg/g) of methyl orange with OH/Al molar ratio.

Altunlu, M. et al, 2007 investigated the pillaring of MMT at different OH/Al and Al/clay molar ratios. They also assessed the effect of OH/Al and Al/clay ratios on the adsorption of phenol and chlorophenol. The authors reported that the amount of phenol adsorbed decreased with increase in the OH/Al molar ratio, which agrees with the findings in this study though the adsorbates are different.

7.3.5 Competitive adsorption of methyl orange from binary mixtures with (Cd^{2+} and Pb^{2+}) onto PMPSgLig-NaMMT nanocomposite

The competitive adsorption of methyl orange (MetO) from a binary mixture with either Cd^{2+} or Pb^{2+} is reported in this section. The competitive adsorption experiments were carried out in such a way as to generate both isotherm and kinetics data. The data were processed as presented in Section 6.2.

7.3.5.1 Adsorption isotherms

Figure 7.20 shows the adsorption isotherms for the adsorption of MetO from a binary mixture of MetO&Cd^{2+} and MetO&Pb^{2+}. The isotherm for MetO adsorption (as a single component) onto PMPSgLig-NaMMT nanocomposite has already been presented in Section 7.3.3.1 but was included here for comparison purposes only. The isotherms were classified according to Giles, C. H. et al, 1960 and 1974 as all belonging to the *S* class and subgroup 3. As discussed in Section 7.3.3.1, it was observed that as the concentration of MetO increased, the uptake of the MetO also increased. This behavior shows cooperative adsorption of the MetO molecules together with the heavy metal ions (Giles, C. H. et al, 1960; Jaoui, M. et al, 1998and 1974; Hinz, C., 2001).
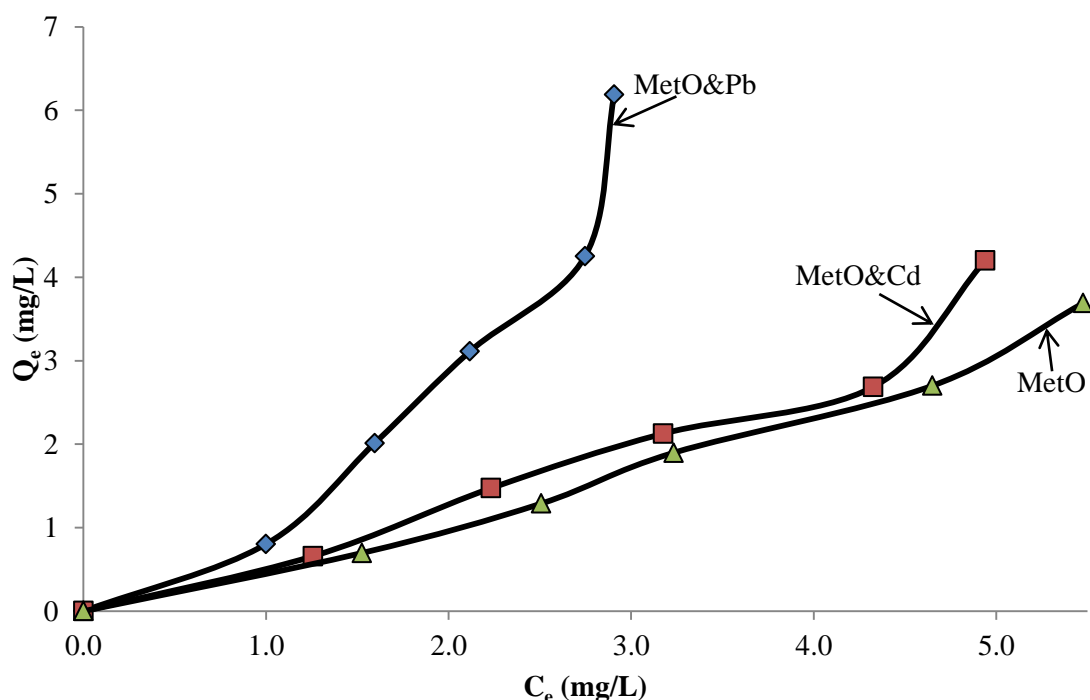
Figure 7.20: Isotherms for MetO, MetO&Cd and MetO&Pb adsorption onto PMPSgLig-NaMMT nanocomposite.

From the isotherms, it was observed that the least amount of MetO was adsorbed when it was present as a single component in solution. The presence of Cd^{2+} in solution caused a slight increase in the uptake in the uptake of MetO from solution. Pb^{2+} caused an even larger increase in the uptake of

MetO than Cd^{2+}. It has also been highlighted in Section 6.3.5.3 that the *S*-curve appears when the solute meets strong competition for adsorption sites due to presence of impurities. The improved uptake of MetO from binary mixtures of either Cd^{2+} or Pb^{2+} can be attributed to the presence of these heavy metals which act as impurities and provide strong competition for the adsorption sites. Apart from inducing competition, the adsorbed heavy metals can also act as adsorption sites for MetO through electrostatic interaction.

The adsorption data were further analysed by fitting to the Freundlich equation and to the Langmuir equation. Figures 7.21 and 7.22 display the plots of the Freundlich and Langmuir isotherms (respectively) generated for the adsorption of MetO from binary mixtures with Cd^{2+} or Pb^{2+}.
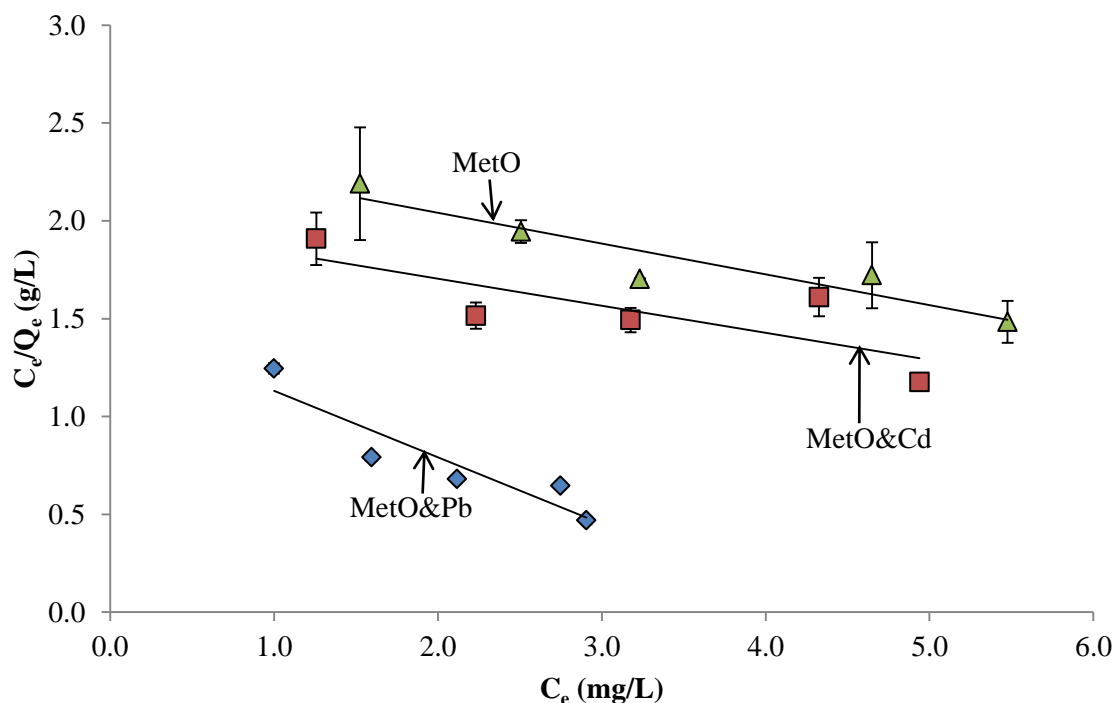
Figure 7.21: Langmuir plots for MetO, MetO&Cd and MetO&Pb adsorption onto PMPSgLig-NaMMT nanocomposite.
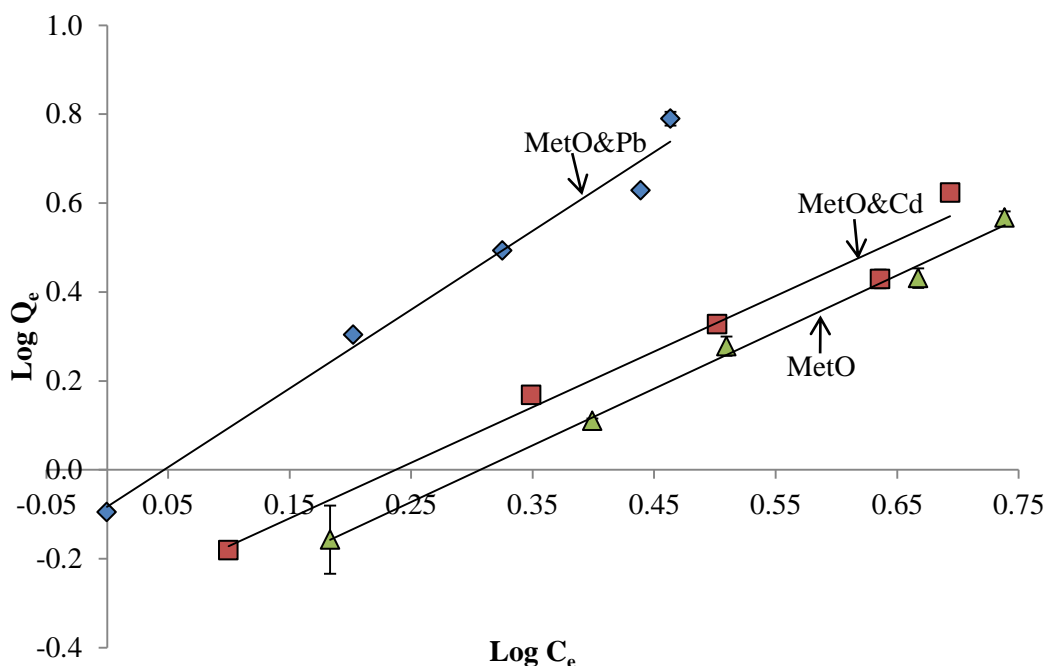
Figure 7.22: Freundlich plots for MetO, MetO&Cd and MetO&Pb adsorption onto PMPSgLig-NaMMT nanocomposite.

The parameters for the Freundlich and Langmuir models are shown in Table 7.7 together with the correlation coefficients (R^2). The Freundlich model showed higher R^2 values compared with the Langmuir isotherm. The Freundlich model describes multilayer adsorption onto heterogeneous surfaces. These findings agree with the plots in Figure 7.20 which showed *S*-curves (a deviation from Langmuir monolayer adsorption). The Freundlich constant, K_f, increased in the order MetO < MetO&Cd < MetO&Pb.

Table 7.7: Freundlich and Langmuir parameters for the adsorption of MetO from binary mixtures with Cd^{2+} or Pb^{2+} onto PMPSgLig-NaMMT.

Mixture	Isotherm	Slope	R^2	Intercept	Q_0/K_f	n/b
MetO	Langmuir	-0.1573	0.8752	2.3562	-6.357	-0.067
	Freundlich	1.2753	0.9952	-0.3912	0.4063	0.7841
MetO&Cd	Langmuir	-0.1384	0.6239	1.9815	-7.2254	-0.070
	Freundlich	1.2503	0.9768	-0.2966	0.5051	0.7998
MetO&Pb	Langmuir	-0.3392	0.8566	1.4701	-2.9481	-0.231
	Freundlich	1.7726	0.9828	-0.0828	0.8264	0.5641

The Langmuir R^2 values were poor (< 0.8900) and negative adsorption capacities were also obtained in all cases. In addition, the Langmuir affinity constants (*b*) obtained for all the cases were negative.

This essentially means the Langmuir model is not applicable to describe the adsorption process of MetO from these mixtures onto the PMPSgLig-NaMMT nanocomposite.

The following section presents the results from the kinetic studies of MetO adsorption from the binary mixtures with Cd^{2+} or Pb^{2+} onto the PMPSgLig-NaMMT nanocomposite.

7.3.5.2 Adsorption kinetics

Figure 7.23 presents the plots of adsorbed amount (mg/g) of MetO from the binary mixtures against time (min). It can be seen from the plots that the adsorbed amount of MetO increased again in the order: MetO < MetO&Cd < MetO&Pb. The plots were characterized by a rapid uptake in the initial stages (1 h) of the adsorption process and systems approached equilibrium in about 4 h.

The adsorption data were further analysed by fitting to the pseudo first-order and pseudo second-order equations.
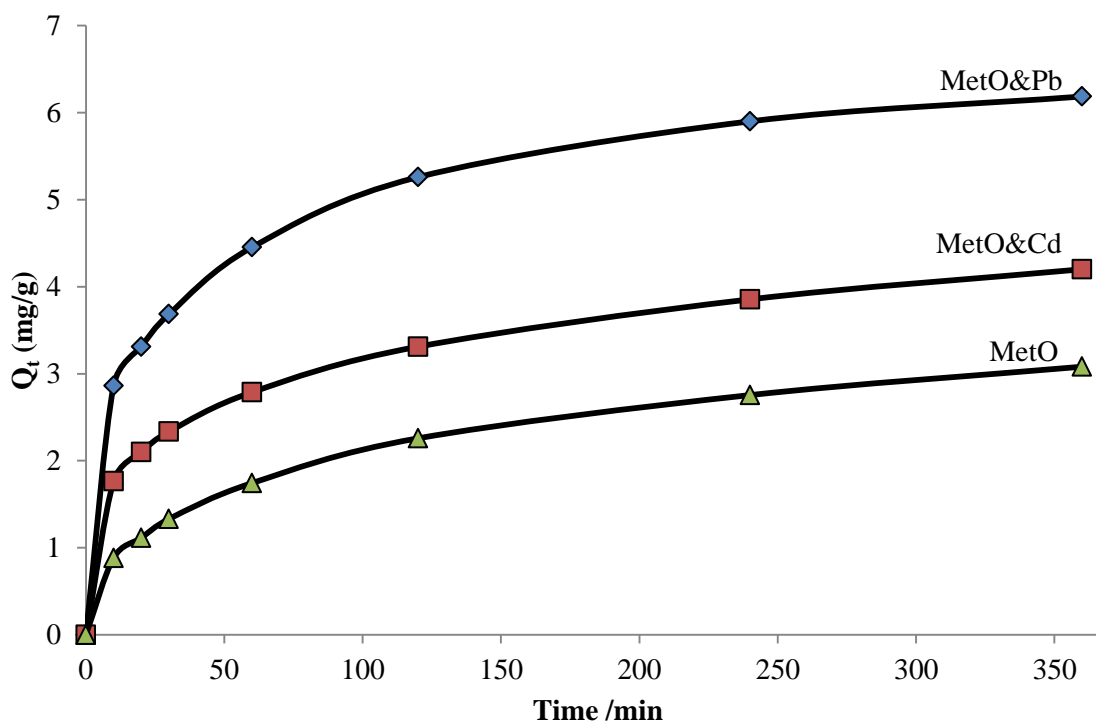
Figure 7.23: Plots of adsorbed amount (mg/g) of MetO, Met&Cd and MetO&Pb onto PMPSgLig-NaMMT nanocomposite against time (min).

Figures 7.24 and 7.25 display the pseudo first-order and pseudo second-order plots for MetO adsorption from the binary solutions containing Cd^{2+} or Pb^{2+}.
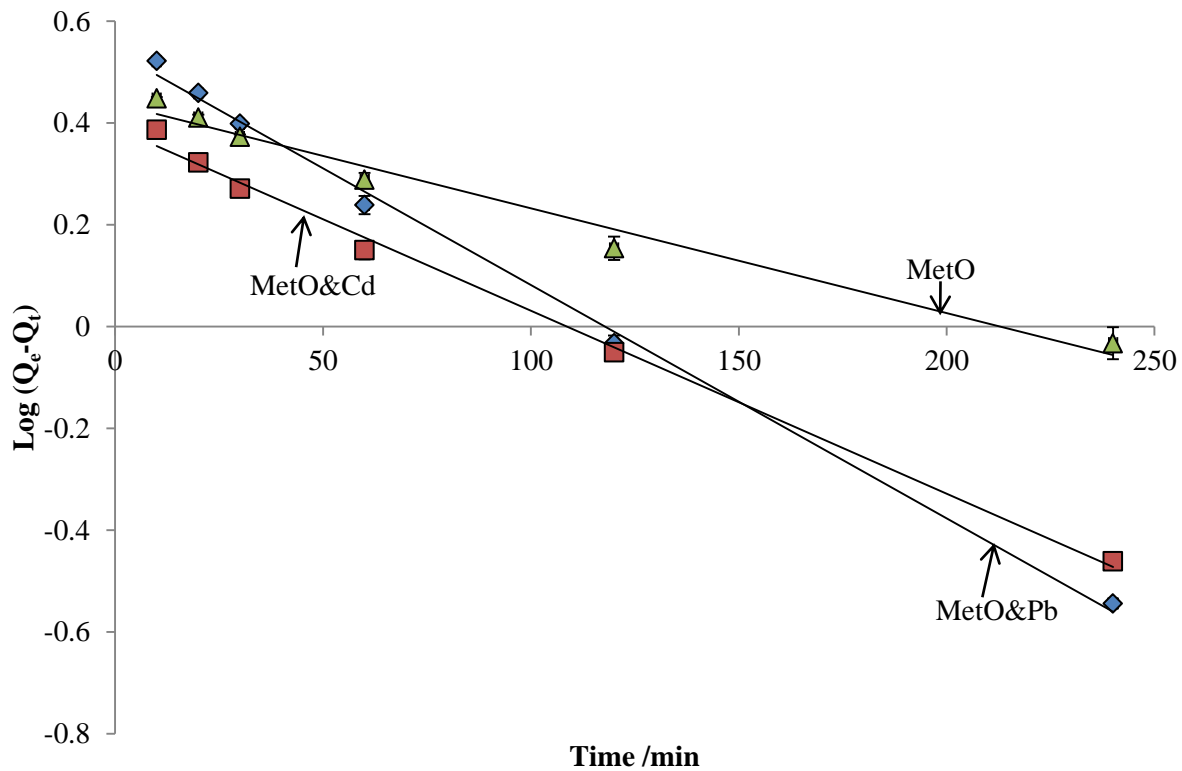
Figure 7.24: Pseudo first-order plots for MetO, MetO&Cd and MetO&Pb adsorption onto PMPSgLig-NaMMT nanocomposite.
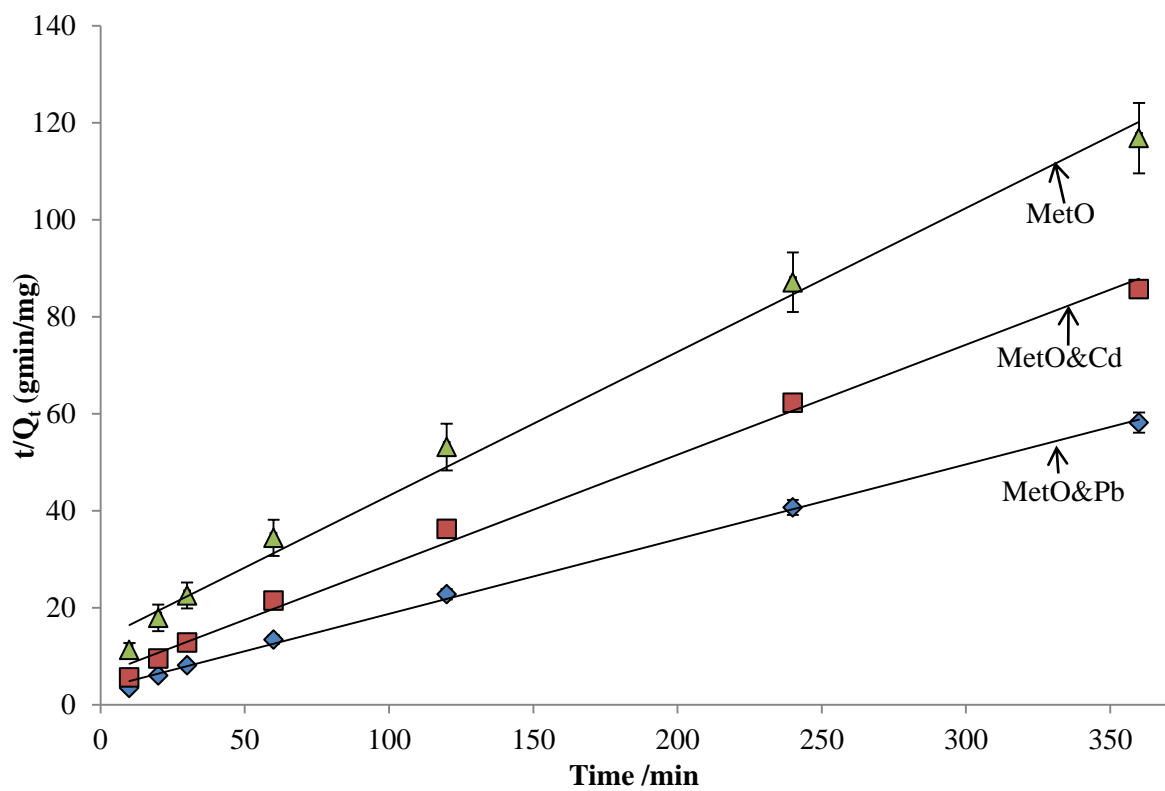
Figure 7.25: Pseudo second-order plots for MetO, MetO&Cd and MetO&Pb adsorption onto PMPSgLig-NaMMT nanocomposite.

The parameters and correlation coefficients (R^2) of the pseudo first-order and pseudo second-order models are shown in Table 8. Adsorption of MetO from a single component solution (MetO only) showed a very poor pseudo first-order R^2 value of 0.0218. The pseudo first-order and pseudo second-order R^2 values for MetO adsorption from MetO&Cd and MetO&Pb binary mixtures were relatively close to 1.0 and quite comparable. The relatively high pseudo first-order R^2 values suggested a departure from the assumption of strict chemisorption according to the pseudo second-order model. The adsorption mechanism of MetO from these mixtures can therefore, be represented by both models.

Table 7.8: Pseudo first-order and pseudo second-order parameters for MetO adsorption from binary mixtures containing Cd^{2+} or Pb^{2+} onto PMPSgLig-NaMMT.

Mixture	Model	Slope	R^2	Intercept	Q_e	k_1/k_2
MetO	1st	-0.0002	0.0218	-1.3181	2.7441	0.0048
	2nd	0.2964	0.9923	13.485	3.3738	0.0065
MetO&Cd	1st	-0.0036	0.9960	0.3908	2.4592	0.0083
	2nd	0.2270	0.9950	6.1600	4.4053	0.0084
MetO&Pb	1st	-0.0046	0.9971	0.5405	3.4714	0.0106
	2nd	0.1542	0.9983	3.3273	6.4851	0.0071
MetO&Cd&Pb	1st	-0.0046	0.9969	0.5398	3.4658	0.0106
	2nd	0.1548	0.9981	3.5533	6.4599	0.0067

The adsorption of MetO from a ternary mixture containing both Cd^{2+} and Pb^{2+} was also assessed. The results showed that the uptake of MetO from such a mixture was just the same as for a binary mixture of MetO and Pb^{2+} mixture. This essentially means that Pb^{2+} exerts greater influence on the uptake of MetO from aqueous solution. It has been highlighted in Section 6.3.3.1 that Pb^{2+} showed a higher affinity than Cd^{2+} for all the adsorbents evaluated. It can, therefore, be postulated that the Pb^{2+} ions get adsorbed onto the adsorbent surface first, thus, creating adsorption sites where the MetO molecules then adsorb. The same mechanism should be at play for MetO adsorption from a MetO and Cd^{2+} binary mixture. However, Rauf, M. A. et al, 2008 found that the adsorption of coomassie blue, malachite green and safranin orange onto sand decreased in the presence of potassium, nickel and zinc ions.

The ability of PMPSgLig-NaMMT nanocomposite to adsorb both organics (methyl orange) and heavy metals (Cd^{2+} and Pb^{2+}) from aqueous solution is attractive since most industrial waste waters contain both organic and inorganic contaminants. This was one of the objectives of this study. This novel

nanocomposite can be used for the simultaneous removal of both heavy metals and organic pollutants in one step, thus cutting down on time and effluent treatment cost.

The following sections discuss the results from the adsorption of neutral red onto the different adsorbents prepared and evaluated in this study.

7.3.6 Adsorption of neutral red onto montmorillonite based adsorbents.

7.3.6.1 Adsorption isotherms

Figure 7.26 displays the isotherms for the adsorption of neutral red (NeuR) onto montmorillonite based adsorbents. The isotherms for neutral red adsorption onto the adsorbents, NaMMT, PMMAgMMT, PMAAgMMT and PMPSgMMT show an exponential increase in the adsorption as the concentration of neutral red increases. The isotherms can be classified as S-curves according to the Giles classification system (Giles, C. H. et al, 1960). S-shaped isotherms are said to indicate multilayer adsorption (Freundlich model). However, the isotherm for neutral red adsorption onto AlpMMT can be classified as L_3 and this shows conformity to the Langmuir model of adsorption. The Langmuir model describes monolayer adsorption. The isotherms indicate neutral red adsorption to more or less the same extent for the adsorbents, NaMMT, PMMAgMMT, PMAAgMMT and PMPSgMMT. Adsorption of neutral red onto AlpMMT was less than that recorded for the other adsorbents in Figure 7.26.
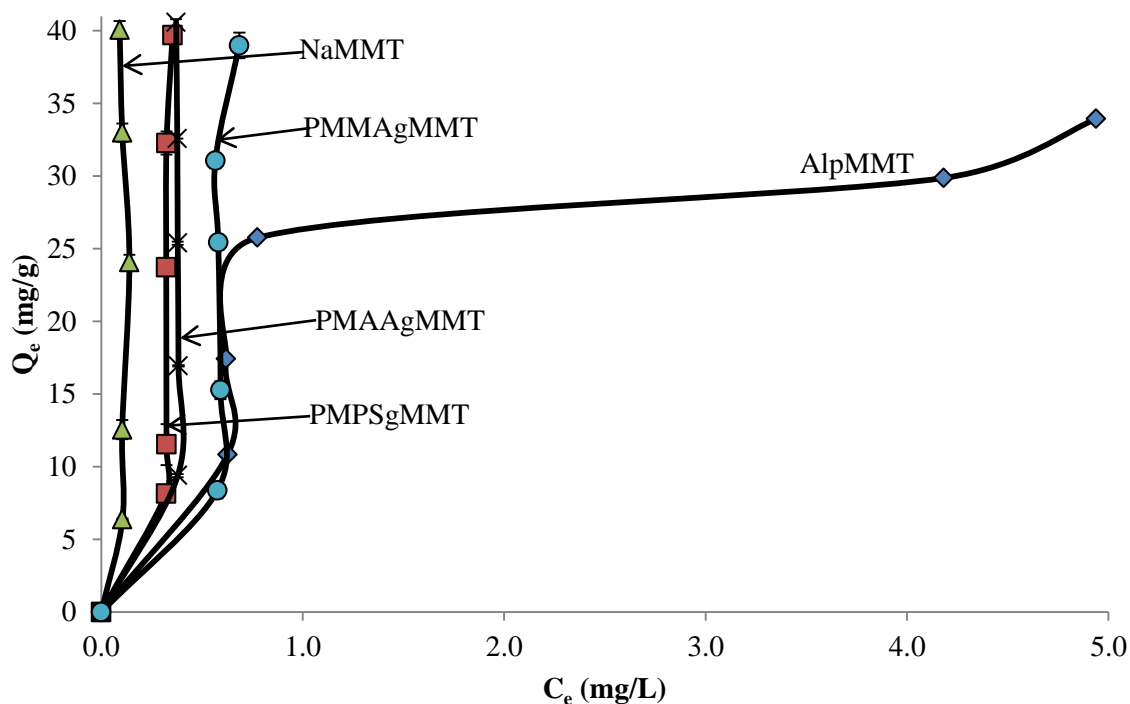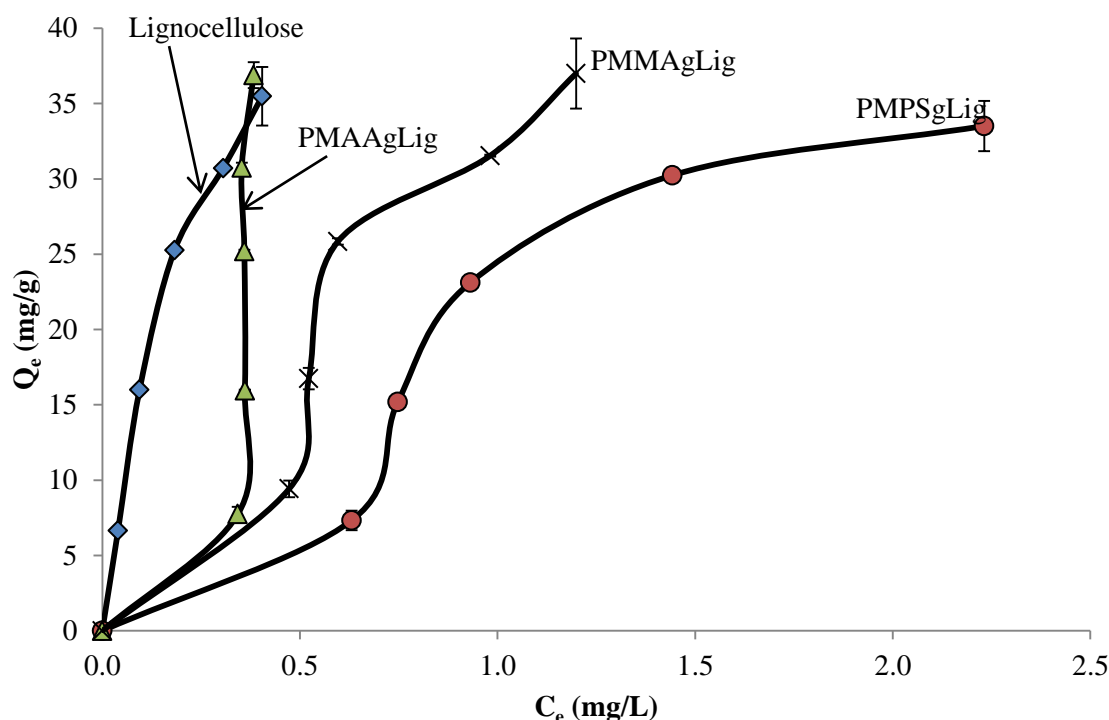

Figure 7.26: Isotherms for neutral red adsorption montmorillonite-based adsorbents.

The adsorption data was fitted to the Freundlich and Langmuir model equations as described in Section 6.2.2. Due to the poor fitting of the adsorption data to these equations, the Freundlich and Langmuir plots had to be plotted individually and are shown in Figures B-1 to B-10 of Appendix B. The respective parameters of the Freundlich and Langmuir equations for neutral red adsorption onto the montmorillonite based adsorbents are shown Table 7.9.

Table 7.9: Freundlich and Langmuir parameters for neutral red adsorption onto montmorillonite based adsorbents.

Adsorbent	Isotherm	Slope	R^2	Intercept	Q_0/K_f	n/b
NaMMT	Langmuir	0.0520	0.1760	-0.0009	19.2308	-57.78
	Freundlich	0.7275	0.0711	2.0385	109.27	1.3746
AlpMMT	Langmuir	0.0262	0.9475	0.0245	38.168	1.0693
	Freundlich	0.4992	0.9686	-0.3112	0.4884	2.0032
PMPSgMMT	Langmuir	-0.4346	0.2609	0.1618	-2.0301	-2.686
	Freundlich	0.1024	0.3916	-0.8436	0.1434	9.7656
PMAAgMMT	Langmuir	1.1135	0.8684	-0.4062	0.8981	-2.741
	Freundlich	-25.901	0.7328	-11.662	2×10^{-12}	-0.039
PMMAgMMT	Langmuir	-0.1659	0.1332	0.1329	-6.028	-1.248
	Freundlich	4.0202	0.2503	2.2148	163.98	0.2487

A look at the data in Table 7.9 shows that the correlation coefficients (R^2) for both the Freundlich and Langmuir models were very poor. This is with the exception of neutral red adsorption onto AlpMMT where the Freundlich and Langmuir R^2 values were all > 0.9400. The adsorption of neutral orange onto AlpMMT can be said to be represented by both the Freundlich and Langmuir models. However, the poor R^2 values for the other adsorbents mean that both the Freundlich and Langmuir were not applicable to describe neutral red adsorption onto these adsorbents. The true adsorption capacities could not be accurately determined from these isotherm models since the correlation coefficient values were poor.

7.3.6.2 Adsorption kinetics

The plots of adsorbed amount (mg/g) of neutral red onto montmorillonite based adsorbents against time (min) are shown in Figure 7.27. The plots were characterized by a rapid uptake of neutral red in the first 30 min, with equilibrium being reached in about 60 min for the adsorbents, NaMMT, PMPSgMMT, PMAAgMMT and PMMAgMMT. However, the uptake of neutral red onto AlpMMT was relatively slow and the system had not achieved equilibrium even after six hours. As observed from the isotherms in Figure 7.26, the amount of neutral red adsorbed onto AlpMMT was lower than

that adsorbed by the other four adsorbents. There was also a relatively greater variation in the adsorption data for AlpMMT compared with NaMMT, PMAAgMMT, PMPSgMMT and PMMAgMMT.
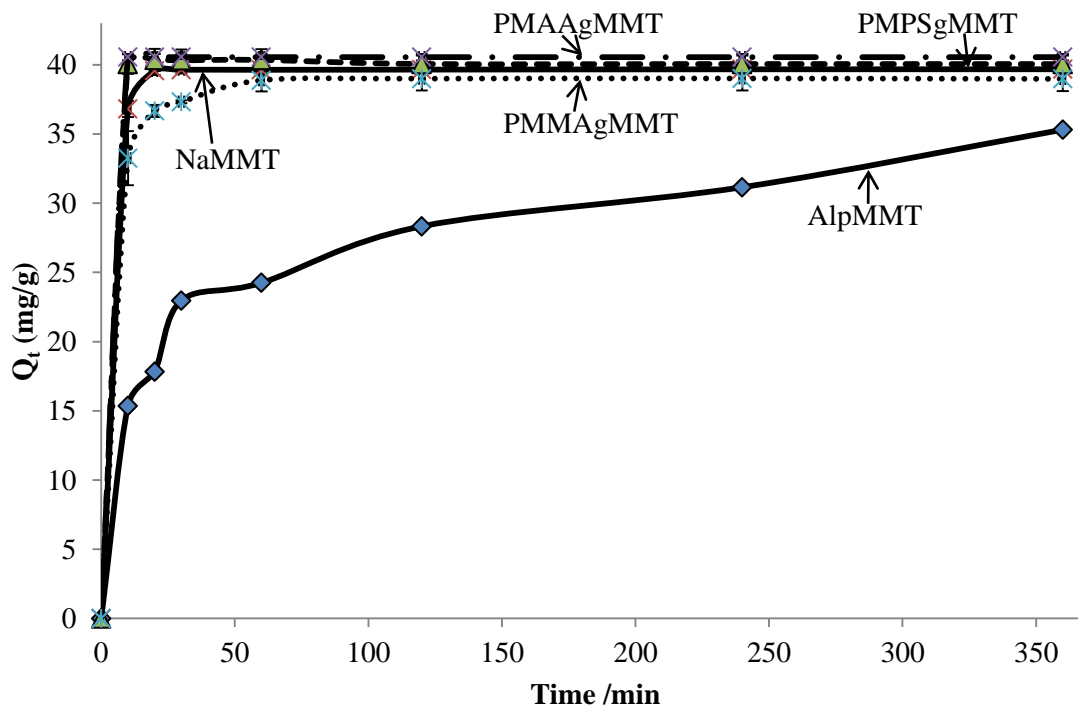
Figure 7.27: Plot of adsorbed amount (mg/g) of neutral red onto montmorillonite-based adsorbents against time (min).

The adsorption data were fitted to the pseudo first-order and pseudo second-order kinetic equations and plots are displayed in Figures 7.28 and 7.29, respectively.
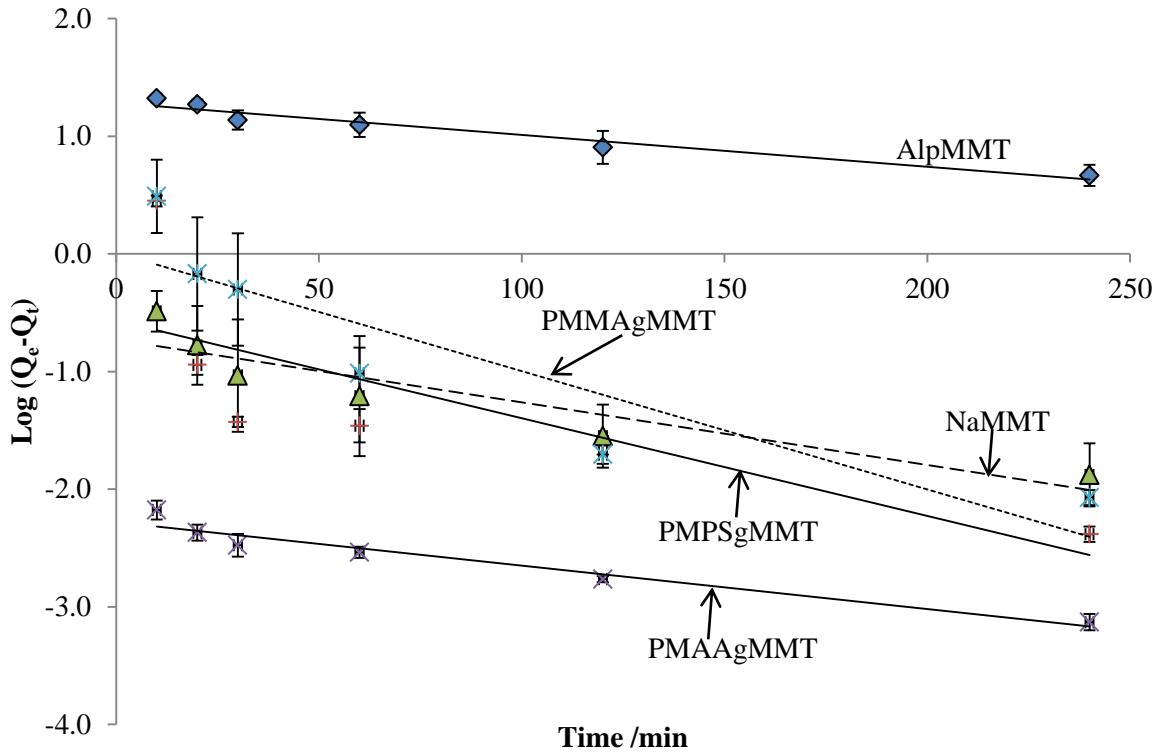
Figure 7.28: Pseudo first-order plot for neutral red adsorption onto montmorillonite based adsorbents.
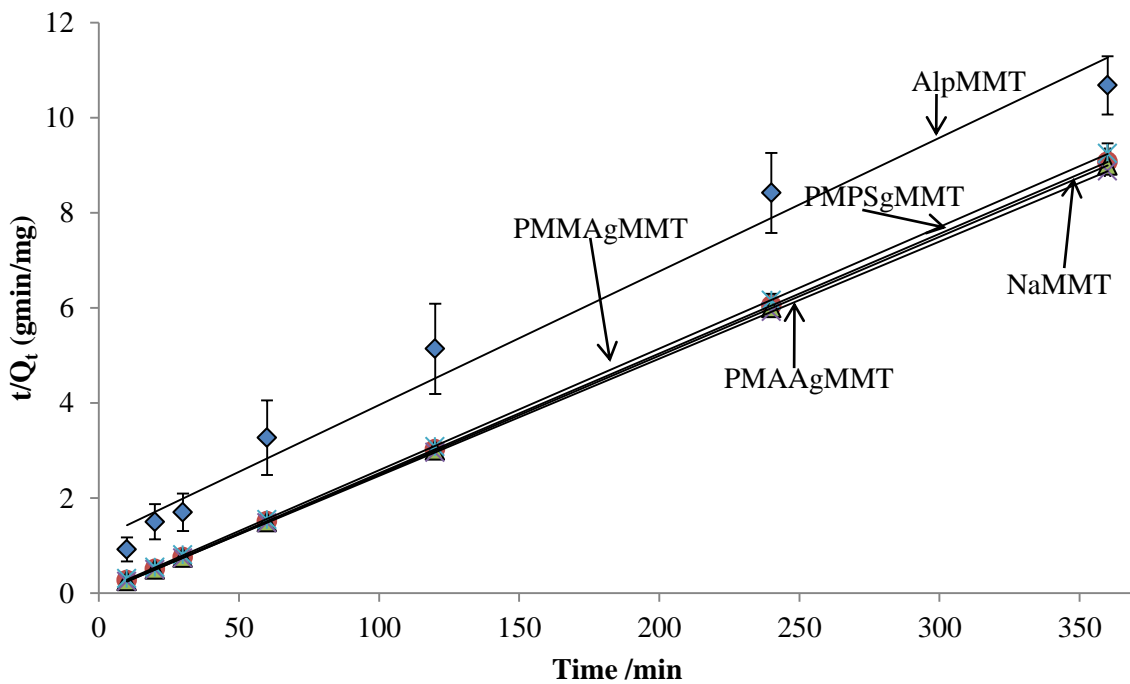
Figure 7.29: Pseudo second-order plot for neutral red adsorption onto montmorillonite based adsorbents.

The respective pseudo first-order and pseudo second-order parameters for neutral red adsorption onto montmorillonite based adsorbents are shown in Table 7.10. Generally, the adsorption data were found to follow the pseudo second-order kinetic model as judged from the relatively high R^2 values. Neutral

red adsorption onto AlpMMT, however, could also be described by pseudo first-order model since the R^2 value found was 0.9506 (> 0.8900).

Table 7.10: Pseudo first-order and pseudo second-order parameters for neutral red adsorption onto montmorillonite based adsorbents.

Adsorbent	Model	Slope	R^2	Intercept	Q_e	k_1/k_2
NaMMT	1st	-0.0053	0.8551	-0.7296	0.1864	0.01221
	2nd	0.0250	1.0000	-0.0043	40.000	0.1454
AlpMMT	1st	-0.0027	0.9506	1.2825	19.1646	0.006218
	2nd	0.0281	0.9815	1.1457	35.587	0.000689
PMPSgMMT	1st	-0.0083	0.5937	-0.5678	0.2705	0.01912
	2nd	0.0252	1.0000	0.0065	39.6825	0.09770
PMAAgMMT	1st	-0.0037	0.9434	-2.2808	0.00524	0.008521
	2nd	0.0247	1.0000	3.0×10^{-5}	40.4858	20.336
PMMAgMMT	1st	-0.0101	0.8155	0.0079	1.01836	0.02326
	2nd	0.0256	1.0000	0.0292	39.0625	0.02244

Since the pseudo second order R^2 values were very high (≥ 0.9800), the adsorption capacities were computed using this model. Table 7.10 shows that AlpMMT had the least adsorption capacity (35.6 mg/g) while PMAAgMMT had the highest (40.5 mg/g).

7.3.7 Adsorption of neutral red onto lignocellulose based adsorbents

7.3.7.1 Adsorption isotherms

Figure 7.30 displays the isotherms for neutral red adsorption onto lignocellulose based adsorbents. The isotherms for neutral red adsorption onto lignocellulose, PMPSgLig, PMAAgLig and PMMAgLig were classified as L_1, S_2, S_1 and S_3, respectively. As already discussed in Section 7.3.3.1 for methyl orange, the *S*-curve indicates 'cooperative adsorption' with solute molecules tending to be adsorbed packed in rows or clusters. In the case of planar aromatic molecules like neutral red, this implies adsorption with the aromatic nuclei face-to-face and perpendicular to the surface (Giles, C. H. et al, 1974).

Figure 7.30: Isotherms of neutral red adsorption onto lignocellulose based adsorbents.

The adsorption data were also fitted to the Freundlich and Langmuir equations. The Freundlich and Langmuir plots are displayed in Figures B-11 to B-18 of Appendix B. The Freundlich and Langmuir parameters for neutral red adsorption onto the lignocellulose based adsorbents are listed in Table 7.11. Again, as observed and discussed for neutral red adsorption onto montmorillonite based adsorbents, both the Freundlich and Langmuir R^2 values were found to be poor (< 0.8900).

Table 7.11: Freundlich and Langmuir parameters for neutral red adsorption onto lignocellulose based adsorbents.

Adsorbent	Isotherm	Slope	R^2	Intercept	Q_0/K_f	n/b
Lignocellulose	Langmuir	0.0157	0.9224	0.0051	63.694	3.0784
	Freundlich	1.1701	0.5868	2.0723	118.11	0.8546
PMMAgLig	Langmuir	-0.0096	0.0800	0.0415	-104.17	-0.231
	Freundlich	1.1750	0.7830	1.5248	33.481	0.8511
PMPSgLig	Langmuir	-0.0016	0.0028	0.0608	-625.00	-0.026
	Freundlich	0.6581	0.7576	1.5667	36.872	1.5195
PMAAgLig	Langmuir	-0.5955	0.4794	0.2342	-1.6793	-2.543
	Freundlich	5.6445	0.6998	4.7732	5.9×10^4	0.1772

The only exception was lignocellulose whose Langmuir R^2 value was 0.9224. Moreover, the adsorption capacities computed for some of the adsorbents (PMMAgLig, PMPSgLig and PMAAgLig)

were negative, indicating that the two models may not be applicable to describe the adsorption process of neutral red under the conditions described.

7.3.7.2 Adsorption kinetics

The adsorbed amount of neutral red (Q_t, mg/g) onto the lignocellulose based adsorbents was plotted against time (min) to generate the plots shown in Figure 7.31. The plots showed rapid adsorption in the first 1 h with all systems reaching equilibrium in about two hours. From the plots, it can be seen that neutral red uptake by PMPSgLig and PMMAgLig was slightly lower compared with PMAAgLig and lignocellulose.

The adsorption data were further processed by fitting to the pseudo first-order and pseudo second-order equations. Figures 7.32 and 7.33 display the pseudo first-order and pseudo second-order plots for neutral red adsorption onto the lignocellulose based adsorbents.
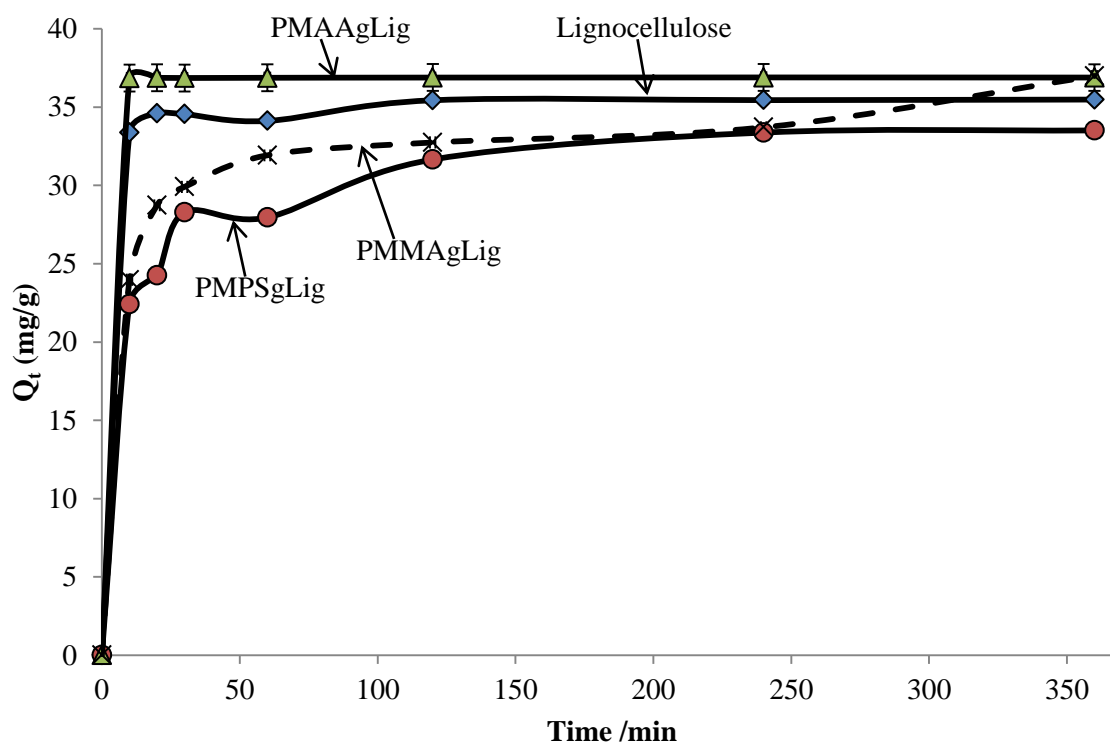
Figure 7.31: Plots of adsorbed amount of neutral red (mg/g) onto lignocellulose based adsorbents against time (min).
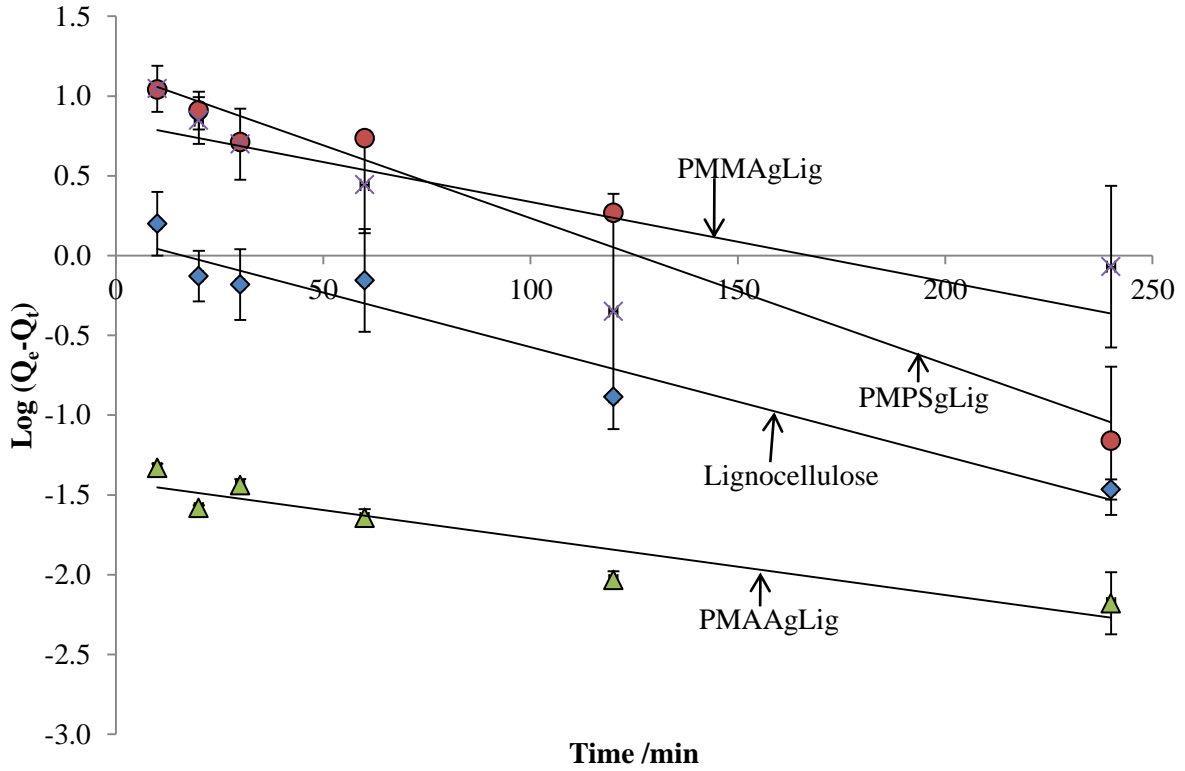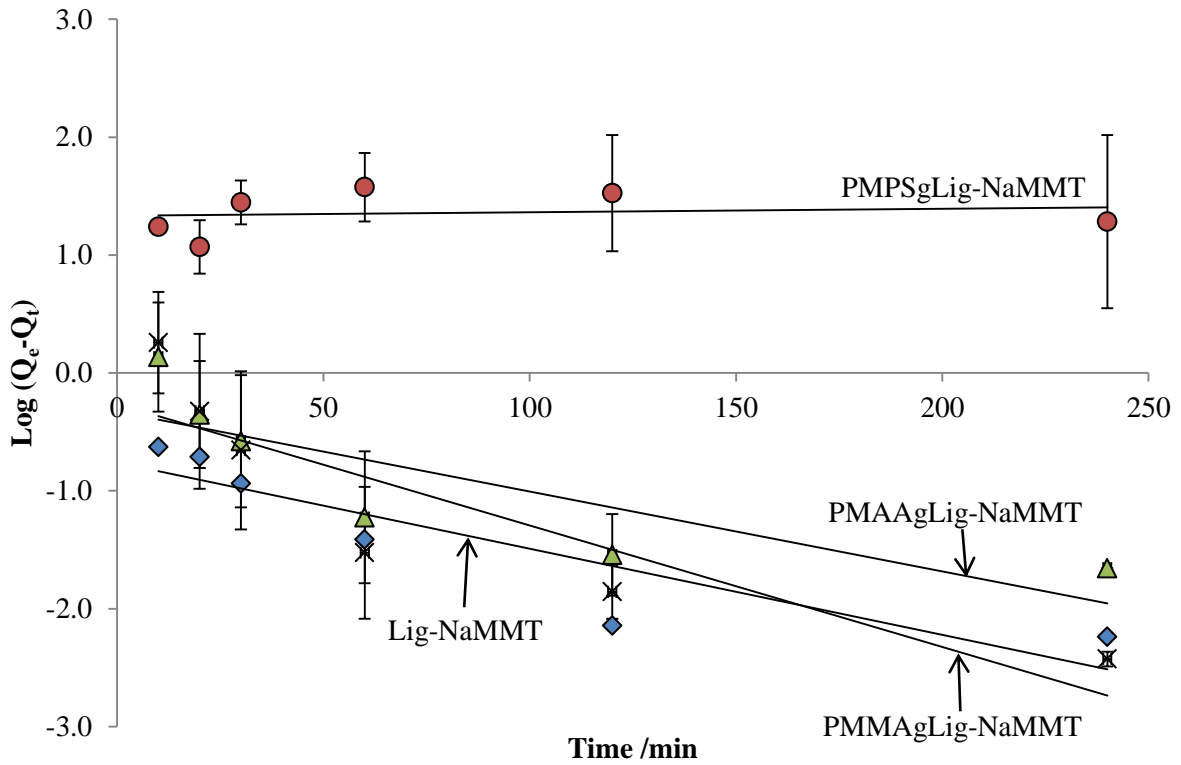
Figure 7.32: Pseudo first-order plots for neutral orange adsorption onto lignocellulose based adsorbents.
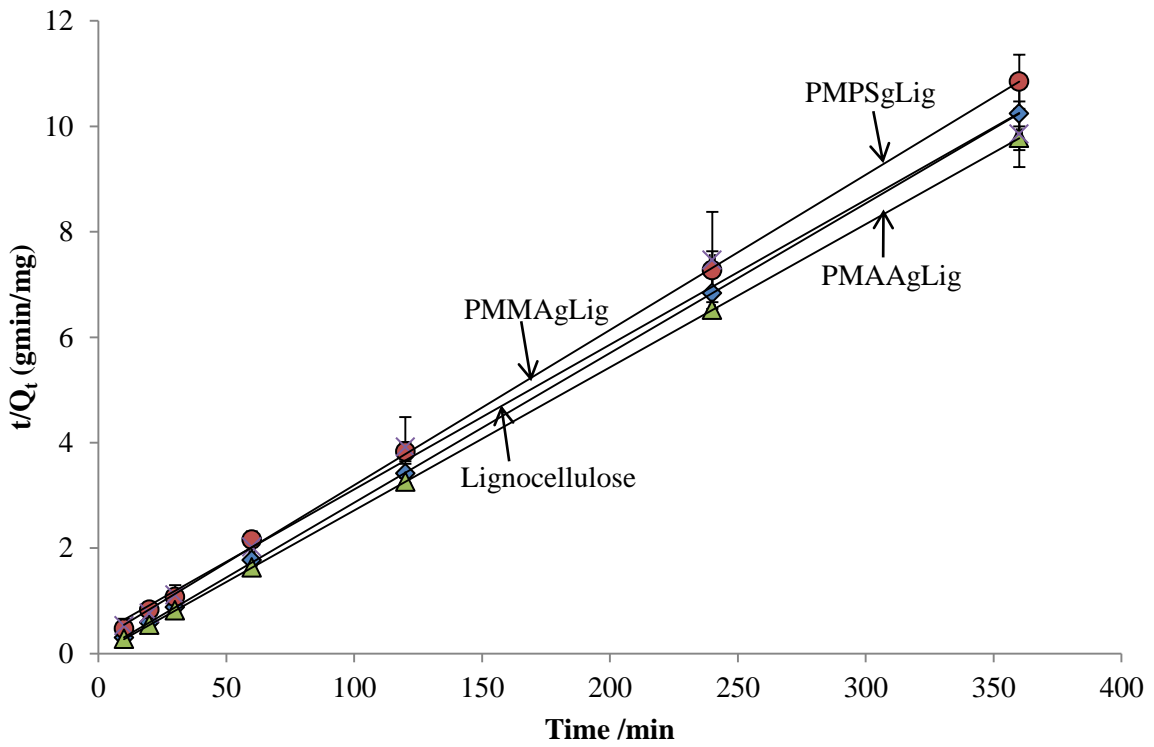
Figure 7.33: Pseudo second-order plots for neutral red adsorption onto lignocellulose based adsorbents.

Table 7.12 shows the pseudo first-order and pseudo second-order parameters for neutral red adsorption onto lignocellulose based adsorbents. The pseudo second-order model gave higher R^2 values than the pseudo first-order model for all the lignocellulose based adsorbents. The adsorption mechanism was, therefore, best described by the pseudo second-order model, though the pseudo first-order model could also be used to describe neutral red adsorption onto lignocellulose and PMPSgLig.

Table 7.12: Pseudo first-order and pseudo second-order parameters for neutral red adsorption onto lignocellulose based adsorbents.

Adsorbent	Model	Slope	R^2	Intercept	Q_e	k_1/k_2
Lignocellulose	1st	-0.0068	0.9479	0.1110	1.291	0.01566
	2nd	0.0284	1.0000	0.0258	35.21	0.03126
PMMAgLig	1st	-0.0050	0.6502	0.8355	6.847	0.01152
	2nd	0.0275	0.9935	0.3660	36.36	0.0021
PMPSgLig	1st	-0.0091	0.9676	1.1480	14.06	0.02096
	2nd	0.0294	0.9996	0.2484	34.01	0.00348
PMAAgLig	1st	0.0035	0.8666	-1.4179	0.038	0.0081
	2nd	0.0271	1.0000	0.0005	36.90	1.4688

The adsorption capacity computed using the pseudo second-order model and was taken as the equilibrium adsorbed amount (Q_e, mg/g). PMPSgLig showed the least uptake of neutral red under the conditions described and PMAAgLig showed the highest uptake. The adsorption capacities found for the lignocellulose based adsorbents were generally lower than those found for the montmorillonite based adsorbents.

7.3.8 Adsorption of neutral red onto lignocellulose-montmorillonite clay nanocomposites

7.3.8.1 Adsorption isotherms

Figure 7.34 displays the isotherms for neutral red adsorption onto lignocellulose-montmorillonite clay nanocomposites. The isotherms were classified as follows: PMAAgLig-NaMMT (S_3), PMMAgLig-NaMMT (S_3), Lig-NaMMT (S_1) and PMPSgLig-NaMMT (S_3). Adsorption of neutral red occurred to more or less the same extent for all the adsorbents.
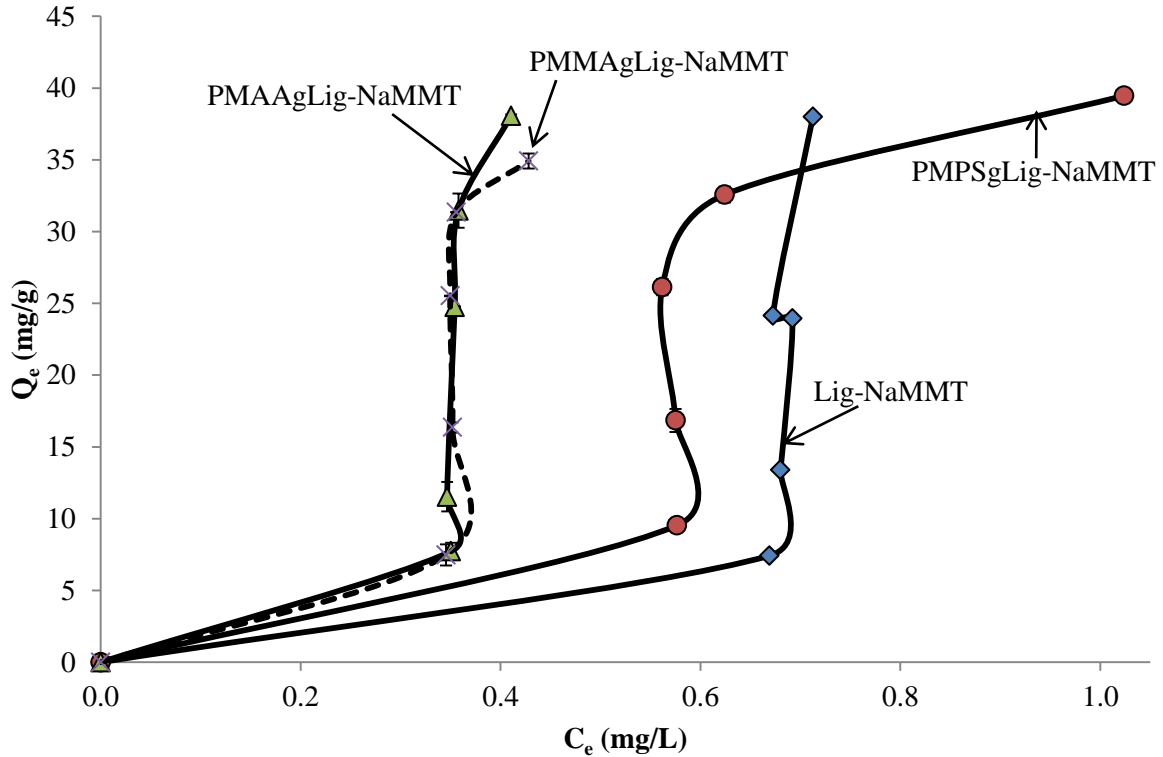
Figure 7.34: Isotherms of neutral red adsorption onto lignocellulose-montmorillonite nanocomposite adsorbents.

The adsorption data were further processed by fitting to the Freundlich and Langmuir equations. The respective Freundlich and Langmuir plots are displayed in Figures B-19 to B-26 of Appendix B. The Freundlich and Langmuir parameters for neutral red adsorption onto the lignocellulose-montmorillonite nanocomposites are presented in Table 7.13.

Table 7.13: Freundlich and Langmuir parameters for neutral red adsorption onto lignocellulose-montmorillonite nanocomposites.

Adsorbent	Isotherm	Slope	R^2	Intercept	Q_0/K_f	n/b
Lig-NaMMT	Langmuir	-1.1069	0.4596	0.8018	-0.9034	-1.380
	Freundlich	19.255	0.6039	4.4307	2.7×10^4	0.0519
PMMAgLig-NaMMT	Langmuir	0.1483	0.1902	0.0738	6.7431	2.009
	Freundlich	0.8458	0.8866	2.0915	123.45	1.1823
PMPSgLig-NaMMT	Langmuir	-0.0191	0.0544	0.0445	-52.356	-0.4292
	Freundlich	1.2354	0.3732	1.6136	41.077	0.8095
PMAAgLig-NaMMT	Langmuir	-0.261	0.2897	0.116	-3.8314	-2.25
	Freundlich	8.4429	0.9951	7.1481	1.4×10^7	0.1184

It can be seen from Table 7.13 that both the Freundlich and Langmuir correlation coefficients (R^2) were very poor except for the PMAAgLig-NaMMT Freundlich R^2 value (0.9951). The Freundlich model describes multilayer adsorption onto heterogeneous surfaces. The high R^2 value suggests that Freundlich model is the best fit for neutral red adsorption onto PMAAgLig-NaMMT.

7.3.8.2 Adsorption kinetics

Figure 7.35 displays the plots for the adsorbed amount (mg/g) of neutral red onto the lignocellulose-montmorillonite nanocomposites against time (min).
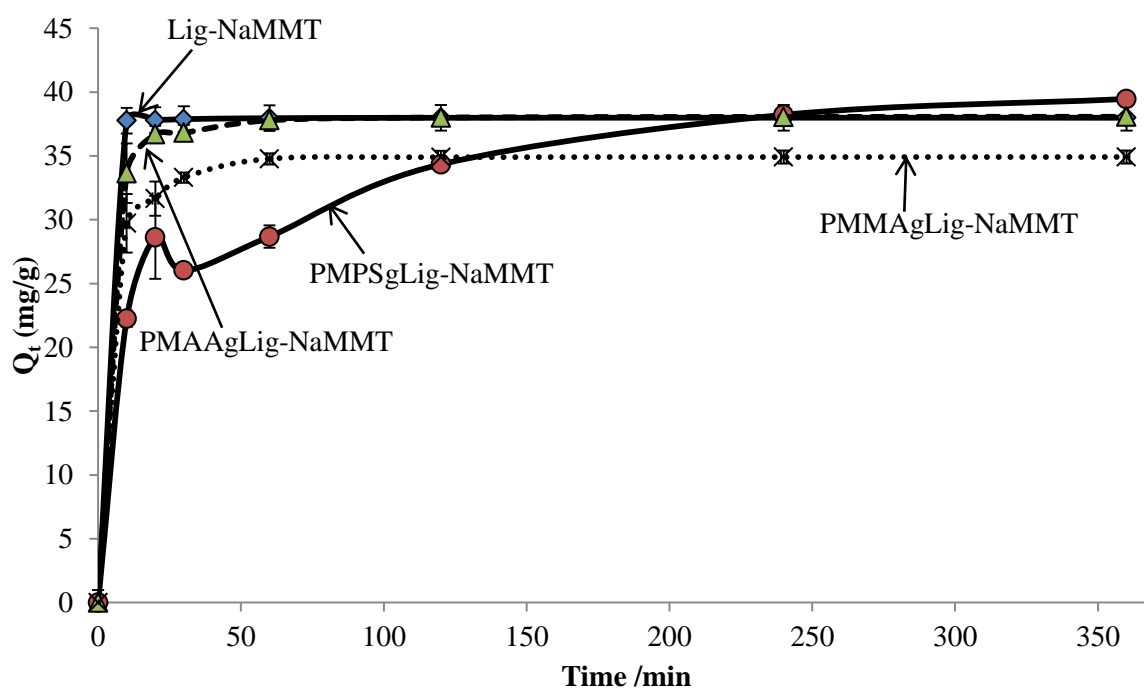
Figure 7.35: Plots of adsorbed amount (mg/g) of neutral red onto lignocellulose-montmorillonite nanocomposite adsorbents against time (min).

The PMPSgLig-NaMMT system was characterized by adsorption and desorption during the first 1 h. Such events were possibly due to the instability of the adsorbent-adsorbate complex, which stabilized later with time. Adsorption of neutral red onto Lig-NaMMT, PMAAgLig-NaMMT and PMMAgLig-NaMMT reached equilibrium in about 1 h, and the amount of neutral red adsorbed remained constant for six hours. The uptake of neutral red onto PMMAgLig-NaMMT was the least compared with the other nanocomposites.

The adsorption kinetics data were fitted to the pseudo first-order and pseudo second-order equations. Figures 7.36 and 7.37 display the pseudo first-order and pseudo second-order plots for neutral red adsorption onto the lignocellulose-montmorillonite nanocomposites, respectively.

Figure 7.36: Pseudo first-order plots for neutral red adsorption onto lignocellulose-montmorillonite nanocomposite adsorbents.
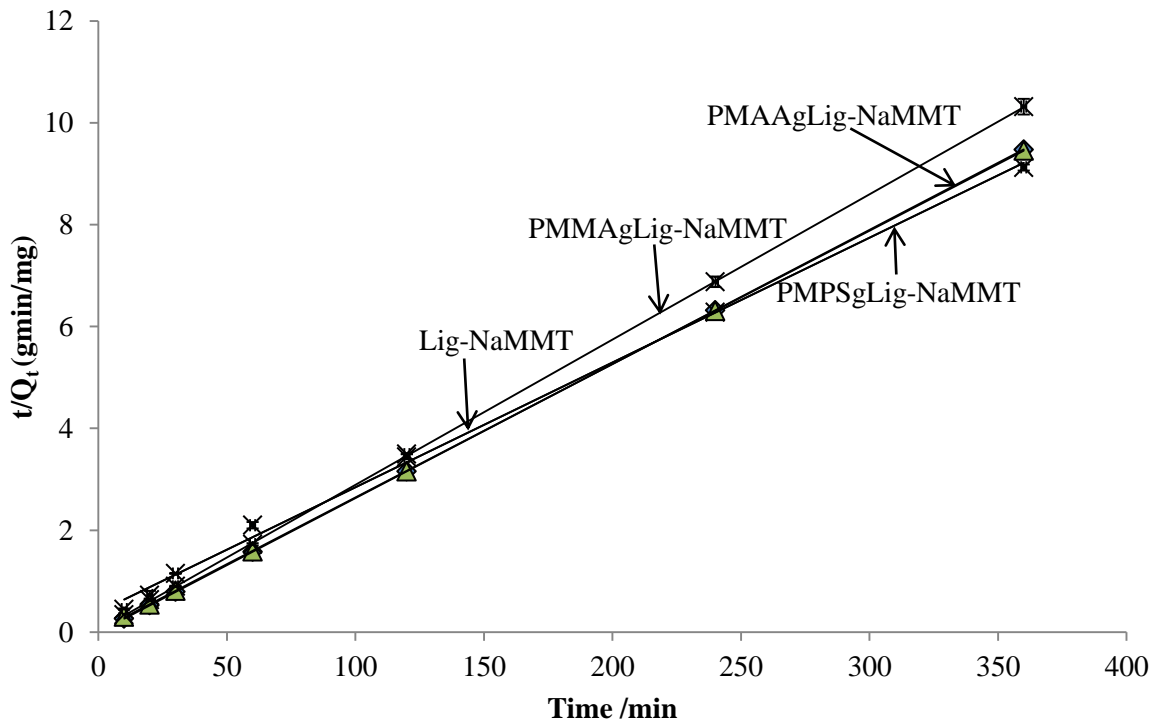
Figure 7.37: Pseudo second-order plot for neutral red adsorption onto lignocellulose-montmorillonite nanocomposite adsorbents.

The pseudo first-order and pseudo second-order parameters for neutral red adsorption onto lignocellulose-montmorillonite adsorbents are displayed in Table 7.14. The pseudo second-order model showed higher R^2 values than the pseudo first-order model. This again suggests that the pseudo second-order model was the best fit for the adsorption of neutral red onto the lignocellulose-montmorillonite nanocomposite adsorbents.

Table 7.14: Pseudo first-order and pseudo second-order parameters for neutral red adsorption onto lignocellulose-montmorillonite nanocomposites.

Adsorbent	Model	Slope	R^2	Intercept	Q_e (mg/g)	k_1/k_2
Lig-NaMMT	1st	-0.0073	0.8184	-0.7609	0.173	0.016812
	2nd	0.0263	1.0000	0.0020	38.02	0.345845
PMMAgLig-NaMMT	1st	-0.0103	0.7954	-0.2646	0.543	0.023721
	2nd	0.0285	1.0000	0.0427	35.09	0.019022
PMPSgLig-NaMMT	1st	0.0003	0.0191	1.3326	21.51	-0.00069
	2nd	0.0245	0.9976	0.3933	40.82	0.001526
PMAAgLig-NaMMT	1st	-0.0068	0.6925	-0.3288	0.469	0.01566
	2nd	0.0262	1.0000	0.0256	38.17	0.026814

The least amount of neutral red was adsorbed onto PMMAgLig-NaMMT and the highest was recorded for PMPSgLig-NaMMT. There were no major differences in the uptake of neutral red onto all the nanocomposites evaluated. A comparison between adsorption onto lignocellulose-montmorillonite nanocomposites, montmorillonite and lignocellulose based adsorbents did not show major differences. Gong, R. et al, 2005 investigated the use of peanut hull for the adsorption of cationic dyes (methylene blue, brilliant cresyl blue and neutral red) from aqueous solution. The Langmuir equation was found to be the best fit for neutral red adsorption, they reported an adsorption capacity of 87.72 mg/g. Runping, H. et al, 2008 assessed the adsorption of neutral red onto peanut husk. The authors reported an adsorption capacity of 37.5 mg/g and their data were best fitted by the Langmuir equation and the adsorption kinetics were best described by both the pseudo first-order and pseudo-second order models. Luo, P. et al, 2010 reported the adsorption of neutral red onto halloysite nanotubes and reported an adsorption capacity of 54.85 mg/g. Their data followed the Langmuir and pseudo second-order models. Differences in the adsorption capacities can be attributed to different experimental conditions employed, otherwise the values obtained in this study were comparable to those reported in the literature.

7.3.9 Effect of OH/Al molar ratio on the uptake of neutral red onto AlpMMT

Figure 7.38 shows a plot for the equilibrium adsorbed amount (Q_e, mg/g) of neutral red against OH/Al molar ratios.
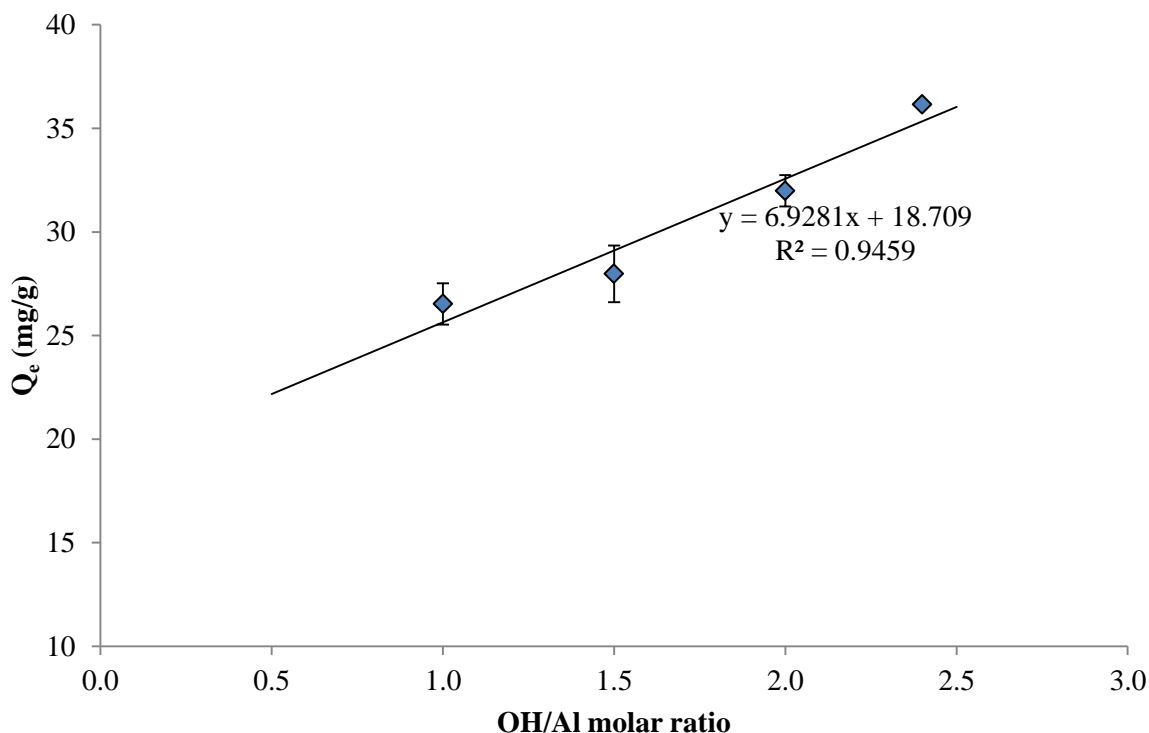
Figure 7.38: Effect of OH/Al molar ratio on neutral red adsorption onto AlpMMT.

The effect of OH/Al molar ratio was assessed by shaking 80 mL of neutral red (50 ppm) solutions with 0.1 g of AlpMMT samples of different OH/Al molar ratios for six hours. Each data point is the average of three replicates. The equilibrium adsorbed amount was then determined.

It was observed that the uptake of neutral red onto AlpMMT increased with increase in the OH/Al molar ratio. The increase in the uptake of neutral red with OH/Al molar ratio can be attributed to the increasing amount of Al^{3+} in the AlpMMT samples. The trend can also be explained in terms of the increase in surface area of the aluminium-pillared clays as the OH/Al molar ratio increases. However, at molar ratios > 2.4, the amount of neutral red adsorbed decreased drastically, and the cause for the decrease was not clear. It can therefore, be said that the optimum OH/Al molar ratio for neutral red adsorption was 2.4.

7.3.10 Desorption studies

Figure 7.39 displays the plot for the amount of MetO adsorbed (mg/g) against the number of regeneration cycles using 80 mL of 0.01 M NaOH solution. It was observed that the adsorption

capacity of the PMPSgLig-NaMMT decreased as a result of the regeneration (desorption) process. It can be said that some of the active sites were lost during the desorption process, thus resulting in a decrease in the uptake of methyl orange.
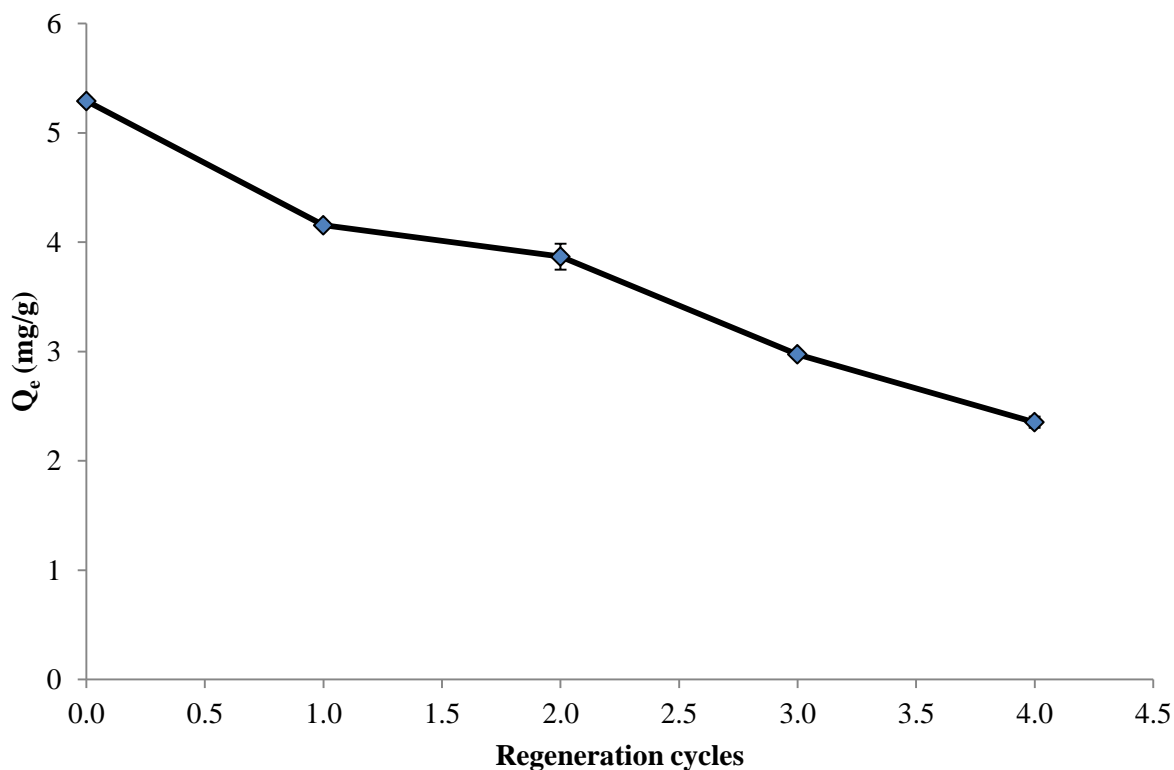
Figure 7.39: A plot of MetO adsorbed (mg/g) against the number of regeneration cycles.

The uptake of MetO decreased to about 40% percent after carrying out adsorption-desorption cycles for four times. It would be desirable to develop an adsorbent whose adsorption capacity does not drastically change in order to reduce the cost of adsorption technology. Similar adsorption-desorption studies were carried out using neutral red (NeuR) onto PMPSgLig-NaMMT.

Figure 7.40 shows the plot for the amount of NeuR adsorbed (mg/g) against the number of regeneration cycles. As mentioned above, the complete desorption of NeuR from the adsorbent proved to be difficult, but the partially desorbed adsorbent was reused still. The adsorbed amount of NeuR remained relatively constant during the first and second cycles. At the third cycle, a decrease in neutral red uptake was observed though the adsorbed amount still remained above 30 mg/g.
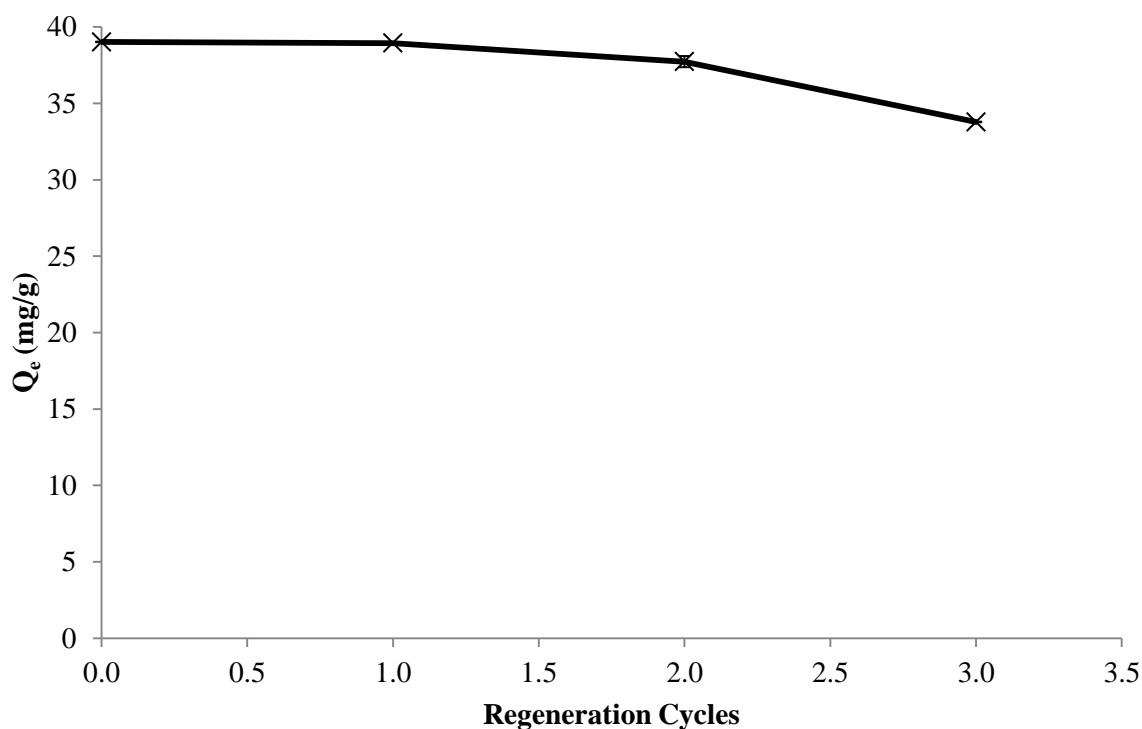
Figure 7.40: A plot of NeuR adsorbed (mg/g) against the number of regeneration cycles.

The difficulty in the desorption of neutral red from PMPSgLig-NaMMT nanocomposite can be explained in terms of its high affinity for the adsorbent compared with methyl orange. It was observed that neutral red displayed a very high affinity for all the adsorbents compared with methyl orange, as judged from the high adsorption capacities obtained for neutral red (Table 7.14).

7.4 Conclusion

Aluminium-pillaring of NaMMT resulted in a slight improvement in the adsorption of methyl orange. However, pillaring of the NaMMT at OH/Al molar ratios greater than 2 caused a sharp decline in the uptake of methyl orange. OH/Al molar ratios of about 1.0 were found to give relatively higher adsorption levels of methyl orange. The adsorption of neutral red was found to increase with increase in the OH/Al molar ratio, with a sharp decrease in uptake at OH/Al molar ratios above 2.4. The grafting of NaMMT with organic polymers caused a decrease in the amount of methyl orange adsorbed for all polymer-grafted montmorillonite adsorbents except PMPSgMMT which showed some comparable adsorption capacity to the NaMMT. There was no major difference in the adsorption of neutral red to NaMMT and polymer-grafted montmorillonite adsorbents.

Lignocellulose based adsorbents showed relatively lower methyl orange and neutral red uptake compared with montmorillonite based ones. Grafting of lignocellulose with MPS caused an

improvement in the adsorption of methyl orange. PMMA-grafted lignocellulose gave the same adsorption of methyl orange as the raw lignocellulose, while a decrease in uptake was found for PMAA-grafted lignocellulose. Neutral red adsorption onto all lignocellulose based adsorbents was relatively the same.

Among the nanocomposite adsorbents, PMPSgLig-NaMMT showed significantly improved adsorption of methyl orange, while the other nanocomposites did not show any significant improvement. PMMAgLig-NaMMT had the least uptake of neutral red, while the other three nanocomposites had comparable adsorption.

Adsorption of methyl orange from binary mixtures with Cd^{2+} or Pb^{2+} showed increased uptake in both cases. However, greater methyl orange uptake was observed for a binary mixture containing Pb^{2+} and methyl orange. PMPSgLig-NaMMT can therefore be used for the simultaneous adsorption of heavy metals and methyl orange from aqueous solution.

Methyl orange could be desorbed completely from PMPSgLig-NaMMT nanocomposite using 0.01 M NaOH solution making it a recyclable nanocomposite, thus fulfilling one of the objectives of the study. The uptake of methyl orange decreased with the number of regeneration cycles. However, neutral red proved difficult to desorb but the adsorbent could be used three times without significant loss in the adsorption capacity.

7.5 References

1. Ai, L.; Jiangb, J.; Zhang, R. Uniform polyaniline microspheres: A novel adsorbent for dye removal from aqueous solution. *Synthetic Metals*, **2010**, *160*, 762–767.
2. Altunlu, M.; Yapar, S. Effect of OH^-/Al^{3+} and Al^{3+}/clay ratios on the adsorption properties of Al-pillared bentonites. *Colloids and Surfaces A: Physicochemical and Engineering Aspects,* **2007***, 306,* 88-94.
3. Anbia, M.; Hariri, S. A.; Ashrafizadeh, S. N. Adsorptive removal of anionic dyes by modified nanoporous silica SBA-3. *Applied Surface Science*, **2010**, *256*, 3228–3233.
4. Annadurai, G.; Juang, R. S.; Lee, D. J. Use of cellulose-based wastes for adsorption of dyes from aqueous solutions. *Journal of Hazardous Materials,* **2002**, *B92*, 263–274.
5. Atmani, F.; Bensmaili, A.; Mezenner, N. Y. Synthetic textile effluent removal by skin almonds waste. *Journal of Environmental Science and Technology*, **2009**, *2* (4), 153-169.

6. Chen, S.; Zhang, J.; Zhang, C.; Yue, Q.; Li, Y.; Li, C. Equilibrium and kinetic studies of methyl orange and methyl violet adsorption on activated carbon derived from *Phragmites australis*. *Desalination*, **2010**, *252*, 149–156.

7. Giles, C. H.; D'silva, A. P.; Easton, I. A. A General Treatment and Classification of the Solute Adsorption Isotherm Part II. Experimental Interpretation. *Journal of Colloid and Interface Science,* **1974**, *47* (3), 766-778.

8. Giles, C. H.; Macewans, T. H.; Nakhwa, N.; Smith, D. Studies in adsorption Part XI. A system of classification of solution adsorption isotherms, and its use in diagnosis of adsorption mechanisms and in measurement of specific surface areas of solids. *Journal of Chemical Society*, **1960**, *111*, 3973-3993.

9. Gong, R.; Li, M.; Yang, C.; Sun, Y.; Chen, J. Removal of cationic dyes from aqueous solution by adsorption on peanut hull. *Journal of Hazardous Materials*, **2005**, *B121*, 247–250.

10. Haque, E.; Jun, J. W.; Jhung, S. H. Adsorptive removal of methyl orange and methylene blue from aqueous solution with a metal-organic framework material, iron terephthalate (MOF-235). *Journal of Hazardous Materials*, **2011**, *185*, 507–511.

11. Hinz, C. Description of sorption data with isotherm Equations. *Geoderma*, **2001**, *99*, 225–243.

12. Ho, Y. S. Review of second-order models for adsorption systems. *Journal of Hazardous Materials*, **2006**, *B136*, 681–689.

13. Ho, Y. S. Second-order kinetic model for the sorption of cadmium onto tree fern: A comparison of linear and non-linear methods. *Water Research*, **2006**, *40*, 119–125.

14. Igwe, J. C.; Mbonu, O. F.; Abia, A. A. Sorption kinetics, Intra-particle diffusion and equilibrium partitioning of azo-dyes on Great millet (*Andropogon sorghum*) waste biomass. *Journal of Applied Sciences*, **2007**, *7* (19), 2840-2847.

15. Jalil, A. A.; Triwahyonob, S.; Adama, S. H.; Rahima, N. D.; Aziz, M. A. A.; Hairom, N. H. H.; Razali, N. A. M.; Abidin, M. A. Z.; Mohamadiah, M. K. A. Adsorption of methyl orange from aqueous solution onto calcined Lapindo volcanic mud. *Journal of Hazardous Materials*, **2010**, *181*, 755–762.

16. Jaoui, M.; Achard, C.; Hasnaoui, N.; Rogalski, M. Adsorption isotherms of phenol and 4-chlorophenol on petroleum asphaltenes. *Revue De L'institut Français Du Pétrole*, Janvier-Février, **1998**, *53* (1).

17. Jeon, Y. S.; Lei, J.; Kim, J. H. Dye adsorption characteristics of alginate/polyaspartate hydrogels. *Journal of Industrial and Engineering Chemistry*, **2008**, *14* (6), 726-731.

18. Kumar, K. V. Linear and non-linear regression analysis for the sorption kinetics of methylene blue onto activated carbon. *Journal of Hazardous Materials*, **2006**, *B137*, 1538–1544.

19. Kumar, K. V.; Porkodi, K. Pseudo Second Order Kinetics for the Sorption of Auramine O onto Activated Carbon. *Indian Chemical Engineer*, **2008**, *50* (3), 227-238.

20. Lazarević, S.; Janković-Častvan, I.; Jovanović, D.; Milonjić, S.; Janaćković, D.; Petrović, R. Adsorption of Pb^{2+}, Cd^{2+} and Sr^{2+} ions onto natural and acid-activated sepiolites. *Applied Clay Science*, **2007**, *37*, 47–57.

21. Li, F.; Rosen, M. J. Adsorption of Gemini and Conventional Cationic Surfactants onto Montmorillonite and the Removal of Some pollutants by the Clay. *Journal of Colloid and Interface Science*, **2000**, *224*, 265–271.

22. Luo, P.; Zhao, Y.; Zhang, B.; Liu, J.; Yang, Y.; Liu, J. Study on the adsorption of Neutral Red from aqueous solution onto halloysite nanotubes. *Water Research*, **2010**, *44*, 1489–1497.

23. Mittal, A.; Malviya, A.; Kaur, D.; Mittal, J.; Kurup, L. Studies on the adsorption kinetics and isotherms for the removal and recovery of methyl orange from wastewaters using waste materials. *Journal of Hazardous Materials*, **2007**, *148*, 229–240.

24. Morais, W. A.; de Almeida, A. L. P.; Pereira, M. R.; Fonseca, J. L. C. Equilibrium and kinetic analysis of methyl orange sorption on chitosan spheres. *Carbohydrate Research*, **2008**, *343*, 2489–2493.

25. Ökte, A. N.; Yılmaz, Ö. Characteristics of lanthanum loaded TiO_2-ZSM-5 photocatalysts: Decolorization and degradation processes of methyl orange. *Applied Catalysis A: General*, **2009**, *354*, 132–142.

26. Rauf, M. A.; Bukallah, S. B.; Hamour, F. A.; Nasir, A. S. Adsorption of dyes from aqueous solutions onto sand and their kinetic behaviour. *Chemical Engineering Journal*, **2008**, *137*, 238–243.

27. Runping, H.; Pan, H.; Zhaohui, C.; Zhenhui, Z.; Mingsheng, T. Kinetics and isotherms of Neutral Red adsorption on peanut husk. *Journal of Environmental Sciences*, **2008**, *20*, 1035–1041.

28. Saha, T. K.; Bhoumik, N. C.; Karmaker, S.; Ahmed, M. G.; Ichikawa, H.; Fukumori, Y. Adsorption of Methyl Orange onto Chitosan from Aqueous Solution. *Journal of Water Resource and Protection,* **2010**, *2*, 898-906.

29. Samarghandi, M. R.; Hadi, M.; Moayedi, S.; Askari F. B. Two-parameter isotherms of methyl orange sorption by pinecone derived activated carbon. *Iran Journal of Environmental Health Science & Engineering*, **2009**, *6* (4), 285-294.

30. Sawunyama P.; Jackson M.; Bailey G. W. Interactions of methyl orange with cyclodextrin/sodium-montmorillonite systems probed by UV-Visible spectroscopy. *Journal of Colloid and Interface Science*, **2001**, *237* (2), 153-157.

31. Seyis, I.; Subasioglu, T. Comparison of live and dead biomass of fungi on decolorization of methyl orange. *African Journal of Biotechnology*, **2008**, *7* (13), 2212-2216.

32. Subasioglu, T.; Bilkay, I. S. Determination of biosorption conditions of methyl orange by *Humicola fuscoatra*. *Journal of Scientific and Industrial Research*, **2009**, *68*, 1075-1077.

33. Teng, M. Y.; Lin, S. H. Removal of methyl orange dye from water onto raw and acidactivated montmorillonite in fixed beds. *Desalination*, **2006**, *201*, 71–81.

34. Vinoth, M.; Lim, H. Y.; Xavier, R.; Marimuthu, K.; Sreeramanan, S.; Mas Rosemal H. M. H.; Kathiresan, S. Removal of methyl orange from solutions using yam leaf fibers. *International Journal of ChemTech Research*, **2010**, *2*(4), 1892-1900.

35. Yu, L.; Li, W. W.; Lam, M. H. W.; Yu, H. Q. Adsorption and decolorization kinetics of methyl orange by anaerobic sludge. *Applied Microbiology Biotechnology*, **2011**, *90* (3), 1119-1127.

36. Zhuannian, L.; Anning, Z.; Guirong, W.; Xiaoguang, Z. Adsorption behavior of methyl orange onto modified ultrafine coal powder. *Chinese Journal of Chemical Engineering*, **2009**, *17* (6), 942-948.

Chapter 8

Conclusions and Recommendations

8.1 Conclusions

Montmorillonite and lignocellulose based adsorbents were prepared together with lignocellulose-montmorillonite clay nanocomposite adsorbents. The montmorillonite and lignocellulose were separately modified through the grafting of organic polymers (PMPS, PMAA and PMMA). Apart from the grafting with polymers, montmorillonite was also modified through aluminium-pillaring. The prepared materials were then evaluated for their adsorption properties by using Cd^{2+}, Pb^{2+}, methyl orange and neutral red as model pollutants in aqueous solutions.

Al-pillaring of montmorillonite clay resulted in an increase in surface area and a shift of the texture of the pillared clays to become microporous as indicated by scanning electron microscopy results. XRD showed that the basal spacings of the pillared clays were higher than what was observed for NaMMT. The basal spacings were found to increase with increase in the OH/Al molar ratio. Pillaring at pH 2 resulted in a decrease of surface area, probably due to the collapse of clay sheets upon each other as evidenced by a lower d-spacing than the original NaMMT. The surface area was generally dependent upon the porosity (pore sizes). The greater the pore size the greater the surface area. Microporous to mesoporous materials were successfully prepared. Pore sizes were found to generally decrease with increase in the OH/Al molar ratio. FTIR, TGA, XRD and BET surface area analyses results showed that the ideal conditions for the Al-pillaring of montmorillonite clay were: pH 4.3, temperature – 50 °C, OH/Al molar ratio – 2.3 and Al/clay ratio – 10 mmol/g.

Novel adsorbent materials (PMMAgLig-NaMMT nanocomposite, PMAAgMMT, PMPSgLig-NaMMT and PMAAgLig-NaMMT nanocomposite) were prepared through condensation as well as free-radical graft polymerization reactions. The intended modification of the lignocellulose and NaMMT separately was confirmed by FTIR, TGA, XRD and TEM. XRD showed some partial intercalation of PMMA into the interlayer space of the clay sheets in PMMAgMMT. All the nanocomposites prepared also showed an increase in thermal stability, which was attributed to the presence of clay in the lignocellulose matrix. Some partial intercalation of PMAA and PMMA into the interlayer space of the NaMMT was observed for the nanocomposites, as judged from XRD and TEM data. The XRD results for PMPSgLig-NaMMT nanocomposite also showed an increase in the

d-spacing of the NaMMT. However, the TEM results showed some aggregation of clay particles, indicating the formation of a microcomposite (phase separated composite).

The grafting of montmorillonite clay with poly (methyl methacrylate) (PMMA) and poly (methacrylic acid) (PMAA) resulted in enhanced adsorption of both Cd^{2+} and Pb^{2+} from solution. However, the grafting of lignocellulose with PMMA did not show enhanced adsorption of heavy metals from aqueous solution. Modification of NaMMT with methacryloxypropyl trimethoxysilane (MPS) caused a slight decrease in the adsorption capacity for both Cd^{2+} and Pb^{2+} while the aluminium-pillaring of NaMMT caused a drastic decrease in the adsorption capacity of the clay for both metal ions, showing that this type of clay modification is not suitable for the adsorption of heavy metals. Modification of lignocellulose with PMPS and PMAA resulted in improved uptake of both heavy metals from aqueous solution.

There was a marked improvement in the adsorption capacity of the PMAAgLig-NaMMT nanocomposite for both Cd^{2+} and Pb^{2+} relative to the raw lignocellulose and NaMMT. The other nanocomposites (PMPSgLig-NaMMT and PMMAgLig-NaMMT) did not show improved adsorption capacity for both Cd^{2+} and Pb^{2+}. The amount of Cd^{2+} and Pb^{2+} adsorbed onto the two nanocomposites was comparable with that of the separately modified adsorbents. The composite of lignocellulose and montmorillonite without a polymer (Lig-NaMMT) did not show improvement in the uptake of both heavy metals. This indeed showed that the choice of polymer had an influence on the adsorption properties of the prepared nanocomposite materials.

Pb^{2+} was observed to have a higher affinity than Cd^{2+} for most of the adsorbents evaluated in this study. Relatively higher correlation coefficients (isotherms and kinetic models) were also obtained for Pb^{2+} adsorption onto almost all the adsorbents than were obtained for Cd^{2+} adsorption. The higher affinity of Pb^{2+} than Cd^{2+} for the adsorbents was attributed to the differences in their hydration energies as well as the radii of their hydrated ions.

The Langmuir isotherm model showed higher correlation coefficients than the Freundlich model for most adsorbents evaluated in this study, regardless of the heavy metal. The adsorption process of Cd^{2+} and Pb^{2+} from aqueous solution onto the prepared adsorbents could best be described by the Langmuir model. The pseudo second-order model gave consistently high R^2 values for all the adsorbents, and there was a good correlation between the Langmuir adsorption capacities and the pseudo second-order equilibrium adsorbed amount (Q_e). Therefore, Q_e values derived from the pseudo second-order could be used to compute adsorption capacities for all the adsorbents evaluated in this study.

Competitive adsorption studies of Cd^{2+} and Pb^{2+} onto PMMAgMMT showed a decrease in the uptake of both heavy metals but the amount of each heavy metal adsorbed still remained relatively high. The decrease observed in the uptake of both heavy metals was due to competition for the same adsorption sites (the number of which is fixed). The co-adsorption of Cd^{2+} and Pb^{2+} from solution did not significantly affect the adsorption process of each metal ion and the mechanism of adsorption. The data from the competitive adsorption studies still could be best represented by the Langmuir model (isotherms) and pseudo second-order model (kinetics).

The adsorption capacities found for most of the adsorbents evaluated in this study for the adsorption on Cd^{2+} and Pb^{2+} were comparable to those reported in the literature. Desorption of heavy metals studies showed that PMMAgMMT could be regenerated by using 0.1 M HNO_3 without significant loss in the adsorption capacity.

The adsorbent materials prepared were also evaluated to assess their adsorption properties for organic dyes, methyl orange and neutral red. Aluminium-pillaring of NaMMT resulted in a slight improvement in the adsorption of methyl orange. However, pillaring of the NaMMT at OH/Al molar ratios greater than 2.0 caused a sharp decline in the uptake of methyl orange. OH/Al molar ratios of about 1.0 were found to give relatively higher adsorption levels of methyl orange. The adsorption of neutral red was found to increase with increase in the OH/Al molar ratio, with a sharp decrease in uptake at OH/Al molar ratios above 2.4. The grafting of NaMMT with organic polymers caused a decrease in the amount of methyl orange adsorbed for all polymer-grafted montmorillonite based adsorbents except PMPSgMMT which showed more or less the same adsorption capacity as the NaMMT. There was no major difference in the uptake of neutral red onto NaMMT and the polymer-grafted montmorillonite adsorbents.

Lignocellulose based adsorbents showed relatively poor methyl orange and neutral red uptake compared with montmorillonite based ones. However, grafting of lignocellulose with MPS caused an improvement in the adsorption of methyl orange. PMMA-grafted lignocellulose gave the same uptake of methyl orange as the raw lignocellulose, while a decrease in uptake was found for PMAA-grafted lignocellulose. Neutral red adsorption onto all the lignocellulose based adsorbents was more or less the same.

Among the nanocomposite adsorbents, PMPSgLig-NaMMT showed significantly improved uptake of methyl orange from aqueous solution. The enhanced adsorption of methyl orange onto PMPSgLig-NaMMT was attributed to some synergy contributed by the presence of lignocellulose, NaMMT and MPS which is what this study was aiming for. The other nanocomposites did not show much

improvement in the uptake of methyl orange. In the adsorption of neutral red, PMMAgLig-NaMMT had the least uptake, while the other nanocomposites had comparable adsorption.

PMPSgLig-NaMMT was also observed to simultaneaously adsorb both heavy metals and methyl orange from aqueous solution. It also had a high uptake of neutral red. Adsorption of methyl orange from binary mixtures with Cd^{2+} or Pb^{2+} showed increased uptake in both cases when this nanocomposite was used. However, greater methyl orange uptake was observed for the binary mixture containing Pb^{2+} and methyl orange. PMPSgLig-NaMMT can therefore be used for the simultaneous adsorption of heavy metals and methyl orange from aqueous solution, thus cutting down on time and effluent treatment cost.

Desorption studies were carried out to assess whether the PMPSgLig-NaMMT could be regenerated for further use. Methyl orange could be desorbed completely from PMPSgLig-NaMMT nanocomposite using 0.01 M NaOH solution although the uptake of methyl orange decreased with the number of regeneration cycles. This makes PMPSgLig-NaMMT a recyclable nanocomposite thus fulfilling one of the objectives of the study. However, neutral red proved difficult to desorb but the adsorbent could be used three times for the adsorption of this dye without significant loss in adsorption capacity.

The choice of coupling polymer had a significant bearing on the adsorption properties of the prepared materials with PMAA modified materials giving the greatest uptake for heavy metals. This is especially with reference to PMAAgLig and PMAAgLig-NaMMT. However, PMAA modified adsorbents showed poor uptake for methyl orange. The adsorption of organic dyes was observed to depend on the chemical structure or nature of the particular compound, as well as the surface chemistry of the adsorbents. Neutral red displayed a very high affinity for all the adsorbents with nearly complete uptake of the dye from aqueous solution at the concentrations used.

8.2 Recommendations

PMMAgMMT could be regenerated several times and used for the adsorption of heavy metals without a significant loss in the adsorption capacity. The adsorbents (PMMAgMMT, PMAAgMMT, PMPSgLig, PMAAgLig and PMAAgLig-NaMMT) which showed improved uptake of heavy metals can be further investigated under continuous flow conditions to check their performance under such conditions. The adsorbents can be packed into a suitable column that can be connected to a waste water pipe, and the contaminated water can be run through the column at an appropriate flow rate.

Since the method of modification used in this study did not give exfoliated nanocomposites, the use of a different coupling method can be explored. It would be interesting to assess the adsorption properties of an exfoliated lignocellulose-montmorillonite nanocomposite. Organic surfactants can be used to promote the exfoliation of the montmorillonite clay sheets. However, some authors have reported a decrease in adsorption capacity as a result of surfactant modification. Lignocellulose-montmorillonite nanocomposites can also be prepared by using the method of solution blending where the lignocellulose is completely or partially solubilised by a suitable solvent.

For lignocellulose pre-treatment a different method (like acid hydrolysis) can be employed. Acid hydrolysis removes both lignin and hemicellulose, and gives a cellulose-like material. Therefore, there is a need to investigate the use of hydrolysed biomass as an adsorbent for both heavy metals and organic dyes. A comparative adsorption study of the hydroysed biomass and pure cellulose can also be performed. Nanocomposites based on the hydrolysed biomass and montmorillonite clay can be prepared and investigated as adsorbents for heavy metals and organic pollutants.

Other organic groups with biocidal activity such as 2,2-dibromonitrilopropionamide (DBNPA) can be used for the modification of both lignocellulose and montmorillonite clay. Such adsorbents can be used for the simultaneous removal of organic pollutants, heavy metals and biological contaminants from water. Because of the biocidal activity of DBNPA, such adsorbents are expected to be resistant to biofouling.

Appendix A

N$_2$ adsorption and desorption curves of AlpMMT prepared under different conditions
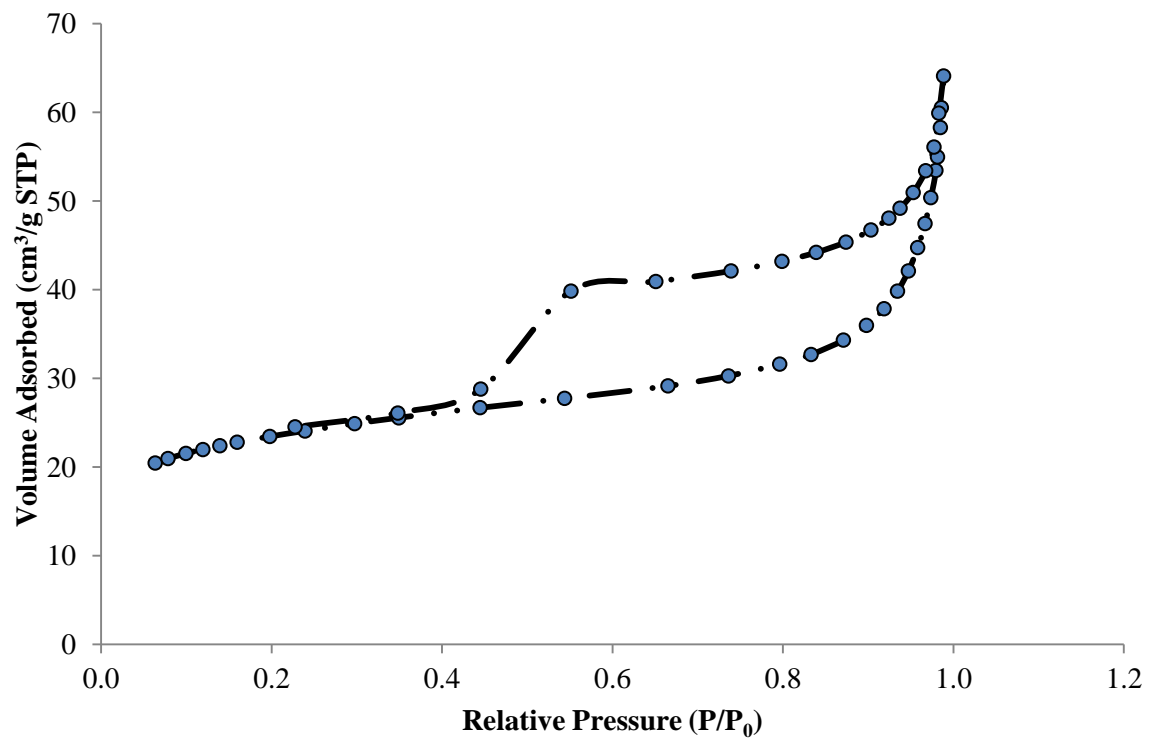
Figure A-1: N$_2$ adsorption-desorption curve for NaMMT.
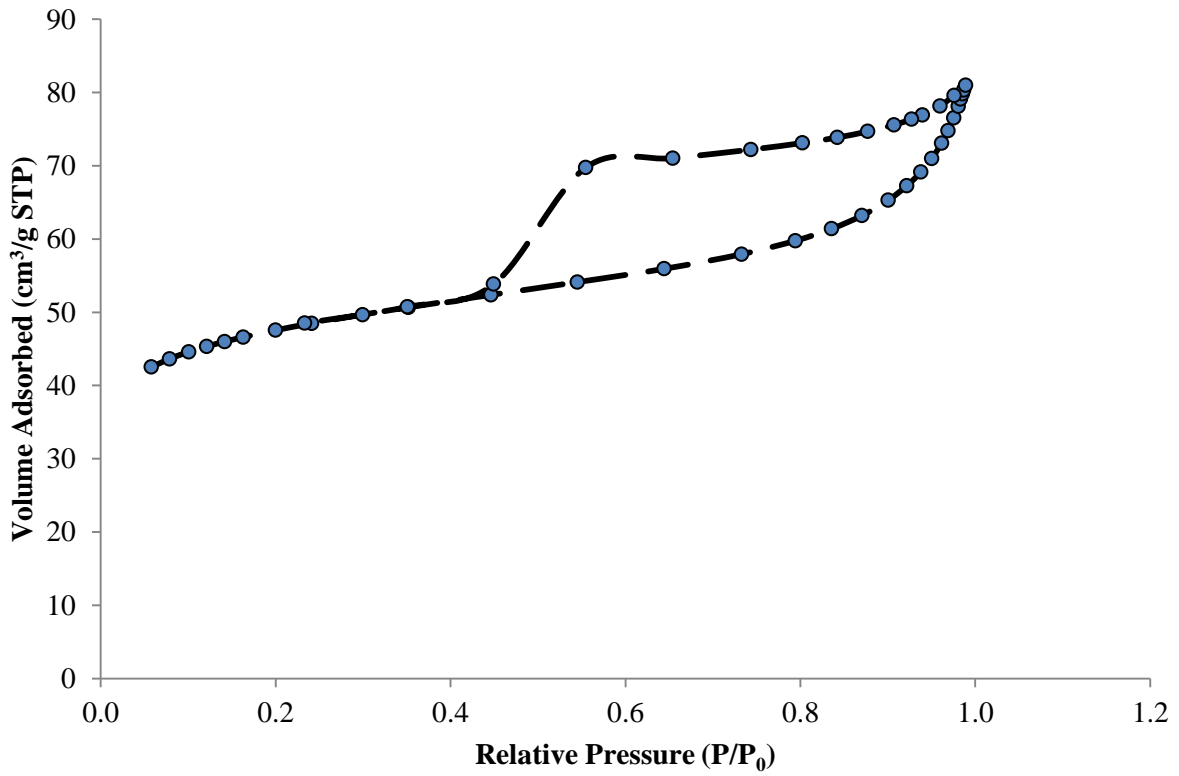
Figure A-2: N_2 adsorption-desorption curve of AlpMMT pillared at Al/clay ratio of 5 mmol/g.
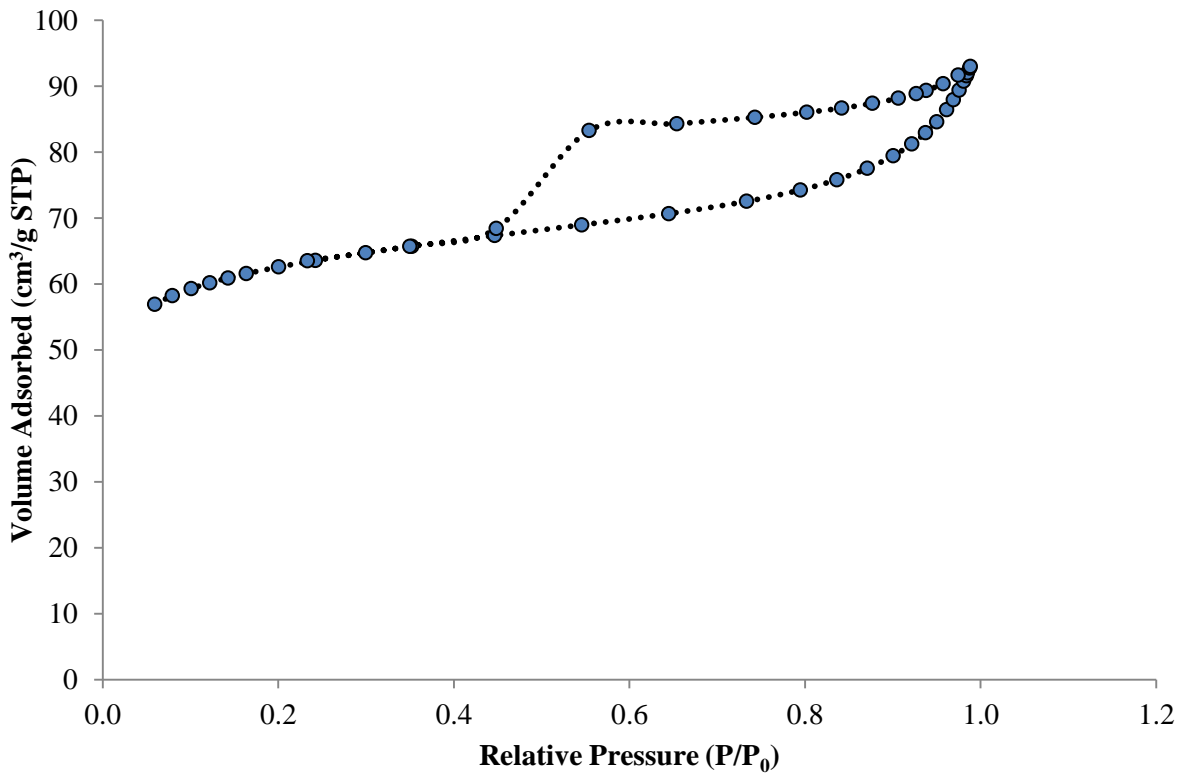
Figure A-3: N_2 adsorption-desorption curve of AlpMMT pillared at Al/clay ratio of 10 mmol/g.
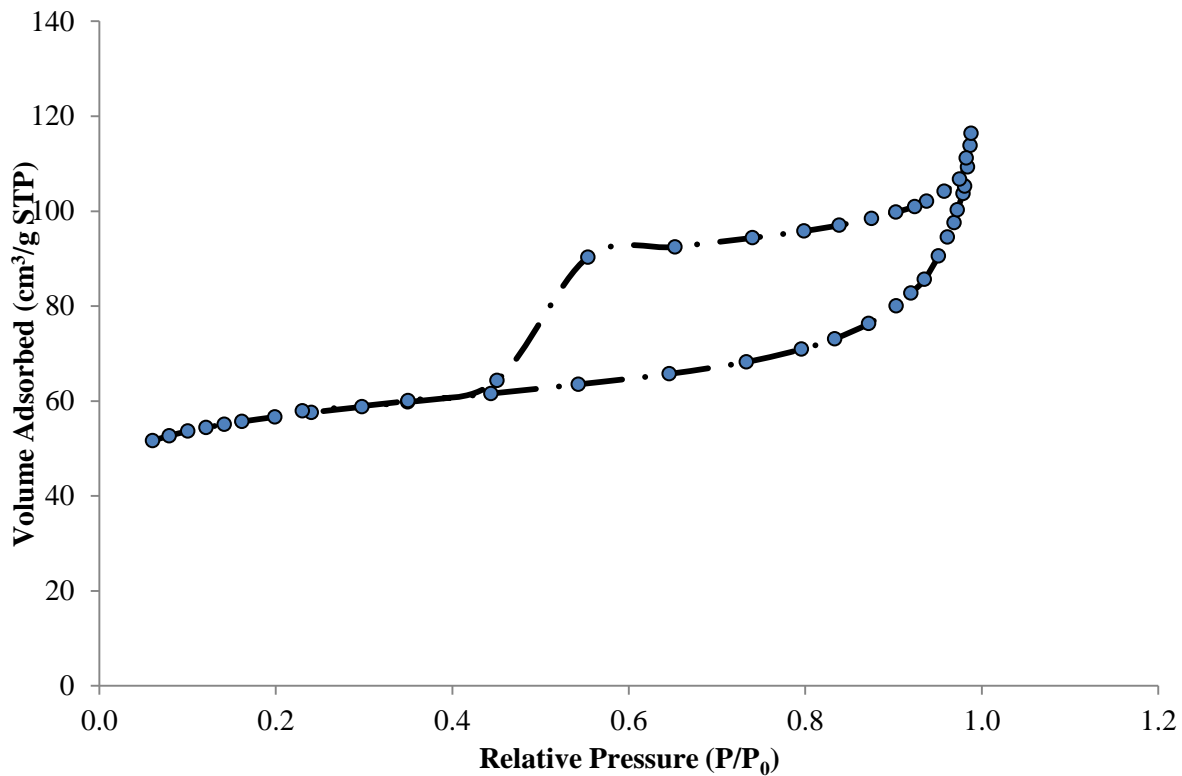
Figure A-4: N_2 adsorption-desorption curve of AlpMMT pillared at Al/clay ratio of 15 mmol/g.
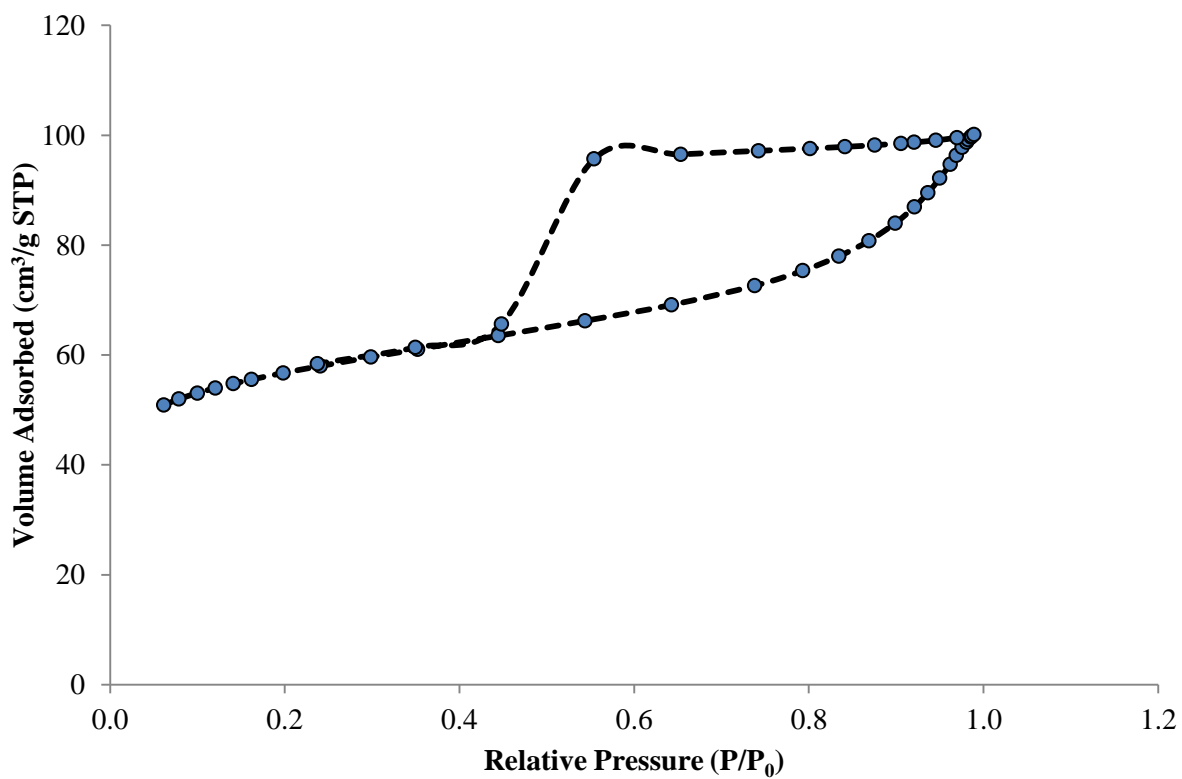
Figure A-5: N_2 adsorption-desorption curve of AlpMMT pillared at Al/clay ratio of 20 mmol/g.
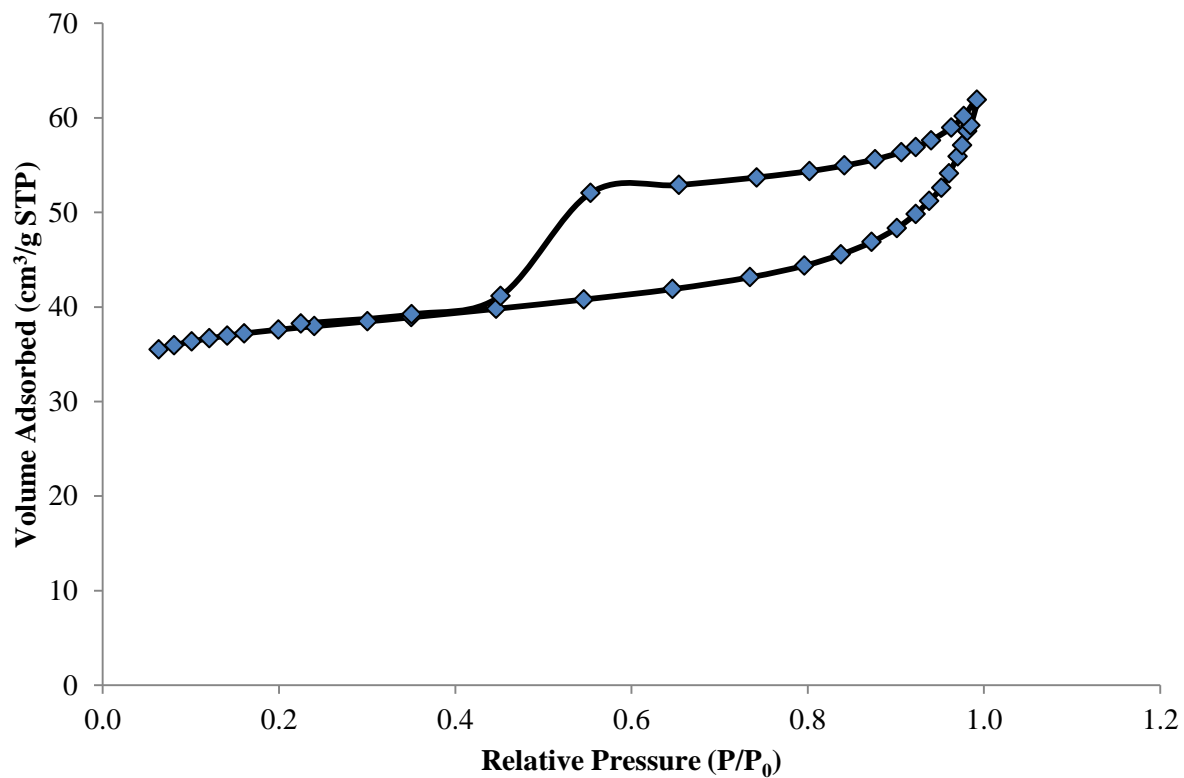
Figure A-6: N_2 adsorption-desorption curve of AlpMMT pillared at OH/Al ratio of 1.0.
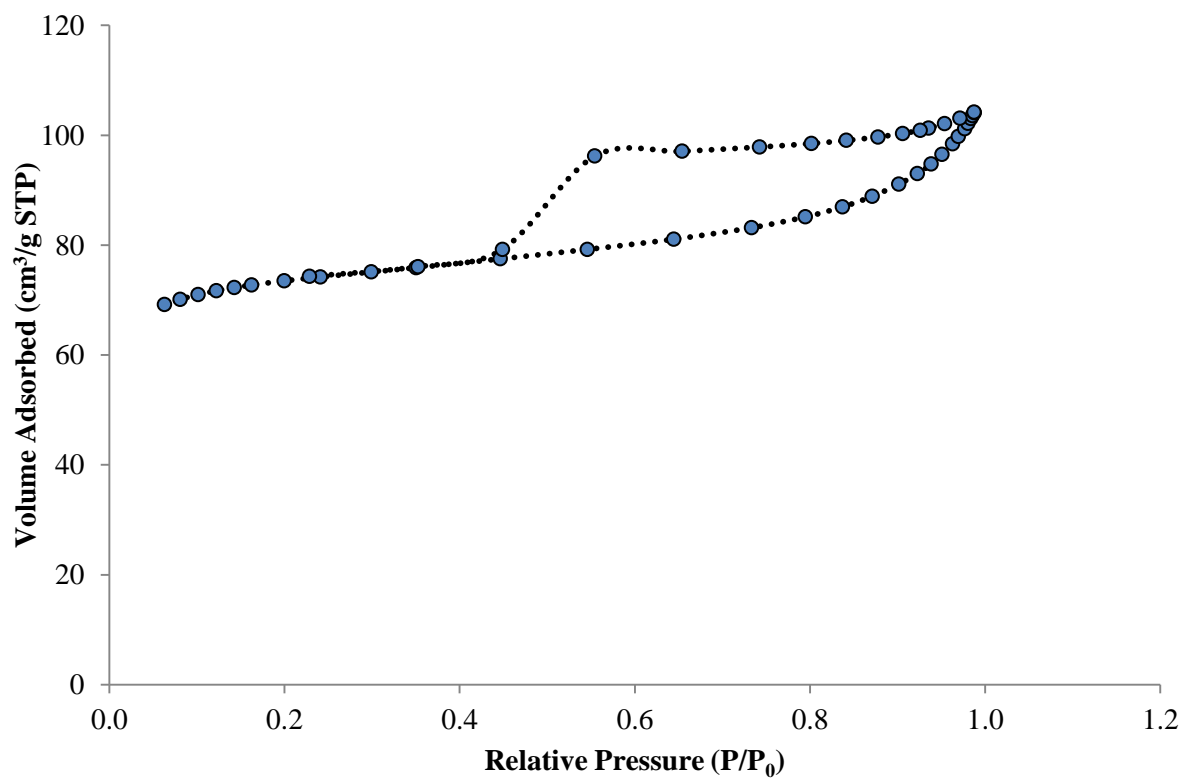
Figure A-7: N_2 adsorption-desorption curve of AlpMMT pillared at OH/Al ratio of 1.5.
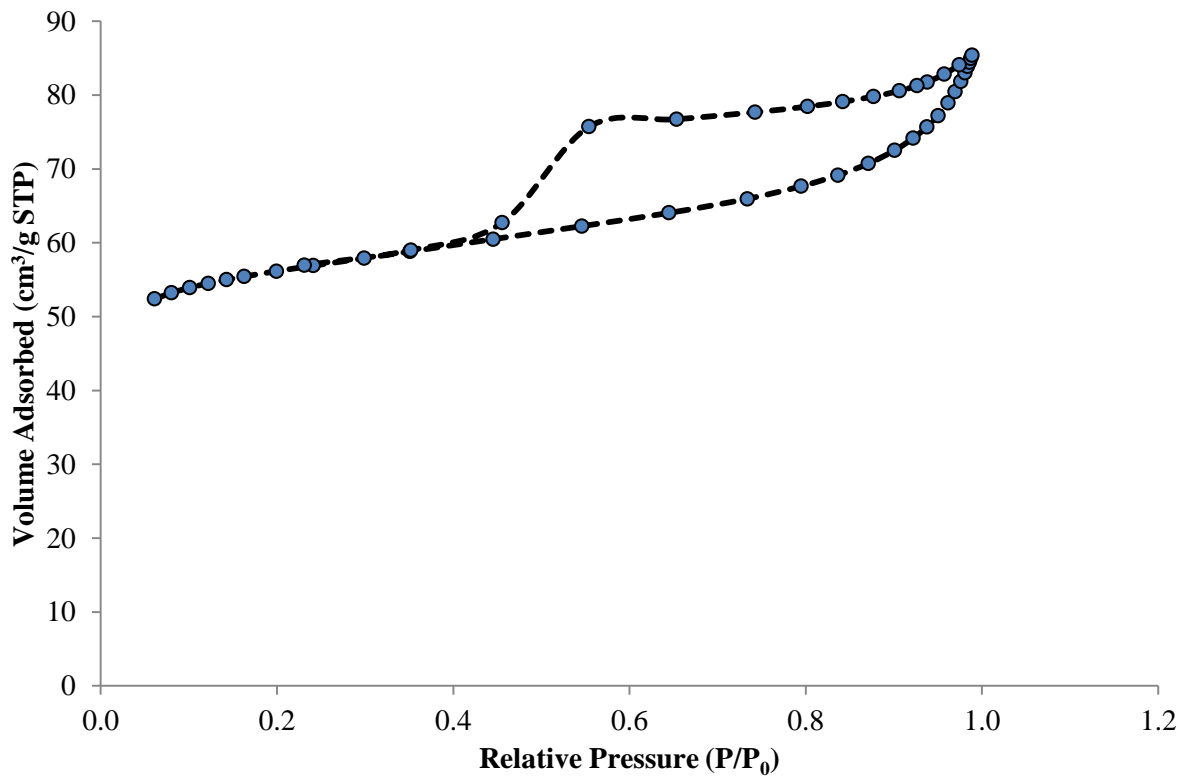
Figure A-8: N$_2$ adsorption-desorption curve of AlpMMT pillared at OH/Al ratio of 2.0.
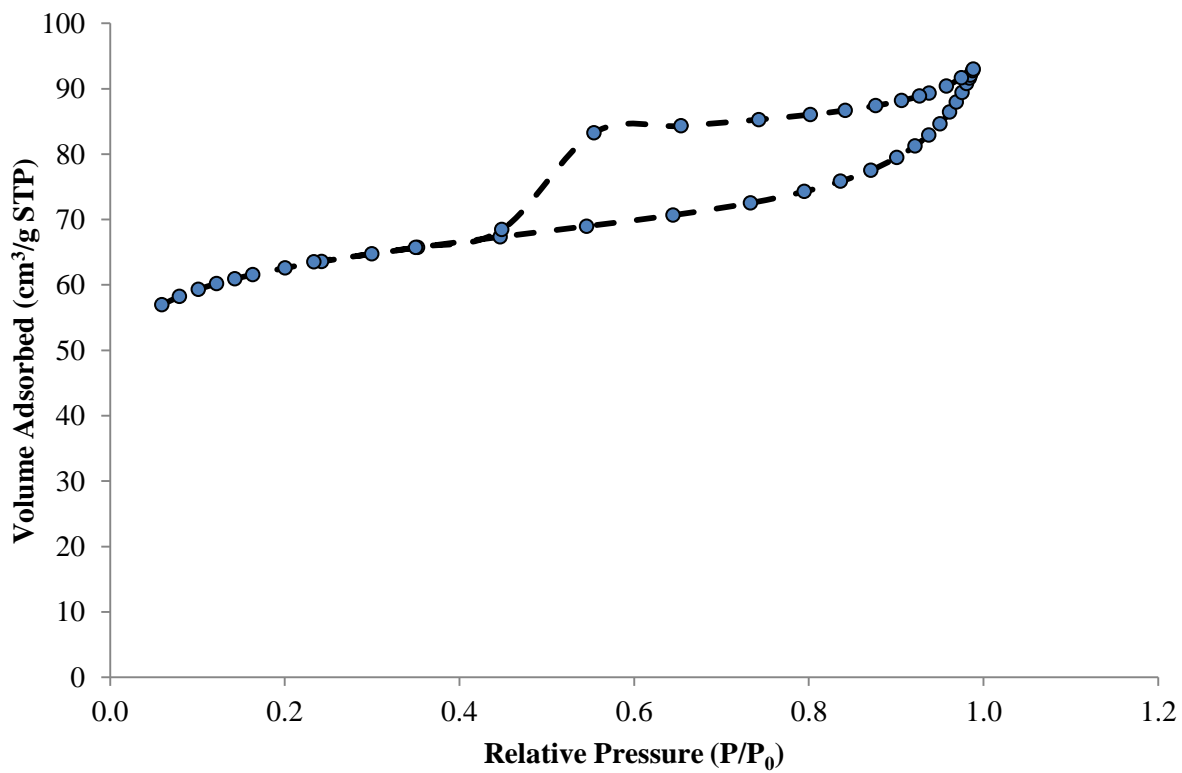
Figure A-9: N$_2$ adsorption-desorption curve of AlpMMT pillared at OH/Al ratio of 2.3.
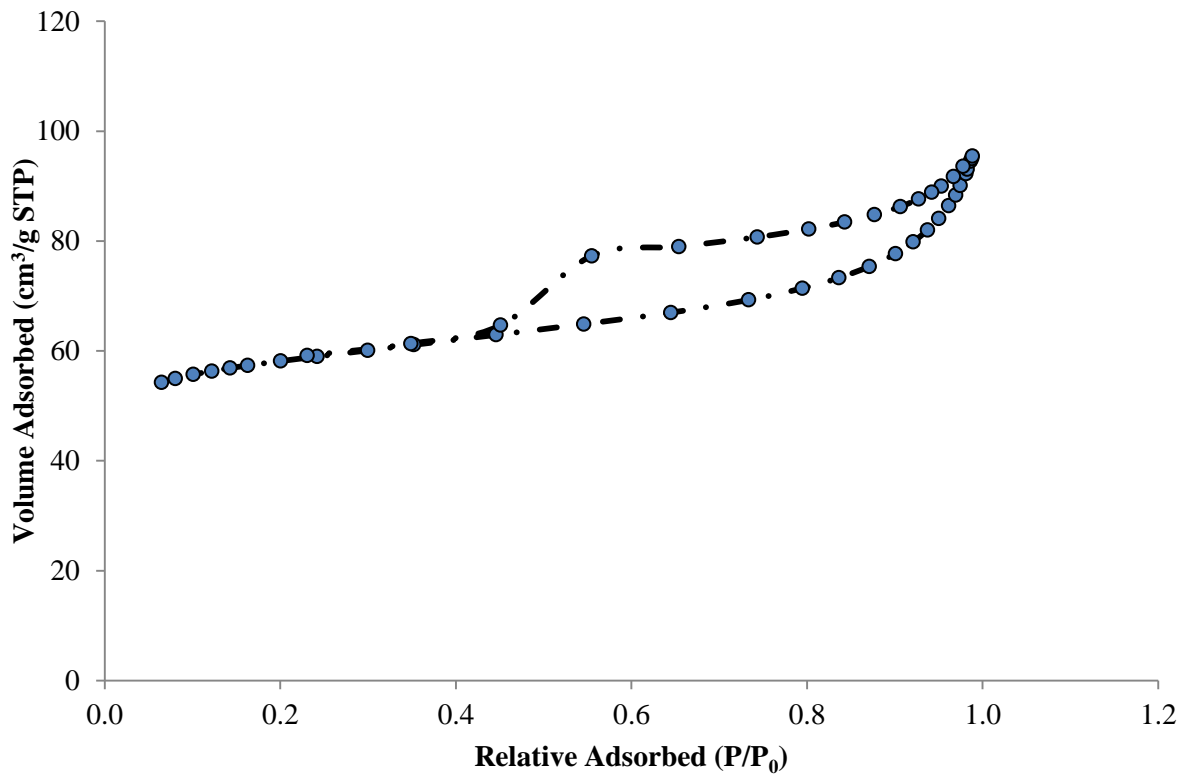
Figure A-10: N_2 adsorption-desorption curve of AlpMMT pillared at OH/Al ratio of 2.4.
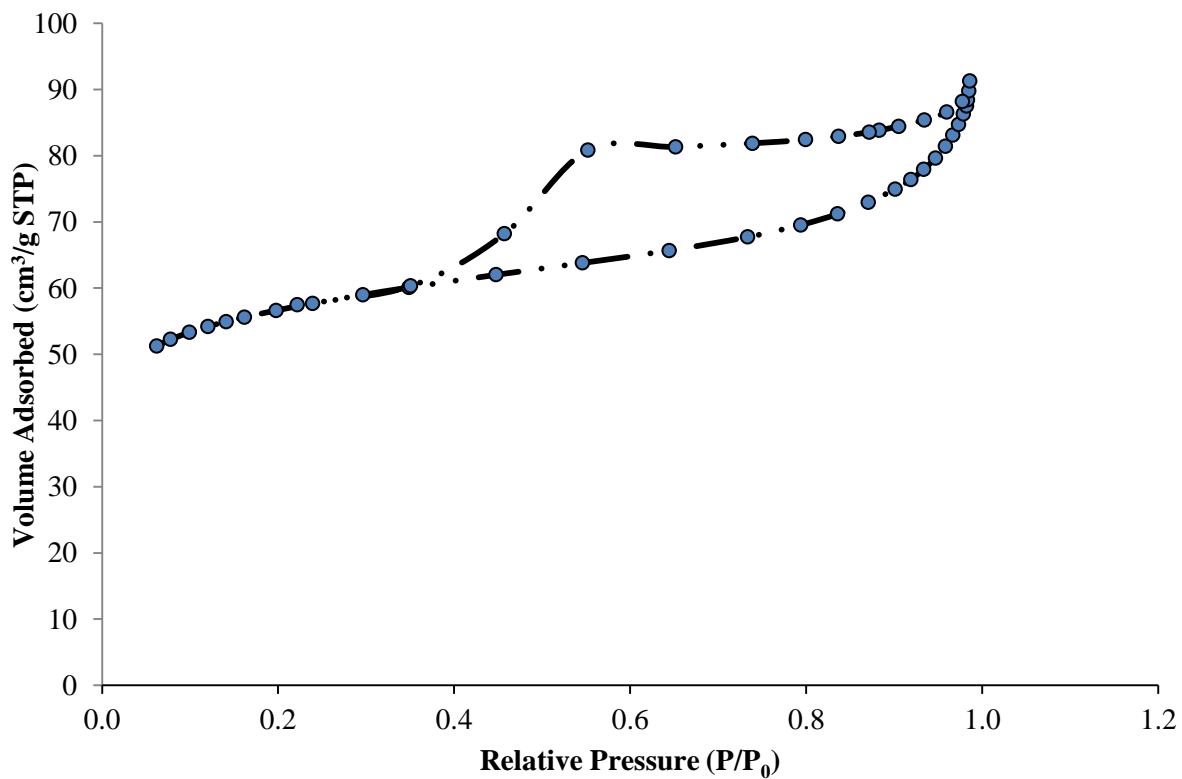
Figure A-11: N_2 adsorption-desorption curve of AlpMMT pillared at OH/Al ratio of 2.6.
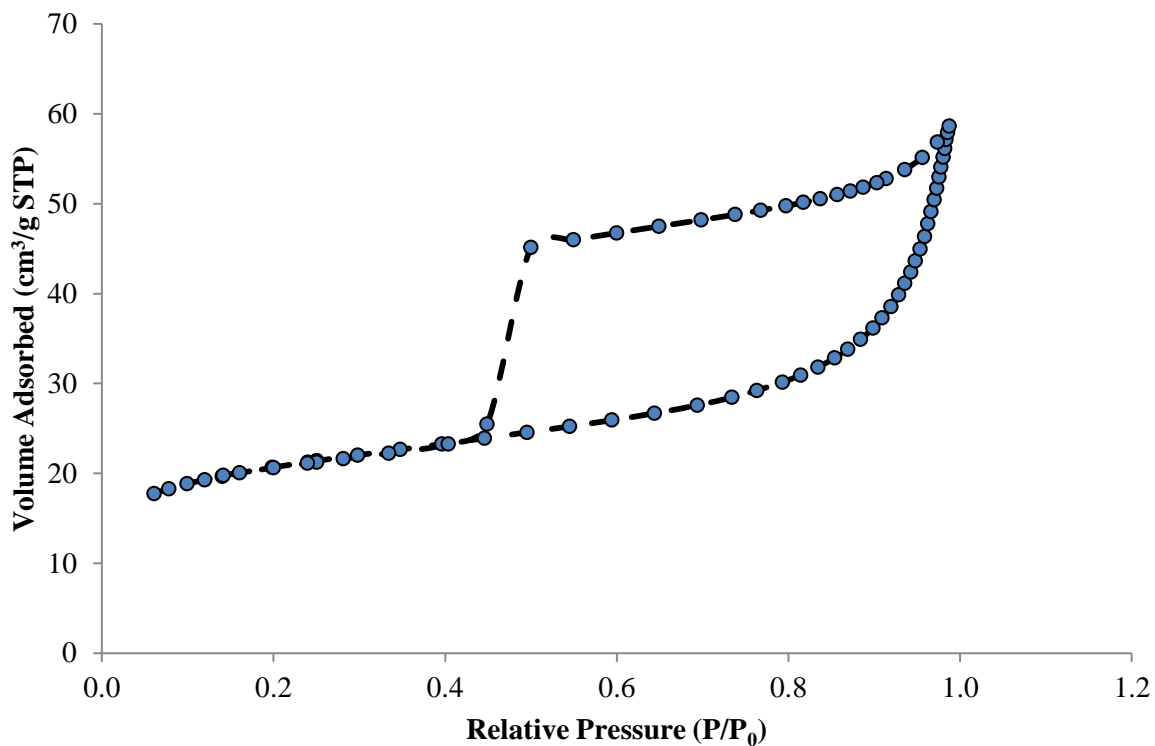
Figure A-12: N$_2$ adsorption-desorption curve of AlpMMT pillared at pH 2
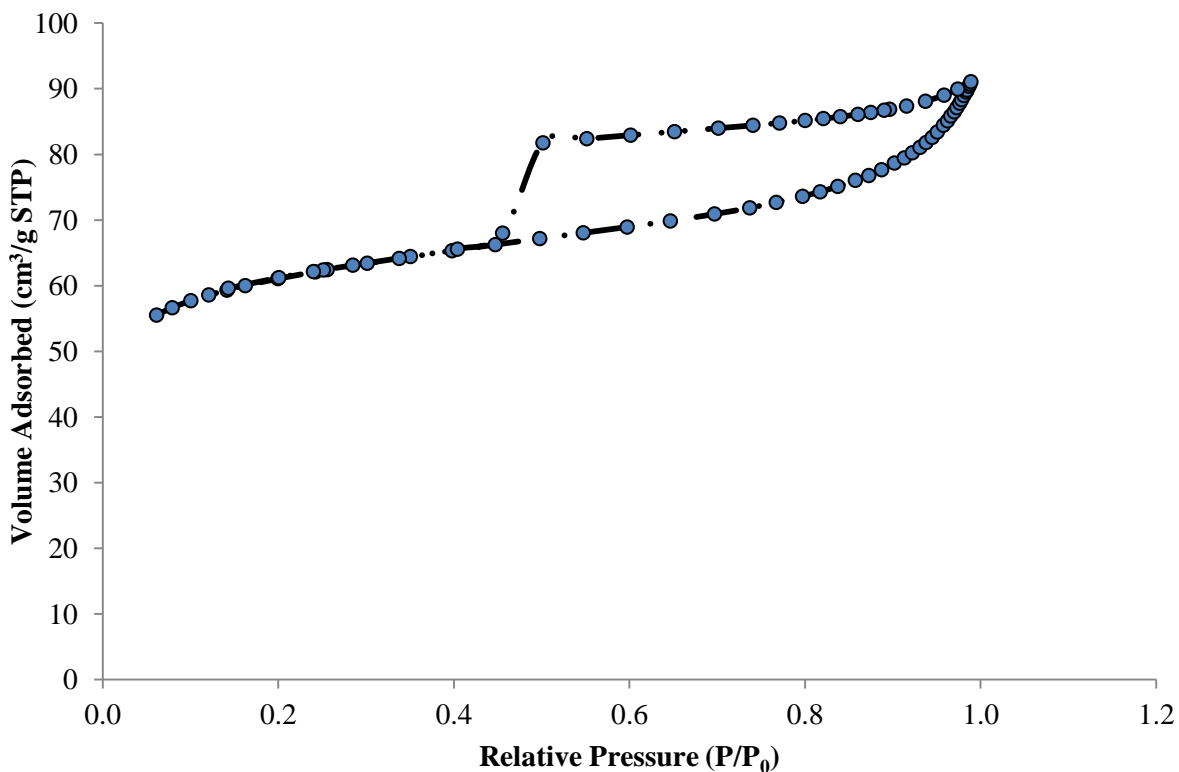
Figure A-13: N$_2$ adsorption-desorption curve of AlpMMT prepared at pH 4.0.
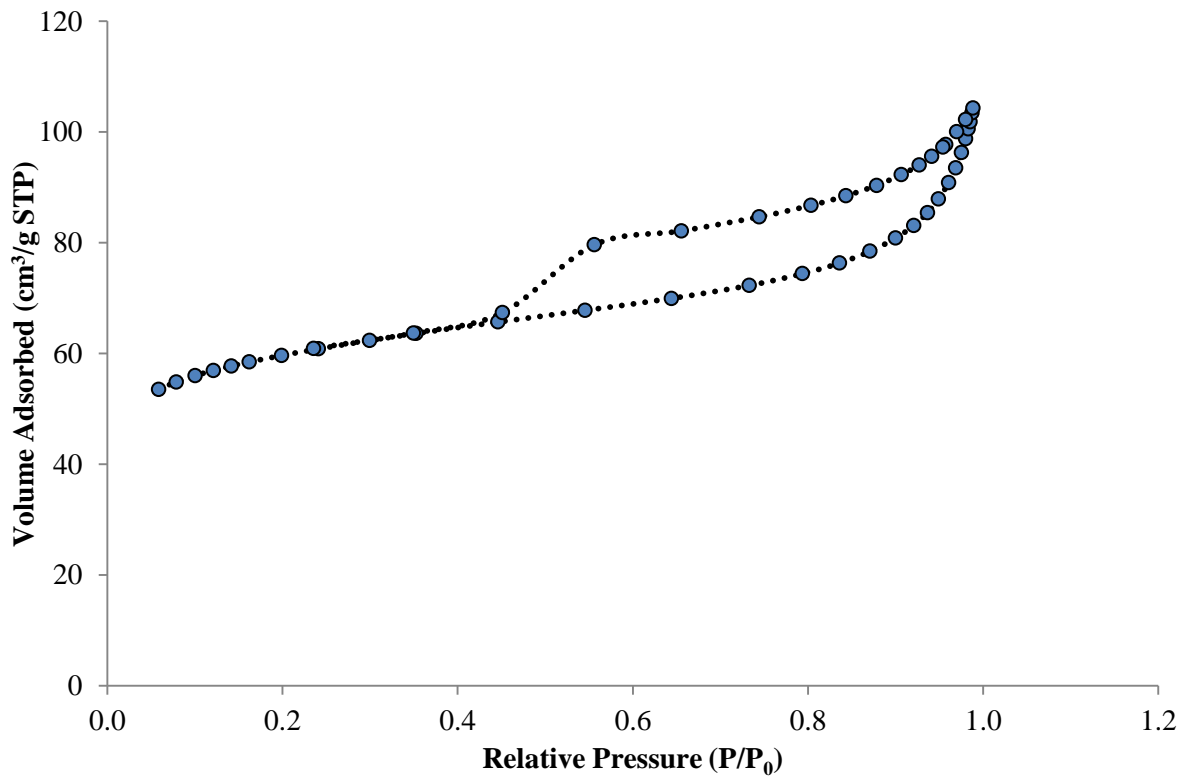
Figure A-14: N$_2$ adsorption-desorption curve of AlpMMT prepared at pH 5.7.
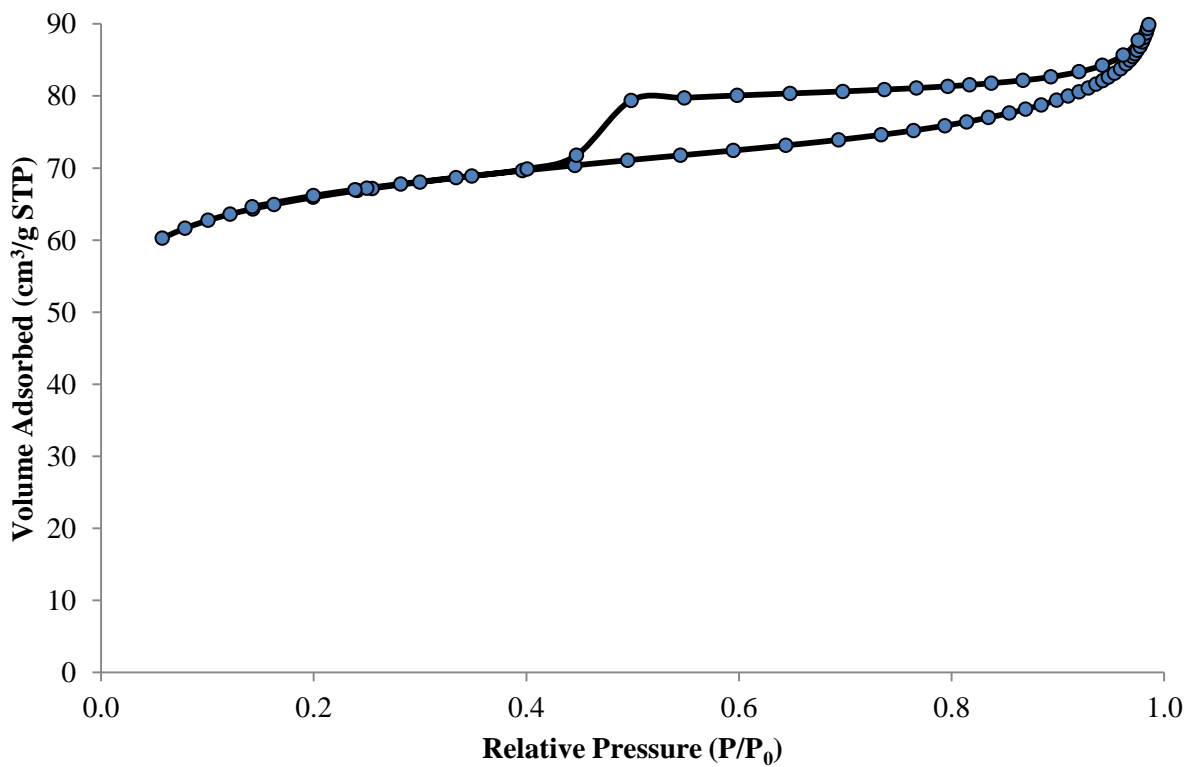
Figure A-15: N$_2$ adsorption-desorption curve of AlpMMT prepared at 25 °C.
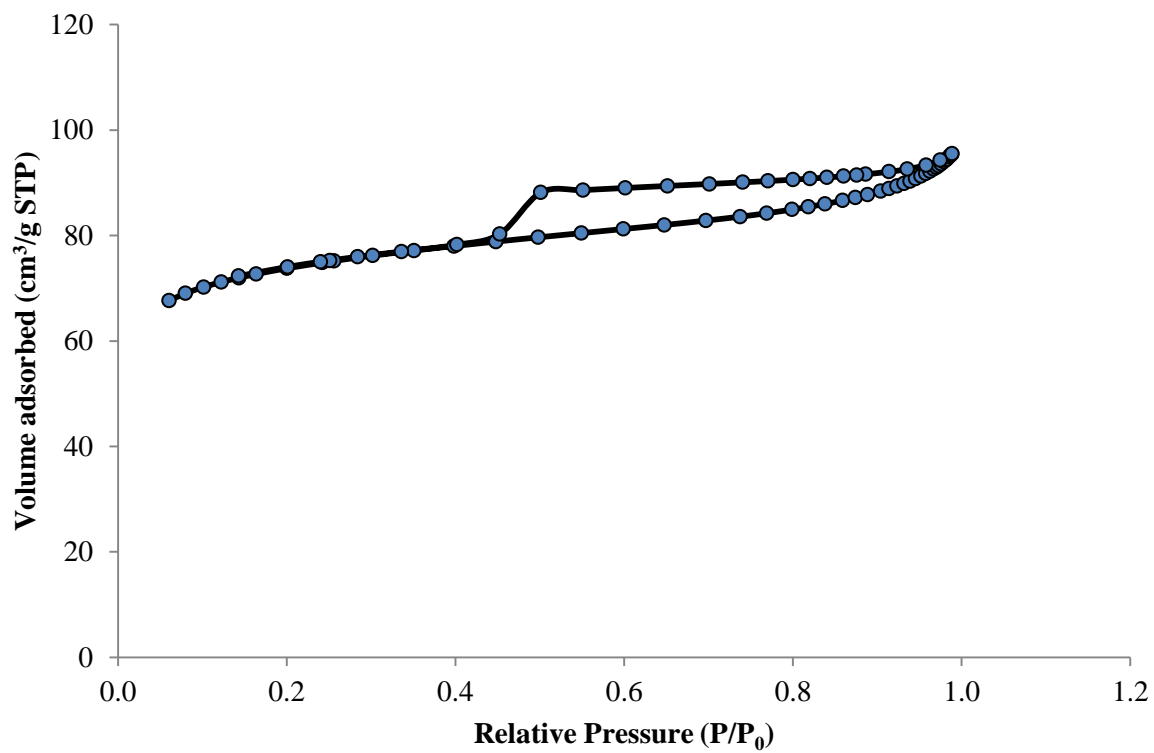
Figure A-16: N_2 adsorption-desorption curve of AlpMMT prepared at 80 °C.

Appendix B

Langmuir and Freundlich isotherms for neutral red adsorption
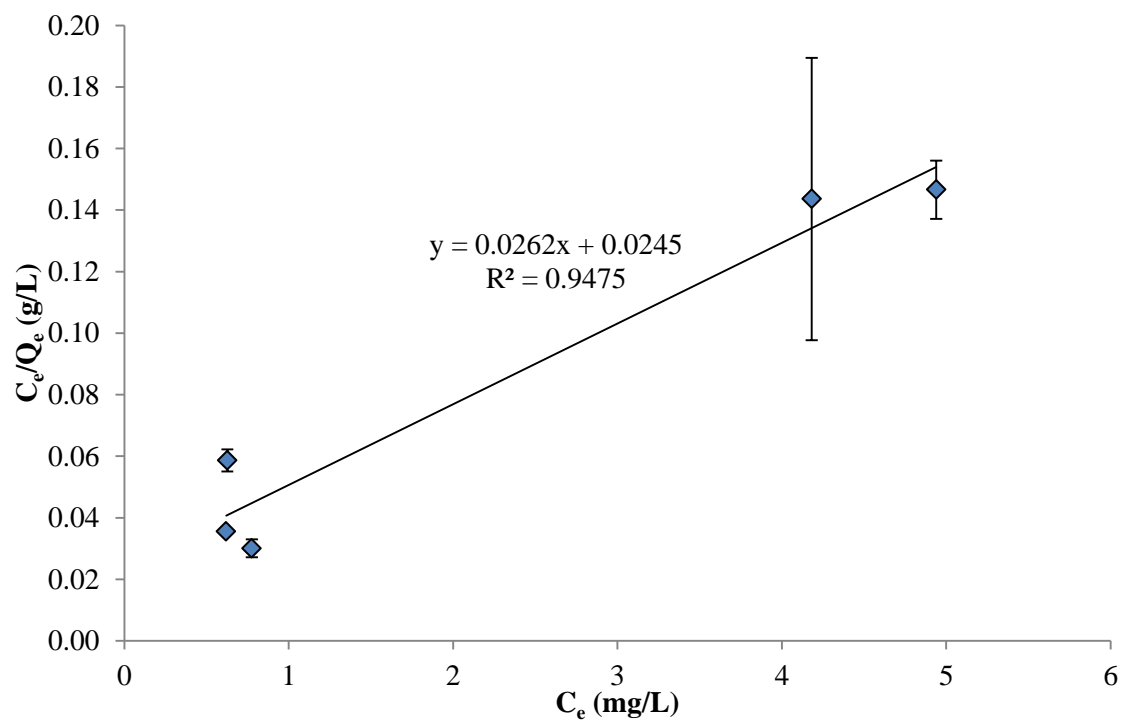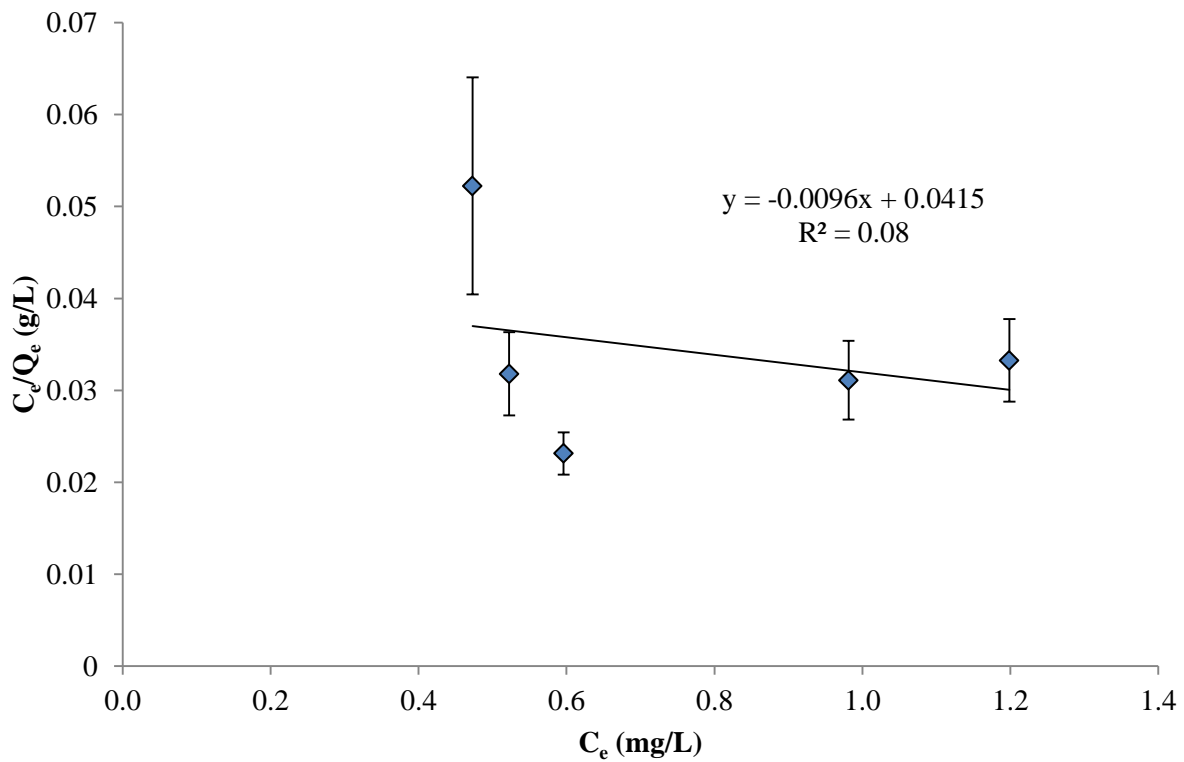

Figure B-1: Langmuir plot for neutral red adsorption onto AlpMMT.
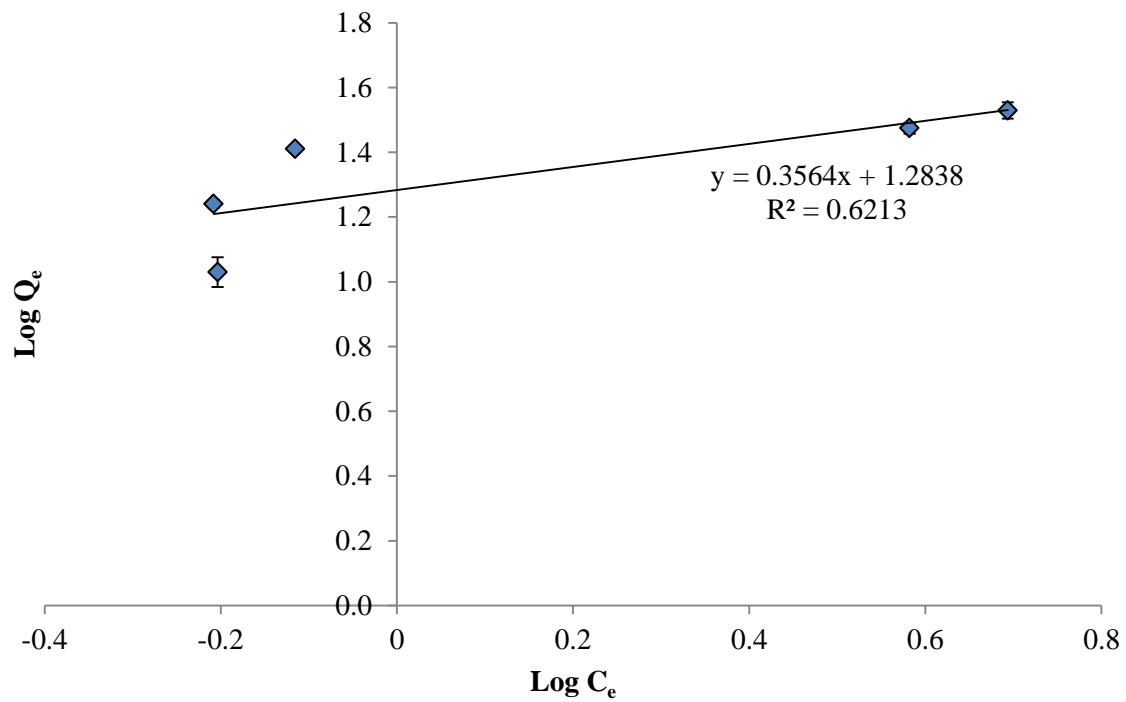
Figure B-2: Freundlich plot for neutral red adsorption onto AlpMMT.
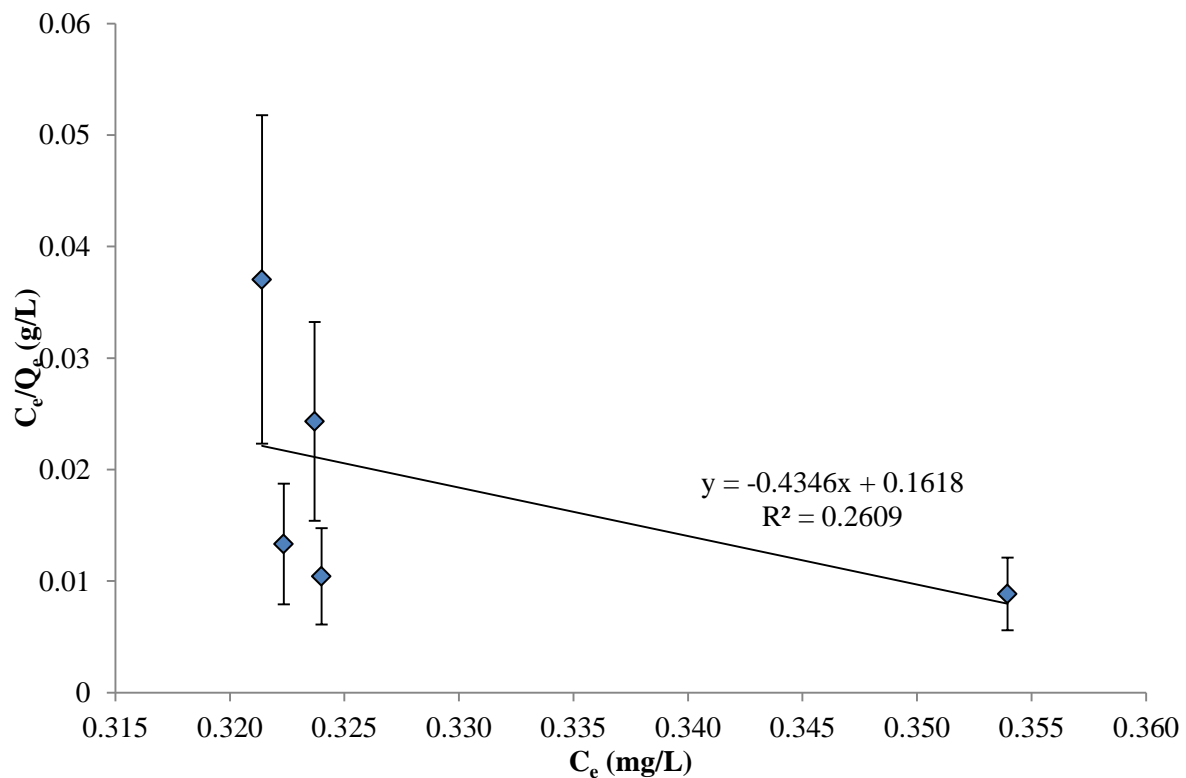
Figure B-3: Langmuir plot for neutral red adsorption onto MPSgMMT.
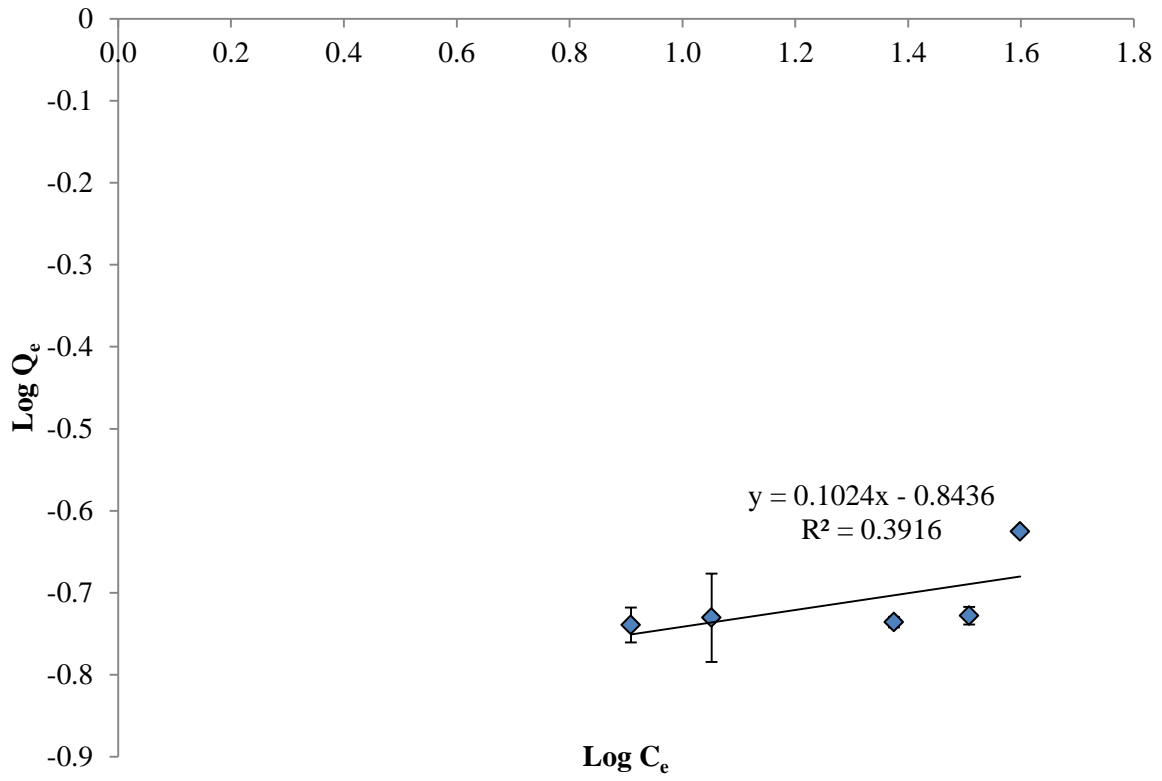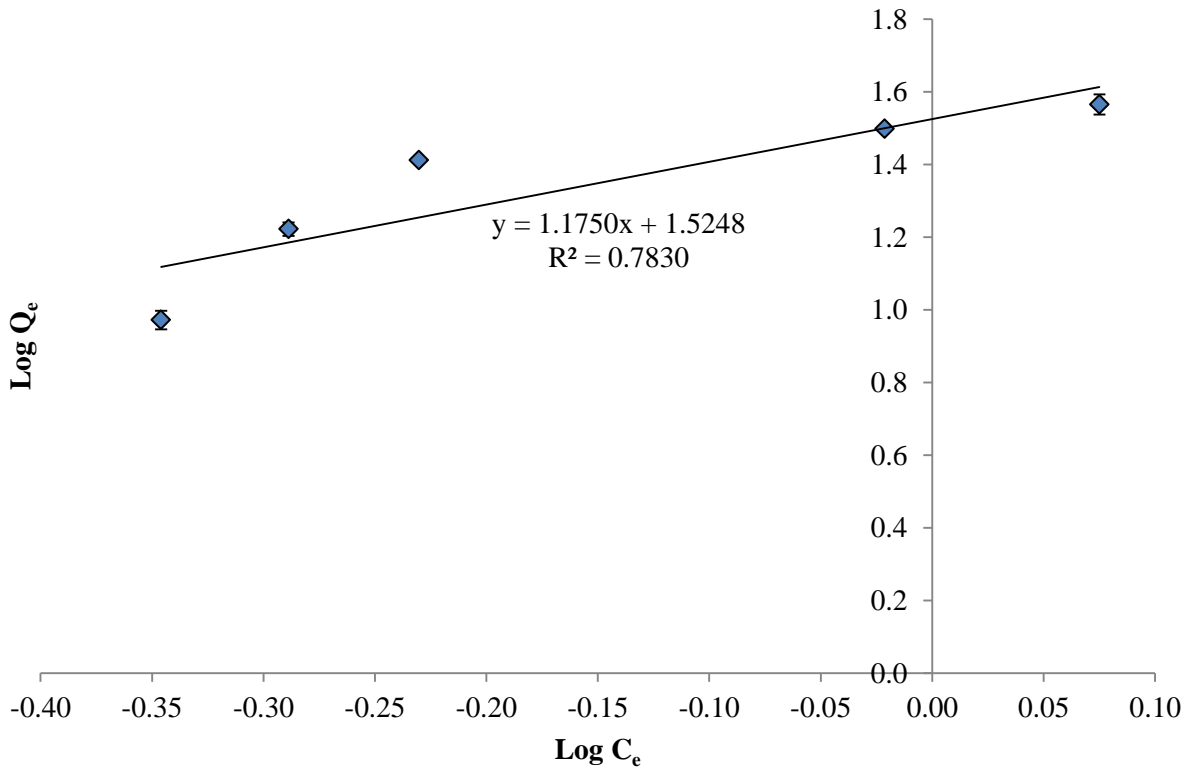
Figure B-4: Freundlich plot for neutral red adsorption onto MPSgMMT.
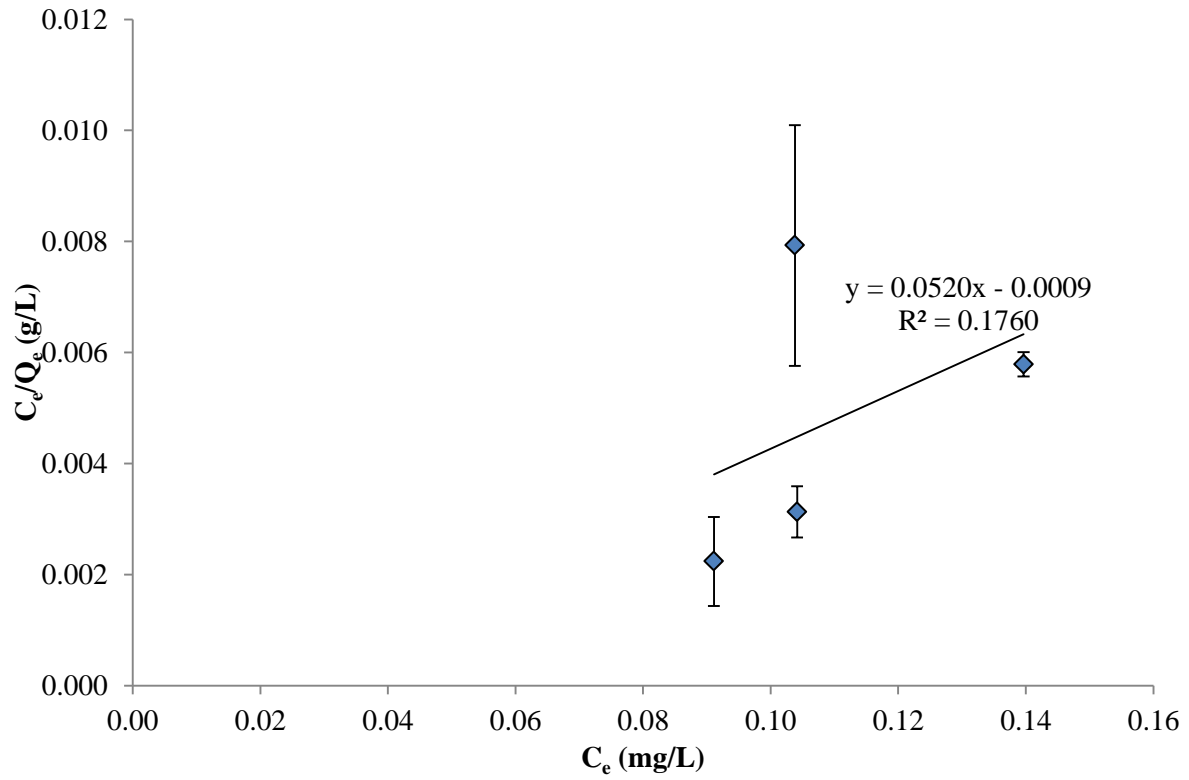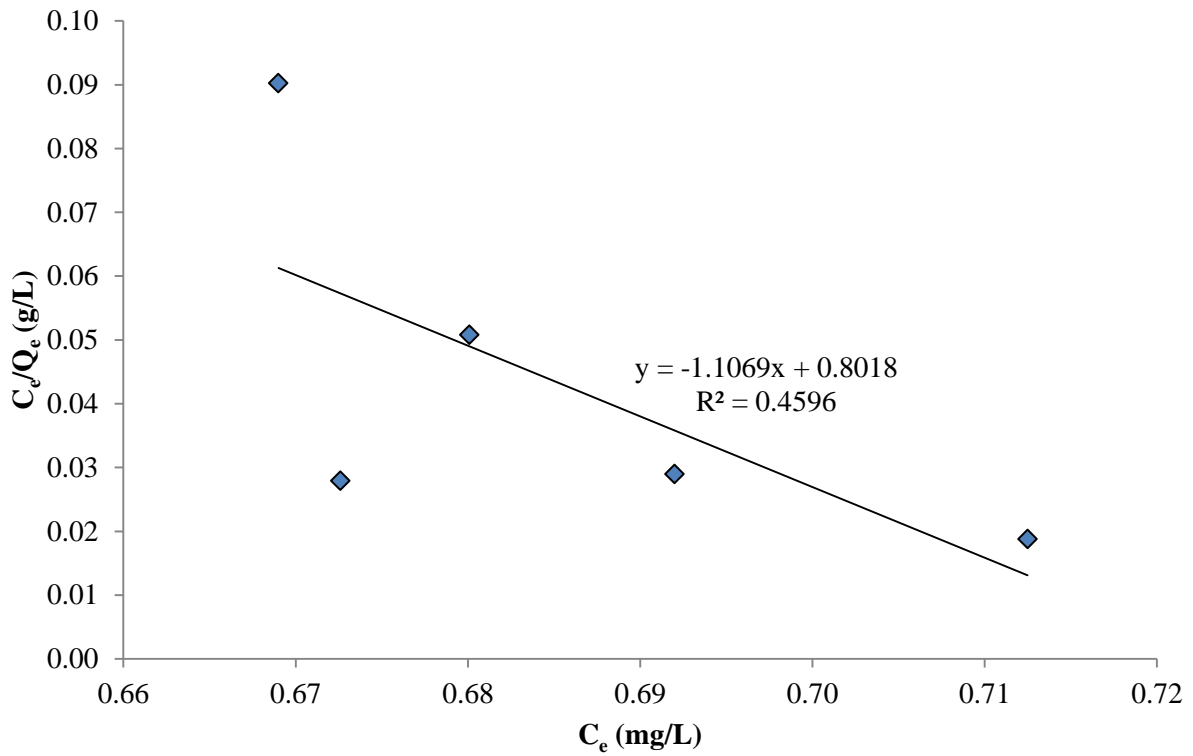

Figure B-5: Langmuir plot for neutral red adsorption onto NaMMT.
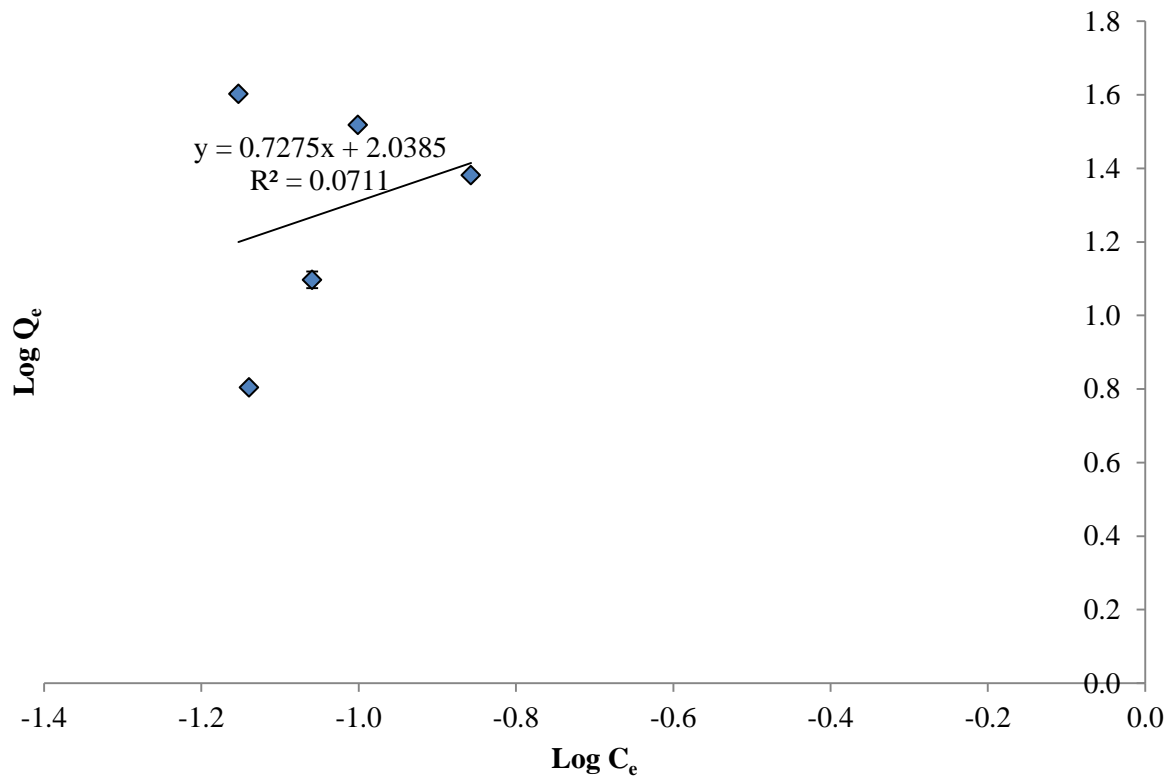
Figure B-6: Freundlich plot for neutral red adsorption onto NaMMT.
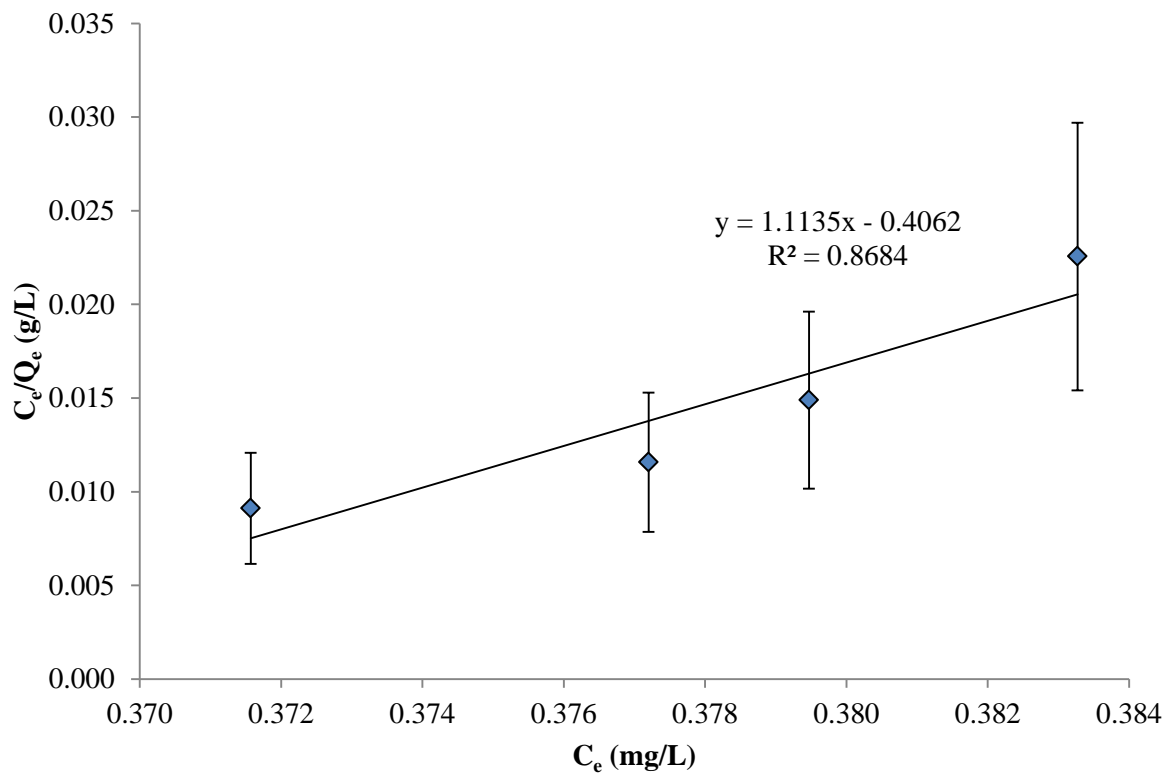
Figure B-7: Langmuir plot for neutral red adsorption onto PMAAgMMT.
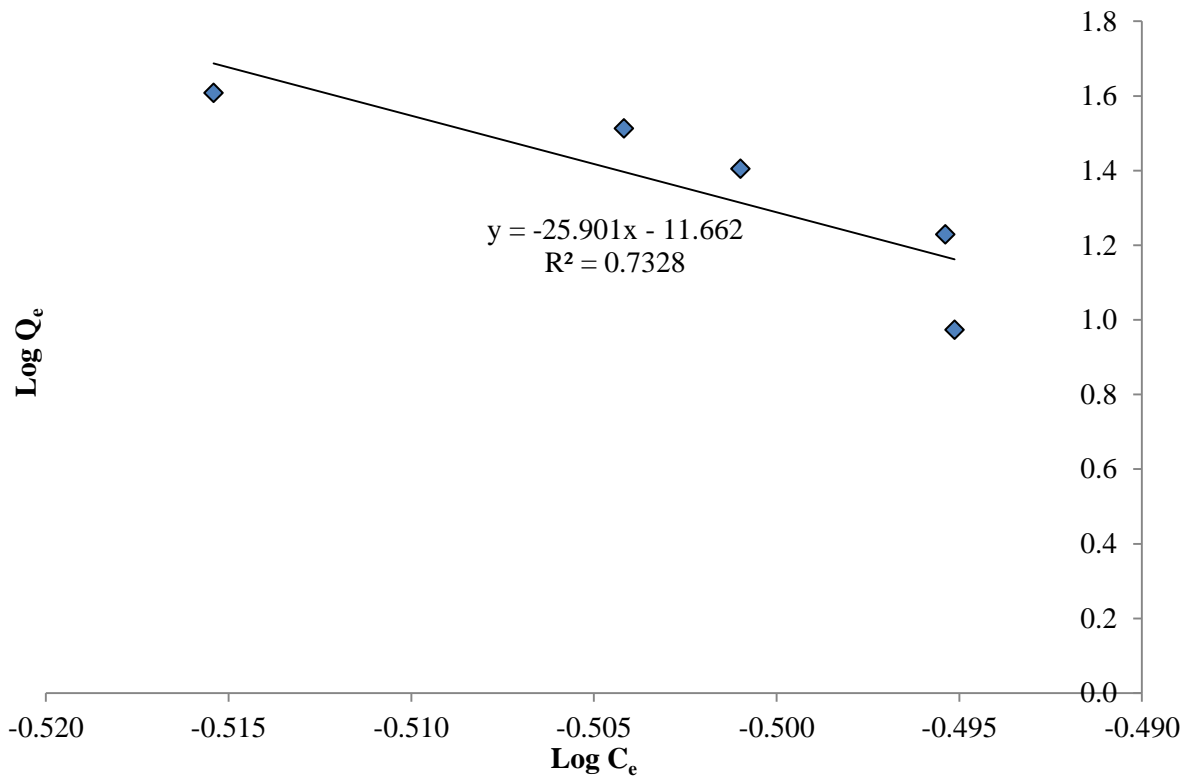
Figure B-8: Freundlich plot for neutral red adsorption onto PMAAgMMT.
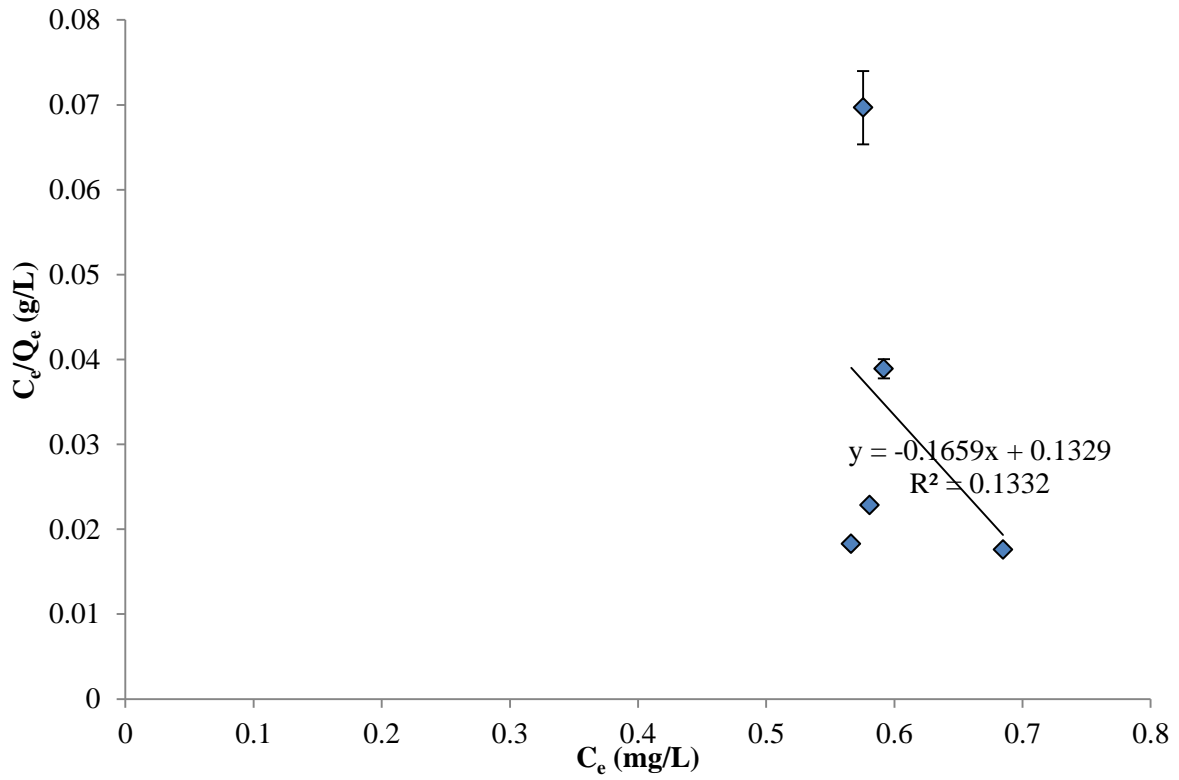
Figure B-9: Langmuir plot for neutral red adsorption onto PMMAgMMT.
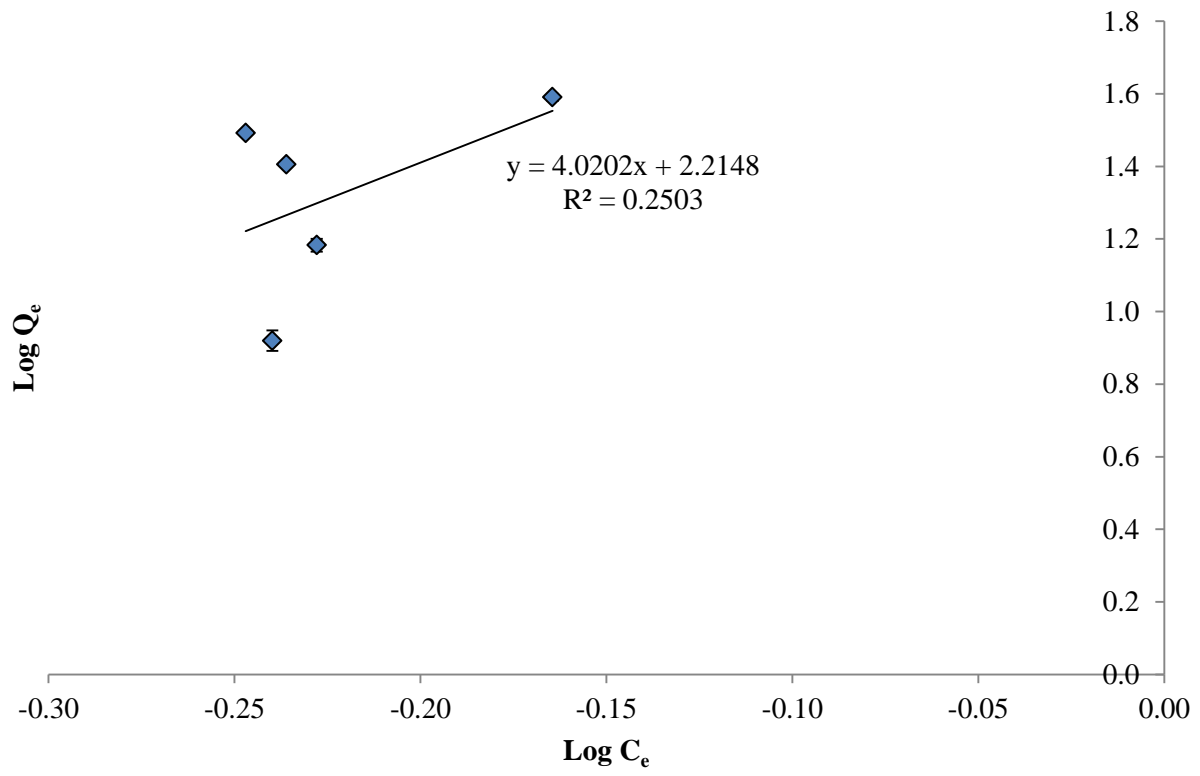
Figure B-10: Freundlich plot for neutral red adsorption onto PMMAgMMT.
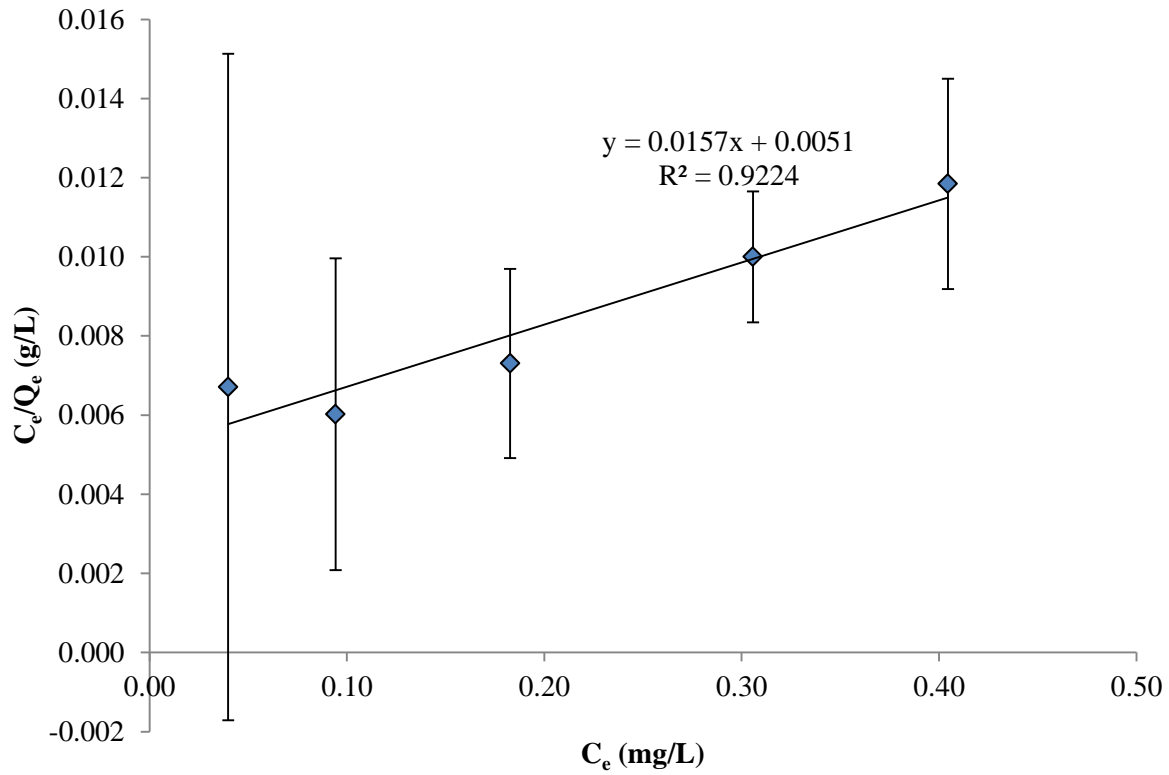
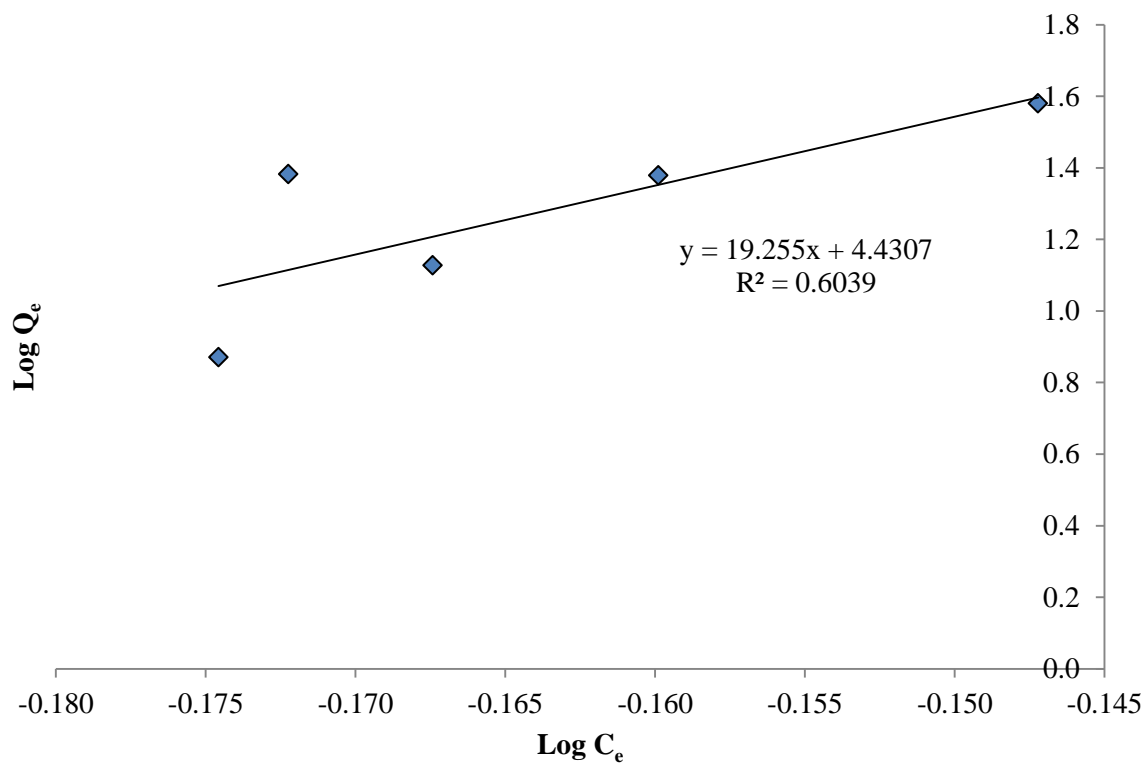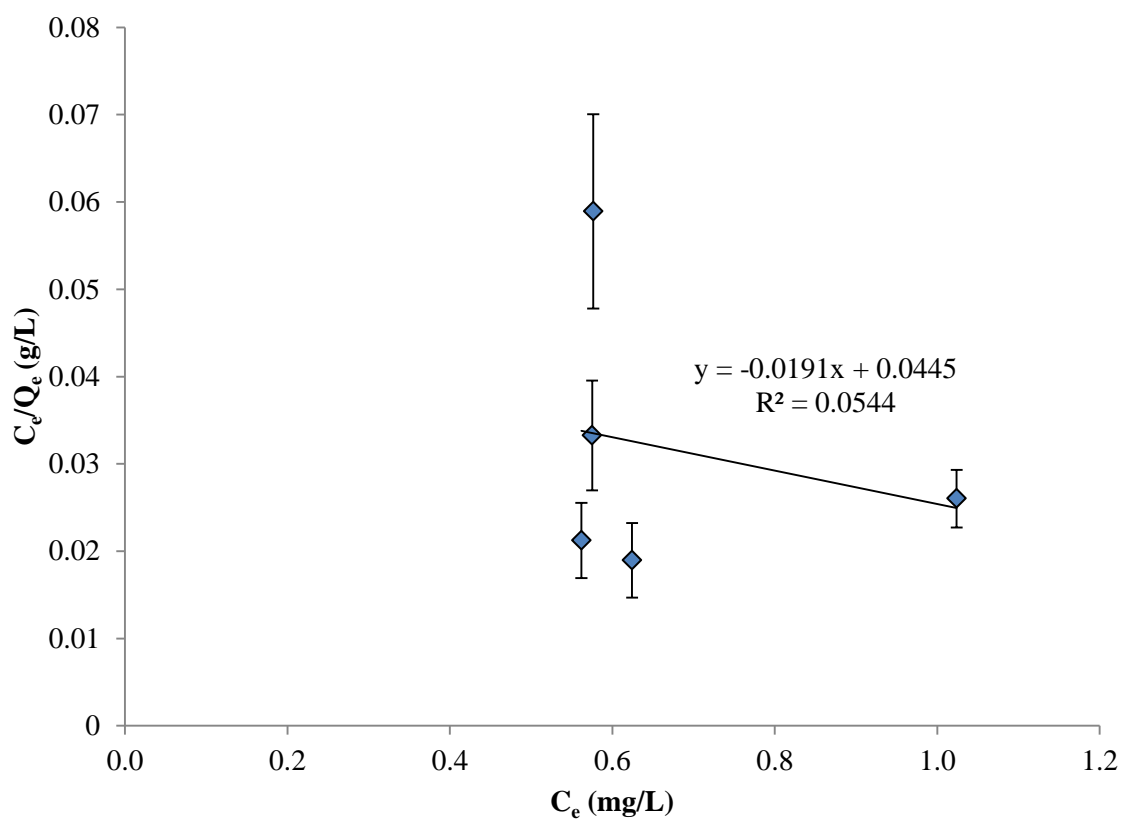Figure B-11: Langmuir plot for neutral red adsorption onto lignocellulose.
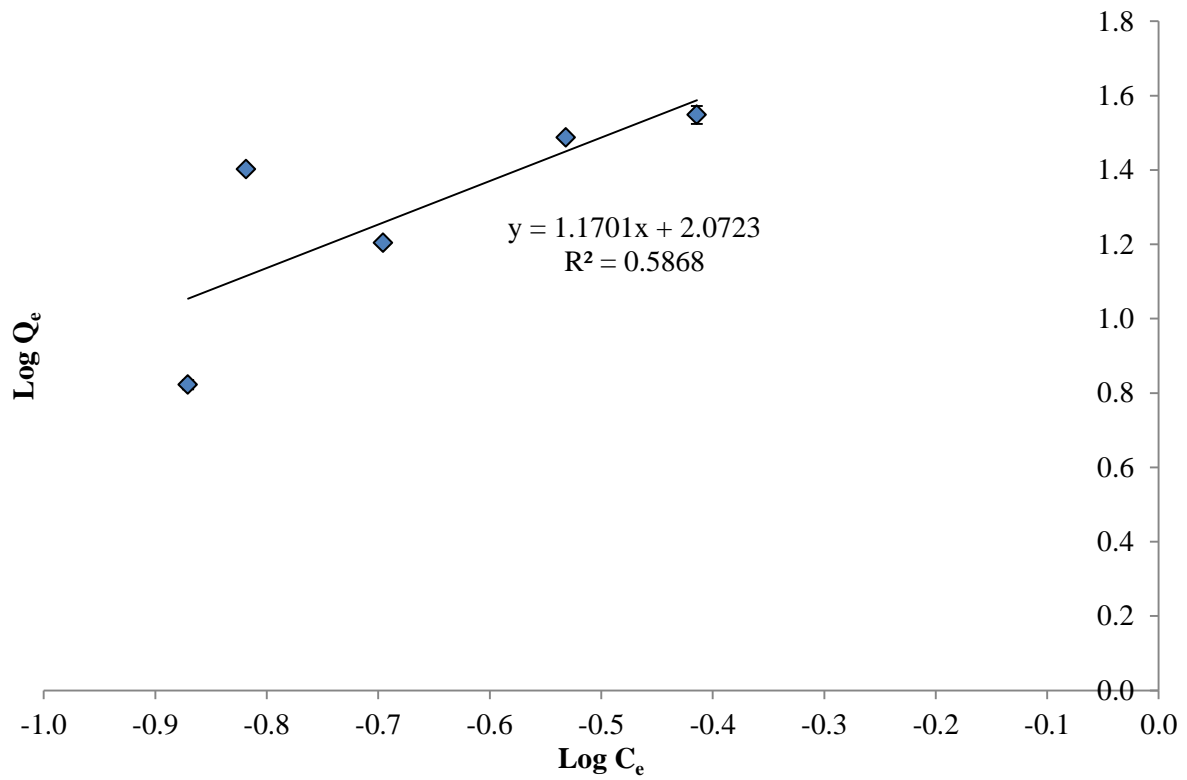
Figure B-12: Freundlich plot for neutral red adsorption onto lignocellulose.
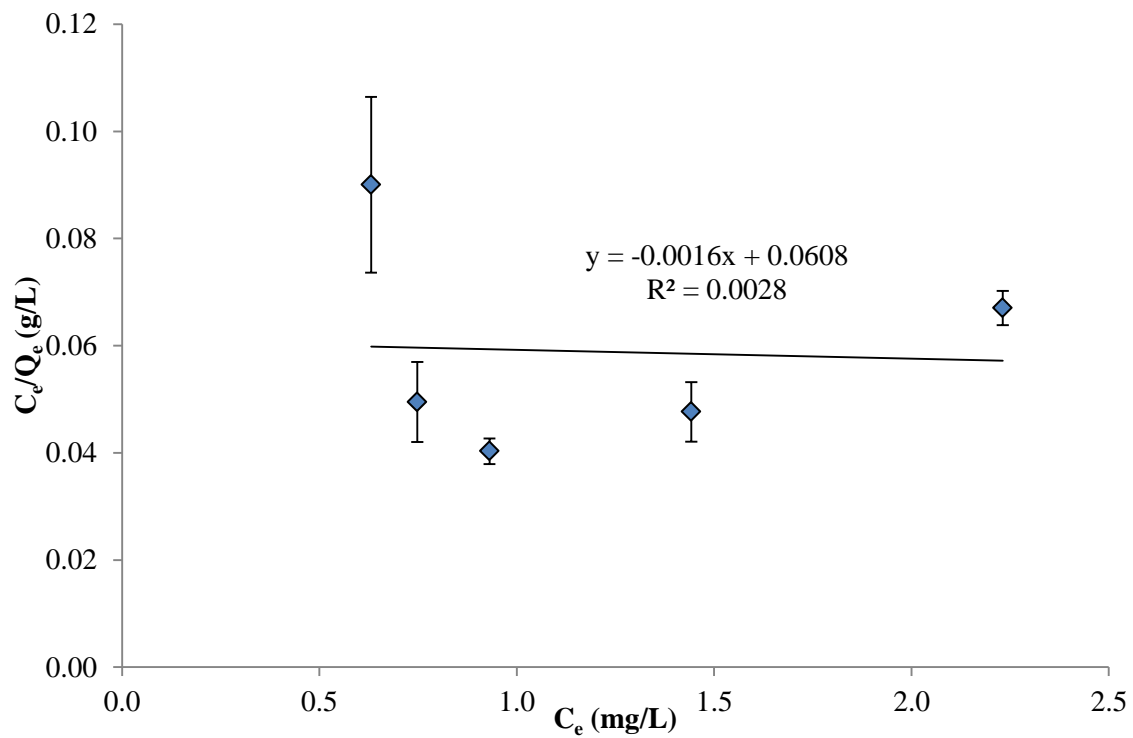
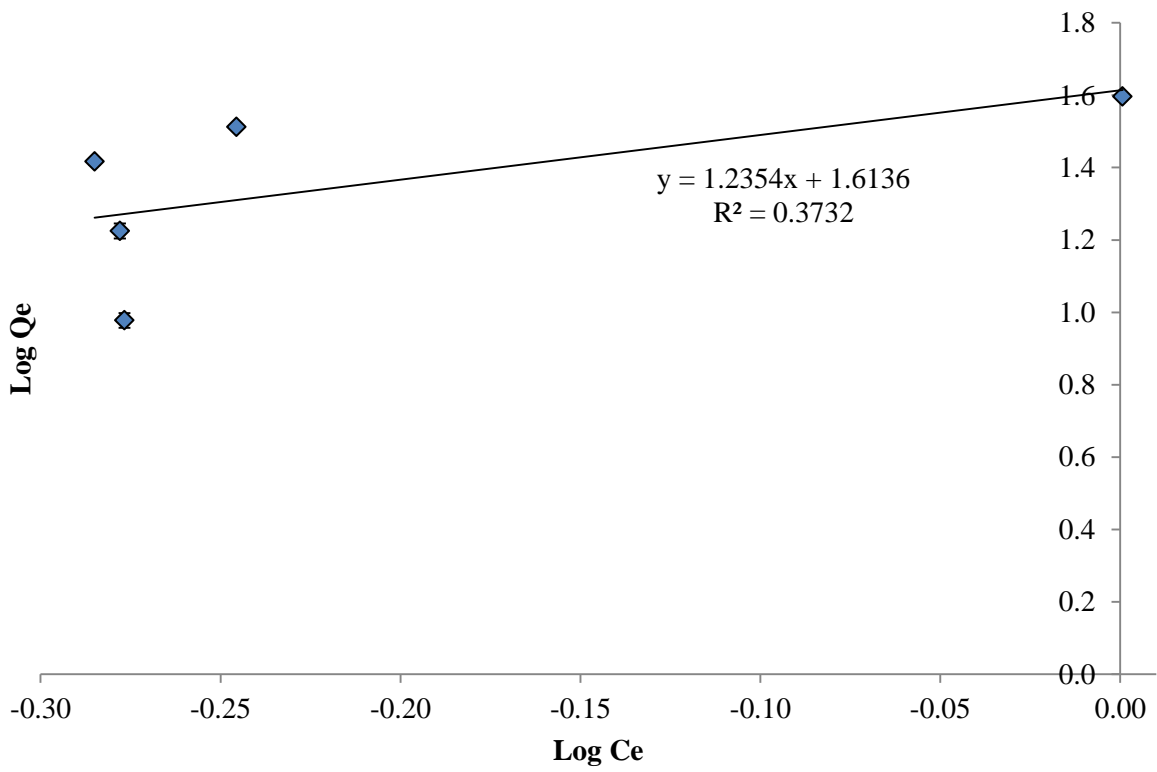Figure B-13: Langmuir plot for neutral red adsorption onto MPSgLig.
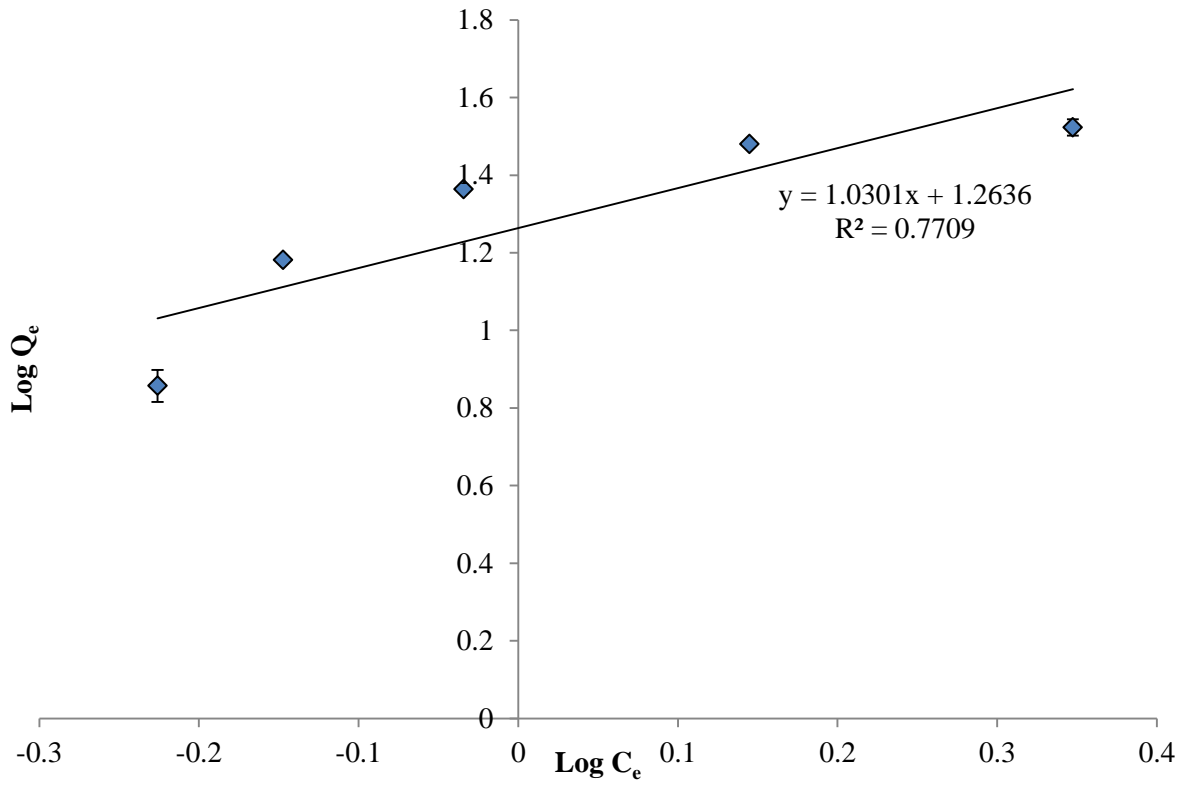
Figure B-14: Freundlich plot for neutral red adsorption onto MPSgLig.
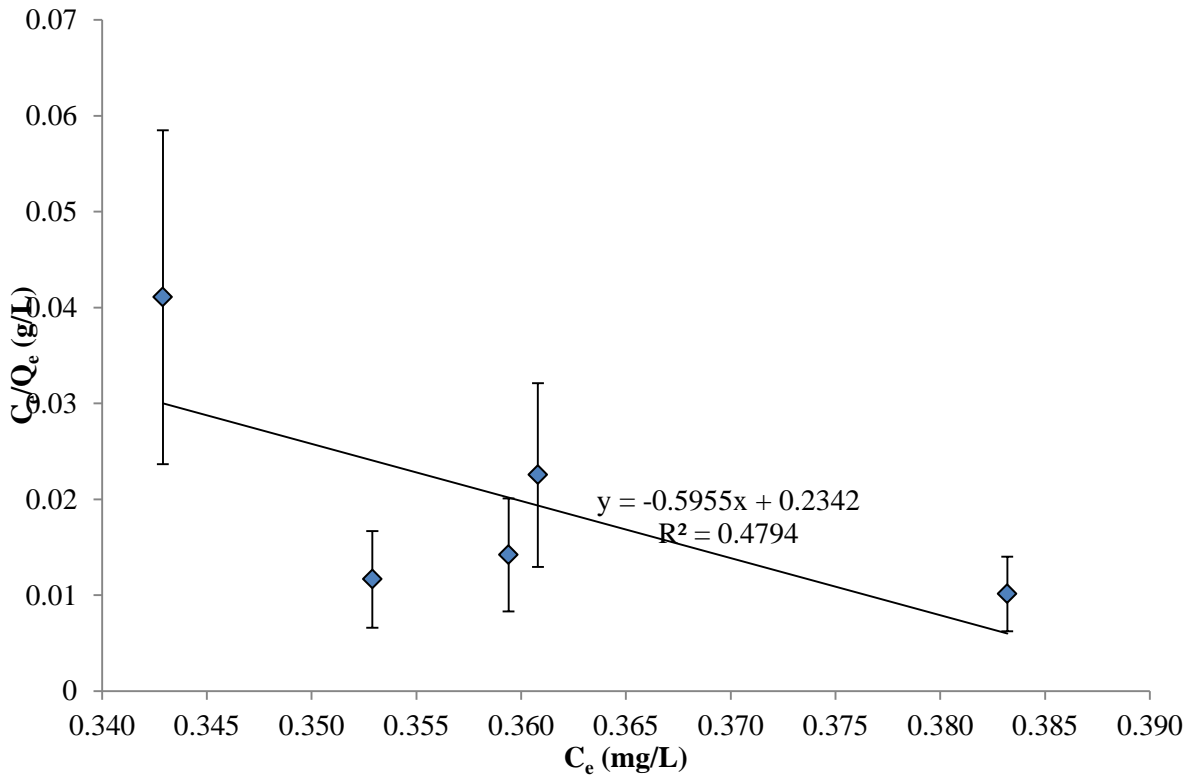
Figure B-15: Langmuir plot for neutral red adsorption onto PMAAgLig.
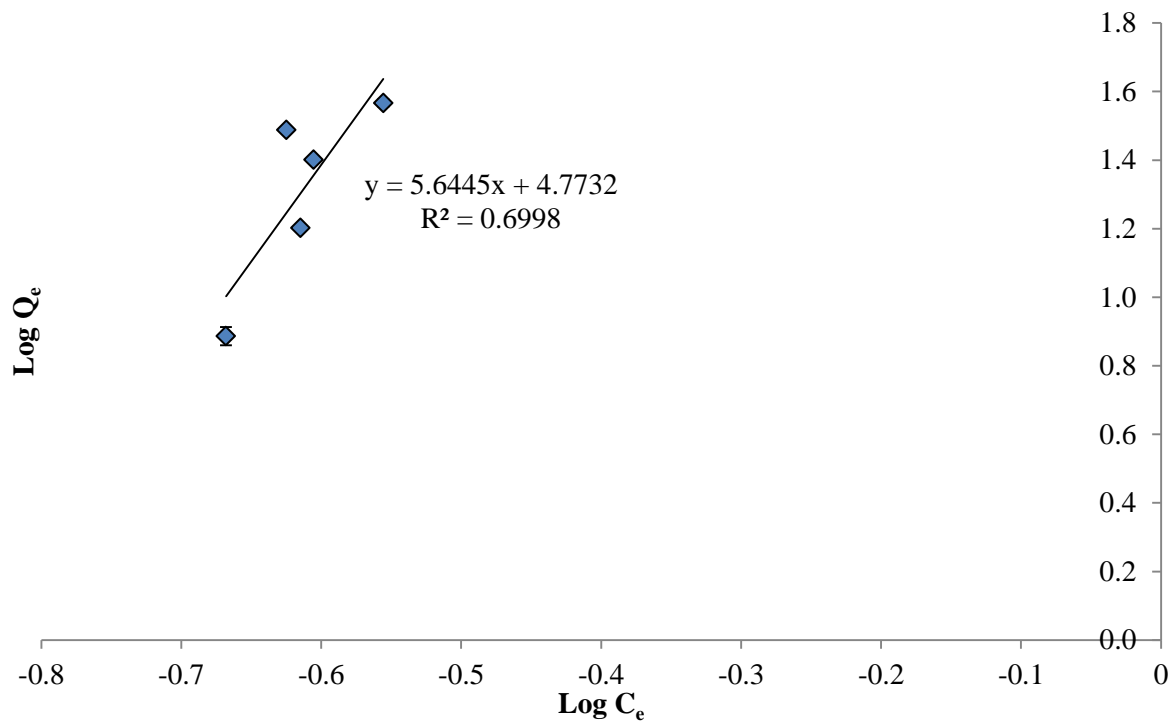
Figure B-16: Freundlich plot for neutral red adsorption onto PMAAgLig.

$y = 5.6445x + 4.7732$
$R^2 = 0.6998$

Figure B-17: Langmuir plot for neutral red adsorption onto PMMAgLig.

$y = -0.0096x + 0.0415$
$R^2 = 0.08$

Figure B-18: Freundlich plot for neutral red adsorption onto PMMAgLig.

Figure B-19: Langmuir plot for neutral red adsorption onto Lig-NaMMT.

Figure B-20: Freundlich plot for neutral red adsorption onto Lig-NaMMT.

Figure B-21: Langmuir plot for neutral red adsorption onto PMPSgLig-NaMMT.

Figure B-22: Freundlich plot for neutral red adsorption onto PMPSgLig-NaMMT.
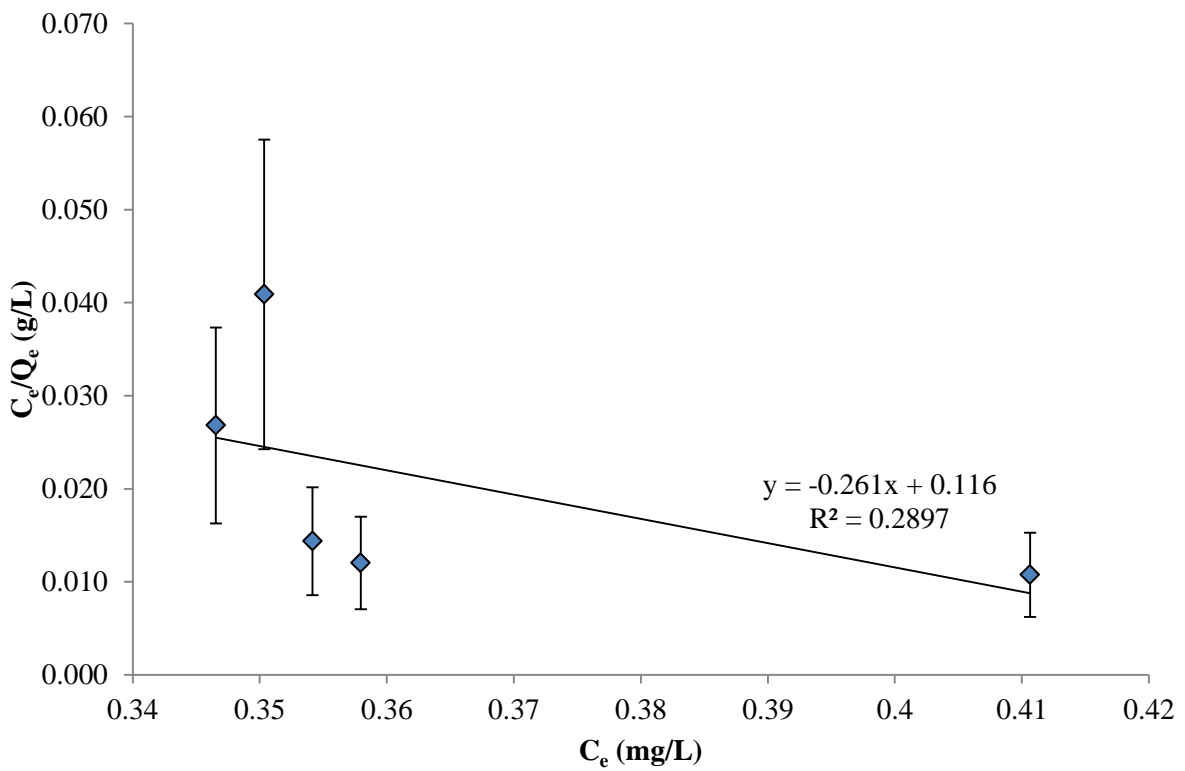

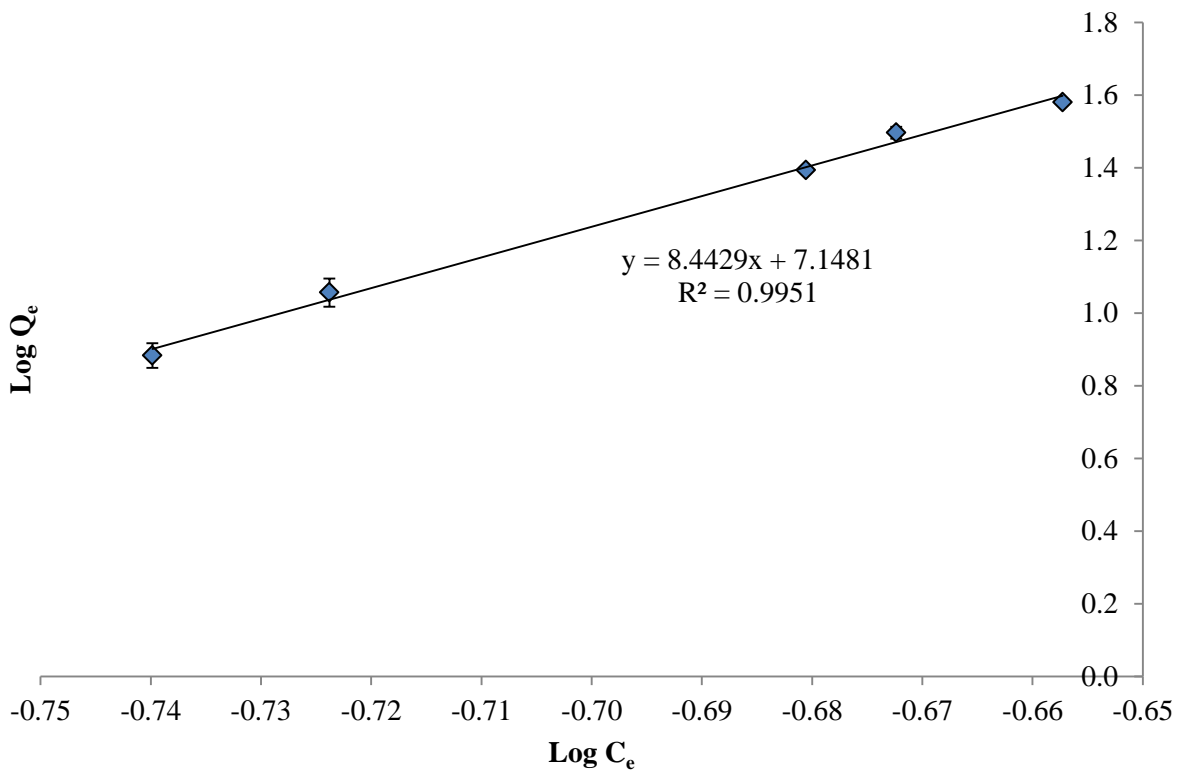Figure B-23: Langmuir plot for neutral red adsorption onto PMAAgLig-NaMMT.

Figure B-24: Freundlich plot for neutral red adsorption onto PMAAgLig-NaMMT.
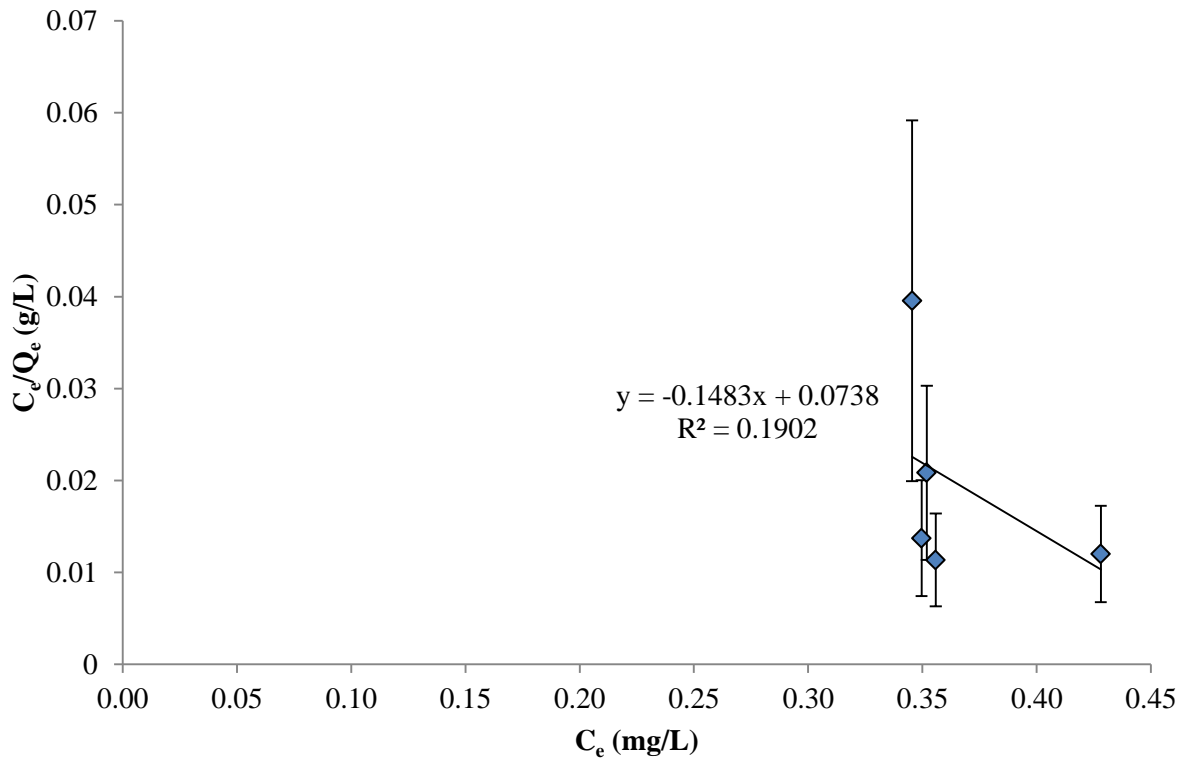

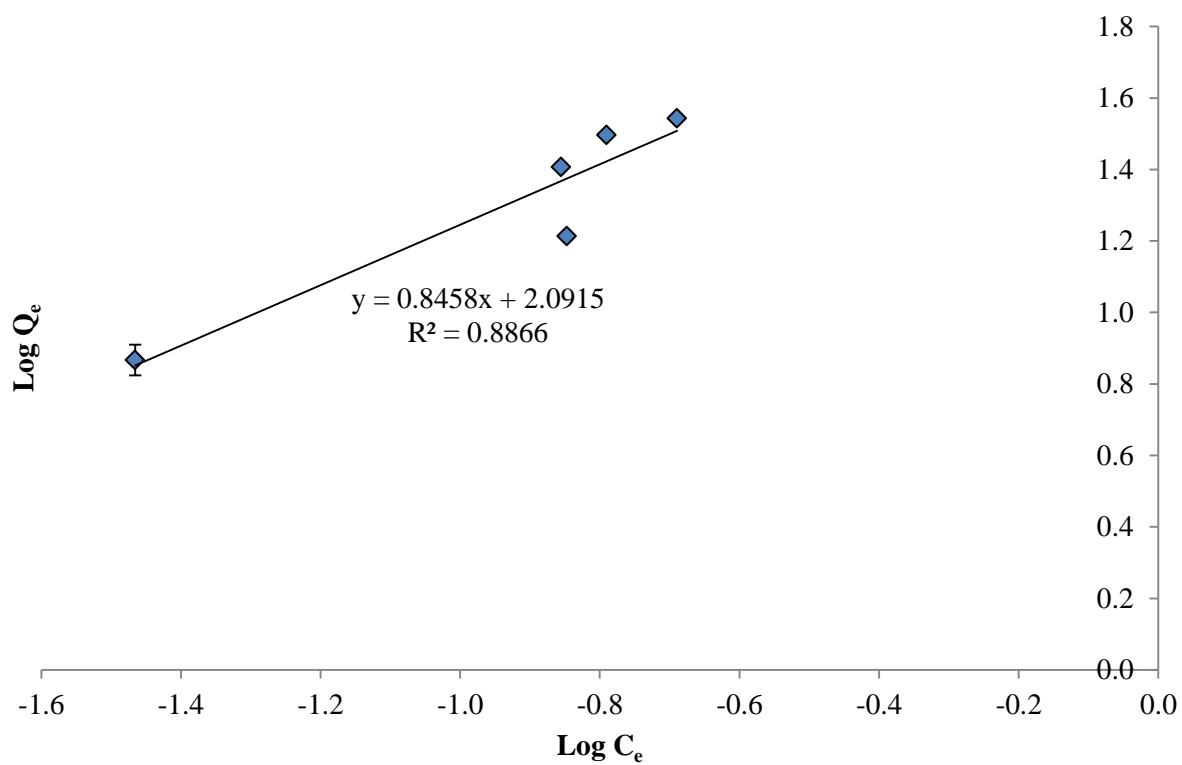Figure B-25: Langmuir plot for neutral red adsorption onto PMMAgLig-NaMMT.

Figure B-26: Freundlich plot for neutral red adsorption onto PMMAgLig-NaMMT.

Appendix C

Conferences and Seminars

The following have been presented at conferences:

- T. Bunhu and L. Tichagwa. Adsorption of heavy metals (Cd^{2+} and Pb^{2+}) from aqueous solution onto montmorillonite based adsorbents. *ASSAf-DST-NRF Second Annual South African Young Scientists' Conference, Diep in Die Berg Conference and Function Centre, Pretoria, South Africa, 26-28 September 2011.*

- L. Tichagwa and T. Bunhu. Composites of clay and lignocellulose materials for water treatment. *11th Annual UNESCO/IUPAC Workshop and Conference on Functional Polymeric Materials & Composites, Stellenbosch, South Africa, 26 – 29 April 2011.*
  T. Bunhu and L. Tichagwa. Adsorption of methyl orange, Pb^{2+} and Cd^{2+} from aqueous solution by composites of lignocellulose-montmorillonite modified with methacryloxypropyl trimethoxysilane. Accepted for publication in *Macromolecular Symposia, 2011.*

- T. Bunhu and L. Tichagwa. Preparation of polymer-grafted lignocellulose/clay composites as adsorbents for the removal of heavy metals from aqueous solution. *Workshop on the NRF Flagship Programme: Nanotechnology for Water Treatment, at the University of Stellenbosch, Stellenbosch, South Africa, 29 – 30 April, 2011.*

- T. Bunhu and L. Tichagwa. Preparation of polymer-grafted lignocellulose/clay composites as adsorbents for the removal of heavy metals from aqueous solution. *2010 Annual SACI/ASPEN Pharmacare Regional Post-graduate Chemistry Seminar, on the 22nd of October, 2010.*

- T. Bunhu and L. Tichagwa. Development and evaluation of polymer-grafted lignocellulose/clay nanocomposites as adsorbents for the removal of heavy metals and chlorinated organics from water *Workshop on the NRF Flagship Programme: Nanotechnology for Water Treatment, at the University of Stellenbosch, South Africa on the 7th of December, 2009.*

- T. Bunhu and L. Tichagwa. Development and evaluation of polymer-grafted lignocellulose/clay nanocomposites as adsorbents for the removal of heavy metals and chlorinated organics from water. *University of Fort Hare, Chemistry Department, on the 6th of September, 2010 and 25th of May, 2009.*

- T. Bunhu and L. Tichagwa. Development and evaluation of polymer-grafted lignocellulose/clay nanocomposites as adsorbents for the removal of heavy metals and chlorinated organics from water. *Pan Africa Chemistry Network Conference in Nairobi, Kenya on the 27th of August, 2009. Also presented a poster at the same conference.*